

GL-TR-90-0301
ENVIRONMENTAL RESEARCH PAPERS, NO. 1070

AD-A229 228

Proceedings of the 11th Annual DARPA/AFGL Seismic
Research Symposium, 2-4 May 1989

DTIC FILE COPY

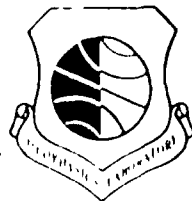
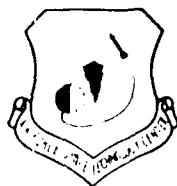
Editors:
JAMES F. LEWKOWICZ
JEANNE M. McPHETRES



6 November 1990



Approved for public release; distribution unlimited.

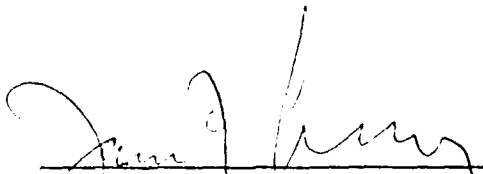


EARTH SCIENCES DIVISION PROJECT 7600
GEOPHYSICS LABORATORY
HANSCOM AFB, MA 01731-5000


90 11 13 202

"This technical report has been reviewed and is approved for publication."

FOR THE COMMANDER



JAMES F. LEWKOWICZ
(Branch Chief
Solid Earth Geophysics Branch
Earth Sciences Division



DONALD H. ECKHARDT
Director
Earth Sciences Division

This report has been reviewed by the ESD Public Affairs Office (PA) and is releasable to the National Technical Information Service (NTIS).

Qualified requestors may obtain additional copies from the Defense Technical Information Center. All others should apply to the National Technical Information Service.

If your address has changed, or if you wish to be removed from the mailing list, or if the addressee is no longer employed by your organization, please notify GL/IMA, Hanscom AFB, MA 01731-5000. This will assist us in maintaining a current mailing list.

Do not return copies of this report unless contractual obligations or notices on a specific document requires that it be returned.

6 November 1990

Scientific, Interim

Proceedings of the 11th Annual DARPA/AFGL Seismic
Research Symposium, 2-4 May 1989

PE 62101F

PR 7600

TA 09

WU 08

Editors: James F. Lewkowicz
Jeanne M. McPhetres

Air Force Geophysics Laboratory, AFSC
AFGL/LWH
Hanscom AFB, MA 01731-5000

GL-TR-90-0301
ERP, No. 1070

DARPA/NMRO
1400 Wilson Boulevard
Arlington, VA 22209-2308

This research was supported by DARPA under PE 61101E and 62714E.

Approved for Public Release; distribution unlimited

These proceedings contain papers presented at the Eleventh Annual Defense Advanced Research Projects Agency/Air Force Geophysics Laboratory (DARPA/AFGL) Seismic Research Symposium held 2-4 May 1989, in San Antonio, Texas. In its capacity as a Technical Agent, the AFGL's Solid Earth Geophysics Branch (LWH) manages the DARPA Nuclear Monitoring Research Office's (NMRO) basic research program in seismology. The scientific objective of this program is to improve the Air Force's capability to seismically detect, locate, identify and estimate the yield of underground nuclear explosions. The purpose of this symposium, which is organized annually by LWH, is to provide the NMRO staff an opportunity to review the research accomplished during the preceding year and outline areas of investigation for the coming year. For the researchers, it provides a forum for the exchange of scientific information, as well as occasions to meet personally with the NMRO and LWH staff to discuss individual projects, ideas and results. In addition, the technical presentations

underground nuclear explosion, seismic waves, regional
seismology arrays, yield estimation, source coupling

517

UNCLASSIFIED

UNCLASSIFIED

UNCLASSIFIED

UL

serve as a means to inform representatives from other Government agencies about advances in seismic monitoring research, technologies and techniques as part of the important process of technology transition. The papers include studies on regional seismic wave propagation, attenuation and scattering, array processing and seismic techniques of yield estimation.

Accession For	
FTIS - SPARI	<input checked="checked" type="checkbox"/>
DEIC CAS	<input type="checkbox"/>
Immunized	<input type="checkbox"/>
Justification	
By	
Signature/	
Date	
Time	
Place	
A-1	



PAPERS PRESENTED
AT THE
11TH ANNUAL DARPA/AFGL SEISMIC RESEARCH SYMPOSIUM

2-4 MAY 1989
HOLIDAY INN RIVERWALK
SAN ANTONIO, TEXAS

Handwritten: Table of Contents
TABLE OF CONTENTS

PAGE

Near-Source Observations of Quarry Explosions, by LANE R. JOHNSON and T. V. McEVILLY	1
Small Explosion Discrimination and Yield Estimation by ROBERT B. HERRMANN, KEVIN D. HUTCHENSON and M. JOST	11
Regional Discrimination of Quarry Blasts, Earthquakes and Underground Nuclear Explosions by T.J. BENNETT, B.W. BARKER, K.L. McLAUGHLIN and J.R. MURPHY	23
Rg as a Depth Discriminant for Earthquakes and Explosions: A Case Study in New England by ALAN L. KAFKA	32
The Time-Frequency Characteristics of Quarry Blasts, Earthquakes and Calibration Explosions Recorded in Scandinavia and Kazakhstan U.S.S.R. by MICHAEL HEDLIN, JOHN ORCUTT, BERNARD MINSTER and HAROLD GURROLA	40
A Comparative Study of High Frequency Seismic Noise at Selected Sites in the USSR and USA, by H. GURROLA, J.B. MINSTER, F.L. VERNON, J. BERGER, H.K. GIVEN and R. ASTER	49
Chemical Explosions and the Discrimination Problem by PAUL G. RICHARDS, ARTHUR LERNER-LAM, RUSSELL SUCH, DAVID W. SIMPSON and DOUGLAS A. ANDERSON	63
Analysis of High-Frequency Data by ANNE SUTEAU-HENSON, HANS ISRAELSSON, VLAD RYABOY and ALAN S. RYALL, JR.	67
Application of Simulated Annealing to Joint Hypocenter Determination, by CHIA-YU CHANG, WILLIAM H. MENKE and ARTHUR L. LERNER-LAM	89
A Study of Soviet PNE's and Spectral Differences Between Below and Above Water Table NTS SHOTS by I.N. GUPTA, C.S. LYNNEs and R.A. WAGNER	92
NTS Surface Wave Moments from a Regional Network by B.B. WOODS and D.G. HARKRIDER	102
Frequency Dependence of Q_L and Q in the Continental Crust, by B.J. MITCHELL and J.K. XIE	130
Determination of Q as a Function of Depth and Tectonic Province by XIAO-YANG DING and STEPHEN GRAND	135

	<u>PAGE</u>
High-Frequency Measurement of Coda Q in Central France by Y. CANSI, S. GAFFET and B. MASSINON	152
Near Source Ground Motions and Scaling from NTS Explosions by BRIAN W. STUMP	160
Spectral Analysis of Eastern Kazakh Events by PIERRE MECHLER and FLORENCE RIVIERE	176
Statistical Approaches to Testing for Compliance with a Threshold Test Ban Treaty by R.H. SHUMWAY and Z.A. DER	183
P_n from The Nevada Test Site by L.J. BURDICK, C.K. SAIKIA and N.F. SMITH	200
The Effects of Three-dimensional Structure on Crustally Guided waves by B.L.N. KENNETT and M.G. BOSTOCK	213
Optimal Digital Elevation Model Resolution for the Interpretation of Morphotectonics by E.J. FIELDING, T.L. GUBBELS and B.L. ISACKS	221
Broad-band Studies of Seismic Sources at Regional and Teleseismic Distances using Advanced Time Series Analysis Methods by ZOLTAN A. DER, DOUG R. BAUMGARDT and ROBERT H. SHUMWAY	231
Strain Amplitude Dependence of Seismic Attenuation and Nonlinearity by KARL B. COYNER	244
Observations of High-Frequency Waveform Coherence in the Northeastern United States by ARTHUR L. LERNER-LAM and WILLIAM H. MENKE	255
Near-Source Contributions to Teleseismic P Wave Coda and Regional Phases by THORNE LAY and CHRISTOPHER S. LYNNE	260
Effects of Depth of Burial and Tectonic Release on Regional and Teleseismic Explosion Waveforms by K.L. McLAUGHLIN, T.G. BARKER, J.L. STEVENS, B. SHKOLLER, and S.M. DAY	266
Comparative Seismic Observations on a Downhole Network verses a Vertical Array by P.E. MALIN	278
Finite-Difference Simulations of Seismic Wave Excitation at Soviet Test Sites with Deterministic Structures, by RONG-SONG JIH, WILMER RIVERS and CHRISTOPHER LYNNE	286
Variability of Ground Motion at Fennoscandian Arrays by M. NAFI TOKSÖZ, EDMOND E. CHARRETTE and ANTON M. DAINTY	290
Synthetic Seismograms and Radiation Patterns for an Explosion in Anisotropic Media by B. MANDAL and M.N. TOKSÖZ	301
Energy Flux Models for Seismic Wave Propagation in a Scattering Layer by CHARLES A. LANGSTON	313

	<u>PAGE</u>
Stochastic Geologic Effects on Near-Field Ground Motions, by R.E. REINKE, K.R. ANDERSON, R.V. GOERKE, J.A. LEVERETTE, M.A. BOGAARDS and B.W. STUMP	329
The Damage Mechanics of Porous Rock by CHARLES G. SAMMIS and MICHAEL F. ASHBY	339
Nonlinear Attenuation Mechanism in Salt at Moderate Strain, by GARY McCARTOR and WILLIAM WORTMAN	356
Nonlinear Finite Difference Simulations of Cavity Decoupled Explosions in Salt and Tuff by J.L. STEVENS, J.R. MURPHY and N. RIMER	364
Structure Effects on Regional Waveforms by TERRY C. WALLACE	372
High-Frequency Regional Discrimination Studies using NRDC and CDSN Seismic Networks by W. WINSTON CHAN, ROBERT K. CESSARO and RICHARD BAUMSTARK	381
A Study of Teleseismic P and P Coda from U.S. and Soviet Nuclear Explosions by I.N. GUPTA, C.S. LYNNEs, R.S. JIH and R.A. WAGNER	389
Siting Survey and Configuration Optimization of a New Regional Array in the Federal Republic of Germany by HANS-PETER HARJES	400
Systematic Analysis of Vertical- and Three-Component High Frequency Phase-Ratio Regional Discrimination by CHRISTOPHER LYNNEs, W. WINSTON CHAN and ROBERT K. CESSARO	420
Compressional- and Shear-Wave Polarizations at the Anza Seismic Array by R. ASTER, P. SHEARER, B. MINSTER and J. BERGER	426
A Generalized Beamforming Approach to Real Time Network Detection and Phase Association, by FRODE RINGDAL and TORMOD KVAERNA	440
Processing of Regional Events Recorded on the NORESS/ARCESS/FINESA Arrays by SVEIN MYKKELTVEIT, JAN FYEN, TORMOD KVAERNA and ROGER A. HANSEN	454
Multiple Crustal Phases from Regional Events Recorded at NORESS by KRISTIN S. VOGFJORD and CHARLES A. LANGSTON	466
Effects of Source Positions on the Diffracted Field at Short Distances by S. GAFFET and M. BOUCHON	474
Regional Seismic Event Location in Kazakhstan, U.S.S.R. by CLIFFORD H. THURBER	485
Nuclear Monitoring Research and Development System (NMRD) by THOMAS C. BACHE	492
A Geophysical Data Base for NTS: A New Interpretation for the Shallow Structure of Silent Canyon Caldera, Pahute, Mesa, Nevada by J.F. FERGUSON, A.H. COGBILL, R.G. WARREN and H.D. AXILROD	505

Near-Source Observations of Quarry Explosions

Lane R. Johnson and T. V. McEvilly

University of California, Berkeley

Contract Number F19628-87-K0032

Objective

The general objective of this research effort is directed toward the problems of detection and identification of underground explosions through the study of radiated seismic waves. Particular emphasis is on the collection and analysis of broadband seismic data at near and regional distances. Specific areas of research include the application of moment tensor inversion to near and regional data, the recording of any new seismic events of special interest at near distances, and the analysis of near and regional data for the purposes of separating effects of propagation, scattering, and intrinsic attenuation.

The present report describes some of the results which have emerged from a special experiment in which a series of chemical explosions detonated in a quarry were recorded with a near-source network of seismometers. The objective is to compare the results of these experiments with results from similar experiments involving nuclear explosions, and also to determine if certain fundamental aspects of elastic wave generation by explosions can be more easily investigated with small controlled chemical explosions than with larger nuclear explosions.

Summary

Seismic waveform data have been recorded from a series of chemical explosions in the Kaiser Permanente Quarry near Menlo Park, California. The explosions were arranged by Dr. Willie Lee of the U.S. Geological Survey. The University of California's part of the experiment was to record broadband waveform data at a network of stations surrounding the sources.

Ten different explosive events were recorded, including single explosions at various depths in drilled holes, regular quarry blasts consisting of simultaneous explosions in clusters of shallow drilled holes, and one event consisting of the combination of a quarry blast and a single explosion in a drilled hole with both fired at about the same time. The recording network contained 11 triggered digital event recorders, with the sensors being three-component force-balance accelerometers. The data were digitized at 200 samples per second with a resolution of 12 bits per sample and the complete system response was flat to acceleration between frequencies of 0.2 and 50 Hz. The stations of the network were distributed more or less uniformly over an area of slightly less

than 1 km, and for all but one of the events there was at least one station within 200 meters of the epicenter.

The recording experiments at the quarry were very similar to experiments performed in the past for nuclear explosions at the Nevada Test Site, with all distances and depths scaled down by a factor of about 10 for the quarry experiments. This series of controlled experiments has several potential advantages over similar experiments we have performed at the Nevada Test Site. The same network was used to record a series of different explosions, so the possibility exists that the separate effects of source, propagation, and recording site can be isolated. Three separate explosions were detonated at different depths in the same drilled hole, thus permitting a direct comparison of the effects of source depth.

The present report concentrates upon the particular question of how source depth may affect the waveforms. This can be studied by examining the records produced by 3 different explosions of about the same size at different depths in the same drilled hole. Figure 1 shows the relative locations of this drilled hole and the recording stations. Epicentral distances of the 11 recording sites ranged between 183 and 596 meters. The depths (and sizes) of the explosions were 217 meters (1000 pounds), 106 meters (900 pounds), and 42 meters (900 pounds). A comparison of the vertical accelerations from the deepest and shallowest explosions can be seen in Figures 2 and 3, respectively. Note that the maximum accelerations at the surface are about 5 times smaller for the shallow explosion than for the deep explosion. The accelerations from the explosion at intermediate depth (106 meters) are similar in amplitude and waveform to the deep event.

The travel times of the first-arriving P-waves were used to estimate an approximate 1D velocity model for the limestone rocks of the quarry in the vicinity of the experiment. Figure 4 shows the results of this process. The S velocity was obtained from the P velocity by assuming a constant Poisson's ratio. Note that the shallow explosion (denoted by the number 5 in Figure 4) is in the part of the section where there are steep near-surface velocity gradients, while the two deeper explosions are in a part of the section where the velocity gradients are more gentle. In this respect, the shallow event is similar to nuclear explosions at Pahute Mesa which are above the water table, while the two deeper events are similar to events which are below the water table.

Using the velocity models of Figure 4 to calculate Green functions, the accelerations of Figures 2 and 3 were inverted to obtain estimates of the source time functions of the second-order force-moment tensors of these events. Figures 5 and 6 show the elements of the moment-rate tensors for the deep and shallow explosions, respectively. Note that for both events the moment-rate tensors are dominated by the diagonal elements of the tensor, which is what one would expect for a simple explosion. The deep event is particularly simple, consisting primarily of a single concentrated pulse on the diagonal elements. This corresponds to a moment tensor consisting of a simple step having a rise time of about 0.03 second. The moment-rate tensor for the shallow event is more complicated, with the initial pulse less well defined and larger longer

period disturbances following it. Results of this type were also obtained for the intermediate depth explosion, and they were quite similar to those of the deep explosion.

Note that the maximum values of the moment-rate tensor for the deep explosion are about 5 times greater than those for the shallow explosion. Recalling that the size of the shallow explosion is only about 10% less than the deep one, this indicates that the two explosions differ significantly in the efficiency with which they convert chemical energy into elastic waves.

The effect of source depth can also be examined by comparing the moment rate tensors in the frequency domain. Figure 7 shows the modulus of the Fourier transform of the trace of the moment-rate tensors which were estimated for the three different source depths. These represent the isotropic parts of the moment tensors and are the only part which one would expect to be non-zero for a simple explosion. The point of interest here is that, while the three explosions have similar spectral levels for frequencies less than 10 Hz, they differ considerably at higher frequencies. In particular, the deep and intermediate explosions have relatively flat spectrums out to corner frequencies near 30 Hz, while the spectrum of the shallow explosion is markedly deficient in higher frequencies, with a corner frequency which is less well defined, but possibly as low as 10 Hz. These results are entirely consistent with the differences that were noted between Figures 2 and 3 with regard to maximum accelerations.

Conclusions and Recommendations

These controlled experiments with chemical explosions have indicated that source depth may significantly affect the efficiency with which explosions generate elastic waves. Furthermore, this effect seems to be strongly frequency dependent. The results generated so far must still be regarded as preliminary, as they will have to be compared with results from the other explosions in this series of experiments before a complete picture is likely to emerge. However, they have suggested several interesting questions which will have to be examined in future analysis. An obvious one is to determine if the depth effects for these small chemical explosions scale in a similar manner to the much larger nuclear explosions. Another critical question is whether the apparent source depth effect is due primarily to differences in overburden pressure or differences in material properties.

An impression acquired from the analysis completed so far is that, with respect to the recorded waveforms and the estimated moment tensors, these small chemical explosions seem to exhibit similar characteristics to large nuclear explosions. However, the experiments with the chemical explosions are much easier to perform. In particular, the potential for isolating and studying a particular phenomenon through a series of carefully controlled experiments is much higher for the chemical explosions. Thus, the study of small chemical explosions offers an attractive approach to investigating some of the remaining problems associated with the generation of elastic waves by nuclear explosions.

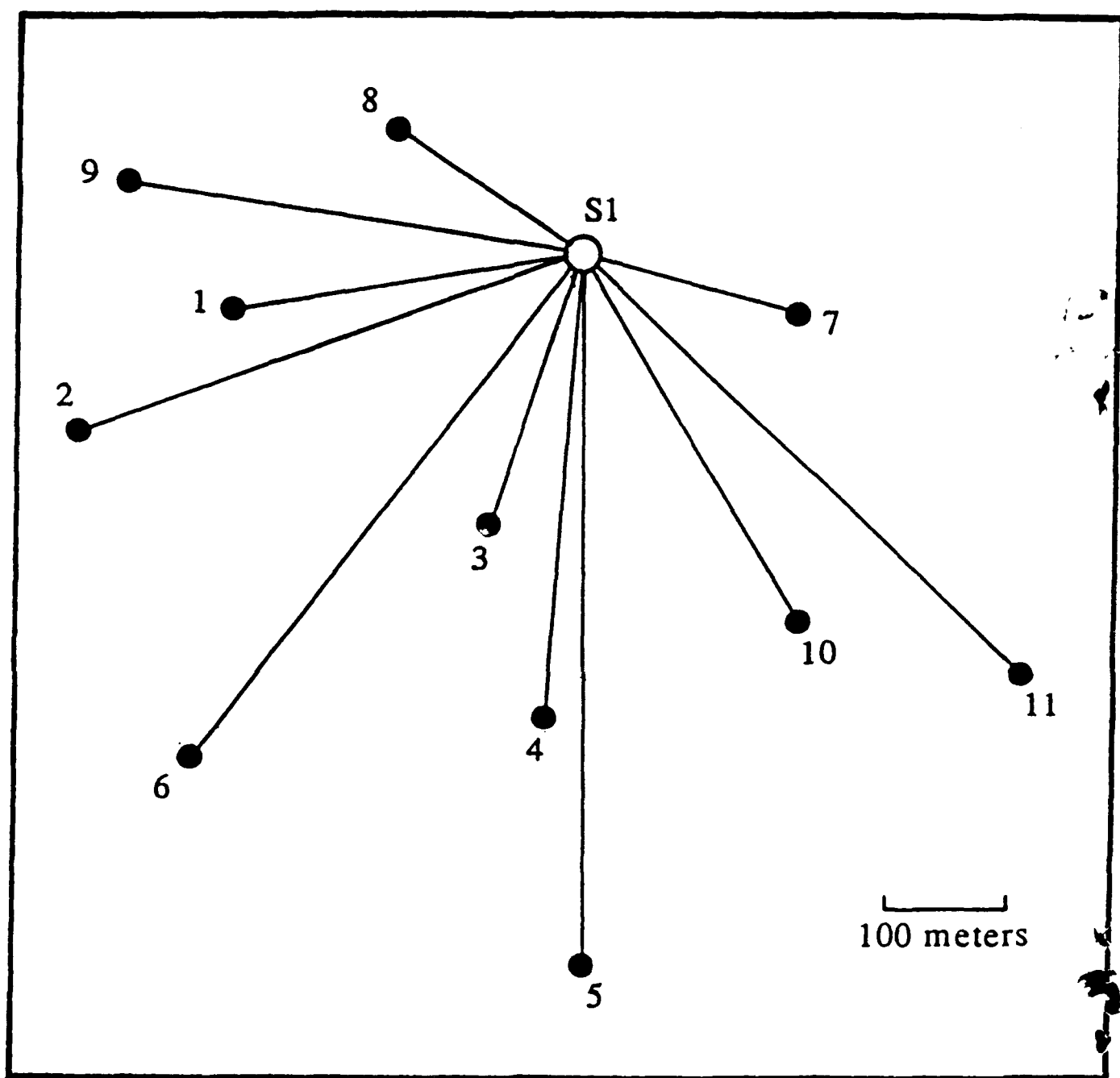


Figure 1. Map showing the location of recording stations (1 - 11) and the location of the deep drilled hole (S1) at the Kaiser Permanente Quarry.

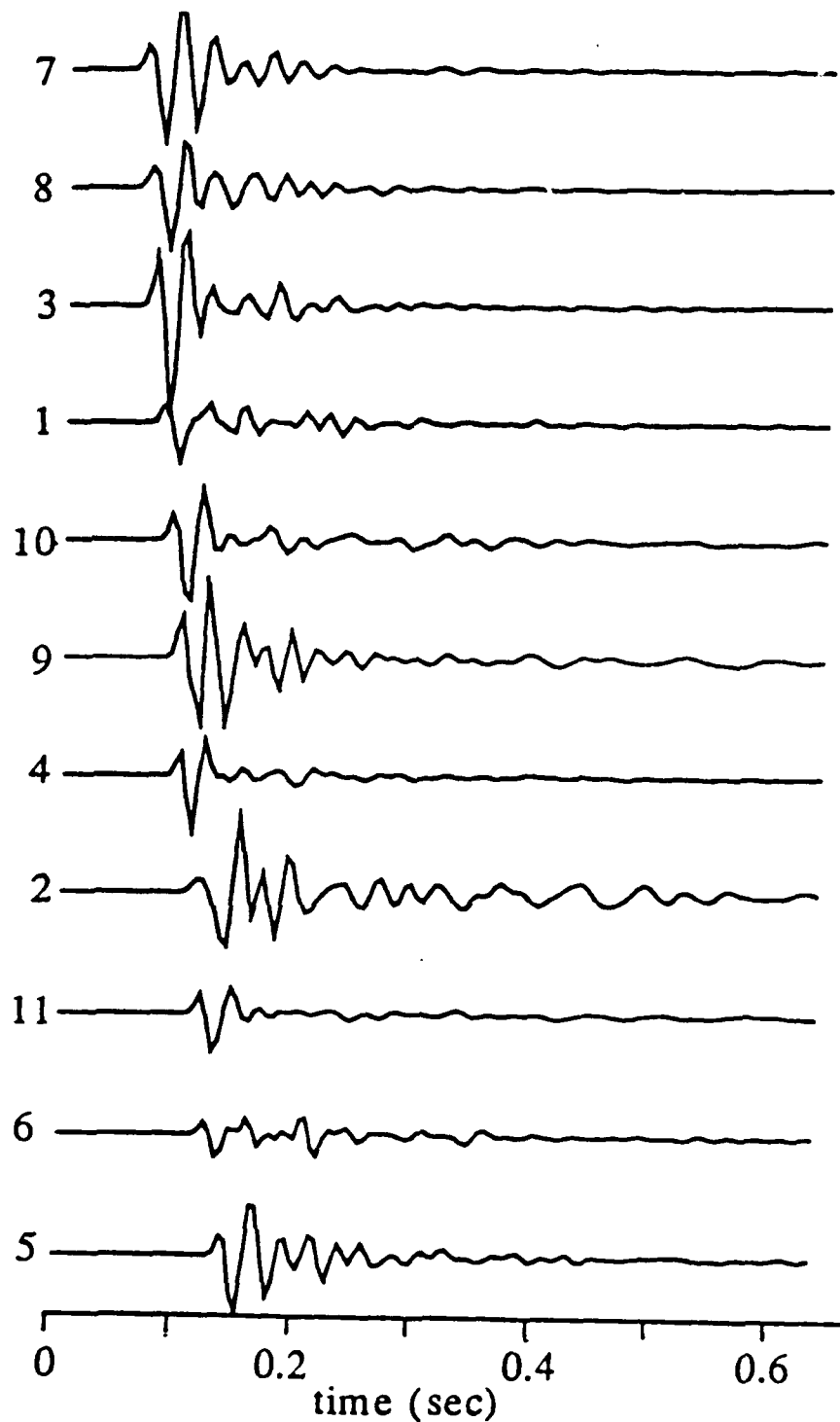


Figure 2. Vertical accelerations of ground motion for a 1000 pound explosion at a depth of 217 meters in the drilled hole S1 at the Kaiser Permanente Quarry. The number on the left indicates the recording station (see Figure 1). The accelerations in this plot have been scaled by multiplying by the epicentral distance, but the maximum accelerations from this event were 0.40 g.

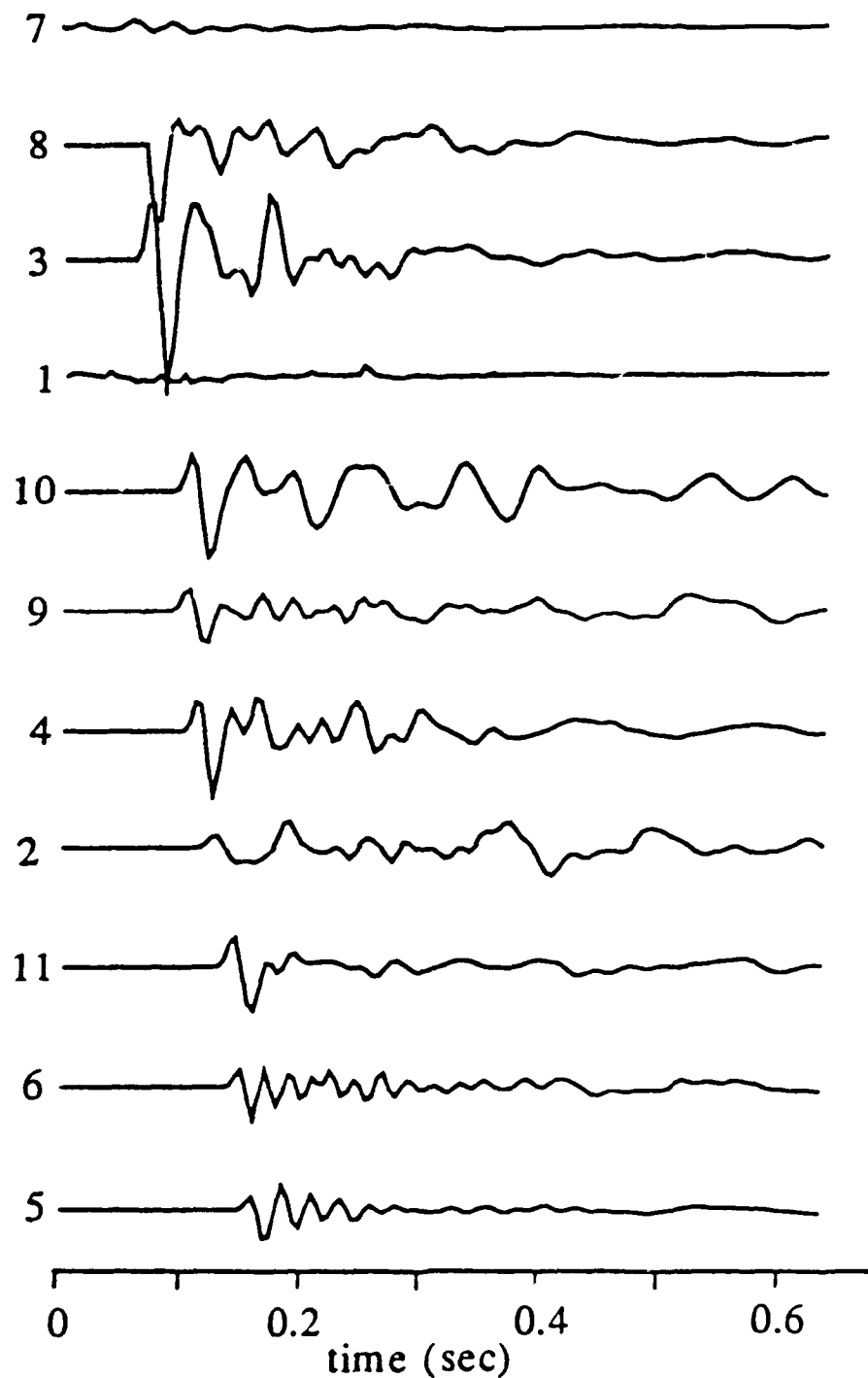


Figure 3. Similar to Figure 2 for a 900 pound explosion at a depth of 42 meters in the drilled hole S1. The amplitude scale has been increased by a factor of 5 relative to that used in Figure 2, so the maximum accelerations from this event were only 0.09 g.

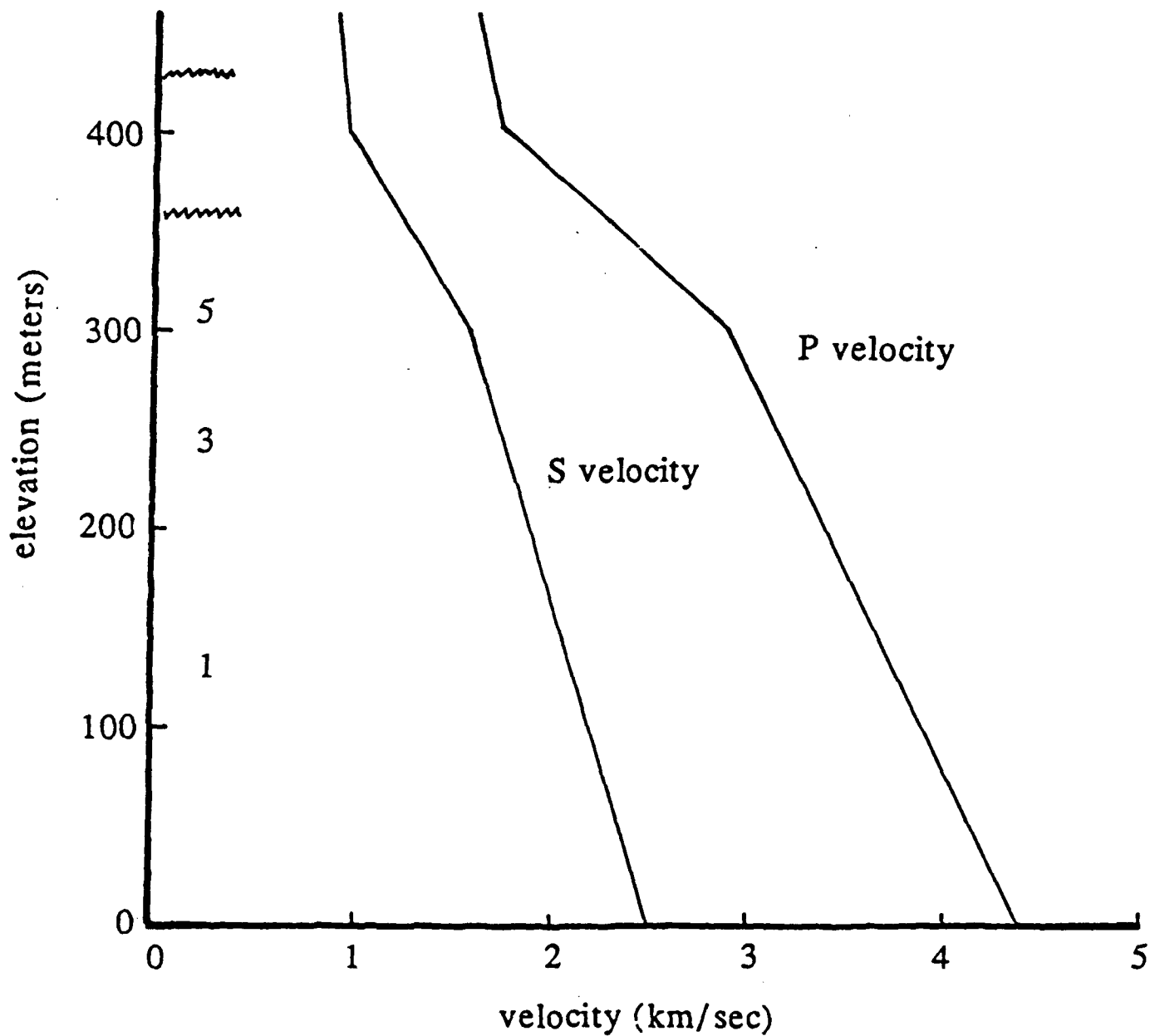


Figure 4. Estimates of the average P and S velocities as a function of elevation in the Kaiser Permanente Quarry. The boundaries at elevations of 360 and 430 meters indicate the approximate floor and rim, respectively, of the quarry. The numbers 1, 3, and 5 indicate the locations of the 3 explosions in the drilled hole S1.

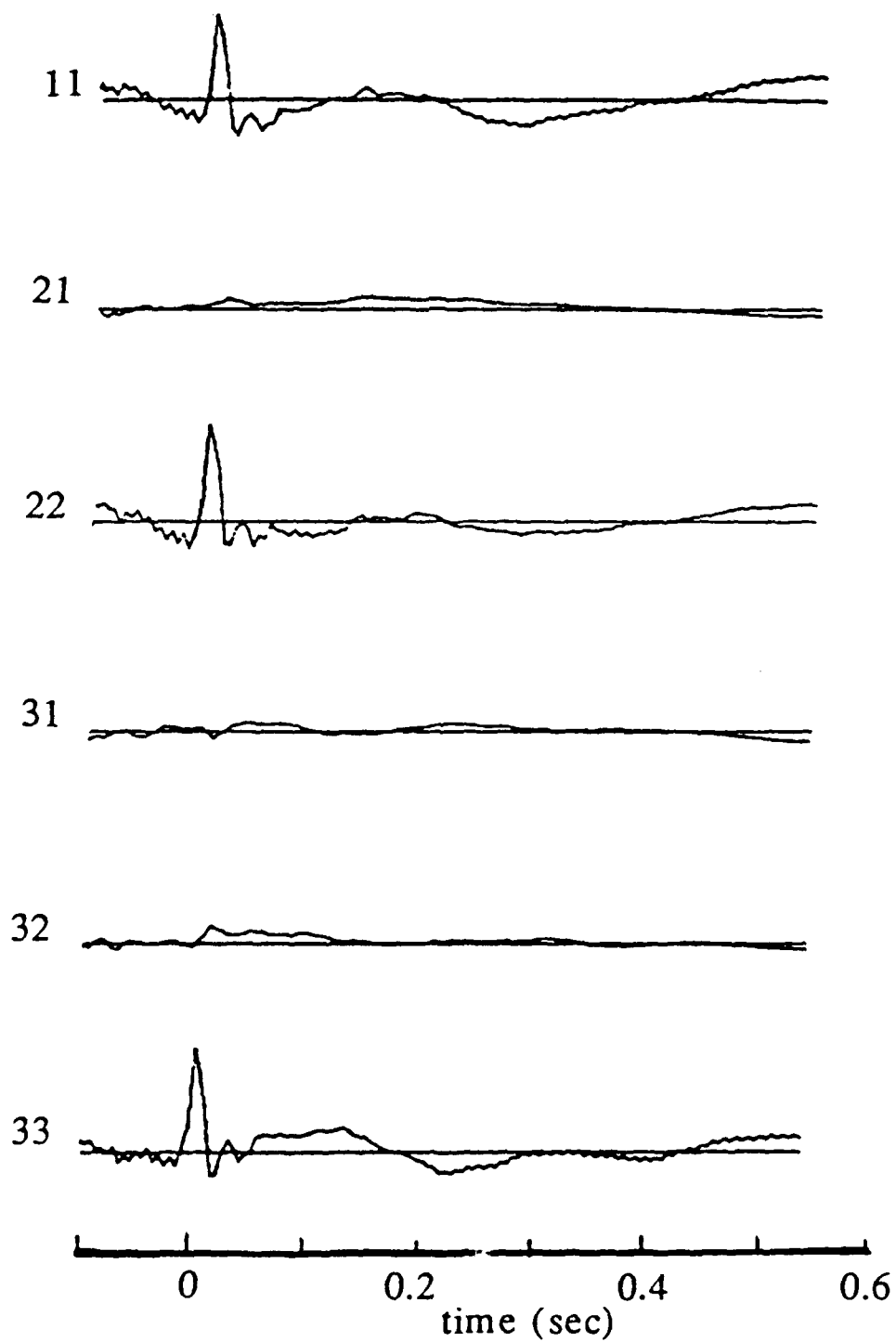


Figure 5. Second-order force-moment rate tensors which were estimated for the explosion at 217 meters. The maximum values are 1.7×10^{20} dyne-cm/sec.

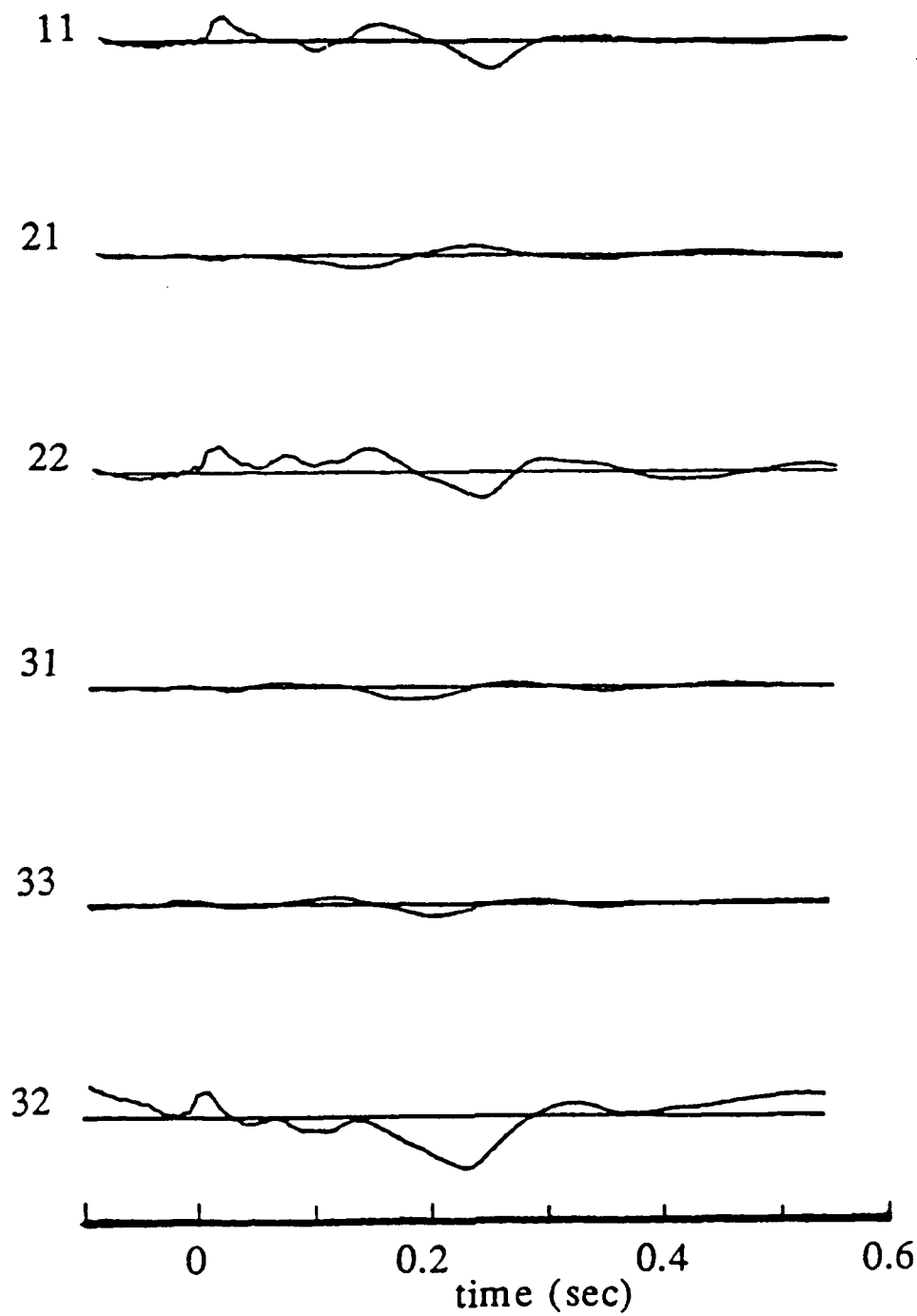


Figure 6. Similar to Figure 6 for the explosion at a depth of 42 meters. The maximum values in this case are 0.3×10^{20} dyne-cm/sec.

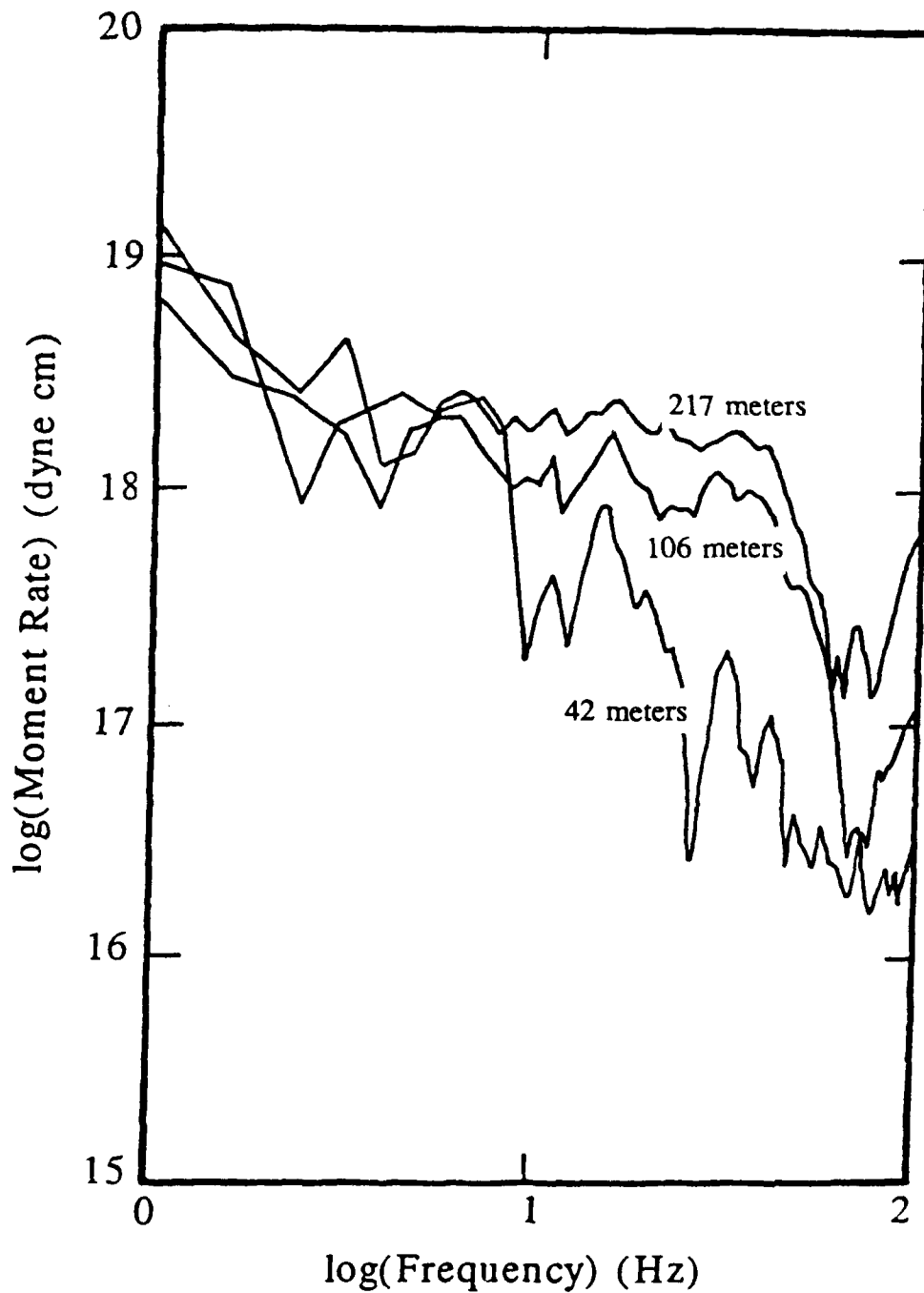


Figure 7. Moduli of the Fourier transform of the trace of the moment-rate tensor for the three different explosions in the drilled hole S1. The labels on the curves are the depths of the explosions.

PAPER TITLE: **SMALL EXPLOSION DISCRIMINATION
AND YIELD ESTIMATION**

PAPER AUTHORS: **R. Herrmann, K. Hutchenson, and M. Jost**
Department of Earth and Atmospheric Sciences
Saint Louis University
P.O. Box 8099
St. Louis, MO 63156

CONTRACT NO.: F19628-87-K-0049

OBJECTIVE: Improved Computational Techniques for Regional Studies

SUMMARY:

This paper reports on the characteristics of small explosions, as recorded by refraction surveys. This data set is used to provide the redundancy for testing computational algorithms, to define medium transmission parameters independent of source assumptions, and to estimate the source spectrum using the separately defined medium parameters.

By using the surface waves, we are able to define the medium to depths of about 1.5 km, to graphically demonstrate lateral variations in the waveguide, and to estimate the source spectrum in the frequency band of 0.4 - 5.0 Hz. The small chemical source *requires a significant*, compared to larger nuclear explosions, component of overshoot. Estimated values of the moment-rate tensor are comparable to those made by Stump (1987).

CONCLUSIONS AND RECOMMENDATIONS:

The estimation of source yield from small chemical explosions requires correct specification of the source function. Whereas yield estimates of nuclear explosions use the RDP spectrum at low frequencies, the level of the RDP-rate spectrum seems important for these small explosions. Since the source also excites Lg waves, it is expected that the Lg spectrum will not be flat in the 0.4-4.0 Hz range, but will rather increase with frequency in the same range.

Since a study of very small yield chemical explosions is outside normal experience, the extrapolation of these effects to larger sources is unknown. In addition, spall effects and directionality effects of distributed chemical explosions will complicate the wavefield, but may introduce other characteristics that can be used for discriminating between chemical and nuclear explosions and for yield estimation, from the surface- or body- wavefields.

SMALL EXPLOSION DISCRIMINATION AND YIELD ESTIMATION

INTRODUCTION

Considerable effort has been expended in this program to understand the seismic signal of the 150 kT source, with consideration of source medium bias as well as robust estimators of yield. One may claim that there is confidence in what is happening at the 150 kT level. On the other hand, the research community may be called upon to be as confident at much lower yields. The functional representation and regional dependence of the yield curve passing through the 150 kT point may now be the focus of future research.

Other, perhaps more difficult, problems also arise at lower yield levels. In addition to the usual problem of discriminating between explosions and earthquakes, the problems of distinguishing between chemical and nuclear explosion as well as of yield estimation become important. Unfortunately, while industrial chemical explosions are very common, very little is known about the seismic wavefield of these sources, both in their own right and in comparison to small nuclear explosions. The only recent studies are source studies by Stump and his associates (Stump, 1987, for example) and searches for ripple fire patterns by Baumgardt *et al.*, (1988).

This is not to say that chemical explosions are not being studied. Certainly mining blasts detected by the NRDC stations are being examined (Bennett and Murphy, 1988), and a JVE calibration shot would be useful to further distinguish between chemical and nuclear explosions. But in the context of treaty data exchange, small JVE nuclear explosions distributed throughout the U. S. are not feasible, and thus by reciprocity, neither is a direct comparison of chemical mining blasts and nuclear explosions for all areas within the Soviet Union.

In order to use the recorded signal of chemical explosions, we need to separate propagation effects, both elastic and anelastic, from source effects. In order to focus on the source component, a well tested method is required to constrain the propagation effects first. This paper reports on one such controlled experiment.

SOURCE THEORY

Mueller and Murphy (1971) proposed a model for characterizing the far-field P-wave displacement spectrum of a nuclear explosion:

$$U(\omega) = \left[\frac{P(\omega)r_e}{4\mu} \right] \frac{\alpha^2}{(\omega_0^2 - i\omega_0\omega - B\omega^2)} \left(\frac{i\omega}{r\alpha} \right) \quad (1)$$

where $P(\omega)$ is the Fourier transform of the pressure profile at the elastic radius, r_e :

$$p(t) = (p_0 e^{-at} + p_{0c})H(t) \quad (2)$$

and hence

$$P(\omega) = \left(\frac{p_0}{a + i\omega} + \frac{p_{0c}}{i\omega} \right) \quad (3)$$

where r is the distance from the source, μ is the rigidity, α is the P-wave velocity, $B = (\lambda + 2\mu)/4\mu = \alpha^2/4\beta^2$, and $\omega_0 = \alpha/r_c$. The specification of p_0 and p_{0c} is based on empirical studies.

Murphy (1977) shows that for models of Pahute Mesa detonations, the reduced displacement potentials are essentially steplike, with little overshoot. The far-field displacement spectra are essentially flat with a high frequency rolloff. His figures show that for Pahute Mesa, the p_0 term is not very significant. Studies of the Gasbuggy explosion reduced displacement potential records (Perret, 1972) also show the predominance of the p_{0c} term. The importance of this is that low frequencies are excited and their level is linearly proportional to yield.

Extrapolation of the Murphy (1977) figures to a 1 ton yield (0.001 kT) would yield a far-field displacement spectrum flat to about 10 Hz. However, Mokhtar *et al.* (1988) required a source spectrum that increased with frequency for this size source (e.g., the predominance of the p_0 term in (3)). Stump (1987) inverted waveforms due to a 253 lb TNT sphere (0.000125 kT) for the moment tensor and moment tensor rate. The moment tensor source time function consisted of a combination of a delta-like pulse followed by a spall contribution. This evidence, the lack of a strong p_{0c} term, indicates that source yield estimations will not be the same as for large nuclear explosions because the retarded potential is not the same shape.

DATA ANALYSIS

To understand the source time function of chemical explosions, the wave propagation effect must be independently estimated. Refraction data provide a useful set of redundant data to do this. In particular, surface-wave data can be used, since they sample the low frequency portion of the spectrum and contain the information required to define the medium and their own propagation. Data from a USGS Maine refraction profile are used because of the excellent surface waves reported by Reiter *et al.* (1988).

Figure 1 shows the surface-wave data from one profile (E and E1 of Reiter *et al.*, 1988) plotted at a reduction velocity of 2.5 km/s. These data are corrected for overall instrument gain levels and have had the 2 Hz seismometer response removed and replaced by a 0.5 Hz seismometer in an effort to enhance low frequency signals in the plots. We performed a group velocity stack (Barker, 1988) to obtain average group velocities and anelastic attenuation coefficients. A phase velocity stack (McMechan and Yedlin, 1981) was performed to obtain an initial phase velocity estimate which was refined by using a multichannel phase match filter (Russell, 1987). The phase velocity and attenuation data were then inverted, assuming a causal constant Q model (Table 1).

Table 1. Velocity Model

H(km)	VP	VS	RHO	QP	QS
0.2500	4.3960	2.6376	2.3754	58.0	29.0
0.2500	5.2022	3.1213	2.5404	62.0	31.0
0.2500	5.3255	3.1952	2.5651	64.0	32.0
0.2500	5.3345	3.2007	2.5669	66.0	33.0
0.2500	5.4317	3.2590	2.5863	66.0	33.0
0.2500	5.6212	3.3728	2.6249	68.0	34.0
0.2500	5.8344	3.5006	2.6669	74.0	37.0
0.2500	5.9848	3.5909	2.6970	82.0	41.0
0.5000	6.1266	3.6759	2.7380	94.0	47.0
0.5000	6.2729	3.7637	2.7819	114.0	57.0
0.5000	6.3489	3.8093	2.8047	148.0	74.0
	6.3674	3.8204	2.8102	212.0	106.0

To see how well such a model characterizes the data, synthetic seismograms can be constructed. Since the profile crosses several geologic units, lateral variation in the waveguide is expected and is visible somewhat in the moveout of the observed data. To focus on isolating any lateral variation, all data can be propagated to the same reference distance r_0 . If we represent the spectra of a single mode, attenuated surface wave at a distance r by the relation:

$$U(r, \omega) = A_0 r^{-1/2} e^{-\gamma r} e^{-ikr}, \quad (4)$$

then to make this trace seem as if it were recorded at r_0 instead, we only need to form a new spectra by the operation

$$U(r, \omega) (r/r_0)^{1/2} e^{-\gamma(r_0-r)} e^{-ik(r_0-r)}. \quad (5)$$

This is converted to a time history and plotted at the distance r to compare the traces. This may be viewed as being analogous to a reduced travel time plot for body-wave studies, and has been previously been used to map lateral variations in coal seams (Beresford-Smith and Mason, 1980).

Figure 2 shows the result of adjusting all the data in Figure 1 for dispersion to a reference distance of 25 km. No attempt was made to isolate the fundamental mode by using phase match filters. In doing this, original data at short distances are attenuated and dispersed, while data at large offsets are compressed and unattenuated, increasing the high frequency noise. If this figure is viewed edge on, breaks in the moveout are seen at about 7 km as well as at 30 km. This lateral variation was noted by Reiter *et al.* (1988), but was not graphically presented. It is interesting to note from Figure 1 that the direct shear wave arrival becomes significant in amplitude at 7 km where the dispersion becomes faster. In addition, the direct shear-wave arrival is delayed in time at distances greater than 25 km, indicating an indirect relation between the slower surface waves and the shear-wave delay. We also note that the peak amplitudes are roughly the same level, indicating the appropriateness of the Q model. Obvious outliers will be investigated later for errors in instrument gain in our processing.

We also processed the other half of the line from the same shot, but recorded in the other direction (D in Reiter *et al.* 1988). The dispersion is different in this direction, but we applied the same phase velocity and anelastic coefficient dispersion to this side. Figure 3 shows the result of projecting the wavefield to a reference distance of 10 km. Here it seems that the reference dispersion is too fast for the data at distances up to 17 km, and too slow at greater offsets.

We have found lateral variations in the surface-waveguide, and should be able to perform one more iteration to define different velocity models for each segment of the line.

Figure 4 shows the observed data, corrected for gain, and with the 2.0 Hz seismometer response removed and replaced with a 0.5 Hz seismometer for the purpose of enhancing the lowpass display. In addition the signal is lowpass filtered using a 3-pole Butterworth filter with a 5.0 Hz corner frequency. Figure 5 shows synthetic seismograms using the earth model of Table 1 for a point explosion source at a depth of 10m and with a Dirac delta function source function of strength 1.0×10^{20} dyne-cm/sec. By comparing peak amplitudes, it seems that an isotropic moment-rate of 1.5×10^{20} dyne-cm/sec will fit the overall levels for this 2000 lb shot. Using the velocity and density from Table 1, we can compute a $d\psi/dt(\infty)$, derived from the isotropic moment tensor rate, we obtain $d\psi/dt(\infty) = 1.1 \times 10^7 \text{ cm}^3 \text{ sec}^{-1}$. Using results from Stump (1987) (Tables 1 and 3), an isotropic moment tensor rate of 1.0×10^{18} dyne-cm/sec, a density of 1.9 gm/cc and a compressional velocity of 500 m/sec, we compute a $d\psi/dt(\infty) = 1.6 \times 10^7 \text{ cm}^3 \text{ sec}^{-1}$, for a 253 lb sphere of TNT. Given the work required to review the proper gains for the USGS instruments, the similarity of these results for similarly sized sources is remarkably consistent.

DISCUSSION

This work has demonstrated with surface waves for the first time the determination of sharp changes in the surface-waveguide. Further work will be done to search for more examples and to invert for the lateral velocity variation. Such data sets will provide constraints for computer programs for 2-D wave propagation, which are needed for understanding Lg-wave scattering.

We have the ability to define the source excitation in the limited range of 0.3 to 4.0 Hz by using these surface waves. This must also provide the excitation of the Lg wave at larger distances, and so we can learn better how to infer source properties from the Lg for these small events. The source time function for these small blasts must be different than what one would predict for small earthquakes, e.g., a derivative of the earthquake source time function, or a large overshoot ratio when talking about explosions. Of course there are tradeoffs with Q and always problems with synthetics, so further careful work is required.

Because of the difference in the source time function, some other relation between yield and the source function is required. The retarded potential rate may be a useful candidate.

We hope to continue this work in the future, by looking at all data within this data set and then proceeding to larger mining blasts in the Illinois coal fields, where we will deploy three component digital recorders in addition to the current regional seismic network to define not only the path, but also to document any non-isotropic source radiation, due to the asymmetry and placement of the mining blast.

Further study will provide the empirical evidence for estimating yields of chemical explosions and for classifying explosions as chemical on the basis of asymmetric shot geometry. In addition, examination of the various regional phases may provide additional high frequency discrimination results and a more basic understanding of the excitation of Lg and other regional phases.

Finally, we emphasize the need for controlled experiments to address the problem posed in the title, so that we can learn how to do this as well as to build confidence in our ability to do so.

REFERENCES

- Barker, T. G. (1988). Array processing of Rayleigh waves for shallow shear wave velocity structure (abs), *Seism. Res. Letters* 59, 12.
- Baumgardt, D.R., and K. A. Ziegler (1988). MERSY: An intelligent multiple seismic event recognition system for regional arrays (abs), *Seism. Res. Letters*. 59, 101.
- Bennett, T. J., B. W. Barker, and J. R. Murphy (1988). Regional phases from East Zazakh seismic events (abs). *Seism. Res. Letters*. 59, 101.
- Beresford-Smith, G., and I. M. Mason (1980). A parametric approach to the compression of seismic signals by frequency transformation, *Geophys. Prospecting* 28, 551-571.
- Mokhtar, T. A., R. B. Herrmann, and D. R. Russell (1988). Seismic velocity and Q model for the shallow structure of the Arabian shield from short period Rayleigh waves, *Geophysics* 53, 1379-1387.
- McMechan, G. A., and M. J. Yedlin (1981). Analysis of dispersive waves by wave field transformation, *Geophysics* 46, 869-874.
- Murphy, J. R. (1977). Seismic source functions and magnitude determinations for underground nuclear explosions, *Bull. Seism. Soc. Am.* 67, 135-158.
- Mueller, R. A., and J. R. Murphy (1971). Seismic characteristics of underground nuclear detonations: Part I. Seismic spectrum scaling, *Bull. Seism. Soc. Am.* 61 1675-1692.
- Perret, W. R. (1972). Gasbuggy seismic source experiments, *Geophysics* 37, 301-312.

- Reiter, E., M. N. Toksöz, and A. M. Dainty (1988). Influence of scattering on seismic waves: velocity and attenuation structure of the upper crust in southeast Maine, *AFGL-TR-88-0094*
- Russell, D. R. (1987). Multi-channel surface wave processing, *Ph. D. Dissertation*, Saint Louis University.
- Stump, B. W. (1987). Mathematical representation and physical interpretation of a contained chemical explosion in alluvium, *Bull. Seism. Soc. Am.* **77**, 1312-1325.

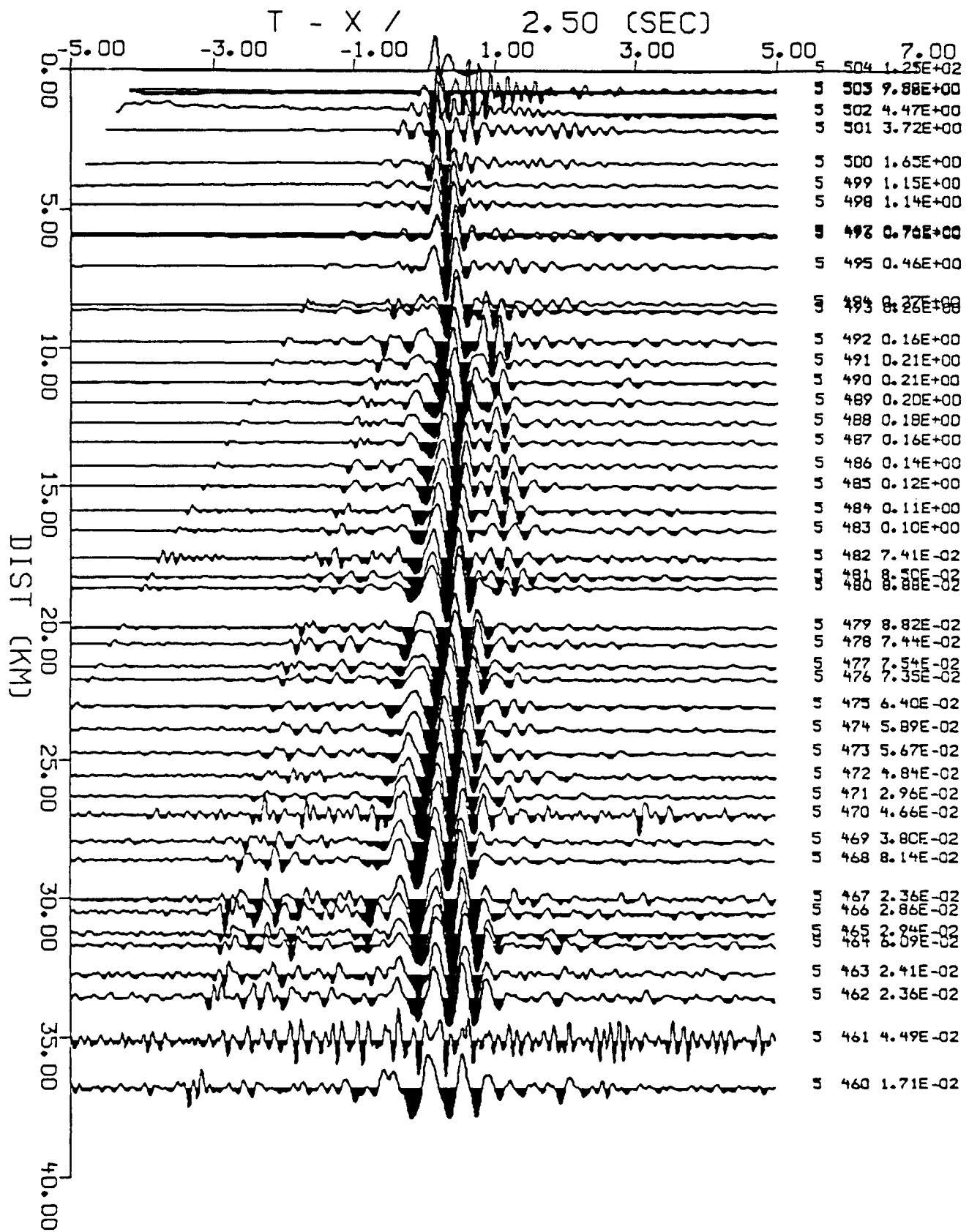


Figure 1. Reduced travel time plot of refraction data.

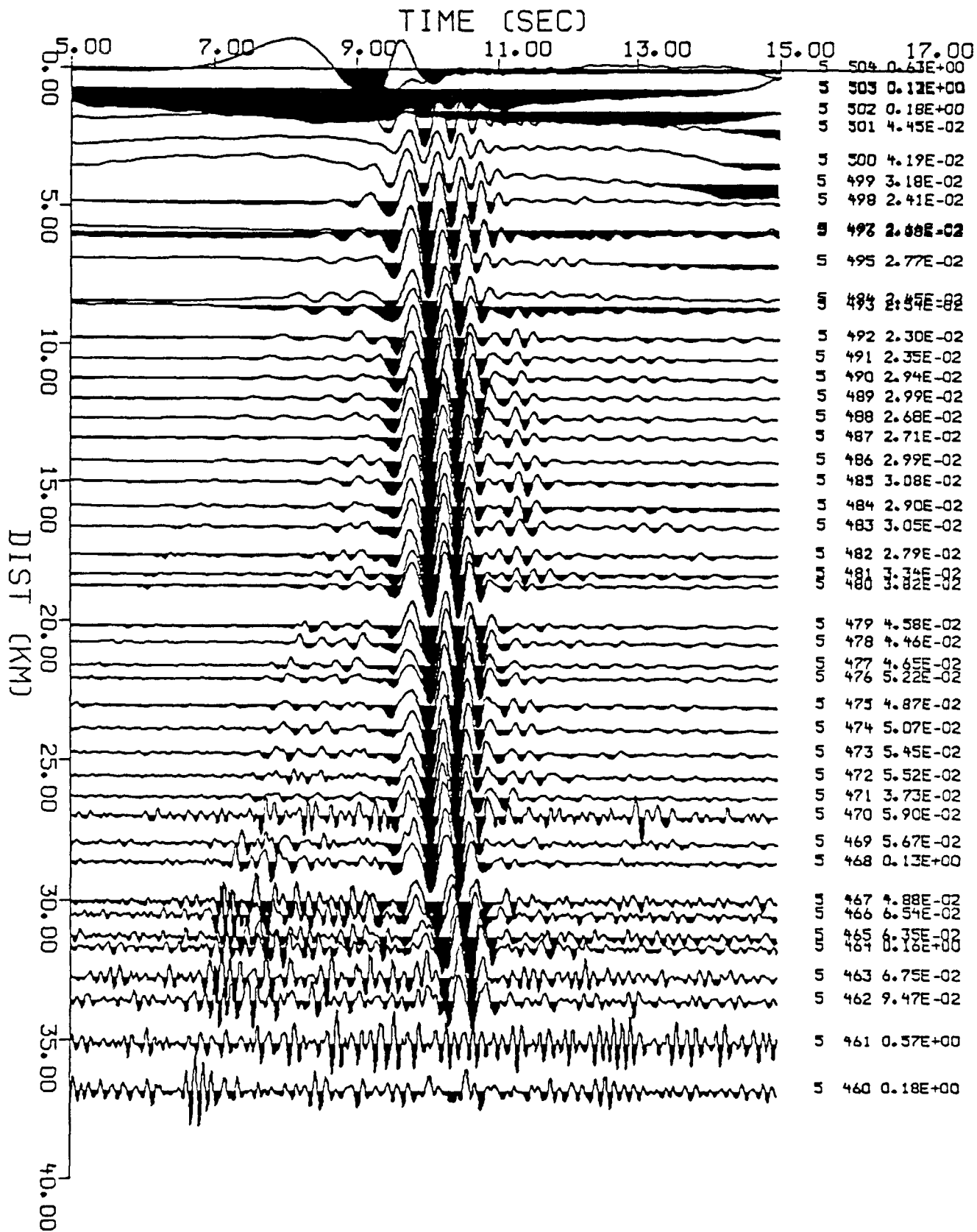


Figure 2. Data corrected for surface-wave dispersion to a reference distance of 25 km.

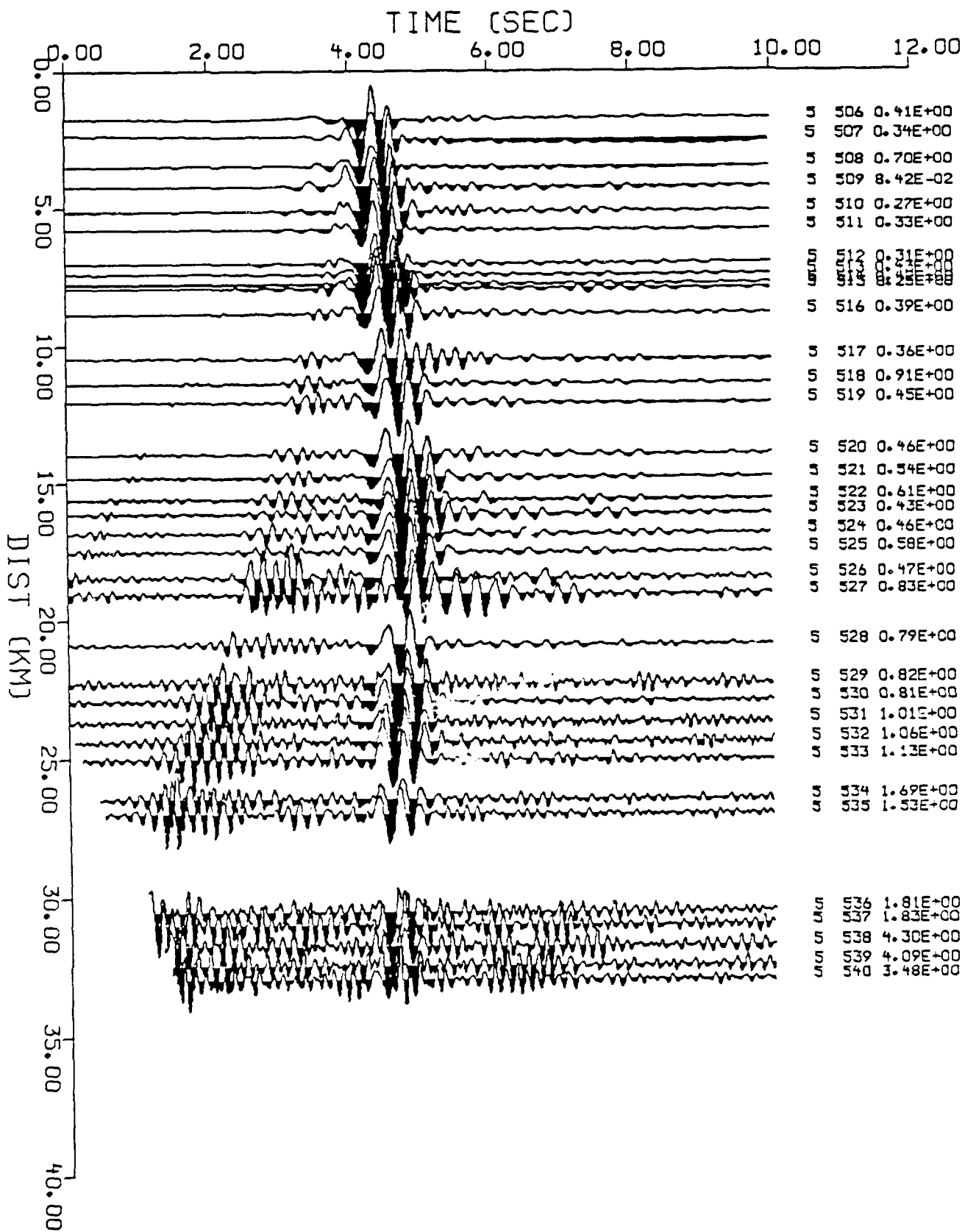


Figure 3. Data corrected for surface-wave dispersion to a reference distance of 10 km.

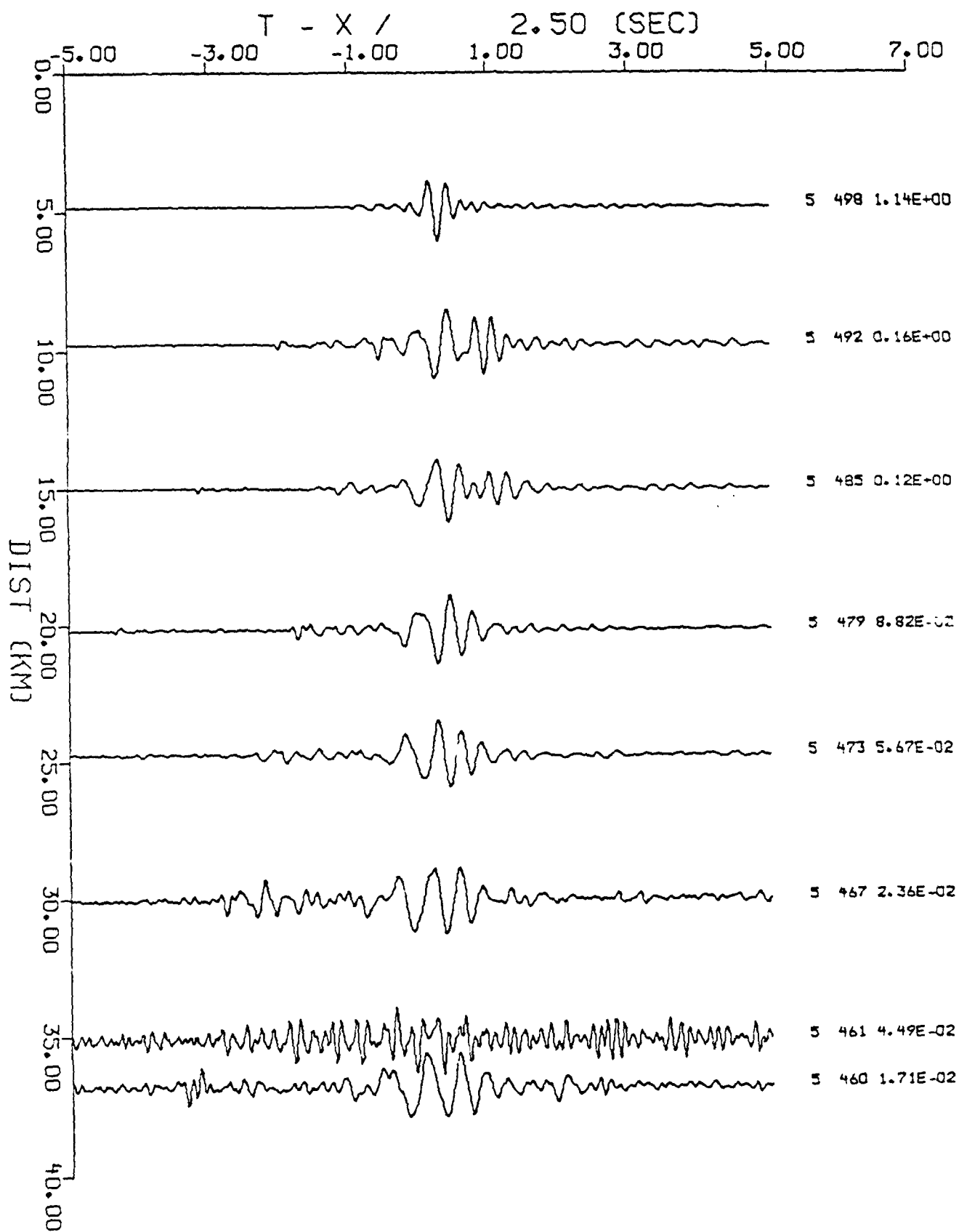


Figure 4. Observed data at selected distances.

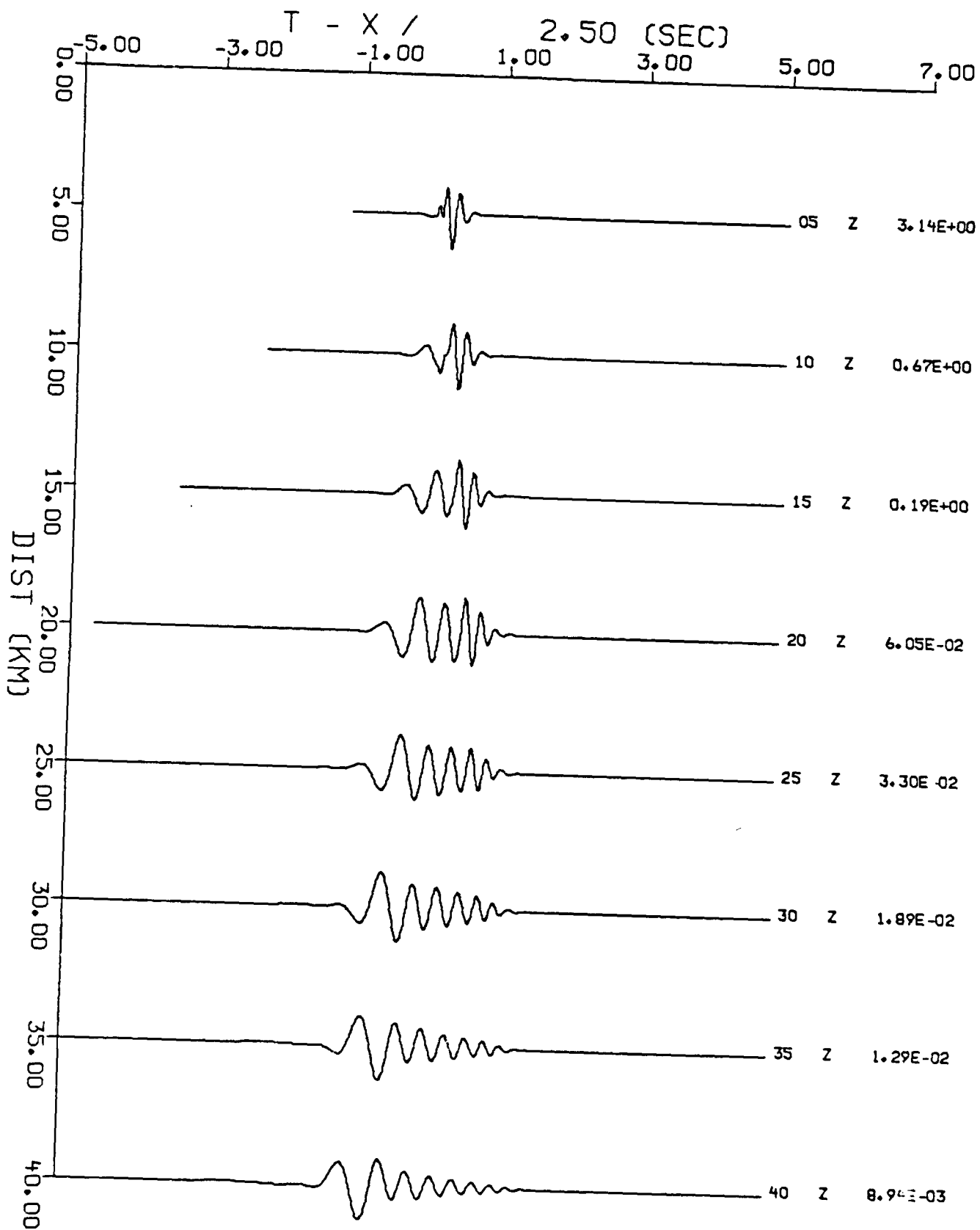


Figure 5. Synthetic predictions at selected distances.

Regional Discrimination of Quarry Blasts, Earthquakes and Underground Nuclear Explosions

T. J. Bennett, B. W. Barker, K. L. McLaughlin and J. R. Murphy
S-Cubed

Contract No. F19628-87-C-0093

OBJECTIVE

Our research efforts consisted of an empirical investigation of the characteristics of regional seismic signals from different source types as observed in a variety of tectonic environments. In this investigation we have focused on higher frequency phases observed at regional distances from underground nuclear explosions, earthquakes and mine or quarry blasts. We have systematically compared the time-domain amplitude and spectral characteristics of the observed regional seismic signals while seeking to identify diagnostic differences which would be indicative of the source. The tectonic environments included (1) eastern North America for which we used data from the Regional Seismic Test Network (RSTN) and the Eastern Canada Telemetered Network (ECTN), (2) the southern Soviet Union for which we used data from the Chinese Digital Seismic Network (CDSN) and the Soviet/Natural Resources Defense Council (NRDC) network surrounding the East Kazakh test site, and (3) the western United States for which we used data from the Lawrence Livermore National Laboratory (LLNL) network and some RSTN stations. The data in all cases were high-quality digital recordings, but the useful frequency range of the different systems varied between stations. Because of the potential interest in extending discrimination capability to lower thresholds, added focus in these investigations has been given to identification of commercial blasts which appear to be frequent contributors to the regional event samples in areas of interest for nuclear monitoring.

SUMMARY

Stable continental areas of central and eastern North America are thought to be analogous in many ways to platform regions of the Soviet Union with regard to regional seismic wave generation and transmission. A particular problem in such monitoring environments is known to be the identification of frequent, small commercial explosions. This discrimination problem could be greatly facilitated if simple procedures could be determined to distinguish these commercial blasts from small underground nuclear explosions. Therefore, part of our research effort was devoted to analysis of the regional signals from such blasts and nearby earthquakes recorded at stations of the RSTN and ECTN.

Our analysis of RSTN data focused on 23 presumed mine blasts, 14 earthquakes and a mine collapse recorded at station RSCP. The blasts with magnitudes from 2.2 to 3.5 $m_b(L_g)$ were at ranges from 210 to 369 km, and the earthquakes with magnitudes from 2.2 to 4.1 $m_b(L_g)$ were at ranges from 147 to 490 km (cf. Bennett *et al.*, 1988). The records showed good P and L_g phases for all events and strong R_g in many cases for the mine blasts and mine collapse. Although the L_g/P_{max} ratio, measured on the vertical component, was generally larger for the earthquakes than the blasts, the data showed considerable intermingling (cf. Figure 1). Failure of some blasts to produce strong R_g could be related to variations in shooting practice or lack of continuity in the waveguide. With regard to spectral characteristics of the regional signals, we saw evidence in both the L_g and P_g spectra of more rapid spectral decay, above the corner frequency, for the blasts in comparison to the earthquakes.

For the ECTN network we recovered the regional phase signals from 36 events with magnitudes between 1.0 and 5.1. These events included seven presumed quarry blasts and are generally recorded at multiple stations in the network. Selected events from this data sample have been processed to examine the use of cepstral analysis from multiple stations to distinguish the quarry blasts from the earthquakes. The results indicate evidence of deterministic multiplicity in the source functions for both the quarry blasts and the earthquakes corresponding to delay times which are generally greater than 0.2 sec.

Past studies of regional phases from Soviet nuclear explosions were frequently forced to rely on measurements at far-regional stations where the signals were extremely weak (cf. Bennett *et al.*, 1984; Nuttli, 1981, 1986). Recent installation of the CDSN and the temporary Soviet/NRDC network have enabled observation of regional phases at ranges from the East Kazakh test site more typical of regional monitoring. Figure 2 shows the locations of 12 East Kazakh underground nuclear explosions and 20 earthquakes for which we analyzed the regional signals recorded at the CDSN station at Urumchi (WMQ). The magnitudes of the events were between 4.7 and 6.1 m_b for the explosions and between 4.5 and 5.9 m_b for the earthquakes. Because of the lack of natural seismicity near East Kazakh, commonality of propagation path cannot be achieved in discrimination studies for this region. The records at WMQ show strong regional P and L_g signals from explosions and earthquakes for which we analyzed the amplitude and spectral characteristics. We found that the broadband L_g/P amplitude ratios tended to be larger for earthquakes than for explosions, but the differences were concentrated in certain frequency bands. As a result the separation between the earthquakes and explosions is much greater at higher frequencies (cf. Figure 3).

In addition to these large events, we analyzed regional phase signal behavior from a large sample of small events from the region surrounding the East Kazakh test site (cf. Figure 4) which were recorded by the Soviet/NRDC network stations. These events were located by the staff at CSS, and the majority are presumed to be mine

blasts. The events normally produce strong P_g and L_g phases and frequently strong R_g to ranges of 400 km or more. Although the amplitudes of the P_g and L_g signals were generally about equal on the broadband recordings, observed variations in relative amplitudes in some cases suggested blasting practice could be an important factor. This also holds true for R_g signals which were clearly weaker for some events. Finally, for some events we have found evidence of spectral scalloping (cf. Figure 5) which has been attributed to shot delays in commercial blasting. However, the observations suggest that this may be difficult to detect at large ranges and will require broad-band, high-frequency monitoring capability.

For the western U.S. we have analyzed regional signals from underground nuclear explosions and earthquakes at comparable ranges. These studies utilize a controlled source sample and thus permit a better understanding of source factors which affect regional phase generation. We have analyzed a sample of 10 NTS underground nuclear explosions from Yucca Flat and eight nearby earthquakes recorded by the four LLNL network stations at ranges between 160 and 485 km (cf. Bennett *et al.*, 1988). The magnitudes of the events were between 4.2 and 5.5 M_L for the explosions and between 3.5 and 4.2 M_L for the earthquakes. P_n , P_g and L_g phases appeared as clear regional signals in all cases except at ranges less than the P_n - P_g crossover distance. We performed spectral analyses on the P_g and L_g signals for these events and found that for both P_g and L_g the average spectral shapes for explosions and earthquakes were comparable up to about 2 Hz, but above 2 Hz the explosion spectra appeared to fall off more rapidly. This result was consistent with observations previously reported by Murphy and Bennett (1982) and Bennett and Murphy (1986) that the L_g signals from earthquakes near NTS appeared to be relatively richer in high frequencies. These latest observations using the LLNL data suggest that the differences which were used to develop the L_g spectral ratio discriminant may be enhanced at higher frequencies.

We have also analyzed regional phases from NTS explosions and comparable earthquakes recorded at larger regional distances at station RSSD. This database included seven NTS explosions with magnitudes from 4.8 to 5.9 m_b and three California earthquakes with magnitudes from 5.6 to 6.1. The earthquake ranges averaged about 1500 km compared to 1300 km for the explosions, and the azimuths from RSSD were about the same. At this distance range the regional signals are dominated by early P phases, including P_n and P^* , and L_g ; P_g is frequently buried in the coda of the other P phases. Spectra of comparable phases for the different source types are not greatly different, but the L_g spectra for the explosions may be somewhat more sharply peaked than for the earthquakes. This generally agrees with our previous findings at closer ranges.

CONCLUSIONS

New observations of East Kazakh nuclear explosions and comparable earthquakes recorded at CDSN station WMQ indicate that L_g/P_{\max} amplitude ratios for earthquakes and explosions are well-separated at high frequencies. Western U.S. nuclear explosions and nearby earthquakes continue to show spectral differences in P_g and L_g signals at smaller regional distances which extend to relatively high frequencies. Commercial blasts in eastern North America and East Kazakh frequently generate strong R_g phases, but these may not always be diagnostic. Spectral scalloping associated with shot delays appears to occur in regional signals for some small apparent mine blasts in East Kazakh but may not always be easy to detect.

REFERENCES

- Bennett, T. J. and Murphy, J. R. (1986). Analysis of seismic discrimination capabilities using regional data from western United States events, Bull. Seism. Soc. Am., 76, 1069-1086.
- Bennett, T. J., Lambert, D. G., Murphy, J. R. and Savino, J. M. (1984). Advanced seismological research: regional discrimination (U), S-Cubed Report, SSS-CR-84-6639.
- Bennett, T. J., Murphy, J. R. and Barker, B. W. (1988). Observation and synthesis of regional phase signals from quarry blasts, earthquakes and underground nuclear explosions, in Papers Presented at 10th Annual DARPA/AFGL Seismic Research Symposium, Pala Mesa Resort, Fallbrook, California.
- Murphy, J. R. and Bennett, T. J. (1982). A discrimination analysis of short-period regional seismic data recorded at Tonto Forest Observatory, Bull. Seism. Soc. Am., 72, 1351- 1366.
- Nuttli, O. W. (1981). On the attenuation of L_g waves in western and central Asia and their use as a discriminant between earthquakes and explosions, Bull. Seism. Soc. Am., 71, 249-262.
- Nuttli, O. W. (1986). L_g magnitudes of selected East Kazakhstan underground explosions, Bull. Seism. Soc. Am., 76, 1241-1251.

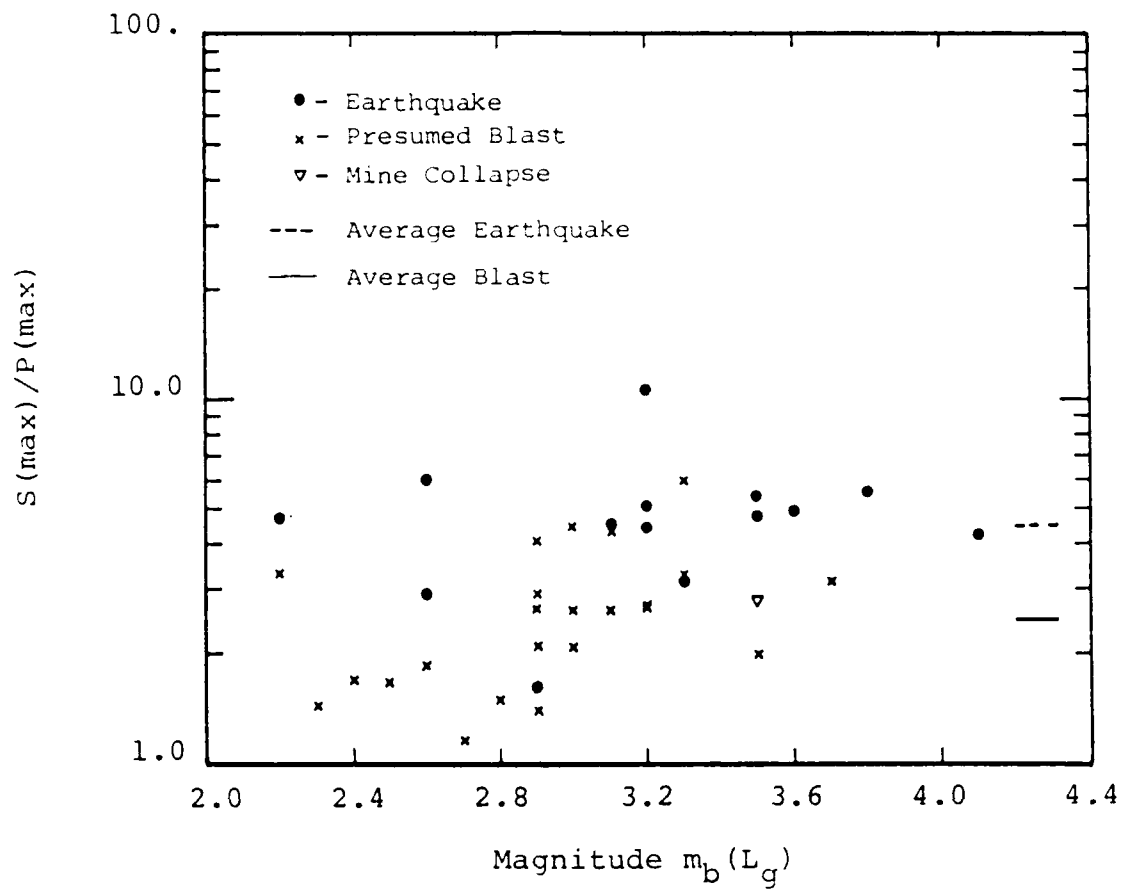


Figure 1. Comparison of L_g/P amplitude ratios for small earthquakes and presumed mine blasts recorded at RSCP.

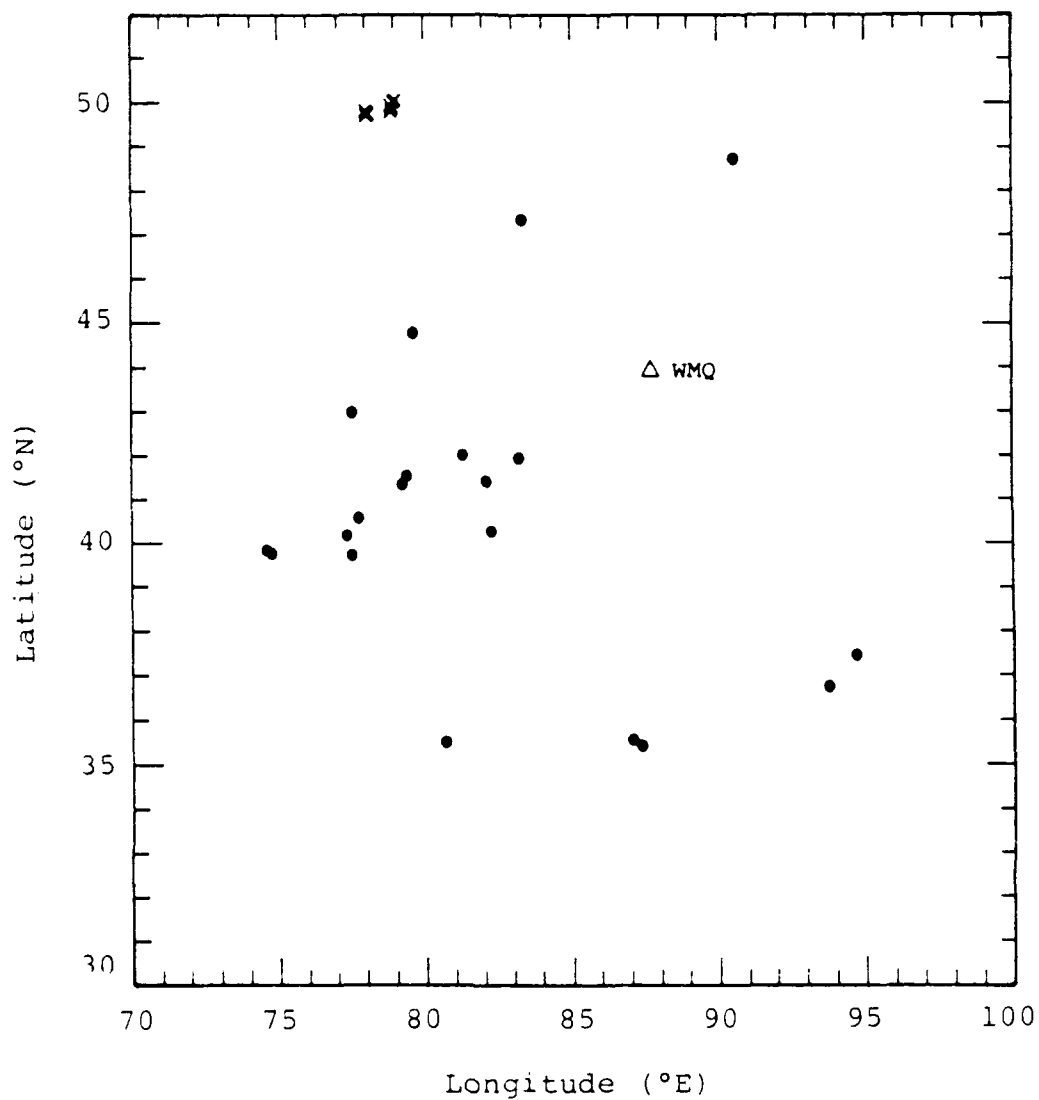


Figure 2. Locations of East Kazakh explosions (x) and earthquakes (•) analyzed using data recorded at WMQ.

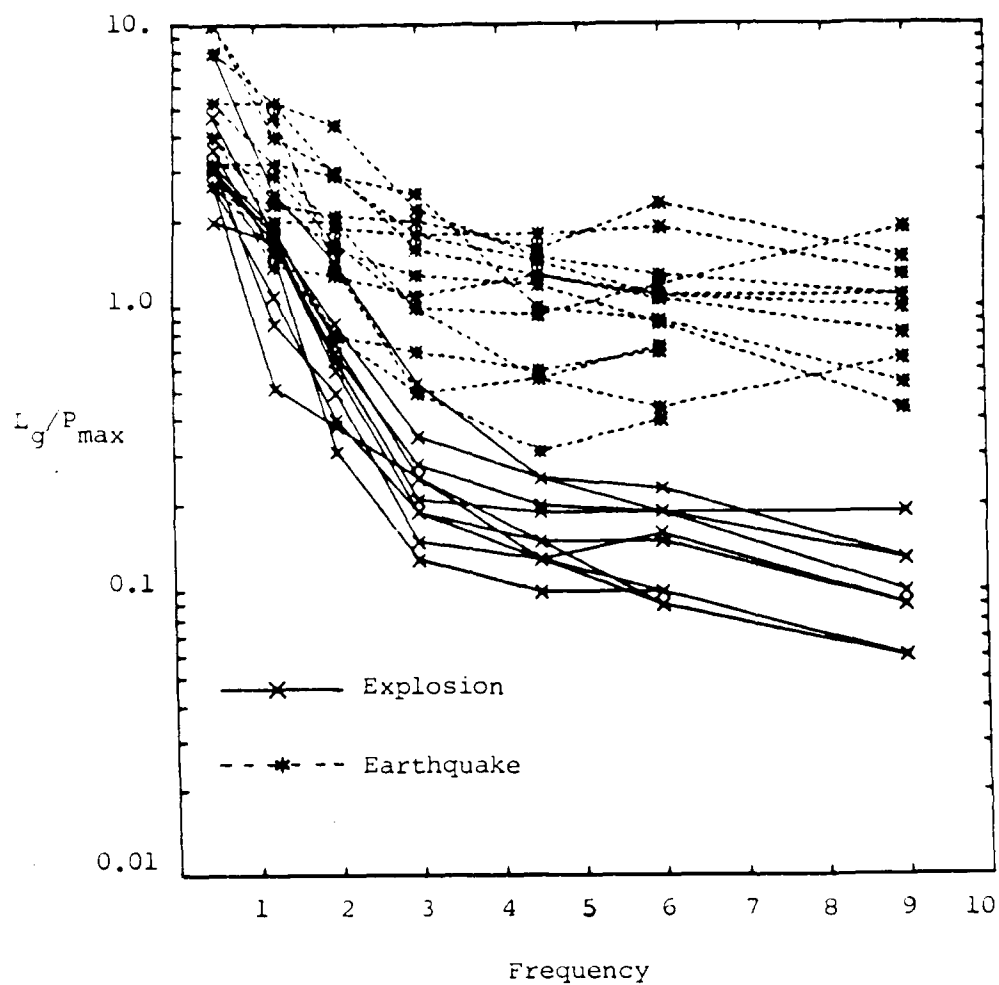


Figure 3. L_g/P_{max} ratios measured at station WMQ for East Kazakh nuclear tests and earthquakes as a function of filter center frequency.

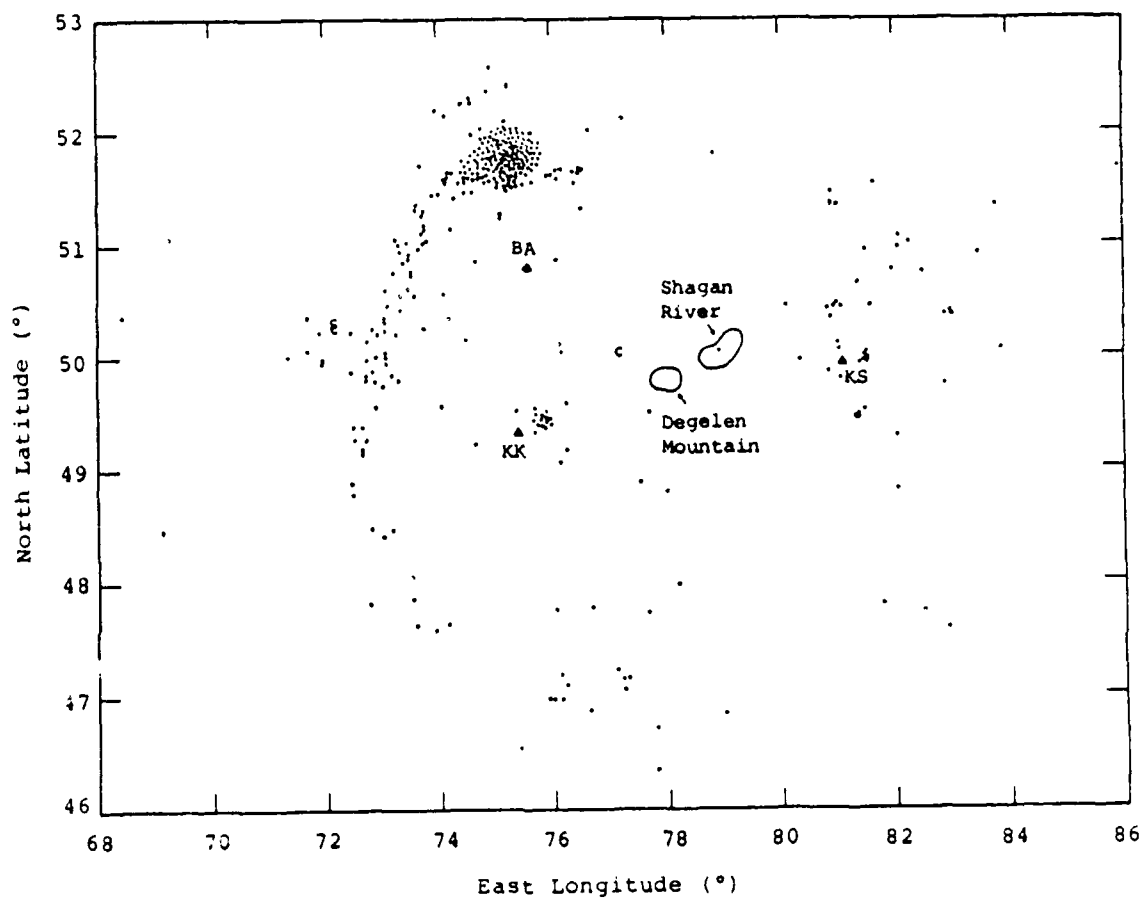


Figure 4. Events near East Kazakh located by CSS analysts using Soviet/NRDC network data.

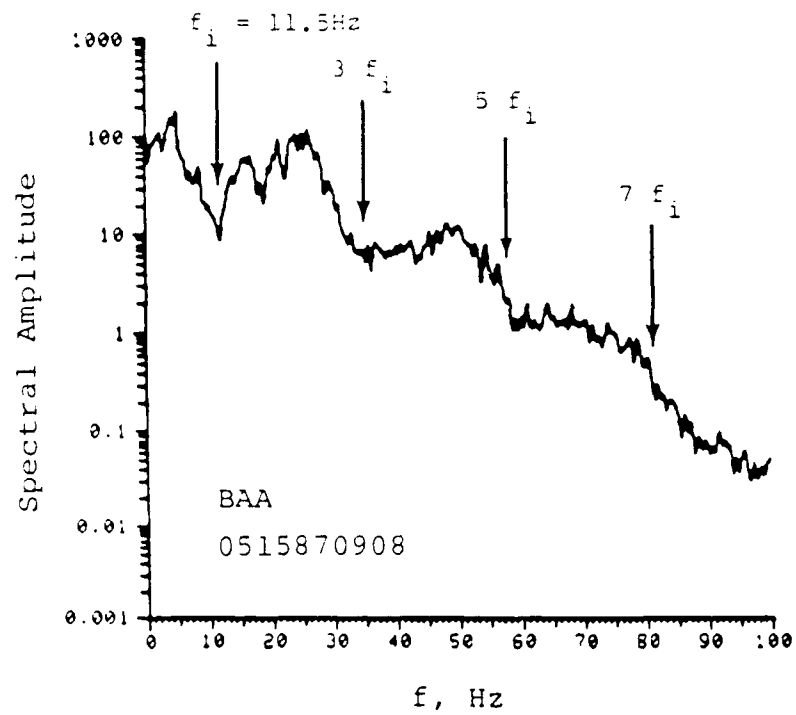


Figure 5. Evidence of spectral scalloping in Lg signal from presumed mine blast near East Kazakh.

Rg AS A DEPTH DISCRIMINANT FOR EARTHQUAKES AND EXPLOSIONS: A CASE STUDY IN NEW ENGLAND

Alan L. Kafka
Weston Observatory
Department of Geology and Geophysics
Boston College

Contract #F19628-87-K-0004

OBJECTIVE

Fundamental mode Rayleigh waves with periods ranging from about 0.4 to 2.5 sec (Rg) are often observed on seismograms of explosions and very shallow-focus earthquakes in New England as well as in other parts of the world. Since Rg is a fundamental mode surface wave, it is not surprising that near-surface sources generate Rg signals. Based on the principles of surface wave and body wave excitation, Bath (1975) proposed that Rg could be used as a depth discriminant for events recorded at local and regional distances. The principles underlying the use of Rg as a depth discriminant are that Rg amplitudes are very dependent on source depth, while amplitudes of other phases such as Pg and Sg are, on average, less dependent on depth. Although these principles are straight forward, applying them to actual data can be problematic because of the complexity of short-period local and regional seismograms. In this study, I am investigating seismograms of earthquakes and explosions recorded in New England to evaluate the extent to which Rg can be used as a depth discriminant. Specifically, observed amplitudes of Rg waves recorded by the New England Seismic Network (NESN) are compared with amplitudes of other recorded phases to test how effectively such comparisons work as a depth discriminant.

The strongest Rg signals recorded by the NESN are in the period range of about 0.5 to 1.5 sec. In that period range, Rg displacement is essentially confined to depths of less than 5 km, with most of the Rayleigh wave energy in the upper 2 or 3 km. Thus, sources deeper than about 4 km would not be expected to generate strong Rg signals; and, if Rg can be clearly identified on a seismogram, the source is most likely very shallow. The task of developing a method for using Rg as a depth discriminant is therefore (to a large extent) a matter of developing a method for identifying the Rg phase and distinguishing it from other phases.

SUMMARY

Most of the sources analyzed in this study were quarry blasts and small earthquakes recorded in New England. A few additional sources were refraction blasts detonated in Maine by the U.S. Geological Survey. Although regional phases recorded by the NESN are generally quite complicated, the Rg phase is often a relatively simple, dispersed wave train. This dispersion appears to be caused by relatively low seismic velocities in the upper few kilometers of the crust (e.g. Kafka and Dollin, 1985; Kafka and Reiter, 1987).

Figure 1 shows examples of seismograms from three quarry blasts and one earthquake recorded in southern New England. The Rg phase is prominent on the seismograms of the quarry blasts, but it is absent on the seismogram of the earthquake. The earthquake had a fairly well-constrained depth of about 5 km, and the lack of an Rg wave is consistent with that depth.

NESN seismograms with prominent Rg waves often have spectral peaks located between about 1 and 3 Hz. These spectral peaks appear to be characteristic of Rg waves. If such a low-frequency spectral peak is indeed characteristic of Rg, then one

way to identify Rg would be to calculate an amplitude ratio that compares the amplitudes in that low-frequency band with amplitudes in other frequency bands. For example, Kafka (1987) used amplitudes in the 1 to 3 Hz band to characterize Rg wave energy, and amplitudes in the 5 to 12 Hz band to characterize S and Lg wave energy. Such an amplitude ratio discriminant is straight forward to apply, but it ignores some of the expected characteristics of the seismograms. In particular, differences in arrival times of various regional phases and the dispersion of Rg waves should be considered as part of the identifying characteristics of regional phases. In this paper, I suggest a method of identifying the Rg phase that takes into account the arrival times of Rg and other regional phases. The method involves comparing amplitudes in the part of the seismogram where the Rg wave energy is expected to arrive with amplitudes in the part of the seismogram where P, S and Lg waves are expected to arrive. The amplitudes in the various arrival time windows are measured for specific periods using a narrow bandpass filter (NBF) analysis (Dziewonski et al., 1969).

To test the idea of using Rg as a depth discriminant on actual data, it is important to identify events with well-constrained depths recorded at a range of distances and azimuths. Identifying such events was one of the difficult parts of this study. The relatively sparse distribution of stations and the low level of earthquake activity make it difficult to find earthquakes in the study area that are recorded by several nearby stations. Two earthquake sequences for which good depth estimates were available from aftershock surveys are the 1987 Moodus CT, earthquakes and the 1985 Ardsley, NY earthquakes. For the purpose of this study, the depth of the Moodus earthquakes is assumed to be 1.6 km (see Mrotek et al., 1988), and the depth of the Ardsley earthquakes is assumed to be 5.2 km (see Locke, 1985). Other events in this study are quarry and refraction blasts (which occur at the surface) and several earthquakes whose depths are poorly constrained.

Figure 2 shows an NBF analysis of a seismogram with a small, but observable, Rg wave as well as prominent arrivals in the S and Lg arrival time windows. Since S and Lg waves are difficult to separate at these distances and frequencies, the notation "Lg" will (in the remainder of this paper) refer to the entire wave train from the onset of the S wave to the end of the S and Lg coda.

The shaded areas in Figure 2(a) are parts of the velocity - period plane where the spectral amplitude is the highest. Because the seismogram shown in Figure 2 has high amplitudes in both the Lg arrival time - frequency window and the Rg arrival time - frequency window, there are two shaded areas. This example suggests that the ratios of Rg amplitudes to Lg or P wave amplitudes can be estimated by narrow bandpass filtering each seismogram and then taking the ratios of amplitudes within the appropriate velocity - period windows. To do this, it is necessary to estimate the group velocity dispersion of Rg waves in the area being investigated. One reason for choosing New England for this study is that dispersion of Rg waves is fairly well-known in that region (e.g. Kafka and Dollin, 1985; Kafka and Reiter, 1987; Kafka, 1988).

To estimate the ratio of Rg amplitudes to amplitudes of Lg and P waves using an NBF analysis, the amplitudes are entered into a matrix, with a given cell representing an amplitude at a particular point on the velocity - period plane. Amplitudes in the cells corresponding to P waves are averaged to give an estimate of the average P wave amplitude. Similarly, the amplitudes in the cells corresponding to Lg and Rg are averaged to give an estimate of the average Lg and Rg amplitudes. In addition, the cells corresponding to a given wave type are searched to find the maximum amplitude for each wave type. The following four ratios are then calculated:

- (1) $Rg/Lg (AV) = Rg(average)/Lg(average)$
- (2) $Rg/P (AV) = Rg(average)/P(average)$
- (3) $Rg/Lg (MAX) = Rg(maximum)/Lg(maximum)$
- (4) $Rg/P (MAX) = Rg(maximum)/P(maximum)$.

Figure 3 shows histograms of the first two ratios calculated for blasts (zero depth) and for the Ardsley, NY earthquakes (5.2 km depth). Except for Rg/Lg (AV), all of the ratios listed above yield a distribution for the Ardsley earthquakes that overlaps with the distribution for the blasts. Thus, the Rg/Lg (AV) ratio appears to be the best of the four ratios to use as a measure of the presence of Rg wave energy on a seismogram. Based on this analysis, I decided to use the Rg/Lg (AV) ratio as a measure of the presence of Rg wave energy on a seismogram. In the discussion that follows, the notation "Rg/Lg" is used to refer to the Rg/Lg (AV) ratio.

Figures 4 shows histograms of the Rg/Lg ratios for blasts and for the Moodus, CT; Erving, MA; and the Boxboro, MA earthquakes. All of the ratios for the Moodus, CT earthquake overlap with those of the blasts. The average value of Rg/Lg for the Moodus earthquake (0.93) is lower than the average value for the blasts (2.50), which is consistent with the 1.6 km depth of the earthquake. The Erving, MA earthquake ratios do not overlap with those of the blasts, and the average value of Rg/Lg was 0.22 for that earthquake. These ratios for the Erving, MA event are almost as low as those of the Ardsley, NY earthquakes (average Rg/Lg = 0.16), which may indicate that the Erving, MA earthquake was more than a few km deep. However, the presence of a low amplitude Rg wave on the seismogram shown in Figure 2 implies that the depth of that earthquake was probably less than about 4 km. The Boxboro, MA earthquake ratios cluster around the lower end of the ratios for the blast population, and the average value of Rg/Lg for that earthquake was 0.86. These higher values of Rg/Lg suggest that the Boxboro earthquake was a shallow event (perhaps no deeper than about 2 km).

Most of the seismograms discussed in this paper were recorded at distances of less than 100 km. A few were recorded as close as 17 km from the sources. If Rg is to be of practical value as a depth discriminant, it is important to ask how close a station must be to the source in order to use Rg as a depth discriminant. One point to be noted in this regard is that the quarry blasts discussed in this paper are quite small, so that none of the phases are recorded very far from the source. For the largest blasts in this study, Rg and other phases were recorded at distances as great as 155 and 168 km.

The effect of distance on Rg/Lg ratios appears to be less significant in the distance range of 50 to 170 km than in the 17 to 50 km range. Comparing the data set of Rg/Lg ratios for blasts recorded at 50 to 170 km, to the data set of Rg/Lg ratios for the earthquakes (all of which were recorded at more than 50 km), lowers the number of ratios that can be analyzed for blasts. However, that restricted data set is more appropriate (in terms of distance) to compare with the earthquake ratios. To test the difference between the Rg/Lg ratios for the earthquakes and those for this smaller data set of blasts, the Student's t-Test was applied to the data using formulas given in Weiss and Hassett (1982). Since all of the earthquakes occurred at some depth below the surface and all of the blasts occurred at zero depth, one would expect that, if the Rg/Lg ratio is a measure of the presence of Rg waves, the earthquake ratios should generally be lower than the blast ratios. The null hypothesis for the t-Test was that the mean of the earthquake ratios was the same as the mean of the blast ratios, and the alternative hypothesis was that the mean of the earthquake ratios was lower. Applying the t-Test, I found that the null hypothesis must be rejected at the 99% confidence level, implying that there is a statistically significant difference between the ratios for blasts and earthquakes.

The following approach to estimating depth from observed amplitudes of Rg is similar to that of Bath (1975), although his observed ratios were based on trace amplitudes rather than spectral amplitudes. Let $r(h)$ represent the average Rg/Lg ratio for an earthquake at depth h , and let $r(0)$ represent the average ratio for sources at the surface. The specific value of $r(h)$ for a given earthquake will depend on a number of factors (in addition to depth) including: the level of excitation of the different wave types that are generically referred to as "Lg", the attenuation of the

different wave types that contribute to Rg/Lg ratios, the azimuths and distances at which recordings are available, the focal mechanism, and the instrument response. For the purpose of this case study, I am assuming that (in the 50 to 170 km distance range) all of the factors contributing to the average Lg wave amplitude are, on average, not very dependent on depth (provided that data are available at a range of azimuths). However, the Rg amplitude varies by more than order of magnitude between events located at the surface and events at about 5 km depth. Furthermore, I assume that the variation in Rg amplitude with depth is approximately characterized by the 0.8 sec displacement-depth eigenfunction calculated for a (flat-layered) model of the upper crust. The observed ratios are normalized by dividing by $r(0)$, and the resulting values are referred to $r_n(h)$. If $f(h)$ is the normalized eigenfunction, then an approximation to $r_n(h)$ will be:

$$r_n(h) = f(h) + K \quad (1)$$

where K is the value of $r_n(h)$ for an event deeper than 5.0 km. K is likely to be greater than zero because there is probably some energy in the various arrival time - frequency windows even when no Rg wave is present. For this illustration, I use 0.10 (the average Rg/Lg ratio for the Ardsley, NY earthquakes) as an estimate of K. The depth of an earthquake can then be estimated by finding the value of h for which:

$$r_n(h) = f(h) - 0.10. \quad (2)$$

CONCLUSIONS AND RECOMMENDATIONS

The ratio determined by dividing the average amplitude in the Rg wave arrival time - frequency window by the average amplitude in the Lg wave arrival time - frequency window was the best measure that I found for determining whether Rg is present on a seismogram. For the Ardsley, NY earthquakes (5.2 km depth), all of the seismograms yielded an Rg/Lg ratio that was lower than any Rg/Lg ratio found for blasts, and using equation (2), the depth of that earthquake was found to be >4.5 km. The Moodus, CT earthquake (1.6 km) yielded Rg/Lg ratios that overlapped with the ratios determined for the blasts, and applying equation (2) to that event yields a depth of 1.1 km. Thus, in these two cases, the observed seismograms are generally consistent with what might be expected from the theory of surface wave and body wave excitation. In addition, using all seismograms recorded in the 50-170 km distance range, the difference in Rg/Lg ratios for blasts and earthquakes was found to be statistically significant at the 99% confidence level.

Based on equation (2), the Boxboro, MA and Erving, MA earthquakes were found to have depths of 1.2 and 3.0 km, respectively. These depths were determined from five stations at distances of 75 to 136 km for the Boxboro earthquake and from five stations at distances of 85 to 131 km for the Erving earthquake. With that type of station distribution, it would not be possible to constrain such shallow depths based only on arrival times of P and S waves.

In regions where there is more complex structure in the shallow crust and where there is greater topographic relief, Rg might not be as good a discriminant as it would be in New England. However, in any region where event depth must be determined from a limited number of seismic observations, it seems that some measure of the presence (or absence) of Rg wave energy on seismograms should be considered as a possible depth discriminant for events in the upper crust.

REFERENCES

- Bath, M. (1975). Short-period Rayleigh waves from near-surface events, Phys. Earth Planet. Int., **10**, 369-376.
- Dziewonski, A.M., S. Bloch and M. Landisman (1969). A technique for the analysis of transient seismic signals, Bull. Seis. Soc. Am., **59**, 427-444.
- Kafka, A.L. (1987). Rg waves as a depth discriminant for earthquakes and explosions in New England, 9th Annual Defense Advanced Research Projects Agency/ Air Force Geophysics Laboratory Symposium, Nantucket, MA, June 1987, 236-241.
- Kafka, A.L. (1988). Earthquakes, geology and crustal features in southern New England, Seism. Res. Lett., **59**(4), 173-181.
- Kafka, A. L. and M. F. Dollin (1985). Constraints on Lateral Variation in Upper Crustal Structure beneath Southern New England from the Dispersion of Rg Waves, Geophys. Res. Lett., **12**, 235-238.
- Kafka, A.L. and E.C. Reiter (1987). Dispersion of Rg waves in southeastern Maine: evidence for lateral anisotropy in the shallow crust, Bull. Seis. Soc. Am., **77**, 925-941.
- Locke, K. (1985). Quarterly Seismicity Bulletin of the New York - New Jersey Network, 1 October - 31 December 1985, Published by Lamont-Doherty Geological Observatory of Columbia University, Palisades, NY.
- Mrotek, K.A., R.C. Quittmeyer, P.G. Naumoff and C.T. Statton (1988). Observations of the earthquake swarm near Moodus, Connecticut: September/October 1987,(Abstract), EOS, Trans. Am. Geophys. Un., **69**(16), 495.
- Weiss, N. and M. Hassett (1982). Introductory Statistics, Addison-Wesley Publishing Company, Reading, Massachusetts.

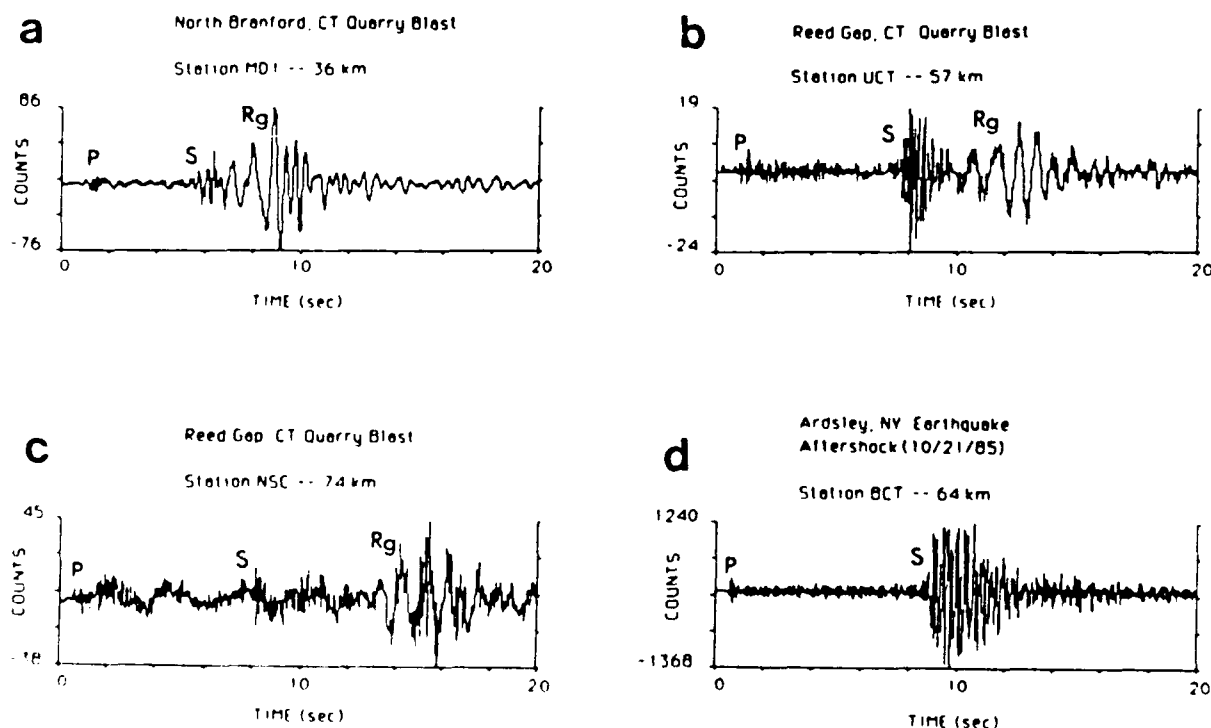


FIGURE 1: Examples of vertical component seismograms from this study. (a) North Branford, CT quarry blast recorded at station MD1 (36 km). (b) Reed Gap, CT quarry blast recorded at station UCT (57 km). (c) Reed Gap, CT quarry blast recorded at station NSC (74 km). (d) Ardsley, NY earthquake recorded at station BCT (64 km).

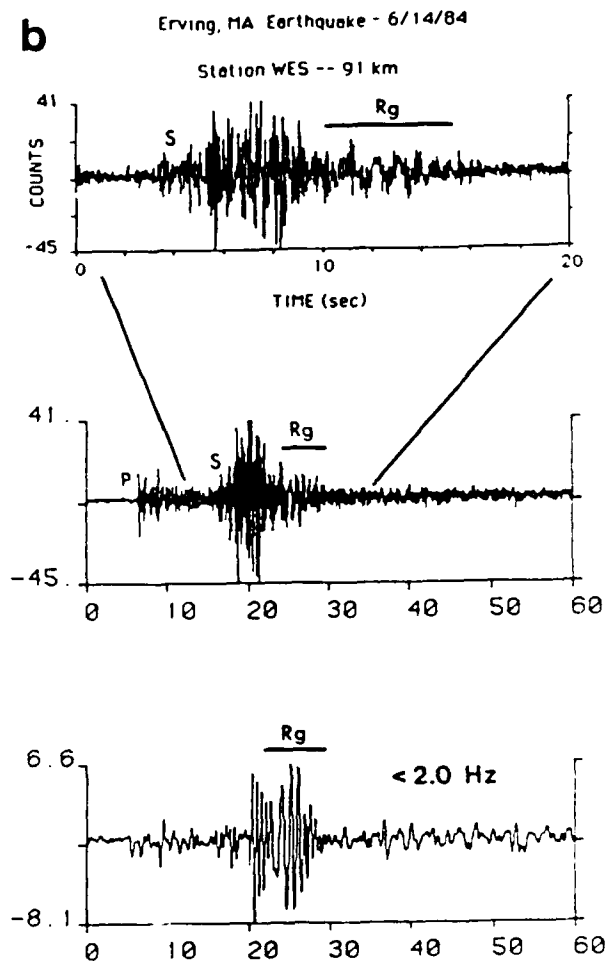
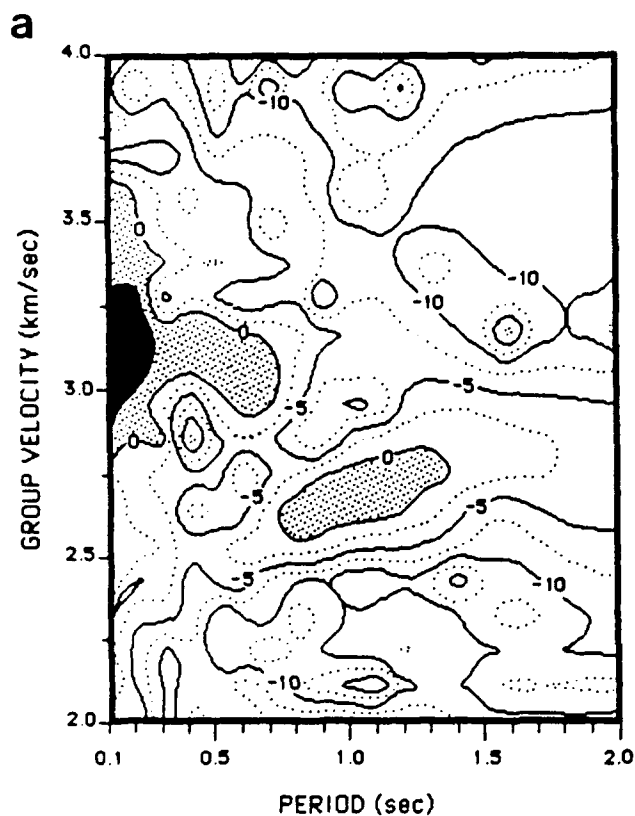


FIGURE 2: Narrow bandpass filter analysis of seismogram recorded from Erving, MA earthquake at station WES. On the left is a plot of group velocity vs. period. The vertical axis is amplitude; each unit of amplitude in the contour plot represents a difference of 2 db. Shaded areas are areas of highest amplitude.

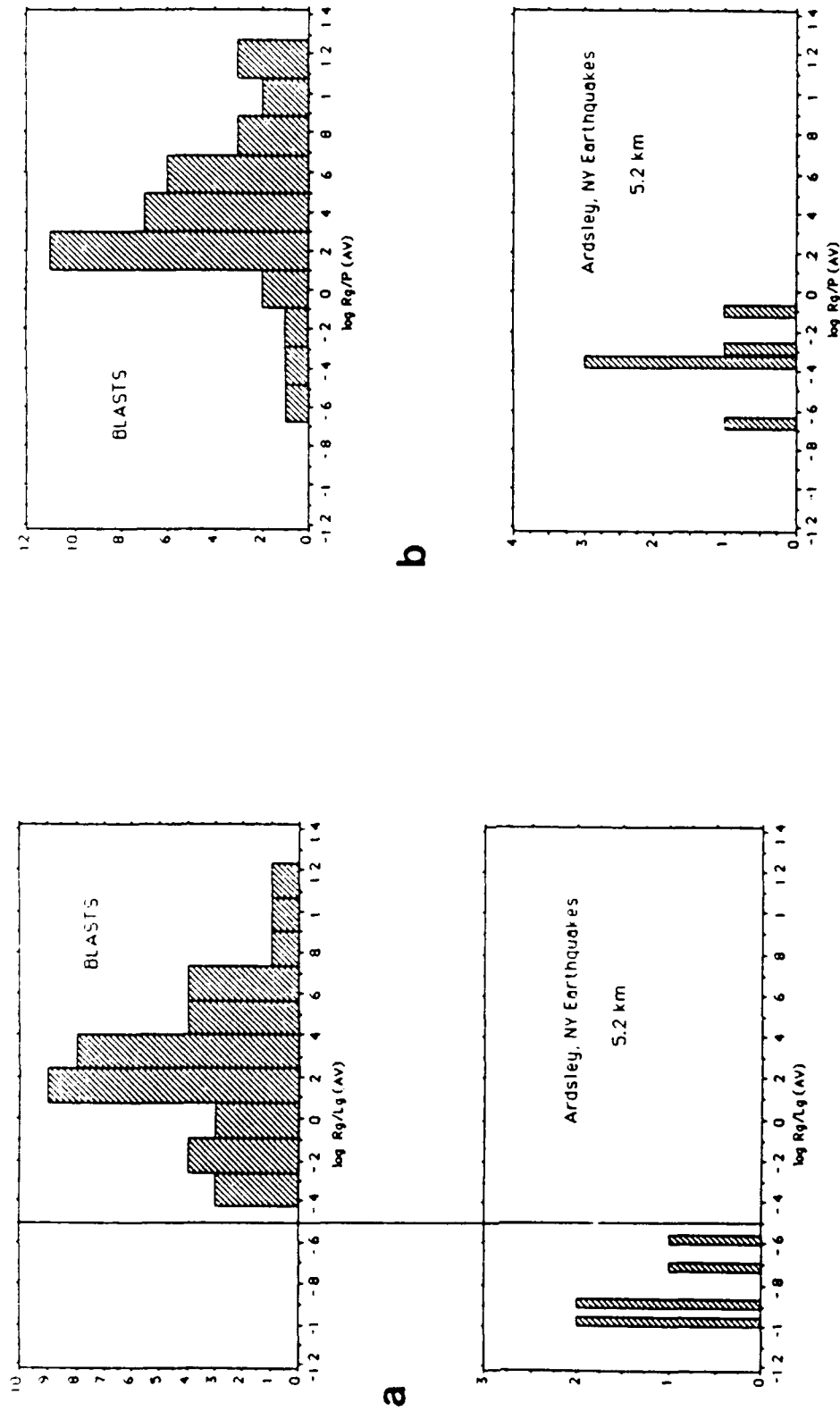


FIGURE 3: Histograms of log of Rg/Lg and Rg/P ratios for quarry and refraction blasts and for the Ardsley, NY earthquakes. (a) Ratios determined from calculating the average amplitude in the arrival time - frequency windows appropriate for Rg and Lg . (b) Ratios determined from calculating the average amplitude in the arrival time - frequency windows appropriate for Rg and P .

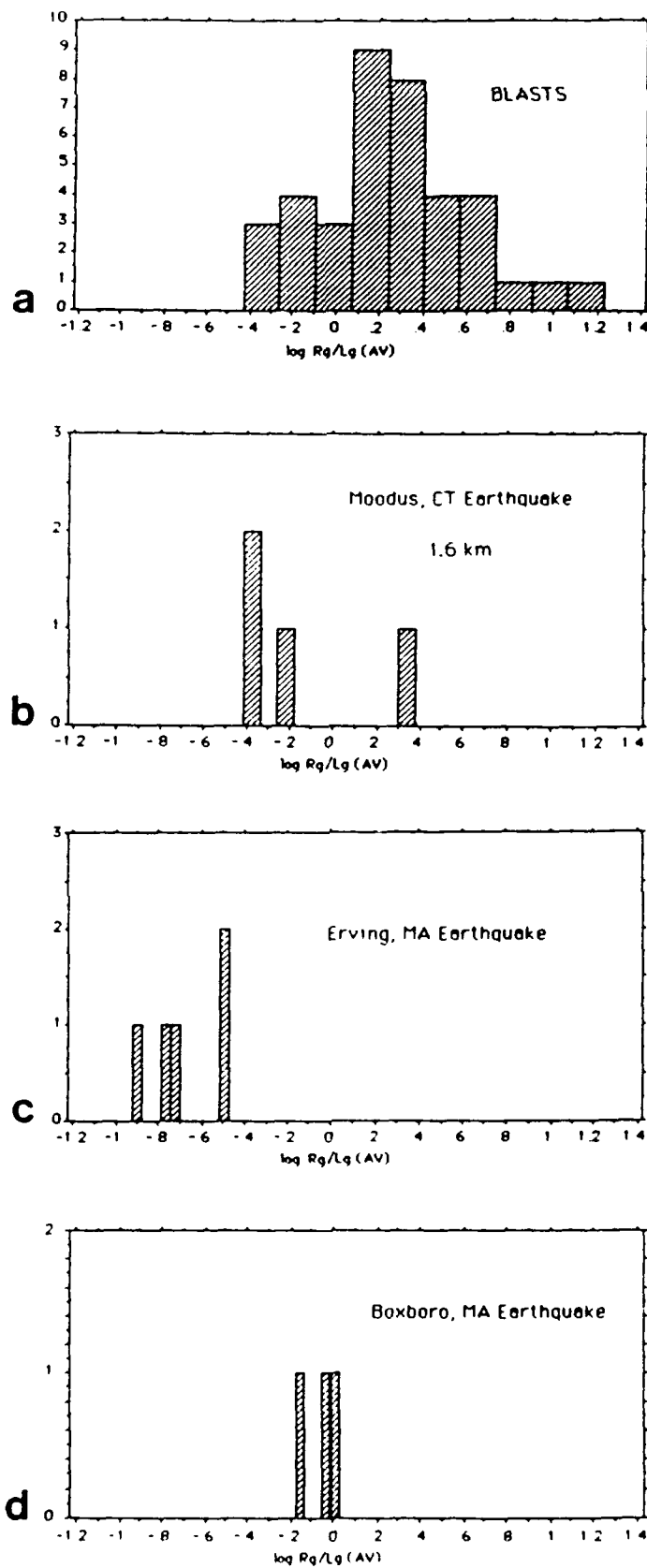


FIGURE 4: Histograms of log of Rg/Lg ratios for (a) quarry and refraction blasts and for (b) the Moodus, CT earthquake; (c) the Erving, MA earthquake; and (d) the Boxboro, MA earthquake. These ratios were determined from calculating the average amplitude in the arrival time - frequency windows appropriate for each specific phase.

THE TIME-FREQUENCY CHARACTERISTICS OF QUARRY BLASTS, EARTHQUAKES AND CALIBRATION EXPLOSIONS RECORDED IN SCANDINAVIA AND KAZAKHSTAN U.S.S.R.

MICHAEL HEDLIN, JOHN ORCUTT, BERNARD MINSTER and HAROLD GURROLA

INSTITUTE OF GEOPHYSICS AND PLANETARY PHYSICS (A-025), SCRIPPS
INSTITUTION OF OCEANOGRAPHY, UNIVERSITY OF CALIFORNIA AT SAN DIEGO, LA
JOLLA CA 92093

CONTRACTS NO. F19628-87-K-0013 and F19628-88-K-0044

OBJECTIVE

The primary objective of this study is to develop an algorithm that will routinely discriminate between ripple-fired mine explosions (events that consist of several sub-explosions closely grouped in space and time) and all other seismic events (including earthquakes and single-event explosions). To develop the algorithm and test its independence from local mining practice and geologic setting we have selected two independent data sets (data collected by the NORESS array in southern Norway and by sensors deployed in Kazakhstan U.S.S.R.). To assess the relative value of these two data sets for this type of work we have conducted a comparative analysis of ambient noise levels at these two sites.

SUMMARY

A commonly used technique in mining practice, known as ripple-firing involves the detonation of a number of sub-explosions offset from each other by small distances and times. The intent of this procedure is to enhance fracturing of the rock and reduce ground motion in areas proximal to the mine. The observation has been made by several researchers (Smith, 1989, Stump and Reamer, 1988, Baumgardt and Ziegler, 1988) that such events tend to give rise to seismic coda possessing highly colored spectra. That is spectra enriched in power at certain, preferred, frequencies and depleted in power at other frequencies.

This spectral color is certainly due to the interaction of the time-offset wavefields produced by each sub-explosion. The manner in which the wavefields interact is not known, and undoubtedly is largely non-linear, however we feel that simple linear theory is sufficient to describe the most obvious result, specifically the pronounced spectral modulation. Briefly, the regular repetition and superposition of similar seismic motions in the time domain leads to regular amplification and suppression of power in the frequency domain. Furthermore, as is demonstrated by Hedlin et al (1989) in the limit where all sub-explosions occur at the same point in space, the spectral features are independent of time in the coda. Because we predict that ripple-fired events should give rise to pronounced, time-independent, spectral features, we have found it useful to calculate frequency-time displays of the seismograms, known as sonograms.

In figure 1 we display the vertical component time series, and sonogram, of a 20 T single-event calibration explosion detonated and recorded in Kazakhstan U.S.S.R. in 1987. The recording was made by a GS-13 seismometer sampled at 250 s^{-1} and deployed at the surface near the town of Bayanaul. The energy in

the coda from this event is distributed fairly randomly as a function of frequency and time. There is no evident organization of the energy into time-independent bands. In figure 2 we show the result of the same processing techniques applied to an unidentified event that occurred 264 km from the station. The spectra of this event are distinctly modulated and furthermore the energy is very clearly organized into time-independent bands. We strongly suspect that this event was a ripple-fired quarry blast.

We have found it useful to suppress the large scale structure provided by the compressional and shear onsets as well as the high frequency spectral falloff and thus enhance any time-independent features that may be present by comparing two versions of each spectral estimate. As figure 3 illustrates we compare a relatively unsmoothed version of the original spectral estimate with one that is heavily smoothed. We represent all regions of the sonogram matrix where the local power is high relative to the *regional* power by a value of +1 (denoted as white for display purposes) and where it is low by a -1 (black). In this manner we discard the bulk of the magnitude information and "flatten" the original sonogram matrix to a very simple, yet informative, binary matrix. In figures 4 and 5 we display the binary sonogram matrices corresponding to the originals displayed in figures 1 and 2 respectively. This method of reducing sonogram matrices to binary form provides simple patterns that allow visual discrimination between mine explosions and single-event explosions.

To extend this work we have examined data collected by the NORESS array in southern Norway. Our goal was to discover whether earthquakes can be as easily distinguished from mine blasts as single-event explosions. We also wanted to determine if the algorithm would be successful in a different geologic setting and in an area of different mining practice than present in central Asia. We have concentrated our efforts thus far on events known to either be earthquakes or mine explosions. The NORESS array data have a distinct advantage over the Kazakh data since typically 30 sensors simultaneously record each event. The obvious disadvantage is that the array data are only digitized at 40 s^{-1} and thus cannot resolve spectral features above 20 Hz. In figure 6 we display the sonogram of a presumed earthquake which occurred 454 km from the array. This display has been produced by stacking the amplitude spectra from each of the 24 vertical channels after converting each spectrum to binary form and assuming infinite phase velocity. The compressional onset occurs at 12 seconds. As expected, little structure can be discerned other than the microseismic noise below 2 Hz. Figure 7 was computed from the coda produced by a Blasjo mine explosion which occurred 302 km from the array. The compressional onset occurs at 15 seconds and is followed by a very obvious time-independent banding. The time-independent structure present prior to the onset is due to long lived spectral lines in the noise and does not correlate with the spectral features present in the coda.

In figures 8 and 9 we display the ambient noise levels present at the high-frequency element of the NORESS array (site NRF0 ; sampling at 125 s^{-1}) and in the boreholes at the Kazakh sites near the towns of Bayanaul and Karkaralinsk. All seismometers recorded the vertical component of velocity and were deployed at 60, 66 and 99 meters depth respectively. The noise levels are represented by three curves which illustrate the average and 95% confidence limits of acceleration power. Above 1 to 2 Hz the Kazakh noise levels are generally slightly (up to 10 dB) higher. The apparent rise in power above 40 Hz at the NORESS array is probably not natural but due to digitization noise. Below 1 to 2 Hz the NORESS noise levels are significantly higher than in central Asia. Although these curves do not extend across the entire

microseism band, the suggestion is that microseismic noise levels are higher in Norway than in central Asia. This seems intuitively reasonable given the relative proximity of the NORESS array to an ocean. This appears to be a long-range extension of the observation made by Hedlin et al (1988) that microseismic noise levels appeared to be inversely correlated with the distance from the shoreline in the range of 1 to 100 km.

CONCLUSIONS AND RECOMMENDATIONS

We observe significant differences between ripple-fired mine-explosions and earthquakes and single-event explosions. The close grouping in space and time of several sub-explosions appears to be responsible for the impression of prominent time-independent spectral modulation on the frequency spectrum of the resultant coda.

We plan to extend further the pattern-based discriminant by reducing the binary sonogram matrices to scalars which reflect the presence or absence of time-independent modulation.

It appears that lower microseismic noise levels will be realized at sites far removed from large bodies of water.

REFERENCES

- Baumgardt, D. R. & Ziegler, K. A., 1988. Spectral Evidence for Source Multiplicity in Explosions: Application to Regional Discrimination of Earthquakes and Explosions. *Bull. seism. Soc. Am.*, **78**, 1773-1795.
- Hedlin, M. A. H., Fels, J. F., Berger, J., Orcutt, J. A. & Lahav, D., 1989, Seismic Broadband Signal and Noise Levels on and Within the Seafloor and on Islands, *Proceedings of a Workshop on Broad-Band Downhole Seismometers in the Deep Ocean, W.H.O.I., Woods Hole, MA, April 26-28, 1988*.
- Hedlin, M. A. H., Minster, J. B. & Orcutt, J. A., 1989, The Time-Frequency Characteristics of Quarry Blasts and Calibration Explosions Recorded in Kazakhstan U.S.S.R., *Submitted for publication in the Geophysical Journal*.
- Smith, A. T., 1989. High-Frequency Seismic Observations and Models of Chemical Explosions: Implications for the Discrimination of Ripple-Fired Mining Blasts. *Submitted for publication in the Bull. seism. Soc. Am.*
- Stump, B. W. & Reamer, S. K., 1988. Temporal and Spatial Source Effects from Near-Surface Explosions. *Paper presented at the 10th annual AFGL/DARPA seism. Res. Symp.*

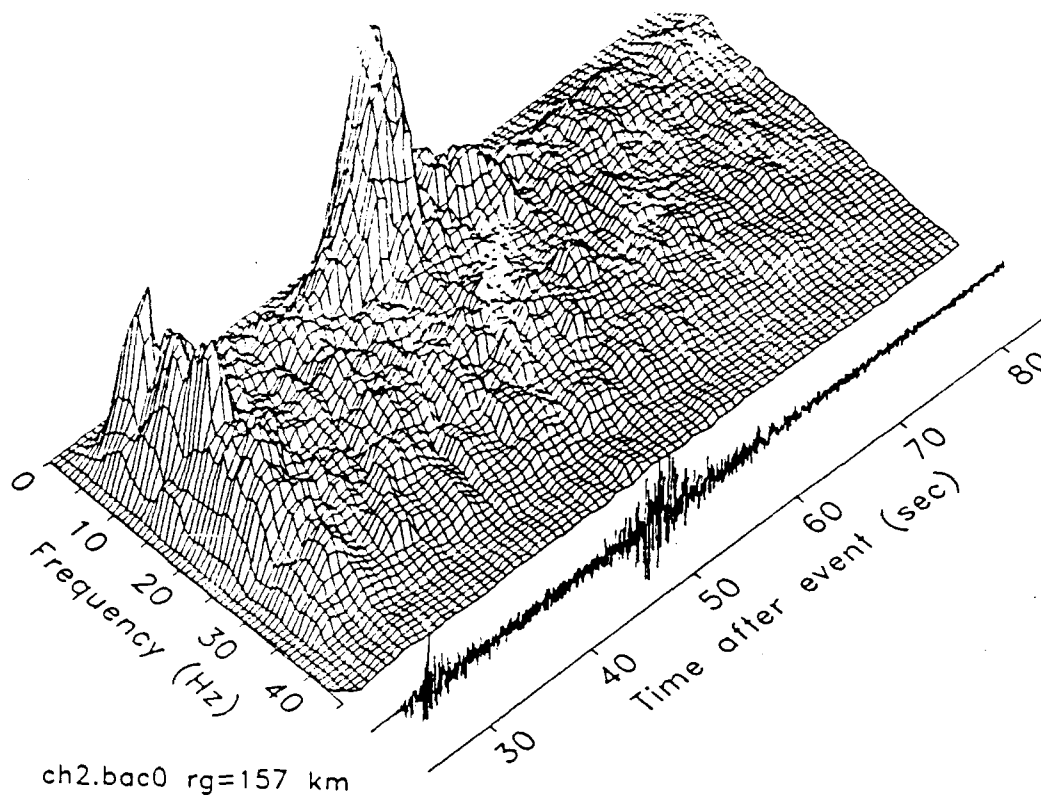


Figure 1. Seismogram resulting from a single-event calibration explosion recorded at a range of 157 km by the vertical surface seismometer at Bayanaul and corresponding sonogram.

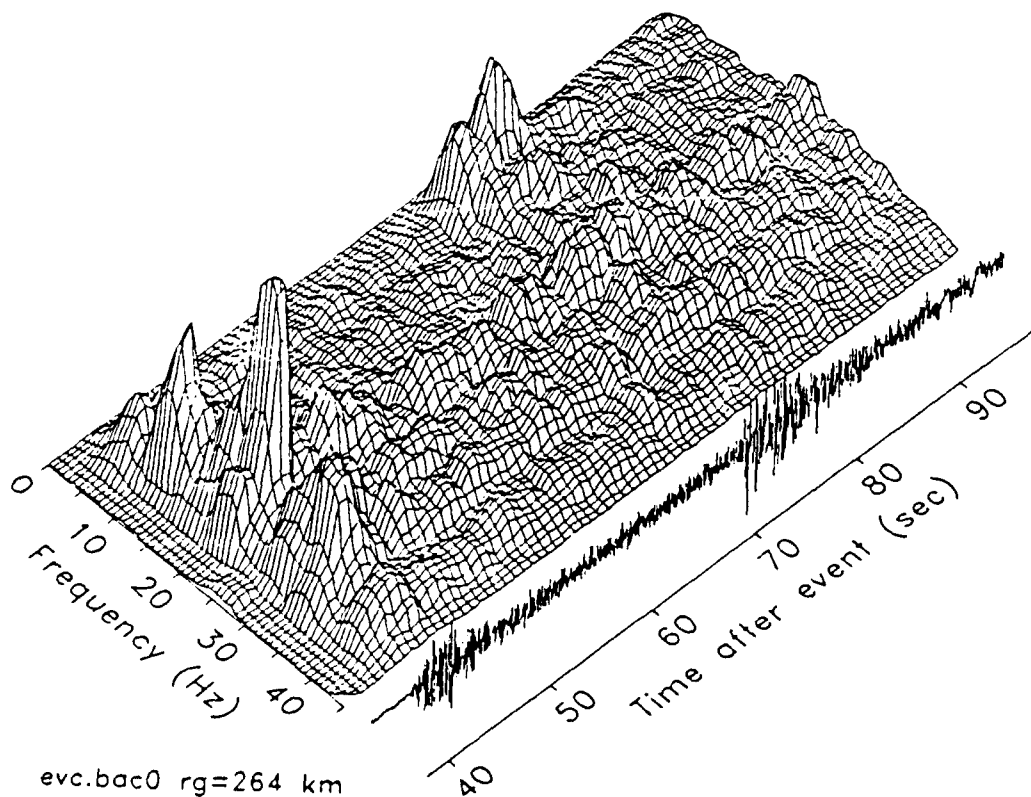


Figure 2. Seismogram resulting from a suspected mine-explosion recorded at a range of 264 km by the vertical surface seismometer at Bayanaul and corresponding sonogram.

evc.bac0

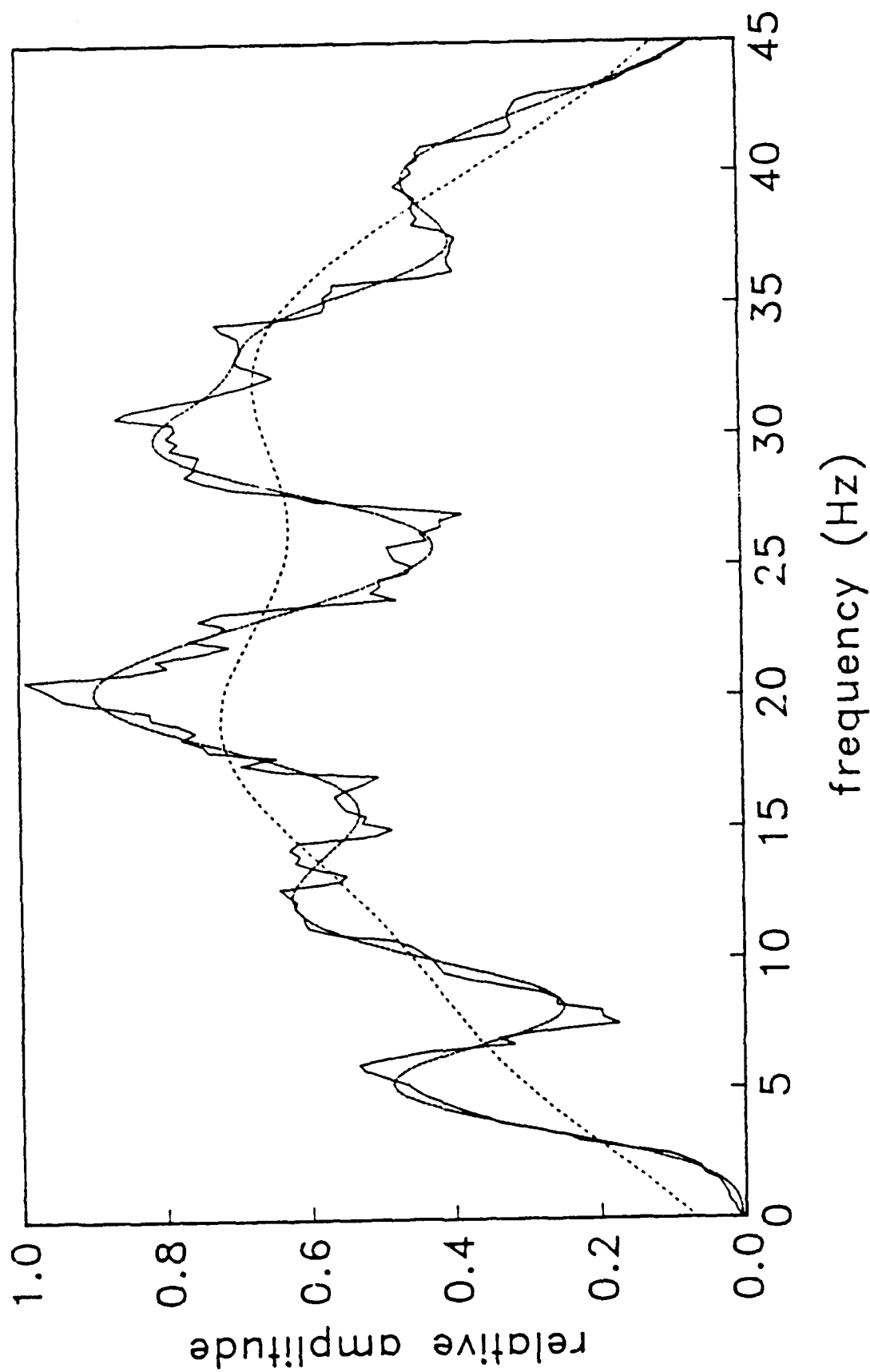


Figure 3. Original spectral estimate and two versions, one relatively unsmoothed and the other relatively highly smoothed. This figure is intended to illustrate the means by which we reduce each spectral estimate to a "binary spectral estimate". The regions of locally high power are represented by a +1 (white). Regions deficient in power are represented by a -1 (black).

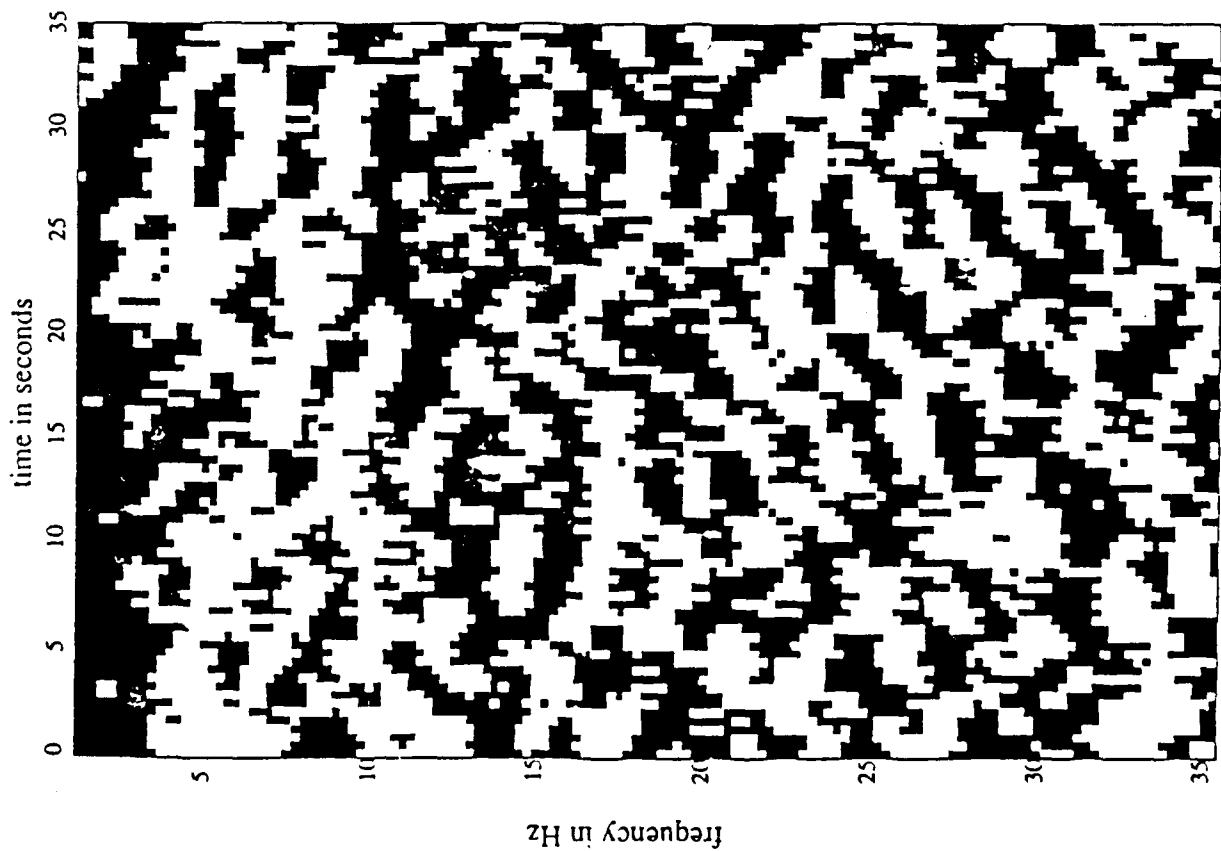


Figure 4. Vertical component binary sonogram matrix corresponding to the single-event calibration explosion recorded at Bayanaul (refer to figure 1). The first 35 seconds of coda after the compressional onset are represented in this and the following figure.

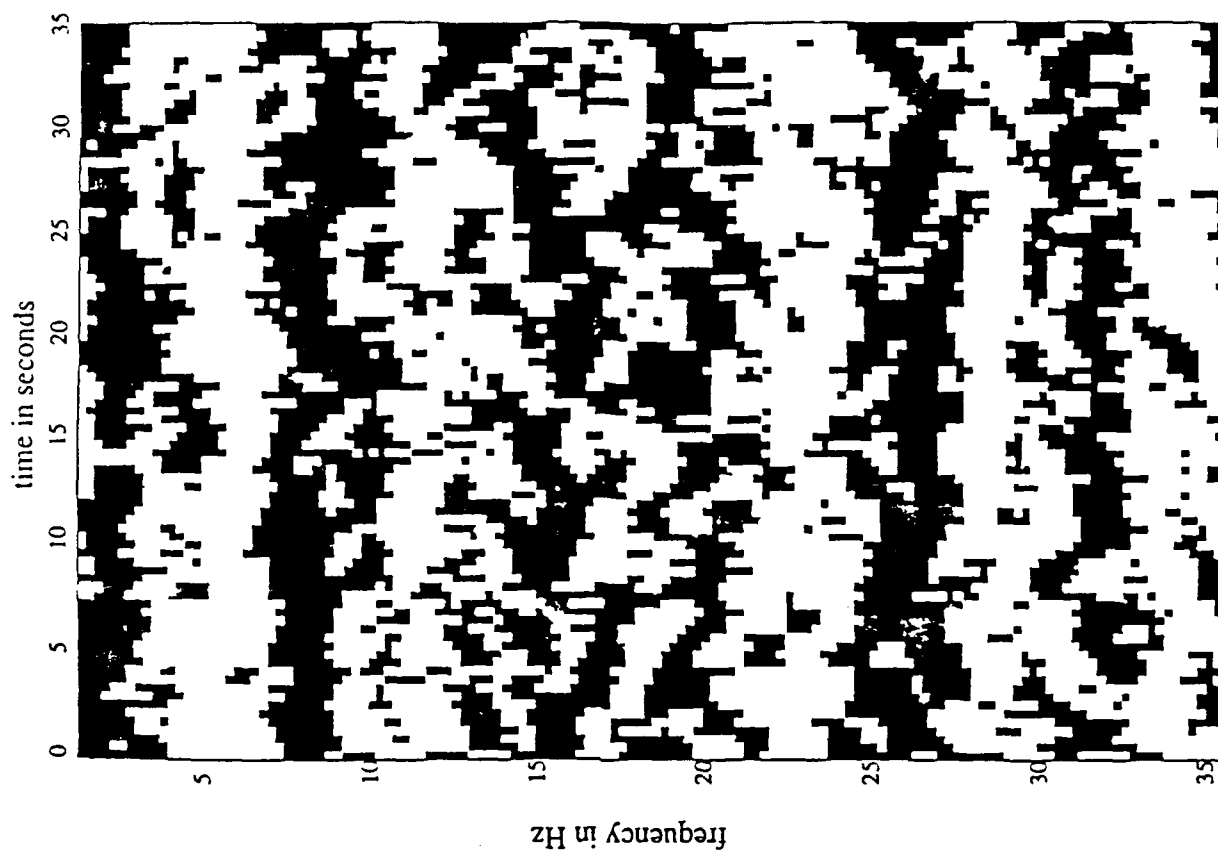
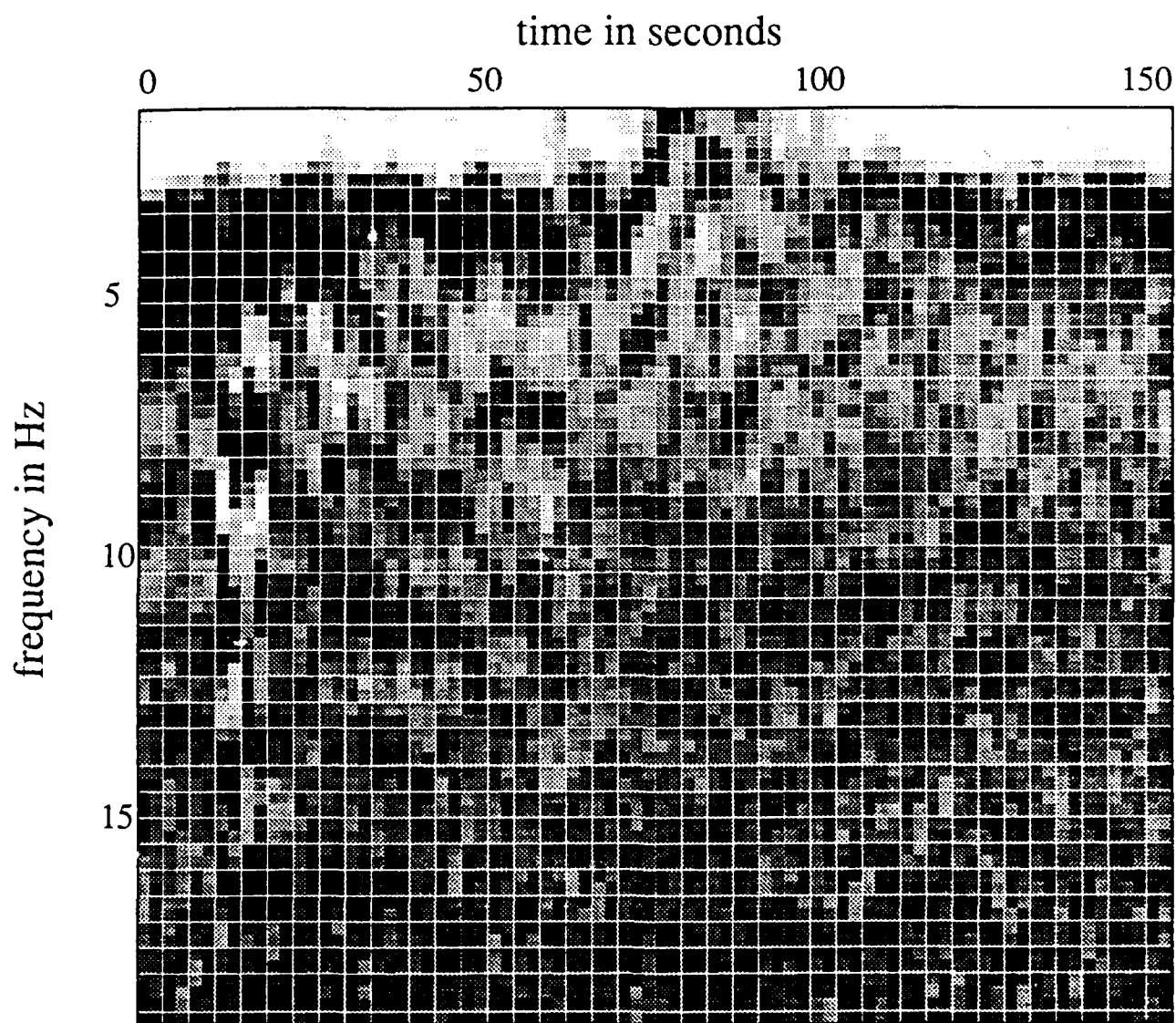
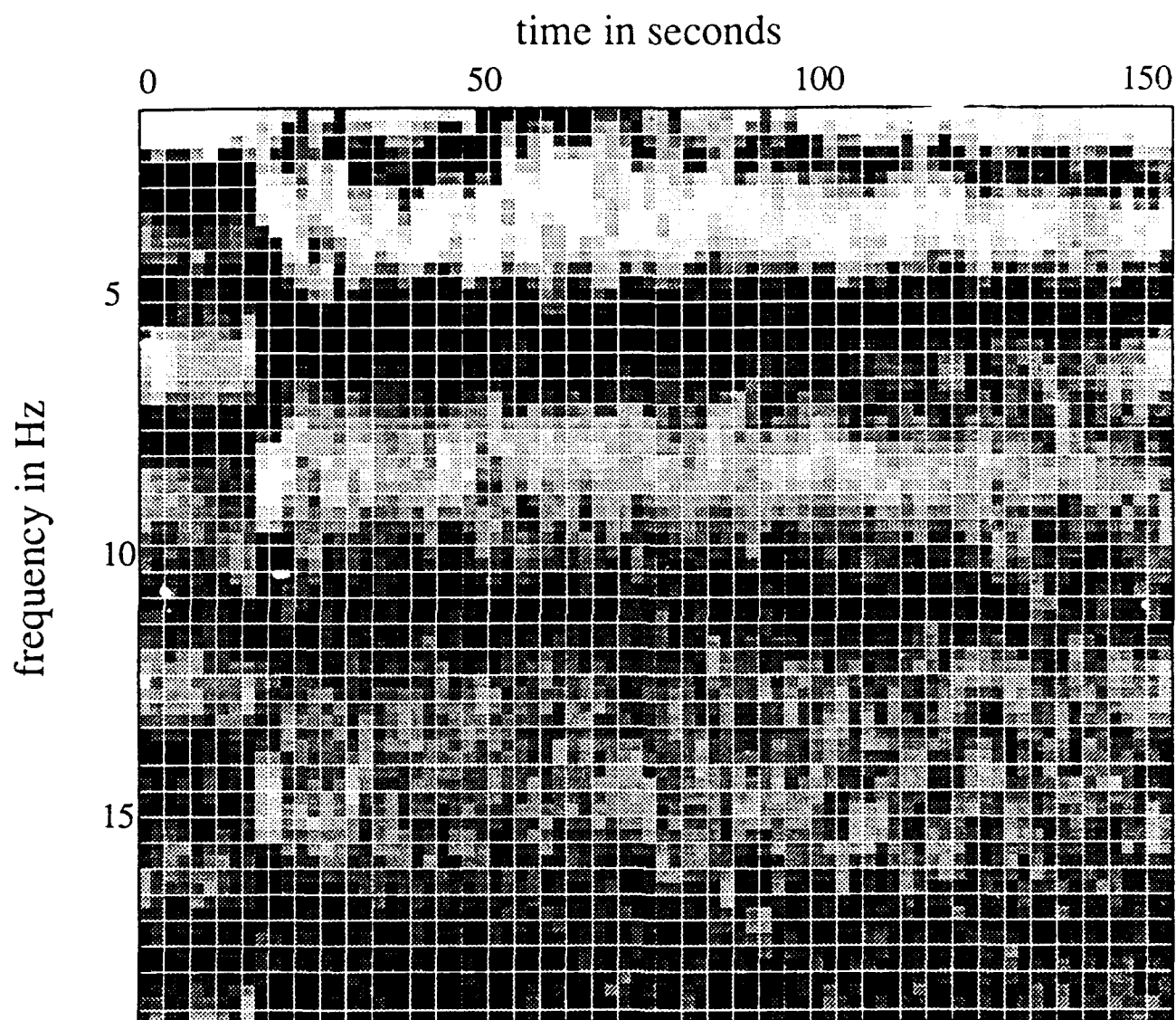


Figure 5. Vertical component binary sonogram matrix corresponding to the suspected mine-explosion recorded at Bayanaul.



Presumed earthquake 0422 - 454 km from NORESS

Figure 6. Vertical component sonogram matrix corresponding to a presumed earthquake recorded at the NORESS array.



Blasjo explosion 0039 - 302 km from NORESS

Figure 7. Vertical component sonogram matrix corresponding to a Blasjo mine explosion recorded at the NORESS array.

Kazakhstan (BAA0) and NORESS (HF-NRFO) Borehole Noise Levels

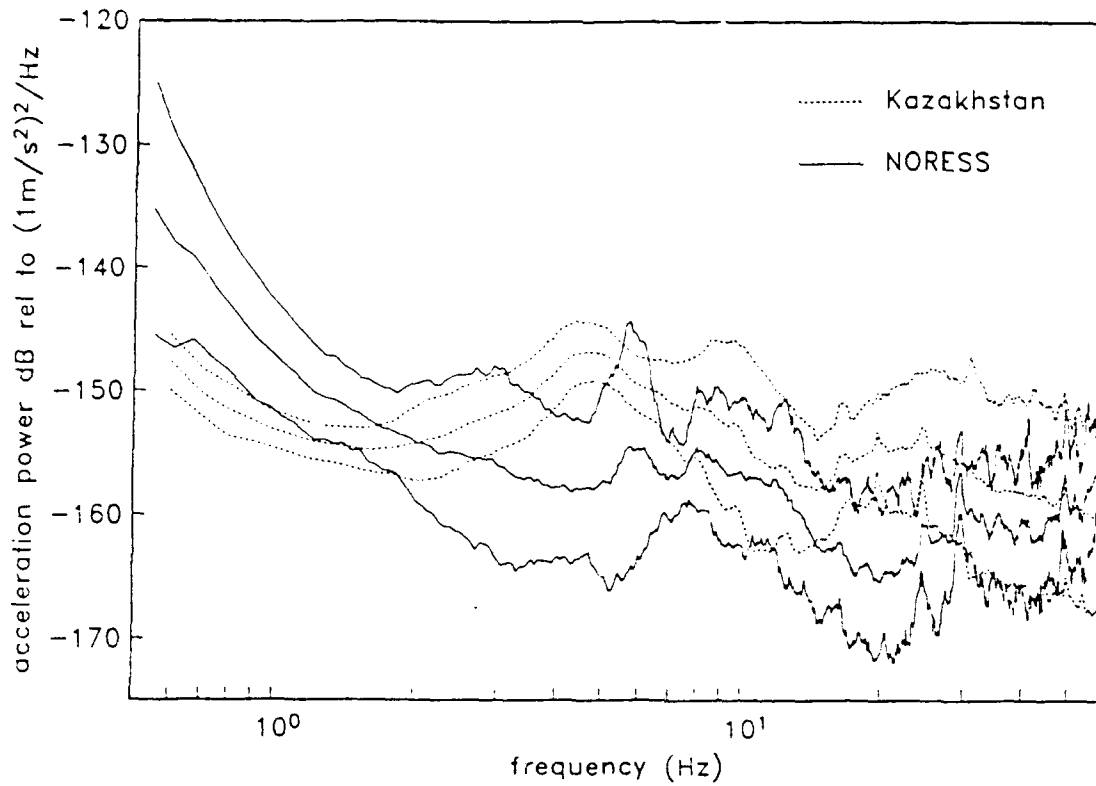


Figure 8. The average and 95% confidence limits of ambient noise levels recorded at the NORESS array and near the town of Bayanaul in Kazakhstan, U.S.S.R.

Kazakhstan (KKA0) and NORESS (HF-NRFO) Borehole Noise Levels

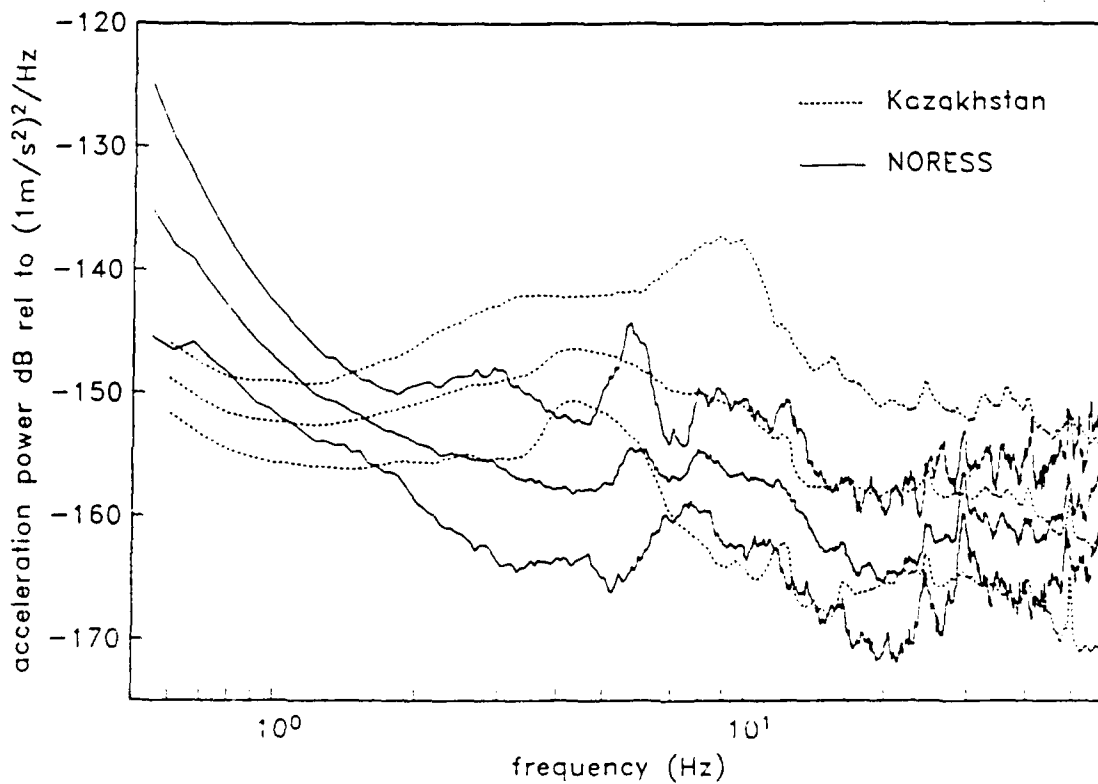


Figure 9. The average and 95% confidence limits of ambient noise levels recorded at the NORESS array and near the town of Karkaralinsk in Kazakhstan, U.S.S.R.

A Comparative Study of High Frequency Seismic Noise at Selected Sites in the USSR and USA

H. Gurrola, J.B. Minster, F.L. Vernon, J. Berger, H.K. Given, R. Aster

Scripps Institution of Oceanography
I.G.P.P. A-025, UCSD
San Diego, CA 92093

Contracts No. F19628-88K-0026 and F19628-88K-0044

OBJECTIVES:

The objective of this study is to compare noise levels observed at three seismic stations located within 250 km of the Nevada Test Site (NTS) with those recorded at three stations located within 250 km of the Kazakh Test Site (KTS), and to seek a better understanding of noise conditions at high frequencies for these sites. For this purpose we have analyzed nearly 2,000 noise samples collected at the US stations and have systematically reexamined several hundred noise samples measured at USSR sites and described by Berger et al. (1988). The principal emphasis of this study is a comparison of average high frequency noise levels at these US and USSR sites, both for surface and borehole emplacements, and a systematic investigation of the effect of wind speed on surface and borehole noise levels at all stations.

SUMMARY:

Through a joint USA-USSR project, seismographic stations have been operated for several months during 1987 at three sites within 250 km of KTS and through most of 1988 and early 1989 at three sites within 250 km of NTS. These periods of operation yield a reasonable sampling of varied meteorological conditions, although the overall duration of occupation of each site is too short to permit reliable characterization of seasonal noise variations. The three Soviet sites —Karkaralinsk, Bayanaul, and Karasu— are shown on figure 1 (Berger et al., 1988), and the three US sites —Nelson, Deep Springs, and Troy Canyon— are depicted on figure 2.

All these stations were equipped with high-frequency, three-component surface and 100 m borehole instruments (Berger et al., 1988). All channels were recorded digitally at 250 samples per second, through a low-pass anti-aliasing filter with a corner frequency of 80 Hz. At the low frequency end of the pass-band, system characteristics were as follows:

- All surface vault installations had a low frequency roll-off with a 1 Hz corner.
- All USSR borehole systems responses had a 0.2 Hz low frequency corner.
- US borehole systems were initially set with a 2 Hz low frequency corner, but were modified to have a 0.2 Hz corner (thus matching USSR installations) during the second half of their deployment (since June, 1988)

Figure 3 illustrates the various system response functions. These were used to correct the corresponding noise spectra. It should be noted, therefore, that comparison of surface and borehole noise levels is affected by larger instrument corrections for surface systems below 1 Hz. System noise spectra were discussed by Berger et al. (1988).

We computed noise spectra for all channels from time windows ranging from 50 s to 120 s. Since our primary interest was to characterize ground noise, each time series sample was examined carefully, mainly to eliminate small events which might color the spectrum. Power

spectra were calculated using a section averaging algorithm, thus allowing use of long time windows and resulting in spectral estimates with reduced variances (e.g. Welch, 1967). The influence of monochromatic spikes —typically at 50 Hz in the USSR and 60 Hz in the USA— and their harmonics was reduced by smoothing spectra through a 1 Hz running median. In each case, the surface wind speed was also recorded; noise samples for which wind speed was not available were not used. Using this procedure, we computed approximately 50 noise spectra for each component at each station in the USSR, or nearly 1,000 spectra from USSR data. We computed approximately twice this number of spectra from US data.

Figures 4 and 5 illustrate the type of noise statistics compiled in this fashion. They show noise spectra —acceleration noise power levels in dB relative to $1 \text{ (m/s}^2\text{)}^2/\text{Hz}$ — observed under low wind ($< 2 \text{ m/s}$) conditions at Karkaralinsk, USSR and Nelson, USA, respectively. On each frame are plotted the mean —for the corresponding channel— of all available spectra for which wind speed was less than 2 m/s, as well as a “high-noise” and a “low-noise” spectrum extracted from this population. The latter were simply selected as the spectra with the highest and lowest integrated power in the 1-80 Hz band, respectively. The spectra shown on figures 4 and 5 are felt to be representative of the general variability in noise levels we have observed in both regions under quiet wind conditions.¹

The large number of spectra we have calculated allows us to examine in greater detail the variation of noise characteristics on each component as a function of wind speed, both for surface and borehole installations. The results are summarized in figures 6 through 11, which show contour plots of noise level as a function of wind speed and frequency (note: each station experienced a different range of wind speeds over the duration of the deployment so that the extent of the contoured data varies from site to site). The grids used to produce these contour plots were obtained by averaging spectra in wind speed “bins” of 0.1 m/s and spline-interpolating the results (e.g. Thompson, 1970). These figures show considerable variability in the noise character exhibited at the various sites of this study, although some general patterns do emerge.

Surface noise vs borehole noise

Not unexpectedly, borehole installations show a marked improvement over surface installations at frequencies above 10 Hz. On the other hand, at frequencies between 1 and 10 Hz, it is not uncommon to observe higher noise levels in the borehole than at the surface. Although a clear explanation is still lacking, comparison of these surface noise levels with the noise spectra recorded by shallow borehole broad band instruments is favorable. This may therefore be indicative of the presence of stronger noise conditions in that band for some of the borehole installations discussed here. In fact, some of the surface noise levels we calculated are lower than the theoretical noise curve of the borehole sensor provided by the manufacturer and shown by Berger et al. (1988, figure 6). At frequencies lower than 1 Hz, surface noise level estimates have been subjected to a substantial instrument correction, and are therefore less certain, but it is clear that the spectral shape is controlled primarily by the height of the microseismic peak which lies just outside the accessible frequency band.

The dependence of noise level on wind speed is generally stronger at high frequencies (above 10 Hz) than at lower frequencies, although much less so for borehole installations than for surface installations. At high frequencies, in the 10-80 Hz band, surface noise levels are considerably higher than borehole levels, by 3 to 15 dB, at all wind speeds.

¹ We have deleted from our sample all spectra calculated from Troy Canyon data collected during the month of May, 1988. The seismograms recorded at that site during this short period of time are significantly noisier than at any other time at all frequencies. We suspect that the dry wash near the station was filled by unusual runoff during that time, although this was not observed directly. Similarly, the surface recordings from Karasu are noticeably noisier than those from other Kazakh sites. Hedlin et al. (1988), and other workers have concluded that this highly structured noise, with a strong peak at or near 5 Hz is associated with very localized site characteristics.

Surface noise vs wind speed

At Troy Canyon and Deep Springs the surface noise levels did not change much with wind speed over the range of observed winds. At Nelson and at the three Soviet sites no significant correlation of surface noise with wind speed is observed for wind speeds below 4 m/s. However, for wind speeds above 4 m/s an increase in surface noise level of 1 to 2 dB for each increase in wind speed by 1 m/s is apparent, indicating a stronger dependence in surface noise on wind conditions in that range. In other words, wind speed appears to be a noise controlling factor above the 4 m/s threshold. This is reflected in the abrupt change of dominant contour directions at or near the threshold.

Borehole noise vs wind speed

At most sites, we find that the noise in the borehole is essentially unaffected by wind speed for the range of conditions observed: there may be at most a 3 dB increase in borehole noise level for a large (5 to 10 m/sec) increase in wind speed. This lack of a strong influence of surface wind on borehole noise holds for all USSR and US stations except Nelson, which exhibits a notable increase in noise level with wind speed (a 3 to 10 dB increase for a 7 m/sec increase in wind speed).

Nevada vs Kazakhstan

The high frequency (> 10 Hz) surface noise levels found at the three Nevada stations are approximately 5 to 10 dB higher than at Karkaralinsk and Bayanaul in Kazakhstan; they also cover a wider range (-130 dB to -160 dB in Nevada versus -145 dB to -155 dB at USSR stations). This may well be due to a better design (primarily lower profile) of the surface vaults at Kazakh installations than at the Nevada sites. On the other hand, the surface noise levels observed at Karasu are the highest in our data set, but there is clear evidence that this is due to a local site effect.

In the range of wind speeds 0 to 5 m/s, for which data are available at all sites, it appears that the surface noise at the Nevada sites is more colored than at the Kazakh sites, in the sense that these US stations show rising noise levels at high frequencies, whereas the Kazakh sites exhibit flatter spectra. Note that we have few or no observations of high (> 5 m/s) wind speed conditions at Soviet sites, so that it is difficult to generalize and extend this conclusion to higher wind speeds.

The shapes of borehole noise spectra measured at the Soviet stations also tend to be somewhat different from those observed at the American sites. We can distinguish three main regimes:

- Below 1 Hz, the Nevada spectra are seen to rise significantly, whereas the Kazakh spectra remain rather flat. This is in agreement with the independent observation made on broad band recordings that the microseismic peak is much stronger and better developed in Nevada than in Kazakhstan.
- In the 1-10 Hz band, all spectra are more or less flat, but the levels recorded in Nevada are lower than those recorded in Kazakhstan.
- In the 10-80 Hz band, Kazakh spectra typically drop with increasing frequency. A similar behavior —flat or slowly decreasing spectrum— is seen at Deep Springs and Nelson, but the spectra collected at Troy Canyon actually increase in that range. In any case, there appears to be little variation in overall spectral levels from site to site at frequencies in excess of 30 Hz.

In the 1-20 Hz band, the surface noise levels observed at all stations except Karasu are not systematically different from those recorded at NORESS (see Hedlin et al., 1989), and the borehole noise levels recorded in this study are comparable to those observed in the Regional Seismic Test Network (Rodgers, et al., 1987). At Deep Springs, noise levels in the same band are within a few dB of the low levels reported by Li et al. (1984) for Lajitas, Texas.

CONCLUSIONS:

From our analysis of surface and borehole noise samples collected in 1987 at three sites in Kazakhstan and in 1988-89 at three sites in Nevada, we conclude that:

1. In general, noise levels in the 100m deep boreholes were unaffected by wind speeds in the range of observations for both groups of stations.
2. Wind did not become a noticeable source of noise at the surface emplacements until a minimum wind speed was reached (typically 4 to 5 m/sec at the sites studied).
3. In the 1-10 Hz band, surface and borehole emplacements in Nevada were generally quieter than those in Kazakhstan.
4. At high frequencies, in the 10-80 Hz band, surface installations in Nevada were considerably noisier than surface installations in Kazakhstan, but borehole installations in both regions yielded comparable noise levels. The difference in surface vault engineering quality between the two sets of stations may be a significant factor.

REFERENCES:

- Berger, J., H. K. Eissler, F. L. Vernon, I. L. Nersesov, M. B. Gokhberg, O. A. Stolyrov, and N. T. Tarasov, Studies of high-frequency noise in eastern Kazakhstan, *Bull. Seismol. Soc. Am.*, **78**, 1744-1758, 1988.
- Hedlin, M., J. Orcutt, J. B. Minster, H. Gurrola, The time-frequency characteristics of quarry blasts, earthquakes and calibration explosions recorded in Scandinavia and Kazakhstan, U.S.S.R, *This Issue*, 1989.
- Li, T.M.C., J.F. Ferguson, E. Herrin, and H.B. Durham (1984), High-frequency seismic noise at Lajitas, Texas, *Bull. Seis. Soc. Am.*, **74**, 2015-2033.
- Rodgers, P.W., S.R. Taylor, and K.K. Nakanishi (1987), System and site noise in the Regional Seismic Test Network from 0.1 to 20 Hz, *Bull. Seis. Soc. Am.*, **77**, 663-678.
- Thompson, R. F., Spline interpolation on a digital computer, (X-692-70-261), 1970, Goddard Space Flight Center.
- Welch, P.D. (1967), The use of Fast Fourier Transform for the estimation of power spectra: A method based on time averaging over short, modified periodograms, *IEEE Trans. Audio and Electroacoustics*, **AU15**, 70-73.

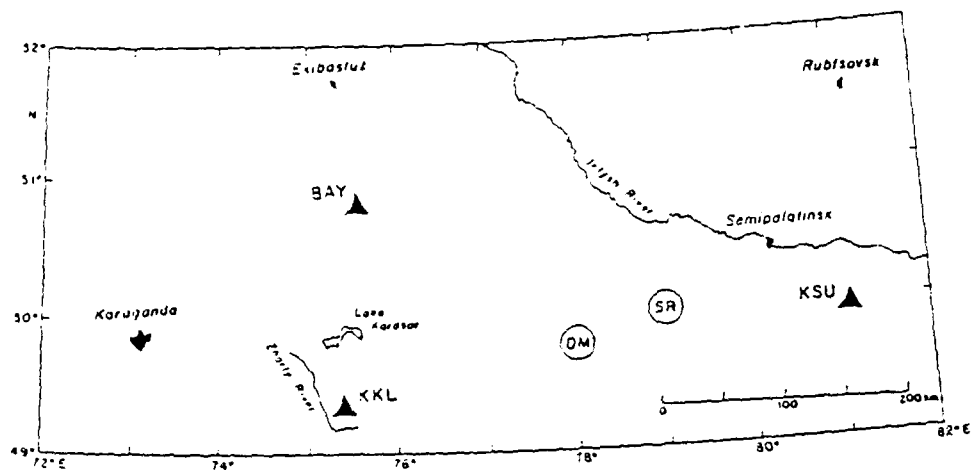


Figure 1. Locations of the three Kazakh seismic stations, Karasu (KSU), Karkaralinsk (KKL), and Baysunbul (BAY).

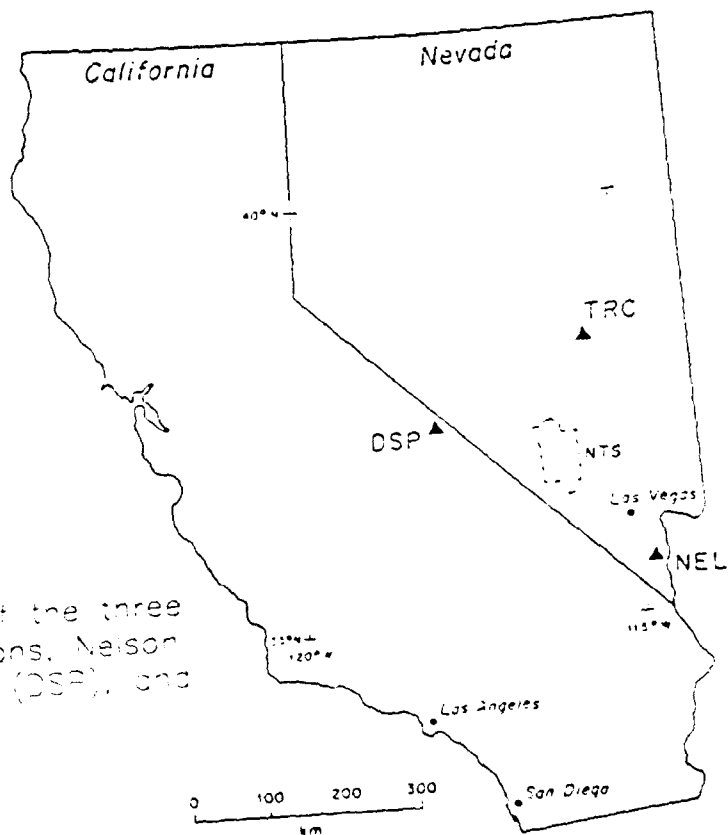
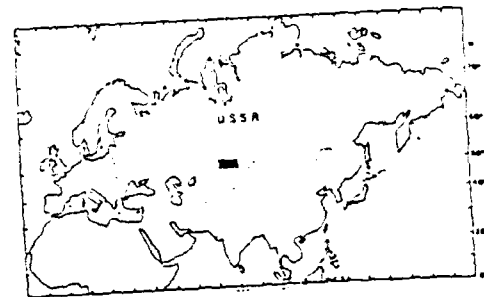


Figure 2. Locations of the three Nevada seismic stations, Nelson (NEL), Deep Springs (DSP), and Troy Canyon (TRC).

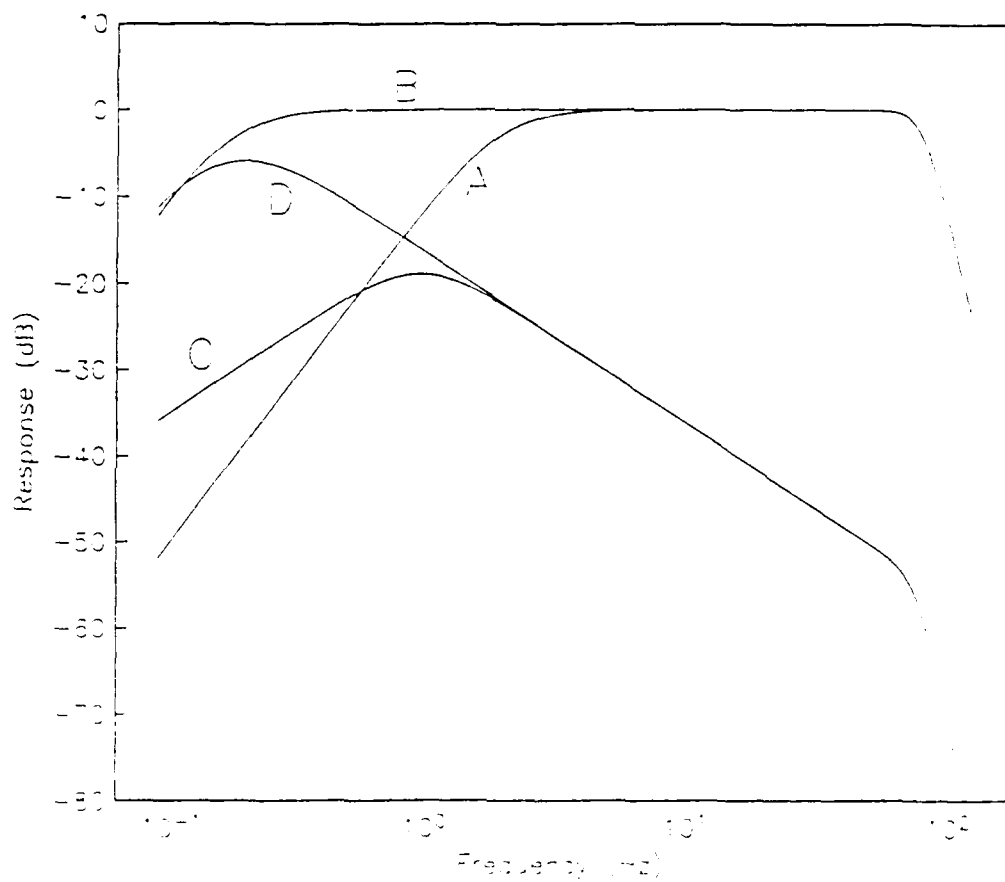


Figure 3. System response (without gains and corrected to acceleration). A and B are the responses of the USA defense systems before and after June 1985, respectively. C is the response of the USA and USSR surface systems. D is the response of the USSR defense system.

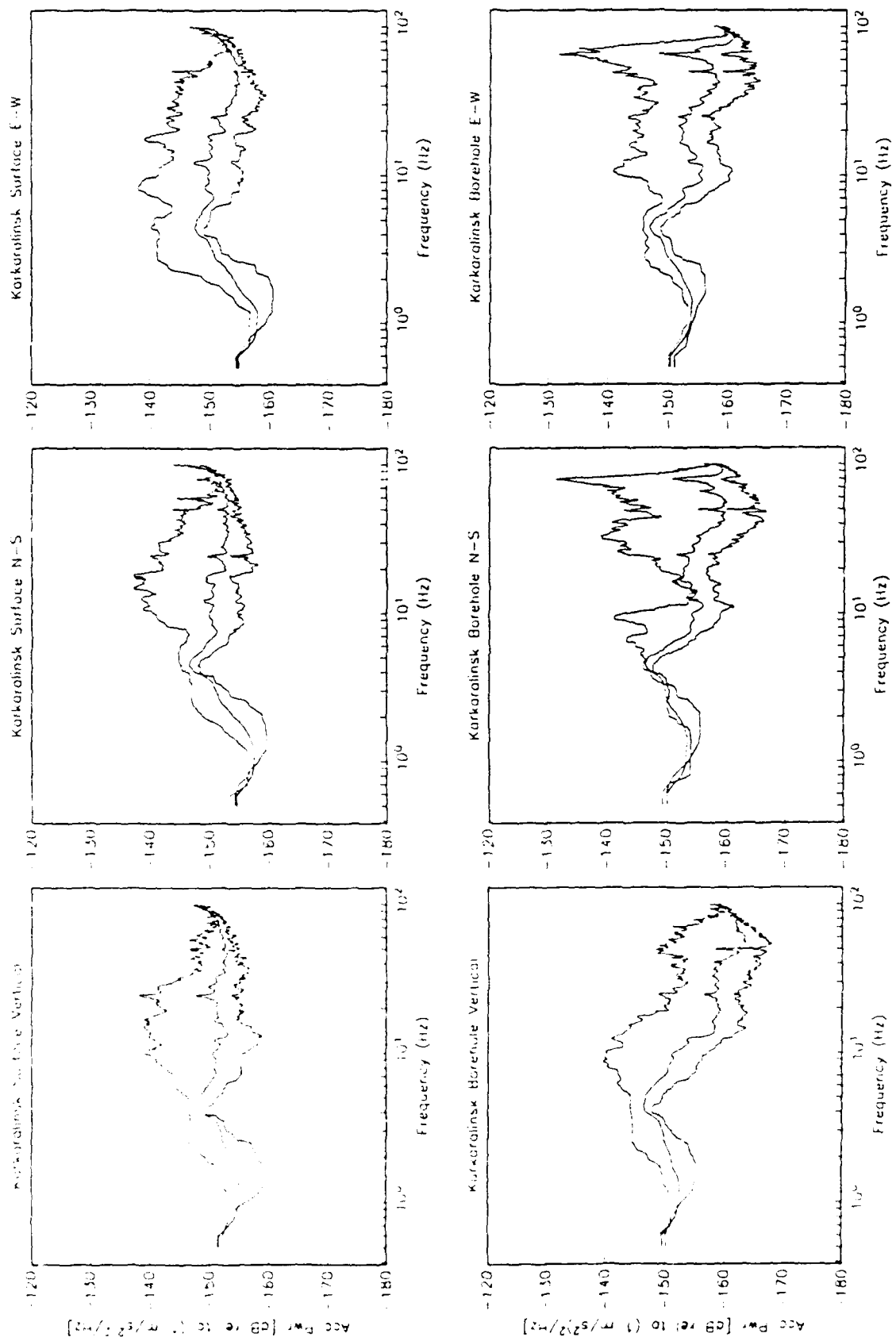


Figure 4. Mean, Maximum, and Minimum noise levels at Korkorlinsk with wind speed less than 2 m/sec.

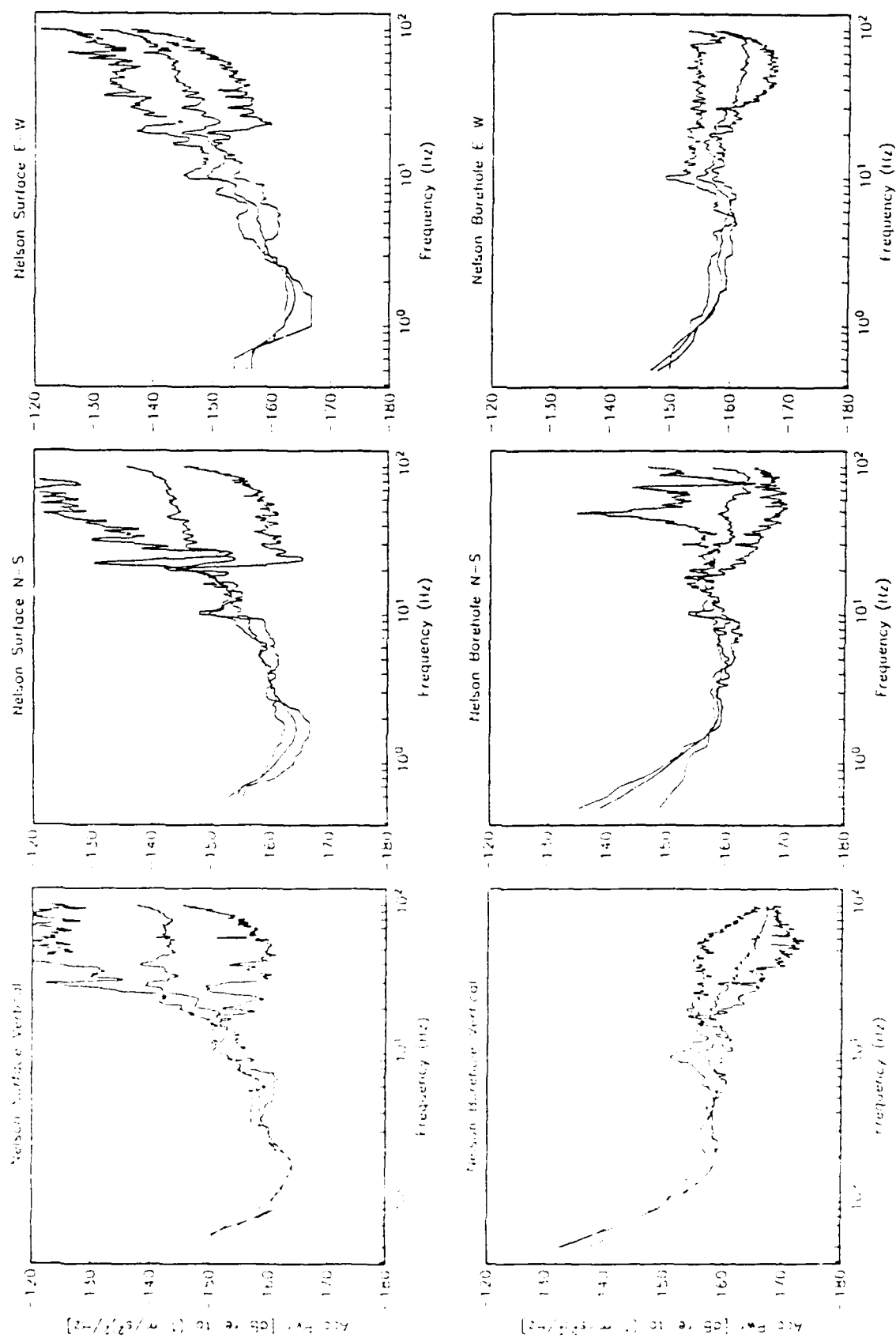


Figure 1. Mean, Maximum, and Minimum noise levels at Nelson with wind speed less than 2 m/sec.

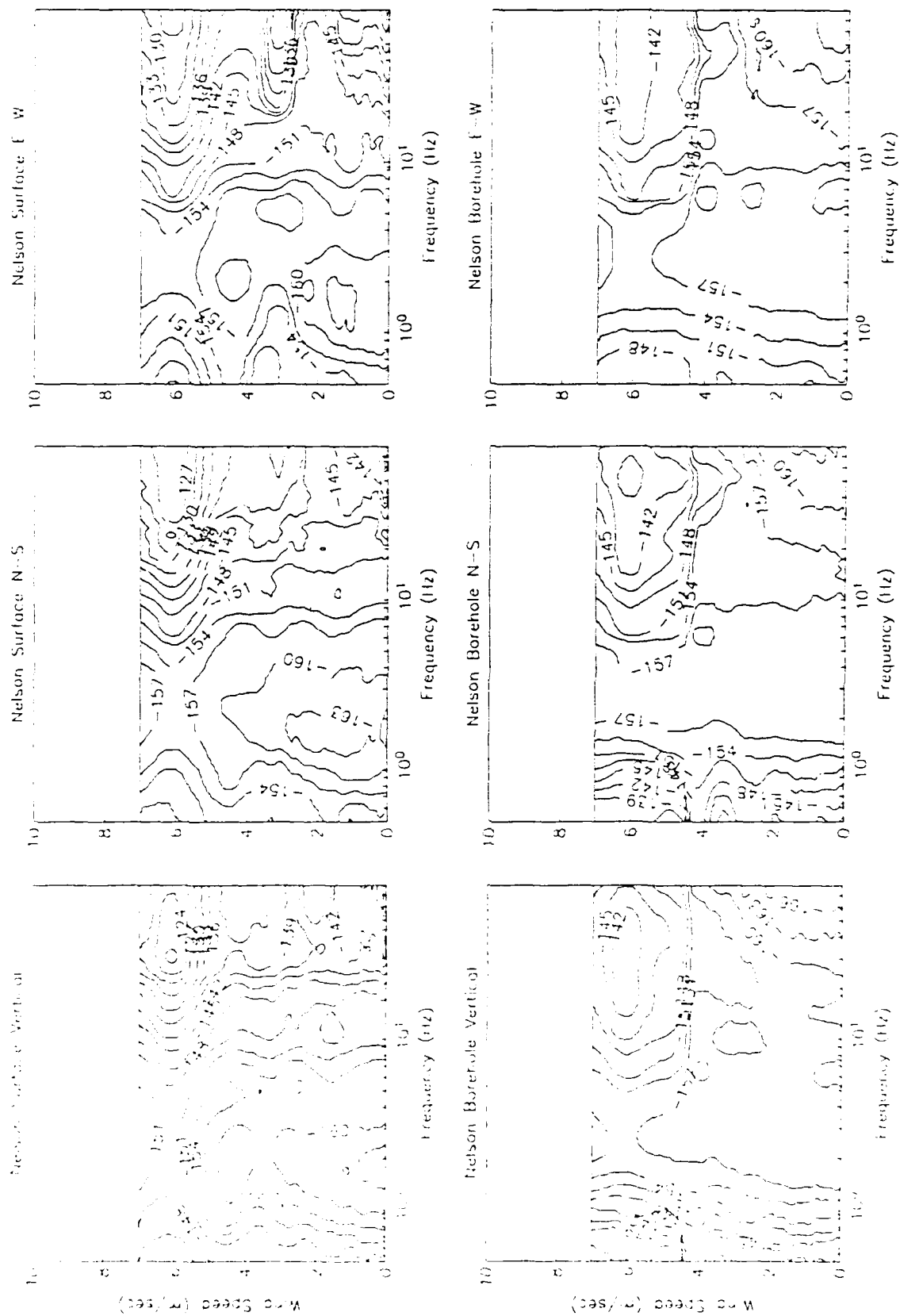


Figure 6. Contour plot (3 dB contour interval) of noise levels at Nelson vs. frequency and wind speed.

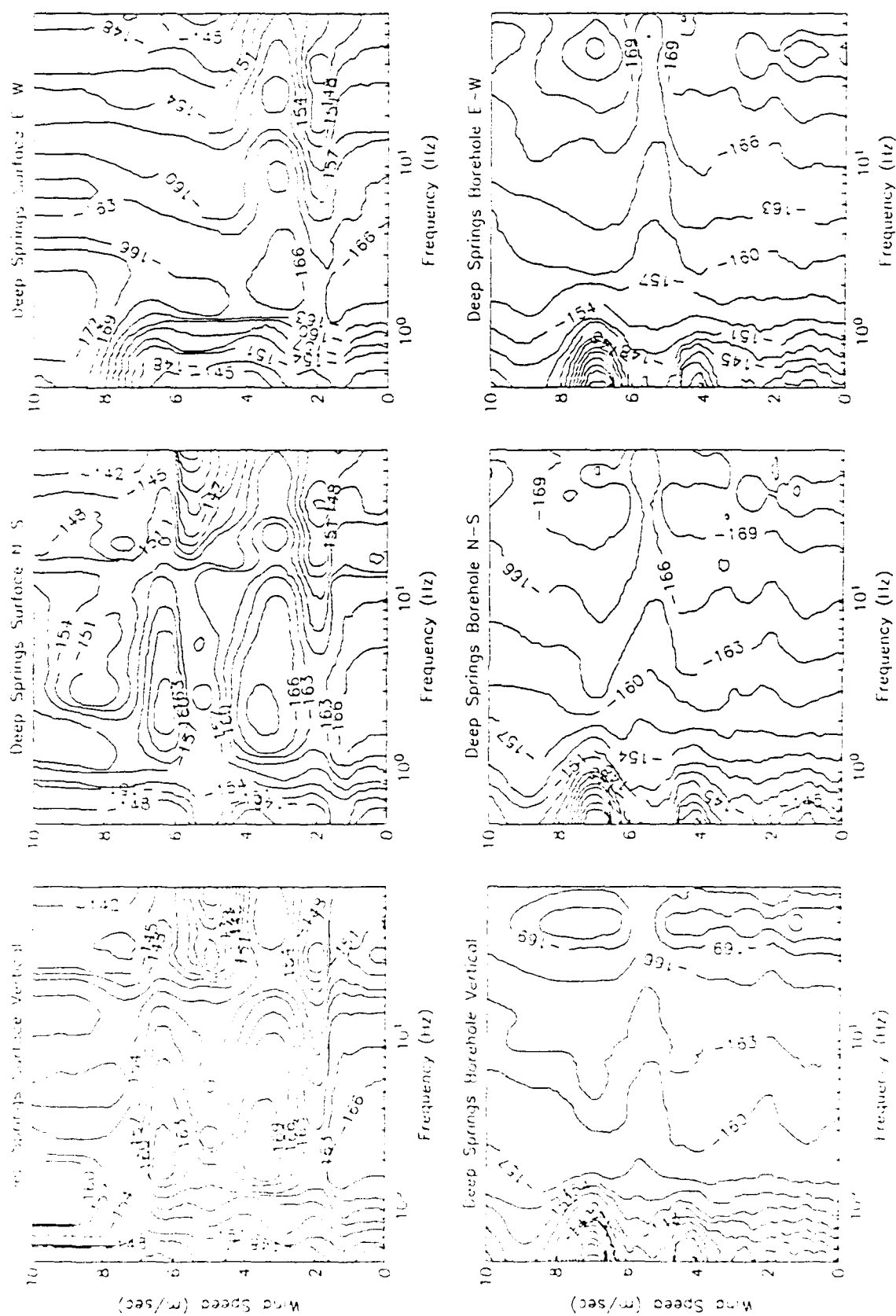


Figure 7. Contour plot (3 dB contour interval) of noise levels at Deep Springs vs. frequency and wind speed.

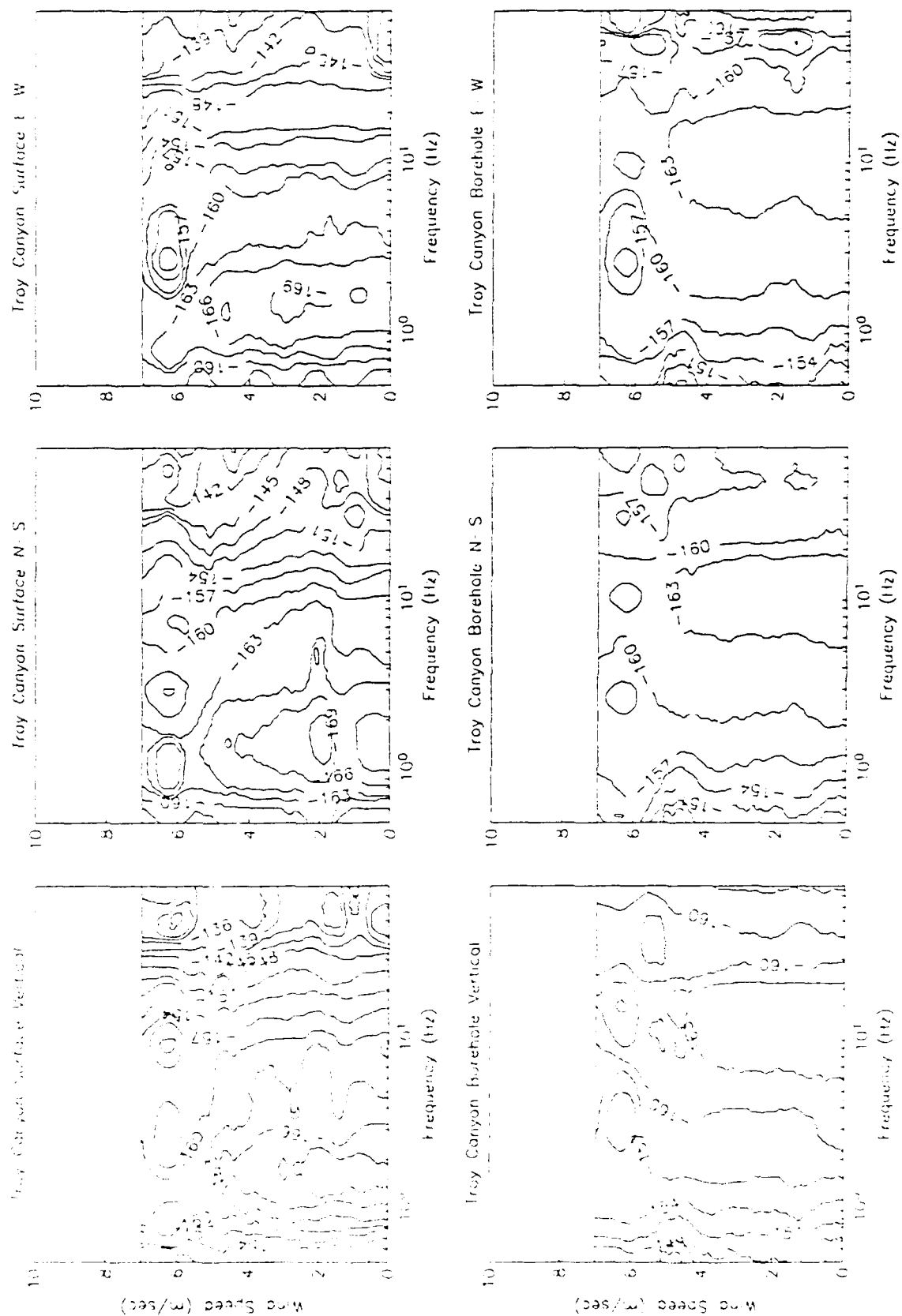


Figure 2. Contour plot (5 dB contour interval) of noise levels at Troy Canyon vs. frequency and wind speed.

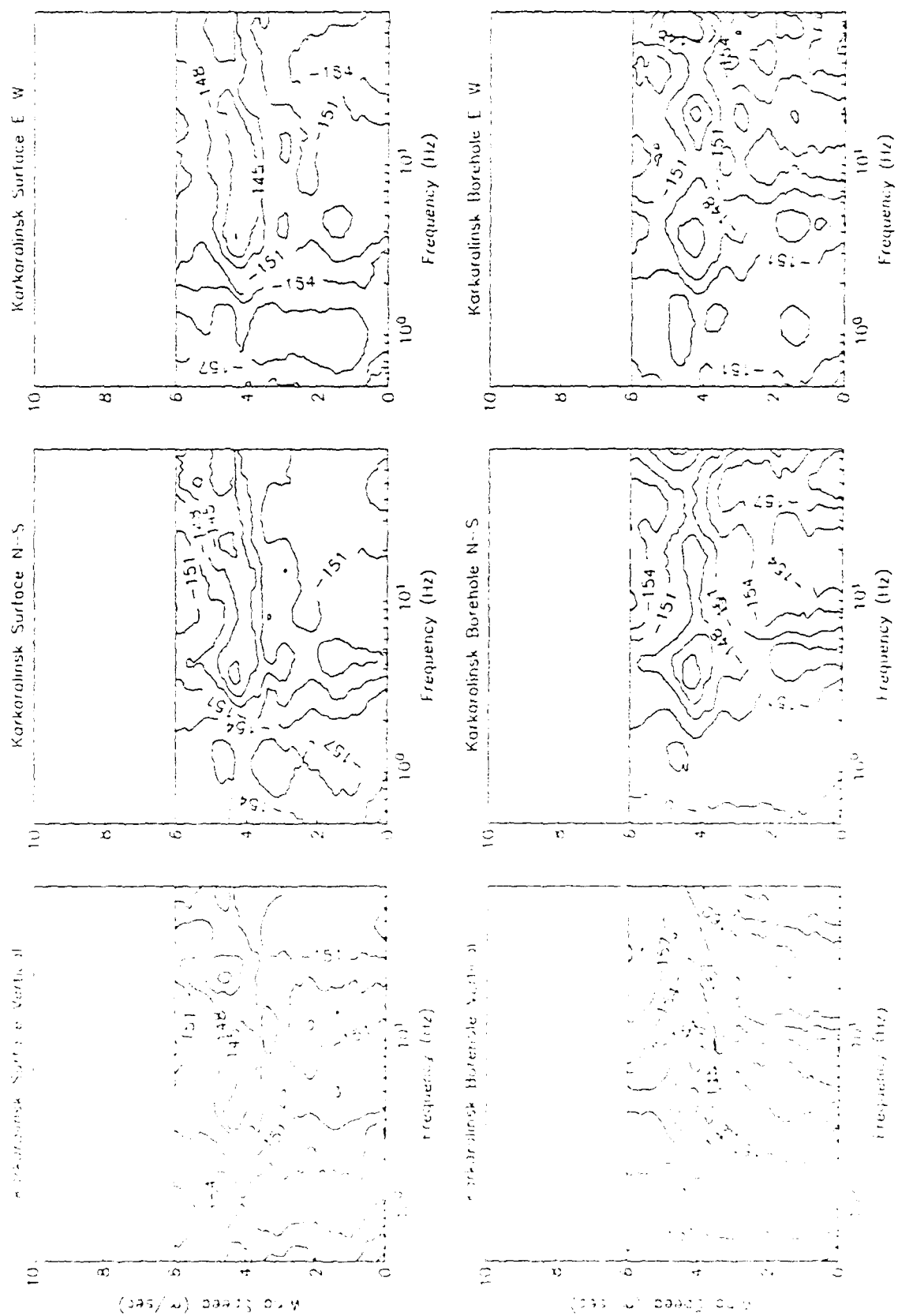


Figure 1. Contour plot (3 db contour interval) of noise levels at Karkaralinsk vs. frequency and wind speed.

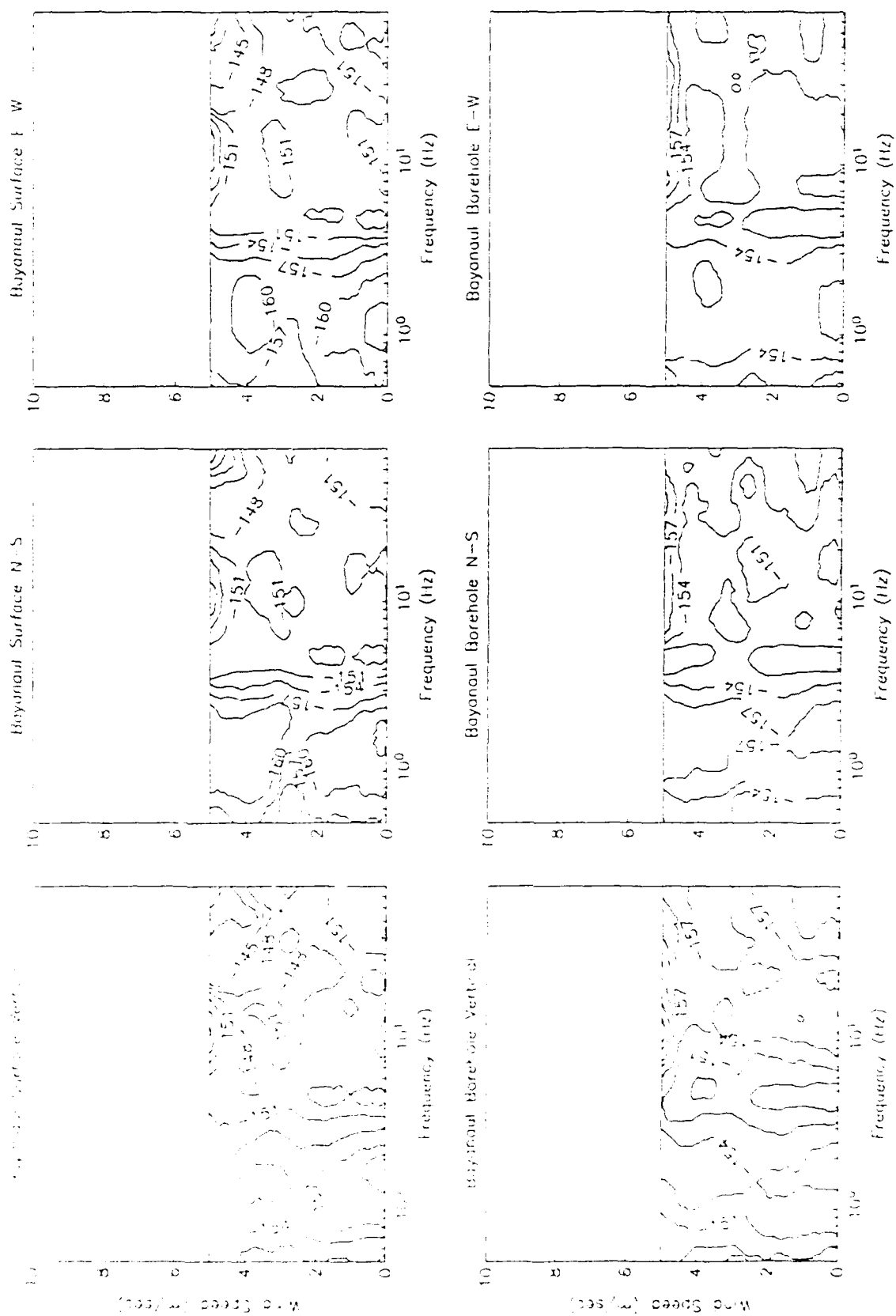


Figure 10. Contour plot (3 dB contour interval) of noise levels at Boyanaul vs. frequency and wind speed.

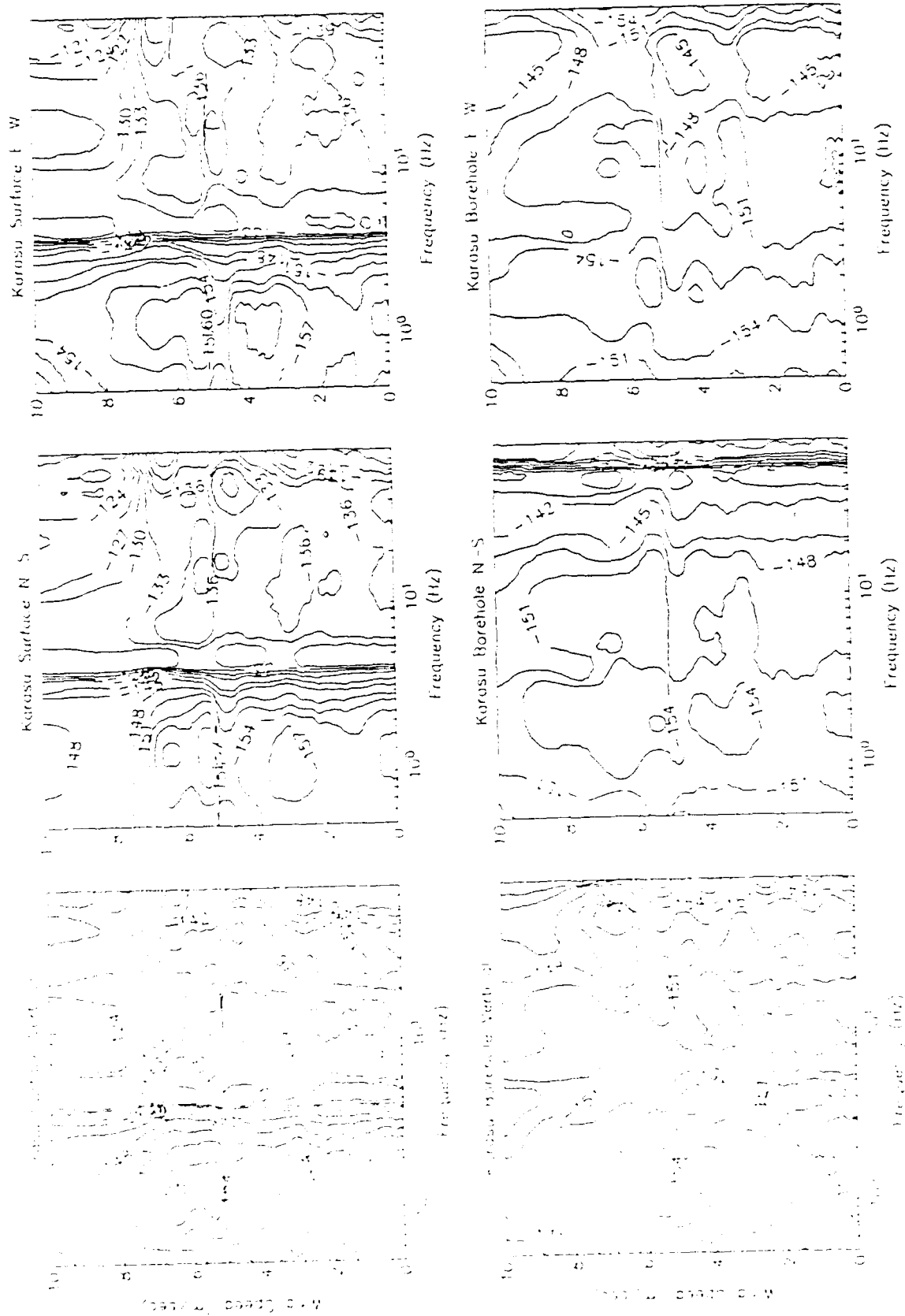


Figure 11. Contour plot (3 dB contour interval) of noise levels at Karasu vs. frequency and wind speed.

CHEMICAL EXPLOSIONS AND THE DISCRIMINATION PROBLEM

Paul G. Richards, Arthur Lerner-Lam, Russell Such, David Simpson

(Lamont-Doherty Geological Observatory of Columbia University, Palisades, NY 10964),

and Douglas A. Anderson (Vibra-Tech Engineers Incorporated, Hazleton, PA 18201-0577)

CONTRACT NO. F19628-88-K-0041

OBJECTIVE

For networks of seismometers that routinely detect signals down to magnitudes around 2 – 2.5, the technically most challenging aspect of identification of nuclear explosions is the problem of distinguishing between chemical and nuclear explosion signals. Our objective is to explore the extent of this problem.

SUMMARY

We have begun two projects. The first, is the acquisition of basic information on the scale of chemical explosion activity (frequency of occurrence, geographic distribution, explosion sizes). The second, is an examination of regional data recorded in New York, to see when "ripple-firing" (called "millisecond delay initiation" by the blasting industry) can be recognized in seismic signals. Results in each project are just beginning to be developed at this time of writing, six months after the contract starting date.

Scale of chemical explosion activity

We are generating a list of chemical explosions in the United States for calendar year 1987 (times, locations, pounds of explosive per delay for each shot, and total pounds of explosive for each shot). A typical report on explosion activity at one location will for example include histograms as shown in Figures 1 and 2. Figure 1 is for a mine that favors a standard number of pounds per delay (750 lbs), using these to build up shots with a variety of total poundage. Figure 2 is for a mine that favors a standard number of total pounds per shot (50000 lbs), built up from delays that cover a range of sizes.

Once developed, this list, and associated maps and histograms describing the activity, can be expected to assist in a practical assessment of detection capability for a variety of seismic networks. For example, various empirical measures of signal strength (such as coda duration) can be calibrated directly in terms of explosion yield; and, at a fixed level of signal strength, the variability of yield (due to differences in source environment) can be assessed.

Observability of ripple-firing in regional seismic signals

Evidence of ripple-firing has been demonstrated recently by Baumgardt and Ziegler (1988), Smith (1988), and Hedlin *et al.* (1989), using spectra and sonograms of regional seismic signals. This success leads in turn to the need to explore what level of seismic data quality is required, both to reveal the occurrence and to characterize the practice of ripple-firing. Thus, for a shot whose total yield (tons of explosive) Y is roughly known, the shot may be a candidate for consideration as n delays with delay time Δt . The need is to develop practical experience in finding what frequency range to instrument, at what distances from the source, in order to gain information on n and Δt .

We are just beginning the study of signal spectra and spectrograms for chemical explosions recorded in New York. An example is shown in Figure 3, of a spectrogram recorded at a standard station of the New York network, that indicates a spectrum with time-independent scalloping of the type expected for ripple-fired explosions.

CONCLUSIONS AND RECOMMENDATION

Our preliminary results indicate the possibility of characterizing chemical explosion activity within the US, and confirm the utility of sonograms/spectrograms for revealing certain chemical explosions as being ripple-fired. We recommend that efforts be extended to survey the extent of chemical explosion activity, at least for large events, in areas of interest for potential future nuclear explosion monitoring.

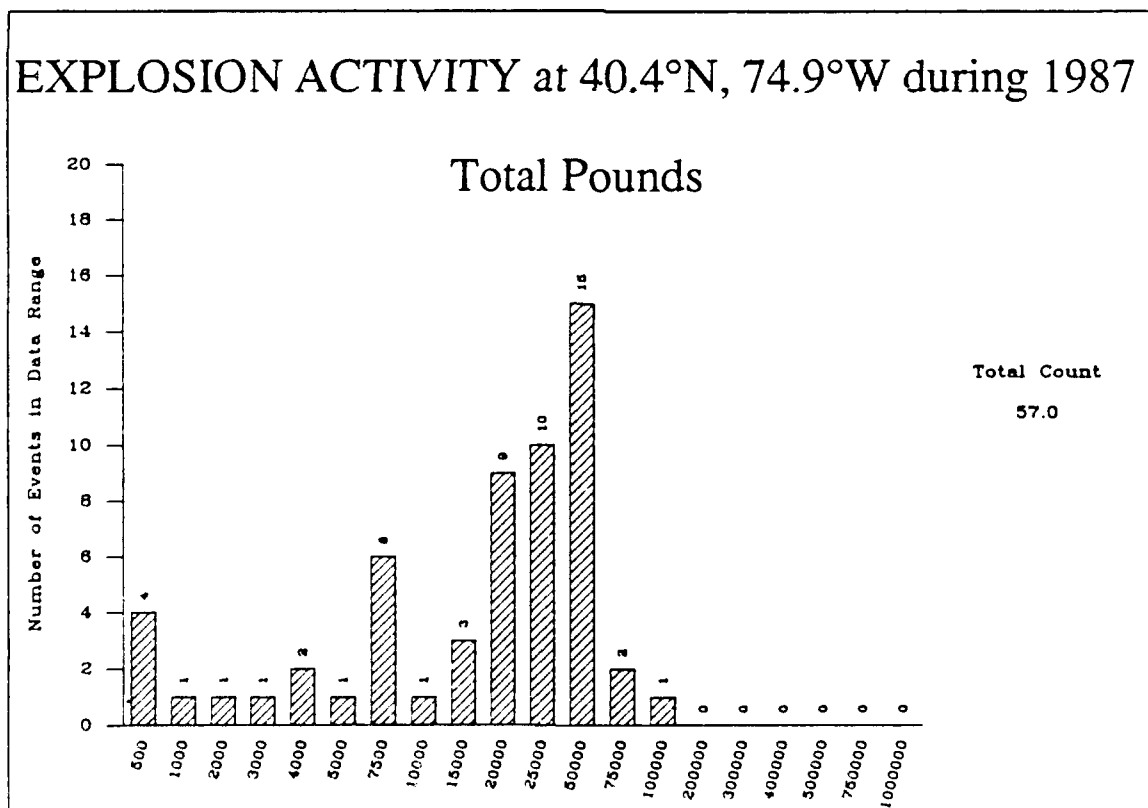
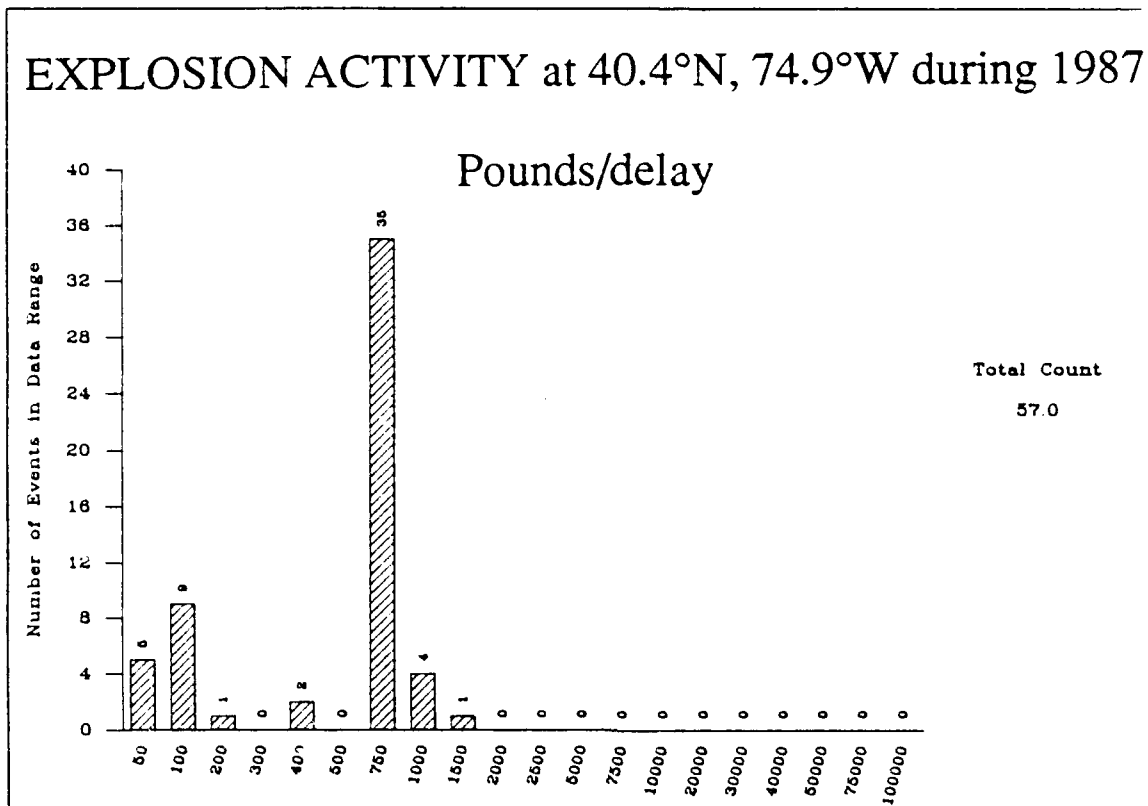
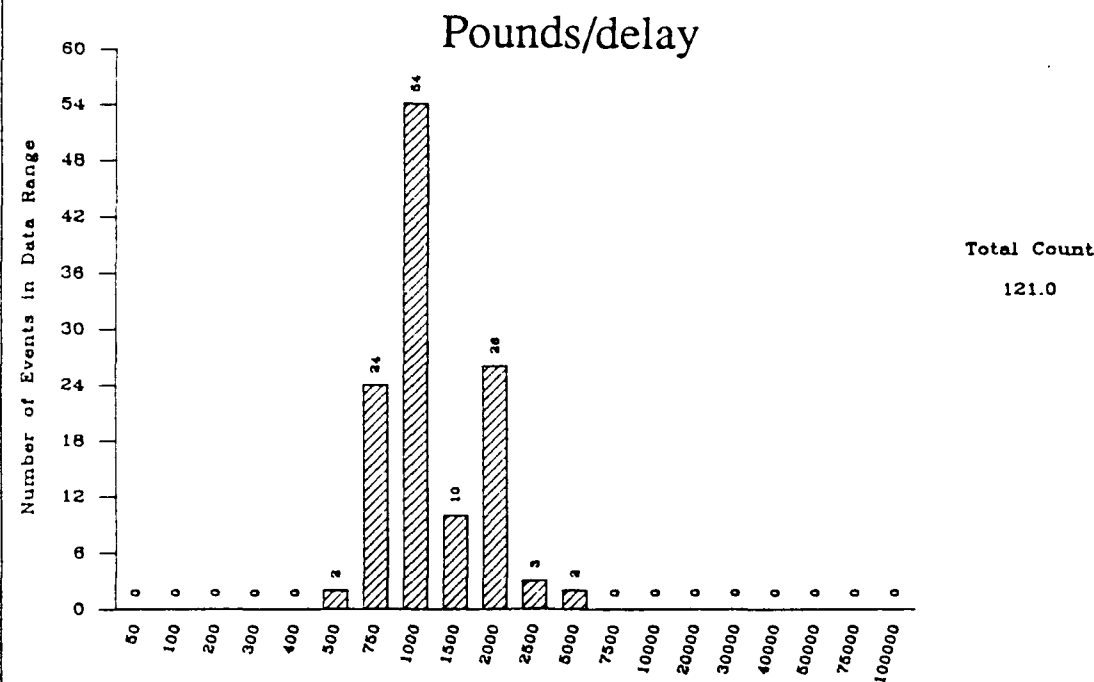


Figure 1. Histograms for pounds of explosive per delay per shot, and total pounds per shot, for a mine in Pennsylvania that favors a standard number of pounds per delay.

EXPLOSION ACTIVITY at 40.8°N, 75.8°W during 1987



EXPLOSION ACTIVITY at 40.8°N, 75.8°W during 1987

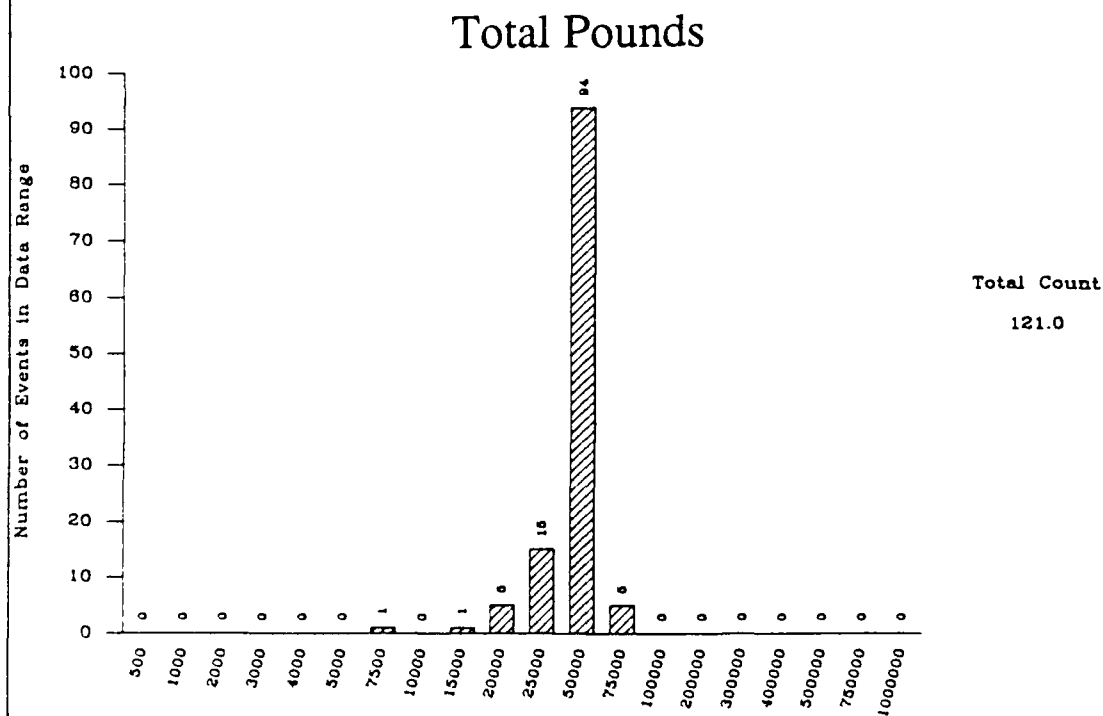


Figure 2. Histograms for pounds of explosive per delay per shot, and total pounds per shot, for a mine in Pennsylvania that favors a standard total number of pounds per shot.

Spectrogram (Linear) Saturated above 3%
of a Ripple Fired Blast
Recorded 890213.150731 at GPDZ 10.5 Km from the Source

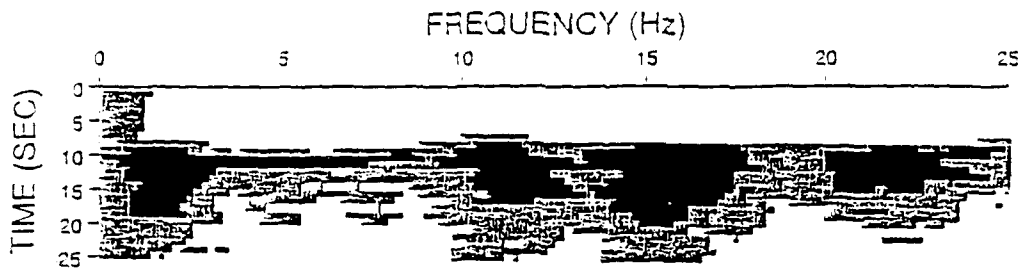


Figure 3. Black and white copy of a color-shaded spectrogram (spectrum as a function of time), for a standard station of the New York State network operated by Lamont-Doherty Geological Observatory.

References

- Baumgardt, D.R., and K.A. Ziegler, Spectral evidence for source multiplicity in explosions: application to regional discrimination of earthquakes and explosions, *Bulletin of the Seismological Society of America*, 78, 1773-1795, 1988.
- Hedlin, M.A.H., J.B. Minster, and J.A. Orcutt, The time-frequency characteristics of quarry blasts and calibration explosions recorded in Kazakhstan U.S.S.R., preprint, 1989.
- Smith, Albert T., High-frequency seismic observations and models of chemical explosions: implications for the discrimination of ripple-fired mining blasts, Lawrence Livermore National Laboratory preprint UCRL-99353.

ANALYSIS OF HIGH-FREQUENCY DATA

Anne Suteau-Henson, Hans Israelsson, Vlad Ryaboy and Alan Ryall

Center for Seismic Studies
1300 N. 17th St., Suite 1450
Arlington, VA 22209

Contract No. F19628-88-C-0159

In this paper we summarize separately three studies currently in progress under Contract Number F19628-88-C-0159, "*Analysis of High-Frequency Seismic Data*." The first and second studies, by Anne Henson and Hans Israelsson, are aimed at developing techniques that can be used in a seismic analysis system for characterization of repeated events such as industrial explosions at specific mines in an area being monitored by a seismic network. The third study, by Vlad Ryaboy, uses NORESS recordings of mine explosions in Scandinavia and the western USSR to modify current models of crust/upper mantle structure in that region, with the objectives of improving NORESS event location capability and of explaining what appears to be an abrupt decrease in high-frequency content of seismic signals at regional distances of 700-800 km. Additional details on these investigations will be reported in a semiannual technical report, C-89-01, to be issued in April.

1. CHARACTERIZATION OF REGIONAL EVENTS RECORDED AT NORESS AND THE NRDC STATIONS

Abstract

Use of 3-D spectrogram plots to characterize regional events is being investigated by Anne Henson, using NORESS recordings of repeated events at distances of 800-1300 km. Small explosions from a mine in northern Sweden show distinctive modulations attributed to ripple-firing for the entire wavetrain, but earthquakes in the vicinity of the mine have smooth spectrograms that are very similar for nearby events. The contamination of secondary phases by the coda of previous arrivals in some frequency ranges is clearly observed. At far-regional distances the usefulness of this method is limited by the narrower bandwidth of the signal. Events recorded by the NRDC network in Eastern Kazakhstan near the Semipalatinsk Test Site were also analyzed. Single explosions, such as three HE calibration shots and the JVE2 nuclear explosion recorded by the University of Nevada-Reno, do not show spectral modulations, as expected. However, spectrograms of presumed mine blasts often have modulations that are similar at different stations, indicating ripple-firing.

Objective

Accurate location and source type identification of small seismic events recorded at local/regional distances depend on our ability to characterize their signals. Regional discriminants have been proposed, including *P*- to *S*-wave spectral ratios, depth phases, and other waveform and spectral characteristics (such as spectral complexity and cepstral peaks). Recent studies using data from the NORESS array include Dysart and Pulli (1988), Baumgardt and Ziegler (1988) and Suteau-Henson and Bache (1988). Although these methods of event characterization have met with some success, there is a need to assess their performance

- as signal-to-noise ratio (SNR) decreases or epicentral distance increases,
- with data recorded at a single station without the benefits of array-averaging,
- when little or no independent information is available, such as with data from the NRDC network within the Soviet Union.

In this paper we begin to address these questions for events at both local and far-regional distances. Event characterization is performed using spectrograms, built from high-frequency spectra covering the entire event. "Control" experiments are performed on a NORESS dataset of earthquakes and mine explosions, calibration shots recorded by the NRDC network of single stations in Eastern Kazakhstan, and recordings of the Soviet nuclear explosion "JVE2" at the same sites. Then, this technique is tested on a dataset of unidentified events in that area.

Summary

The technique used to characterize regional events combines the advantages of waveform and spectral techniques, by making it possible to view and analyze the entire seismic wavefield throughout the event, in both time and frequency. "Spectrograms" displayed as 3-D perspective plots show the variation of spectral content above noise level, as a function of time, for a data segment containing the event. Spectra are calculated for fixed-length (3 to 5 seconds) time windows, using a technique similar to that of Suteau-Henson and Bache (1988). They are formed for the vertical channel (in the case of single-station data), or for each vertical channel and then averaged over all channels for array data. Then, they are instrument-corrected, smoothed, and noise-corrected.

Our first dataset includes events recorded at the regional array NORESS and detected by the Helsinki network, which were located at distances of 800 to 1300 km, in a N-NE direction. The Helsinki bulletin also listed their local magnitude (ranging from 2.0 to 3.6), and indicated that most were explosions from known mines. Of particular interest are a set of earthquakes with magnitudes of 2.9 and above from a seismic area in Northern Sweden, and a set of 16 explosions with magnitudes of 2.0 to 2.7 from a nearby mine at ≈ 800 km distance from NORESS (designated as "R1" in the Helsinki bulletin). Since these events are located in the same area, spectral differences due to regional path effects are not expected to be dominant, and source effects can easily be observed.

Figure 1 (top) shows the spectrogram for an R1 explosion. All R1 events have characteristic spectral modulations that last throughout the entire wavetrain. As expected, they become less visible as the magnitude (and SNR) decreases, although they can still be observed for events with magnitude as low as 2.0. The S_n spectral content is very similar to that of P_n for the entire coda. In contrast, L_g is characterized by much lower frequencies. For larger events, S_n arrives in the P_n coda, therefore some frequencies are contaminated by P -type signal. A worse contamination occurs for L_g , which arrives in the P_n/S_n coda.

The spectrogram for one of the nearby earthquakes is shown in *Figure 1* (bottom). As for R1 events, the S_n and P_n spectral contents are very similar for the entire coda, while L_g has much lower frequencies. Also, each secondary phase is contaminated by coda energy from previous arrivals. Apart from this, in spite of nearby locations, the earthquake spectrograms are remarkably different from those for R1 explosions. First, the ratio of P to S energy is much smaller, as expected. Second, the spectrograms do not show any spectral modulations and are generally lacking in character. They are

very similar for two earthquakes located only 14 km apart by the Helsinki network. Explosions from more distant mines V10 (≈ 1100 km from NORESS) and K1 (≈ 1300 km) were also analyzed. At K1, the available signal bandwidth is so narrow, due to strong attenuation of higher frequencies, that spectral modulations could not be observed.

Next, we evaluated the use of this technique for events (mostly local) recorded at one or two single stations of the NRDC network, located in Eastern Kazakhstan near the Soviet Test Site, and consisting of three three-component stations at Karkaralinsk (KKL), Karasu (KSU) and Bayanaul (BAY). Station KSU was not used, because of a pronounced resonance peak due to near-receiver structure. The NRDC short-period data have a Nyquist frequency of 125 Hz, but we found that the useful frequency range was limited to half of that.

Figure 2 (top) shows the spectrogram at station BAY for one of three known H.E. calibration shots. These are single explosions, and, as expected, no spectral modulations are observed. Since no array-averaging could be performed, the non-stationarity of the noise produces many noise peaks. Also, the scatter in the spectrograms is much larger than for NORESS events. We also obtained spectrograms for a nuclear explosion, the JVE2 event at the Soviet Test Site, recorded with UNR instruments. One is shown in *Figure 2* (bottom). As expected, no spectral modulations are observed. Above ≈ 30 Hz, the spectral amplitude above noise level remains roughly constant, instead of continuing to decay, as it does for the calibration shots. The character of the data above 30 Hz seems to indicate an instrument-related artifact, correlated with the actual signal, so we cannot ascertain that the source of the JVE2 event was particularly rich in higher frequencies.

Finally, we analyzed a set of unidentified events recorded at the NRDC stations. *Figure 3* (top) shows the spectrogram for a presumed local mine blast, at station BAY. This and some other presumed explosions show spectral modulations (similar at all stations that detected), but others do not. Hedlin *et al.* (1988) report observing such modulations for presumed explosions, indicating ripple-firing. The spectrogram at station BAY for a presumed earthquake at ≈ 1100 km (*Figure 3*, bottom) has no complex character, as expected.

Conclusions and Recommendations

We have shown how spectrograms can be a useful tool to characterize events, especially during an analyst review, because of the amount of visual information present. For example, distinctive patterns of modulations can help identify an event as an R1 explosion, down to local magnitudes of 2.0. For secondary arrivals, a spectrogram can help select those parts of the wavetrain (as areas in the time-frequency domain) which are the least contaminated by interfering signals from previous arrivals. Such information can then be used for optimal spectral and/or cepstral measurements of potential discriminants. Modulation patterns were not usually observed for more distant mines (although more data should be analyzed before definite conclusions can be reached): small bandwidth due to attenuation of high frequencies limits the usefulness of spectral modulations as a discriminant at distances beyond 1000 km.

The scatter in the spectrograms of events recorded at NRDC stations is larger than at NORESS, due to lack of array-averaging, thus increasing the uncertainty attached to this characterization technique. Spectrograms can still be used as part of event identification at single stations, when no information from independent networks is available. The presence of distinctive spectral modulations can confirm or establish that an event is an explosion. In their absence, no conclusion can be drawn. We recommend evaluating the use of interactive analysis graphics to compare

spectrograms of unidentified and reference events, and extract characterization parameters from carefully selected parts of the spectrogram.

2. WAVEFORM CORRELATION OF CLOSELY SPACED REGIONAL EVENTS

Abstract.

Hans Israelsson has analyzed NORESS high-frequency waveforms of 137 small events in mining districts of Central Sweden, at an epicentral distance of about 200 km. The events were grouped using hierarchical clustering based on correlations involving the covariance matrices (Jurkevics, 1987) and maximum amplitudes of three-component recordings. The events separated into one large group of 98 events and a few smaller groups with 2-5 events each. Epicenters of events in the large group are scattered over an area 20 by 75 km. If one assumes that these events had the same location, the 95% confidence region of the epicenter has an aperture of less than 1 km, which is consistent with the so called quarter-wavelength argument. High cross correlations at frequencies above 15 Hz were obtained for one of the smaller event groups. These frequencies are significantly higher than those reported for short distances in other studies, and the quarter-wavelength argument constrains the epicenters of these events to within 100 m.

Objective

In regional seismic monitoring one sometimes distinguishes between *model* based and *case* based approaches to identify seismic events (Dysart and Pulli, 1987). The model based approach aims at defining some discriminant from the recorded waveforms that will in general identify events regardless of region. The discriminant should also relate to the physics of various seismic source types, like the ratio of radiated P and S wave energy. In spite of a number of studies no single model based method has so far been defined that performs successfully regardless of region. The case based approach attempts to take advantage of the repeatability of records from events in the same source area for location and identification. Similarities of waveforms recorded from closely spaced sources have been reported for several regions in the literature, and experienced analysts are often able to identify events from particular locations from visual inspection of the recorded waveforms. This ability is based on knowledge acquired from the recordings of many events from a particular source area, and a new event is identified by waveform comparisons with events previously recorded in the region.

In spite of known cases of waveform repeatability, the case based approach has not yet been fully explored, and the number of observations used to demonstrate repeatability are usually quite small compared to the total number of regional events that are detected and located. The purpose of this research is to study repeatability and patterns of regional records from a fairly large number of events within a small area. Attempts are made to utilize automatic procedures to compare and group seismic waveforms.

Summary

Selection of events for analysis

The seismic events used in this study were located within an area 50 by 200 km in Central Sweden. This area has the highest density of events that are detected and

located by NORESS, and most of them are located in mining districts and are presumed to be detonated by ripple firing. Because of current interest in high frequency recordings and the short epicentral distances (around 200 km), data recorded by the high frequency (Geotech GS-13) element of NORESS were selected for the analysis.

Waveform data for 222 events in central Sweden were and reviewed for data quality. Eight-five were rejected for various reasons, leaving 137 events to be used in the analysis. The procedure used to arrive at these events, which make up about 10% of the total number of events that were detected and located in the area, can be considered as a random selection.

The events have median ML of 1.2, with a range of 0.8-2.1, and ML is approximately normally distributed for $ML < 1.5$. None of the events were reported in the seismic bulletins based on local station networks in Fennoscandia and the location accuracy was therefore limited by uncertainties in the backazimuth and distance determinations using the NORESS array data.

The P/S wave amplitude ratio ranges almost over half an order of magnitude for the events studied, indicating considerable variation among the waveforms. We also note that The phases P_g/P_n and S_g/S_n have theoretical arrival times within a few seconds or less for a distance of 200 km, so we would expect some interference between these phases. Synthetics calculated with the reflectivity method and with the standard flat layer velocity model used in the NORESS locations suggest, however, that P_g and S_g are the most prominent phases in this distance range.

Signal to noise ratio as a function of frequency

Since most of the events are in the low magnitude range attempts were made to define a frequency band with good signal-to-noise ratio for the subsequent signal processing. The signal-to-noise ratio was calculated as a function of frequency for each event. Each record was filtered by a set of narrow bandpass filters that were obtained from low and high pass Butterworth (three-pole) filters both at frequency f varying from 0.1 to 50 Hz in increments of 0.1 Hz. The SNR at frequency f was then defined by the ratio:

$$SNR(f) = \frac{\max_m |s(m; f)|}{\max_m |n(m; f)|},$$

where $n(m; f)$ is noise prior to signal onset in a time interval of about 12 seconds as shown in Figure 4, and $s(m; f)$ denotes the signal segment. The maximum amplitudes of the noise and of the signal segments was determined in the proper time intervals. Ratios were calculated as marked in Figure 4 for the four signal intervals P, P-coda, S, and S-coda.

The $SNR(f)$ for the two events in Figure 4 is typical of the data, and these functions usually show a pronounced peak at some frequency which we call the *peaking frequency*. If the peaking frequency were the same for all events a bandpass at that frequency would thus provide maximum signal-to-noise ratio. Plots of peaking frequencies for P and S wave intervals against SNR showed a strong concentration of the peaking frequencies in the band 2.5-4.0 Hz for both P and S waves, and we will subsequently use this band for prefiltering of the data.

For only about 10% of the events did the peaking occur at about 15 Hz or higher. The fact that the maximum signal-to-noise ratio mostly occurs at such low frequencies

could be due to the increased noise levels at high frequencies during daytimes when most of the events were recorded. Many of the events are also believed to be ripple-fired, and delayed firing of shots may well reduce the high frequency content (Willis, 1963).

Waveform Similarity measures

In order to compare the waveforms recorded from the events we use quantitative measures based on polarization (Jurkevics, 1987) and relative amplitude of the records. In polarization processing various useful attributes like particle-motion ellipticity and orientation can be extracted from the polarization ellipse, which in turn is defined by the three polarization axes solved from the covariance matrix of the recordings of the three instrument components. Rather than using such polarization attributes we employ the approach by Jurkevics (1987) that simply forms particle motion signatures from the covariance matrix.

Similarity Measures

The filtered (between 2.5-4.0 Hz) seismogram of component i ($i=1,2,3$) for event k is denoted $s_{ik}(m)$. For each event, k , the covariance matrix R_{ijk} of the components i and j as a function of time t is defined as follows:

$$R_{ijk}(t) = \sum_{m=-T/2}^{m=T/2} \frac{(T-2m)}{T} \cdot s_{ik}(t-m) \cdot s_{jk}(t-m)$$

The matrix R_{ijk} is the 3 by 3 matrix of coefficients for a quadratic form which is an ellipsoid and is symmetric with six unique terms. The three diagonal terms of R_{ijk} are simply the envelopes of the three component motions as a function of time. The three unique off-diagonal terms are the cross-products between components, which provide important information about the phase and orientation of the particle motion.

The data were windowed into short overlapping time segments, T seconds wide. The data window was tapered, and its width was related to the center frequency of the pass-band in such a way that each frequency component is assumed to be purely polarized over several cycles of duration. The tapered sliding data window has a smoothing effect that will make the signatures less sensitive to minor variations in source and path properties. We used a window length of about $T=1.5$ seconds and moved the center of the time window in steps (t) of about 0.5 s. *Signature correlations* were calculated from a data window covering the entire wavetrain, including both P and S phases.

Cross correlations between events k and l were obtained by cross correlating the signature traces R_{ijk} and R_{ijl} . A summation of these cross correlations over the channels i and j (in all six unique) was then used to define a similarity measure, $\rho_{kl}(\tau)$:

$$\rho_{kl}(\tau) = \sum_{i \geq j} \left[\sum_t R_{ijk}(t) \cdot R_{ijl}(t-\tau) / \sqrt{\sum_t R_{ijk}^2(t) \cdot \sum_t R_{ijl}^2(t-\tau)} \right]$$

To account for different amplitudes in the comparison of waveforms, we define the maximum amplitude of the three component recordings from the maximum amplitudes (positive or negative) of one of the components (vertical, $i=1$):

$$A_k = \max \left(\max_m (s_{1k}(m)), |\min_m (s_{1k}(m))| \right)$$

The maximum amplitudes defined in this manner can in turn be used to define the following measure of similarity between amplitudes of two recordings:

$$\rho_{kl}(A) = \sqrt{\min \left[A_k/A_l, A_l/A_k \right]}$$

This measure was normalized and was always in the interval (0,1). Because of the square root it is not too different from 1 in cases with minor amplitude differences.

These two correlation measures were finally combined to define the total correlation, ρ_{kl} , between waveforms of events k and l :

$$\rho_{kl} = \rho_{kl}(A) \cdot \max_{\tau} \rho_{kl}(\tau)$$

The total correlation defined in this manner was used in the analysis of the events. Examples of particle signatures and correlations are given in *Figure 5* for event pairs with high and low total correlation values, ρ_{kl} .

Correlation Values

Correlation values ρ_{kl} were calculated for all possible (9,316) event pairs. In order to group similar waveforms we need to specify some cutoff value of ρ_{kl} above which waveforms are considered similar. The correlation ρ_{kl} depends on the signatures of all components and their relation to each other, and will therefore be sensitive to location of the event, in particular backazimuth since the events are presumed to have similar epicentral distances.

We use the uncertainty of the NORESS estimates of backazimuth to define this cutoff value. The standard deviation of backazimuth is between 6 and 7 seven degrees, and we use here a minimum of 6.2 degrees obtained from comparison with locations of local station networks for a regionalized set of events. In other words, we assume that the error in backazimuth determined by NORESS for a group of events with identical sources and locations would have a standard deviation of 6.2 degrees and the difference in backazimuths determined independently of pairs of such events would then have a standard deviation of $\sqrt{2} \cdot 6.2 = 8.8$ degrees. If the events were gradually separated from each other the standard deviation of the difference in backazimuths would increase, and the correlation between waveforms would drop. This behavior was confirmed by plotting the standard deviation of azimuth differences as a function of correlation value for all event pairs. The plot showed that for backazimuth standard deviations above our *a priori* value of 8.8°, correlation increased with decreasing azimuth, up to a correlation value of 0.7; for larger values of the correlation the standard deviation in azimuth stayed pretty much the same as our expected value.

We used $\max_{l \neq k} \rho_{kl}$ as an indicator of the similarity of event k with that of the rest of the events. In other words if this value for a given event k is high there is at least one other event with a similar record, but if it is low the event would appear as "unique" in the data set. A histogram showing the distribution of these maximum values indicated that 24 events (or about 17% of the total) had $\max_{l \neq k} \rho_{kl} < 0.7$ and would therefore be characterized as unique.

Event grouping

The locations and source properties for the events studied here are not precisely known, but from a visual inspection of the records it is reasonable to assume that there are a number of events with close locations and similar source characteristics. We can therefore attempt to group the data so that events within groups are similar and unlike those from other groups without assuming anything about the number of such groups. This problem can be formally analyzed with clustering analysis techniques (Everitt, 1986).

As a first attempt with this technique we apply hierarchical clustering, which operates on the matrix of pairwise correlations between the event waveforms. The hierarchical clustering consists of a series of "fusions" of events into groups, and in each step in this process events or groups of events that are most similar are fused together. We use the single linkage method, in which the groups initially consist of single events. As the clustering proceeds, groups are fused according to members with highest correlation. The correlation between groups is defined as the highest correlation between members.

The results of this clustering are summarized by a *dendrogram* or cluster structure tree in *Figure 6*, which shows the successive fusions of events (Everitt, 1986). If we use 0.7 as a cutoff value between groups, the events can be grouped into one large group with 98 members according to the dendrogram. In addition, there are two groups with four and two groups with two members. In the larger group there are also three sub groups with very high correlation (above 0.85) among the members. That is to say that about 80% of the events can be grouped, in one way or another, with one large group that contains about 70% of the events.

The hierarchical clustering gives a re-ordering of the events as described by the dendrogram, resulting in similar waveforms being adjacent to each other. A plot of all vertical-component waveforms was generated in the order of groupings on the dendrogram. While several waveforms were nearly identical over the entire length of the records, most groups included only two or three events and no large suite of events was observed with nearly identical waveforms. It should be noted that the similarity measure used here depends on the horizontal components as well as the vertical, and that it is not a direct correlation between waveforms but between the smoothed envelopes of the seismograms.

Similarity at High Frequencies

The results for waveform correlation presented above are limited to a band with rather low frequencies, 2.5-4.0 Hz, since the signal-to-noise ratio is usually low at higher frequencies. There were, however, some events with high signal-to-noise ratio at high frequencies, like a suite of five events all with NORESS epicenters at 60.8N and 15.3E. Correlation values based on the particle motion signatures were calculated for these events for portions of the records that were windowed for P and S waves. High correlations (0.90 or more) were obtained for data up to 20 Hz for P waves and 15 Hz for S wave data.

Considering the 200 km epicentral distance for these five events, the frequencies at which their waveforms have strong correlations are high compared to results from other studies. Thorbjarnardottir and Pechmann (1987) study data recorded from mine blasts at about 100 km and obtain correlations (between two traces) around 0.6 or higher in the frequency band 2-4 Hz, but little or no correlation at higher frequencies. Geller and Mueller (1980) observed very high correlations for regional earthquake data at less than 100 km for frequencies up to about 5 Hz. Lack of correlation at higher frequencies was attributed to very small scale crustal heterogeneities and scattering.

Spatial Clustering

As a quantitative statement about the spatial clustering of earthquake aftershocks it has been suggested that events with very similar waveforms at a particular wavelength can be assumed to have source locations within one-quarter of that wavelength (Geller and Mueller, 1980). Results for records of mine blasts by Thorbjarnardottir and Pechmann (1987) provide support for this hypothesis. If we assume that events grouped together by the similarity measure also have the same location, an

improved estimate of the epicenter can be obtained from the NORESS locations of these events and *a priori* assumptions about the uncertainties in the determinations of backazimuth and distance. This topic was considered as part of the present study and is included in an expanded writeup in *Center for Seismic Studies Technical Report C-89-01 (in press)*. If we use this argument for correlations at high frequencies for the group of events near 60.8N and 15.3E, the quarter wavelengths are about 100 m or less (assuming P velocity of 6.2 km/s).

NORESS locations of the events in the large group were scattered over an area of 20 by 75 km. If one assumes that these events had the same location the 95% confidence region of the epicenter has an aperture of about 10 km. If the waveform correlation between nearby events decreases monotonically as a function of source separation, then it should be possible to determine epicentral separation of nearby events from their correlation values. A numerical example of this is provided in Center Report C-89-01.

3. STUDY OF UPPER-MANTLE STRUCTURE ALONG THE PROFILE OSLO-HELSINKI-LENINGRAD

Abstract

Approximately 150 NORESS recordings of mine explosions detonated along a west-east profile from NORESS to Helsinki to Leningrad have been studied by *Vlad Ryaboy*. The events were 250-1,300 km from NORESS, and had mb in the range 2.0-3.5. Event locations listed in the Helsinki Bulletin had less error than NORESS locations, and were used as the basis for constructing record sections. Analysis of mantle wave signals from the explosions showed that first arrivals could be followed continuously to a distance of 750-800 km, where there is a cutoff and shift of approximately 1.5-2.0 seconds in the traveltime curve, and an increase in apparent velocity. An upper-mantle velocity model based on this data consists of two layers, each with increasing velocity with depth, separated by a low-velocity layer. In the lid (depth 40-105 km) velocity increases from 8.1 to 8.55 km/sec; from 105 to 125 km depth, the velocity is 8.0 km/sec; and for 125-200 km velocity increases from 8.55 to 8.65 km/sec. Because of ambiguities in the inverse seismic problem, there is a tradeoff between the thickness of the low-velocity layer and its velocity. This model offers a possible explanation for observations by the NORSAR group (Ringdal *et al.*, 1986; Mykkeltveit and Ringdal, 1988) of an abrupt decrease in the amplitude of high-frequency seismic signals in the 600-800 km distance range.

Objective

The purpose of this study is to answer questions related to the siting of stations in a region (*e.g.*, USSR) for which the US has little or no regional seismic data, but where an extensive body of published geophysical work exists and can be used to develop at least a starting model of crust-upper mantle structure to use in processing data from a verification network. In such a situation procedures would have to be developed for selecting, checking, modifying and extending available structural models using data from the new stations. For a sparse network of stations, in particular, accurate knowledge of structure will be critical in attempting to locate events recorded at far-regional distances (1,000 km or more) by one or two stations or a single seismic array. Structural details will also be important in determining the detectability of specific seismic phases over particular frequency bands and distance ranges, and such information can be used in turn to design networks aimed at achieving specified monitoring capabilities.

Summary

Over the last decade, structure of the upper mantle below the Baltic shield has been the subject of intensive study, using recordings of Soviet nuclear explosions as well as long-range deep seismic sounding profiles such as the Fennolora and Blue Road projects (*e.g.*, Masse and Alexander, 1974; King and Calcagnile, 1976; Lund, 1979; Guggisberg and Berthelsen, 1987). Reference structural models for the Baltic shield have also been published in NORSAR/NORESS and Helsinki bulletins. Results of these studies show distinct contradictions, which could lead to large errors in using one or another model for locating small events recorded by one or two seismic stations. For example, reference models published in the NORSAR and Helsinki bulletins do not contain upper-mantle low-velocity layers, but models constructed for the Fennolora and Blue Road long-range profiles are characterized by laminar structure, with alternating high- and low-velocity layers in the uppermost mantle (*Figure 7*).

To evaluate these results, we are studying NORESS recordings of approximately 150 mine explosions, recorded along a profile from NORESS to Helsinki to Leningrad during the period 1985-1988 (*Figure 8*). These events were in the range of epicentral distance from 250 to 1,300 km, and had magnitude 2.0-3.5 based on listings in the NORESS and Helsinki bulletins. The advantage of using events in this magnitude range, over the smaller explosions used in typical DSS investigations, is that recordings of industrial explosions have better signal-to-noise ratio, which is critical in identifying weak mantle waves at far-regional distance ranges.

The events used in the study are listed by both the NORESS and Helsinki bulletins, which makes possible a comparison of locations and estimated origin times in the two bulletins. Such a comparison shows large discrepancies, up to several seconds in origin time and several tens of kilometers in location. For the purpose of this study we assumed that the Helsinki bulletin, based on recordings from a network of stations closer to the events, had less error than event parameters based only on recordings by the NORESS array. For example, traveltimes for several events identified by the Helsinki bulletin as repeated explosions at the same mine typically agreed within ± 0.3 second. As a result we used the Helsinki bulletin locations and origin times as the basis for constructing record sections and traveltime curves along the profile. For epicentral distances less than 400 km, we analyzed data recorded by NORSAR in 1979 for three of the Fennolora shots (*C*, *D*, and *E* in the publications cited above), which were near the Oslo-Helsinki-Leningrad profile.

Analysis of first and secondary arrivals from the explosions showed that the first arrivals at far-regional distances are characterized by small amplitudes and relatively high frequencies (5-8 Hz), and these are followed by secondary arrivals with larger (up to a factor of 20-30) amplitude and lower frequency (2-3 Hz). In general, analysis of the weak first arrivals was possible only by filtering and beamforming of the NORESS data (as an extension of this study repeated events from the same mine will be stacked for SNR improvement).

Analysis of signals for this profile showed that first arrivals (P_{n1}) can be followed continuously to a distance of 750-800 km, with average apparent velocity increasing with distance, from 8.1-8.2 to 8.4-8.5 km/sec. A second, intensive arrival (P_1) follows P_{n1} in the same distance range. Beyond 750-800 km there is a shift of 2 seconds in the traveltime curve, with P_{n1} and P_1 disappearing and a later phase P_{n2} appearing as the first arrival, followed by another intensive phase P_2 . The apparent velocity of P_{n2} is high, 8.6-8.7 km/sec (*Figure 9*).

The character of these waves was studied by calculating traveltime curves and synthetic waveforms for different theoretical models on the basis of ray theory, according to which the first arrivals P_{n1} and P_{n2} are refracted waves, travelling in two

different layers of the upper mantle. Between these two layers there is a low-velocity layer, which accounts for the shift in the traveltime curve at 700 km. The intensive waves P_1 and P_2 are probably reflected waves, respectively from the top and bottom of the low-velocity layer. We constructed a one-dimensional model of the velocity structure of the upper mantle to a depth of 200 km, based on the observed first arrivals and using the *WKB* ray-tracing program as modified by W. Chan and T. Clarke.

The upper-mantle structure along the profile consists of two layers with increasing velocity with depth, separated by a low-velocity layer. In the lid, between depths of 40 and 105 km, velocity increases from 8.1 to 8.55 km/sec; from 105 to 125 km depth the velocity is 8.0 km/sec; and from 125 to 200 km the velocity increases from 8.55 to 8.65 km/sec. Because of ambiguities associated with the necessarily indirect method of constructing the model, there is a tradeoff between the thickness of the low-velocity layer and its velocity.

Comparison of our results with those in previous studies suggests that some investigators may have interpreted larger secondary arrivals as primary arrivals because the weak first arrivals were buried in noise. However, in one previous investigation of the attenuation structure of northern Eurasia, Der et al. (1986) found a low- Q layer at approximately the same depth range as described above. Masse and Alexander (1974) also found a thin low-velocity layer at depth of about 100 km under the Canadian shield. As shown by *Figure 10*, our upper-mantle velocity model can better explain and predict P-wave traveltimes at far-regional distances along the Oslo-Leningrad profile than results of previous studies.

Ringdal *et al.* (1986) and Mykkeltveit and Ringdal (1988) have noted that the high-frequency content of regional seismic signals decreases at distances of 700-800 km. In our analysis of NORESS high-frequency data, signals at far-regional distance (beyond about 800 km) do not contain detectable frequencies above 20 Hz, and for many events, the spectrum drops sharply at around 10 Hz. This could be explained by the structure obtained in this investigation, as follows. The first arrival P_{n1} travels in the mantle lid, which has relatively high Q permitting the propagation of signals containing high frequencies. However, the wave P_{n2} , recorded as a first arrival at ranges beyond 700-800 km, has traversed the upper-mantle low-velocity layer twice, with the effect of a dramatic reduction in high-frequency content of the recorded signals. We are still in the process of modelling this effect, as well as effects on waves P_1 and P_2 , reflected from the top and bottom of the low-velocity layer, respectively. This will be discussed in detail in *Center Technical Report C-89-01*, to be issued in April.

This new structural model is also being tested to determine whether its use in relocation of events recorded by NORESS will lead to improvements in location accuracy. The model will be improved and similar studies will be conducted for other regions of the USSR, using the DSS literature and data from new digital seismic stations as such data become available.

REFERENCES

- Baumgardt, D. R. and K. A. Ziegler (1988). Spectral Evidence for Source Multiplicity in Explosions: Application to Regional Discrimination of Earthquakes and Explosions, *Bull. Seism. Soc. Am.*, 78, 1773-1795.
- Der, Z. A., A. C. Lees, and V. F. Cormier (1986). Frequency Dependence of Q in the Mantle Underlying the Shield Areas of Eurasia, Part III: The Q Model, *Geophys. Journ.* 1103-1112.

- Dysart, P. S. and J. J. Pulli (1987). Spectral Study of Regional Earthquakes and Chemical Explosions Recorded at the NORESS array. *Center for Seismic Studies Tech. Rept. C87-03*, 3.21-3.44.
- Dysart, P. S. and J. J. Pulli (1988). Waveform and Spectral Characteristics of Regional Earthquakes and Chemical Explosions Recorded at the NORESS Array, in *Technical Report C87-03*, Center for Seismic Studies, Arlington, Virginia, 3-25 - 3-59.
- Everitt, Briant (1986). Cluster Analysis. *Halsted Press, Division of John Wiley & Sons, New York (2nd Edition)*, pp 136.
- Geller, R. J. and C. S. Mueller (1980). Four similar earthquakes in central California. *Geophys. Res. Letters* **7**, 821-824.
- Guggisberg, B. and A. Berthelsen (1987). A Two-Dimensional Velocity Model for the Lithosphere Beneath the Baltic Shield and Its Possible Tectonic Significance, *Terra Cognita*, **7**, 631-638.
- Hedlin, M. A. H., J. B. Minster and J. A. Orcutt (1988). The Time and Time-Frequency Characteristics of Quarry Blasts and Chemical Explosions Recorded in Kazakhstan U.S.S.R. (abstract), *EOS, Trans. Am. Geophys. Union*, **69**, 1331.
- Jurkevics, Andy (1987). Particle motion signatures for source identification, *Center for Seismic Studies Tech. Rept. C87-01*, 3.1-3.11.
- King, D. W. and G. Calcagnile (1976). P-Wave Velocities in the Upper Mantle Beneath Fennoscandia and Western Russia, *Geophys. Journ. R. astr. Soc.*, **46**, 407-432.
- Lund, C. E. (1979). The Fine Structure of the Lower Lithosphere Underneath the Blue Road Profile in Northern Scandinavia, *Tectonophysics*, **56**, 111-122.
- Masse, R. P. and S. S. Alexander (1974). Compressional Velocity Distribution Beneath Scandinavia and Western Russia, *Geophys. Journ. R. astr. Soc.*, **39**, 587-602.
- Mykkeltveit, S. and F. Ringdal (1988). New Results from Processing of DATA Recorded at the New ARCESS Regional Array, *Semiannual Technical Summary, 2-87/88*, NORSAR, Kjeller, Norway.
- Ringdal, F., B.Kr. Hokland and T. Kvaerna (1986). Initial Results from the NORESS High Frequency Seismic Element (HFSE), *Semiannual Technical Report, 2-85/86*, NORSAR, Kjeller, Norway.
- Suteau-Henson, A. and T. C. Bache (1988). Spectral Characteristics of Regional Phases Recorded at NORESS, *Bull. Seism. Soc. Am.*, **78**, 708-725.
- Thorbjarnardottir, Bergthora S. and James C. Pechmann (1987). Constraints on Relative locations from Cross-Correlation of Waveforms, *Bull. Seism. Soc. Am.* **77**, 1626-1634.
- Willis, D. E. (1963). A note on the effect of ripple firing on the spectra of quarry shots, *Bull. Seism. Soc. Am.*, **53**, 79-85.

NORESS Events

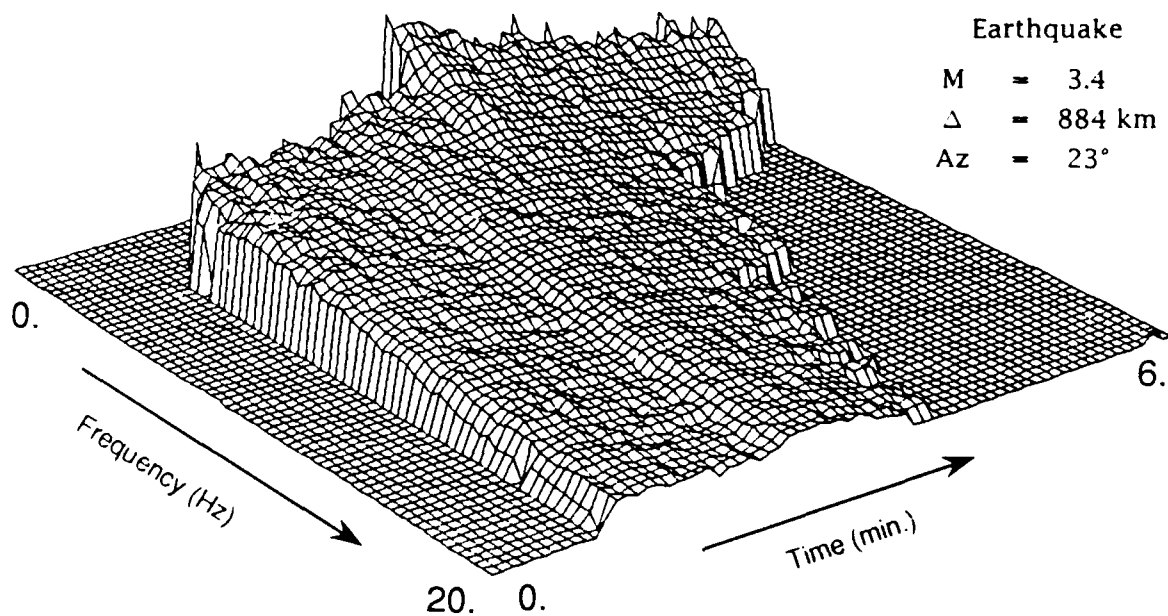
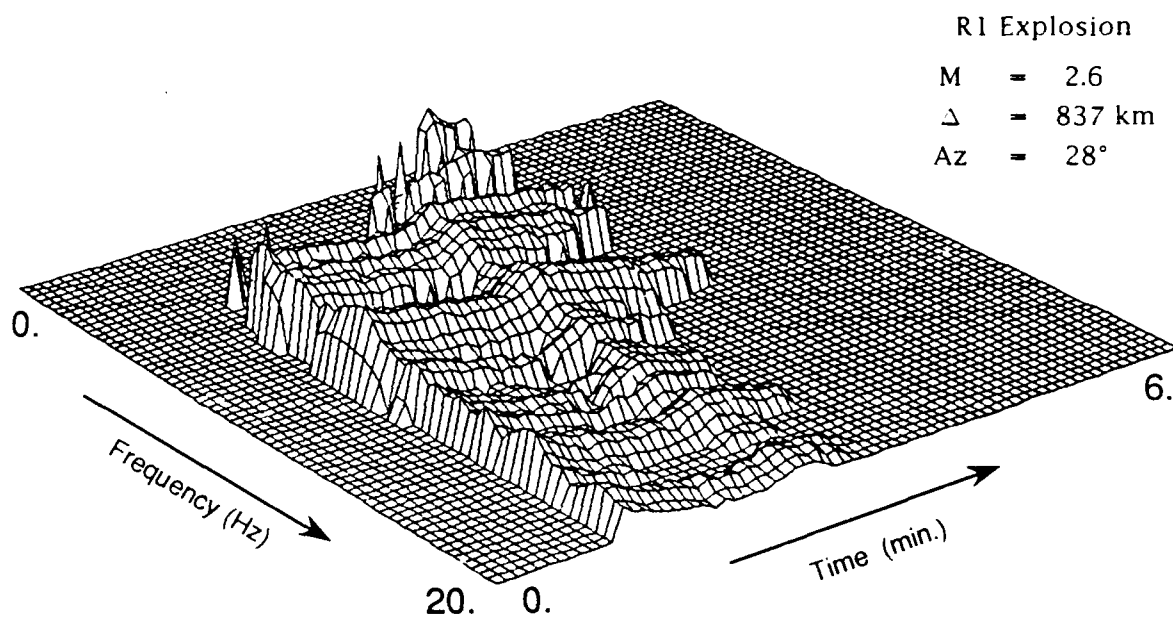


Figure 1. Spectrograms of two Northern Sweden events at NORESS. Top: Explosion from Mine R1. Bottom: Earthquake. The spectral amplitudes above noise level are plotted on a logarithmic scale. Frequencies below 0.5 Hz are masked to avoid spurious peaks due to noise non-stationarity.

NRDC Events at BAY

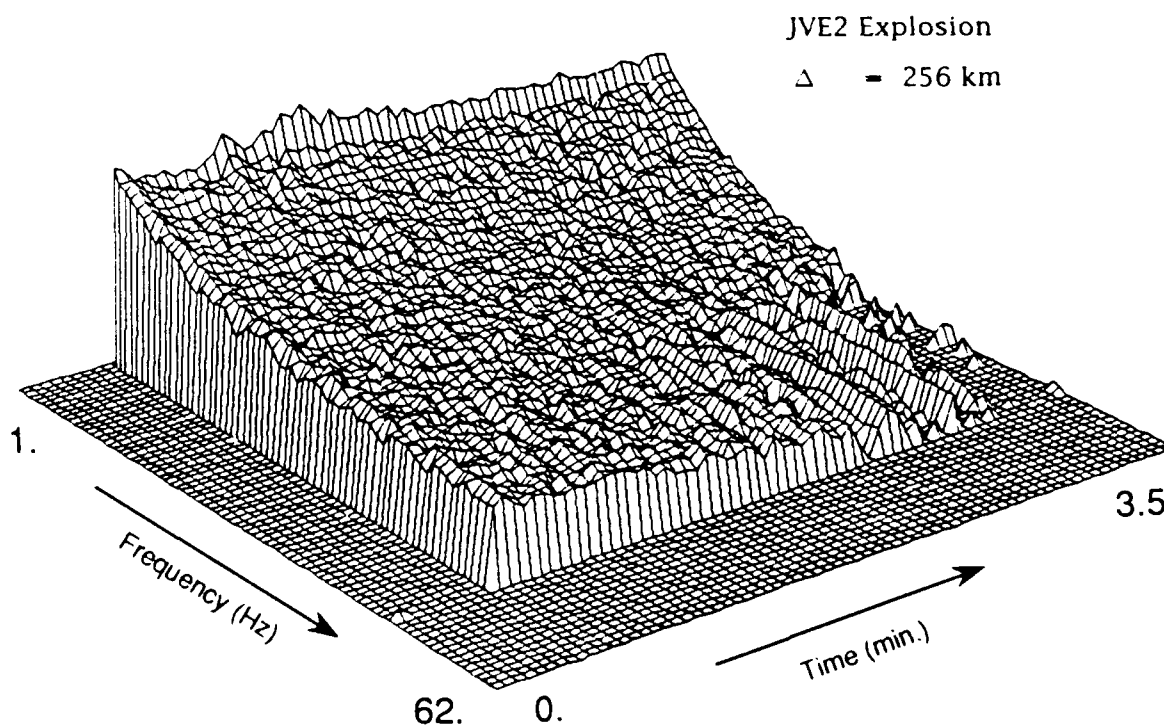
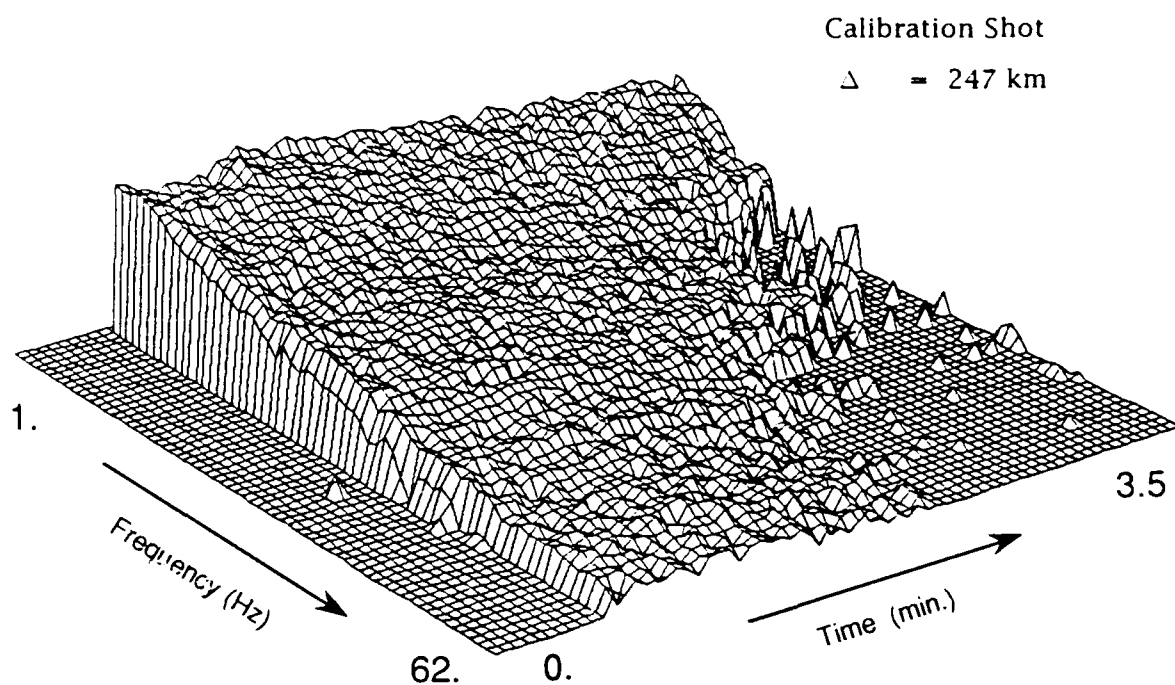


Figure 2. Spectrograms of two single explosions at NRDC station BAY. Top: Calibration shot. Bottom: JVE2 nuclear explosion at Semipalatinsk Test Site, recorded by the University of Nevada-Reno (the data have a Nyquist frequency of 50 Hz).

NRDC Events at BAY

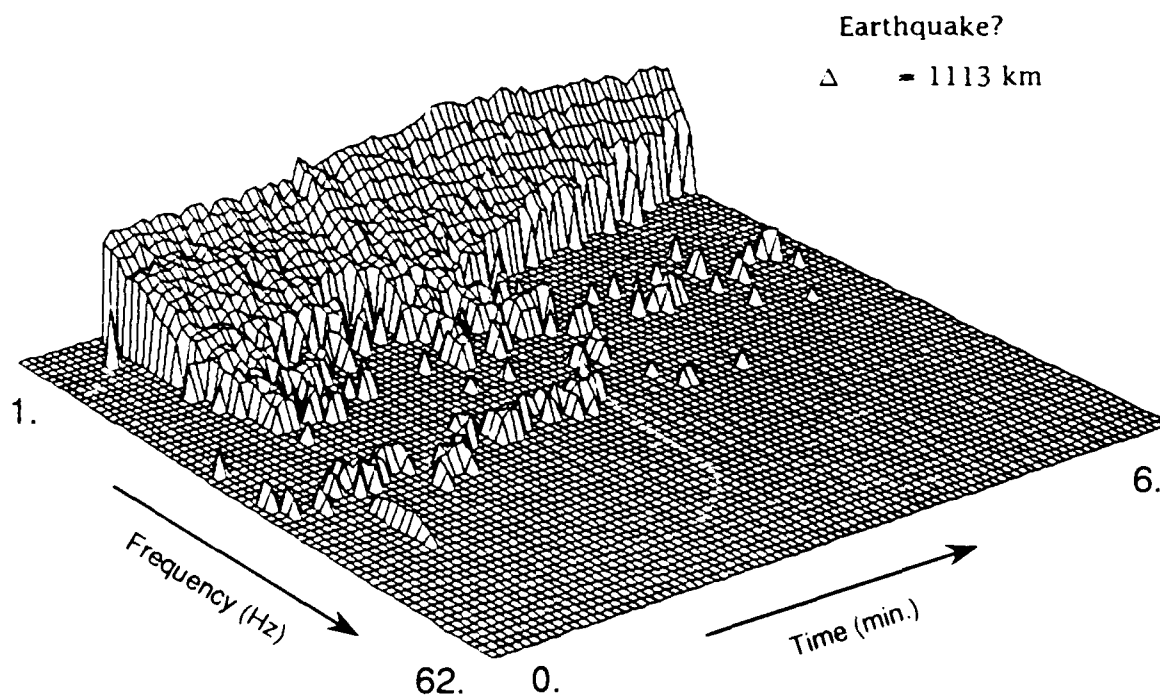
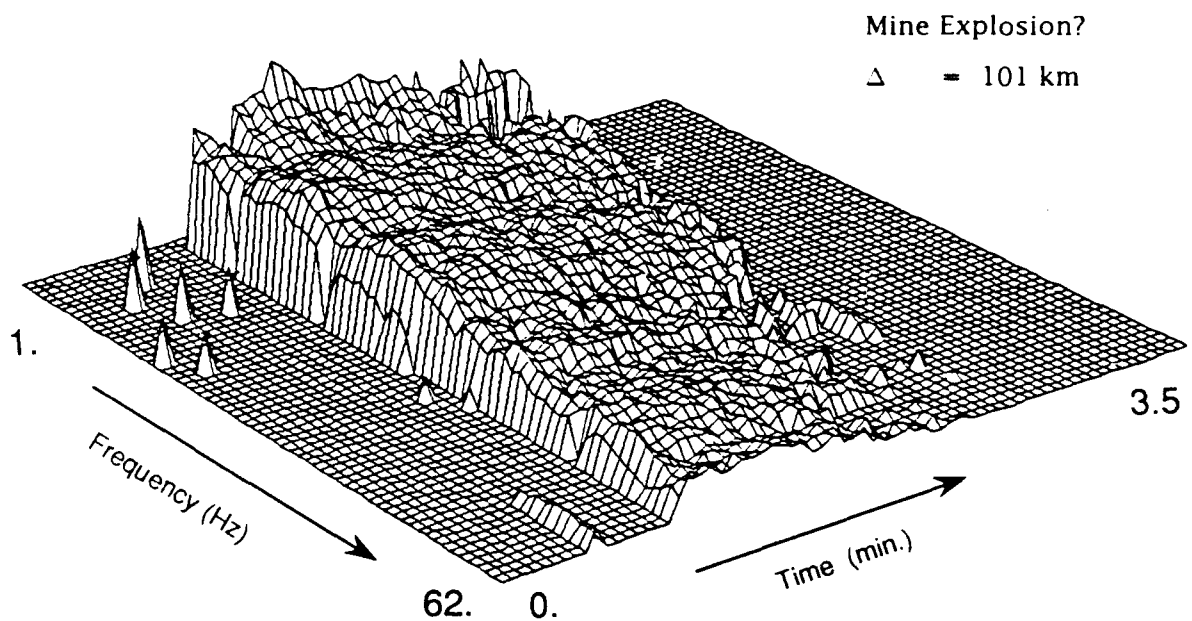


Figure 3. Spectrograms of two unidentified events at NRDC station BAY. Top: Presumed local mine explosion (times beyond the end of the recorded data are masked). Bottom: Presumed regional earthquake.

Waveform Correlation

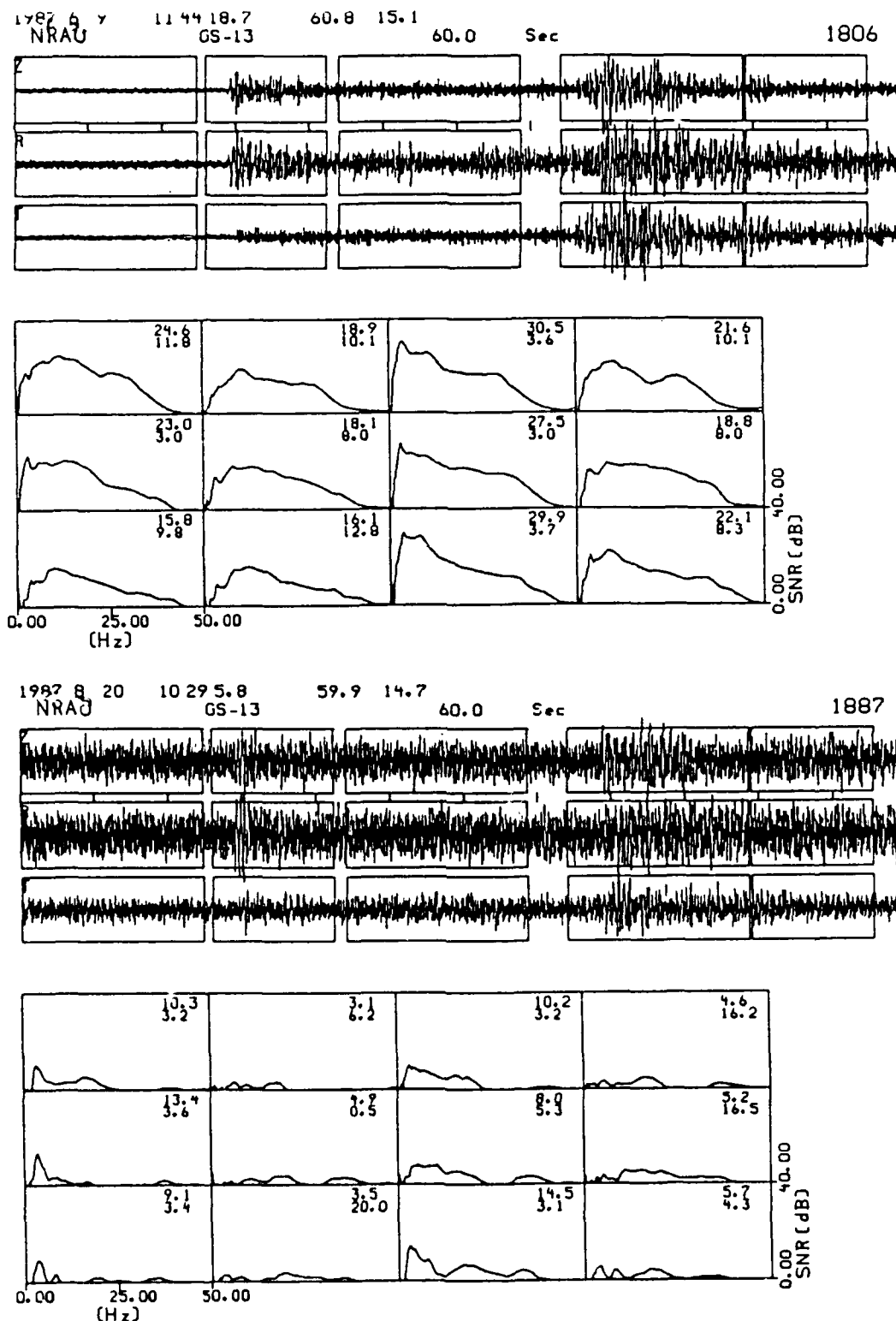


Figure 4. Examples of waveforms for the events analyzed here. The horizontal EW and NS components have been rotated to produce radial and transverse components. The SNR as a function of frequency is plotted below the seismograms for four different segments of the recorded wavetrains. These functions usually have a pronounced peak for the P and S wave intervals.

Waveform Correlation

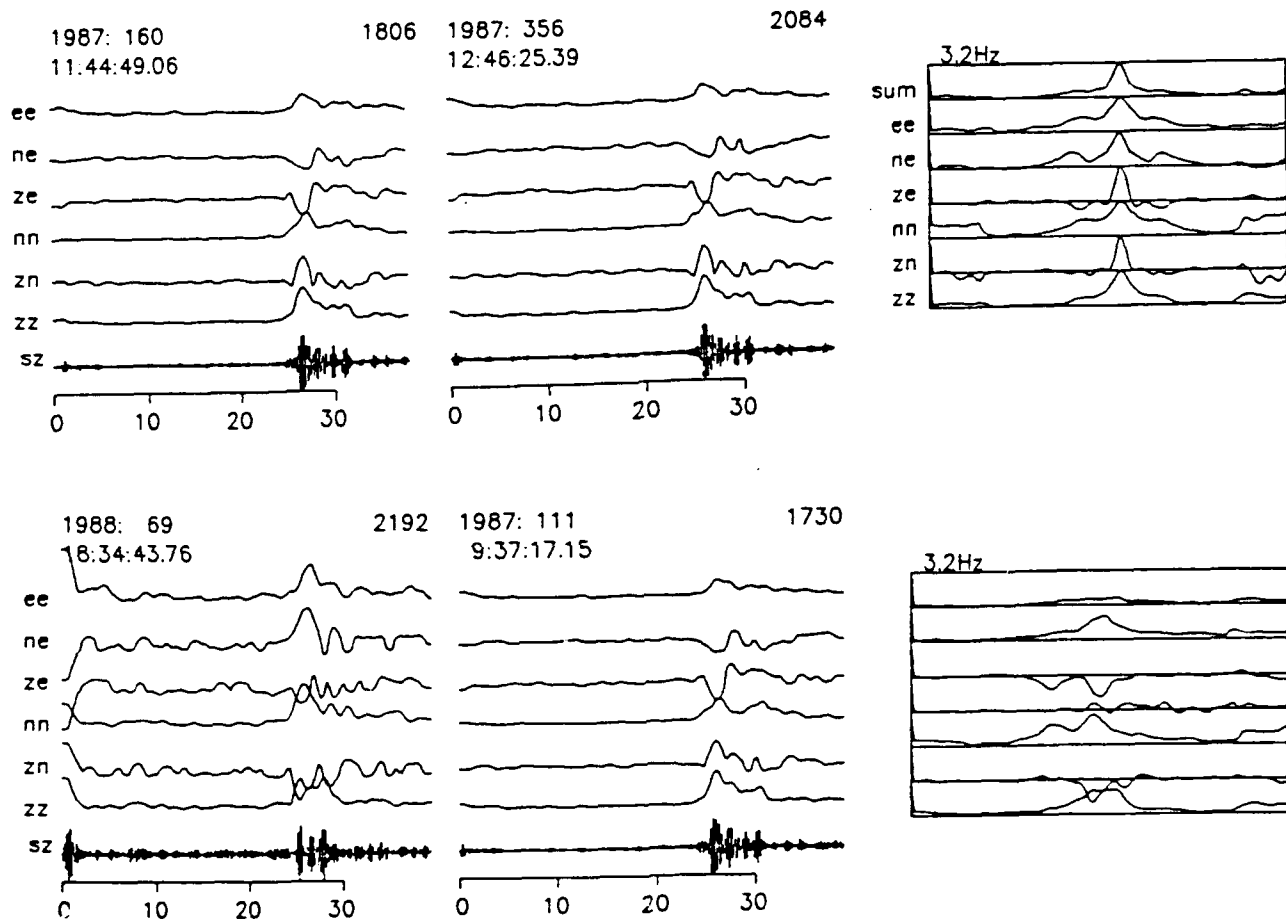


Figure 5. Examples of the output of the cross correlation algorithm for three-component recordings of events with high and low correlation. The vertical-component seismograms are plotted in the center of each diagram, and the six unique components of the covariance matrix as a function of time are shown above the vertical-component trace. The cross correlation functions of the six covariance components and the sum of the cross correlations are displayed to the right for each pair of events.

Waveform Correlation

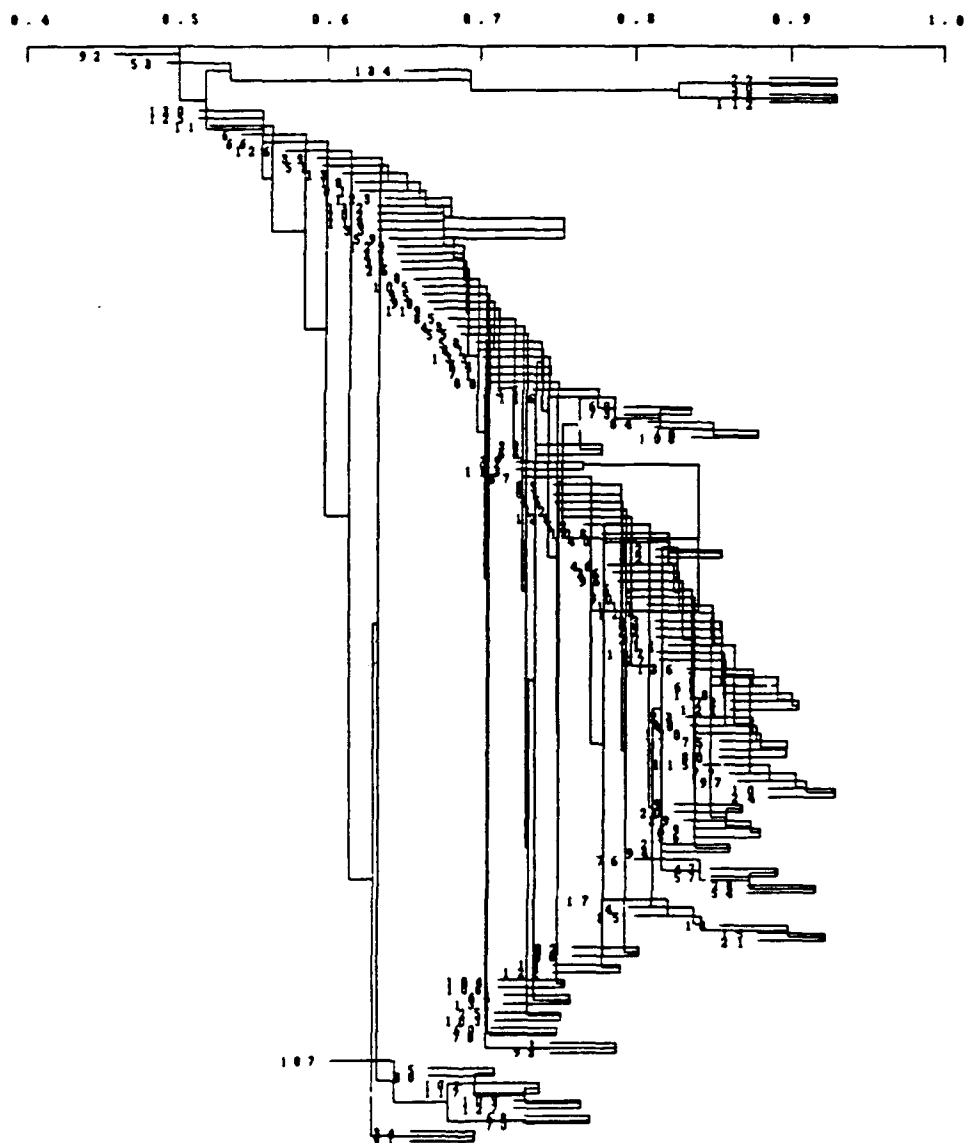


Figure 6. Dendrogram, or cluster tree structure as a result of hierarchical clustering with the single link method. Above the cutoff value of 0.7 the data are shown to cluster in one large *group* and a few smaller *events*.

Oslo-Helsinki-Leningrad Profile

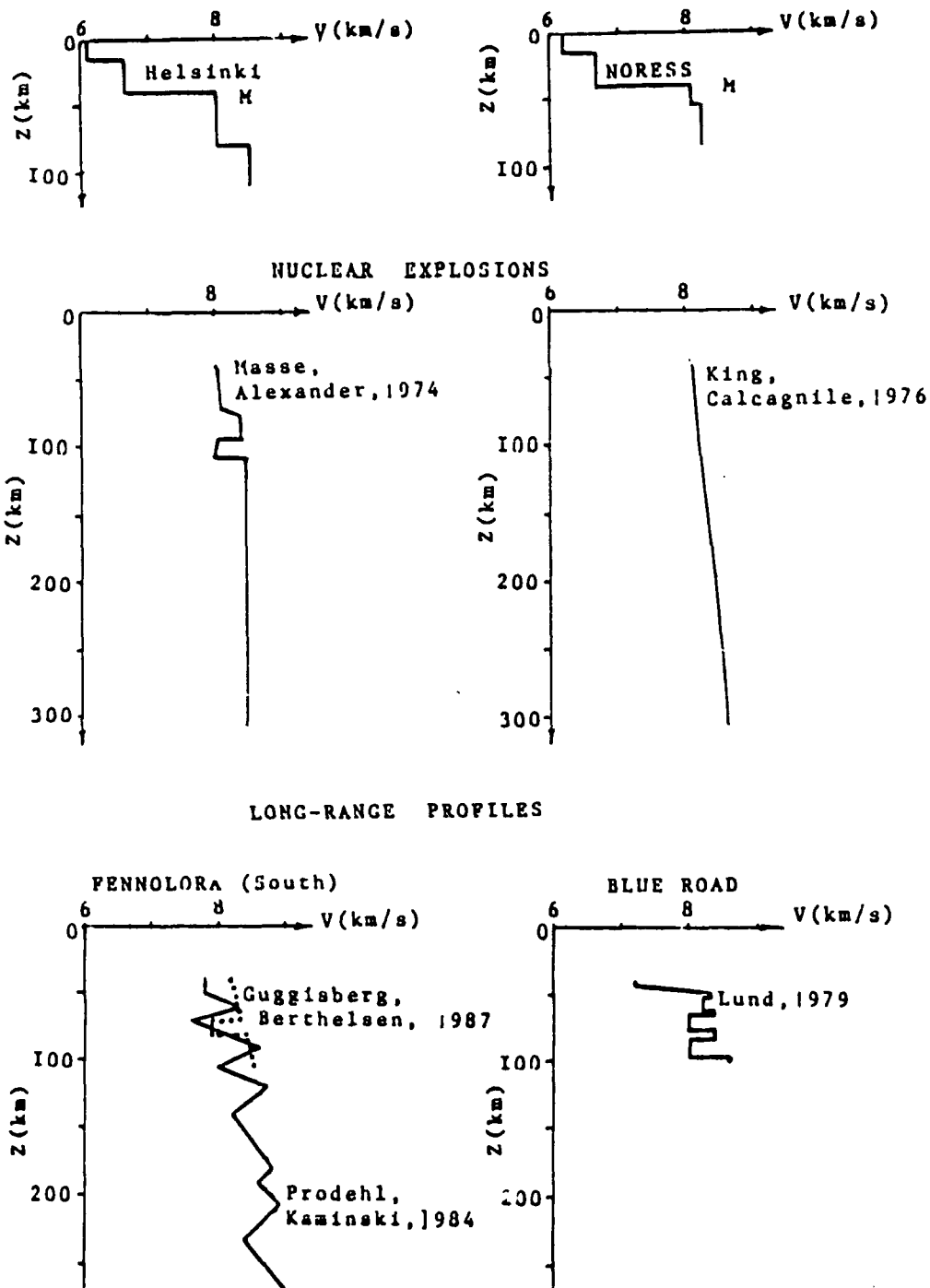


Figure 7. Published upper-mantle velocity models for the Baltic shield. Top -- models used by the Helsinki Seismological Institute and NORSSAR for locating regional events; middle -- models based on nuclear explosions; bottom -- models determined from the *Fennolora* and *Blue Road* long-range profiles.

Oslo-Helsinki-Leningrad Profile



Figure 8. Location of the NORESS array (open circle), Fennolora shots (closed circles with letters) and presumed mine blasts (+'s) used in the analysis. Size of symbols for mine blasts is proportional to ML.

Oslo-Helsinki-Leningrad Profile

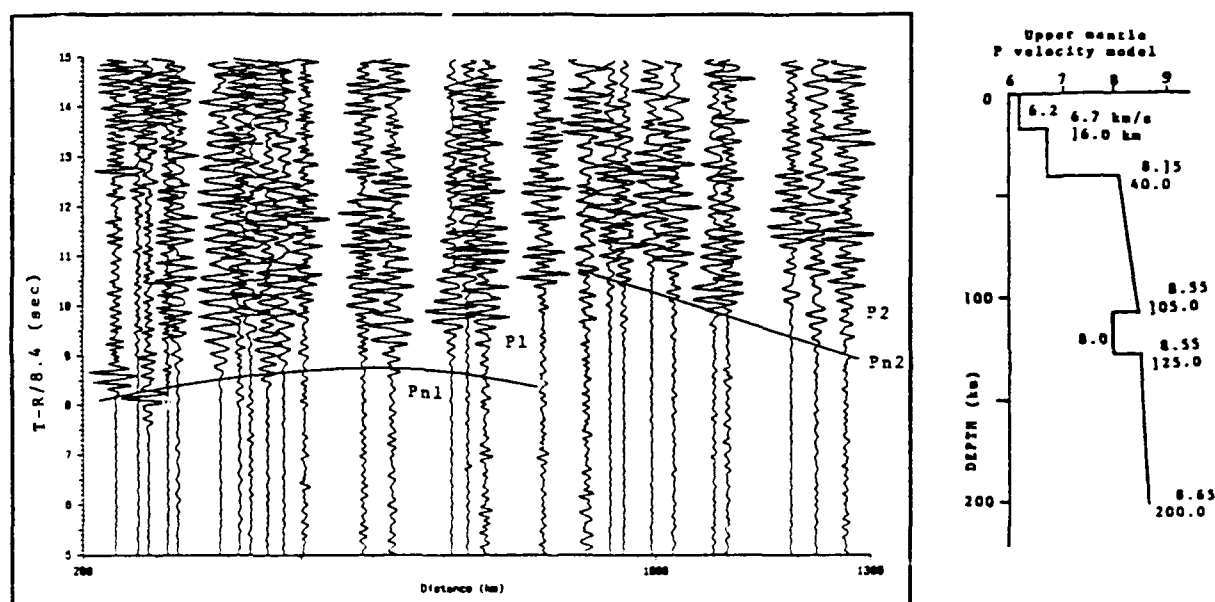


Figure 9. Record section made up of NORESS recordings of presumed mine blasts along Oslo-Helsinki-Leningrad profile. Three of traces at distance less than 400 km were from Fennolara blasts. All signals bandpass-filtered, 3-12 Hz. Velocity model at right was determined from readings made on records of this profile. Theoretical curves for $Pn1$ and $Pn2$ correspond to the velocity model shown.

Oslo-Helsinki-Leningrad Profile

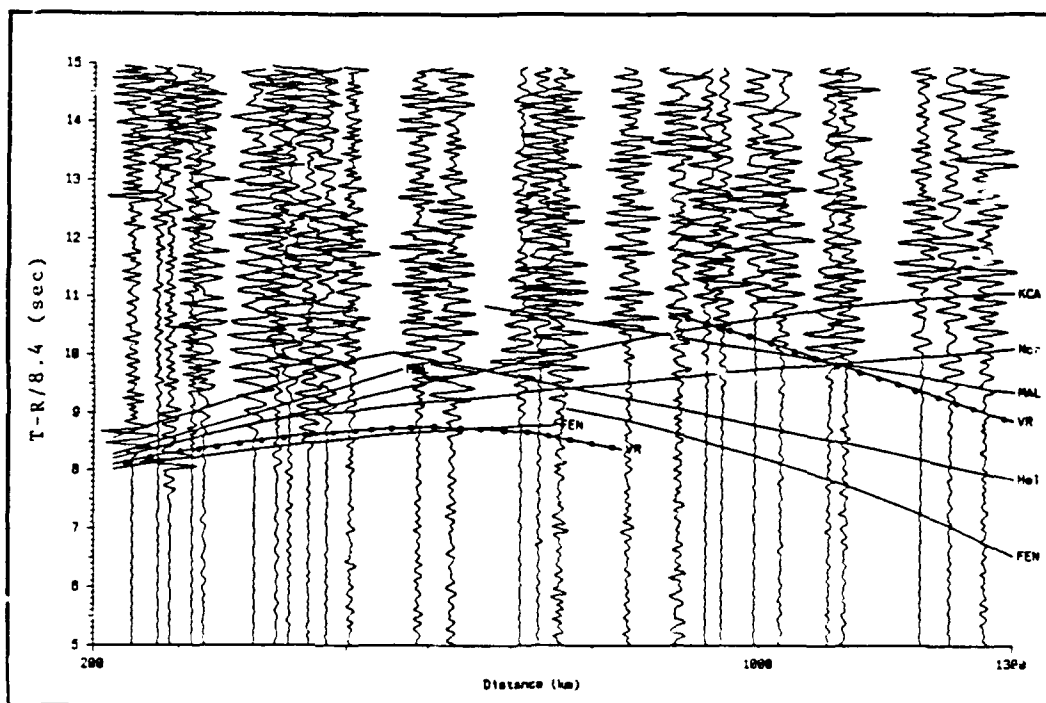


Figure 10. Record section from Figure 9, with theoretical Pn traveltime curves calculated for various velocity models. VR -- this study; Nor -- model used in NORESS Bulletin; Hel -- model used in Helsinki Bulletin; KCA -- King and Calcagnile, 1976; MAL -- Masse and Alexander, 1974; Fen -- Guggisberg and Berthelsen, 1987.

APPLICATION OF SIMULATED ANNEALING TO JOINT HYPOCENTER DETERMINATION

Chia-Yu Chang, William H. Menke, Arthur L. Lerner-Lam

(Lamont-Doherty Geological Observatory)

CONTRACT NO. F19628-88-k-0041

OBJECTIVE

Joint hypocenter determination (JHD) is a nonlinear problem. Linearized methods often lead to undesirable solutions that correspond to local minimal energy states. We are exploring different aspects of the application of a nonlinear optimization technique, Simulated Annealing, to the JHD problem.

SIMULATED ANNEALING

Simulated annealing is a Monte Carlo nonlinear optimization technique that conducts random searches of model parameters iteratively over the model space until an energy (or cost, objective) function, E , is minimized. To avoid being trapped in a local minimum, however, the random model parameter searches are allowed to go "uphill" (i.e., to higher energy states), depending on a probability function, $P(E)$. P depends on both the energy and an *a priori* scaling parameter, T , through the function $P(E, T) = \exp(-E/T)$. $P(E, T)$ is analogous to the Gibb's distribution function in statistical mechanics, where T is identified as the temperature and E as the energy of a physical system. An optimization problem may thus be considered an analogy to the annealing of a crystal, in which the crystal is heated up and then gradually cooled down. In practice, this process is often implemented via an algorithm due to Metropolis et al. (1953). Consider the ratio of the probability functions corresponding to two consecutive model parameter searches, $P(\Delta E, T) = P(E_2, T)/P(E_1, T) = \exp(-\Delta E/T)$. The second search is considered successful under two circumstances: 1) $\Delta E \leq 0$, or 2) $P(\Delta E, T)$ is greater than a random number lying between 0 and 1. High T conditions thus allow the path of stabilization of the system to remain in high energy states in order to sample as much of the model space as possible. T is then gradually decreased to simulate annealing.

SUMMARY

In our first stage of study, we have conducted a series of synthetic experiments. Synthetic arrival times are computed for twelve sources and eight receivers in a 1-D velocity model that has a constant P-velocity of 6 km/sec plus a set of constant static station corrections. The twelve sources are evenly distributed at 5 km and 6.3 km depths and form a rectangular grid. At each depth, there are six sources separated by 1 km. The eight receivers are located on the surface, spaced by 1 km and has a centroid that is aligned vertically with the centroid of the source cluster. One constant static station correction is assigned to each receiver. These static station corrections are gathered from a set of 500 random numbers having a zero mean. The sizes of these station corrections are generally near 5% of the half space P-velocity.

Taking the source coordinates as the model parameters, we estimate the origin times as the averages of arrival time residuals over the receivers. Using these estimates of origin times, the static corrections are then calculated as the averages of residuals over the sources. The energy function is the sum of the square of arrival time residuals, where the arrival time residuals are the difference between observed arrival times and the sum of estimated origin times, travel times and static station corrections. Temperatures are computed as $T_k = T_0 / (T_1 + mk)$, where T_0 , T_1 and m are positive constants and $k = 1, 2, \dots, n$. At each temperature, iteration is stopped if either the number of iteration exceeds a maximum or the number of successful search exceeds another preset limit.

Our results bring out the well-known coupling effect on the residuals between source locations and origin times (and static station corrections). Even though the energy functions are minimized, the errors in estimated source locations and origin times (and static station corrections) may be both equally large (Figure 1). This degeneracy of the energy function with respect to source

parameters implies the solution is nonunique, even using a nonlinear method.

FUTURE WORK

Simulated annealing method is particular useful for JHD problems when the hypocentral locations are constrained to lie on a finite set of points or surfaces within the earth, as the constraints could reduce or even eliminate the nonuniqueness problem discussed previously. The computational effort in random search would also be greatly reduced, as is the danger of finding a local minimum solution. Such constraints, however, are highly nonlinear, and not easily implemented in a linearized inversion technique. A direct application of simulated annealing with constraints is in jointly locating nuclear explosions using teleseismic data, using shot holes recognized from satellite images as accurate constraints. Another possible application of this technique is to locate earthquakes in tectonically complicated areas, using, for example, fault surfaces as constraints. The distribution of seismicity over the fault surfaces may then be used to test or construct a tectonic model.

REFERENCE

Metropolis, N., A. Rosenbluth, M. Rosenbluth, A. Teller, and E. Teller (1953). *J. Chem. Phys.*, V. 21, p. 1087.

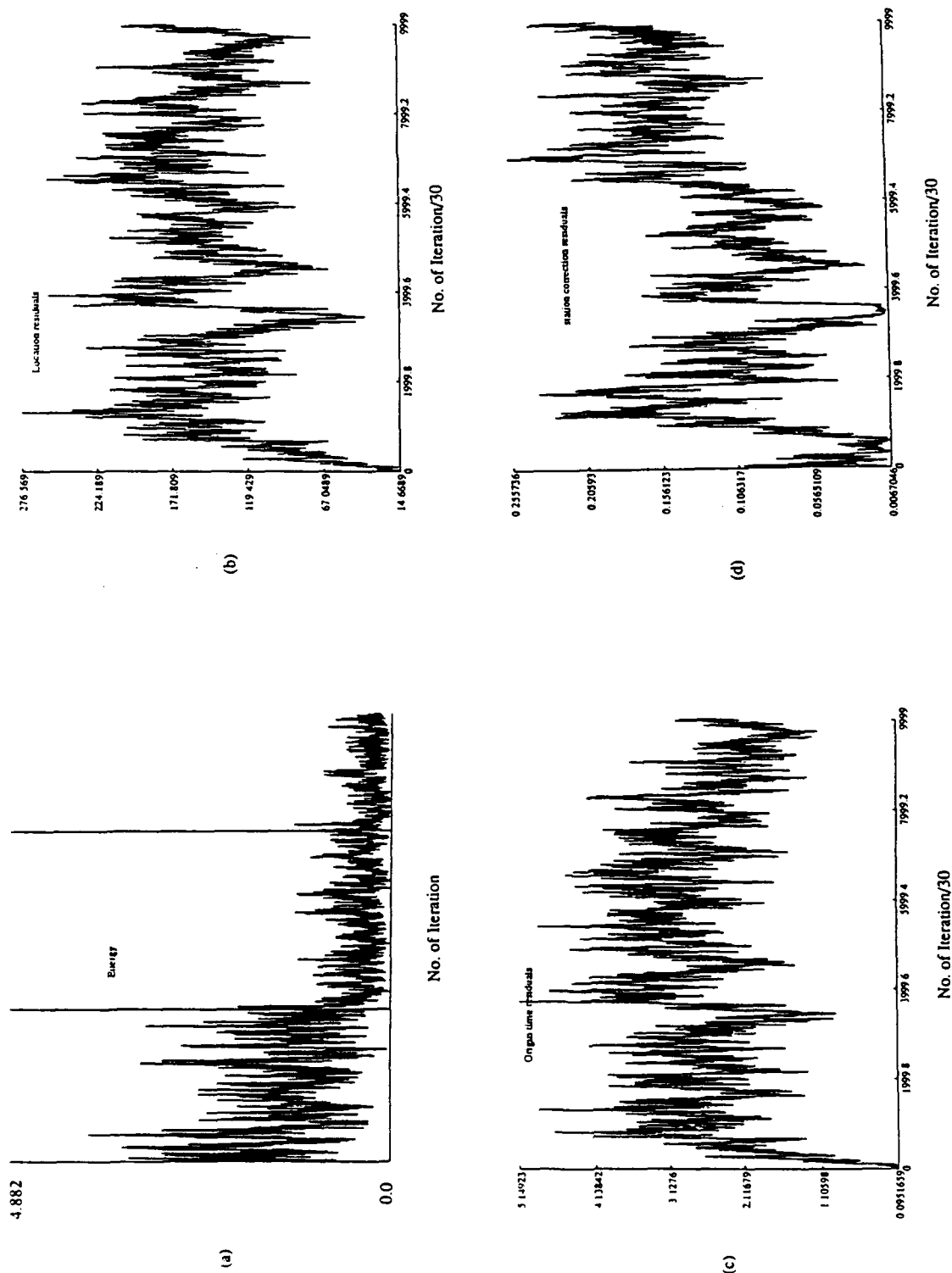


Figure 1: The effects of source locations and origin times (and station corrections) on arrival time residuals are coupled. (a) shows the energy functions for the first 10000 iterations (including both successful and unsuccessful searches). The two long vertical bars indicate changes of the temperature parameter. The energy is decreased almost monotonically to very small numbers. (b), (c) and (d) show the squared residuals (relative to true values) of hypocenter locations, origin times and station corrections, respectively, for 30000 iterations. Notice that these residuals may all assume large values, while the energy is still small.

A STUDY OF SOVIET PNE'S AND SPECTRAL DIFFERENCES BETWEEN BELOW AND ABOVE WATER TABLE NTS SHOTS

I. N. Gupta, C. S. Lynnes, and R. A. Wagner
Teledyne Geotech
314 Montgomery Street
Alexandria, Virginia 22314

CONTRACT No. F19628-88-C-0051

OBJECTIVE

- (a) Investigate prominent arrivals in teleseismic P and P coda for two sets of sequentially fired Peaceful Nuclear Explosions (PNE's) in the Astrakhan and Orenburg regions of the USSR.
- (b) Compare the spectral characteristics of NTS nuclear shots detonated below and above the water table by analysis of the regional phases Pn and Lg recorded at common stations.

SUMMARY

(a) Study of Soviet Peaceful Nuclear Explosions

The maximum-likelihood multichannel deconvolution method of Shumway and Der (1985) was applied to teleseismic P waves from 15 Peaceful Nuclear Explosions (PNE's) from the Astrakhan (9 shots) and Orenburg (6 shots) regions of the USSR. These 15 shots were well recorded at all three RSTN stations, RSNY, RSSD, and RSNT. The epicentral distances from the two sets of explosions to the three stations are 76° and 74° for RSNY, 86° and 83° for RSSD, and 70° and 66° for RSNT, respectively. Both sets of data belong to sequences of shots fired about 5 minutes apart. The value of t^* for the RSTN stations was assumed to be 0.2 sec and the yields of all 15 shots in salt were considered to be 15 kt each; the actual values should not be much different (Borg, 1983; Sykes and Ruggi, 1986). The corresponding von Seggern and Blandford (1972) or "VSB" wavelet for salt has been removed in the deconvolutions. Simultaneous use of all data provided the deconvolved source function for each shot.

Figure 1 shows the deconvolved source time functions for the 9 Astrakhan shots along with the result of stacking the source functions. The first 5 seconds or so of the nine source functions look very similar, probably because the shots are all located close to each other and have nearly the same magnitude. The source function for each shot shows clear P and pP arrivals separated by about 1 sec, suggesting large shot depths. There are also several arrivals which consistently show up between the P and pP, similar to those observed for the U.S. explosion in salt, Salmon. These earlier reflections may be due to strong impedance contrasts, such as those in a salt dome environment. P coda on the stacked or SUM trace does not show any prominent arrivals.

Results of deconvolution for the 6 Orenburg shots are shown in Figure 2. The first several seconds of P again look very similar for all shots. The P and pP arrivals are separated by about 0.4 sec only, suggesting that these shots are much shallower than the Astrakhan shots. Moreover, unlike the source terms in Figure 1, a low-frequency phase arriving about 6 to 7 sec after the first P is clearly present on all traces in Figure 2.

There are numerous observations of large amplitude Sp phases from earthquakes, due to S \rightarrow P conversion at the Moho under the stations, with S - Sp time of about 5 to 6 sec (e.g., Jordan and Frazer, 1975). Similarly, several stations show the Ps phase, with conversion at the Moho under the station, arriving about 5 to 6 sec after P (e.g. Owens et al., 1987; Egorkin et al., 1987). If large amplitude S waves are somehow generated at or near the explosion source, one should therefore expect an

arrival due to S→P conversion at the Moho under the source, appearing at least 5 to 6 sec after the direct teleseismic P. The actual time difference will depend not only on the P and S velocities and thickness of the crust, but also on where and when the S waves are generated. This arrival will be designated hereafter as the SP phase.

The large secondary arrival in the source terms for the Orenburg explosions (Figure 2) is probably the SP phase discussed above. However, it is interesting to note that source functions of the Astrakhan shots in Figure 1 do not show any prominent SP arrivals. A possible reason is that the Astrakhan shots, being much deeper than the Orenburg shots, are not likely to generate as much near-source S as the much shallower Orenburg shots. There are several possible ways by which large S may be generated at or near the source, such as scattering of explosion-generated Rayleigh wave into S (Stead and Helmberger, 1988) and direct S due to source anisotropy (e.g. McLaughlin et al., 1988a). Both of these mechanisms would suggest much smaller explosion-generated S for deeper shots than for shallower shots.

(b) Spectral Differences Between Below and Above Water Table NTS Shots

The geological environment in which a nuclear explosive is emplaced has a major influence on the amplitudes and spectra of the observed seismic signals. Source coupling depends mainly on rock strength and dry porosity. Shots in stronger rocks generally excite smaller P-wave amplitudes as compared to weaker rocks, provided both are saturated or have the same dry porosity. Increased dry porosity also reduces P-wave amplitudes. Typically, a rock with dry porosity is weak so that the conflicting roles of these two parameters serve to mask the effect of each. Non-linear finite difference calculations (Bache, 1982; Figure 11) show a larger low-frequency amplitude and lower corner frequency, f_c for wet tuff in comparison to dry tuff, when yield values are the same. Evernden et al. (1986) also show similar strong dependence of explosion P wave spectra on the material properties of the coupling media (see especially their Figure 8). Gupta and Blandford (1987) examined teleseismic P from shots in saturated (below water table) media and found spectral differences to depend on the shot medium velocity. It is clear therefore that both amplitudes and spectral shapes are strongly influenced by the geological environment of the shot point.

In this study, a comparison of the spectral characteristics of nuclear shots detonated below and above the water table (WT) is made by analysis of mostly the regional phase Pn recorded at two common stations. We first analyzed digital data from 22 NTS shots well recorded at 20 samples/sec at the DWWSSN station Jamestown, JAS at epicentral distances of about 350 km. Out of 22 shots, only 9 are below WT; 19 shots are from the Yucca Flats and only 3 are from the Pahute Mesa regions of the NTS.

Digital, vertical component data from JORNADA and the Joint Verification Experiment (JVE) shot, KEARSARGE (17 August 1988; 37.29° N, 116.31° W) are shown in Figure 3a. The JVE shot was recorded at the new DWWSSN station, CMB, about 10 km away from JAS. JORNADA, detonated below WT, has $m_b = 5.9$ which suggests a yield value close to 150 kt (see, e. g., Bache, 1982). The JVE shot, known to be above WT, also had a yield of probably close to 150 kt although its m_b is only 5.4. The large difference in Pn amplitudes for the two shots is probably due to the large differences in coupling expected for shots below and above the WT. It is interesting to note that although Pg is clipped for both shots, the Pn/Pg amplitude ratio is much smaller for KEARSARGE than for JORNADA. In fact, a comparison of the later, unclipped portion of Pg (or Pg "coda") amplitudes appears to suggest that Pg may not show the effect of the water table. Records of JORNADA and KEARSARGE recorded at the SRO station ANMO (epicentral distance of about 900 km) are shown in Figure 3b. As in Figure 3a, JORNADA has much larger amplitudes than KEARSARGE in the first several seconds of Pn but not in the later wavetrain.

The spectra of Pn, based on a window length of 6.4 sec, and of noise are shown in Figure 4a and 4b for the same two records as in Figure 3a and 3b. The spectra are neither smoothed nor corrected for instrument response. The spectral ratios KEARSARGE/JORNADA, corrected for noise, are shown in Figure 5 in which the mean slope values over the frequency range of 0.2 to 6.0 Hz are also indicated. The mean values of the spectral ratio (in magnitude units), integrated over the frequency range by using the mean values of slope and intercept, denoted by AV INTEG in Figure 5, indicate the average spectral amplitudes in KEARSARGE to be smaller than that for JORNADA.

The far-field source spectra may generally be characterized by three independent parameters: the low-frequency spectral level A_0 , proportional to seismic moment; the corner frequency f_c , and the power of the high-frequency asymptote (Aki and Richards, 1980). The last parameter (n in f^{-n}) may be assumed to be 2 for explosions (Evernden et al., 1986). For explosions in same or similar media, A_0 is a good measure of the explosion yield (Evernden et al., 1986; McLaughlin et al., 1988b). A spectral measure of A_0 is made by correcting for noise, removing the instrument response, applying the appropriate spatial attenuation correction and then least-squares fitting the log-amplitude spectra to a model spectrum with a fall-off rate of f^{-2} . The amplitude spectrum is assumed to have the form (Brune, 1970)

$$A(f) = \frac{A_0}{1 + (f/f_c)^2} \quad (1)$$

Spectral fits to equation (1), using $t^* = 0.1$ (Bakun and Johnson, 1970), were made for JAS records of 22 shots and the values of A_0 and f_c derived. Spectral fits for JORNADA and KEARSARGE, based on S/N power threshold of 1.5, are shown in Figure 6a, clearly demonstrating the latter shot to have significantly lower A_0 and higher f_c than the former. The frequency range used for spectral fits was 0.2 to 6.0 Hz since most shots showed good S/N only in this frequency band. Spectral fits, based on $t^* = 0.25$ for the ANMO data, are shown in Figure 6b and provide results similar to those in Figure 6a.

Plots of f_c versus A_0 for 9 below and 13 above WT shots, are shown in Figures 7a and 7b, respectively. Forcing the theoretically expected slope of $-1/3$ through the data points, the least squares regressions gave mean intercept values of 0.926 (0.044) and 0.754 (0.045), respectively. Thus the below and above WT populations are separated by 0.172 (0.063). In other words, for the same low-frequency spectral level, shots below WT have, on the average, larger (about a factor of 1.5) f_c than those above WT. Figures 8a and 8b show plots of A_0 versus yield (on log-log scale) for 9 below WT and 13 above WT shots, respectively. When the theoretically expected slope of 1 is forced through the data points, the least squares regressions give mean intercept values of 0.789 (0.083) and 0.276 (0.045), respectively. Thus the below and above WT populations are separated by 0.513 (0.095). In other words, for the same yield, A_0 for a shot below WT is, on the average, significantly larger (about a factor of 3) than that for a shot above WT. The low-frequency amplitude values may also be obtained by bandpassing the data and computing the root-mean-square (RMS) amplitudes, after correcting for the instrumental response and noise level. Results for the 0.5-1.5 Hz passband, with window length of 6.4 sec, for the 22 shots recorded at JAS are shown in Figure 9a. The least squares regression lines for the two types of shots, assuming a slope of 1, are separated by 0.542 magnitude unit, nearly identical with that for A_0 (Figure 8). The below WT shots show larger deviations from the mean than the above WT shots. The RMS value from one shot in Figure 9a, denoted by the letter P, is close to that expected for an above WT shot. A possible reason for this may be the fact that this is the only below WT shot with non-zero gas porosity value (viz. 4%). An important factor contributing to the scatter in Figure 9a is perhaps the proximity of the shot cavities of several explosions to the water table. Out of a total of 22 shots, the shot points of 3 are within one cavity radius of WT (marked by

long arrows) and those of 9 other are within two cavity radii of WT (denoted by small arrows). If this were not the case, the RMS values for these 12 shots would move in the direction pointed by the arrows, thereby resulting in somewhat larger separation between the two types of shots.

A plot of the RMS values for Lg with window length of 51.2 sec (but otherwise obtained in the same manner as for Pn) versus yield for 19 shots for which Lg was available (most others were clipped) is shown in Figure 9b. The below and above WT populations are separated by 0.300 magnitude unit, considerably less than the separation for Pn in Figure 9a. It seems therefore that Lg is considerably less sensitive than Pn to whether the shot is below or above WT and Pn/Lg amplitude ratio is a possible discriminant. This is in agreement with an analysis of Blandford and Klouda's (1980) data showing larger separation between below and above WT shots for m_b (Pn) than for m_b (Lg).

Analysis of both regional and teleseismic m_b data from substantially larger data bases also demonstrate that, for a given yield, m_b values for shots below WT are generally larger than those for shots above WT by 0.3 to 0.5 magnitude unit. Gas porosity of the shot medium appears to play an important role in the determination of this large magnitude bias. Yield estimates can be significantly improved if it is known whether the shot point is below or above the water table.

CONCLUSIONS AND RECOMMENDATIONS

Multichannel deconvolution method applied to two sequences of Soviet PNE's provided useful source information such as variations in shot depth and secondary arrivals due probably to the conversion of explosion-generated S→P at the Moho near the source. Data from many more PNE's should be examined since the monitoring and discrimination of PNE's can be a most challenging and difficult task.

A comparison of the spectral characteristics of nuclear shots detonated below and above the water table (WT) is made by analysis of the regional phase Pn recorded at common stations. The largest difference between the below and above WT shots of a given yield appears to lie in their low-frequency spectral level. Yield estimates can be significantly improved if it is known whether the shot was detonated below or above WT. A comparison of Pn and Lg phases at a common recording station can help distinguish between below and above WT explosions. More regional data with good azimuthal coverage and shots with more variable scaled depth (i.e. overburied and underburied shots) should be examined.

REFERENCES

- Aki, K. and P. G. Richards (1980). *Quantitative Seismology*, W. H. Freeman and Company, San Francisco, California.
- Bache, T. C. (1982). Estimating the yield of underground nuclear explosions, *Bull. Seism. Soc. Am.* 72, S131-S168.
- Bakun, W. H. and L. R. Johnson (1970). Short period spectral discriminants for explosions, *Geophys. J. R. Astr. Soc.* 22, 139-152.
- Blandford, R. R. and P. Klouda (1980). Magnitude-yield results at the Tonto Forest Observatory, in *Studies of seismic wave characteristics at regional distances, AL-80-1*, Teledyne Geotech, Alexandria, Virginia.

- Borg, I. Y. (1983). Peaceful nuclear explosions in Soviet gas condensate fields, *Energy and Technology Review* (May 1983), 30-33, Lawrence Livermore National Laboratory, Livermore, California.
- Brune, J. N. (1970). Tectonic stress and the spectra of seismic shear waves from earthquakes, *J. Geophys. Res.* 75, 4997-5009; Correction, *J. Geophys. Res.* 76, 5002.
- Egorkin, A. V. , T. A. Lamova, and N. G. Mikhailova (1987). Possibility of recording upper mantle converted waves, *Computational Seismology* 20, 179-191.
- Evernden, J. F., C. B. Archambeau, and E. Cranswick (1986). An evaluation of seismic decoupling and underground nuclear test monitoring using high-frequency seismic data, *Rev. of Geophysics* 24, 143-215.
- Gupta, I. N. and R. R. Blandford (1987). A study of P waves from Nevada Test Site explosions: Near-source information from teleseismic observations? *Bull. Seism. Soc. Am.*, 77, 1041-1056.
- Jordan, T. H. and L. N. Frazer (1975). Crustal and upper mantle structure from Sp phases, *J. Geophys. Res.* 80, 1504-1518.
- McLaughlin, K. L., T. Barker, and J. Stevens (1988a). An analysis of 2-D axisymmetric nonlinear finite difference explosion simulations using moment tensor expansions, *EOS* 69, 1332 (abstract).
- McLaughlin, K. L., I. N. Gupta, M. E. Marshall, R. A. Wagner, and T. W. McElfresh (1988b). Studies of explosion source functions and amplitudes using available far-field seismic data, *TGAL-87-06*, Teledyne Geotech, Alexandria, Virginia.
- Owens, T. J., S. R. Taylor, and G. Zandt (1987). Crustal structure at Regional Seismic Test Network stations determined from inversion of broadband teleseismic P waveforms, *Bull. Seism. Soc. Am.* 77, 631-662.
- Shumway, R. H. and Z. A. Der (1985). Deconvolution of multiple time series, *Technometrics* 27, 385-393.
- Stead, R. J. and D. V. Helmberger (1988). Numerical-analytical interfacing in two dimensions with applications to modeling NTS seismograms, *PAGEOPH* 128, Nos. 1/2, 157-193.
- Sykes, L. R. and S. Ruggi (1986). Soviet underground nuclear testing: inferences from seismic observations and historical perspective, *NWD 86-4*, Natural Resources Defense Council, Washington, D.C.
- von Seggern, D. H. and R. R. Blandford (1972). Source time functions and spectra for underground nuclear explosions, *Geophys. J.* 31, 83-97.

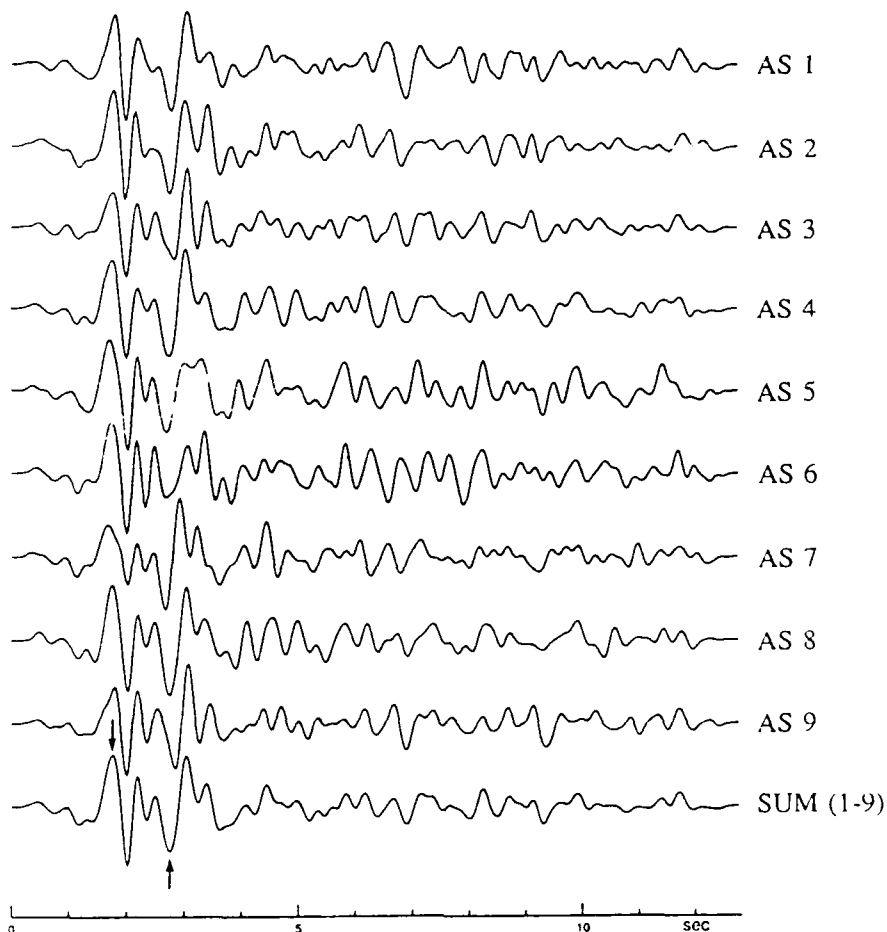


Figure 1. Deconvolved source time functions for the nine Astrakhan shots recorded at three RSTN stations. The stacked trace is shown at the bottom. The arrows denote the peaks of P and pP arrivals separated by about 1.0 sec.

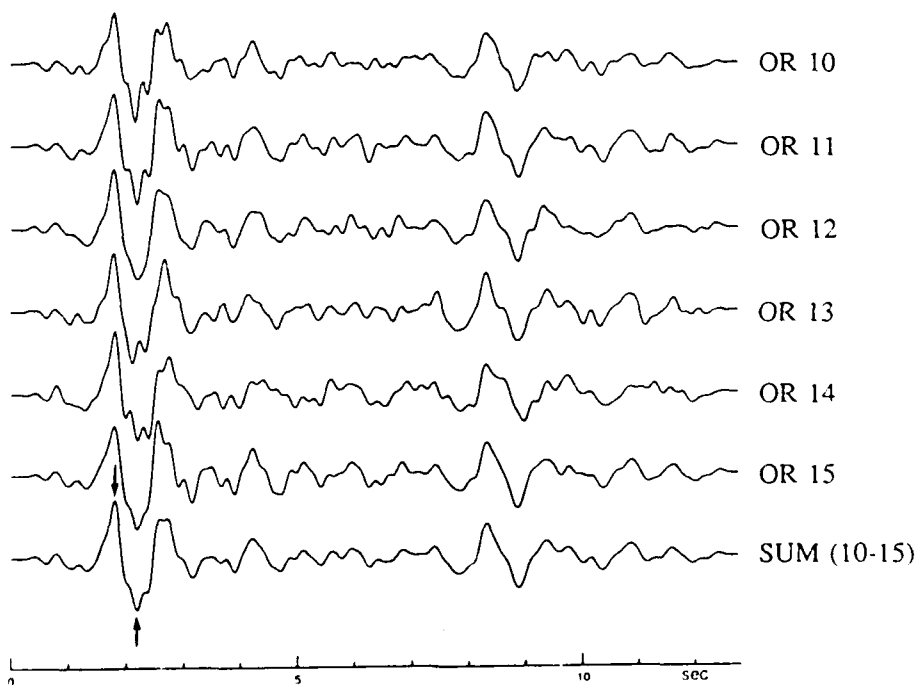


Figure 2. Deconvolved source time functions for the six Orenburg shots recorded at three RSTN stations. The stacked trace is shown at the bottom. The arrows denote the peaks of P and pP arrivals separated by about 0.4 sec. Note the secondary arrival about 6 to 7 sec after P for each shot.

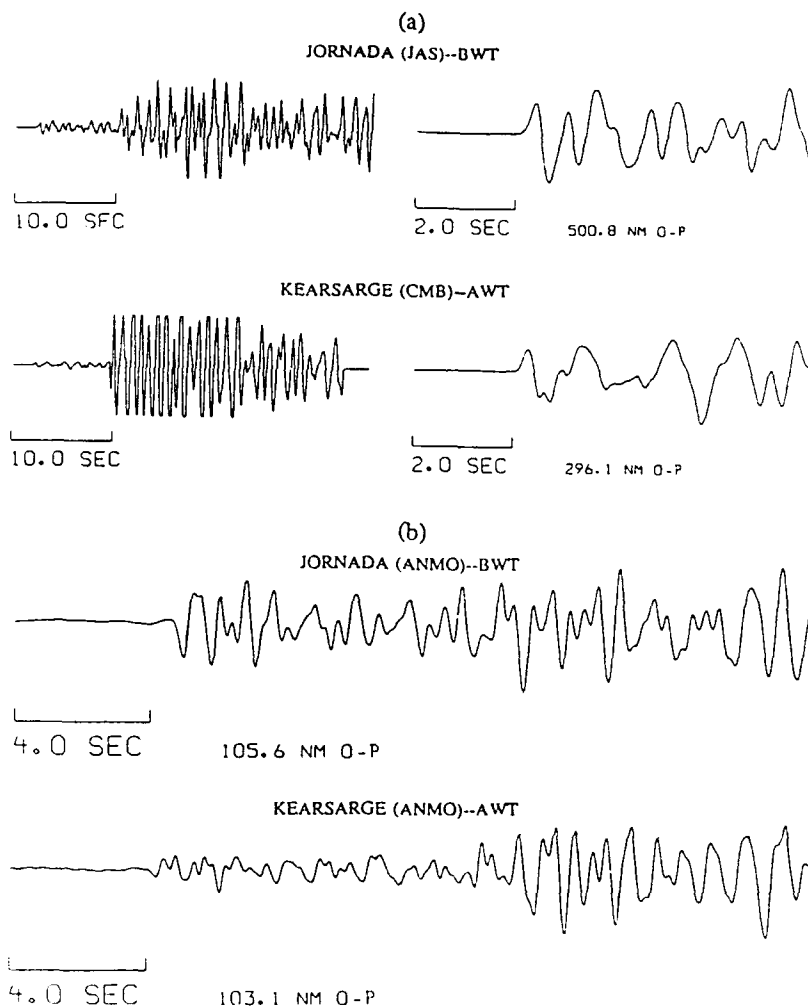


Figure 3. (a) Short-period, vertical-component records of JORNADA (below water table) at JAS and KEARSARGE (above water table) at CMB (located within 10 km of JAS) with 2 sec of noise before the onset of Pn, with two different time scales. Note the large difference in the Pn amplitudes. Pg is clipped for both events but Pn/Pg amplitude ratio is much smaller for KEARSARGE than for JORNADA. (b) Records of the same two shots at ANMO. Again, KEARSARGE has much smaller amplitude than JORNADA in the first several seconds of Pn.

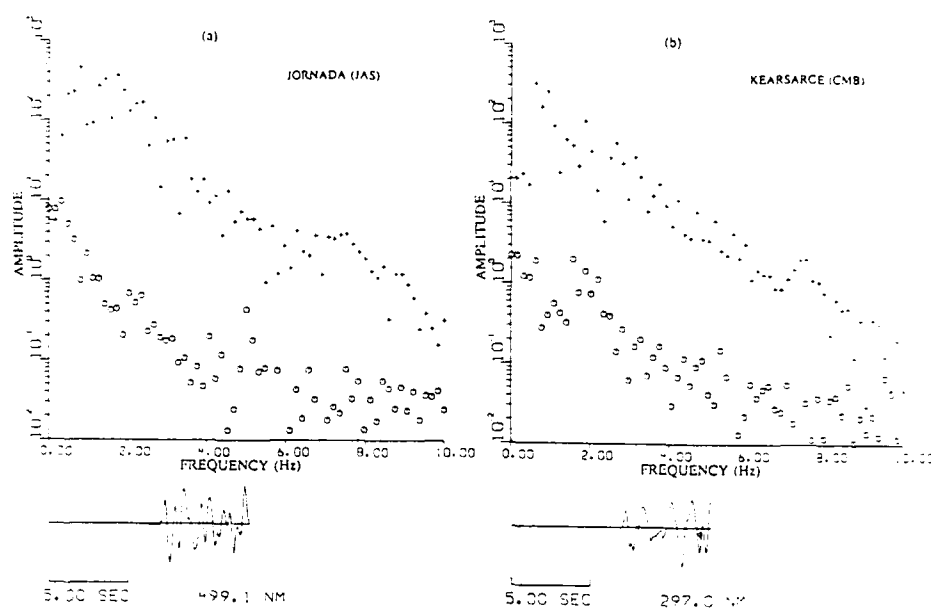


Figure 4a. Vertical-component displacement amplitude spectra (symbol +) of Pn, uncorrected for instrument response and based on 6.4 sec long window with 10% cosine taper, on JAS and CMB records of JORNADA and KEARSARGE, respectively. Spectra of an equal window length of noise (symbol o) are also included. S/N appears good up to the Nyquist frequency of 10 Hz.

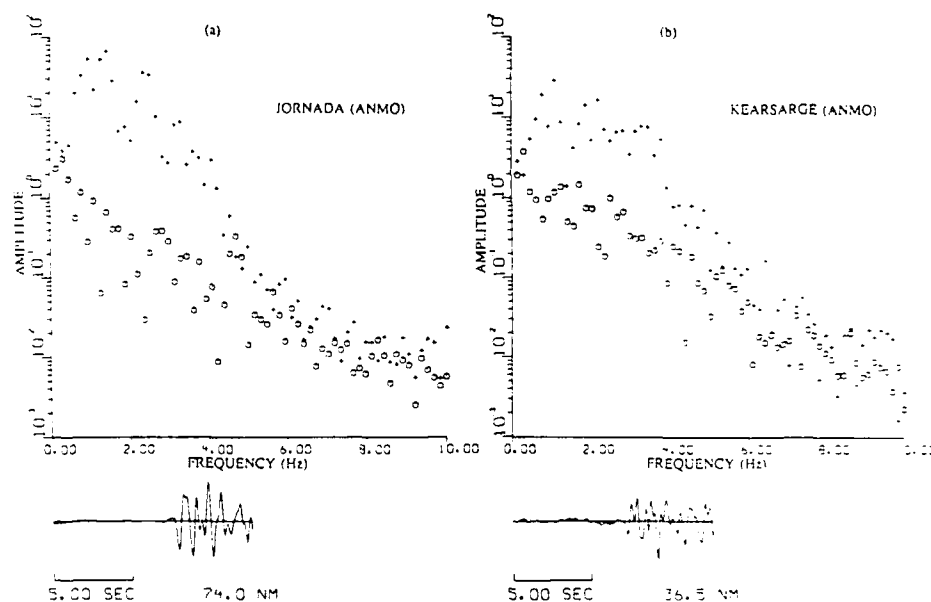


Figure 4b. Similar to Figure 4a based on ANMO records of the same two shots. S/N appears good up to about 6 Hz only.

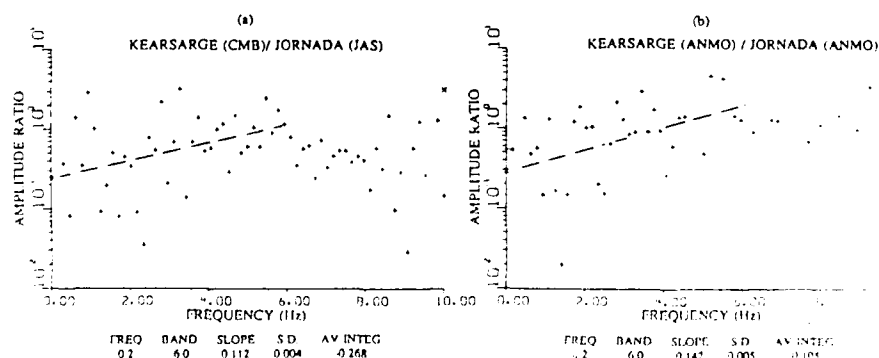


Figure 5. Spectral ratio KEARSARGE/JORNADA of Pn, corrected for noise, based on data from (a) CMB and JAS and (b) ANMO. Points for which S/N power ratio is less than 1.5 are not plotted. The dashed line shows the mean least squares slope over the frequency range of 0.2 to 6.0 Hz. Mean slope, with associated standard deviation, SD and mean value of log amplitude ratio (AV INTEG) is also indicated.

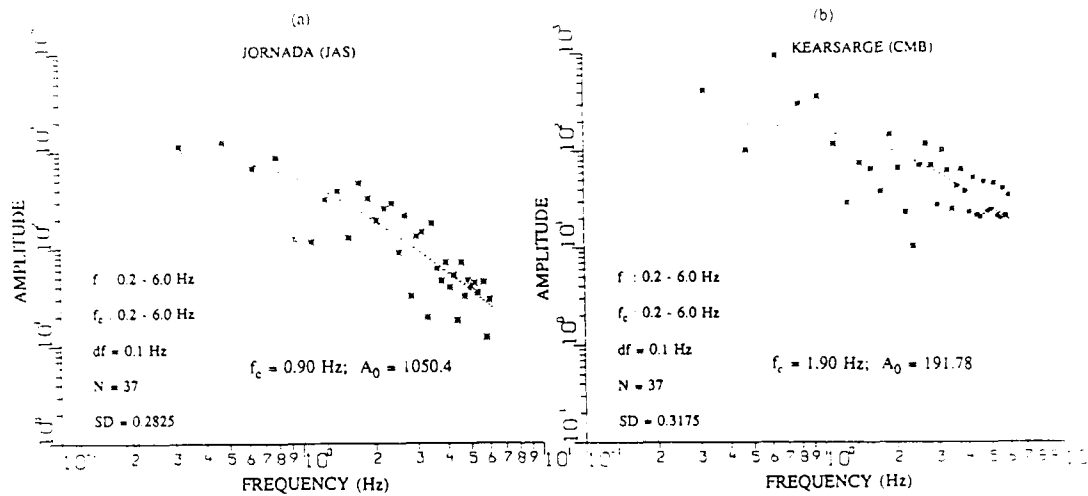


Figure 6a. Displacement spectral fits of (a) JORNADA at JAS and (b) KEARSARGE at CMB for corner frequency, f_c , and low-frequency spectral level, A_0 . Model spectrum (denoted by -) is a least-squares fit to the log-amplitude spectrum (denoted by *). Input parameters and the output results are listed.

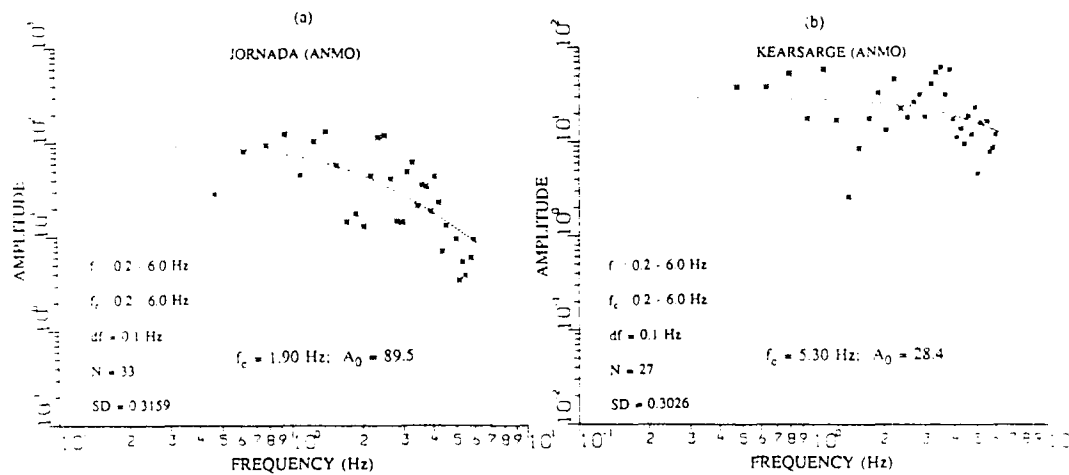


Figure 6b. Similar to Figure 6a for (a) JORNADA and (b) KEARSARGE, both at ANMO.

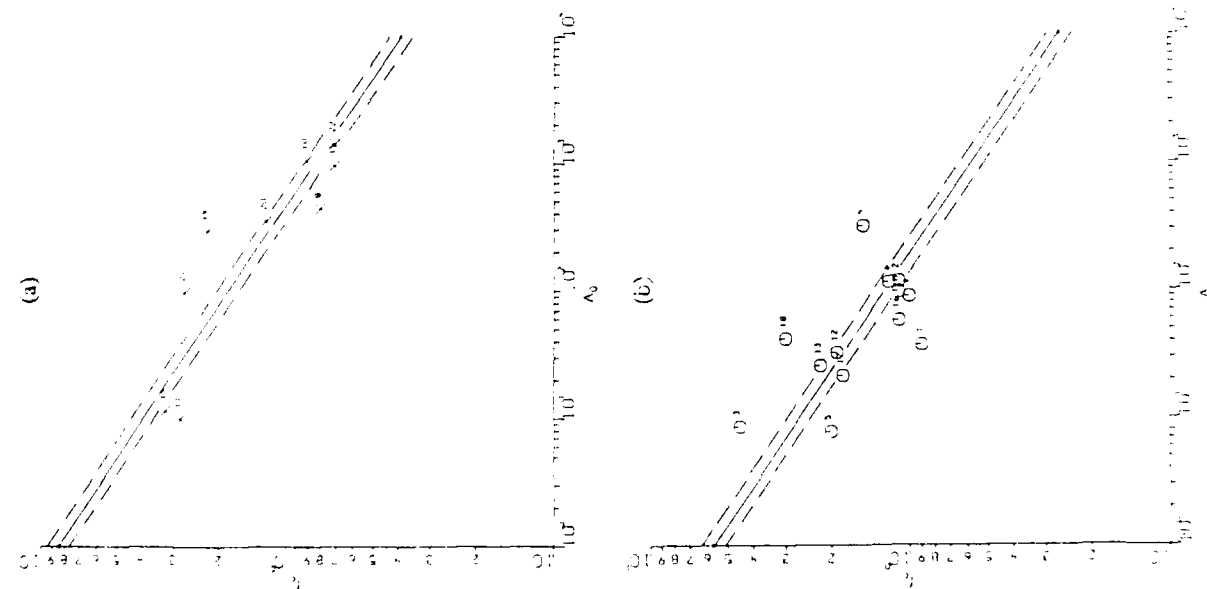


Figure 7. f_c versus A_0 for (a) 9 below water table and (b) 13 above water table shots. Forcing a slope of $-1/3$, the least squares linear regressions (continuous lines) have intercepts of 0.926 and 0.754, respectively. One standard deviation in the intercept value is shown by the dashed lines.

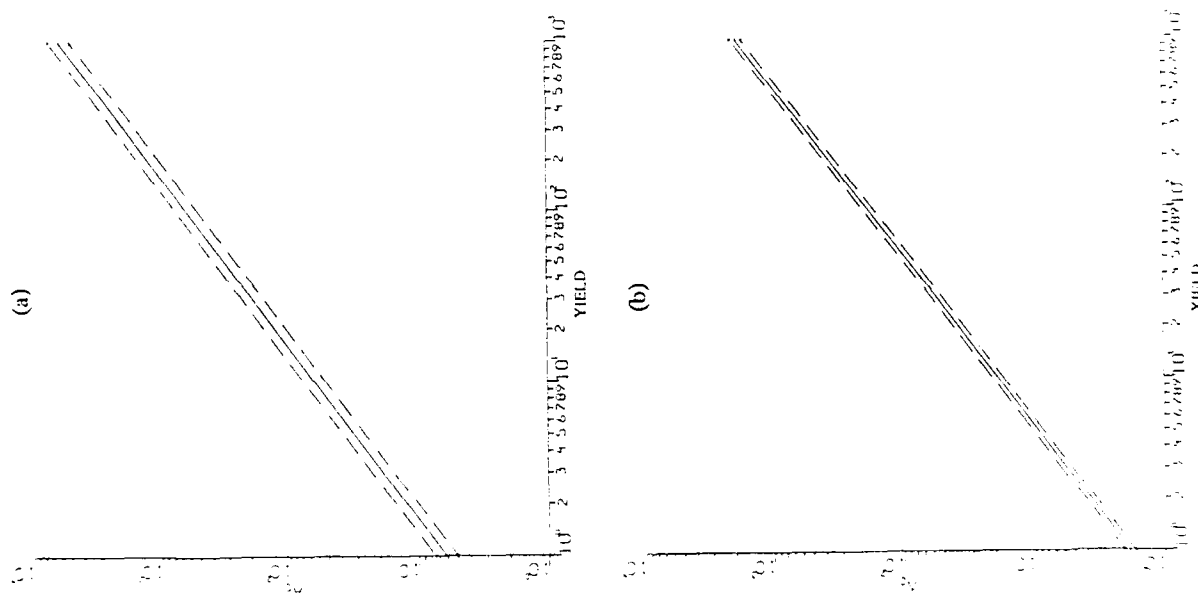


Figure 8. A_0 versus yield for (a) 9 below water table and (b) 13 above water table shots. Forcing a slope of 1, the least squares linear regressions (continuous lines) have intercepts of 0.789 and 0.276, respectively. One standard deviation variation in the intercept value is shown by the dashed lines.

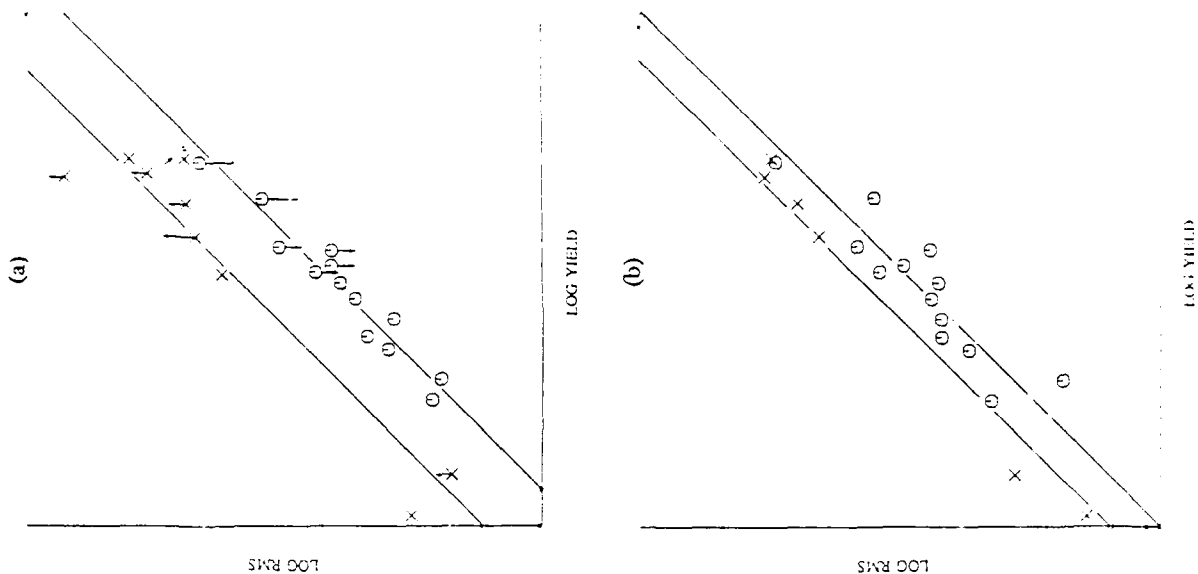


Figure 9. RMS amplitudes of (a) Pn and (b) Lg for the bandpass 0.5 to 1.5 Hz, versus yield for 22 shots recorded at JAS. The two mean lines with slope of unity for the below and above WT populations are separated by 0.542 and 0.300 magnitude unit, respectively. The arrows in Figure 9a indicate explosions with shot points within two cavity radii of the water table.

NTS SURFACE WAVE MOMENTS FROM A REGIONAL NETWORK

B. B. WOODS and D. G. HARKRIDER

Seismological Laboratory, California Institute of Technology,
Pasadena, California, 91125

SUMMARY

We have begun to obtain NTS explosion moments using theoretical fundamental mode surface waves from a network composed of 5 RSTN stations and long period recordings at Pasadena and Jamestown. The stations range in distance to NTS from 375 km at PAS to 3600 km at RSNY (Figure 1). The digital IRIS station at Pasadena is used to calibrate the Pasadena Press-Ewing recordings of earlier events. As more IRIS large dynamic range, broadband stations become routinely available they will be added to the network. The long period microseism noise at Pasadena and Jamestown restricts their use to events with m_b 's greater than 4.1 or 4.2. The PAS and JAS station are especially useful in determining the Love wave estimate of tectonic release from NTS events.

At this time, the moments, M_o , of 14 Pahute Mesa events, with yields in the approximate range of 10 to 100 ktons have been obtained from this network. All the events except one are just above the static water table. The exception is 50 meters below the water table but does not differ significantly in observed moment and m_b from one above the water table. In Figures 2-7, we show seismograms at six of the stations superimposed on the synthetic fundamental Rayleigh waves which are used to window the data and form spectral ratios to determine the moment. Spectral ratios with relative moment and standard deviation at six of the stations for the event Darwin are shown in Figures 8-13. The relative moment is a theoretical spectral amplitude weighted frequency average of the spectral ratio over a period range from 67 to 6.7 secs. For most events we use the vertical seismograms but in Figure 13 we use the rotated radial Press-Ewing recording at Pasadena. At m_b 's above 5.5 for NTS events, the vertical Press-Ewing frequently goes non linear while the horizontals are still useable as in this case.

The station relative moments and standard deviations are then used to determine an inverse station variance weighted least squares fit of this data with an explosion plus tectonic release mechanism which has a $\sin(2\phi)$ variation with ϕ the azimuth measured from the least squares determined strike. The fit as a function of azimuth is shown in Figures 14-25 for 12 of the events. This procedure determines the model explosion moment as well as its standard deviation. The assumed tectonic release model is vertical pure strike slip. The estimated strike azimuths are from 10 to 23 degrees west with a right lateral mechanism. The model fits for these events would not be improved by freeing the dip and slip of the mechanism. In order to reduce the degrees of freedom, we intend to include the Love waves which were also observed for these events.

The events range in NEIC m_b 's from 5.7 to 4.9. A linear regression of NEIC m_b 's against $0.9 \log_{10} M_o$ was made. No station corrections were used and the inversion was weighted by the inverse model variance of each event. The $\log M_o$ intercept was 0.25 m_b units less than Given and Mellman (1986) and the standard deviation was less than 0.12 (Figures 26-27).

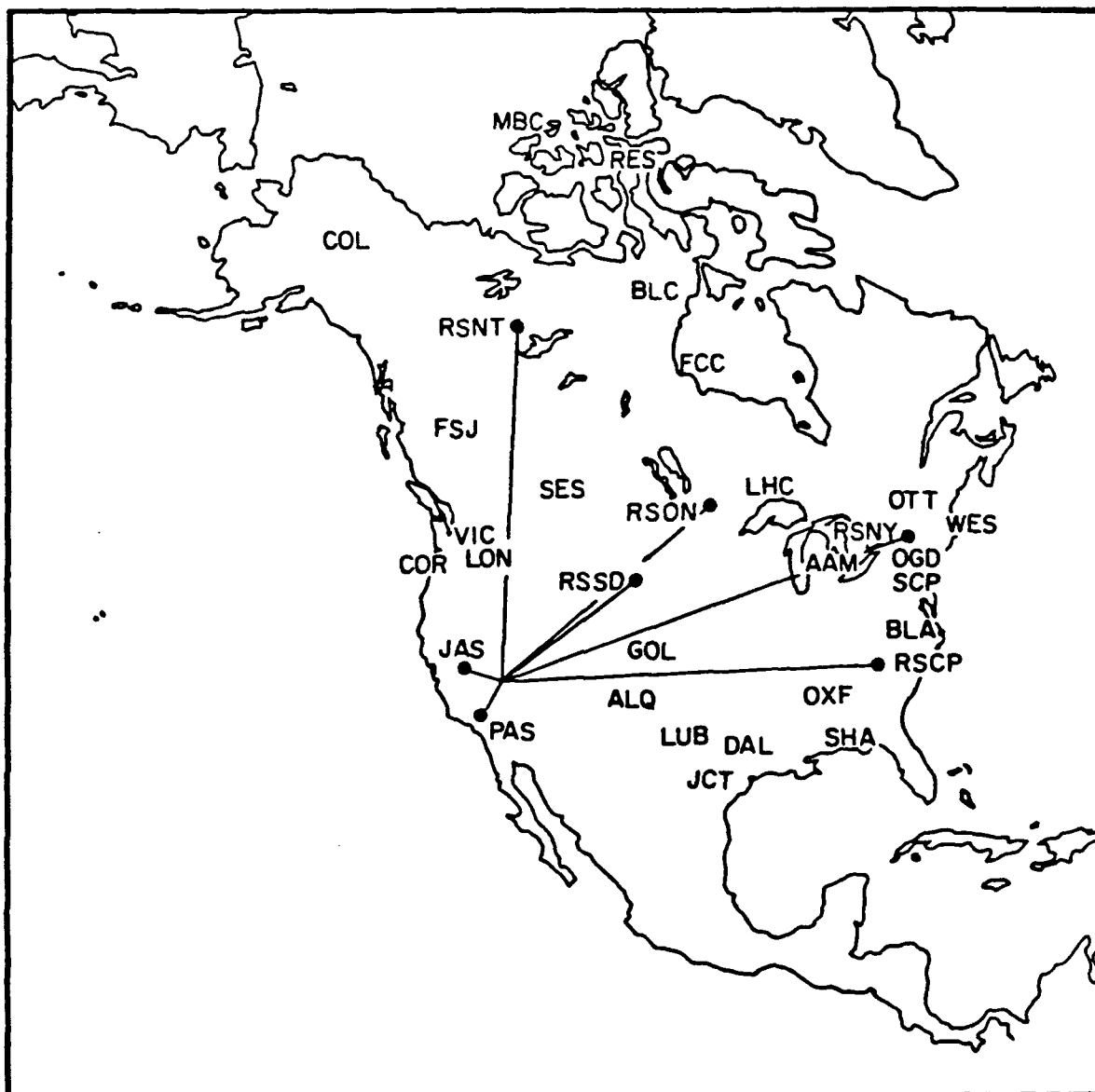


FIGURE 1

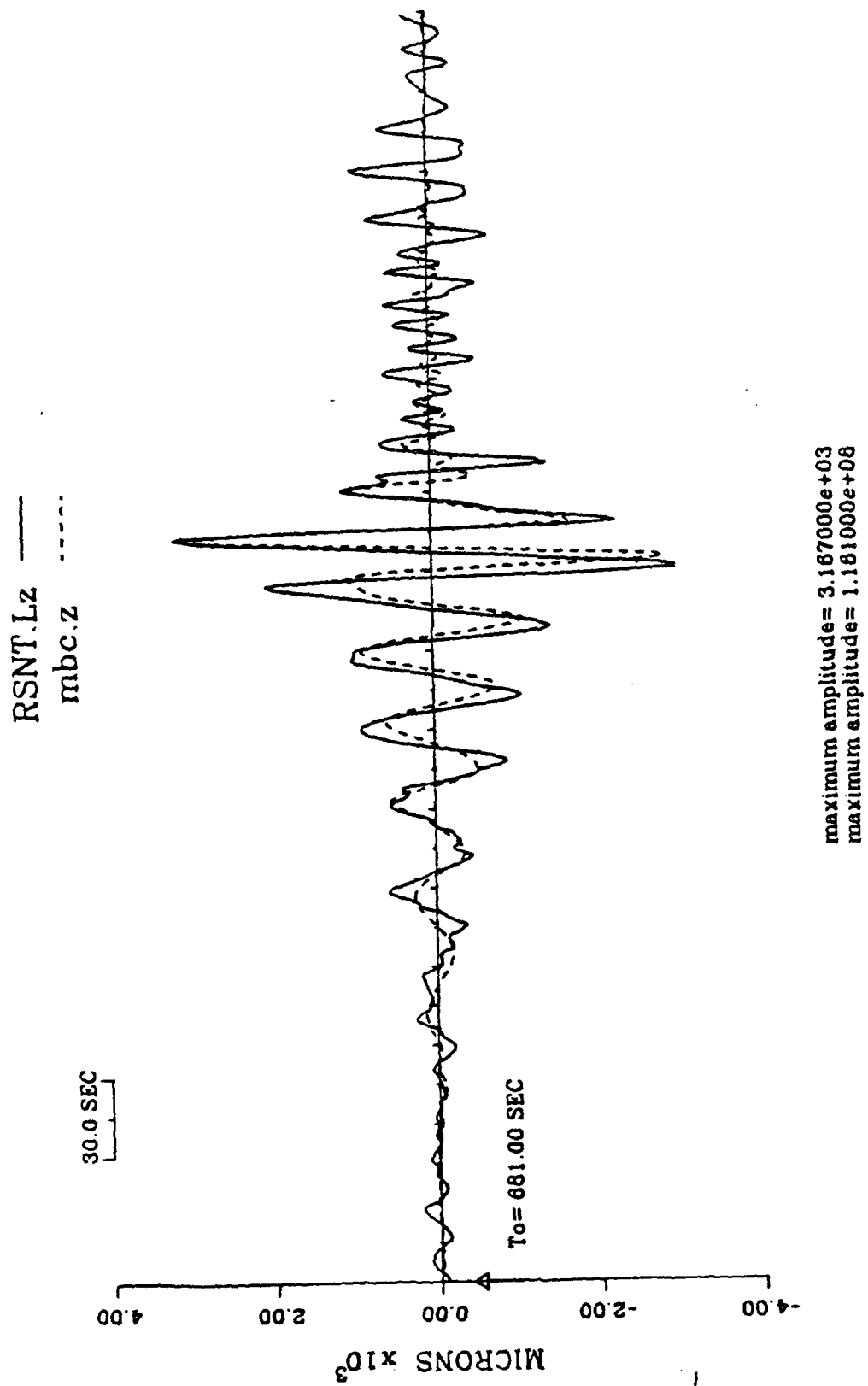


FIGURE 2

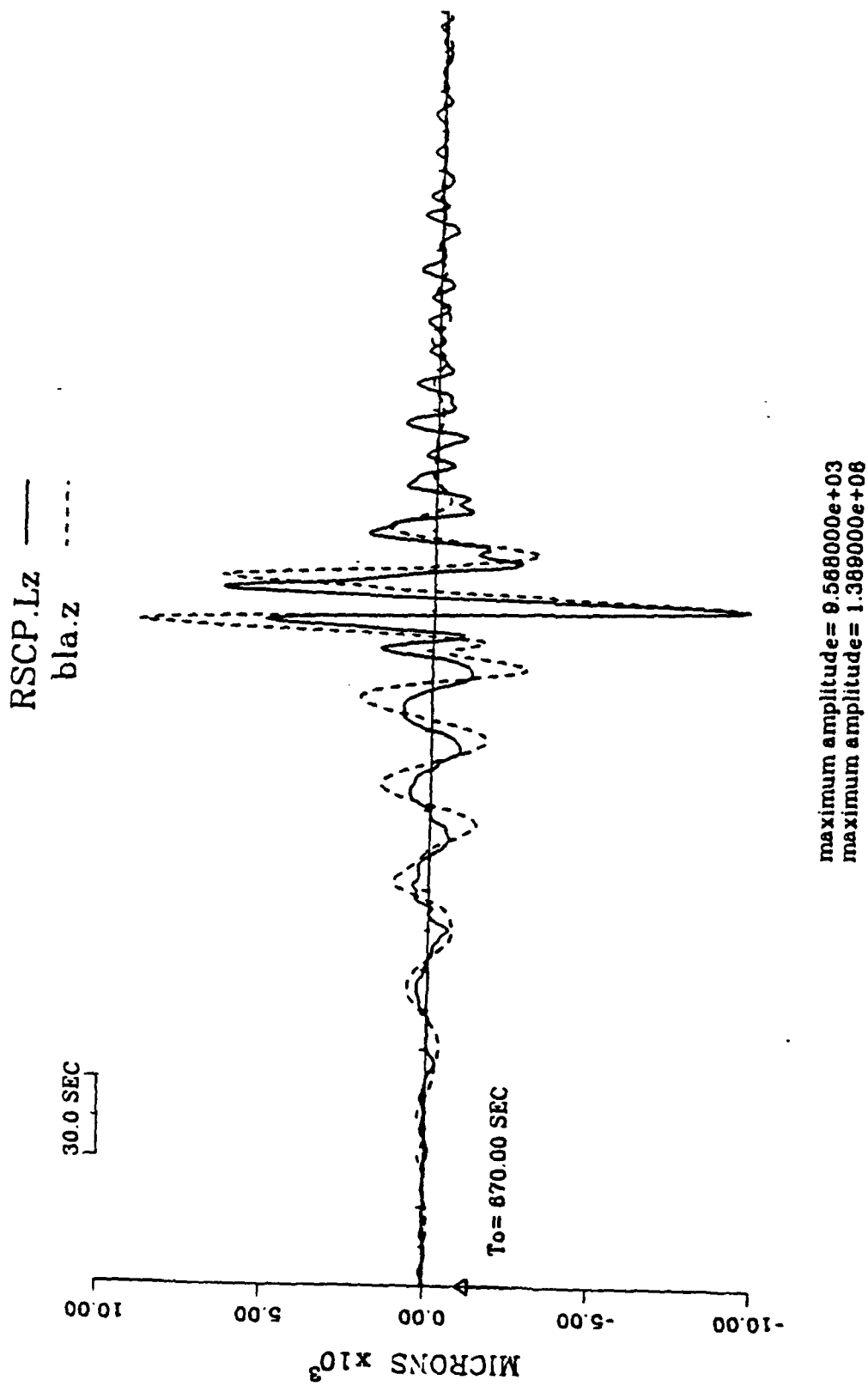


FIGURE 5

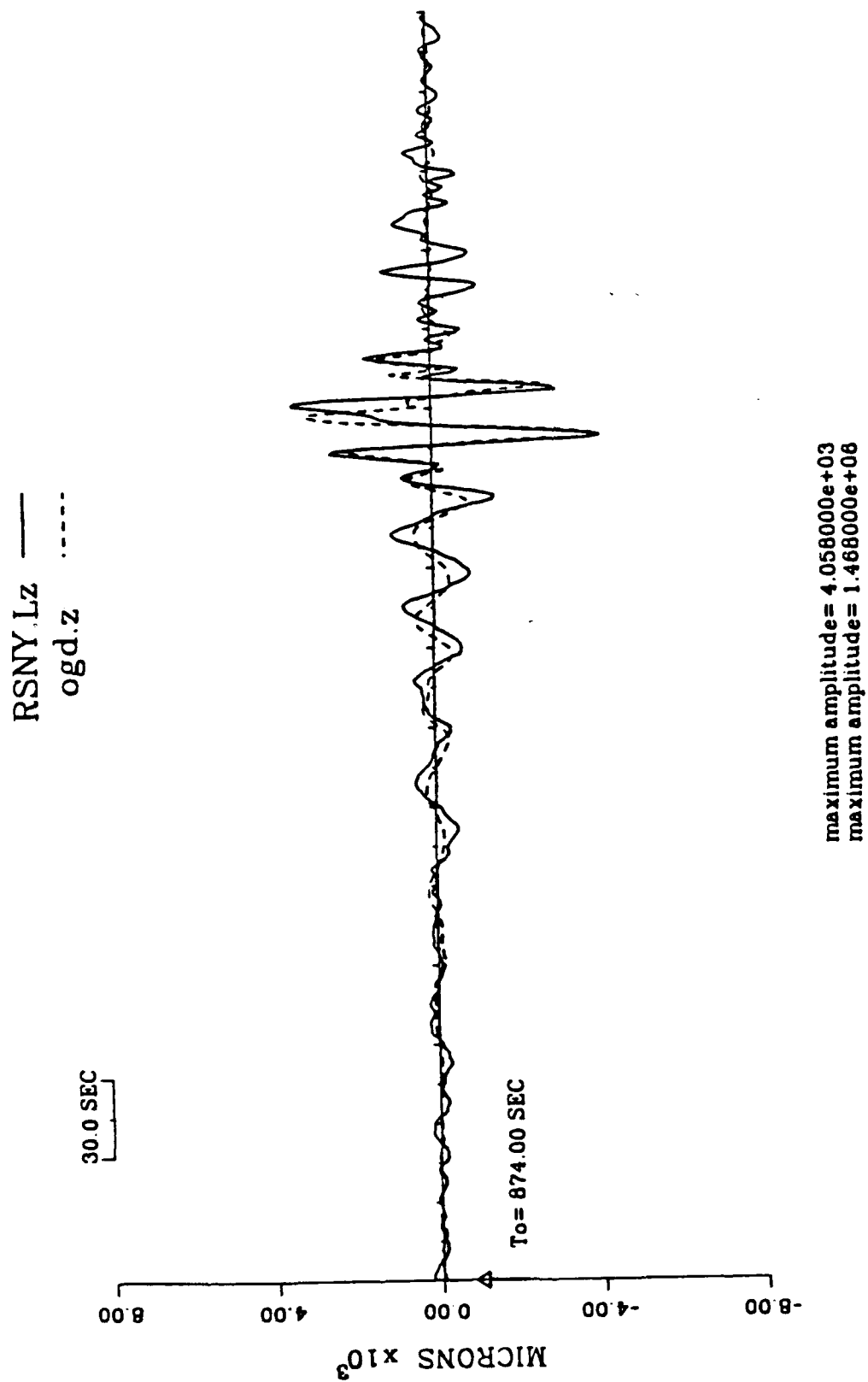


FIGURE 4

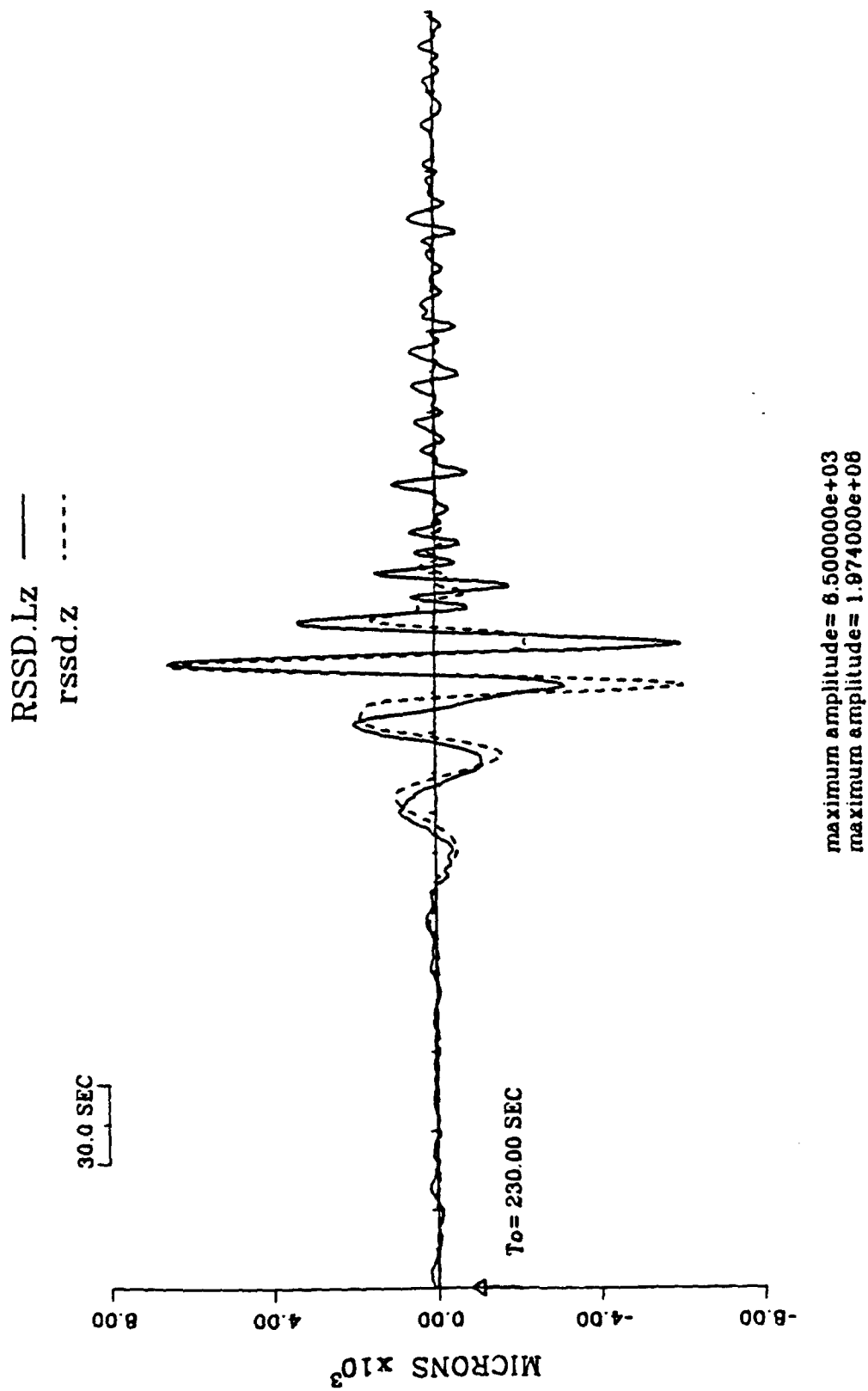


FIGURE 5

bel.z —
NTS-PAS.z - - - -

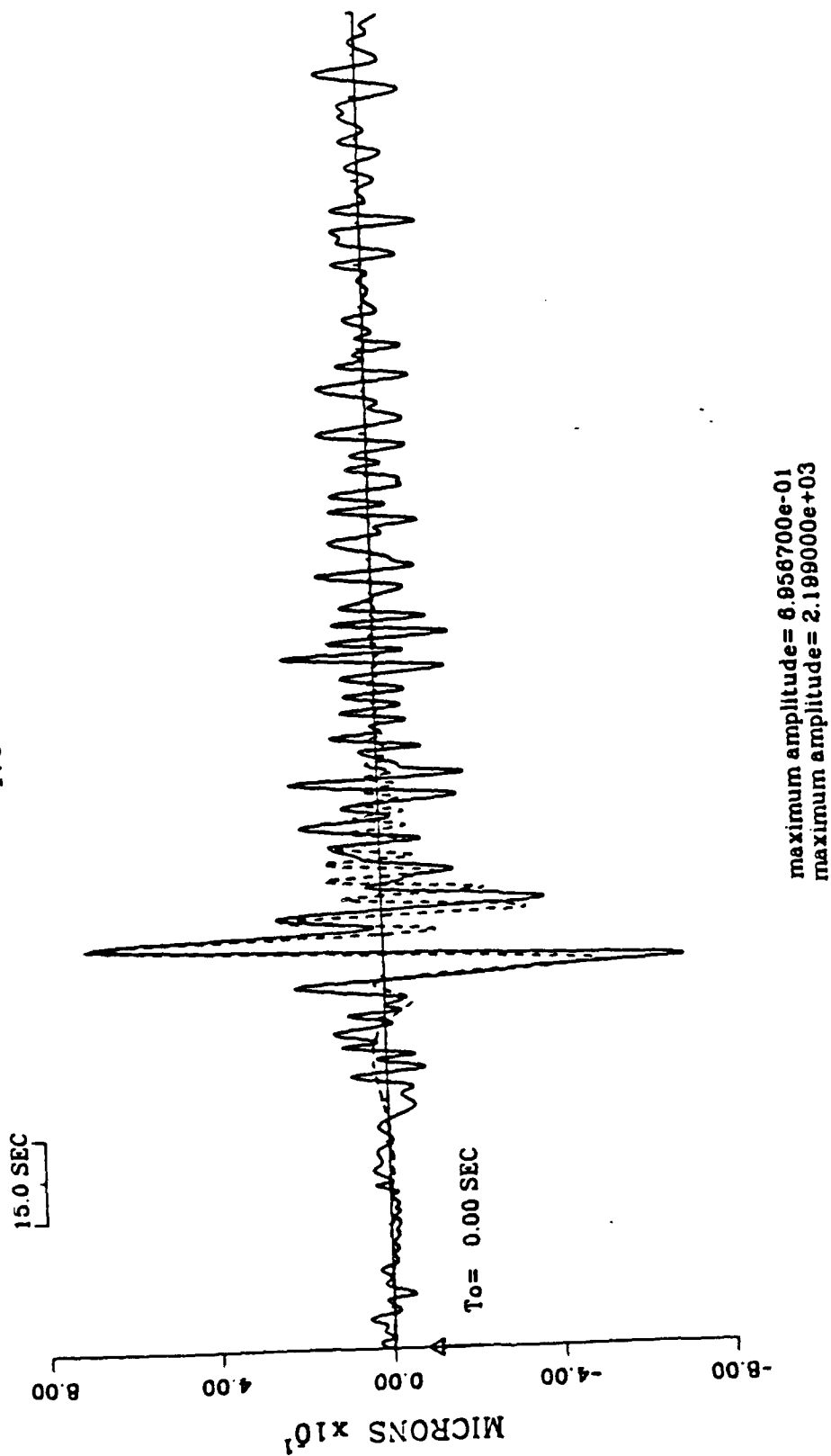


FIGURE 6

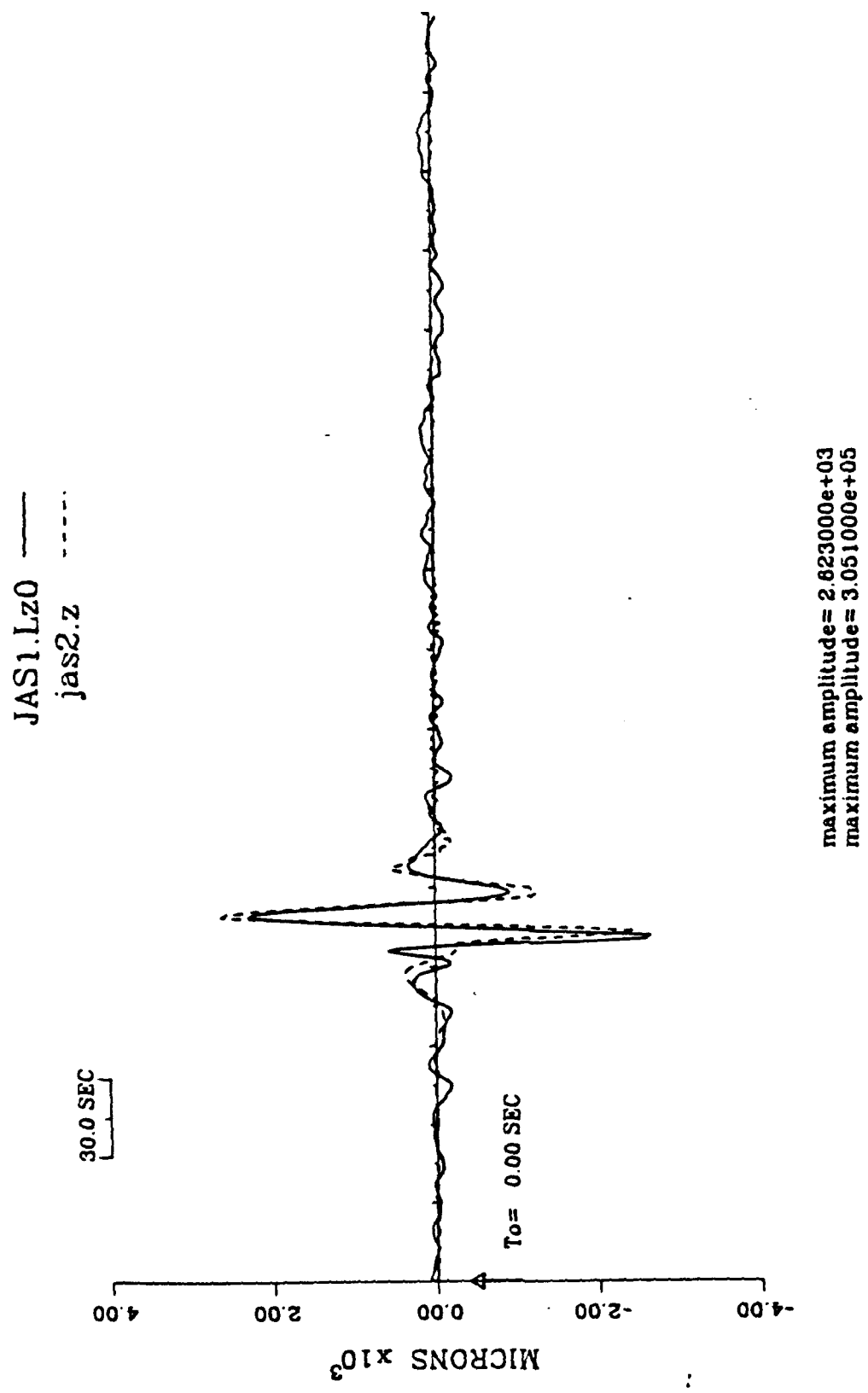


FIGURE 7

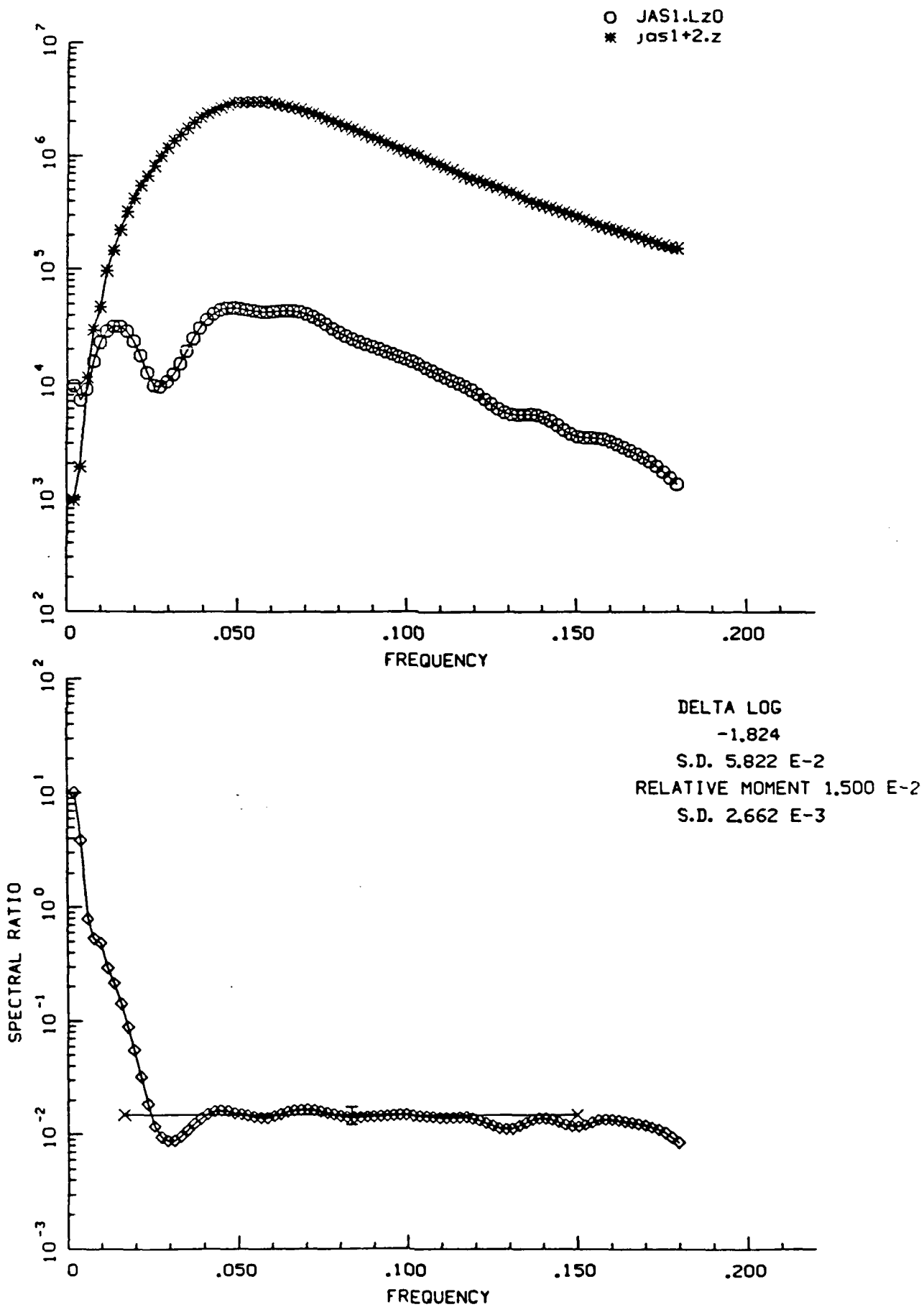


FIGURE 3

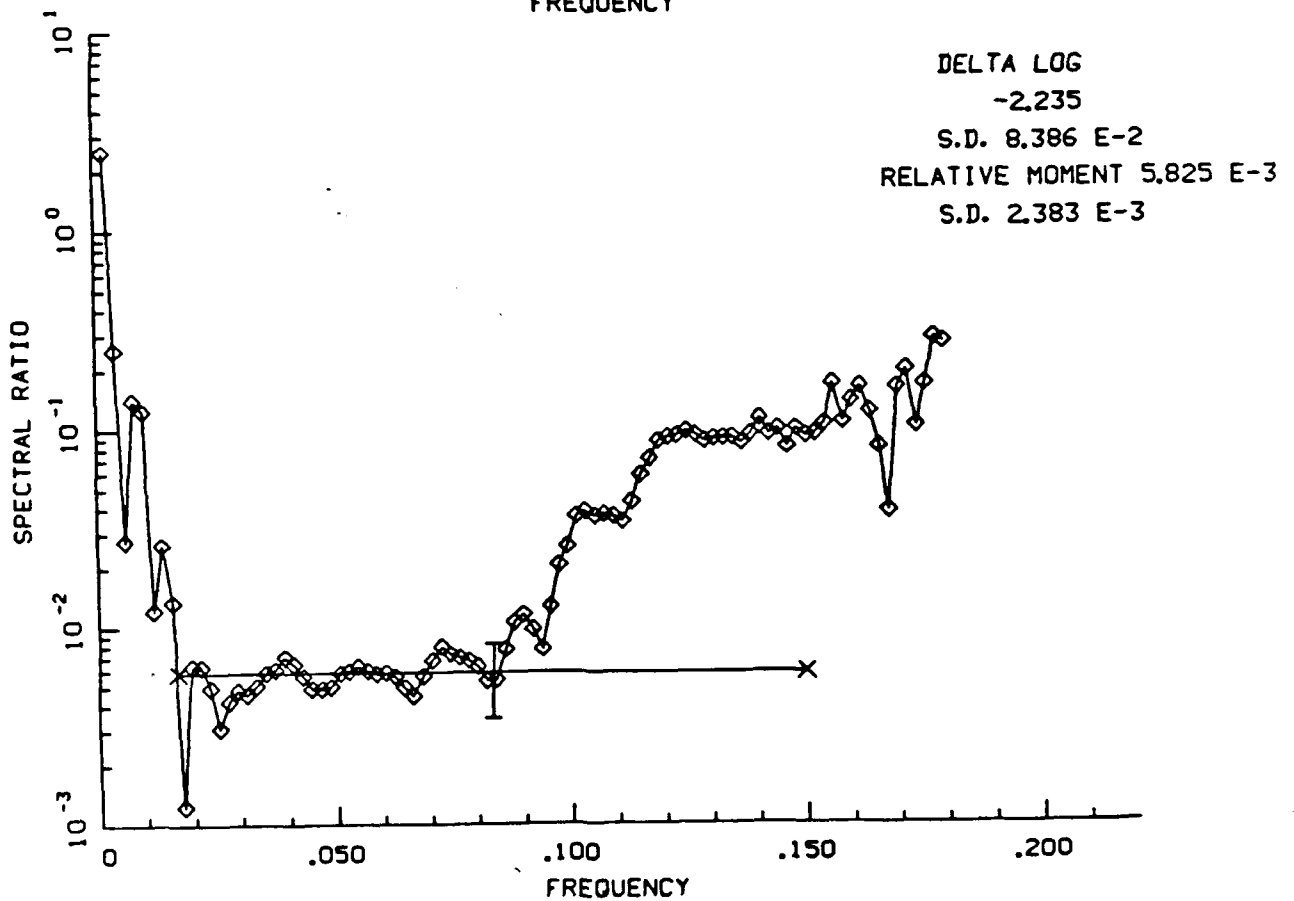
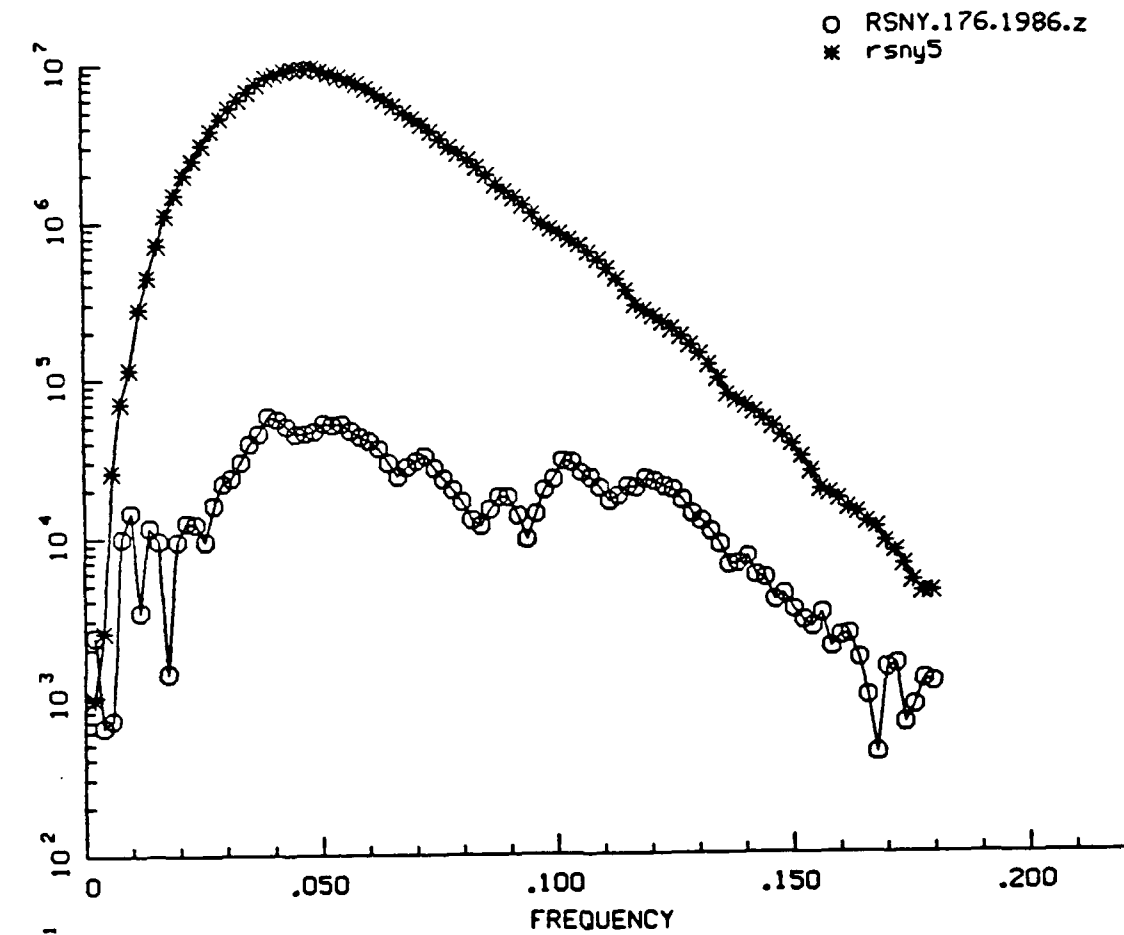


FIGURE 9

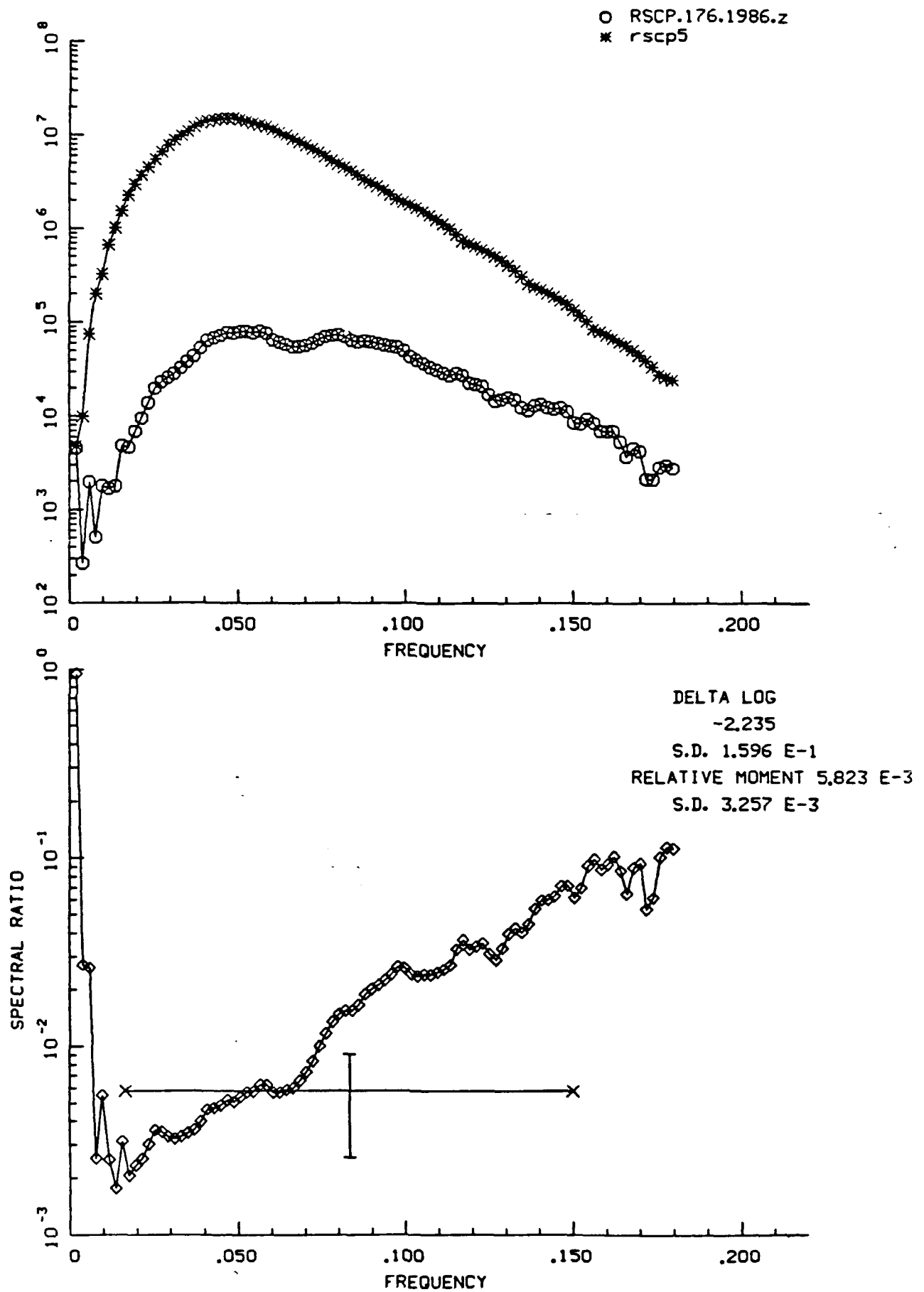


FIGURE 10

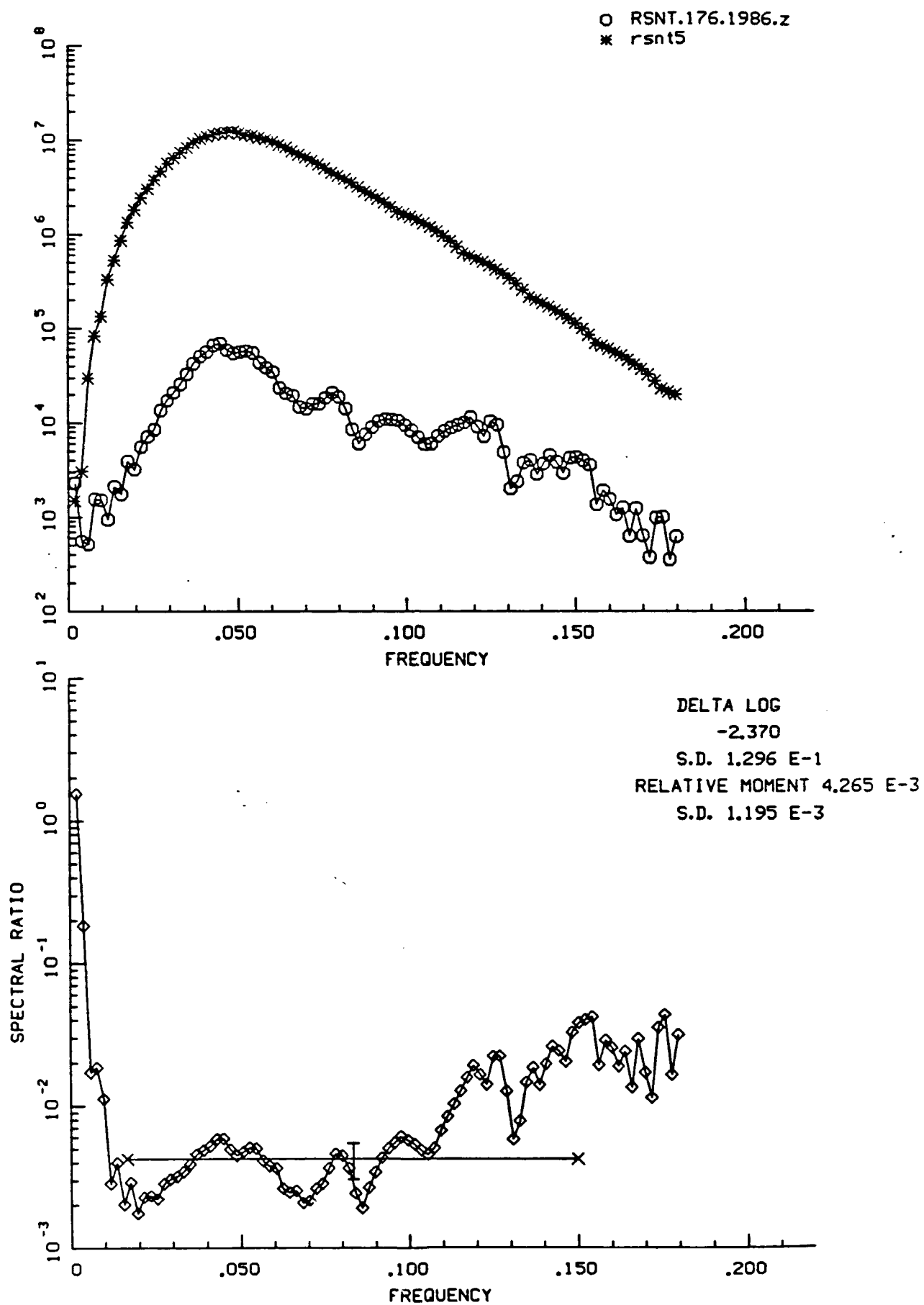
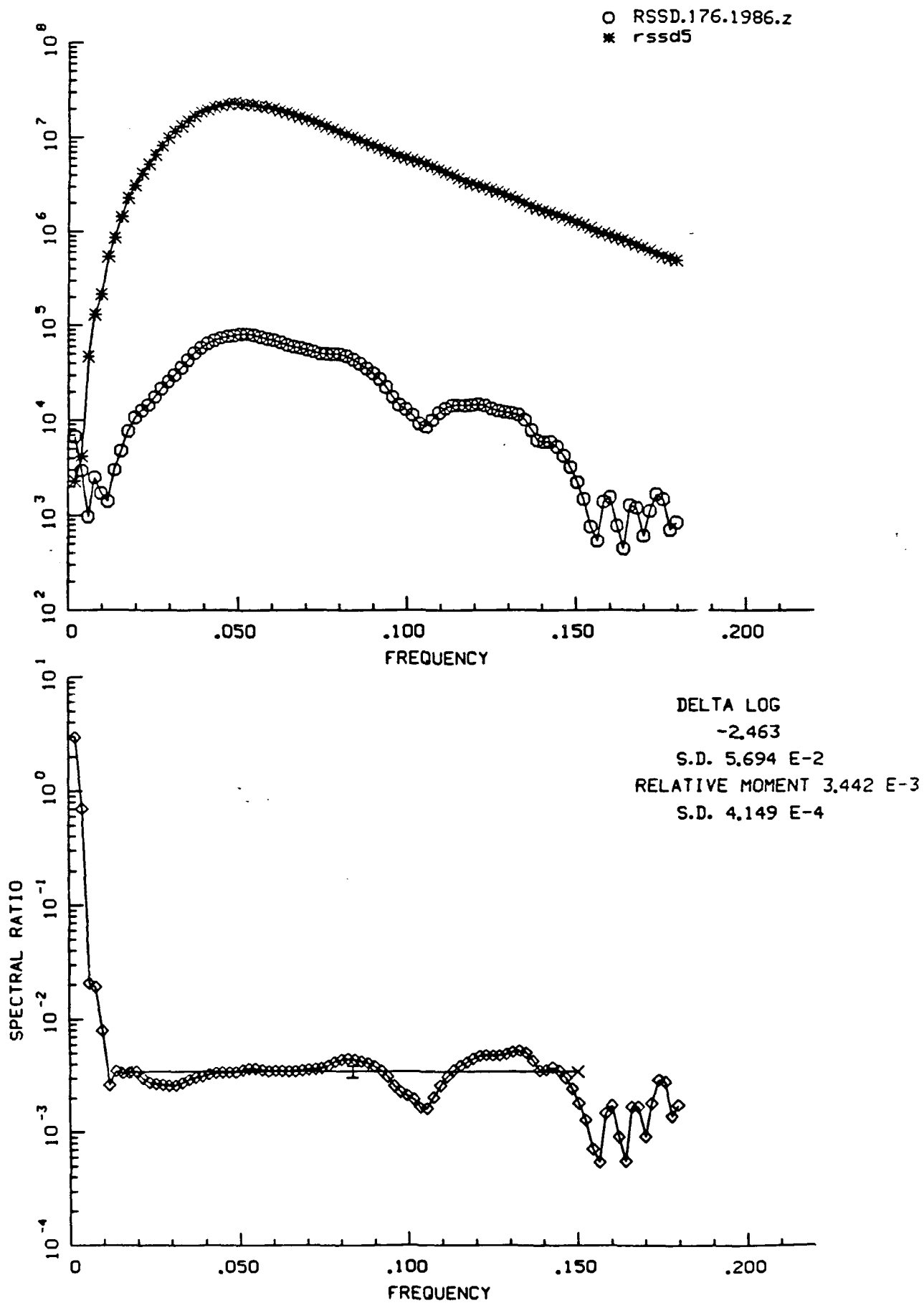


FIGURE 11



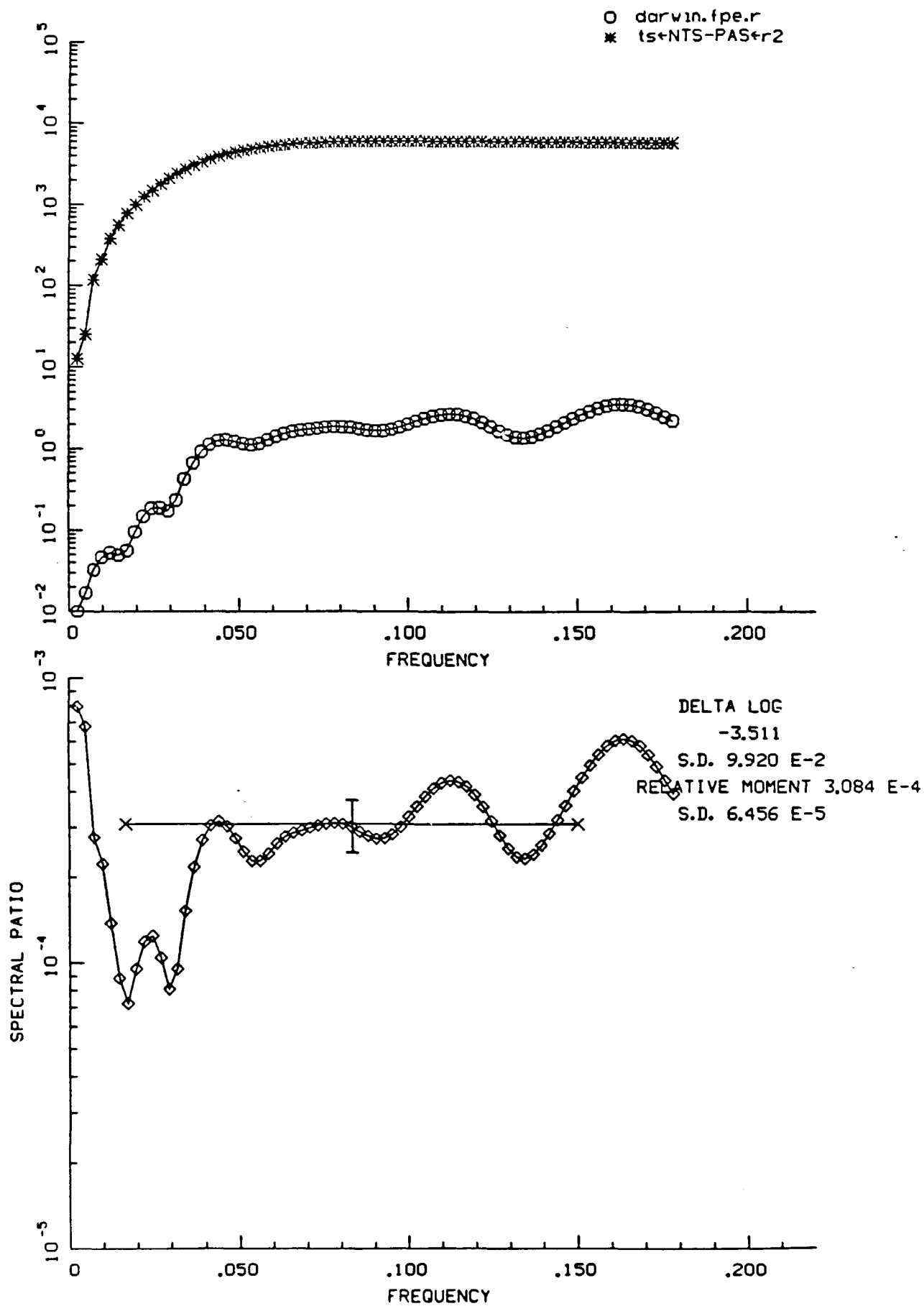


FIGURE 13

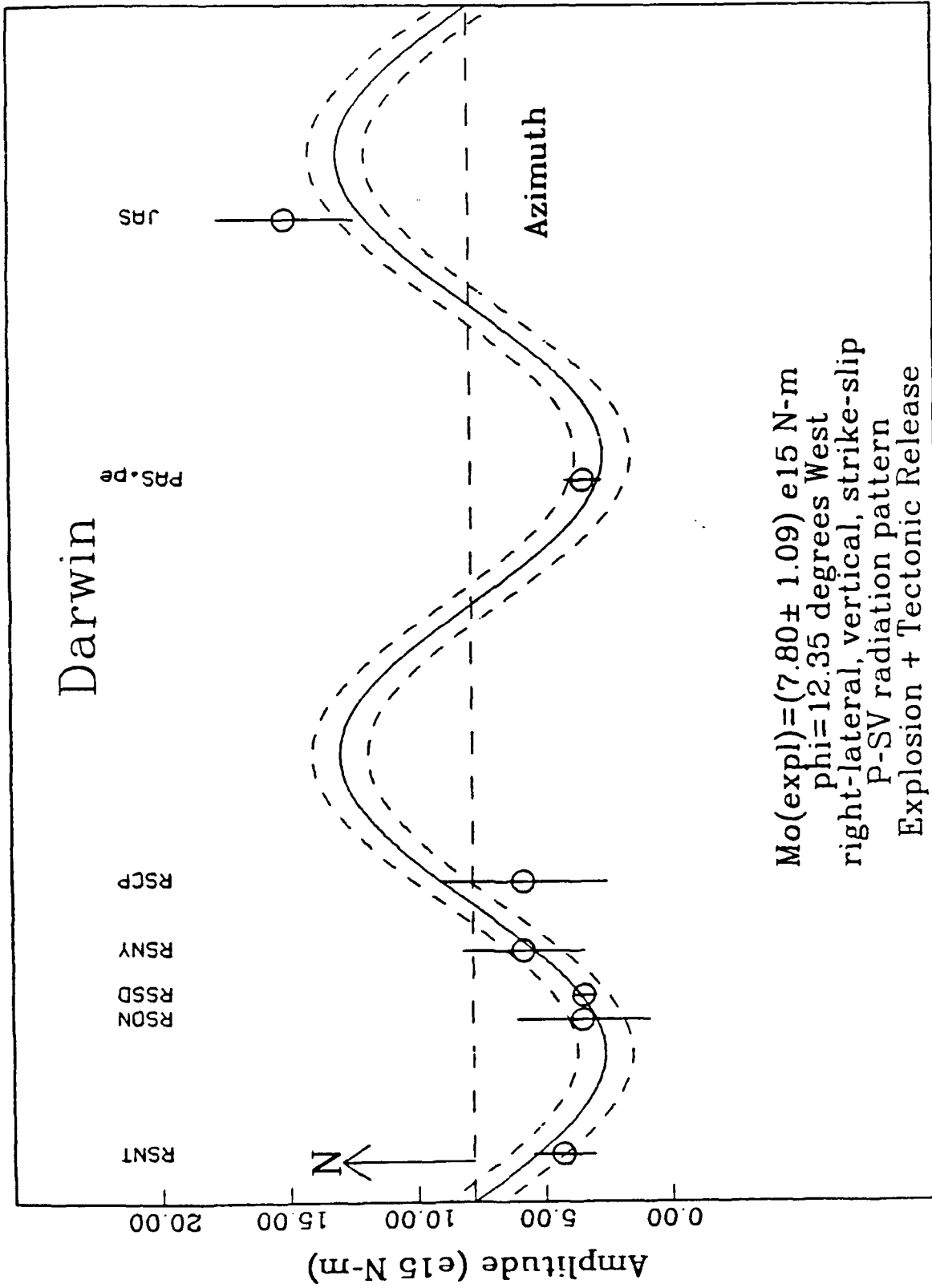


FIGURE 14

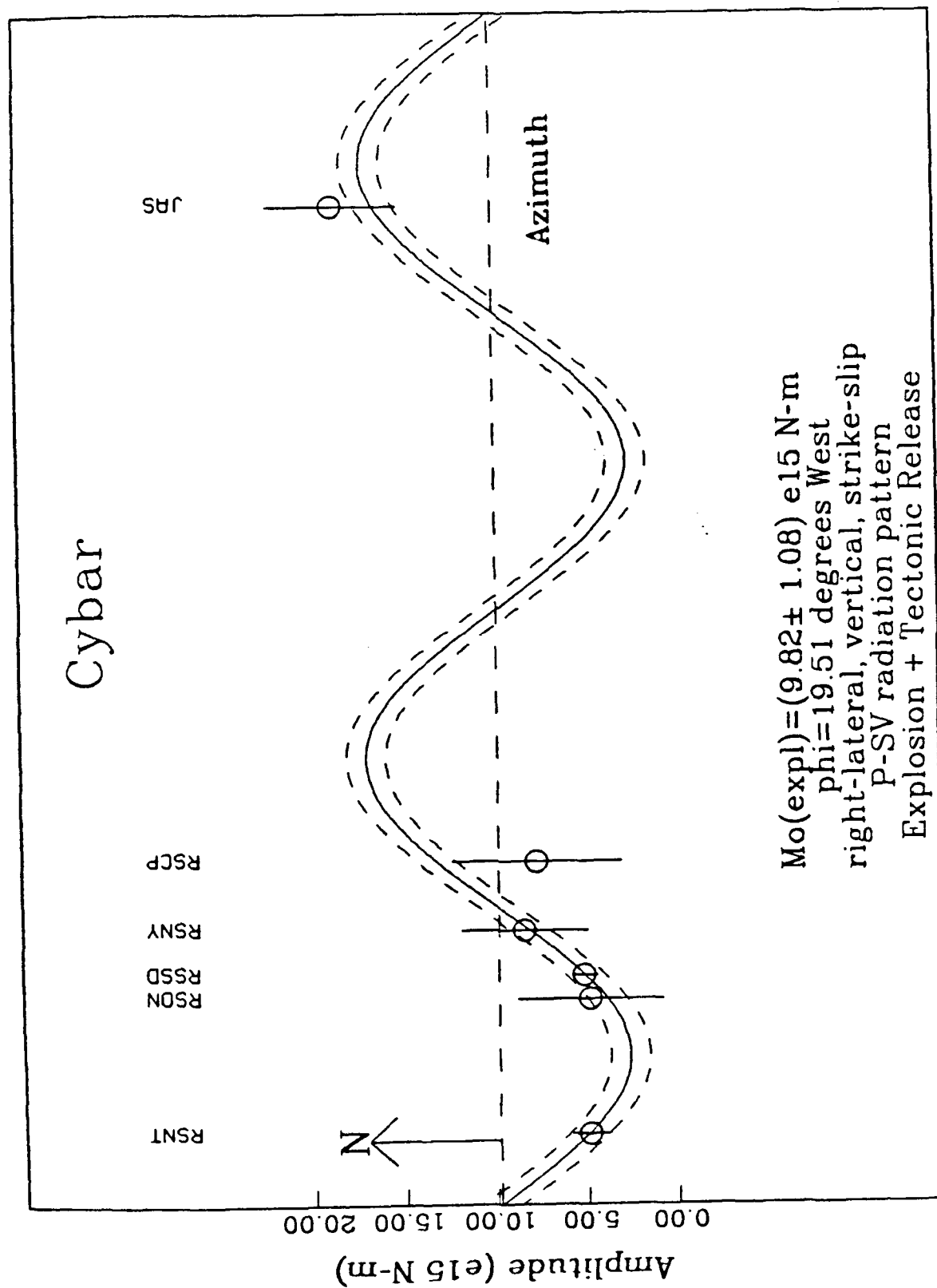


FIGURE 15

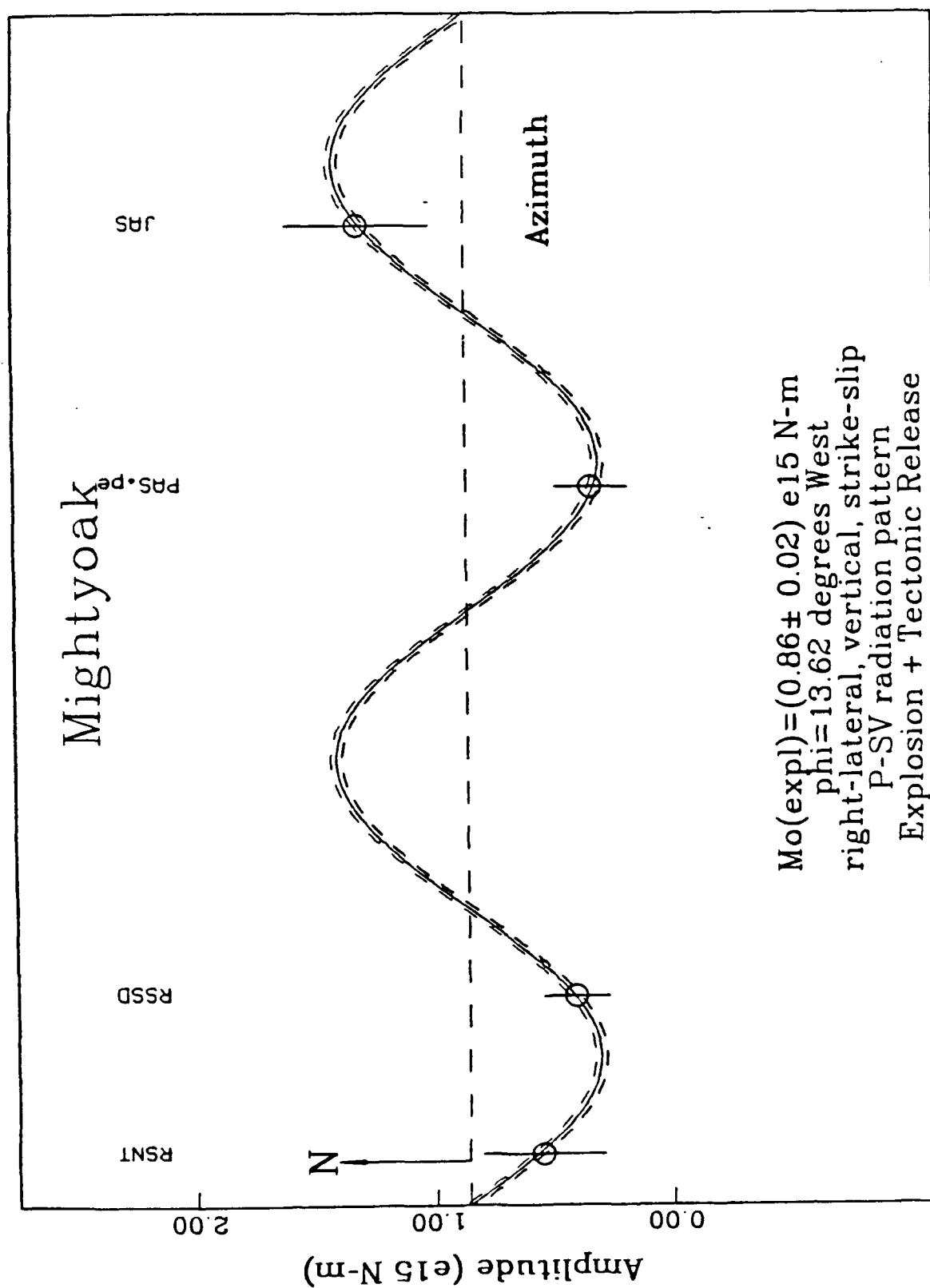


FIGURE 16

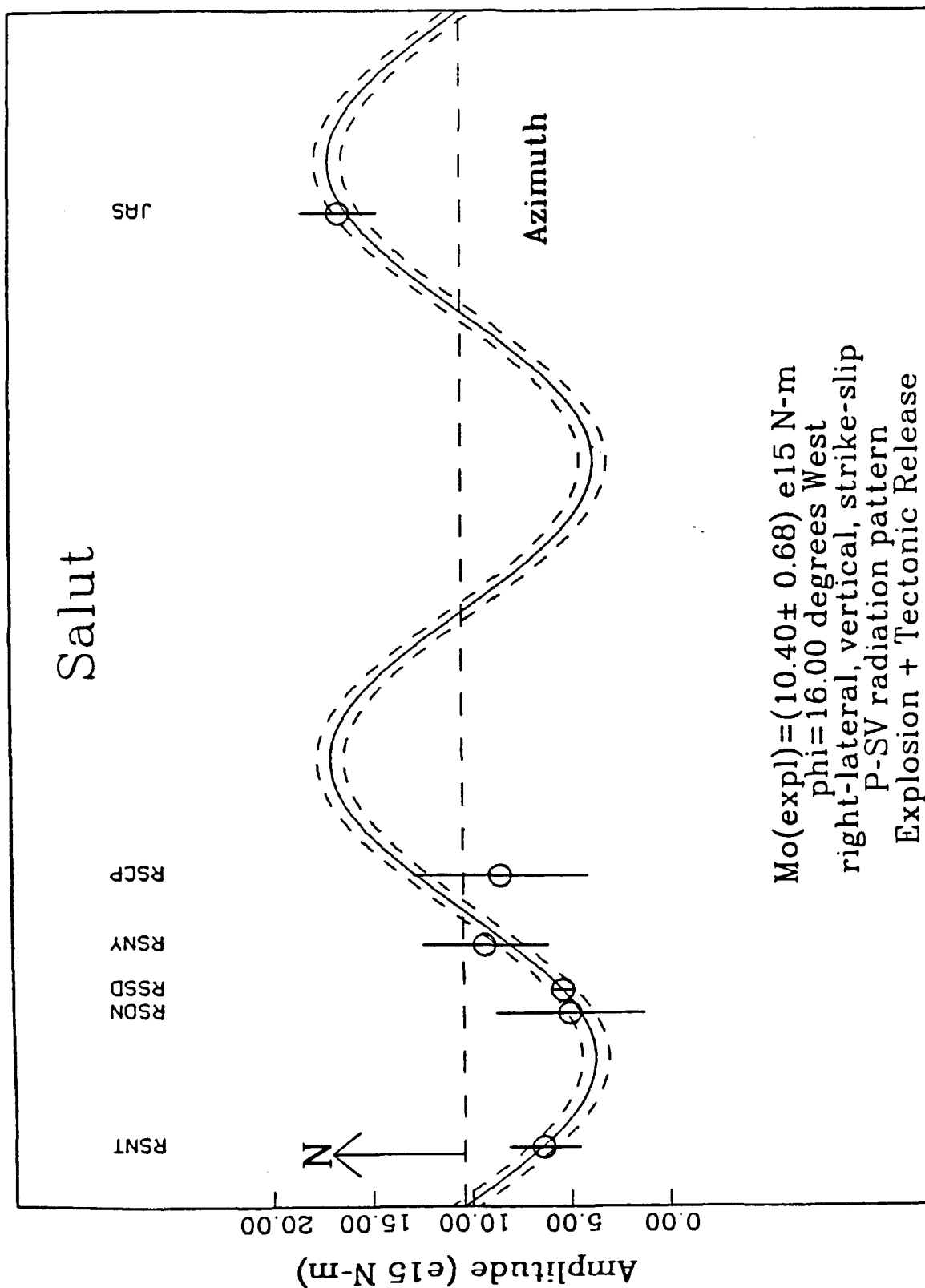


FIGURE 17

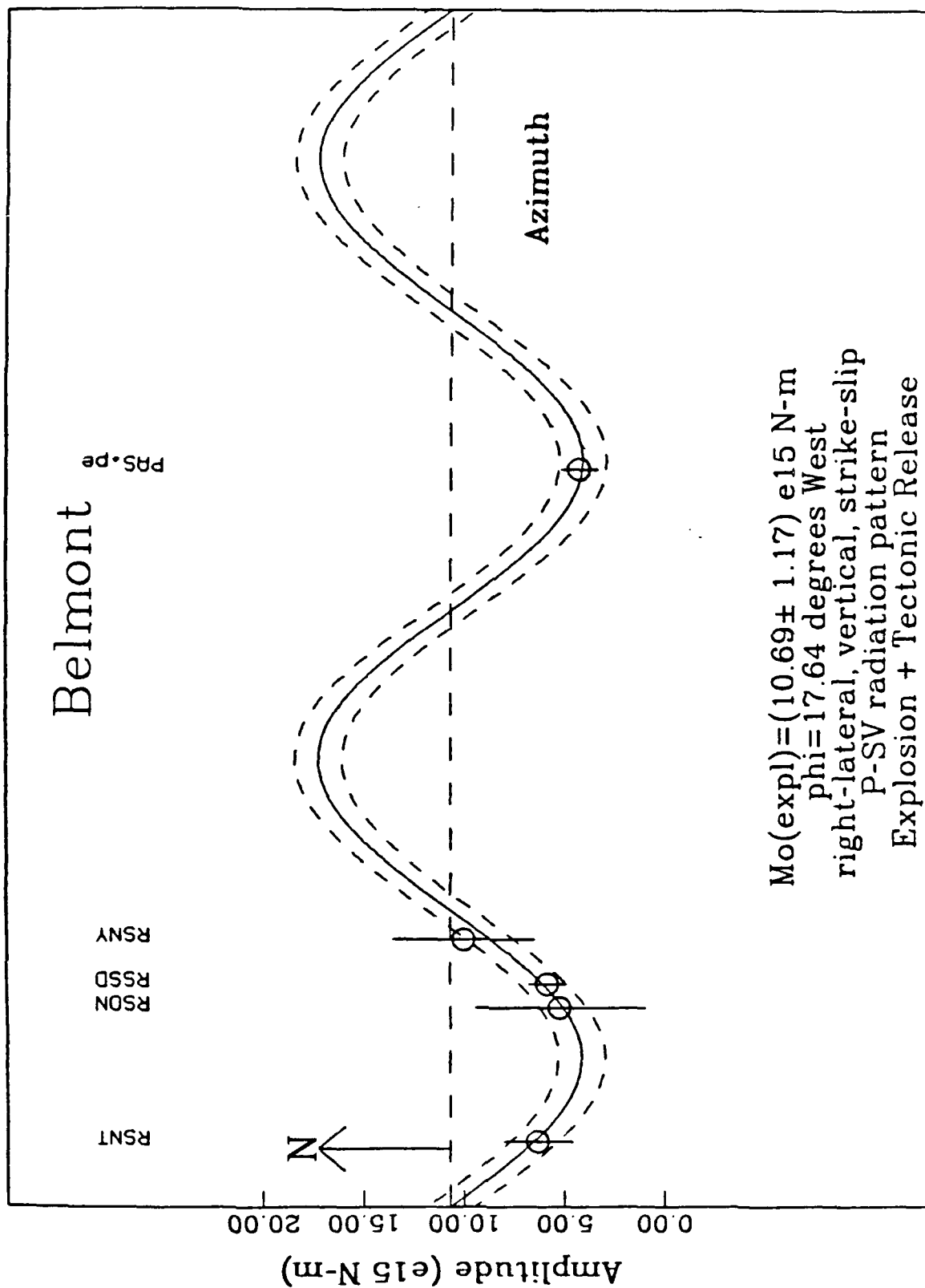


FIGURE 18

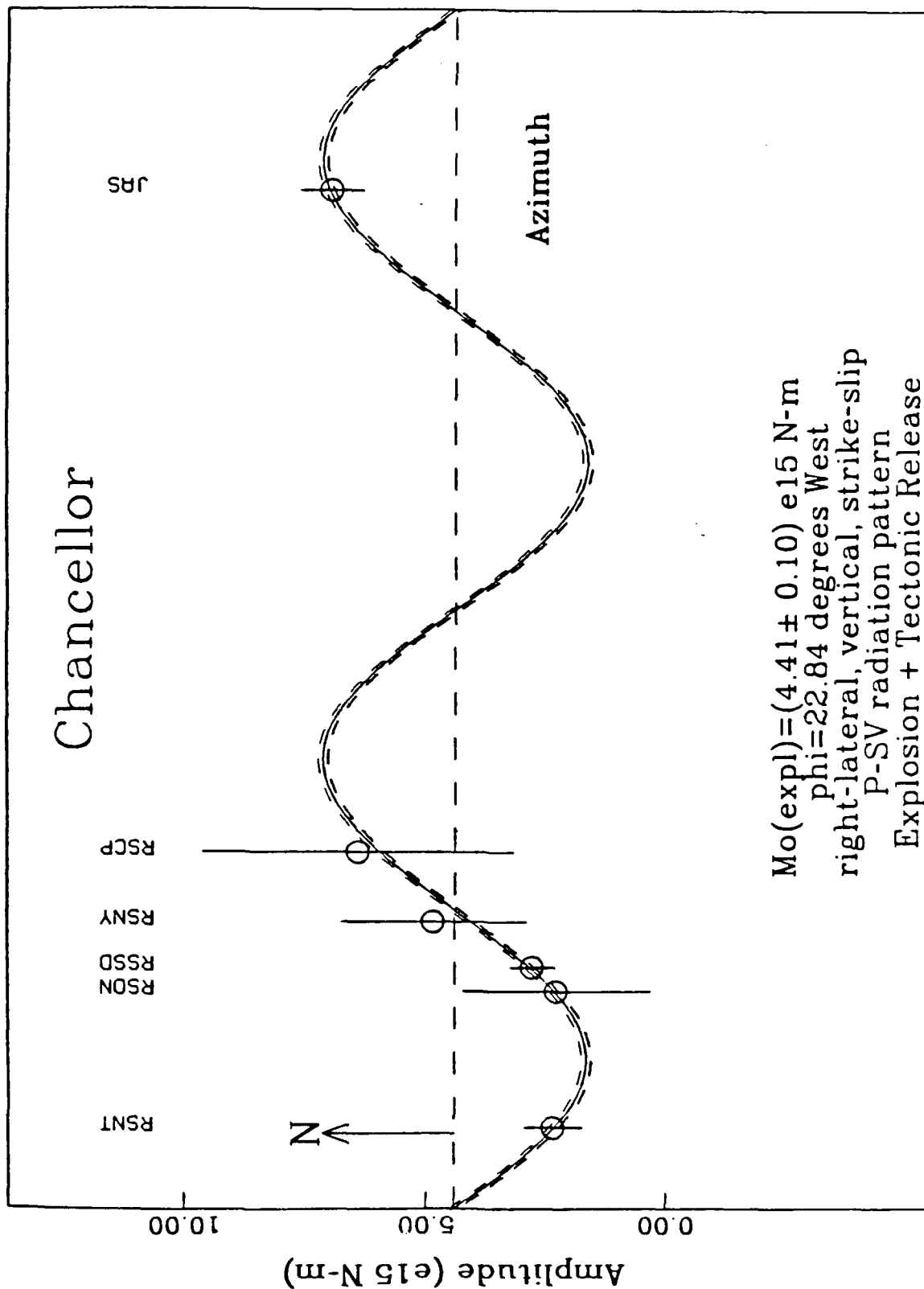


FIGURE 19

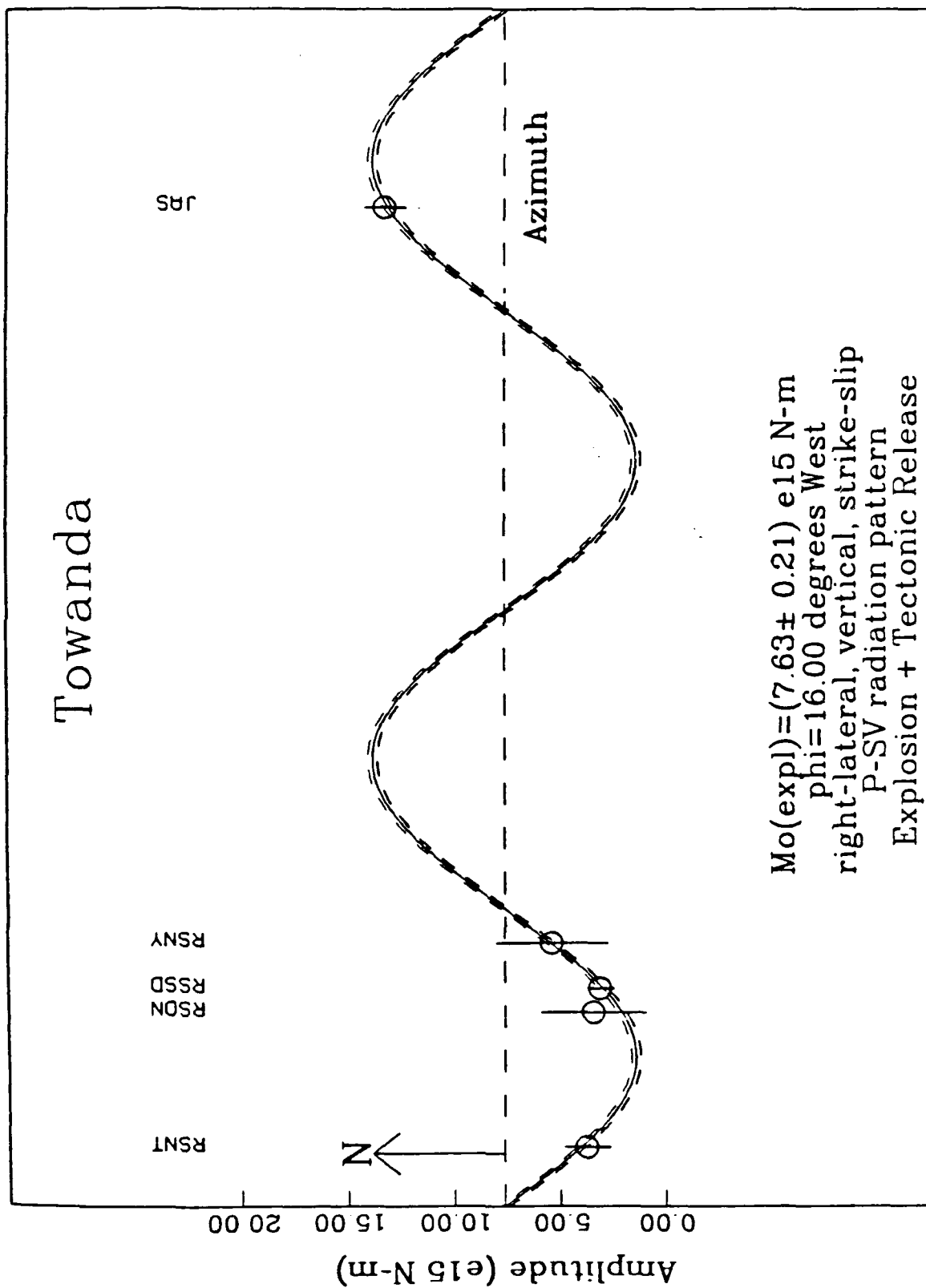


FIGURE 20

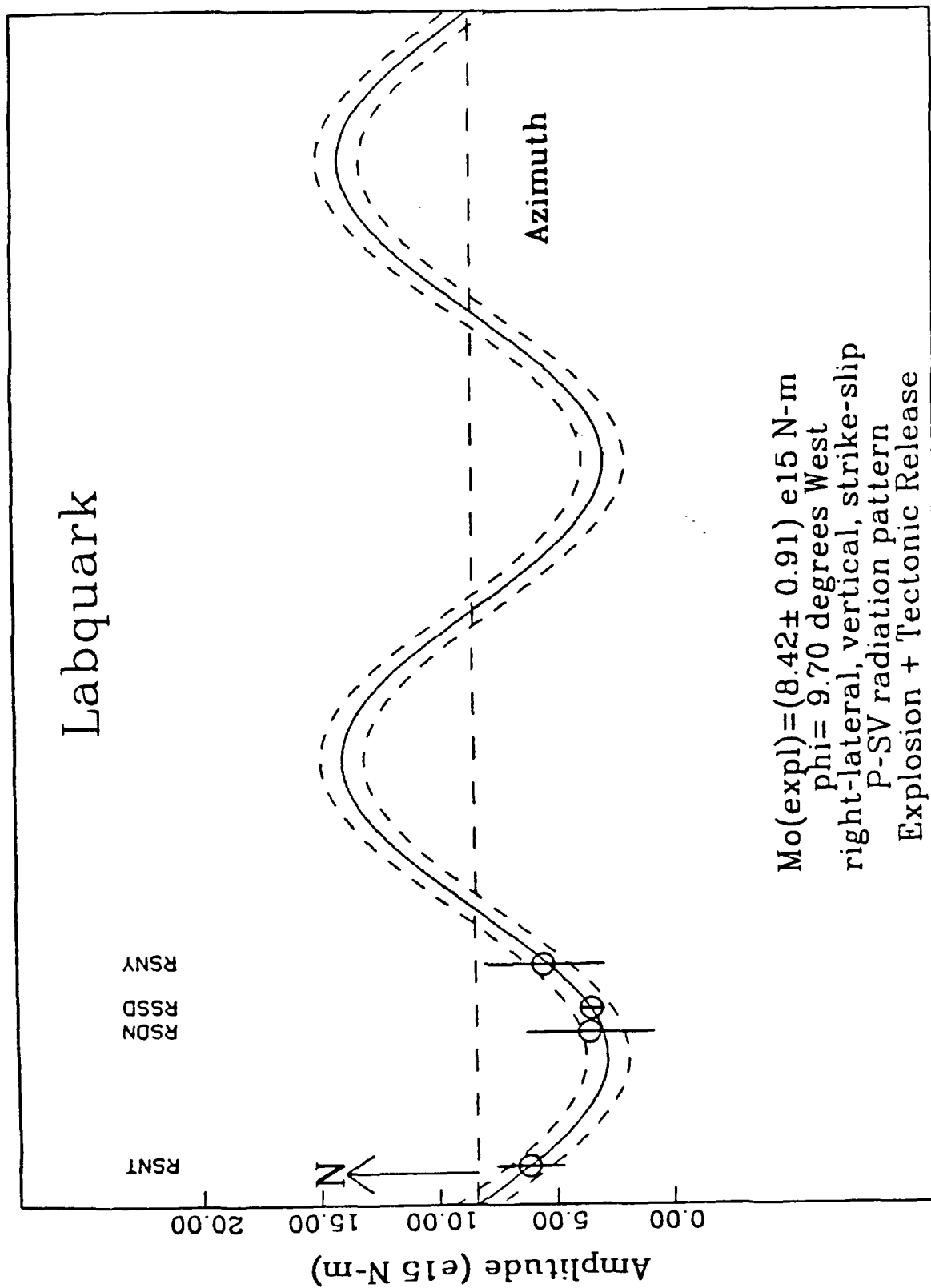


FIGURE 21

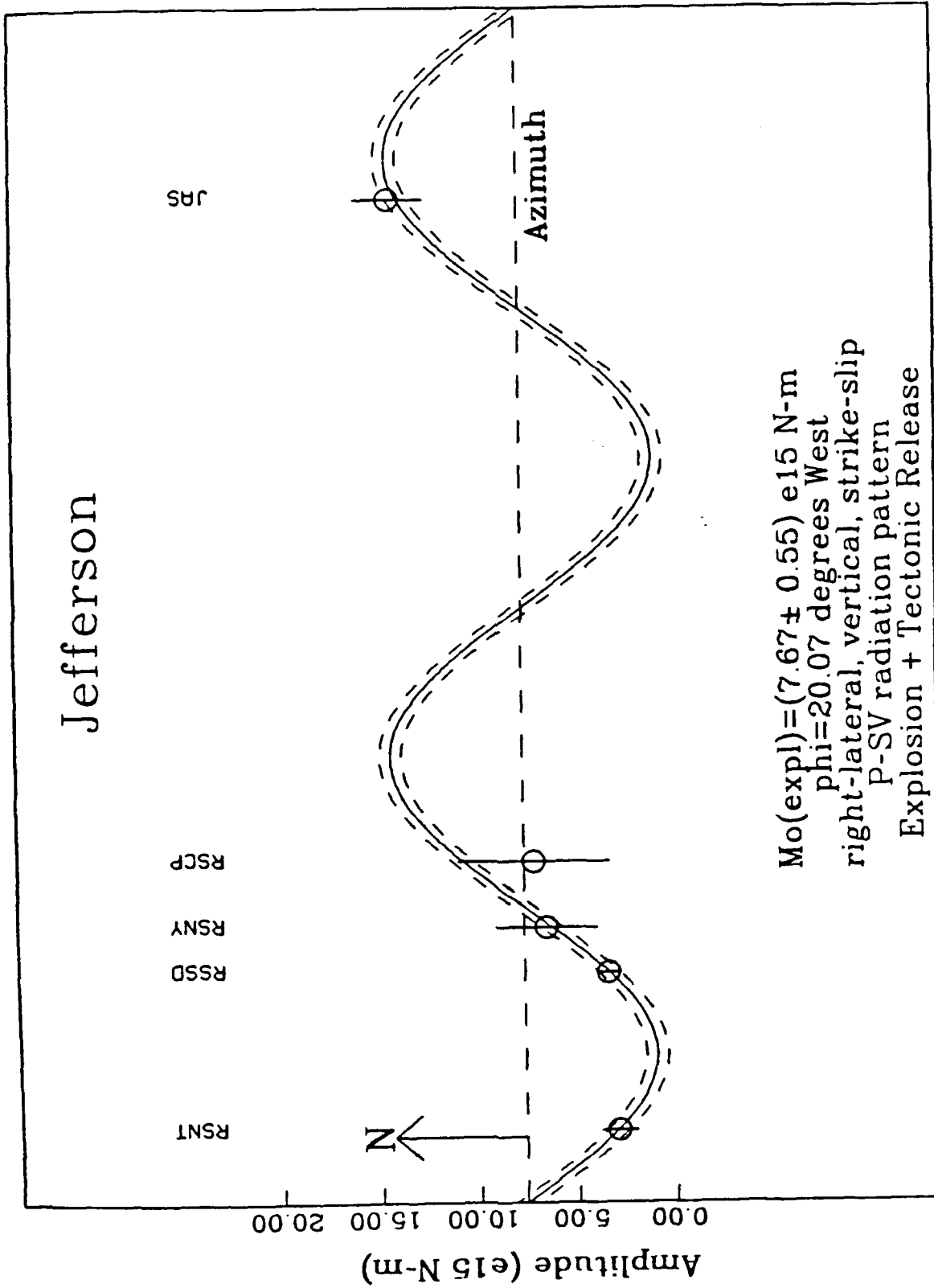


FIGURE 22

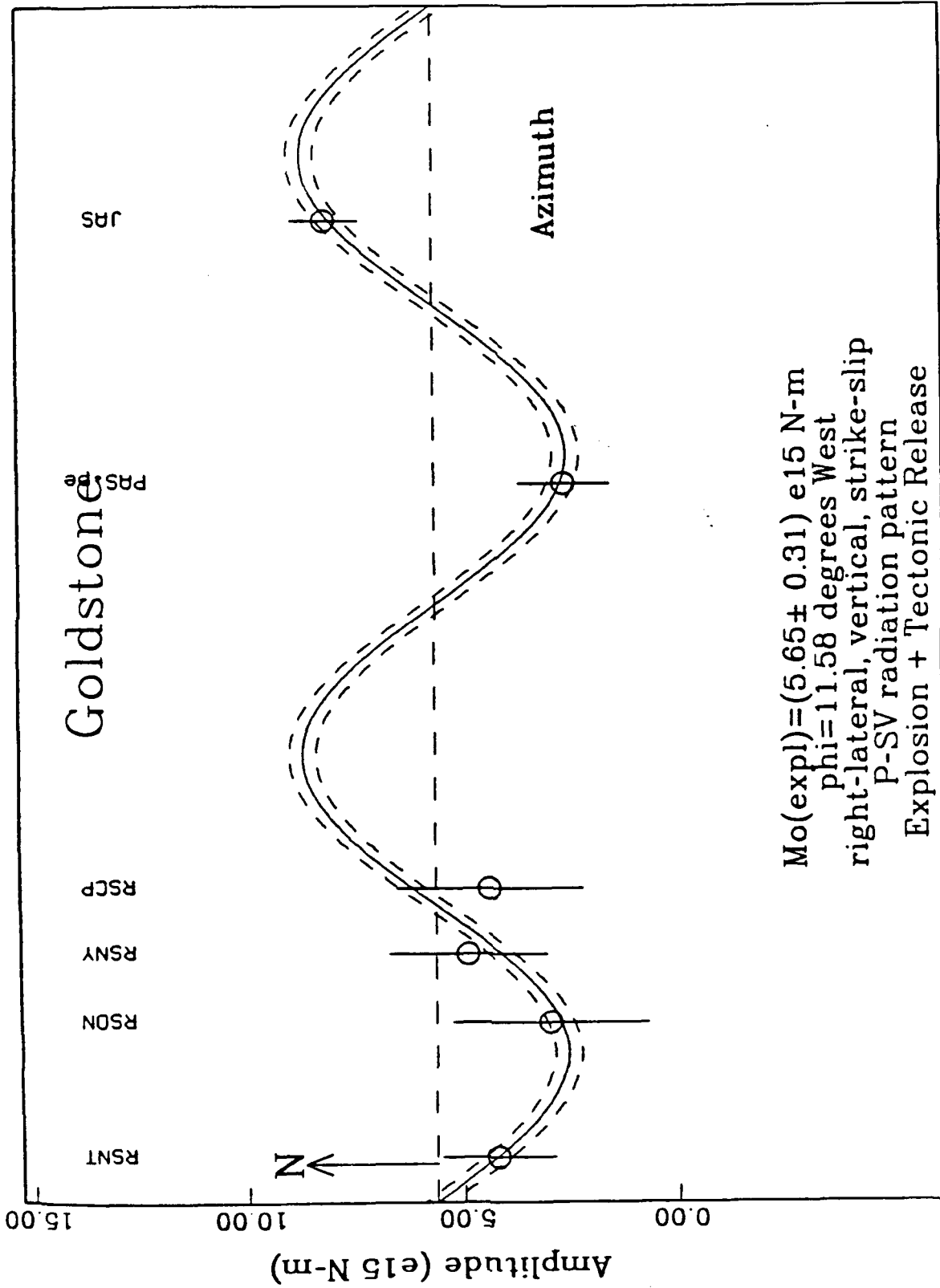


FIGURE 23

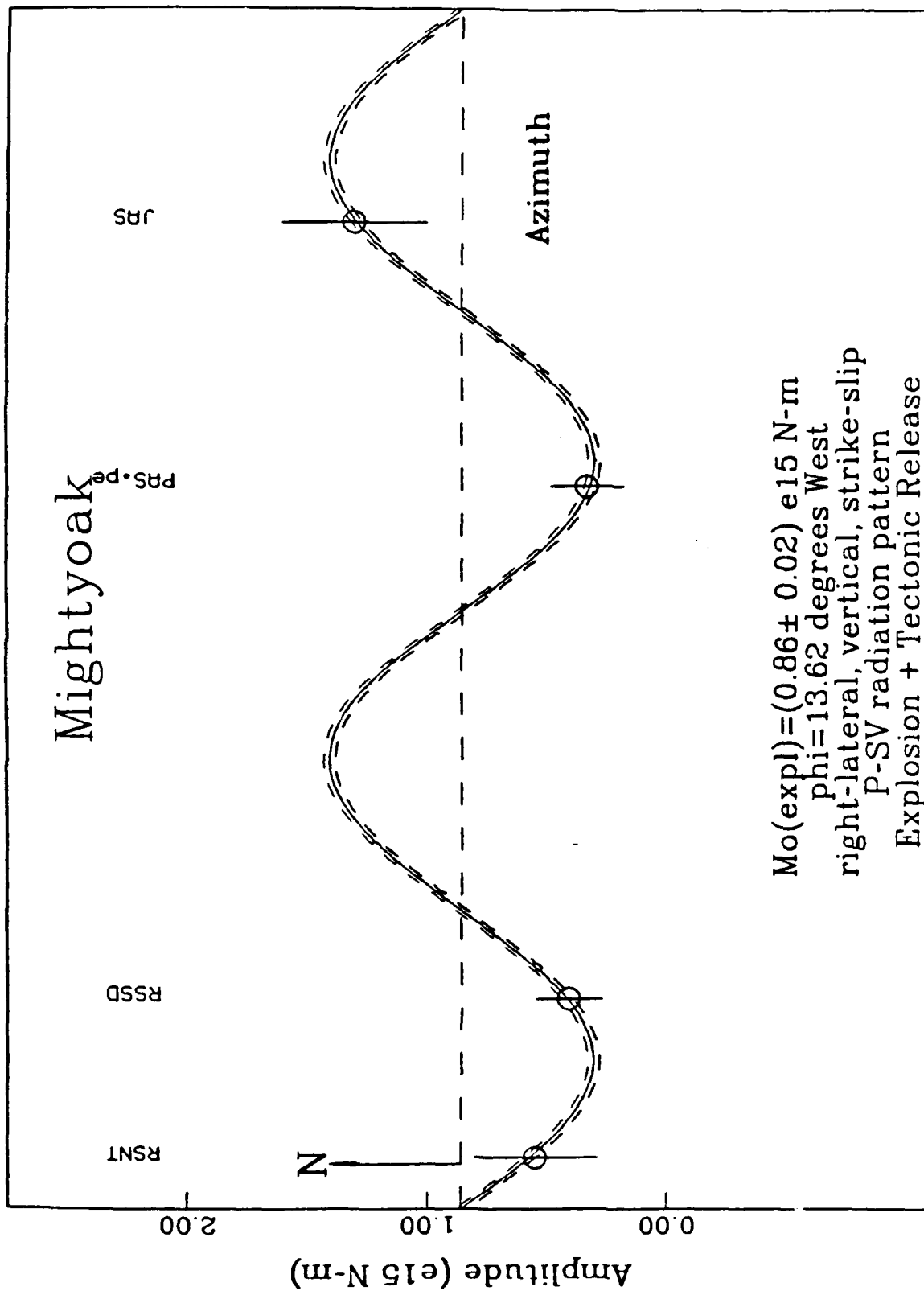


FIGURE 24

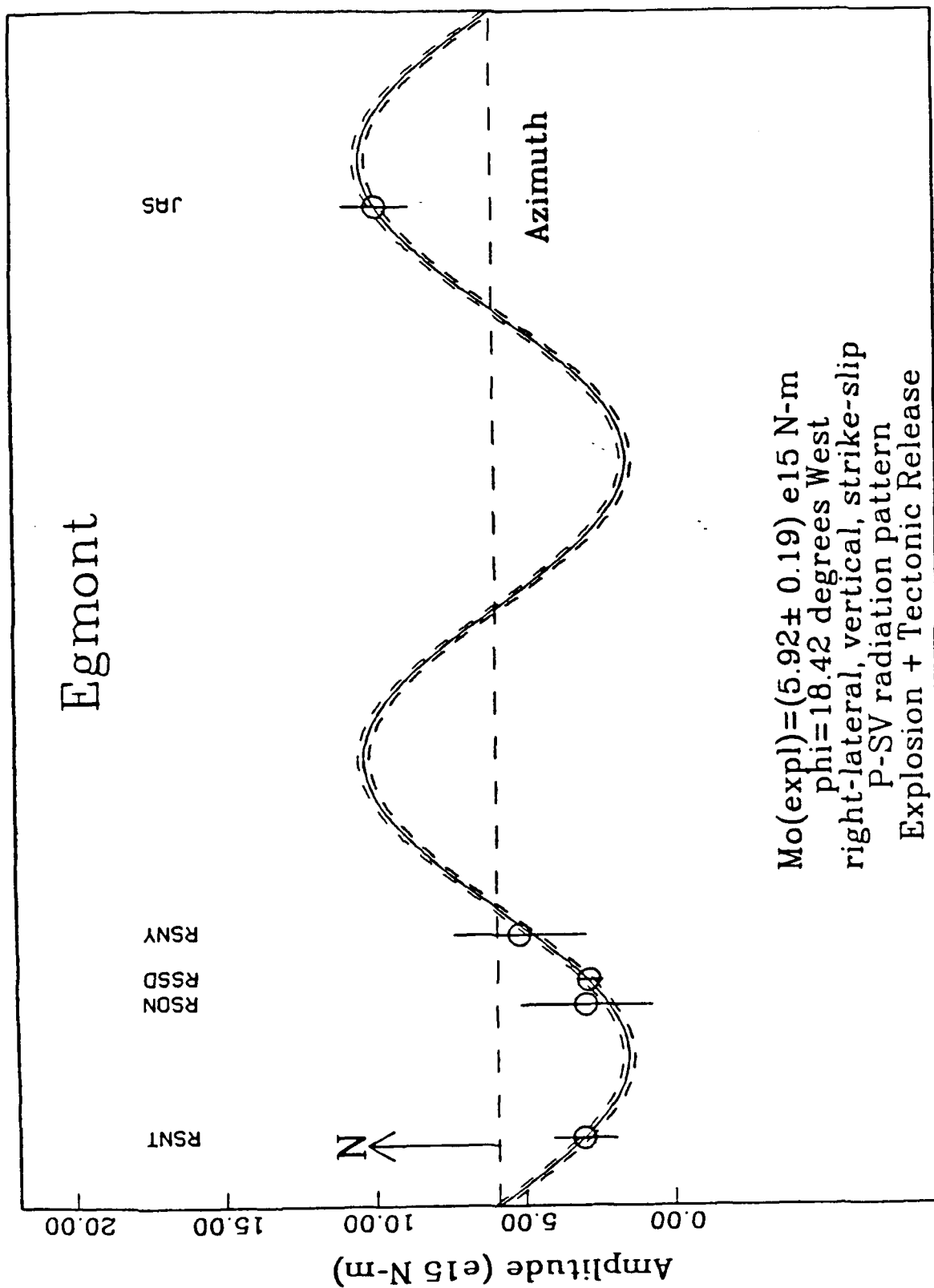
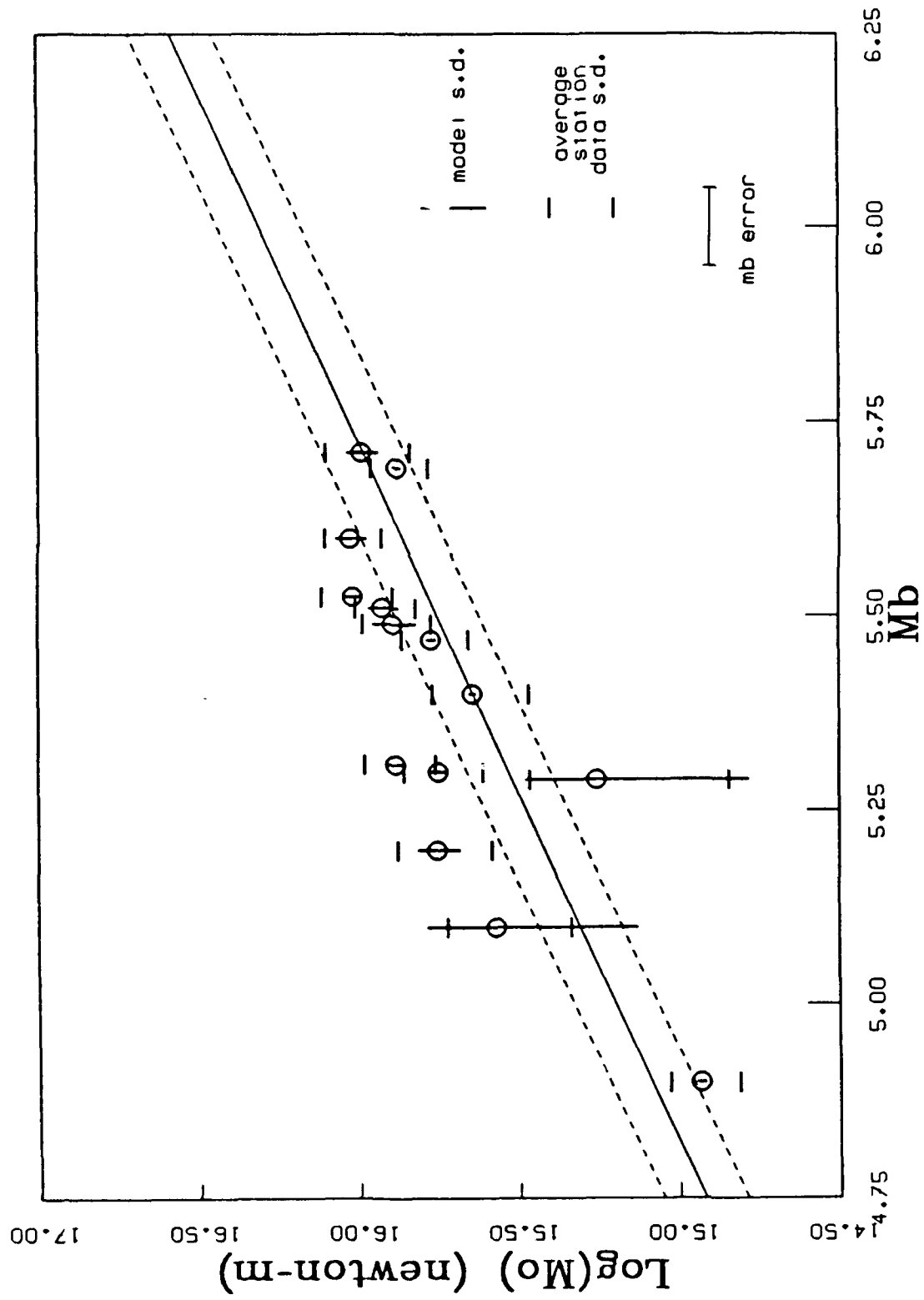


FIGURE 25



$$M_b = 0.9 \log(M_o) - 8.67 \quad (s.d. = 0.12)$$

FIGURE 2b

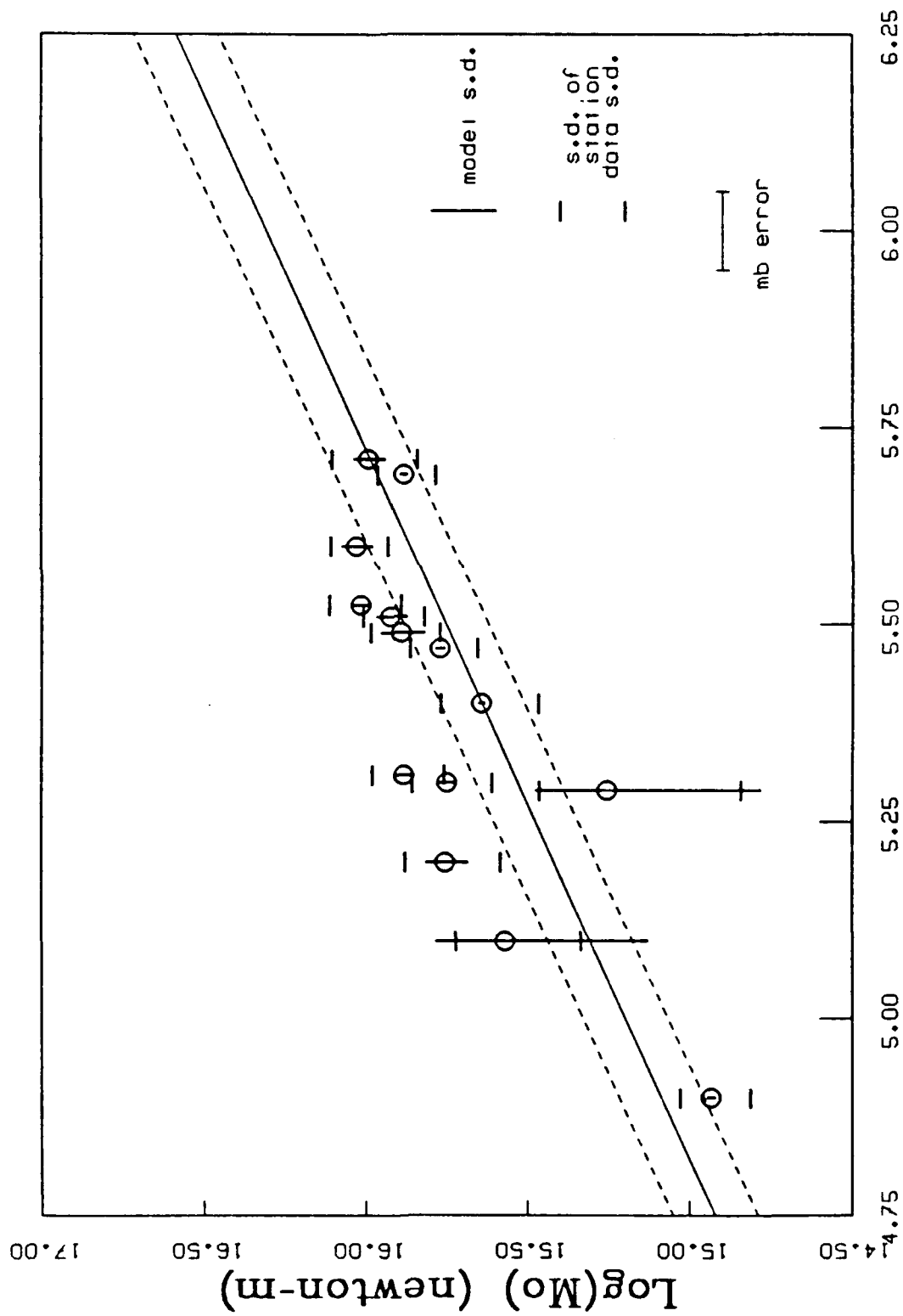


FIGURE 27

TITLE: Frequency dependence of Q_{Lg} and Q_β in the Continental Crust.

AUTHORS AND AFFILIATION: B.J. Mitchell and J.K. Xie, Dept. of Earth and
Atmospheric Sciences, Saint Louis University

CONTRACT NO.: F19628-87-K-0036

OBJECTIVE:

To reconcile observations which indicate the Q_β in the continental crust of the Basin-and-Range province is independent of frequency whereas Q_{Lg} in the same region varies with frequency.

SUMMARY:

A recently developed stacking procedure (Xie and Nuttli, 1988) has provided stable and precise determinations of Q and its frequency dependence for Lg waves in the Basin-and-Range province. Repeated observations using four station pairs leads to $Q_{Lg}(f) = (267 \pm 56)f^{0.4 \pm 0.0}$ over the frequency range 0.2 - 2.5 Hz (Figure 1). The value of the frequency-dependence parameter (0.4) is much higher than that determined for Q_β by Mitchell (1981) and Cong and Mitchell (1988) in the same region.

We computed synthetic seismograms of Lg (Herrmann, 1988) for a frequency-independent Q_β model obtained by Lin and Mitchell (1988) and found that this model predicts the values of Q (210) and its frequency dependence (0.4) which are observed in the Basin-and-Range province (Figure 2). These results indicate that the frequency dependence of Q_{Lg} observed for that region is produced by a layered Q_β structure in which Q_β is independent of frequency over the frequency range 0.2 - 2.5 Hz, but increases with depth in the crust.

Similar experiments in the eastern United States, where Q is relatively high, require that Q_β increases with frequency over the range 0.5 - 5.0 Hz (Figure 3), a result which is consistent with that of Mitchell (1980). The model of Mitchell (1980), for the eastern United States, in which Q_β varies as $f^{0.5}$ predicts Q and power-law frequency dependence values for Lg of 1200 and 0.4, respectively. These values are similar to those reported by Nuttli (1973) and Singh and Herrmann (1983) for that region.

CONCLUSIONS AND RECOMMENDATIONS:

The frequency dependency of Q_{Lg} over a range of frequencies near 1 Hz is caused by different mechanisms in high- Q and low- Q regions. In high- Q regions it is caused by the frequency dependence of Q_β whereas in low- Q regions it is caused by a layered Q structure in which Q_β is independent of frequency. Incorrect values of Q can cause large errors in yield estimates using Lg . It is therefore important that regional variations of Q and its frequency dependence be accurately obtained for all propagation paths used for yield estimates. Since it may be

difficult to obtain data for all possible paths and all frequencies it is important that we be able to make reasonable estimates of Q in those regions where sufficient data are not available. An understanding of the mechanisms for Q and its frequency dependence is therefore important for successful yield estimation.

REFERENCES:

Computer Programs in Seismology (1988). R.B. Herrmann, ed., Saint Louis University.

Cong, L., and B.J. Mitchell (1988). Frequency dependence of crustal Q_β in stable and tectonically active regions, *PAGEOPH* **127**, 581-605.

Lin, W.J., and B.J. Mitchell (1988). Rayleigh wave attenuation in the Basin-and-Range (abs.), *EOS* **69**, 405.

Mitchell, B.J. (1980). Frequency dependence of shear wave internal friction in the crust of eastern North America, *J. Geophys. Res.* **80**, 4904-4916.

Mitchell, B.J. (1981). Regional variation and frequency dependence of Q in the crust of the United States, *Bull. Seism. Soc. Am.* **71**, 1531-1538.

Nuttli, O.W. (1973). Seismic wave attenuation and magnitude relations for eastern North America, *J. Geophys. Res.* **78**, 876-887.

Singh, S.K., and R.B. Herrmann (1983). Regionalization of crustal coda Q in the continental United States, *J. Geophys. Res.* **88**, 527-538.

Xie, J., and O.W. Nuttli (1988). Interpretation of high-frequency coda at large distances: stochastic modelling and method of inversion, *Geophys. J.* **95**, 579-595.

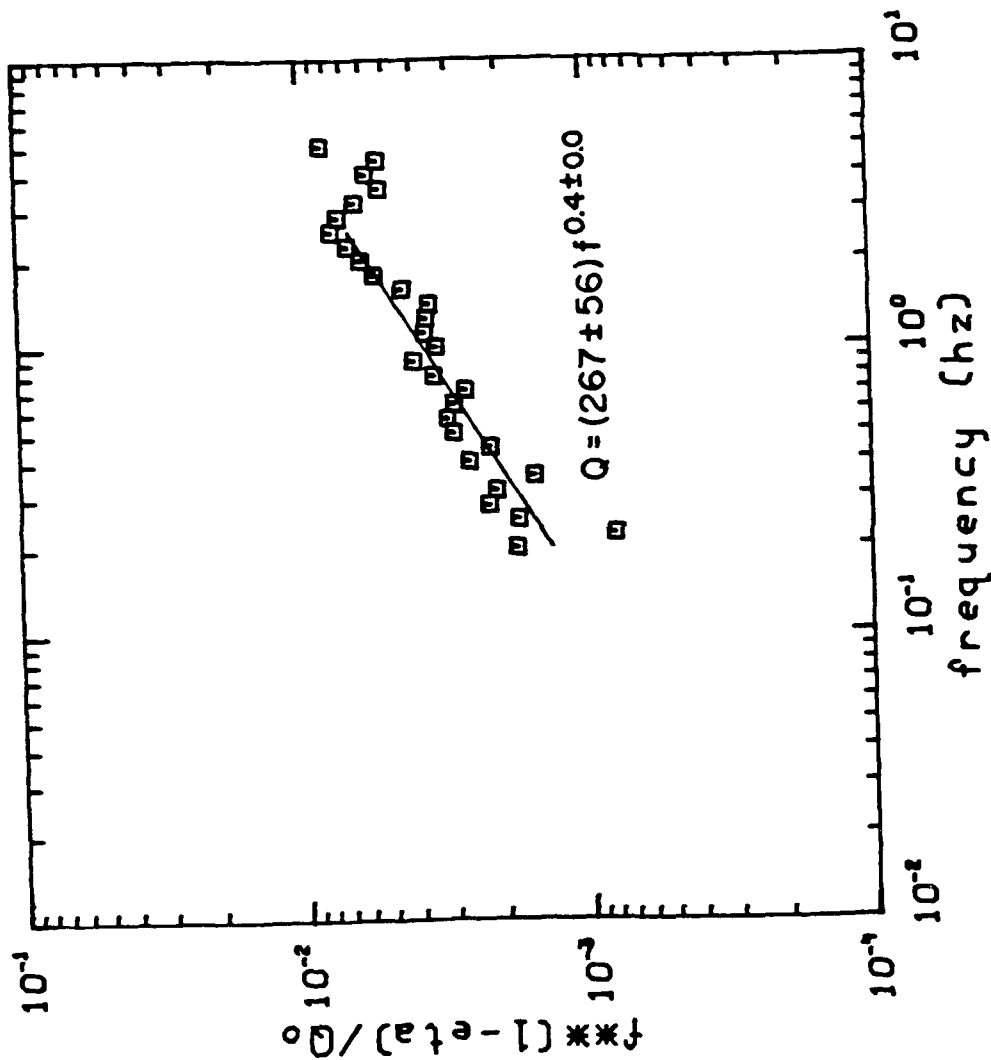


Figure 1. Mean values for the stacked spectral ratio between 0.2 and 5.0 Hz obtained for four stationspairs in the Basin-and-Range province. The solid line is a least-squares fit to the data between 0.2 and 2.5 Hz.

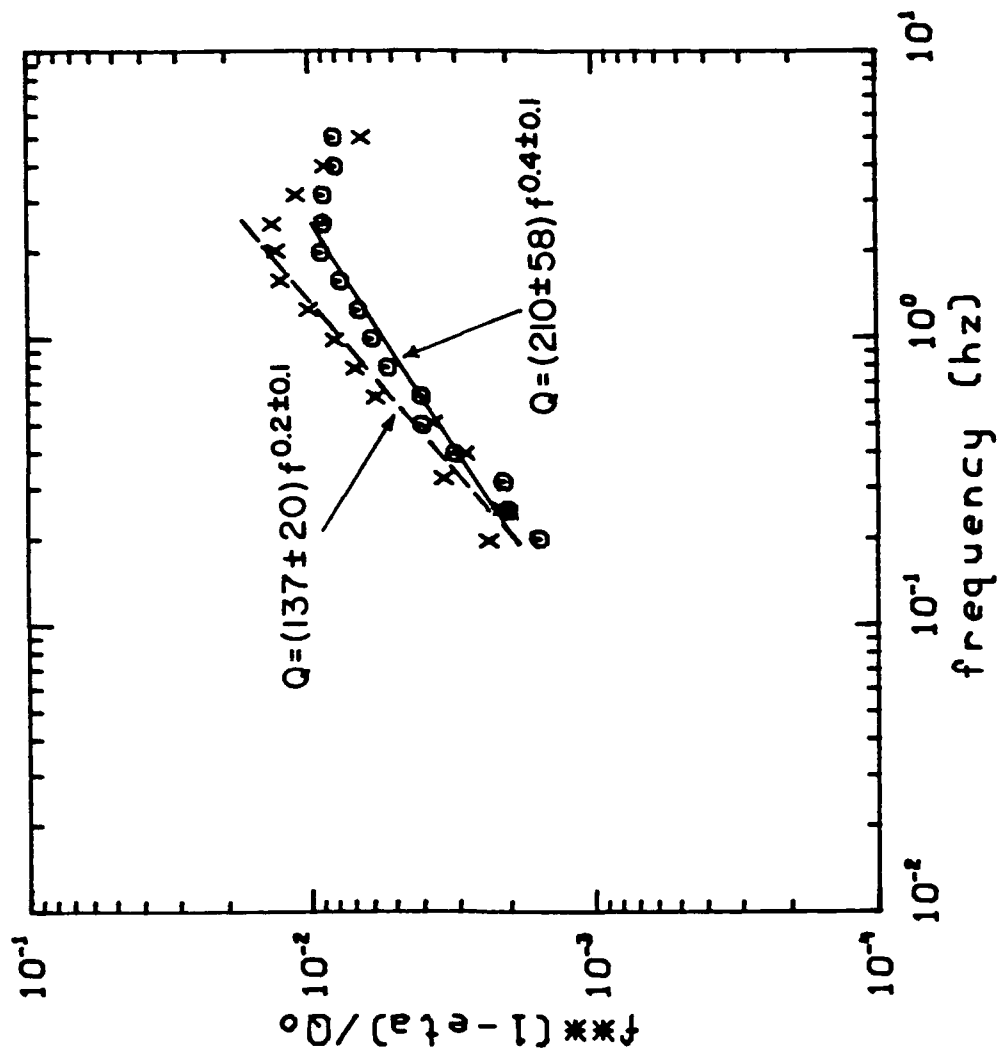
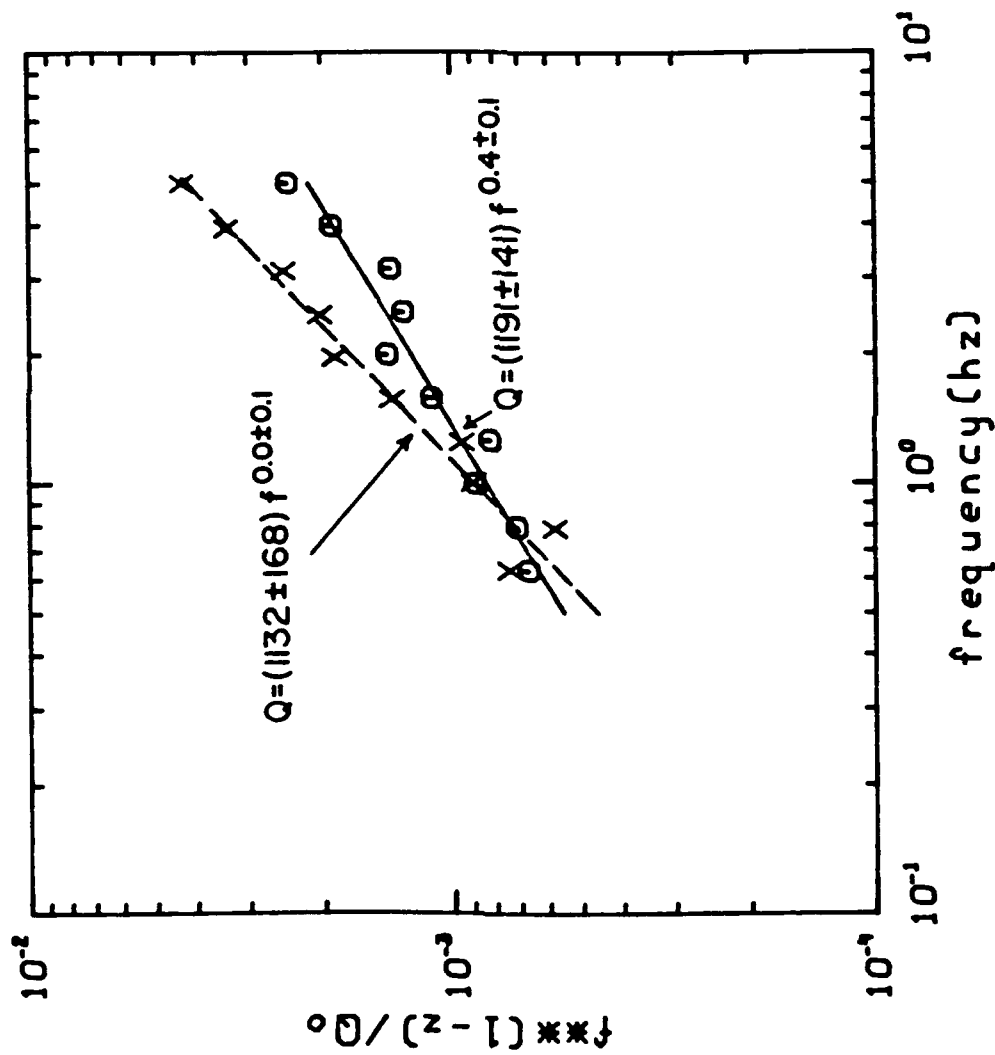


Figure 2. Stacked spectral ratios for synthetic seismograms computed for crustal models of the Basin-and-Range province. The solid line is a least-squares fit for the Q model of Lin and Mitchell (1988) and the dashed line is a least-squares fit for the model of Patton and Taylor (1984).



EUS.SYN.1

Figure 3. Stacked spectral ratios for synthetic seismograms computed for crustal models of the eastern United States. The dashed line is a least-squares fit for a model in which shear-wave Q is independent of frequency and the solid line is a least-squares fit for a model in which shear-wave Q varies with frequency as $f^{0.5}$.

Determination of Q as a Function of Depth and Tectonic Province

Xiao-yang Ding and Stephen Grand
Department of Geology, University of Illinois
Urbana-Champaign, IL 61801

Contract No.: F19628-87-K-0025

Objective

The objective of this work is to try to relate shear velocity, as a function of depth in the Earth's mantle, to Q at those depths. Such a relation would enable one to use mantle shear velocity structures, already determined for much of the Earth, to predict t^* values for particular source-receiver geometries.

Summary

The attenuation of the upper mantle has been shown to correlate with the shear velocity of the upper mantle. Der et. al. (1980) and many others have shown higher t_p^* values for the western United States relative to the eastern United States. It is also well known that the upper mantle shear velocities are higher in the east relative to the west. In this work an attempt is made to quantify the relation between Q and upper mantle shear velocity.

We have approached the problem by developing upper mantle Q structures for two regions which have shear velocity structures representative of the extremes found in the Earth. The two regions are the East Pacific Rise, which has the slowest shallow velocity structure found to date, and the Canadian shield, which is representative of a very high velocity structure. Shear velocity models for the two areas were developed by Grand and Helmberger (1984) and are used in this study. The NTS test site is above mantle similar to that beneath the East Pacific Rise, while the Soviet and French Saharan test sites overlie mantle closer in structure to the Canadian shield.

The Q models were derived by modeling the amplitude decay of multiple bounce SH shear phases with bottoming depths above 700 km depth. The data have predominant periods from 15 to 40 sec. Given the velocity structure of a region, the raypaths of S, SS, SSS and SSSS phases as a function of distance are known and thus given a Q structure the t^* values for each phase are known. Using multiple bounce phases allows sampling of the shallow mantle over long distances and times. Fig. 1 shows the multibounce shear raypaths at 76° for the East Pacific velocity structure. Notice SSSS, with a travel time of about 1800-sec, propagates wholly above 400 km depth. An upper 400 km Q of 60 would produce a t^* 7.5 sec greater than an upper 400 km Q of 80 for SSSS at this distance. The S wave, at this distance, would have less than a 1 sec difference in t^* for the two models. Notice also, that SS at 38° and SSS at 57° sample the same depth range as SSSS at 76° . Since velocity differences associated with tectonic provinces are limited to the upper mantle we have assumed the Q below 700 km depth is uniform and given by the PREM model of Dziewonski and Anderson (1981). With this assumption and the mechanism of the earthquake source, the amplitudes of the multibounce shear phases relative to the S wave amplitudes can be used to determine the upper mantle Q structure. To accomplish this we computed synthetic seismograms using the WKB technique (Chapman, 1978) to compare to the data in the time domain. Each significant arrival in the synthetic corresponds to a raypath and thus, for a given Q structure the appropriate t^* for each arrival can be computed. Futterman Q operators (Futterman, 1962) with the appropriate t^* values were convolved with the Green function for each arrival after which the arrivals were summed to make complete seismograms. By trial and error Q structures were found which fit the amplitudes of the multibounce phases relative to the S wave amplitude for distances from 30° to 80° .

The data and synthetics for the East Pacific Rise experiment are shown in figs. 3-6. The Q model for the East Pacific Rise, QTNA, is shown in fig. 7 and given in table 1. The figure captions give more detailed explanations of how the Q model was determined. In fig. 8 the sensitivity to Q of the relative amplitudes of SSS and SSSS to S is illustrated. Figs. 9 and 10 compare predicted relative amplitudes for other published Q models to the relative amplitude data from the East Pacific. Model QTNA has a Q of 70 to 150 km depth increasing to 180 at 400 km depth. A Q of 180 was found for the transition zone from 400 to 650 km depth. The PREM Q model below 700 km depth has Q equal to 312 and this difference in Q above and below 650 km is considered significant. To test the importance of the assumption of the PREM lower mantle Q, the data were also modeled assuming the lower mantle Q structure SL8 of Anderson and Hart (1978). The resulting upper mantle Q model was very similar to QTNA and we feel that for any reasonable lower mantle Q model our results would not change significantly. Determining Q for the shield mantle presented a more difficult problem. True cratons are generally limited to dimensions of less than 60° so that multibounce phases beyond SSS can not be used. Also, most earthquakes are in tectonic regions so that multibounce shear data with pure shield paths are very rare. The final difficulty is that the shield velocity structure causes rays which turn in the upper 400 km to be spread over large distances and to have relatively small amplitudes. For these reasons we used only the relative amplitudes of the SS and SSS reflections off the 400 km discontinuity to constrain the shield Q structure. With such a restriction we could only constrain the average Q of the upper 400 km beneath the shield. For this case we assumed the lithosphere had a Q of 500 (we define lithosphere as the mantle above 250 km depth with velocity greater than 4.7 km/sec) and that the shield Q below 400 km was given by QTNA since the East Pacific and shield velocity structures are indistinguishable below 400 km depth. With these assumptions model QSNA (table 2) was found to fit the shield amplitude data. The data and synthetics are shown in figs. 11-13. The lithosphere assumption is based on surface wave studies (see Cara, 1981 for example) and coda Q measurements (see Aki, 1980 for example). A higher Q for the lithosphere would not effect the results greatly, lower shallow Q would increase the Q between 200 and 400 km depth.

Conclusions and Recommendations

In tables 3 and 4 t^*_α for S waves as a function of distance are given. Using the relation $t^*_\alpha = .25t^*_\beta$ (Burdick, 1978) we show in table 5 the predicted Δt^*_α for one-way propagation through the two structures. The maximum difference of .16 sec is slightly less but close to the results found by Der et. al. (1982) for the United States. Fitting only the maximum amplitude shield data would increase this value to .18 sec. Given an upper mantle shear structure it appears possible to predict the teleseismic short-period P t^*_α bias due to the upper mantle by combining QTNA and QSNA. This can be done by assigning a Q of 500 to the lid (4.7 km/sec or greater region) and using the range in Q found here to compute Q for velocities below the lid and finally using the relation between P wave t^*_α and S wave t^*_α . Measurements of Q_{ScS} by Chan and Der (1988), Lay and Wallace (1983) and Sipkin and Jordan (1980) among others have found Q_{ScS} values from 93 to over 300. Our two models predict a Q_{ScS} of 217 and 274 respectively. The difference in the range of measurements seems to require substantial variations in Q in the lower mantle. Whether the heterogeneity is confined to the core-mantle boundary or distributed throughout the lower mantle is an important question to be answered. Hager et. al. (1985) have shown the lower mantle to be hot (seismically slow) beneath North Africa. This may be the cause of the apparently high t^*_α values for the Saharan nuclear blasts.

References

- Anderson, D. L. and R. S. Hart, 1978. Q of the earth, *J. Geophys. Res.*, **83**, pp. 5869-5881.
- Burdick, L. J., 1978. t^* for S waves with a continental ray path, *Bull. Seism. Soc. Am.*, **68**, pp. 1013-1030.
- Cara, M., 1981. Differential attenuation coefficients for Rayleigh waves: a new constraint on Q-models, in *Anelasticity in the Earth*, American Geophysical Union, Washington D. C., pp. 23-37.
- Chan, W. W. and Z. A. Der, 1988. Attenuation of multiple ScS in various parts of the world, *J. Geophys.*, **92**, pp. 303-314.
- Chapman, C. H., 1978. A new method for computing synthetic seismograms, *Geophys. J. R. astr. Soc.*, **54**, pp. 481-518.
- Der, Z. A., E. Smart and A. Chaplin, 1980. Short-period S-wave attenuation under the United States, *Bull. Seism. Soc. Am.*, **70**, pp. 101-125.
- Der, Z. A., T. W. McElfresh and A. O'Donnell, 1982. An investigation of the regional variations and frequency dependence of anelastic attenuation in the mantle under the United States in the .5-4Hz band, *Geophys. J. R. astr. Soc.*, **69**, pp. 67-99.
- Dziewonski, A. M. and D. L. Anderson, 1981. Preliminary reference earth model, *Phys. Earth Planet. Int.*, **25**, pp. 297-356.
- Futterman, W. I., 1962. Dispersive body waves, *J. Geophys. Res.* **67**, pp. 5279-5291.
- Grand, S. P. and D. V. Helmberger, 1984. Upper mantle shear structure of North America, *Geophys. J. R. astr. Soc.*, **76**, pp. 399-438.
- Hager, B. H., R. W. Clayton, M. A. Richards, R. P. Comer and A. M. Dziewonski, 1985. Lower mantle heterogeneity, dynamic topography and the geoid, *Nature*, **313**, pp. 541-545.
- Lay, T. and T. C. Wallace, 1983. Multiple ScS travel times and attenuation beneath Mexico and Central America, *Geophys. Res. Lett.*, **10**, pp. 301-304.
- Rial, J. A., S. P. Grand and D. V. Helmberger, 1984. A note on the lateral variation in upper-mantle shear structure across the Alpine front, *Geophys. J. R. astr. Soc.*, **77**, pp. 639-655.
- Sipkin, S. A. and T. H. Jordan, 1980. Multiple ScS travel times in the western Pacific : implications for mantle heterogeneity, *J. Geophys. Res.*, **85**, pp. 853-861.

Table 1 : Q Model for TNA

Depth (km)	Q Value	Depth (km)	Q value
0	400	325	150
12	400	350	160
20	300	385	173
40	70	405	180
50	70	425	180
75	70	450	180
100	70	475	180
125	70	500	180
150	70	525	180
175	80	550	180
200	95	575	180
225	110	600	180
250	120	625	180
275	130	650	312
300	140	675	312

Table 2 : Q Model for SNA

Depth (km)	Q Value	Depth (km)	Q value
0	500	350	170
34	500	375	175
50	500	400	180
75	500	425	180
100	500	450	180
125	500	575	180
150	500	500	180
175	400	525	180
200	120	550	180
225	130	575	180
250	140	600	180
275	150	625	180
300	160	650	312
325	165	675	312

Table 3 : T^* vs. Distance for QTNA

Distance (Deg.)	T^* (sec.)
30	4.0
35	4.3
40	4.4
45	4.6
50	4.8
55	5.0
60	5.2
65	5.3
70	5.5
75	5.7
80	5.8

Table 4 : T^* vs. Distance for QSNA

Distance (Deg.)	T^* (sec.)
30	2.8
35	3.0
40	3.3
45	3.5
50	3.7
55	3.9
60	4.1
65	4.3
70	4.4
75	4.6
80	4.8

Table 5 : $\delta T^*/8$ vs. Distance

Distance (Deg.)	$\delta T^*/8$ (sec.)
30	0.16
35	0.16
40	0.16
45	0.15
50	0.15
55	0.15
60	0.14
65	0.14
70	0.14
75	0.14
80	0.14

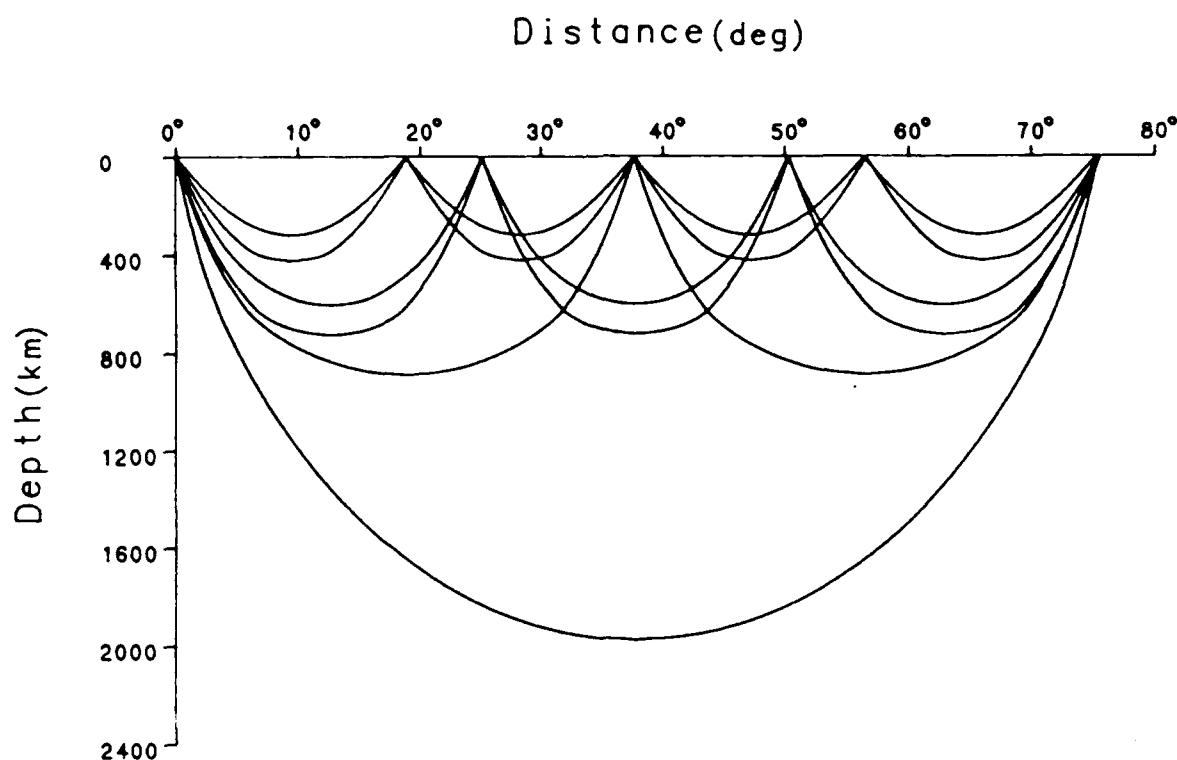


Figure 1. An illustration of S, SS, SSS and SSSS raypaths for a distance of 76° . It shows that most of the S wave raypath is in the lower mantle but the entire SSSS raypath is in the upper 400 km of the mantle. A small change in Q in the shallow mantle would result in a large change in t^* for SSSS phase and thus a large change in amplitude for this arrival relative to the S wave amplitude. The same is true for SSS at 57° and SS near 38° . Note how SSS, at this distance, samples primarily the transition zone from 400 km to 600 km depth. Our approach is to model the amplitudes of multiple bounce arrivals relative to S. Their raypaths determine the depth range over which they are sensitive to Q .



Figure 2. A map showing the location of earthquakes (stars along the East Pacific Rise) and stations, which are labeled, used in this study.

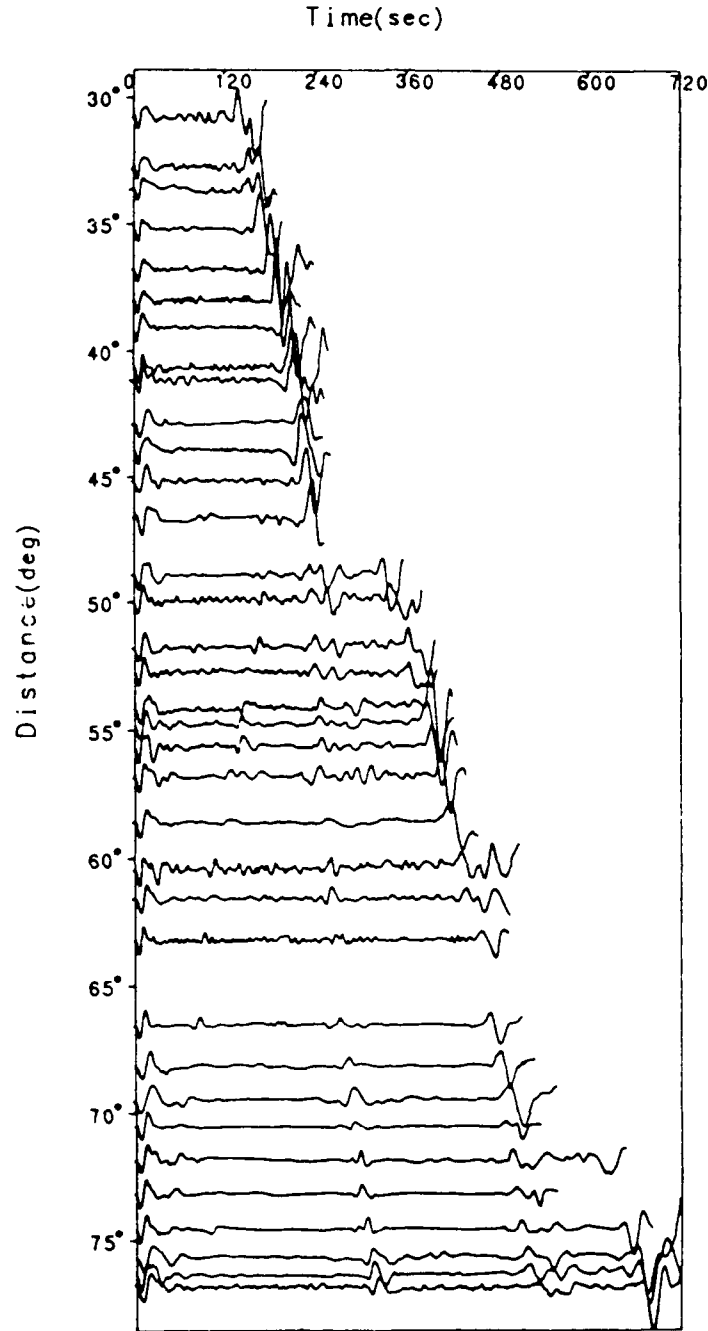
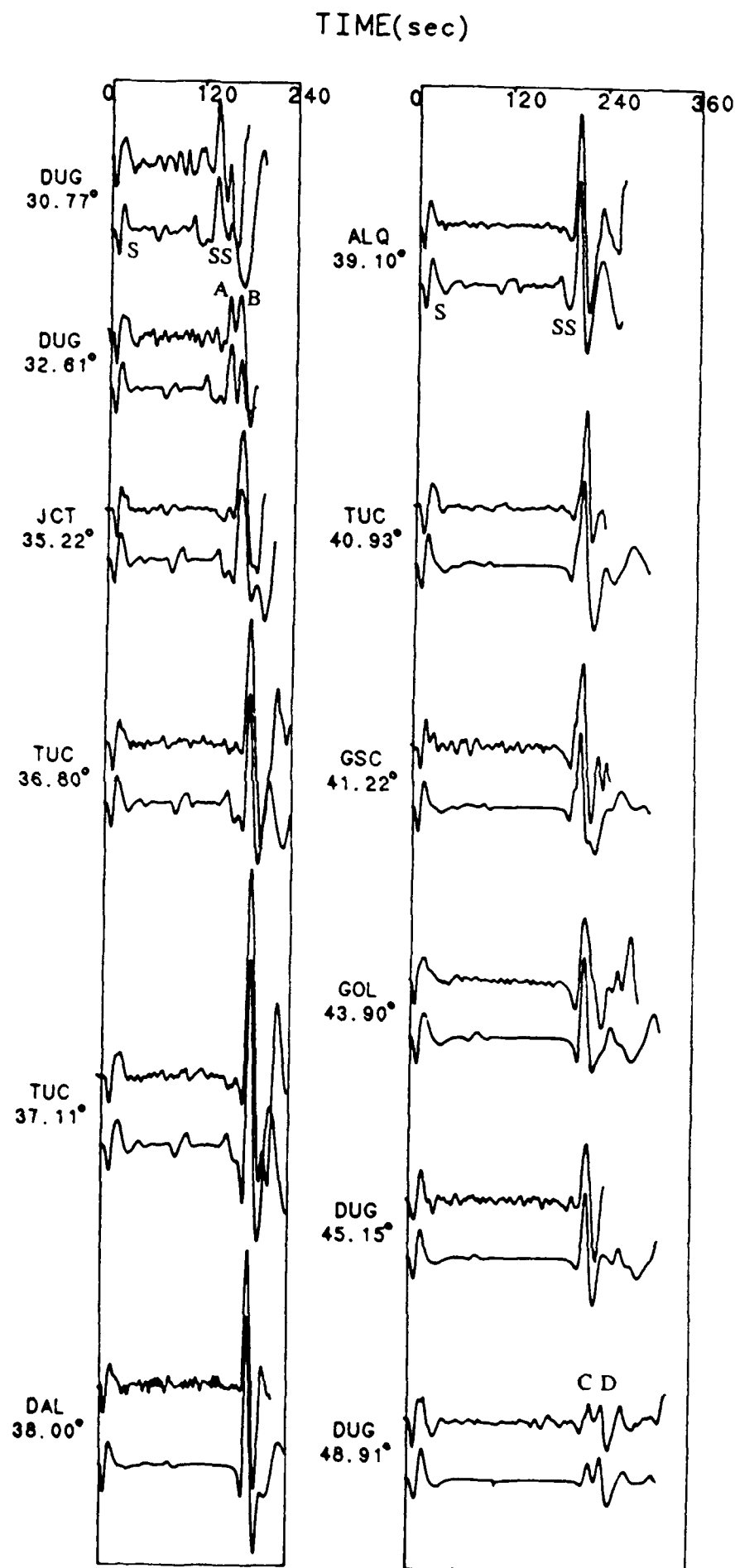


Figure 3. A profile of data which has propagated up the East Pacific Rise is shown. The S waves are aligned at zero time and normalized in amplitude. From 30° to 47° only S and SS waves are apparent. Beyond 48° the upper mantle SSS is visible and reaches a maximum amplitude between 54° to 59°. SSSS is apparent as a large downswing following SSS beyond 74°. Note the effect of the $\frac{\pi}{2}$ phase shift for each bounce. SSS and SSSS have a π phase shift relative to S and SS respectively.

Figure 4. Comparison of amplitudes of SS from 30° to 50° . For each pair of the seismograms the upper one is the observed seismogram, the lower one is a synthetic seismogram. All the S-waves are aligned at zero time and are normalized in amplitude. The synthetics are computed using the Q model labeled model (2) in figure 7. The synthetics shown in the next two figures are the same Q model. The SS arrival labeled A at 32° bottoms near 250 km depth, arrival B is associated with the 400 km velocity discontinuity. At 48° , arrival D comes from just above 650 km depth, arrival C comes from below 650 km depth. Near 37° the SS arrivals from above 300 km and the 400 km reflection arrive at nearly the same time, this causes the large amplitude near that distance.



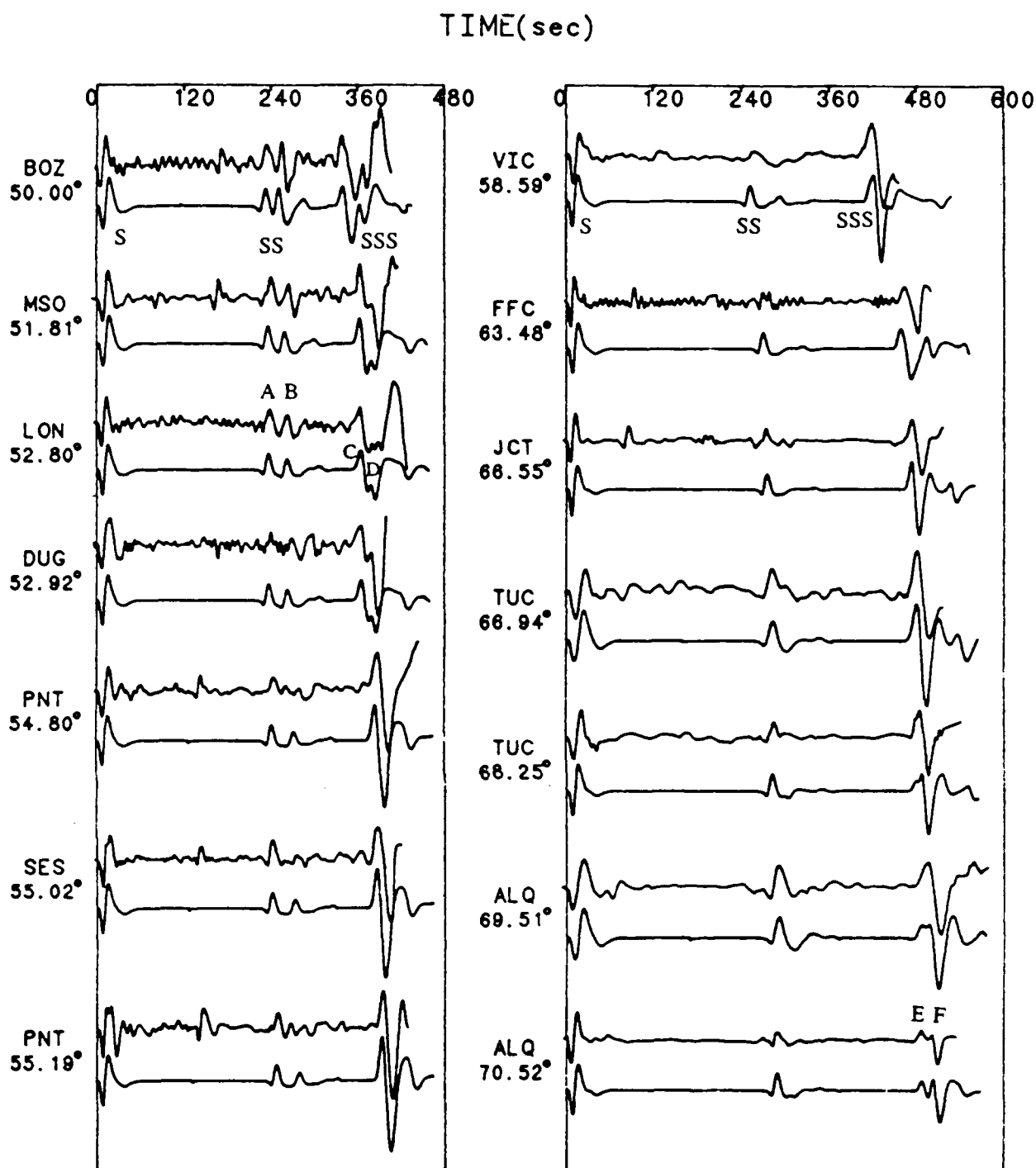
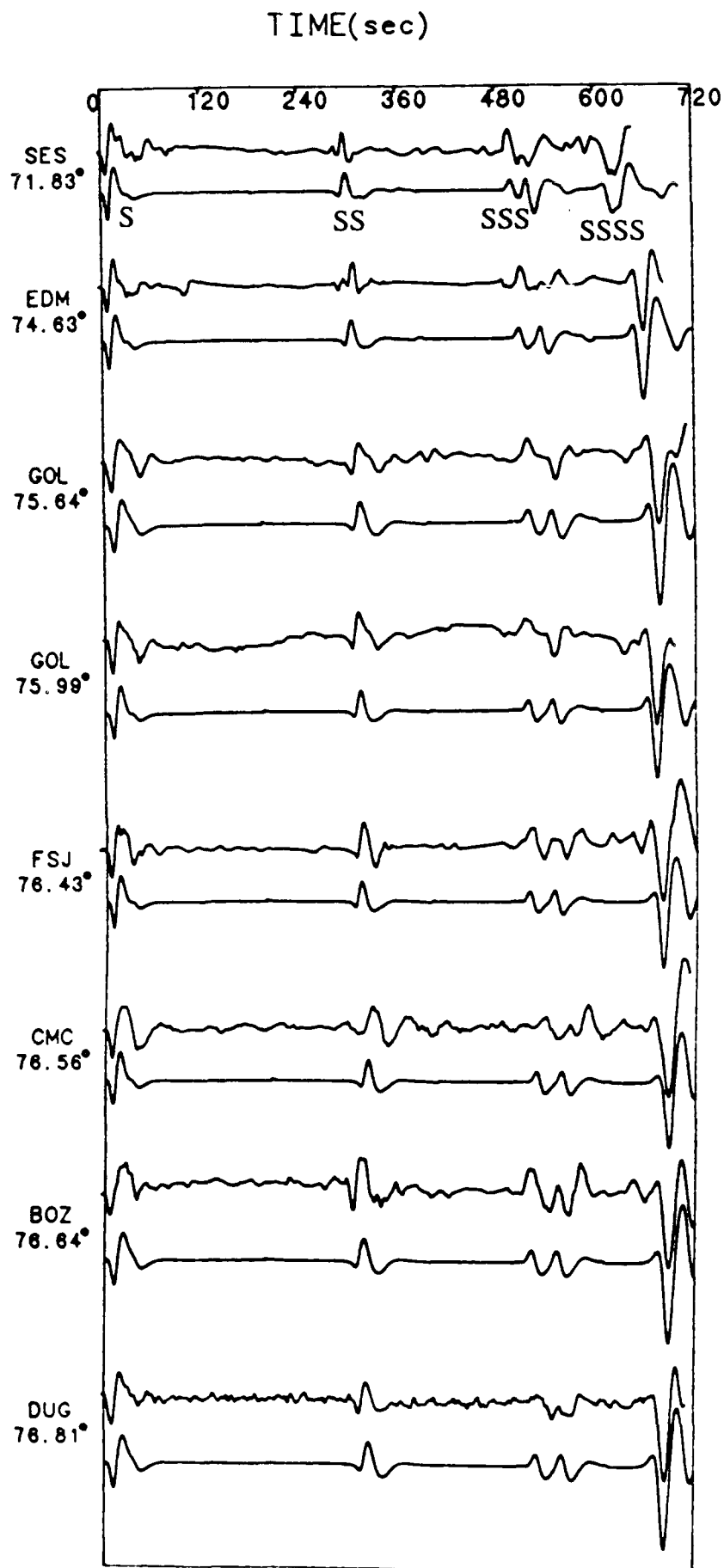
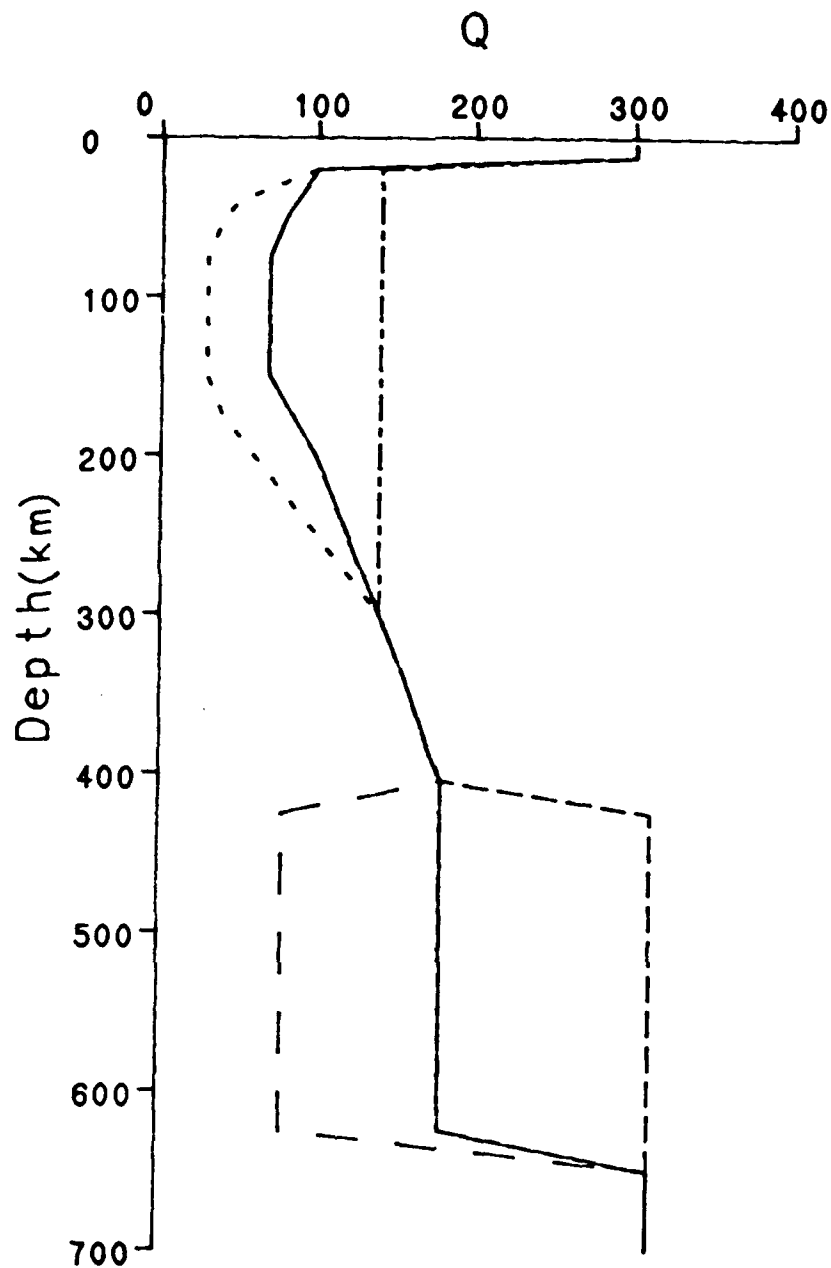


Figure 5. Comparison of SS and SSS data and synthetics from 50° to 70° distance. The data and synthetic seismograms are arranged in the same way as that in Figure 4. The double SS arrivals seen from 50° to 54° , labeled A and B at 52.8° , and the two SSS arrivals seen from 68° to 70° , labeled E and F at 70.5° , are due to the 650 km discontinuity, as mentioned in Fig. 4. Also the two SSS arrivals, C and D, are due to the rays bottoming between 250 km and 300 km and rays reflecting from 400 km discontinuity. These arrivals cross near 55° causing the large SSS amplitudes from 54° to 59° .

Figure 6 . Comparison of SS, SSS and SSSS data and synthetics from 71° to 77° distance. The double SSS arrivals seen at all distances are due to the 650 km discontinuity as mentioned before. The SSSS phase consists of an arrival bottoming near 300 km depth and a reflection from the 400 km discontinuity arriving at nearly the same time. These two arrivals also cause the large SS amplitudes from 36° to 39° in Fig. 4 and the large SSS amplitudes from 54° to 59° in Fig. 5. The single SS arrival seen at all distances bottoms near 900 km depth.





Model (1) : - - - Model (2) : ——— Model (3) : - . - . -
 Model (4) : — — — Model (5) :

Figure 7. The preferred East Pacific Q model (2) is shown relative to four other trial Q models. Synthetics for all five models are shown in the next figure to illustrate the effects of Q structure on particular multiple S phases.

Figure 8. The upper figure shows five synthetics for a distance of 76.8° . They correspond, from top to bottom, to the five Q models from (1) to (5) in Fig. 7. The S waves are normalized in amplitude and are followed by SS, SSS and SSSS. Relative to S, the amplitude of SSSS phase is very sensitive to the shallow Q structure but shows nearly no sensitivity to the Q between 400 km to 650 km. However, the SSS phase shows some sensitivity to the Q structure at that depth. This is shown in the lower figure. The lower figure shows three synthetics for a distance of 68° . They correspond, from top to bottom, to the Q model(4), model(2) and model(5) in Fig. 7, respectively. The S waves are also normalized in amplitude and are followed by SS and SSS. It is seen that the amplitude of the SSS phase shows some sensitivity to the changes of Q between 400 km to 650 km but not as sensitive as SSSS to the shallow Q structure in the upper figure. Note the SS in both figures shows only very little sensitivity to the different Q models. The reason why SSSS at 76.8° shows no sensitivity but SSS at 68° shows some sensitivity to the Q structure between 400 km to 650 km is that, as mentioned in Fig. 4, the arrivals of SSSS at 76.8° are from 300 km to 400 km depth but those for SSS at 68° are from above and below 650 km depth.

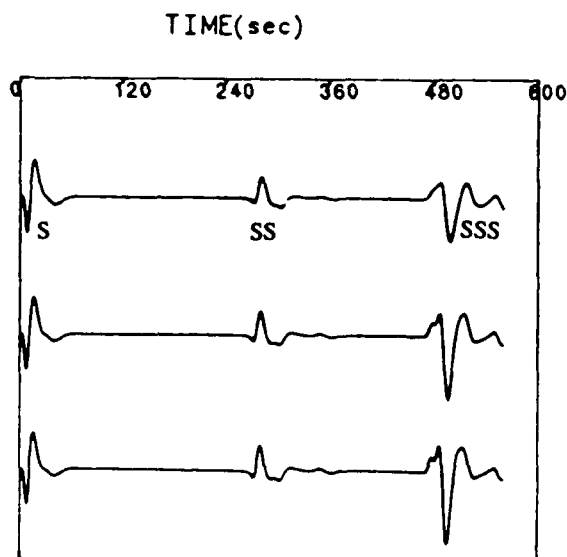
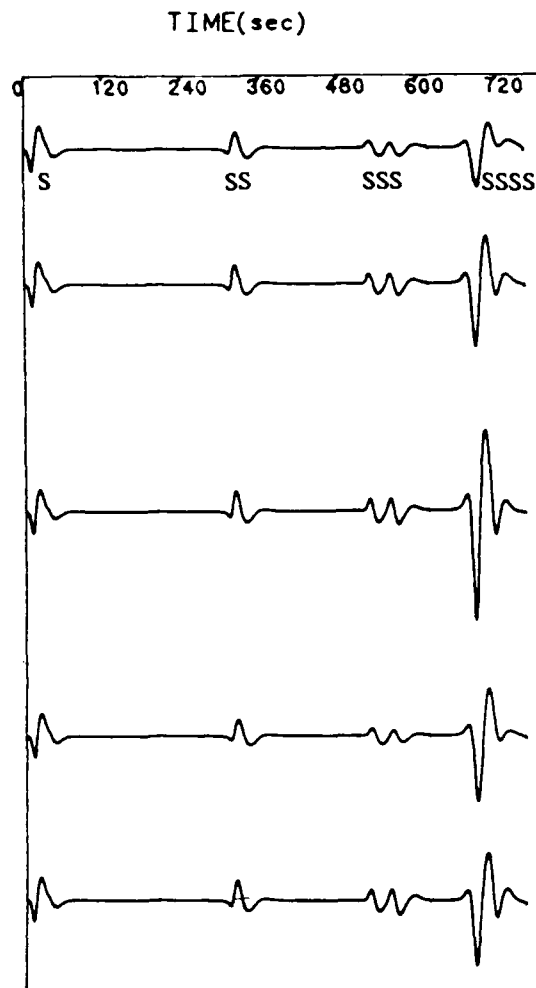
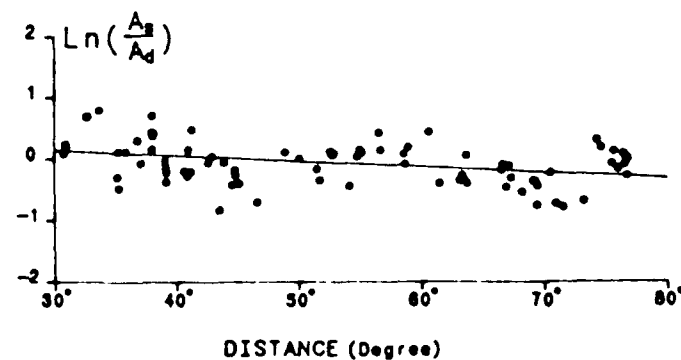
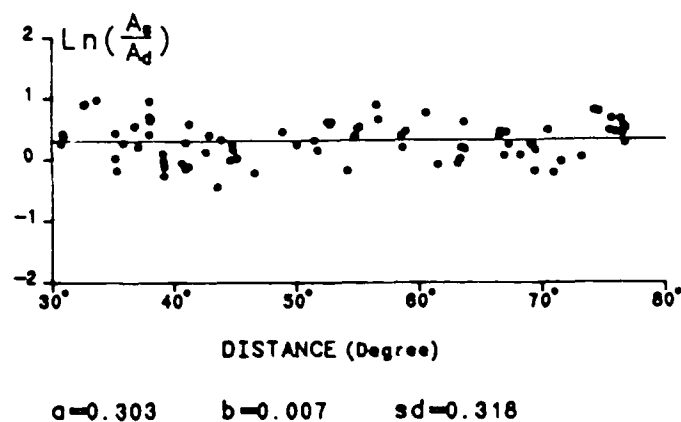
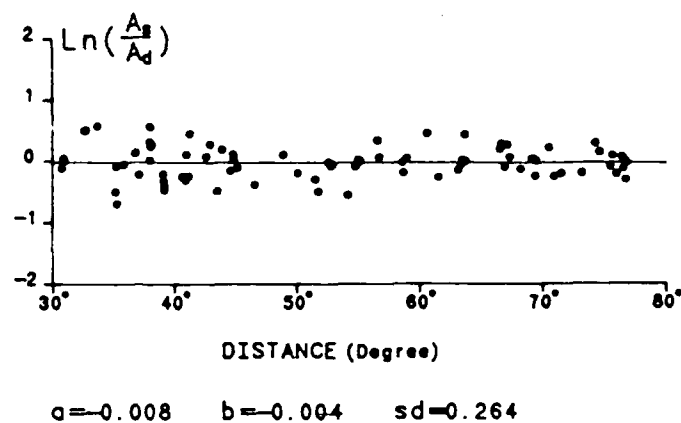
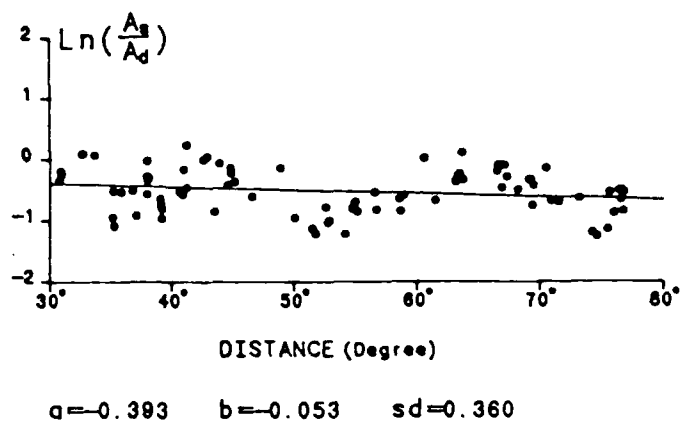


Figure 9. These four figures show the logarithm of the ratio of the amplitudes of synthetics to the amplitudes of data from 30° to 78° distance. They correspond, from top to bottom, to four Q models from (1) to (4) in Fig. 7. The solid line is a least squares fitting line to the data points. a is the intercept on the y-axis, b is the slope and sd is the standard deviation. The amplitudes of SS and SSS were measured from zero to peak, the amplitudes of SSSS were from zero to trough.



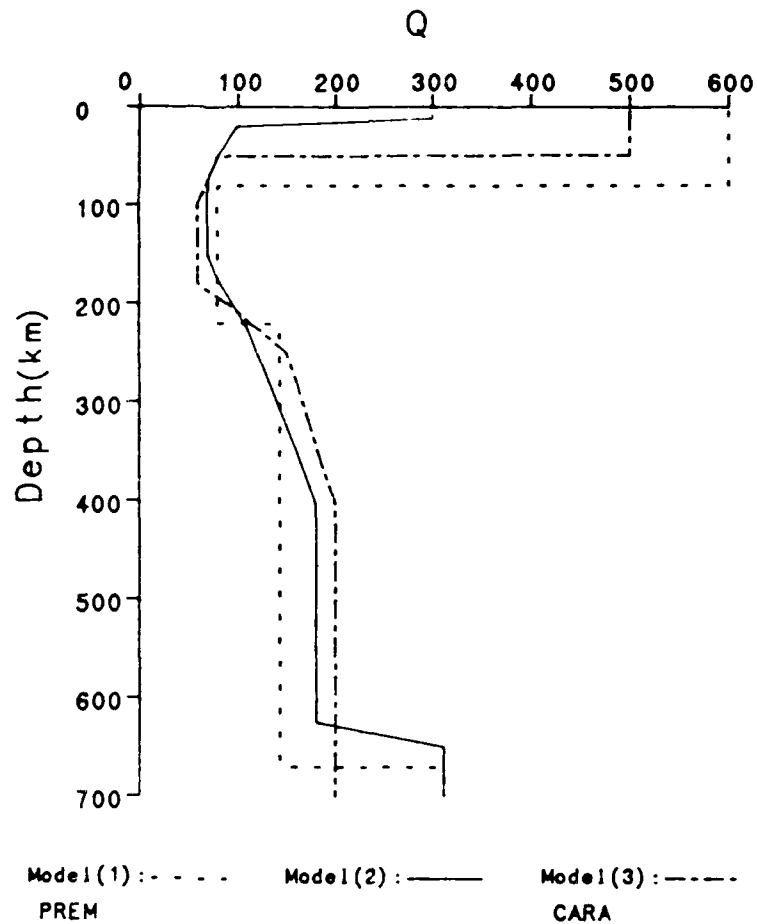
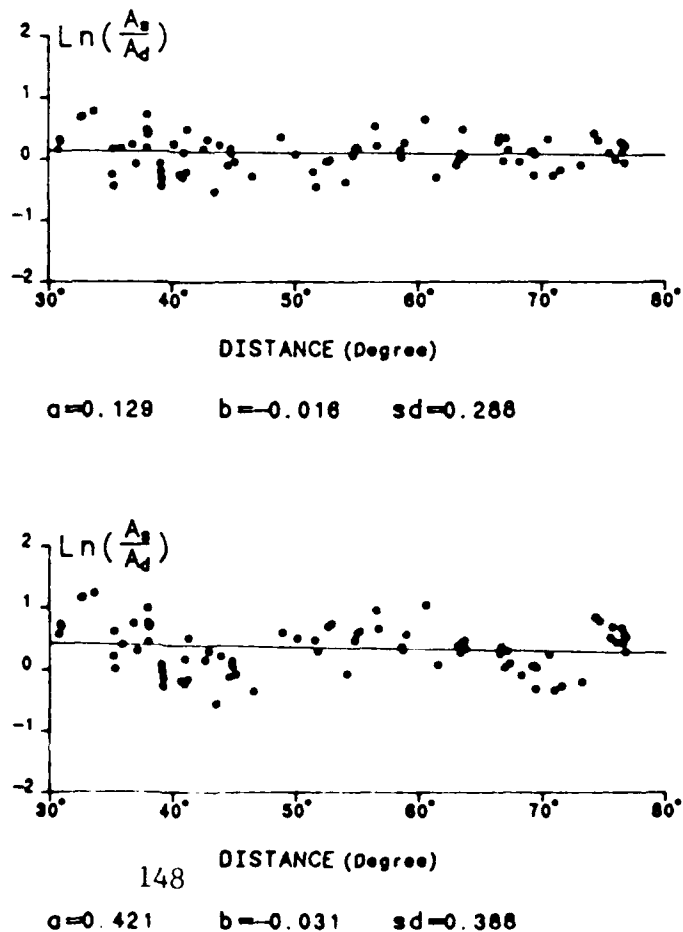


Figure 10. The upper figure shows three different Q models. Model (1) is the PREM Q structure (Dziewonski and Anderson, 1981), model (2) is the same Q model as that in Fig. 7 and model (3) is the Q model from Cara (1981). The lower figure is the same as that in Fig. 9. They correspond, from top to bottom, to Q model (3) and Q model (1) in the upper figure.



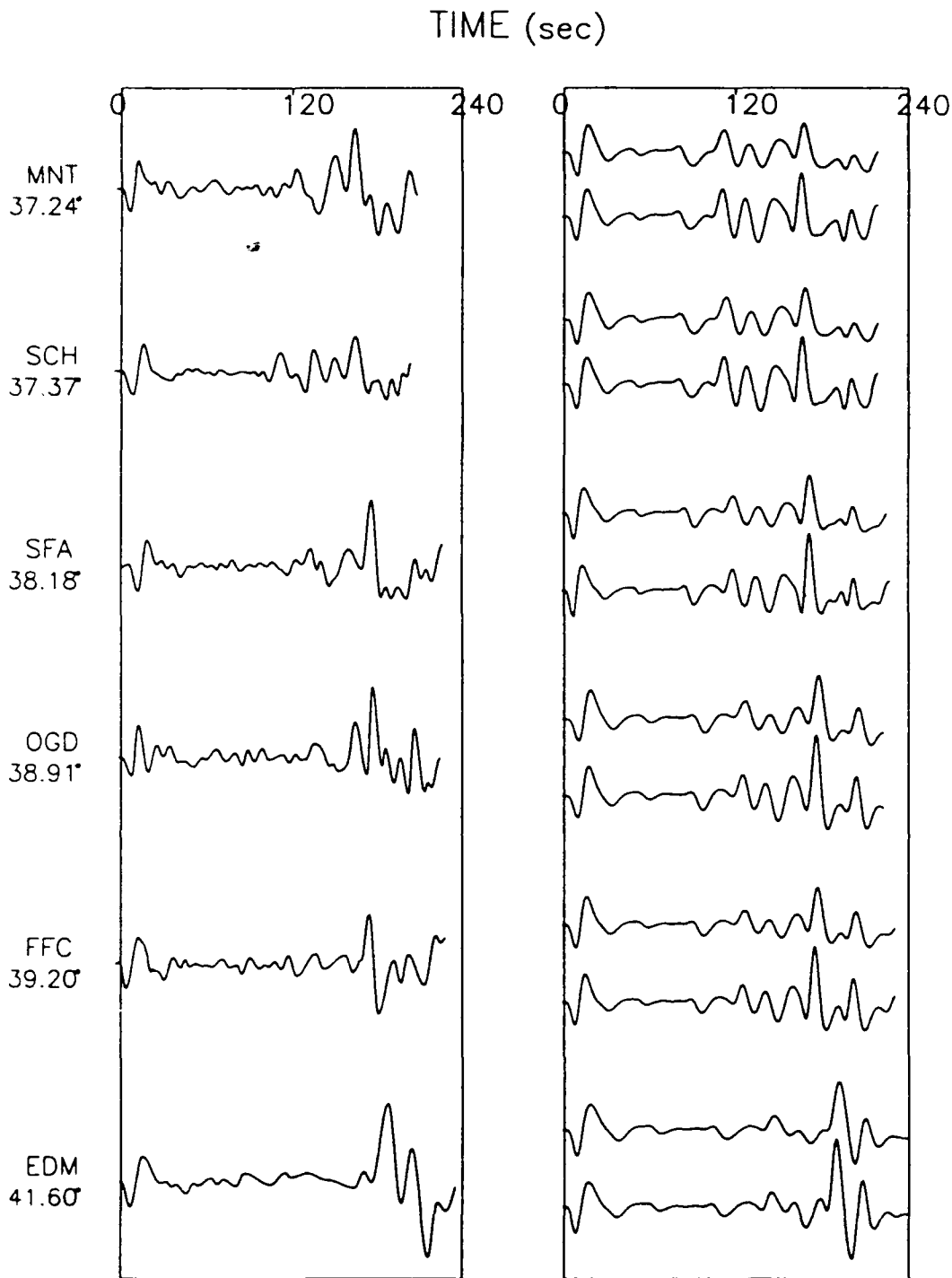


Figure 11. S and SS data are shown on the left. The first four seismograms are from an event near Vancouver with propagation paths across central Canada. The last two are from an Arctic event with stations in central Canada. The largest arrivals in each seismogram are SS reflections from the 400 km discontinuity (see Grand and Helmberger, 1984). Synthetics, on the right, were computed using QTNA (upper synthetic) and QSNA (lower synthetic) using the velocity model SNA.

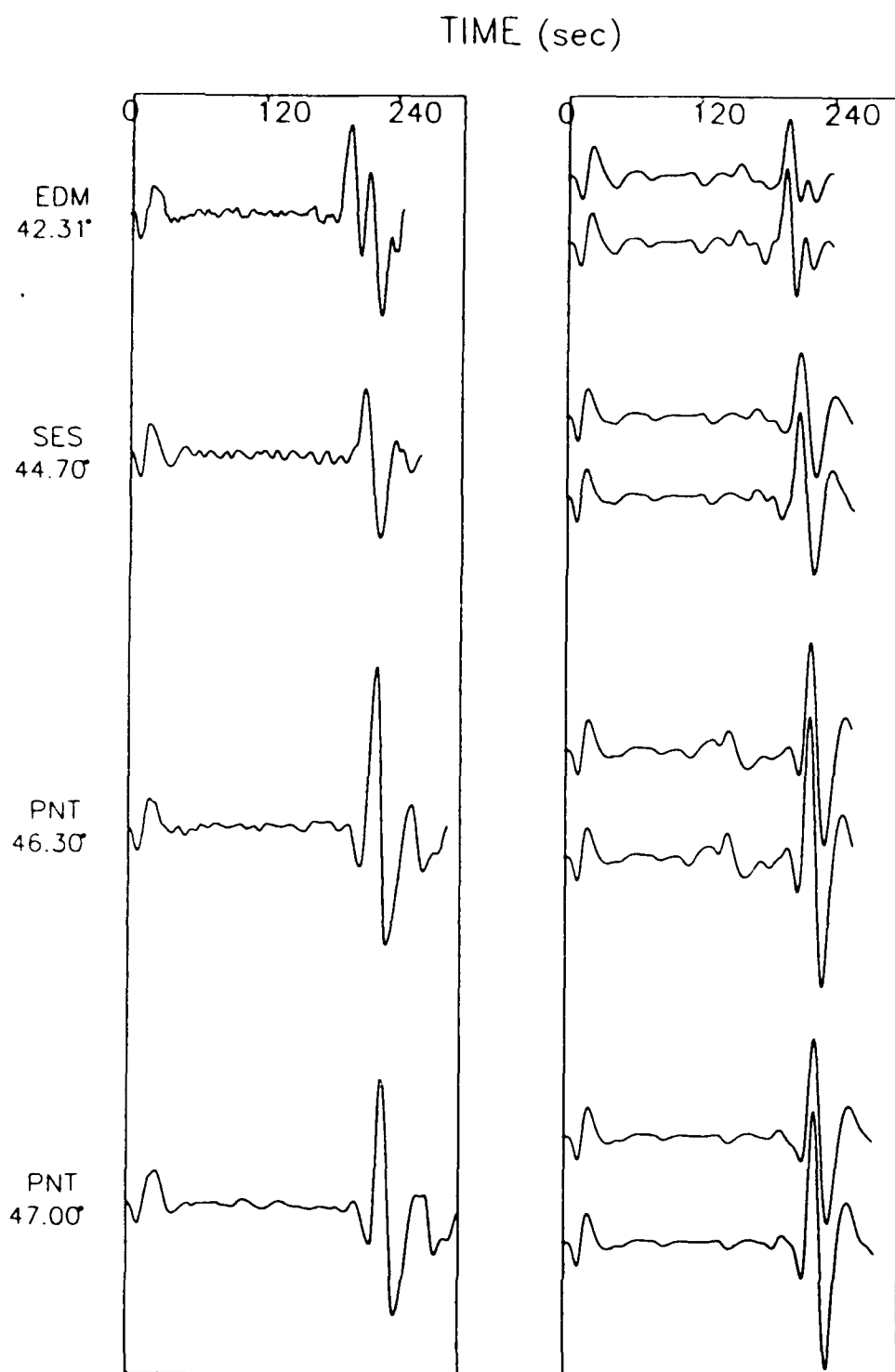


Figure 12. S and SS data shown on the left are from Arctic events recorded in southern Canada. The SS waves are due to reflections from 400 km and 650 km depth. These arrivals cross near 45° giving the large SS amplitudes in the last two seismograms. The synthetics use models QTNA and QSNA respectively as in the previous figure.

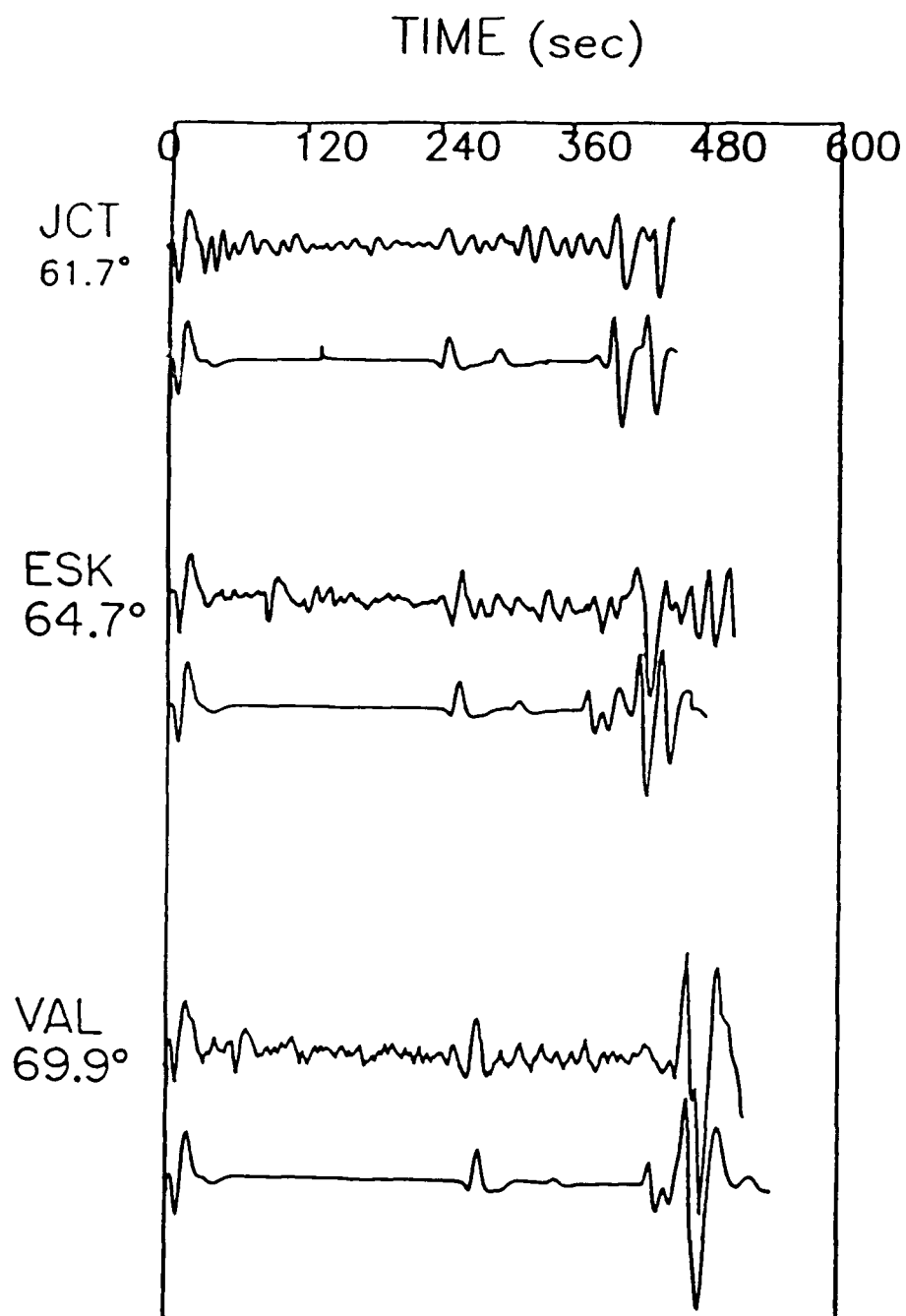


Figure 13. The upper three seismograms show S, SS and SSS waves. The first seismogram followed a path from the Arctic to Texas. The other two records propagated across the Russian platform (the seismic structure is the same as the Canadian shield, see Rial et. al., 1984). The SSS wave at these distances (the last large seismic phase in the above traces), is composed of a 400 km reflection and a 650 km reflection. They arrive at the same time at VAL giving the large SSS amplitude. The synthetics, below the data, were computed using model QSNA.

HIGH-FREQUENCY MEASUREMENT OF CODA Q IN CENTRAL FRANCE

Y. Cansi, S. Gaffet, B. Massinon

Radiomana, 27 Rue Claude Bernard, 75005 PARIS, FRANCE

OBJECTIVE

High frequency investigation in the frequency dependance of the Q factor for coda-waves has been carried out using the Q-coda method applied on digital records of a temporary station (LOR) installed in Central France. The results are compared with the Q_{Lg} factor resulting from inversion of both attenuation and source-function of a set of local earthquakes recorded on the french LDG network.

SUMMARY

We have used high-frequency records of the temporary station LOR to compute anelastic attenuation and scattering effects in central France by using the Q-coda method. Two methods are used to evaluate the coda decay: the time method and the frequency method. They lead to the same results: $Q(f) = 130f^{0.8}$ for the coda of Lg-waves. These results are to be compared to these obtained by Campillo et al. in western Europe. They obtained by simultaneous inversion of anelastic attenuation, source-function and station response a frequency depending Q-factor according to the relation: $Q(f) = 290f^{0.52}$.

DATA

Figure 1 shows the recording system. Five channels with different frequency bands and different sampling frequencies are used to cover the total bandwidth ranging from 0.5 to 110 Hz. Table 1 summarizes the characteristics of the recording system.

N°	Sampling frequency (Hz)	Bandwidth (Hz)	Relative gain
1	100	0.5-27.5	4
2	200	0.5-55	1
3	400	40-110	64
4	400	40-110	32
5	400	16-110	8

Table 1

Each channel is recorded with a magnification adapted to the various frequency bands in order to keep a large dynamic at all frequencies.

Figure 2 shows an example of event. It is a $M_L=3.6$ superficial earthquake located at 270 km from the station. We clearly see the 4 seismic phases usually recorded in France: P_n , P_g , S_n and L_g . Note that the crustal phases P_g and L_g are only visible on the low frequency channels, contrasting with the refracted phases P_n and S_n clearly visible up to 40 Hz.

RESULTS

In the time-method each signal is bandpass filtered in 32 bands with a central frequency f_c ranging from 1 to 90 Hz and bandwidth defined by $[f_c/2, 3f_c/2]$. The coda shape is computed by using the Hilbert transform and then smoothed with a 3s moving time-window. Figure 3 shows 5 traces representing the coda decay for different frequency-bands. The flat level plotted at the end of each trace is the average noise level in the corresponding frequency band. This noise level is removed before the computation of the Q factor by fitting the traces using least-square method. The Q values obtained are displayed on the right side of the figure. They lead to a frequency dependant Q factor described by the relation: $Q(f) = 130f^{0.85}$ as displayed on figure 4.

In the frequency method the amplitude at time t is evaluated at different frequencies by computing the spectrum of a time-window centered on time t, and then smoothing this spectrum. It leads to similar results for the Q(f) relationship.

CONCLUSION

The Q(f) relation is rather different from the one obtained by Campillo et al. who used a set of 18 earthquakes in western Europe recorded on the french LDG network. They have computed Q(f) by inverting simultaneously the anelastic attenuation, each source-function and the station responses. This can be explained by the rather disturbed structure of the crust investigated by the Q-coda method which may allow important scattering effects. Figure 5 shows this region defined by the beginning and the end of the studied time-window. It covers the northern part of the Alps and the Rhinegraben which are active tectonic areas.

REFERENCES

- AKI, K. and B. CHOUET, 1975, *Origin of Coda Waves: Sources, Attenuation and Scattering Effects*, J. Geophys. Res., 80, 3322-3342.
- CAMPILLO, M. et al., *Frequency dependant Attenuation in the Crust beneath Central France from Lg-waves: Data Analysis and Numerical Modeling*, Bull. Seism. Soc. Am., 75, 1395-1441.
- CANSI, Y., *Theoretical and Experimental Study of the Excitation of Seismic Phases versus Depth at Local Distances*, Spring Meeting of the AGU, 1988.
- JIN, A., and K. AKI, 1988, *Spatial and Temporal Correlation between Coda Q and Seismicity in China*, Bull. Seism. Soc. Am., Vol. 78, No. 2, 741-769.
- NICOLAS, M., et al., 1982, *Attenuation of Regional Phases in Western Europe*, Bull. Seism. Soc. Am., 6, 2089-2106.

FIGURES

- Figure 1: The recording system.
- Figure 2: An example of records showing clearly the frequency dependence of the 4 seismic phases.
- Figure 3: The coda shapes obtained after filtering and smoothing. At the right side are displayed the noise level and the Q value computed by least-square.
- Figure 4: The $Q(f)$ relation.
- Figure 5: The studied region delimited by the two ellipses is displayed with its tectonic structure. The star represents the quake. The thin lines delimit the hercynian mountains.

RECORDING SYSTEM

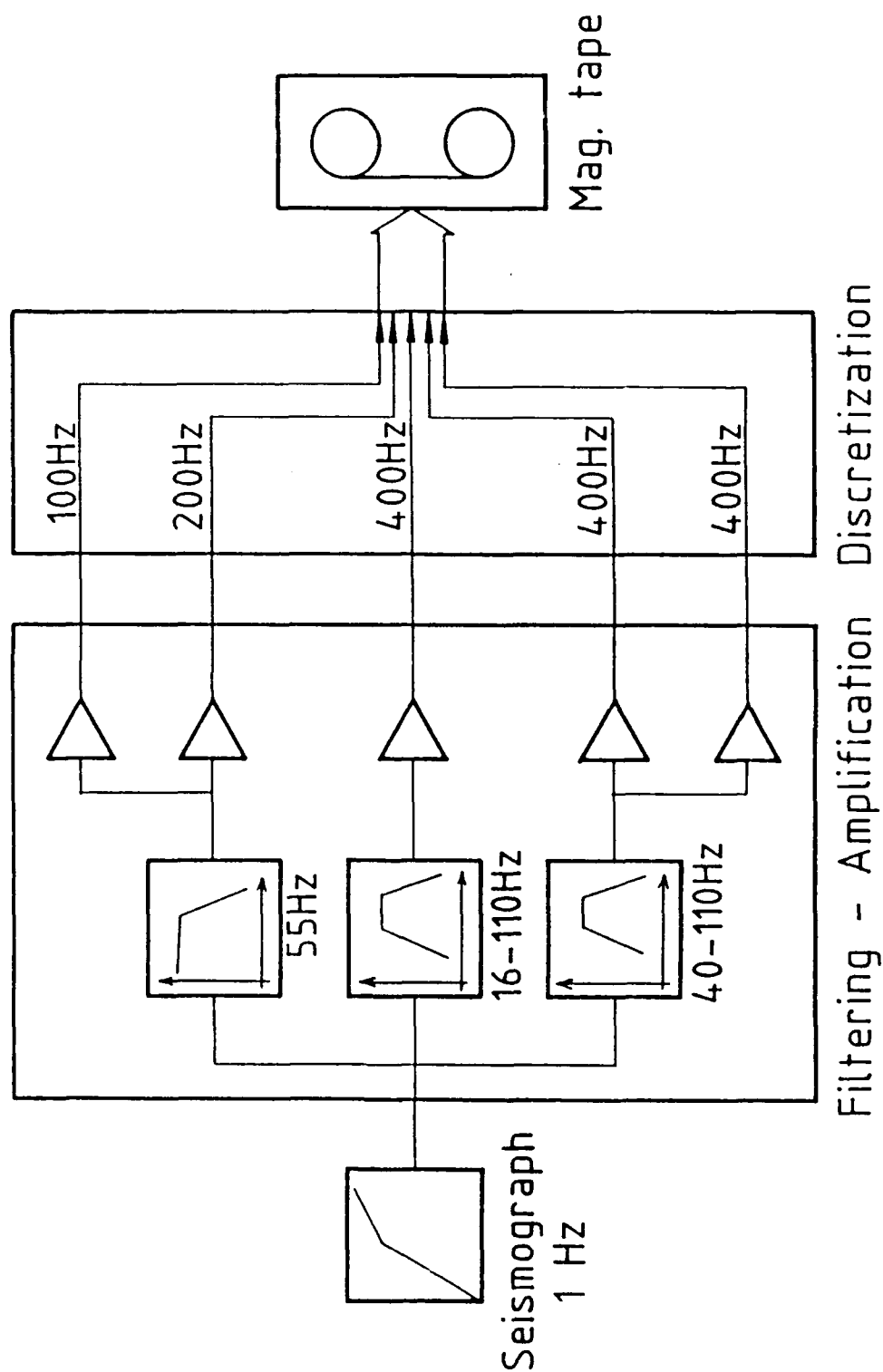
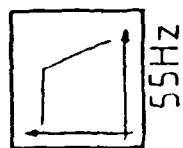


Figure 1

SEI002 LOR 270 km

STUDIED TIME WINDOW

OR 31 0.014

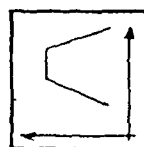


Sn

Pg

Pn

Lg



16-110Hz

TIME (seconds)

Figure 2

SEI002 LOR 270 km

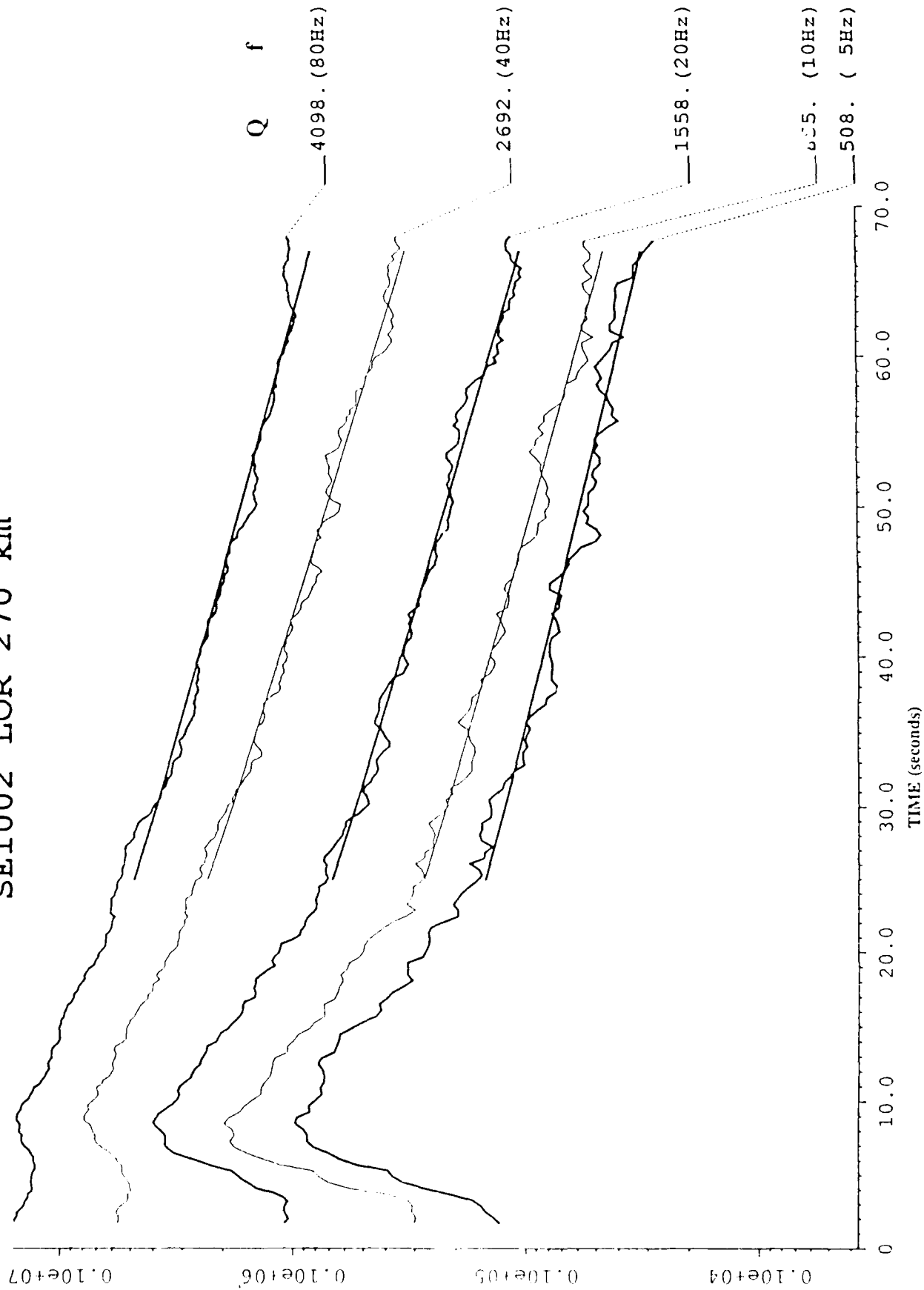


Figure 3

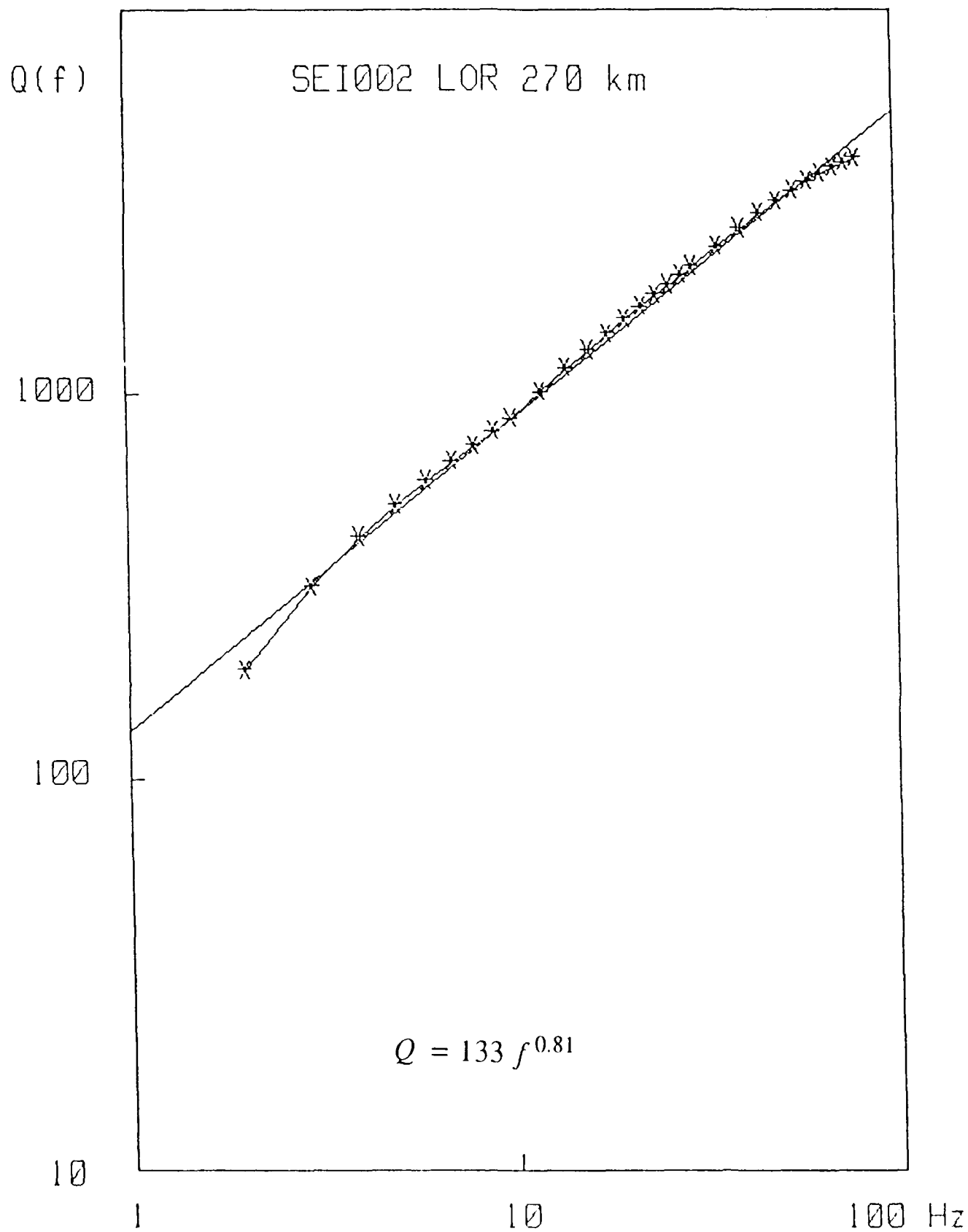


Figure 4

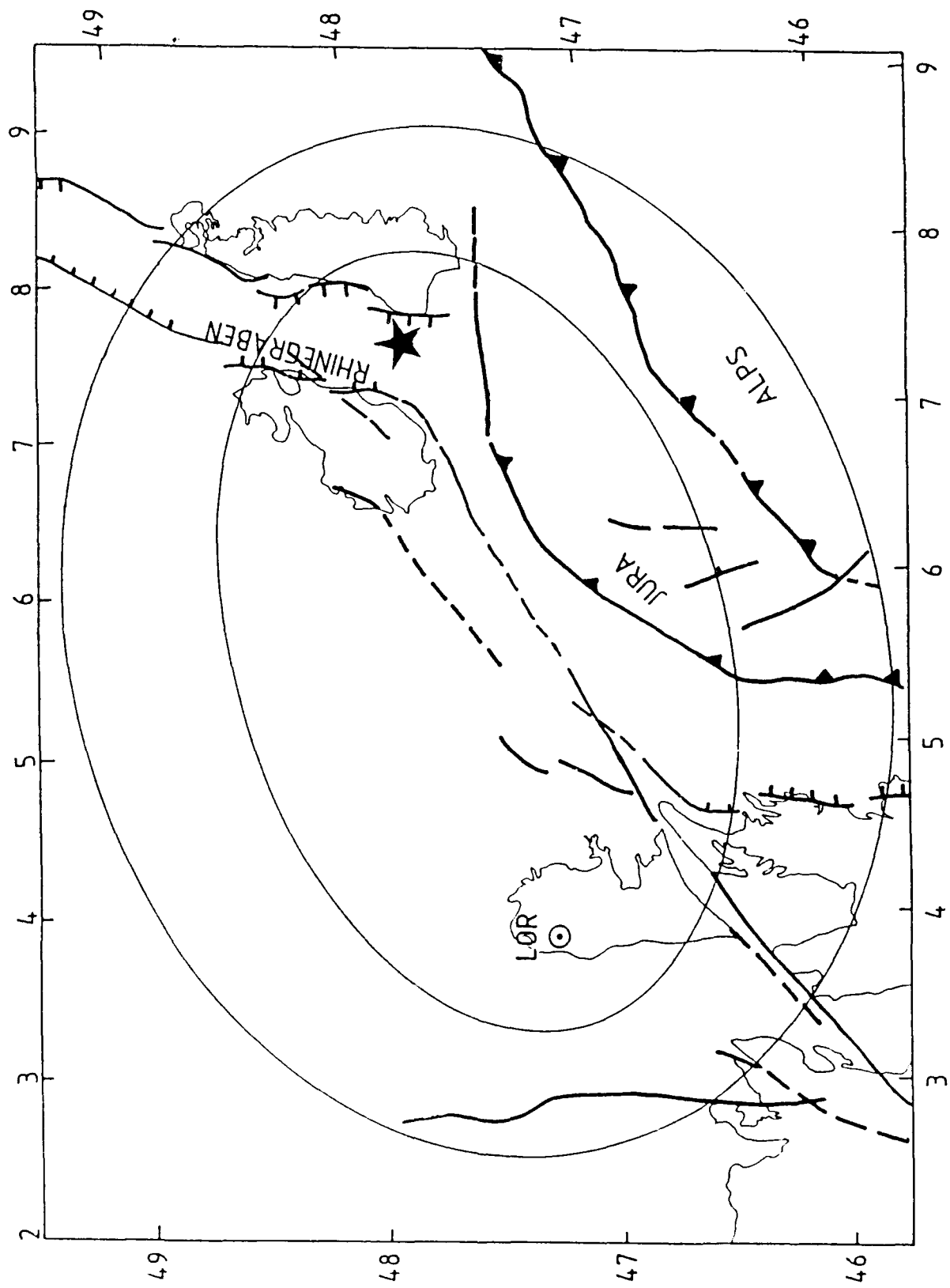


Figure 5

NEAR SOURCE GROUND MOTIONS AND SCALING FROM NTS EXPLOSIONS

Brian W Stump
Department of Geological Sciences
Southern Methodist University
Dallas, Texas 75275

Contract #F19628-87-k-0021

A. OBJECTIVES: The work reported is part of continuing program designed to constrain the physical and mathematical models of near surface explosions. These sources included contained single burst chemical and nuclear explosions, and multiple burst chemical explosions used to fragment near-surface rock masses. This work has focused upon near-source data sets. Explosions, unlike natural events, are controllable in that their time of occurrence and location can be determined by the experimenter. This attribute allows for the design of ground motion experiments whose expressed purpose is the determination of source properties. Not only can the elastic field be determined but the development of the wavefield from very close to the source where the material responds nonlinearly can be documented. Several nuclear explosions at NTS have been instrumented during the past year. These near-source studies are unique because in one case a combination of free-field and free surface data are recovered, and in another case significant amounts of data from within the spall zone are available. Our focus in this paper will be the quantification of these motion fields with particular emphasis placed upon their variability.

B. SUMMARY: The spatial variability of free-field and free surface data must be quantified if such measurements are to be utilized in the constraint of physical characteristics of the explosive source function. In an attempt to explore this topic two near-source experiments have been conducted. This data has been supplemented by motion measurements made available through the LANL data base.

Free surface acceleration measurements can be compared under the assumptions of cube root scaling. In Figure 1 the scaled accelerations for a number of nuclear explosions detonated at Pahute Mesa are compared. This vertical data is typical of the scatter observed in free surface measurements from all types of sources. As the figure

PAHUTE MESA SCALED ACCELERATION

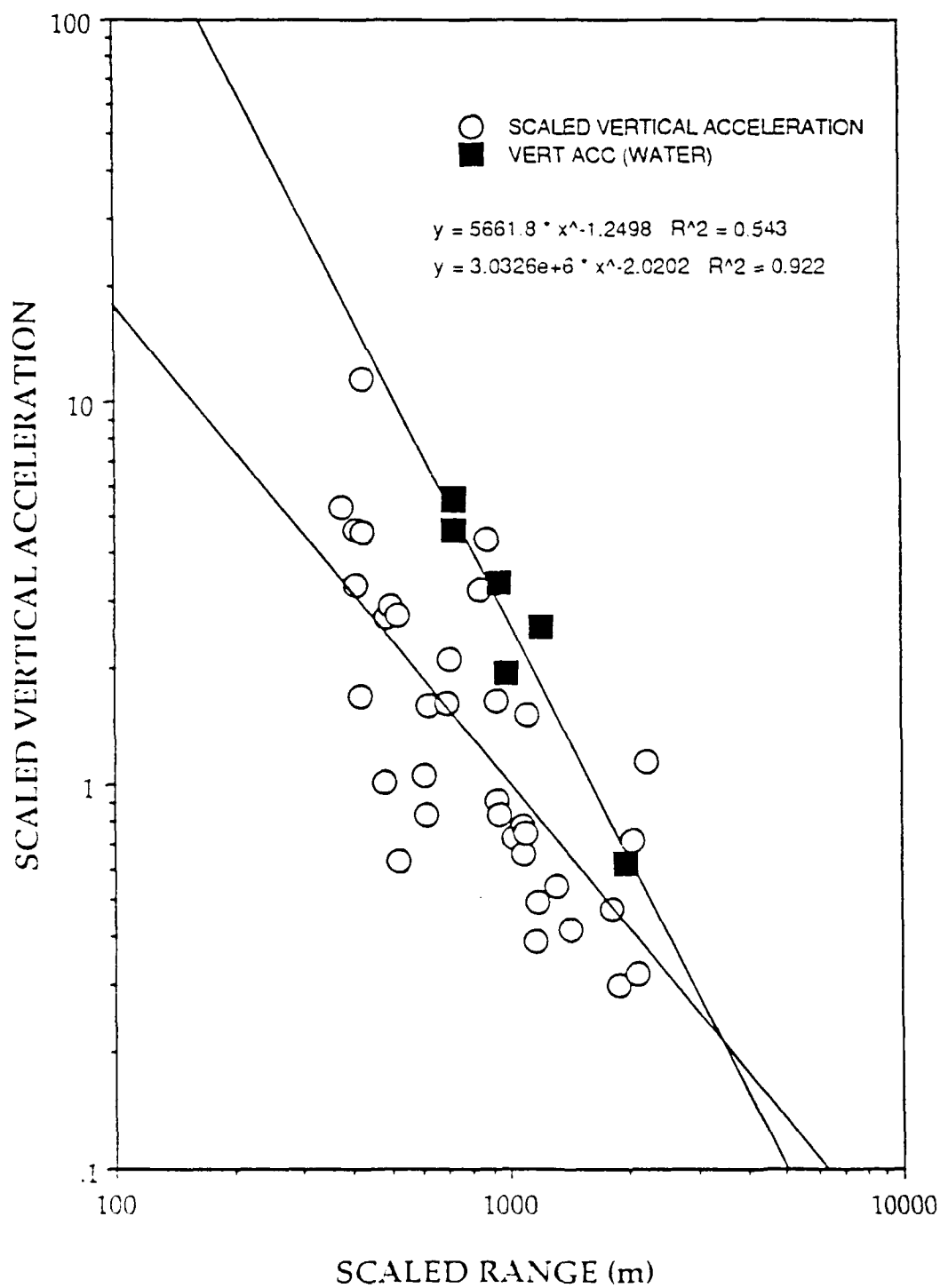


Figure 1: Scaled vertical acceleration (g's) for a number of nuclear explosions detonated at Pahute Mesa.

indicates, there can be over an order of magnitude variation in scaled acceleration at a particular range. It is interesting to note that the data from shots below the water table indicate a positive bias in measured acceleration when compared to the rest of the data. Similar variations are found in the moments estimated from near-source data of earthquakes (Archuleta et al, 1982 and Fletcher et al, 1984). This spatial variability of the observed wavefield extends to small scale lengths. Figure 2 is a plot of peak accelerations from a series of 5 lbs explosions detonated in alluvium (Grant, 1988). The vertical and radial accelerations exhibit the same variation observed in the nuclear data. A single explosion also exhibits strong lateral differences in peak acceleration as well as waveshape at NTS. Figure 3 is a plot of peak vertical acceleration as a function of range from one particular experiment. Again the factor of ten variation is observed. These types of observations cast doubt on the utility of single point measurements in the near-source regime for constraining source properties.

In an attempt to constrain the effect the weathered layer has on this spatial variation in waveforms a second seismic experiment was designed and implemented. As Figure 4 indicates, both free surface and free-field (shot depth) measurements from a single explosion were recovered. In this case 8-three component gages were fielded at shot depth while 9 gages were distributed in the expected spall zone with 10 additional three component free surface gages. The design goals of this experiment included the quantification of the free-field data including range and azimuthal effects, the quantification of spall at the free surface and the determination of the equivalent elastic wavefield. The free-field and free surface radial accelerations are presented in Figure 5. The free surface data, solid squares, reflect the factor of ten scatter documented in the other data sets. The free-field data is in marked contrast, where individual data points diverge by no more than 20% from a linear decay model,

$$\text{Acc (g's)} = 5.42 \times 10^7 R^{-2.62}$$

The scatter observed in the free surface data is dramatically reduced at shot level indicating that geological inhomogeneities are having a significant impact on peak acceleration data at the free surface.

In order to explore these lateral variations in the wavefield the actual waveforms were investigated in the time and frequency domain. The free-field waveforms summarized in the peak

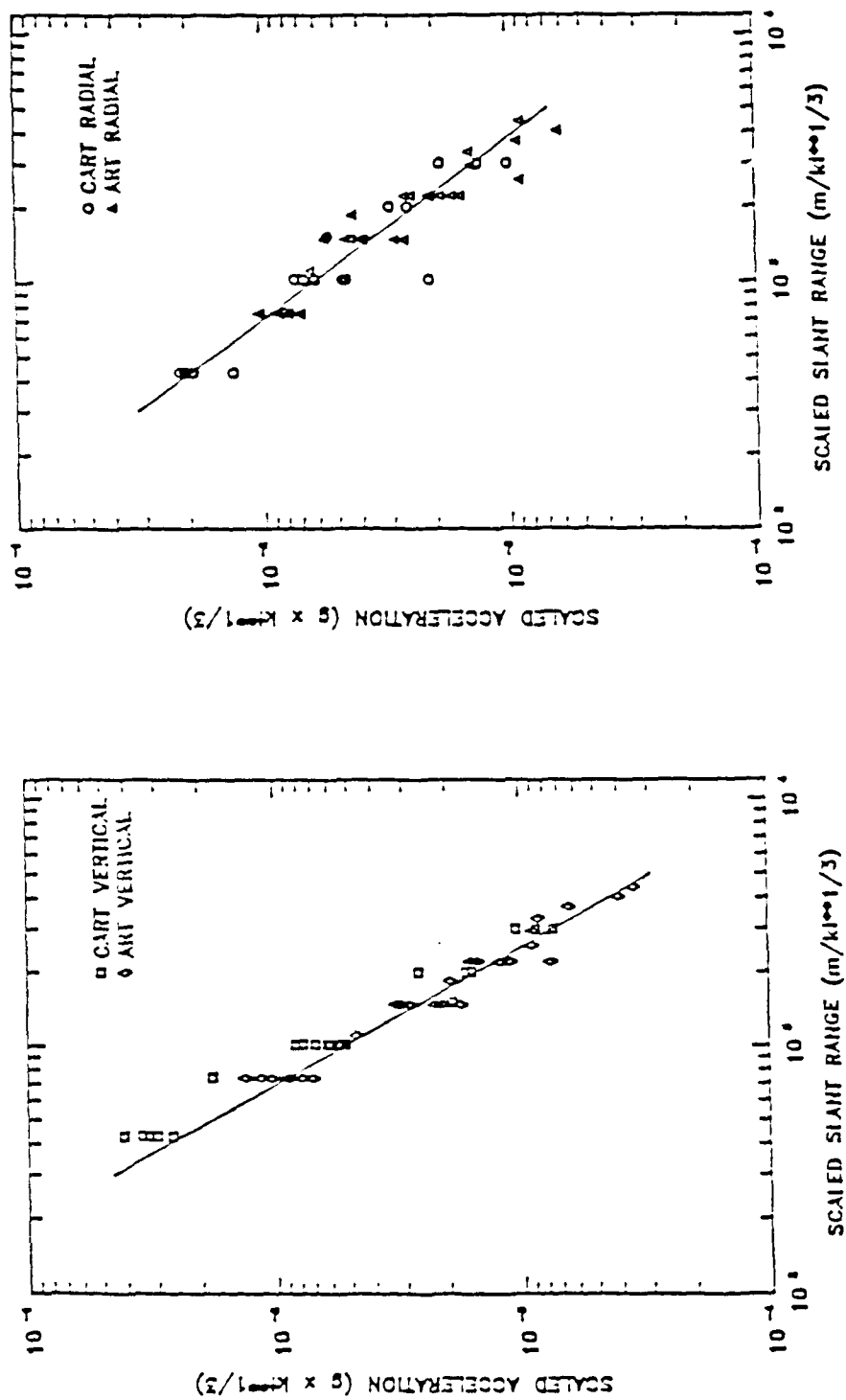


Figure 2: Scaled vertical and radial accelerations from 5 lbs chemical explosions detonated in alluvium.

SINGLE EXPLOSIONS DATA PAHUTE MESA

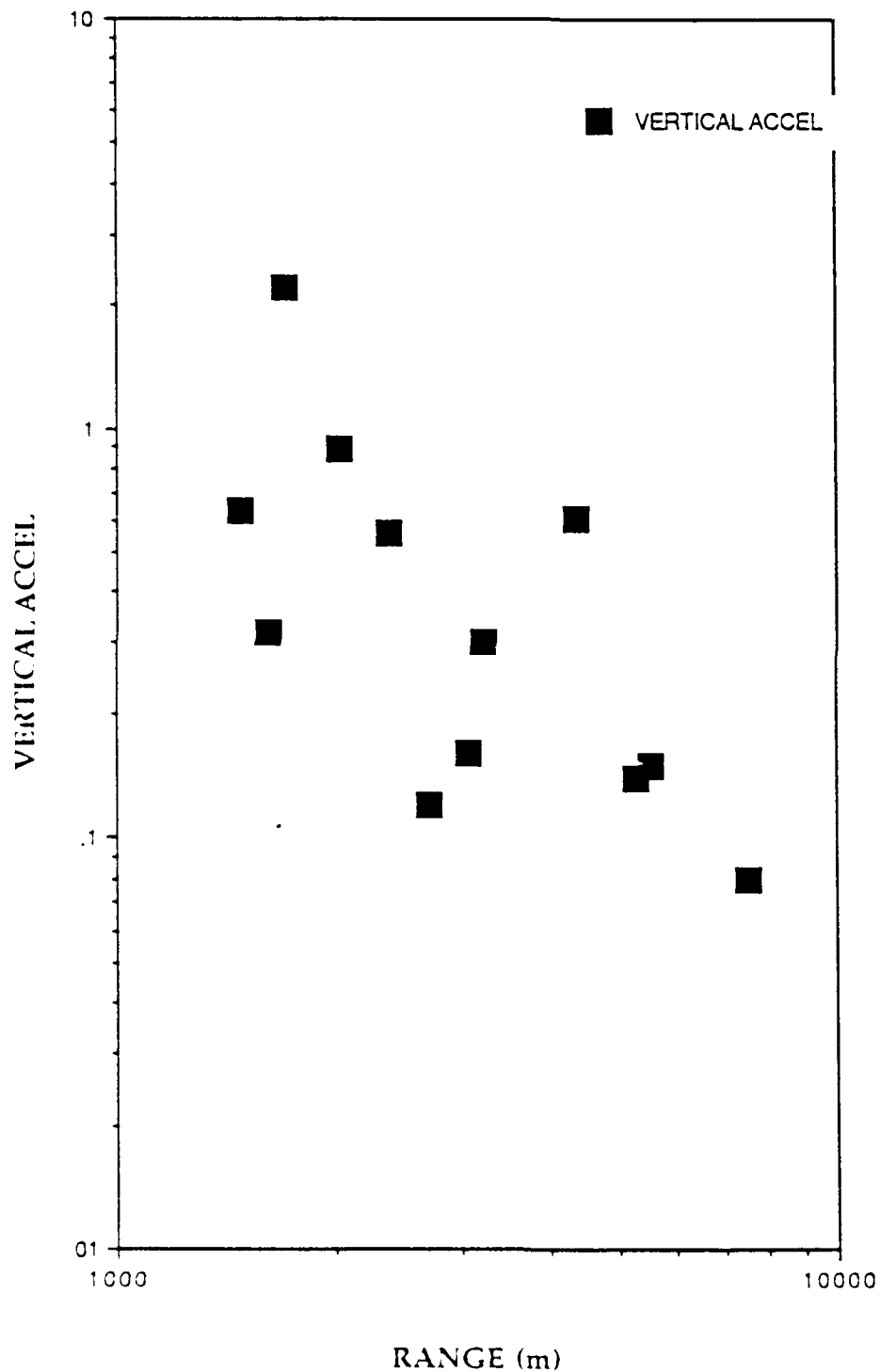


Figure 3: Vertical acceleration (g's) (free-surface) for a single nuclear explosion detonated at Pahute Mesa.

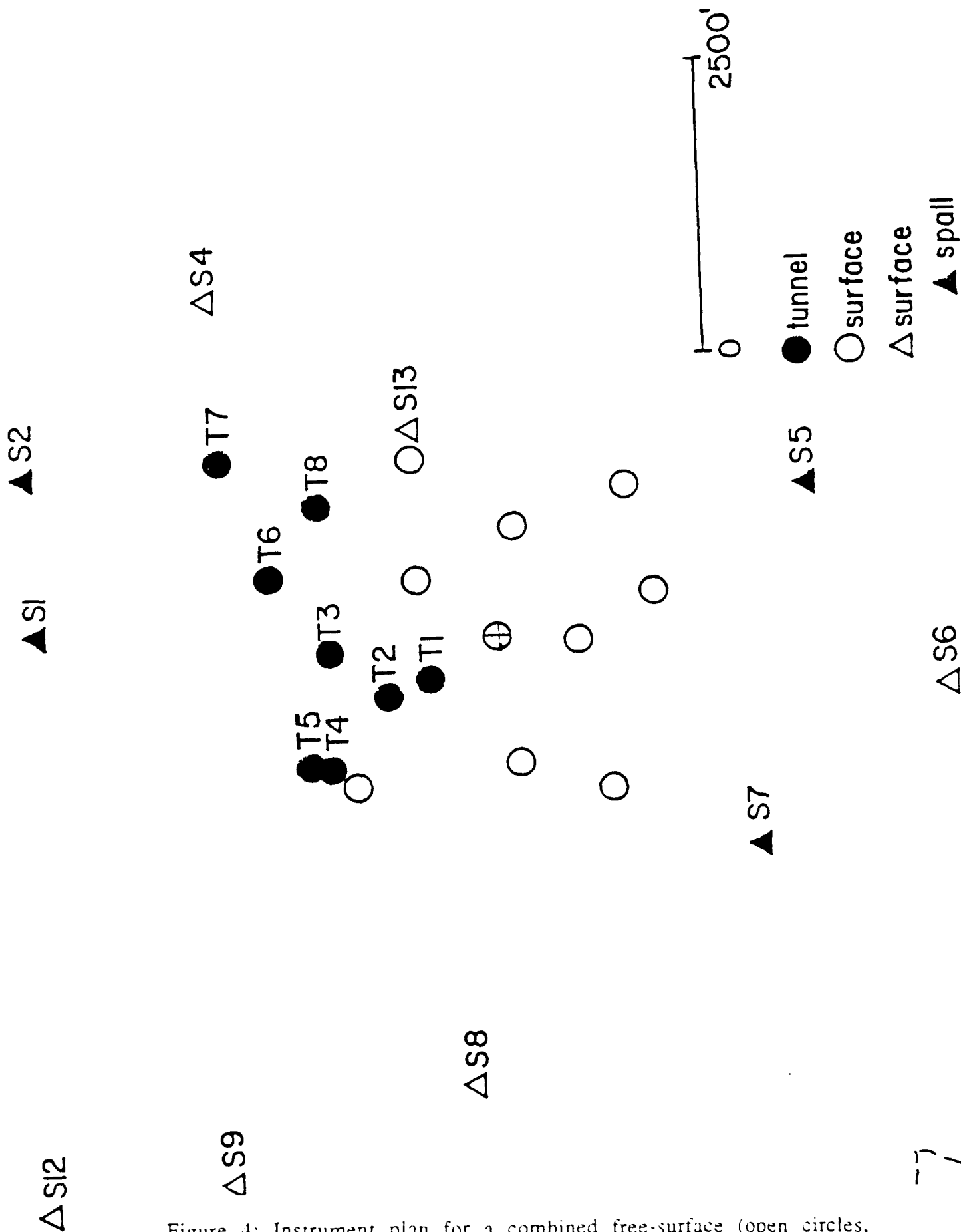


Figure 4: Instrument plan for a combined free-surface (open circles, triangles) and free-field (solid circles) experiment.

FREE SURFACE AND FREE FIELD DATA

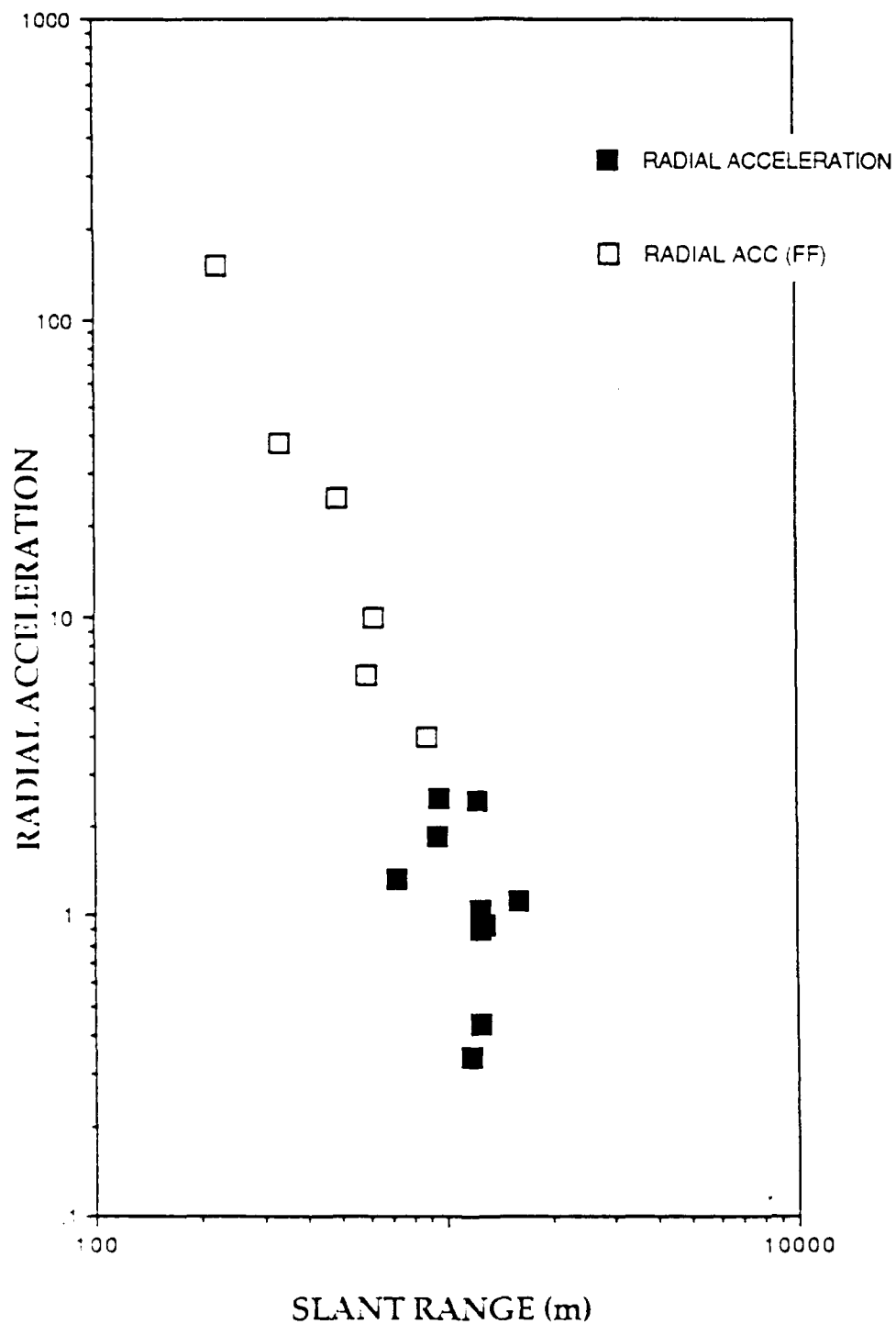


Figure 5: Free-field (open squares) and free-surface (solid squares) measurements from a single nuclear explosion.

amplitude plots are replicated in Figure 6. Comparing the observation at the greatest range with the closest observation indicates a pulse broadening with range. The process by which the high frequencies are lost from the waveforms is not consistent with range. The third observation in Figure 6 is apparently longer period than the more distant fourth observation. As the key in the figure indicates the observations to the northwest are higher frequency than those to the northeast. This apparent azimuthal effect in the waveshapes may be related to structural differences around the shot but have not been substantiated at this point of our studies. Data such as that recovered from this combined free-field/free surface experiment can be used to constrain possible lateral variations in the equivalent elastic source function as well as document the development of this function.

Free-surface waveforms from a small nuclear explosion in alluvium are replicated in Figure 7. This particular explosion, Coalora, was instrumented with a dense array of three component accelerometers (thirty-one) out to a range of 5 km. In this particular example the radial and vertical displacements vary by 30% about the mean of the observations. There is significant similarity between the waveshapes for the radial and vertical motions respectively. These characteristics argue for some degree of cylindrical or spherical symmetry in the source function. The transverse components in comparison are much shorter in duration, delayed in time, and exhibit significant fluctuations including a change in first motion. Displacement spectra were estimated from these records and reproduced in Figure 8. Envelop functions were fit to each spectrum which included a long period level, corner frequency, and high frequency decay. In comparison to the vertical and radial spectral estimates, the transverse displacement spectra exhibit higher corner frequencies, lower long period levels, and faster high frequency decay.

FREE-FIELD RADIAL ACCELERATION

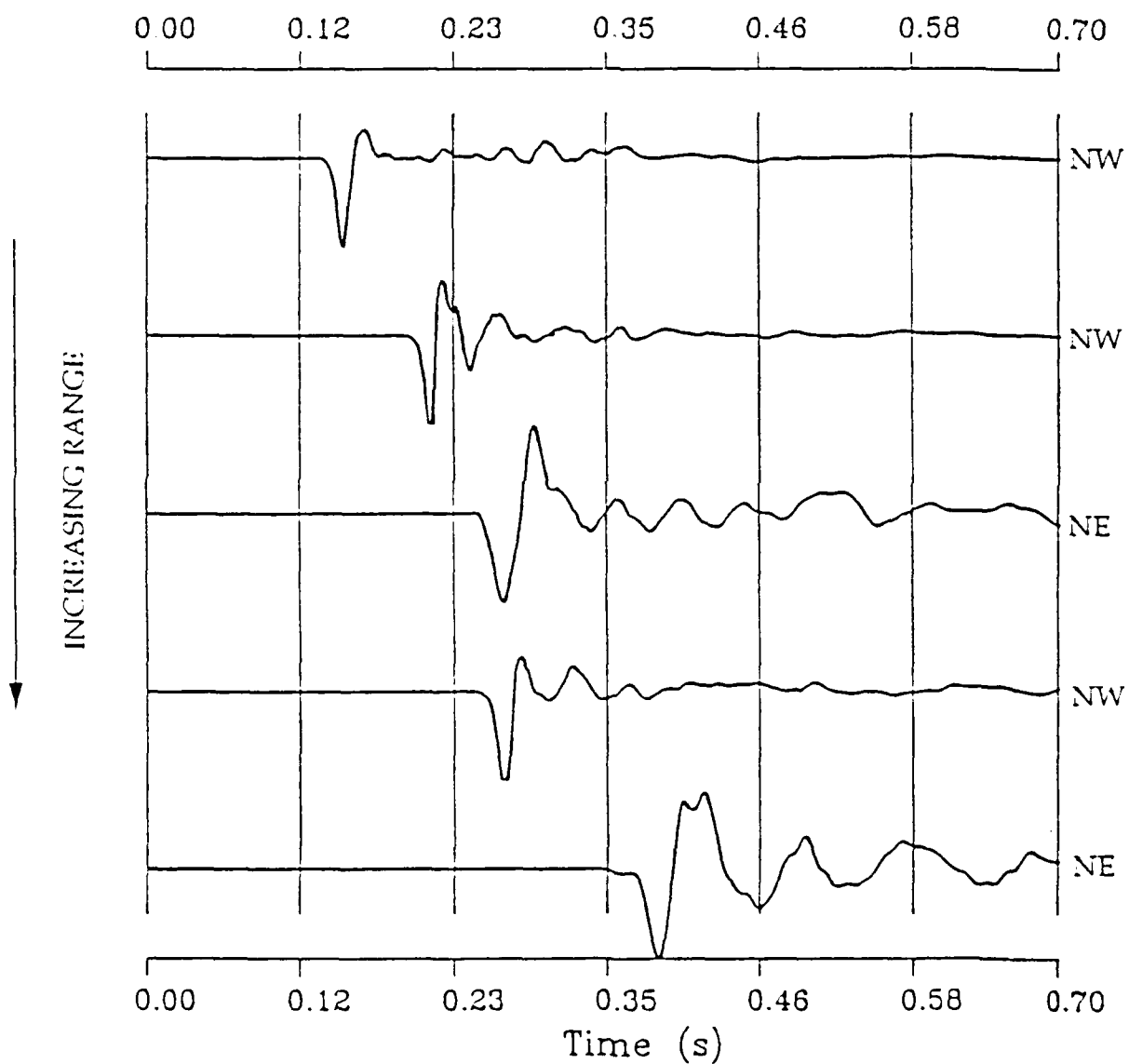


Figure 6: Free-field waveforms from a single nuclear explosion.

COALORA DISPLACEMENT AT 549m RANGE

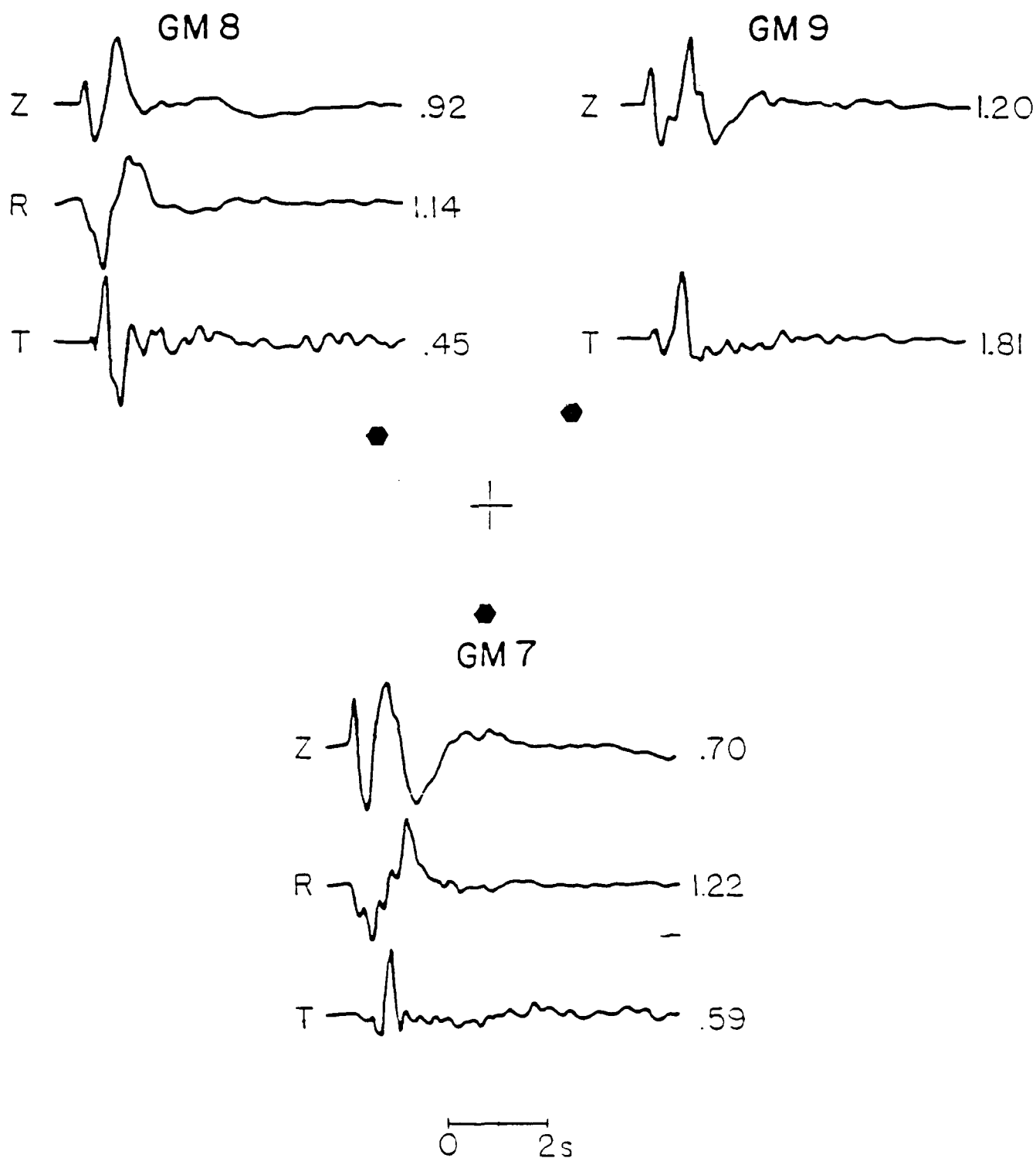


Figure 7: Vertical, radial, and transverse displacements from the nuclear explosion Coalora.

COALORA DISPLACEMENT SPECTRA AT 549m RANGE

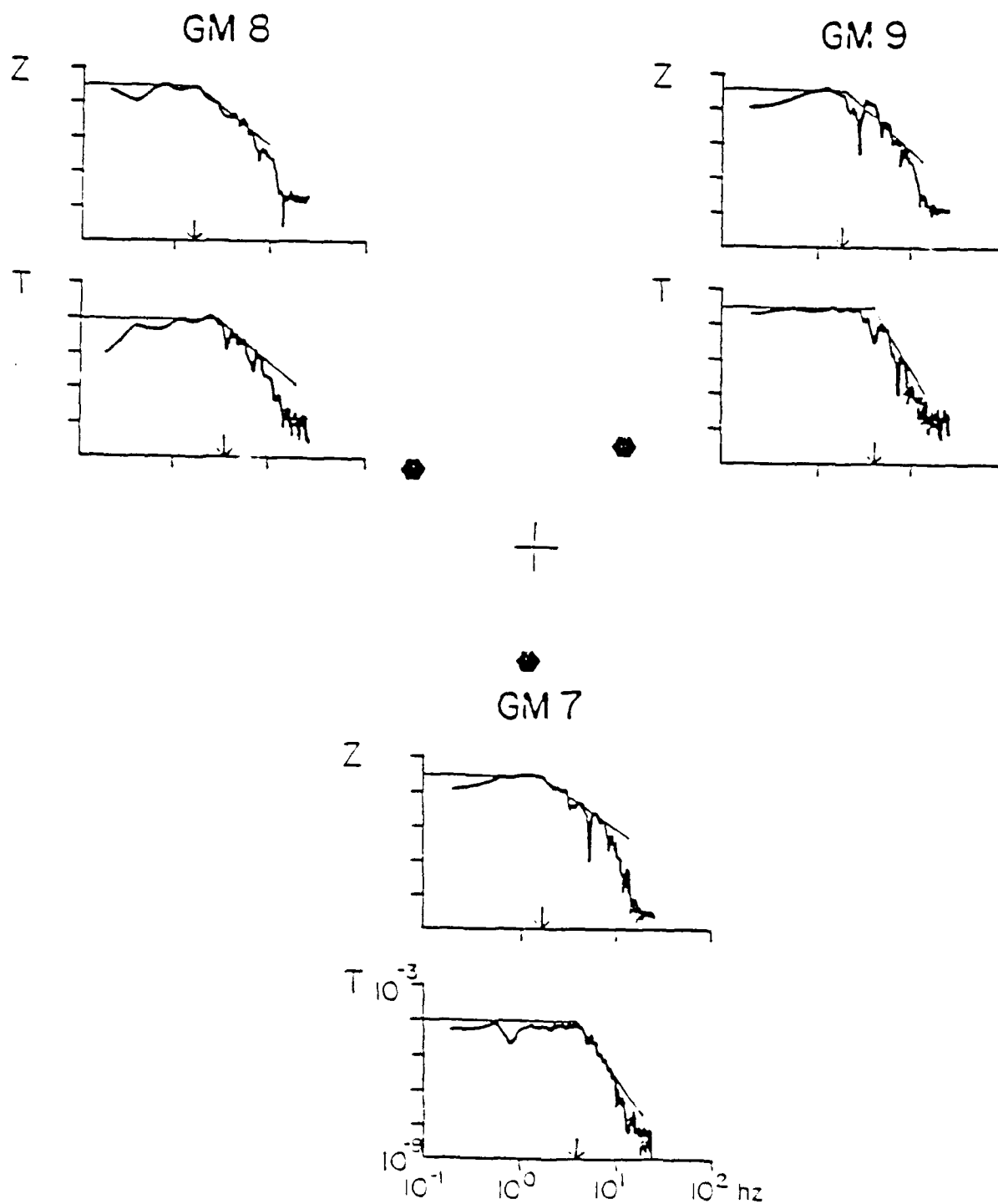


Figure 8: Vertical and transverse displacement spectra from the Coalora explosion.

Station #	Range (m)	DC (cm-s)	f_c (Hz)	Slope
GM7Z	612	0.30	1.8	2
GM7R	612	0.36	2.1	2+
GM7T	612	0.09	4.0	4
GM8Z	614	0.30	1.6	2
GM8R	614	0.36	1.8	2
GM8T	614	0.10	3.5	2+
GM9Z	612	0.34	1.8	2+
GM9T	612	0.30	3.5	3+

These relative close-in spectra show little variation in radial and vertical long period levels, quite a contrast to the peak accelerations. The transverse estimates in comparison have a factor of two increase in corner frequency and an accompanying reduction in long period level. Full wave spectral estimates give an isotropic moment(R&Z Components) of 1.95×10^{21} dynes-cm (multiplicative error of 1.36) and a deviatoric moment(T Component) of 3.97×10^{20} dynes-cm (multiplicative error of 1.44). The accompanying corner frequencies were 1.82 for the isotropic spectra (1.12 multiplicative error) and 3.28 for the deviatoric spectra (1.13 multiplicative error). The isotropic corner frequency lies between a model prediction of 2.5 Hz for 1 kt and 1.7 Hz for 10 kt which is agreement with the announced yield of less than 20 kt. The transverse spectra can be used to make stress drop and source dimension estimates for the deviatoric part of the source. The mean source radius is 124 m with a stress drop of 89 bars and an average displacement of 33 cm. These displacements calculated from the radiated wavefield are similar in magnitude to observed displacements on faults and bedding planes found upon reentering tunnels surrounding nuclear explosions at Rainier Mesa (Kennedy, 1982). The equivalent elastic radii for 1 and 10 kt explosions are predicted to be 133 and 202 m. The deviatoric source radius falls within the bounds of the equivalent elastic source radii.

These peak amplitude and waveform observations of the explosion source indicate that point measurements may lead to significant variations in source estimates of a single explosion. Average spectral estimates offer a means for smoothing along with a quantification of data scatter.

These spectral estimates make only a rudimentary correction for propagation path effects which may lead to bias in the source estimates. This effect may be particularly strong in the case of shallow depth explosions which generate both body and surface waves. In order to better take into account the propagation path effects and account for both the deviatoric and isotropic source components, moment tensor inversions were completed for the Coalora explosion. Wave propagation effects were taken into account with a set of reflectivity Green's functions. Many different stations were utilized simultaneously in the inversion in order to smooth through that part of the data reflective of lateral inhomogeneities in the geologic structure. Both the absolute amplitudes and the waveshapes were modeled with the fits completed in the frequency domain. Characteristic comparisons between the observed and modeled ground motions are reproduced in Figure 9. The seismograms are well modeled with correlation coefficients between 0.71 to 0.94. The resulting source characterization is given in Figure 10 as the moment rate and moment tensors. The source is dominated by the isotropic part of the moment tensor. The initial pulse is symmetric and is followed by a secondary long period contribution, largest on the M_{33} component, the vertical dipole. The size of this secondary vertical force moment is in agreement with an equivalent elastic force model of spall developed from the data within the spall zone. The isotropic moment is 7.9×10^{20} dynes-cm which is a factor of 3 smaller than the average scalar moments estimated from the displacement spectra. The whole record spectral interpretation assumes a simple propagation path effect with no way to return downgoing energy back to the free surface. The moment tensor inversions with the realistic Green's functions take into account energy which returns to the free surface as well as trapped energy such as surface waves. These more realistic propagation path corrections lead to a factor of three reduction in source strength. The off-diagonal elements are a factor of 5-10 smaller than the diagonal elements supporting the small deviatoric source estimates using the transverse waveforms and spectra.

C. CONCLUSIONS AND RECOMMENDATIONS: The spatial variability in free surface near-source data from NTS has been documented. This variation must be accounted for in making source estimates from such data. Point estimates of source strength may vary by as much as a factor of ten. This variability of amplitudes is found at small scales from chemical explosions as well. There is an

COALORA SYNTHETICS

INVERSION II

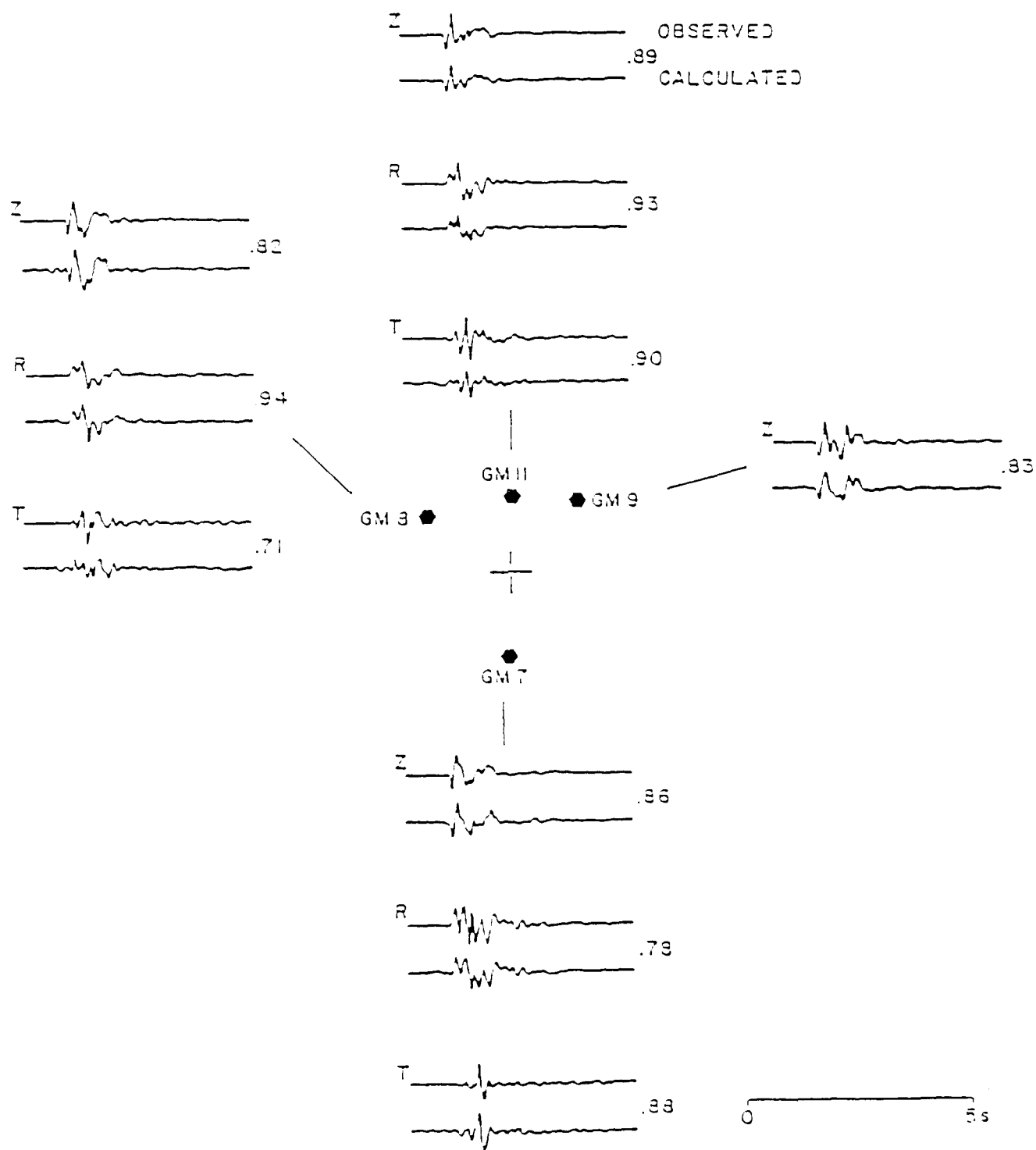
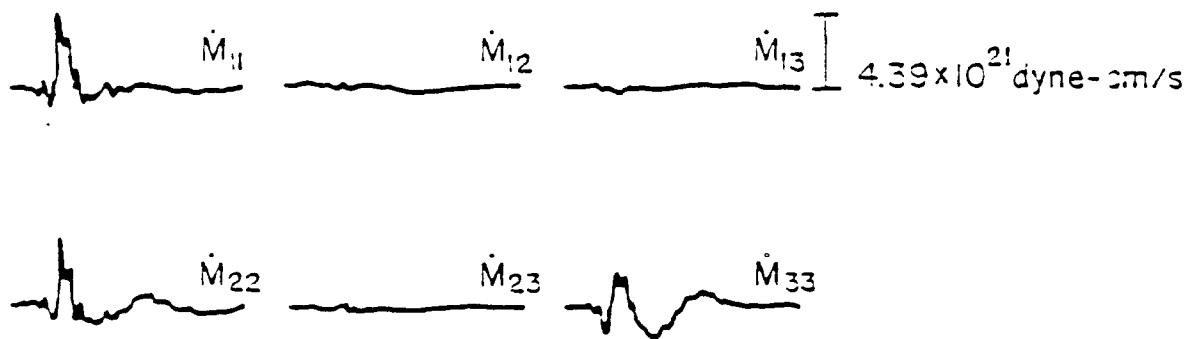


Figure 9: Observed and modeled velocity records from the nuclear explosion Coalora. The modeling was completed with moment tensor inversions.

MOMENT RATE TENSOR (\dot{M})



MOMENT TENSOR (M)

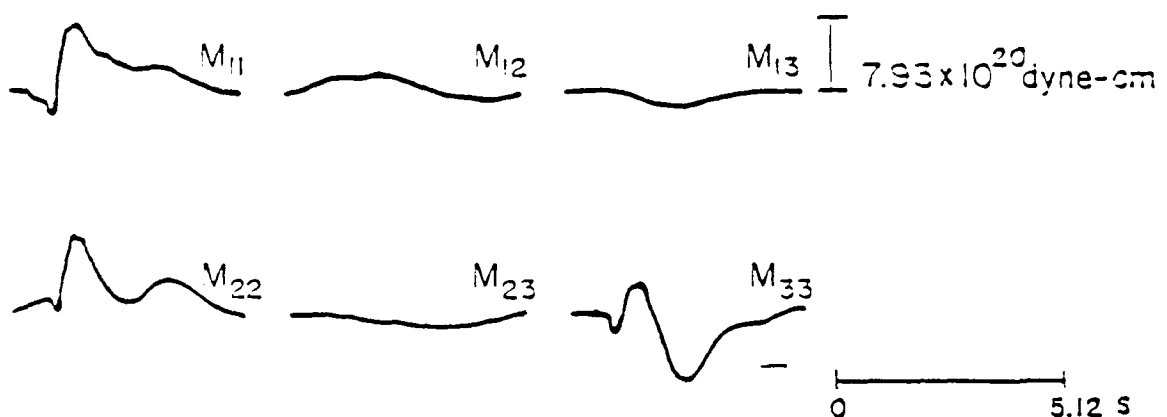


Figure 10: Moment rate and moment tensor estimates for the Coalora explosion.

indication in the data of a positive bias in peak accelerations for sources below the water table.

Free-field data gathered at shot level below near surface weathered layers appears to have greatly reduced scatter although unexplained variations in waveshapes are observed. Comparison of free surface and free-field data from the same explosion indicates a 20% variation in free-field data compared to a factor of 10 variation in free surface data.

In order to stabilize source estimates, corrections for propagation path effects coupled with some type of spatial averaging is tested. Simple average scalar moment estimates from a nuclear explosion are compared to full wave moment tensor inversions. Scalar moment estimates are a factor of three larger than full wave moment tensor estimates. Both spatial averaging and full wave propagation corrections are necessary for source interpretation.

REFERENCES

- Archuleta, R. J., E. Cranswick, C. Mueller, and P. Spudich, 1982. Source parameters of the 1980 Mammoth Lakes, California earthquake sequence, *J. Geophys. Res.* **87**, 4595-4607.
- Fletcher, J., J. Boatwright, L. Harr, T. Hanks, and A. McGarr, 1984. Source parameters for aftershocks of the Oroville, California, earthquake, *Bull. Seism. Soc. Am.* **74**, 1101-1123.
- Grant, L., 1988. Experimental Determination of Seismic Source Characteristics for Small Chemical Explosions, Masters Thesis, Southern Methodist University.
- Kennedy, R. P., 1982. Misty Echo/Diablo Hawk block motion program. DARPA/AFOSR Symposium on the Physics of Nonisotropic Source Effects from Underground Nuclear Explosions, DARPA-GSD-8203/AFOSR-NP-8201, Defense Advanced Research Projects Agency, Arlington, Va 22209.

SPECTRAL ANALYSIS OF EASTERN KAZAKH EVENTS

Pierre MECHLER, Florence RIVIERE

Radiomana, 27 Rue Claude Bernard, 75005 PARIS, FRANCE

Objective

Characterisation of source function for Eastern Kazakh events.
Obtention of energy independently from magnitude.
Influence of seismic station environnement.

Summary

On theoretical source functions, we first determine the order of the optimal predictive filter (the same for all events) and a simple characteristic frequency for which the probability spectral density is maximum. Applied to the real data, the same filter gives several characteristic frequencies, we believed to be representative of the source.

For high enough signal over noise ratio, the increase of characteristic frequency is well correlated to a decrease of magnitude.

Spectral analysis by Maximum Entropy Method

The maximum entropy method is well known, so we will not develop it here. As the Burg's algorithm do not give a precise determination of frequency and is subject to numerical instabilities produced by rounding errors in computations, we used the maximum entropy spectral estimation (MES) described by I. Barrodale and R.E. Erickson (1980).

In this algorithm, a prediction filter is computed on the time serie, by simultaneous minimisation of the forward and of the backward prediction errors.

The first parameter to determine is the order of the prediction filter. As suggested in the quoted article, this was done by computing the first minimum of the mean square residuals versus length of the filter.

Noting N_0 this minimum, m the order of the filter, and

$$E(Z) = 1 - \sum_{j=1}^m a_j Z^{-j}$$

the filter, the MES is given by

$$D(f) = (N_0 \Delta T) \frac{1}{\left| 1 - \sum_{j=1}^m a_j (e^{-i2(\pi f_j \Delta T)}) \right|^2}$$

The plot of this MES shows one or several peaks (according to the filter's order) which are characteristics of the signal.

Application to synthetic signals

The MES was computed on 19 synthetic source's functions (Mueller-Murphy model). The values of the magnitudes m_b selected for this study may seem to be curious, but correspond to the observed m_b values of a series of events used later on in this work, which origin are in Eastern Kazakh.

We took 60 points of signal, corresponding to 1.2 sec (50 samples per seconde is the normal sampling rate in the French Seismic Network). The optimal order for the filter was 6.

Only one characteristic frequency was observed for each signal, with an excellent correlation between the increase of frequency and the the decrease of magnitude.

Theoretical characteristic frequencies versus magnitudes

event	freq.	mb	event	freq.	mb
0	.62	6.18	1	.62	6.15
2	.64	6.09	3	.66	6.06
4	.66	6.05	5	.66	6.04
6	.66	6.02	7	.68	5.96
8	.70	5.93	9	.70	5.92
10	.72	5.84	11	.74	5.81
12	.76	5.74	13	.78	5.70
14	.80	5.65	15	.86	5.63
16	.88	5.52	17	.88	5.44
18	1.02	5.15			

Application to real data

To apply the same kind of analysis to real data, it is important to correct the actual records from the various effects they were affected by. The first one to evaluate is the station's response.

Each record was deconvolved by

- a mean attenuation between France and Eastern Kazakh. We used the model of Bache et al.(1986) with the parameters $t_0 = 0.75s$, $t_1 = 0.01s$ and $t_m = 0.05s$.

- the seismometer's response $\frac{f^3}{\sqrt{f^4 + f_0^4}}$

- a source's function model (Mueller-Murphy).

the mean station's response was obtained by averaging over all events recorded in the station.

The record, $R_{s,e}$, of event e in station s is the convolution of the source function of event e , SO_e , by the station's response, STR_s , the attenuation, A and the seismometer's response, SE . In frequency domain :

$$R_{s,e}(\omega) = SO_e(\omega)STR_s(\omega)A(\omega)SE(\omega)$$

The characteristic frequency was computed for each station and each event, using, as before, a prediction filter of order 6, for comparison with the synthetic results.

Fig. 1 represents two examples of the actual records (a), of the computed source functions (b) and of the MES (c). Even if only the first 1.2 second of the source functions were used in the computation of the MES, they were plotted for a longer time window. The high frequency noise on the source is purely a computational artefact during the processing and could be filtered out as the records do not contain energy for frequencies higher than at least 8 Hz.

On fig. 2, we plotted, for the 19 events, the characteristic frequencies obtained for the synthetic signals and for the real data in two of the stations of the French Seismic Network.

When the amplitude of the recorded signal is small (case of station FLN), we notice anomalies in the relation between characteristic frequency and magnitude. But, in the stations where the signal over noise ratio was large enough (case of station SMF), we obtain again a good correlation between the increase of frequencies and the decrease of magnitudes.

Conclusion

The first results on characteristic frequencies, in good stations, allow to obtain a seismic magnitude independently from the amplitude of the signal. We still have to improve the station response and to understand the local geological influences on the shape of the records.

References

- BACHE.T.C., S.R. BRATT and H. BUNGUM.1986. *High frequency P wave attenuation along five teleseismic paths from Central Asia*. *Geophys. J. R. Astr. Soc.* (and DARPA Report)
- BARRODALE.I. and R.E. ERICKSON.1980. *Algorithms for least-squares linear prediction and maximum entropy spectral analysis*. *Geophysics*. 45.3.420-432.
- MUELLER.R.A. and J.R. MURPHY. 1971. *Seismic characteristics of underground nuclear detonations*. *Bull. Seism. Soc. Am.* 61.6.1675-1704.

Figure caption

Figure 1 :

- a) left : records of the two largest events in the station AVF.
- b) center : corresponding experimental source function.
- c) right : maximum entropy spectrum.

Figure 2 :

- top : characteristic frequencies versus events (in decreasing magnitude order) for synthetic case.
- center : same for station SMF (good signal over noise ratio).
- bottom : same for station FLN (poor signal over noise ratio).

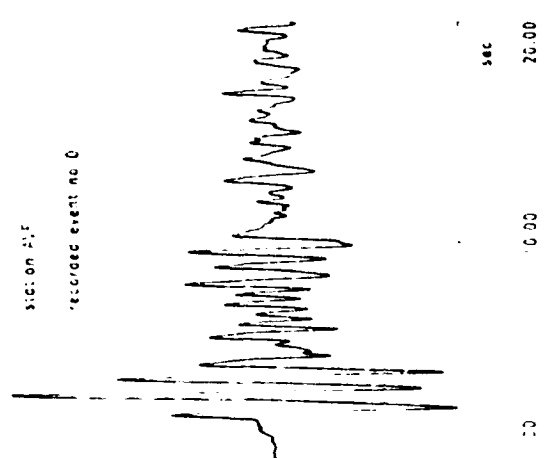
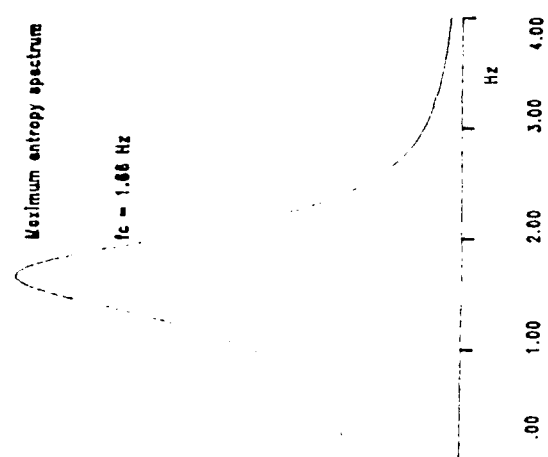
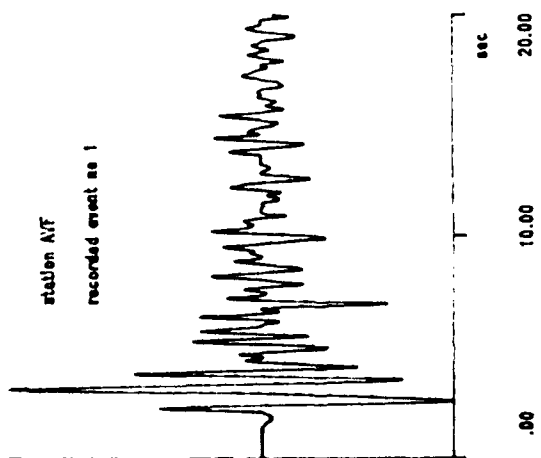
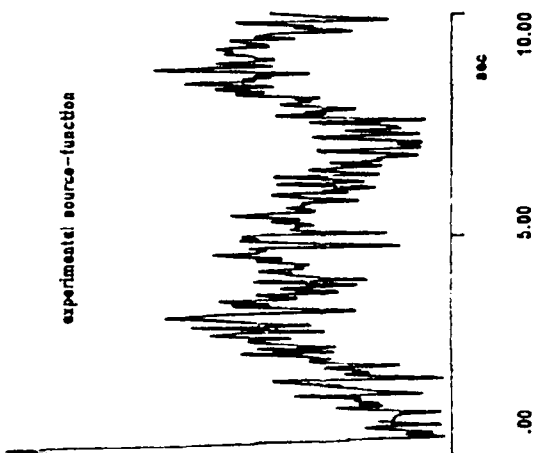
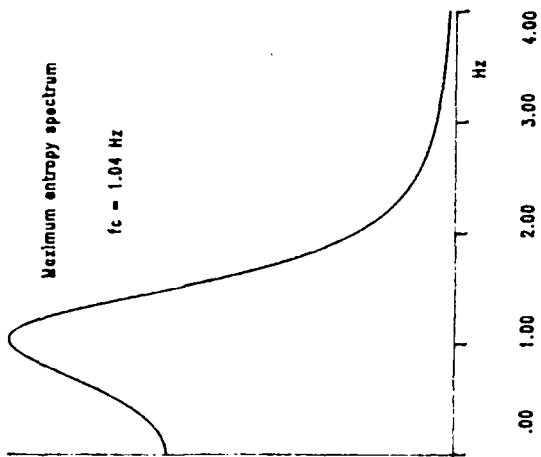
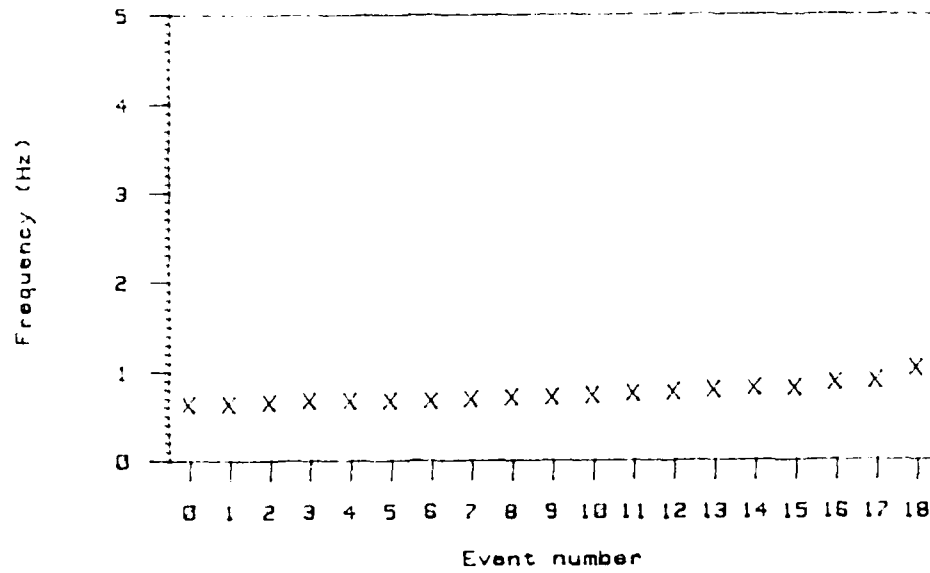
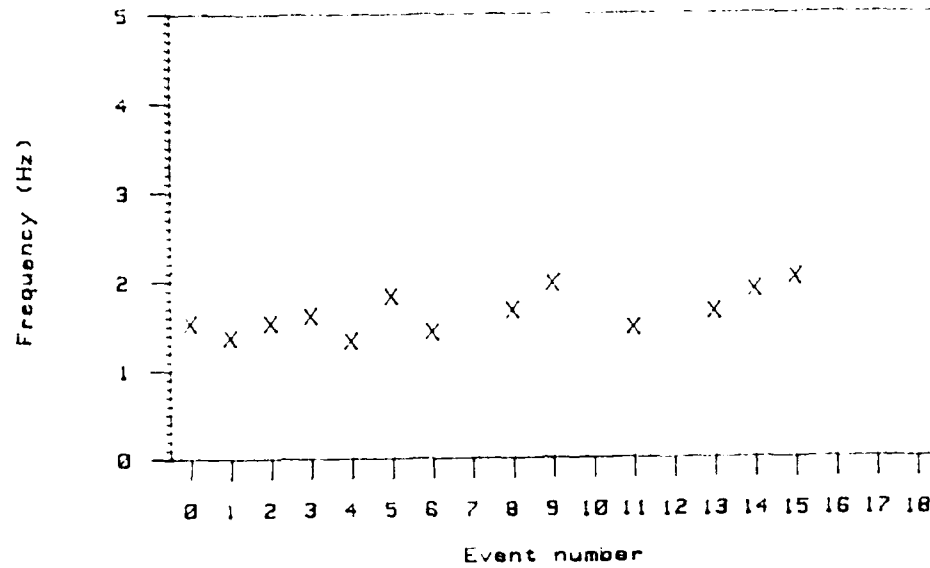


Figure 1

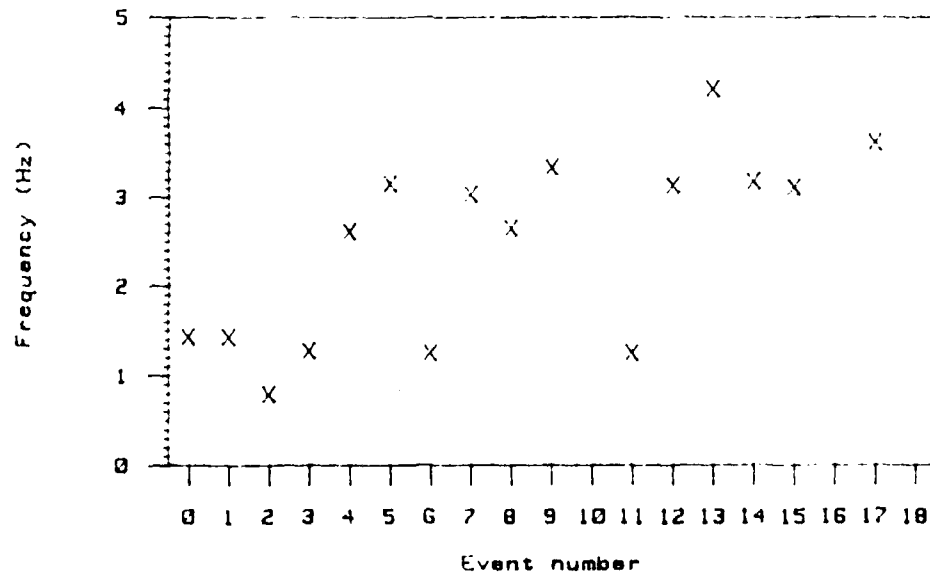
Source Function : Characteristic Frequency



Station SMF : Characteristic Frequency



Station FLN : Characteristic Frequency



STATISTICAL APPROACHES TO TESTING FOR COMPLIANCE WITH A THRESHOLD TEST BAN TREATY.

by R. H. Shumway* and Z. A. Der

ENSCO Inc, 5400 Port Royal Road, Springfield, VA, 22151

* Department of Statistics,
University of California at Davis,
Davis, CA.

ABSTRACT

Classical procedures for estimating the yield of a nuclear test use the fact that the body wave magnitude m_b is linearly related to the logarithm of the yield. When the slope and intercept are assumed to be known, a new magnitude measurement can be inverted to obtain an estimator for the yield of the new event and to give a measure of uncertainty. A test can also be made of the hypothesis that a new event is in compliance with the terms of some proposed threshold test-ban treaty.

The uncertainties associated with yield estimation and test of compliance can be influenced by a phenomenon termed yield clustering which sets forth the hypothesis that subsets of tests may have been conducted at essentially the same yield. There is also the possibility of using measurements in addition to the classical m_b magnitude. Incorporating vector measurements into the yield estimation procedure introduces complications due to missing observations and correlation between the additional magnitude measurements.

In this paper we study the statistical properties of optimal unified yield estimators developed from multiple magnitude measures in the presence of correlation and missing values. Maximum likelihood methodology is used for estimating the yields and covariances and for developing the conventional K-means clustering procedure using distance measures based on the Akaike and Bayesian information criteria (AIC and BIC) for the case where there are multiple magnitude measurements on the same yield. The procedures are illustrated using measurements on m_b , Lg amplitude, Lg root mean square and P-coda magnitudes for 72 Russian explosions at Semipalatinsk.

UNIFIED YIELD ESTIMATION

The use of yield estimates for the purposes of testing whether there has been compliance with the Threshold Test Ban Treaty (TTBT) is only an important end result of an overall estimation procedure. In general, one usually begins with a set of magnitudes that must be converted to yields using an uncertain magnitude-yield model. Recent approaches (see Der et al, 1987, Gupta et al, 1985, Alewine, 1987, Nuttli, 1987) emphasize the importance of combining measures other than simple body wave magnitude into a "unified yield estimation procedure" that may incorporate surface-wave magnitudes, Lg and moments into the computation. Furthermore, the model that converts the vector of magnitudes into the yield estimate contains a highly variable intercept term called the bias that corrects for propagation differences between the various test sites and the networks. While the bias term is mostly used for P wave magnitude biases may conceivably exist for other magnitude measures as well. We assume that the slope term in the linear model for magnitude yield relationships is known. There may also be correlation between the various measurements and these may be taken into account by the estimation procedure if they are significant.

The yields of the nuclear explosions may also cluster around some discrete values due to testing of a few types of nuclear devices. Defining such clusters may be important intelligence to be gained from seismic data.

We consider first the problem of using a vector of magnitudes to estimate log yield in the presence of correlation, bias and missing data. It is useful to suppose that $p \times 1$ magnitude vectors corresponding to the i th yield, say m_{ij} , $j = 1, \dots, n_i$, $i = 1, \dots, K$ can be replicated n_i times, either by clustering like events as in Section IV, or by repeated observations taken over networks or stations. A simplified model then expresses the $p \times 1$ magnitude vector as

$$m_{ij} = a + b w_i + e_{ij} \quad (1)$$

where a is the bias correction vector, b is the slope vector and w_i is the unknown logarithm (base 10) of the yield of the i th cluster. The noise vector e_{ij} are assumed to be mutually uncorrelated zero-mean normal (Gaussian) vectors with $p \times p$ covariance matrix Σ . It is clear that the log likelihood for the model thus defined is proportional to

$$\ln L \propto - \frac{N}{2} \ln |\Sigma| - \frac{1}{2} \sum_{i=1}^K \sum_{j=1}^{n_i} (m_{ij} - a - b w_i)' \Sigma^{-1} (m_{ij} - a - b w_i) \quad (2)$$

The parameters of interest in the above model are (1) the yields $w_1, w_2, w_3, \dots, w_K$, the bias a and the slope b vectors and (3) the covariance matrix Σ . One may consider the problems involved in estimating these parameters at various levels. We shall consider the bias, slope and covariance parameters to be fixed and estimate the yields by maximum likelihood or one can estimate jointly the covariance and yields. The bias, can be estimated by using corroborating CORTEX measurements as in Alewine et al (1987), or by using various types of geophysical measurements and arguments. The covariance matrix can be structured using a random effects model as in McLaughlin et al (1988) or Heasler et al (1988). Assuming that Σ , a and b are known then

$$\hat{w}_i = \frac{1}{s_i^2} b' \Sigma^{-1} (m_{i.} - a) \quad (3)$$

is the maximum likelihood estimator for the yield where

$$m_{i.} = \frac{1}{n_i} \sum_{j=1}^{n_i} m_{ij} \quad (4)$$

is the mean magnitude for cluster i and

$$s_i^2 = b' \Sigma^{-1} b \quad (5)$$

It is clear that

$$\hat{w}_i = w_i + \frac{1}{s_b^2} \underline{b}' \Sigma^{-1} \underline{e}_i, \quad (6)$$

so that the w_i are unbiased for w_i , jointly normal, and uncorrelated with variance

$$E[(\hat{w}_i - w_i)^2] = \frac{1}{n_i s_b^2}. \quad (7)$$

A problem to be considered later in compliance testing requires the distribution of a future estimated yield

$$\hat{\underline{w}} = \frac{1}{s_b^2} \underline{b}' \Sigma^{-1} (\underline{m} - \underline{a}) \quad (8)$$

based on a future observed magnitude conforming to the model

$$\underline{m} = \underline{a} + \underline{b}w + \underline{e} \quad (9)$$

and again the mean is w and the variance is

$$\text{var } \hat{\underline{w}} = \frac{1}{s_b^2}. \quad (10)$$

If the covariance matrix Σ is not known, we can use the maximum likelihood value

$$\hat{\Sigma} = \frac{1}{N} \sum_{i=1}^K \sum_{j=1}^{n_i} (\underline{m}_{ij} - \underline{a} - \underline{b}\hat{w}_i) (\underline{m}_{ij} - \underline{a} - \underline{b}\hat{w}_i)' \quad (11)$$

We follow the usual convention of substituting $\hat{\Sigma}$ for Σ in (5), (8) and (10).

The procedure for maximizing the log likelihood in (2) is iterative, since w_i in (2) involves $\hat{\Sigma}$ and $\hat{\Sigma}$ in (10) involves w_1, \dots, w_K . We employ the usual iteratively reweighted procedure using the following steps.

Maximum Likelihood Estimation

1. Set $\Sigma = I$ and compute w_1, \dots, w_K using Equation (3).

2. Use Equation (11) to estimate .
3. Use Equation (3) to compute w_1, \dots, w_k
4. Go to Step 2.

The procedure is repeated until the log likelihood (3) and the estimated yields fail to change significantly.

MISSING DATA MODIFICATIONS

One will usually not observe the complete vector m_{ij} since certain magnitude measurements will be missing part of the time due to censoring, clipping or non-reporting. When part of the vector is missing, partition it into

$$\underline{m}_{ij} = \begin{pmatrix} \underline{m}_{ij}^{(1)} \\ \underline{m}_{ij}^{(2)} \end{pmatrix} = \begin{pmatrix} \text{observed} \\ \text{missing} \end{pmatrix} \quad (12)$$

where m_{ij} is the recorded vector with the observed values listed first. Let be a similar rearrangement of the mean vector

$$\underline{\mu}_i' = (\underline{\mu}_i^{(1)'} , \underline{\mu}_i^{(2)'}) = \underline{a}_i + \underline{b}w_i \quad (13)$$

with \tilde{a}, \tilde{b} the reordered bias and slope components. Let

$$\tilde{\Sigma} = \begin{pmatrix} \tilde{\Sigma}_{11} & \tilde{\Sigma}_{12} \\ \tilde{\Sigma}_{21} & \tilde{\Sigma}_{22} \end{pmatrix} \quad (14)$$

be the corresponding rearrangement of the covariance matrix Σ . Then, if a missing magnitude in (3) is replaced by

$$\begin{aligned} \underline{\mu}_{ij}^{(2.1)} &= E(\underline{m}_{ij}^{(2)} | \underline{m}_{ij}^{(1)}) \\ &= \underline{\mu}_i^{(2)} + \tilde{\Sigma}_{21} \tilde{\Sigma}_{11}^{-1} (\underline{m}_{ij}^{(1)} - \underline{\mu}_i^{(1)}) \end{aligned} \quad (15)$$

and the single term in the covariance sum (12) is replaced by

$$A = \begin{pmatrix} A_{11} & A_{12} \\ A_{21} & A_{22} \end{pmatrix} \quad (16)$$

where

$$A_{11} = (\bar{m}_{ij}^{(1)} - \bar{\mu}_i^{(1)}) (\bar{m}_{ij}^{(1)} - \bar{\mu}_i^{(1)})', \quad (17)$$

$$A_{12} = (\bar{m}_{ij}^{(1)} - \bar{\mu}_i^{(1)}) (\bar{\mu}_{ij}^{(2.1)} - \bar{\mu}_i^{(2)}), \quad (19)$$

and

$$A_{22} = \bar{\Sigma}_{22.1} + (\bar{\mu}_{ij}^{(2.1)} - \bar{\mu}_i^{(2)}) (\bar{\mu}_{ij}^{(2.1)} - \bar{\mu}_i^{(2)})', \quad (19)$$

with

$$\bar{\Sigma}_{22.1} = \bar{\Sigma}_{22} - \bar{\Sigma}_{21} \bar{\Sigma}_{11}^{-1} \bar{\Sigma}_{12}, \quad (20)$$

and where $A_{21} = A_{12}$. Material related to maximum likelihood estimation for incompletely observed multivariate normal populations can be found in Little and Rubin (1987). Applying the modified equations iteratively in combination with the reweighting procedure of the previous section increases the modified log likelihood version by the results for EM algorithm given in Dempster et al (1977). The following iterative scheme seems to be reasonable.

Maximum Likelihood Estimation--Missing Data)

1. Initialize $\Sigma = I$
2. Compute w_1, \dots, w_K (m_i computed over observed values only)
3. Compute estimators for the mean vectors
4. Update Σ as in (11) using the replacements defined in (15) - (20) when values are missing.
5. Update w_1, \dots, w_K using (3) with Σ from Step 4 and replacing missing m_{ij} using (15).
6. Return to Step 3.

MAGNITUDE-YIELD CLUSTERING

The availability of vector observations involving various magnitudes and moments suggest that multi-dimensional clustering procedures will be useful for establishing clusters of similar

vector magnitudes, defined as arising from a common yield event. Systematic procedures (MacQueen, 1967 and Johnson and Wichern, 1982) such as K-means and hierarchical clustering can be applied to the vector magnitudes to determine a reasonable null configuration of equal magnitude events. Such procedures can be used to define an optimal number of clusters and to identify the vector observations belonging to each cluster. The methods can also be used to identify regional clusters where there is more than a single-station vector magnitude.

The original magnitudes will not have been divided into clusters and the number of clusters K will be undetermined. We consider here adapting the K-means clustering algorithm to assign magnitudes to clusters, with standard goodness-of-fit criteria AIC and BIC used for the purpose of identifying the number of clusters K .

We consider first the assignment of magnitude vectors to clusters for a given number of clusters K . Suppose that we are given an initial arbitrary partition of clusters and we want to consider a method of assigning observations to clusters. The cluster means S and the covariance matrix can be estimated for this configuration using the methods of the previous section. Then, consider computing for each observation its distance from each of the cluster means, say

$$d_i^2(j, k) = (\underline{m}_{jk} - \hat{\underline{\mu}}_i)' \hat{\Sigma}^{-1} (\underline{m}_{jk} - \hat{\underline{\mu}}_i) \quad (21)$$

and reassigning observation m_{jk} to the cluster i for which $d_i(j, k)$ is smallest. An option that is usually taken in this case is to consider the unweighted Euclidean distance

$$d_i^2(j, k) = (\underline{m}_{jk} - \hat{\underline{\mu}}_i)' (\underline{m}_{jk} - \hat{\underline{\mu}}_i). \quad (22)$$

For the missing data case we arbitrarily replace $\underline{m}_{jk}^{(2)}$ by its conditional mean. One might also calculate

$$E[d_i^2(j, k) | \underline{m}_{jk}^{(1)}].$$

The K-means clustering procedure then reduces to the following sequence of steps:

K-Magnitudes Clustering Algorithm

1. Set $\Sigma = I$
2. Calculate w_1, \dots, w_K using Equation (3) (m_i computed over observed values only).
3. Compute the estimators for the group means
4. Calculate d_i for $i = 1, \dots, K$ and reassign m_{ij} if necessary.
5. If observation is reassigned return to 2. If observation is not reassigned return to 4.
6. Stop when no observations are reassigned on a complete pass through all magnitudes.

In order to assign an optimal value for the number of clusters K , we consider the standard goodness-of-fit measures $AIC(K)$ and $BIC(K)$ and choose the value of K which minimizes either $AIC(K)$ or $BIC(K)$. The definitions of the two objective functions are

$$AIC(K) = -2 \ln L + 2 K p \quad (23)$$

and

$$BIC(K) = -2 \ln L + 2 K p \ln N \quad (24)$$

where $\ln L$ is the log likelihood function (2) evaluated at Σ, w_1, \dots, w_K or it is the log-likelihood function of the observed subvectors if there are missing magnitudes.

COMPLIANCE PROBABILITIES

In order to develop measures relating to compliance, we suppose that a new magnitude measurement satisfies

$$\underline{m} = \underline{a}_0 + \underline{b}w + \underline{e} \quad (25)$$

as before except that a_0 is now regarded as the true bias with a , the estimated bias assumed to be normal with mean a_0 and covariance matrix Σ_0 . The estimated magnitude is still

$$\hat{w} = \frac{1}{s_b^2} \underline{b}' \Sigma^{-1} (\underline{m} - \underline{a}) \quad (26)$$

so that

$$\hat{w} = w + \frac{1}{s_b^2} \underline{b}' \Sigma^{-1} ((\underline{a}_0 - \underline{a}) + \underline{e}) \quad (27)$$

The estimator still has mean w , but the variance becomes

$$\sigma_{\hat{w}}^2 = \frac{1}{s_b^2} \left(1 + \frac{1}{s_b^2} \underline{b}' \Sigma^{-1} \Sigma_0 \Sigma^{-1} \underline{b} \right). \quad (28)$$

Then, assuming known Σ and Σ_0 , we may set up a compliance test involving a single yield Y and an assumed testing threshold T as

$$H_0: Y = 10w = T$$

$$H1: Y = 10w > T$$

and reject at level .025 if

$$\hat{w} > \log_{10} T + 1.96 \sigma_{\hat{w}}. \quad (29)$$

Suppose we ask for the yield Y_{50} that will be detected 50 percent of the time. The so called "F-number" (Alewine et al, 1988) of the test is the ratio of this 50 percent detectable yield to the threshold T ,

$$Y_{50} = 10^{w_{50}} \quad (30)$$

where

$$F = \frac{Y_{50}}{T} \quad (31)$$

with w_{50} the log yield that would be exceeded with probability 0.5. Then, the value w_{50} must satisfy

$$\text{Prob}\{\hat{w} > \log_{10} T + 1.96 \sigma_{\hat{w}} \mid w = w_{50}\} = .50$$

which implies that

$$\log_{10} T + 1.96 \sigma_{\hat{w}} - w_{50} = 0. \quad (32)$$

Then, manipulating the above in accordance with (30) and (31) gives

$$F = 10^{1.96\sigma_{\hat{w}}} \quad (33)$$

The F-number thus depends only on σ_w^2 as given in (27), which, in turn, depends on the slope b , error covariance Σ and the bias covariance Σ_0 .

AN EXAMPLE INVOLVING RUSSIAN TESTS AT SEMIPALATINSK

The measurements we processed as a test case come from the NORSAR publication by Kwaerna et al (1988) for *P* wave magnitude (m_b), log Lg amplitudes (LgA), Lg log mean square amplitude (LgR which should not be confused with M_s !) and log Pcoda amplitudes (P-coda). These notations will be used throughout this paper.

In this particular data set, we do not know whether a measurement is absent due to being indistinguishable above the noise, clipping or because the measurement was not available. This being the case, modifications for censoring developed by Ringdal, (1976), Blandford and Shumway (1982), Blandford et al (1984), for the univariate case and by McLaughlin et al (1988), for multivariate vectors with patterned covariances are not necessary. Since the missing point is essentially filled in by a regression on the available points [see Equation (14)], the additional information as to cause is probably not essential.

Our general approach to analyzing this data depends on using several combinations of the vector observations in an effort to (a) determine the optimal configuration of yield clusters, (b) estimate the yields and their variances for the optimal configuration and (c) develop measures of compliance using the results of (a) and (b). Because of the high correlation between the magnitude measures, we looked at three different combinations of measurements, namely m_b alone, m_b and LgA combined and the combination of all four measurements.

For each vector subset of magnitude measures, there is now the difficulty of combining the various algorithms in the previous sections into an overall procedure. For each possible number of clusters, one must estimate the yields and the covariance matrix Σ subject to the missing data restrictions. The clusters can be determined using either the weighted distances (21) or the unweighted sums of squares of the residuals (magnitude-estimated magnitude) given by (22). The latter corresponds to using the former with the identity matrix and we determine the initial cluster using the unweighted distance. The following procedure was adopted for each number of clusters K :

1. Set $\Sigma = I$ and run the K magnitudes clustering algorithm as described.
2. Follow the maximum likelihood estimation (missing data) method at the end of Section 3 to define yield and covariance estimators under the cluster configuration defined by the unweighted distance (21).
3. Use the estimated covariance matrix in to run a weighted K magnitudes clustering algorithm using (22).
4. Follow the maximum likelihood estimation method to obtain the final yields and estimated covariance matrix.

The procedure outlined in Steps 1 through 4 above is followed for each cluster configuration K , with AIC and BIC computed as measures of goodness-of-fit. The cluster configuration chosen was the one minimizing BIC. AIC seemed to drift consistently downward as K increased for all of the examples tried and may have some overfitting tendencies.

In order to illustrate one of the subsets that seemed to fit reasonably well for this set of data, consider using m_b and LgA only. Table 1 shows the estimated log yields [Equation (3)] with standard deviations given by Equation (5). The minimum BIC was obtained using a $K = 3$ cluster model.

Figure 1 shows the clusters as they lie within the two-dimensional m_b -LgA space. Based on the scatter diagram, there may be good reasons to doubt the assumption that the covariance matrices of the three populations are the same in that high log yields may be subset to less variability than low log yields. A quick fix might be to consider a quad-cluster model that approximately equalizes covariances. The correlation between the m_b and LgA residuals after adjusting for log yield was 0.537. The effective weights applied to adjusted magnitude were 0.39 for m_b and 0.86 for LgA. Since the measures were originally scaled to reflect magnitude (m_b)

equivalents, we might infer that since LgA gets a higher weight, it is therefore more important in determining yield. For comparison, the yield estimators for the three clusters using m_b alone had standard deviations 0.032, 0.050 and 0.028 respectively so that adding LgA improves the precision of the yield estimate.

Adding the other two magnitude measures to the procedure gives estimated yields and standard deviations as in Table 1. Although the standard deviations are reduced somewhat, the correlation matrix of the residuals was

$$R = \begin{vmatrix} 1.00 & 0.88 & 0.94 & 0.95 \\ 0.88 & 1.00 & 0.98 & 0.85 \\ 0.94 & 0.98 & 1.00 & 0.91 \\ 0.95 & 0.85 & 0.91 & 1.00 \end{vmatrix}$$

which indicates strong intercorrelations between the various residuals. Of special interest are the high correlation between LgA and LgR of 0.98 and the high correlation between m_b and P-Coda of 0.95. The weights for this case are 0.91, 2.99, -2.85 and 0.20, indicating that the difference LgA-LgR tends to be important and that P-Coda with its low weight may not be important. The difficulty of interpreting the weights combined with the high correlations that may adversely affect the weighting coefficients together indicate that a more prudent procedure might be to use only m_b and LgA for this particular data.

We assumed the same slopes and intercepts for all the magnitude measures in these simulations in the absence of better values. Therefore the values of estimated yields estimated in these calculations may not be reliable. This data set serves only to demonstrate the procedure. In future work we shall attempt to substitute the best estimates available from actual data analyses.

We may also investigate compliance by calculating the F- numbers that might be expected from various measurements and the tri- cluster configuration. This involves using Equations (28) and (32). If the bias covariance matrix is assumed to be zero so that there is no error in the bias given, the entries in Table 2 show the resulting standard errors and F-numbers. For example, using m_b and LgA, it could be inferred that with a false alarm rate of 0.025, there would be only a 50 percent chance of detecting a violation as high as 257 KT (1.7×150) with a 150 KT threshold. Since the F-numbers do not change with the threshold, under equal conditions, these results would hold for lower thresholds. As noted above, it appears that the uncertainty covariance may be larger at lower yields, although one might increase it by extending the analysis to unequal covariance matrices, i.e., not pooling in Equation (12) or by adding more clusters.

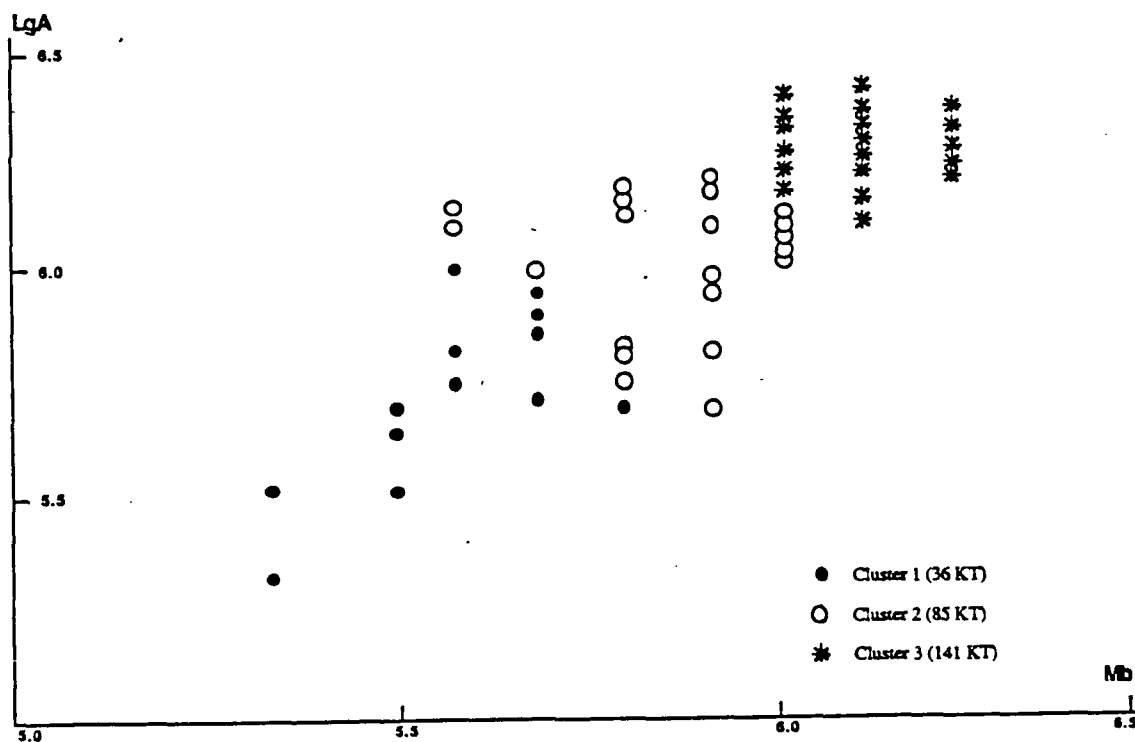
While defining the clusters in this "free-running" mode, i.e recomputing the covariance matrices at each iteration will work well for well-defined clusters, there is a problem with magnitude populations with vague clustering structures. If we set the number of clusters, it is possible to fit that number of clusters, but the various magnitude measures will be strongly correlated due to the fact that all the magnitudes depend on yield. The resulting covariance structure may not be reasonable in the light of independent knowledge about the sizes of variances of the various magnitudes. Therefore it is advisable to run the clustering procedures with preset covariance matrices which were defined based on the known variances of the yield measures. Ideally it would be desirable if did know something about the covariances between two measures (such as m_b and M_0) due to various causes. Presently we have little such knowledge, therefore we must assume that the covariances are zero.

In the following we present the results of a run using the covariance matrix

$$\Sigma = \begin{vmatrix} 0.00625 & 0.00000 & 0.00000 & 0.00000 \\ 0.00000 & 0.02250 & 0.00000 & 0.00000 \\ 0.00000 & 0.00000 & 0.04000 & 0.00000 \\ 0.00000 & 0.00000 & 0.00000 & 0.03000 \end{vmatrix}$$

The diagonal elements are the assumed variances of the magnitude measures which are assumed to be independent. The values of the statistics AIC and BIC shown in Table 3 indicate that the data set can still be modelled by 3 or 4 clusters even if we do not recompute the variances but assume them to be as in the matrix above.

FIGURE 1



Clusters determined using the tri-cluster model on m_b and LgA for the Semipalatinsk explosions.

TABLE 1

Unified Yield Clustering and Estimation Using m_b , Magnitude, Lg Amplitude, Lg RMS and P-Coda. Covariance matrices were estimated from the data for each cluster size.

(Bias and Slope Assumed to be 4.40 and 0.8 respectively)

Number of Clusters	Estimated		Standard Deviation	AIC	BIC
	Log Yield	Yield			
1	1.855	72	0.074		
2	1.808	64	0.019	-14.88	-14.15
	2.126	134	0.014		
3	1.801	63	0.016	-15.35	-14.26
	2.056	114	0.015		
	2.205	161	0.014		
4	1.813	65	0.014	-15.55	-14.09
	1.989	97	0.018		
	2.117	131	0.015		
	2.239	173	0.012		
5	1.812	65	0.012	-15.57	-13.75
	1.985	96	0.026		
	2.151	142	0.013		
	2.058	114	0.025		
	2.276	189	0.012		

TABLE 2

Measurements	Std. Error	F-Number
M_b	.1653	2.11
$M_b, L_g A$.1188	1.71
$M_b, L_g A, L_g R, P\text{Coda}$.0696	1.37

TABLE 3

Unified Yield Clustering and Estimation Using m_b Magnitude, Lg Amplitude, Lg RMS and P-Coda. Covariance matrices for each cluster were kept constant.

(Bias and Slope Assumed to be 4.40 and 0.8 respectively)

Number of Clusters	Estimated		Standard Deviation	AIC	BIC
	Log Yield	Yield			
1	1.885	72	0.074		
2	1.583	38	0.017	-10.65	-9.92
	2.024	105	0.014		
3	1.551	35	0.016	-11.35	-10.26
	1.868	73	0.023		
	2.061	115	0.014		
4	1.497	31	0.017	-11.91	-10.45
	1.892	77	0.029		
	1.821	66	0.024		
	2.070	117	0.013		
5	1.492	31	0.017	-11.77	-9.95
	1.802	63	0.029		
	1.897	78	0.044		
	1.869	73	0.031		
	2.067	116	0.013		

DISCUSSION

We have developed a procedure for clustering multivariate vector magnitudes, estimating cluster yields and calculating compliance statistics. The procedure applies even when there are missing components and correlation is present between the yield-adjusted magnitudes.

The results seem to be reasonably consistent with clustering results previously reported (see McCartor and Gray, 1986) using m_b magnitudes alone and a different clustering method. For the limited data examined, namely m_b , Lg amplitudes, Lg root mean square and P-Coda magnitudes, three clusters seemed to be appropriate whether we used only m_b , a combination of m_b and Lg amplitude, or all four measures together. In general, m_b combined with Lg seemed to reflect a reasonable compromise that considered specific factors such as correlation in residuals and weighting coefficients.

There are still questions remaining as to the performance for thresholds in the low magnitude range; the data set analyzed did not have enough values at low levels to consider this problem in detail. More substantial data sets are needed to investigate adequately such questions as whether the covariance matrix of the low yield cluster is dramatically larger than the others. One would also like to be able to consider changes in the bias and slope values for these lower magnitude ranges. The idealized computations for compliance done in this report also reflect the assumption that there is no uncertainty in the bias and slope.

The general linear model (GLM) approach used here is in the spirit of the one used by Heasler et al (1988), with certain differences. They assume that there is available a more primal data set consisting of the individual station values collected before averaging. In this case, one does not need to consider clustering (one may want to do it for other reasons) as a techniques for producing covariance estimators; this can be done using the individual station magnitudes. They are able to develop structural models for the station errors that emulate spatial correlation caused by differing distances between stations and events (see also Blandford et al, 1982, 1984).

Another difference between this work and Heasler et al (1988) is that here the bias and slope are assumed to be that here the bias and slope are assumed to be known in the yield estimation methodology and to be stochastic in the compliance testing situation with mean and covariance structure determined by other means. Alewine et al (1988) have discussed the problem of estimating these quantities using calibrating CORRTX measurements, whereas Heasler et al (1988) do it within the GLM framework. We also focus on the vector of magnitudes and show in at least one example that there is substantial correlation between the yield-adjusted magnitudes that may severely limit their joint utility in a proposed unified magnitude estimation procedure.

The data set we tested does not show a clear pattern of clustering, the clusters are poorly defined. In the future we shall extend the analyses to more extensive vector data sets that have been reported to show patterns of clustering for at least one magnitude measure.

REFERENCES

- Alewine, R.W. III (1987). Unified Seismic Method For Yield Determination (U). GSD-87- 01. (SECRET). Defense Advanced Research Projects Agency (DARPA), Arlington, VA.
- Alewine, R. W. III, H. L. Gray, G. D. McCartor and G. L. Wilson (1987), Seismic Monitoring of a Threshold Test Ban Treaty (TTBT) Following Calibration of the Test Site With CORRTEx Measurements, *AFGL-TR- 88-0055, Air Force Geophysics Laboratory, Hansom AFB, MA 01731- 5000*.
- Blandford, R. R. and R. H. Shumway (1982). Magnitude Yield For Nuclear Explosions In Granite At the Nevada Test Site and Algeria: Joint Determination With Station Effects With Data Containing Clipped and Low Amplitude Signals. *VSC-TR-82-12, Teledyne-Geotech, Alexandria, Virginia*.
- Blandford, R. R., R. H. Shumway, R. Wagner and K. McLaughlin (1984). Magnitude-yield for Nuclear Explosions In Granite At the Several Test Sites With Allowance For the Effects of Truncated Data, Amplitude Correlation Between Events Within Test Sites, Absorption and pP, *TGAL-TR-83-6, Teledyne Geotech Alexandria, VA*.
- Dempster, A. P., N. M. Laird and D. B. Rubin (1977). Maximum Likelihood Estimation From Incomplete Data Via the EM Algorithm (with discussion), *J. R. Statist. Soc. B39, 1-38*.
- Der, Z. A., T. W. McElfresh, R. Wagner and J. Burnett (1985). Spectral Characteristics of P Waves From Nuclear Explosions and Yield Estimation, *Bull. Seism. Soc. Am 75, 1222-1223*.
- Gupta, I. N., R. R. Blandford, R. A. Wagner, J. A. Burnett and T. W. McElfresh (1985). Use of P Coda For Determination of Yield of Nuclear Explosions, *Geophy. J. Roy. Astron. Soc., 83, 541-554*.
- Heasler, P. G. and W. L. Nicholson (1984). Statistical Analysis of Individual AEDS Station mb Data, *PNL-X-385, Pacific Northwest Labs, Richland, Washington 99352*.
- Heasler, R. G., R. C. Hanlen, D. A. Thurman and W. L. Nicholson (1988). Application of General Linear Models to Event Yield Estimation, *PNL- CC-1801-171, Pacific Northwest Labs, Richland, Washington 99352*.
- Johnson, R. A. and D. W. Wichern (1982). Applied Multivariate Statistical Analysis, Englewood Cliffs: Prentice Hall.
- Kwaerna, T., J. Kibsgaard, S. Mykkelveit and F. Ringdal (1988). Magnitudes of Semipalatinsk Explosions Using P-Coda and Lg Measurements at NORSAR, NORSAR (Norwegian Seismic Array) Scientific Report #1-87- 88, Kjeller, Norway.
- Little, R. J. A. and D. B. Rubin (1987). Statistical Analysis With Missing Data, New York: John Wiley & Sons.
- MacQueen, J. B. (1987). Some Methods For Classification and Analysis of Multivariate Observations, *Proc. 5th Berkeley Symp. on Math. Statist. and Prob., 1n 281-297, Berkeley: University of California Press*.
- McLaughlin, K. L., T. W. McElfresh and R. H. Shumway (1988). Determination of Event Magnitudes With Correlated Data and Censoring. A Maximum Likelihood Approach, *J. Geophy, 95, 31-44*.
- McCartor, G. G. and H. L. Gray (1986). Statistical Methodology for TTBT Monitoring (U), Mission Research Corp., MRC-85-598. SECRET

- Nuttli, O. (1987). Yield Estimates of Nevada Test Site Explosions Obtained From Seismic Lg Waves, *J. Geophys. Res.* 91, 2137-2151.
- Rivers, D. W., R. H. Shumway and R. Wagner (1986). Statistical Analysis of Explosion Magnitudes and Yields, The Vela Program, 771-779, A. Kerr, ed., Arlington Virginia: Executive Graphic Services.
- Ringdal, F. (1976). Maximum Likelihood Estimation of Seismic Magnitude, *Bull. Seismolog. Soc. Amer.* 66, 789-802.
- Sykes, L. R. and D. M. Davis (1987). The Yields of Soviet Strategic Weapons, *Scientific American* 256, 29-37.
- Sykes, L. R. and Cifuentes (1983). Yields of Soviet Underground Nuclear Explosions From Seismic Surface Waves: Compliance With the Threshold Test Ban Treaty, *Proc. Natl. Acad. Sci.* 81, 1922-1923.

P_n from The Nevada Test Site

by L. J. Burdick, C. K. Saikia and N. F. Smith

Contract AFGL-TR-89-0034

OBJECTIVE

High frequency regional data appears to be among the most unstable and difficult to characterize in seismology. For this reason, most of the attempts to solve the regional discrimination problem have been based on highly empirical approaches. Ratios of phase amplitudes in either the time or frequency domain have been tested to find whether they are systematically different for earthquakes and explosions. Recently, Taylor et al. (1988) have demonstrated an impressive capability for event discrimination using spectral ratios of Lg. In essence, they demonstrated that regional signals from explosions are systematically lower in frequency content than earthquakes. This confirms an earlier result of Murphy and Bennett (1982). Though development of this discriminant represents a significant advance, there remain important questions of the transportability of the method. The reason is that a deterministic model for the change of spectral behavior between earthquake and explosion sources is not available. There is no evidence in teleseismic data that explosion sources have a different spectral decay rate than earthquakes. Thus, if the spectral discriminant works consistently on Lg in the western United States, it must be related to phenomena associated with Lg propagation there. We can not rely on the same processes to occur in a consistent fashion in other regions.

To avoid such difficulties in transporting discriminants to new tectonic and seismic regimes, it will be necessary to develop discriminants based on a sound understanding of the physical processes which underlie them. This knowledge will permit an assessment of whether and how the discriminant should be modified for other areas. The investigations discussed here are directed at establishing what the most stable portions of the regional P wave signal are, and if they can be modeled in a deterministic fashion. Specifically, we will discuss observations of NTS nuclear events at stations in the western U.S. digital network. We have used arrays of events to form seismic sections at each station and examined them for stable arrivals. Most of the P_n and P_g wave trains exhibit a low level of coherence. However, we have found that the very onset of P_n is remarkably stable at high frequency and that it has a character strongly influenced by free surface phases. Since free surface phases occur later for earthquakes than explosions, it is possible to develop a discriminant based on P_n onset. Because the physics behind the discriminant is straightforward, transporting the technique to other regions should not pose a significant problem.

SUMMARY

The Western U.S. Digital Array For the purposes of this discussion, we will define the western U. S. digital array as including the four LLNL stations MNV, KNB, LAC and ELK; the two DWWSSN stations ALQ and JAS and the Caltech and UCSD stations, PAS and PFO. Figure 1 is a map displaying the stations of the digital array as they distribute about NTS. Azimuthal coverage is relatively good, and stations LAC and PFO are almost exactly aligned with NTS. Shown as circles are the locations of earthquakes we have used for discrimination studies. The closest station is MNV at a range of 195 km to the nearest NTS events and the farthest

Western U.S. Digital Network

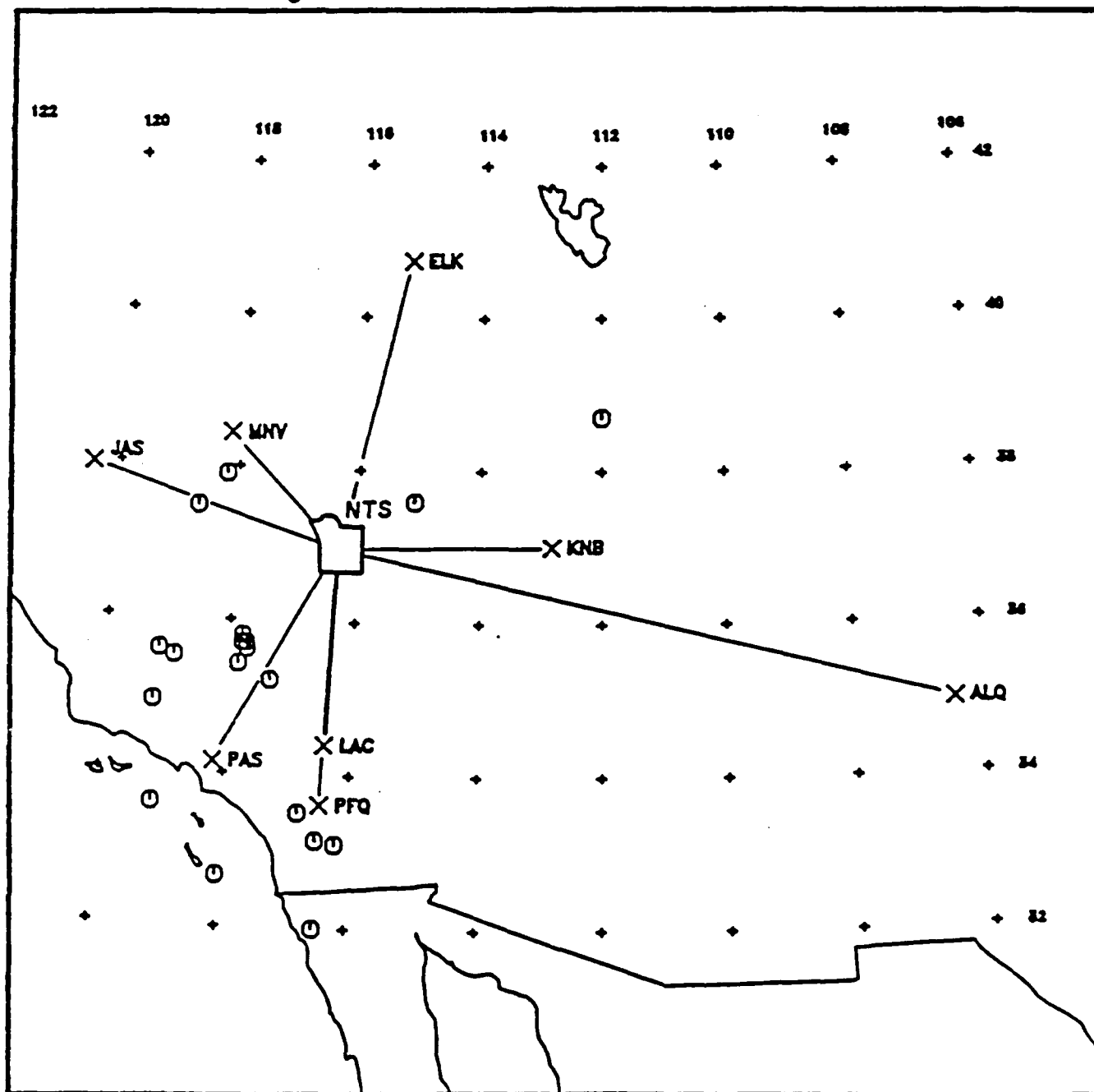


Figure 1. The western United States digital array as defined for the purposes of this study. MNV, KNB, LAC and ELK are LLNL stations. ALQ and JAS are DWWSSN stations and PAS and PFO are university run stations. The open circles are the locations of earthquakes in the discrimination data base.

The Effect of pP On Short Period Records

$t^* = 0.15$

$t^* = 0.35$

$t^* = 0.55$

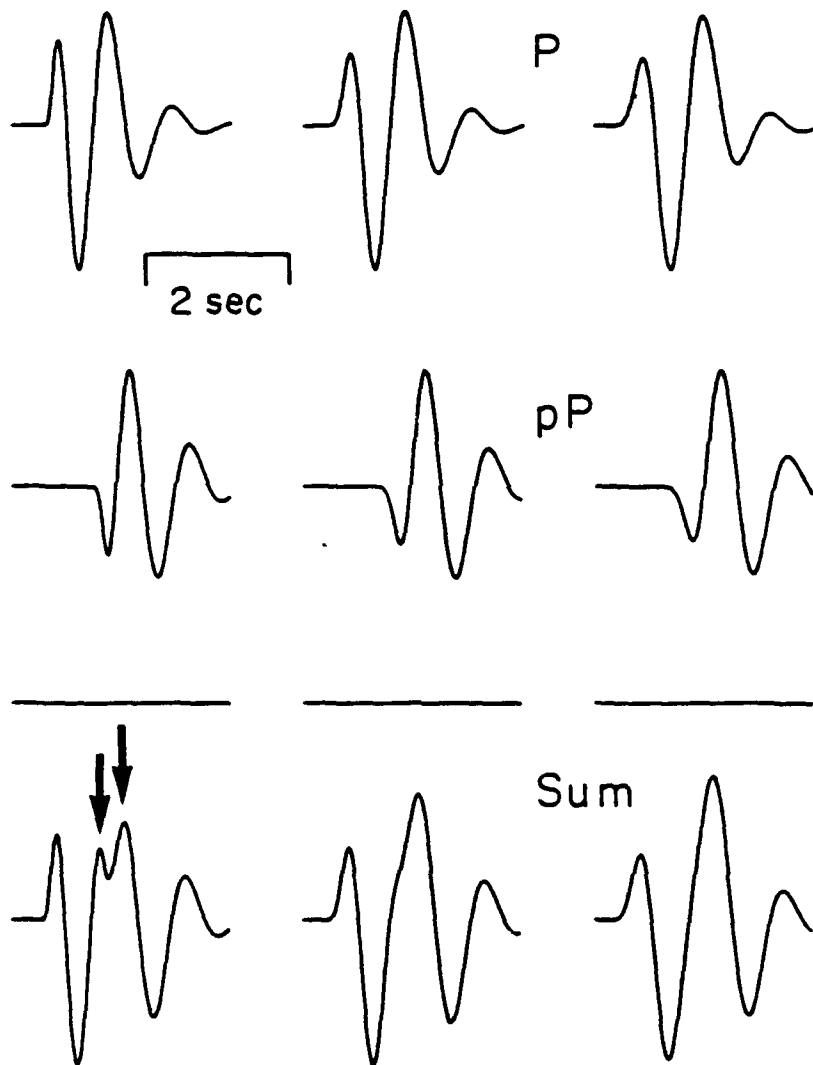


Figure 2. A simple calculation to show the effect of pP on short period WWSSN records of explosions. At low values of t^* , it causes a splitting of the third swing as indicated by the arrows. If t^* is as high as only 0.3, the feature is smoothed out.

is ALQ at 890 km. The other stations are at about 325 to 375 km in range on average. The waveforms shown in the following have been corrected to the DWWSSN short period response, since this is the narrowest band instrument in the net.

Stacking P_n Waveforms The basic approach of our study was to assemble seismic profiles of events at each separate station for suites of Yucca Valley and Pahute Mesa events and to attempt to resolve consistent phases by stacking. In carrying out this procedure we discovered the stable character of the P_n waveform onset. The effect of pP from explosions on short period teleseismic (30° to 90°) WSSN arrivals is subtle. However, synthetic analyses of these arrivals have been carried out for many years (Burdick and Helmberger, 1979); Burdick et al., 1984) and most investigators recognize what the effect should look like. Figure 2 shows a simplified calculation of the pP interference. The top row shows the signal for a direct P wave arrival. We assume a Mueller Murphy wet tuff source with a yield of 150 Kt and variable values of t^* as indicated. We assume that the elastic response of the earth is well approximated as a delta function. This corresponds with the idea that the first energy is associated with a turning ray in the smooth lower mantle and the well known wave front expansion (Aki and Richards, 1980). If t^* is low enough or pP is very much later than elastic predictions, the effect of the interference is to split the third swing as indicated by the arrows. For moderate values of t^* , the effect is smoothed out and the only effect of pP is a change in the ratio of the first to the third swing. This splitting of the third swing has in fact only been observed in teleseismic data for the largest and deepest explosions on record (Burdick et al., 1984). This is not surprising since it is well known that, if the Mueller Murphy wet tuff source is accurate for Pahute Mesa events, the observed teleseismic amplitudes require a t^* of 1.0 s (Burger et al., 1987). Even with a correction of several tenths of a second for non tectonic paths, one would not necessarily expect to see the splitting of the third swing.

In the initial stages of this work (Burdick et al., 1988), observed explosion waveforms were assembled from just the DWWSSN stations ALQ and JAS since this data was most readily accessible. Averages of P wave trains for large numbers of events were formed, and it was noted that the average onset of the P_n resembled the waveform at the lower left of Figure 2 very closely. In the more recent work reported here, data is being assembled from many other stations in the net. A very limited data set is available for many stations, particularly PAS and PFO since they have been installed very recently. We show the average P_n waveforms which exhibit the effect of pP most clearly in Figures 3 and 4. The waveforms shown are the result of stacking 4 to 6 observations for each station and test site. It is important to note that we particularly selected waveforms that showed the split third swing clearly since the feature is caused by pP_n and we are attempting to design an automated discriminant based on detecting it.

The tests at Pahute Mesa are on average larger than those from Yucca Flat. The structure there also appears to be simpler and the scattering less intense. The pP effect seems in general to appear more consistently and more clearly for Pahute events. Figure 3 shows the average P_n for 5 stations in the digital network. The splitting of the "c" swing is indicated by arrows. The only stations in the digital network for which we do not show a result are ELK, LAC and PFO. The former has a complex receiver structure, and the latter two are affected by a triplication due to structure in the lid as we discuss in a following section. Figure 4 shows similar averaging results for 7 stations. All of the digital stations except ELK and PFO are represented. We have obtained the result

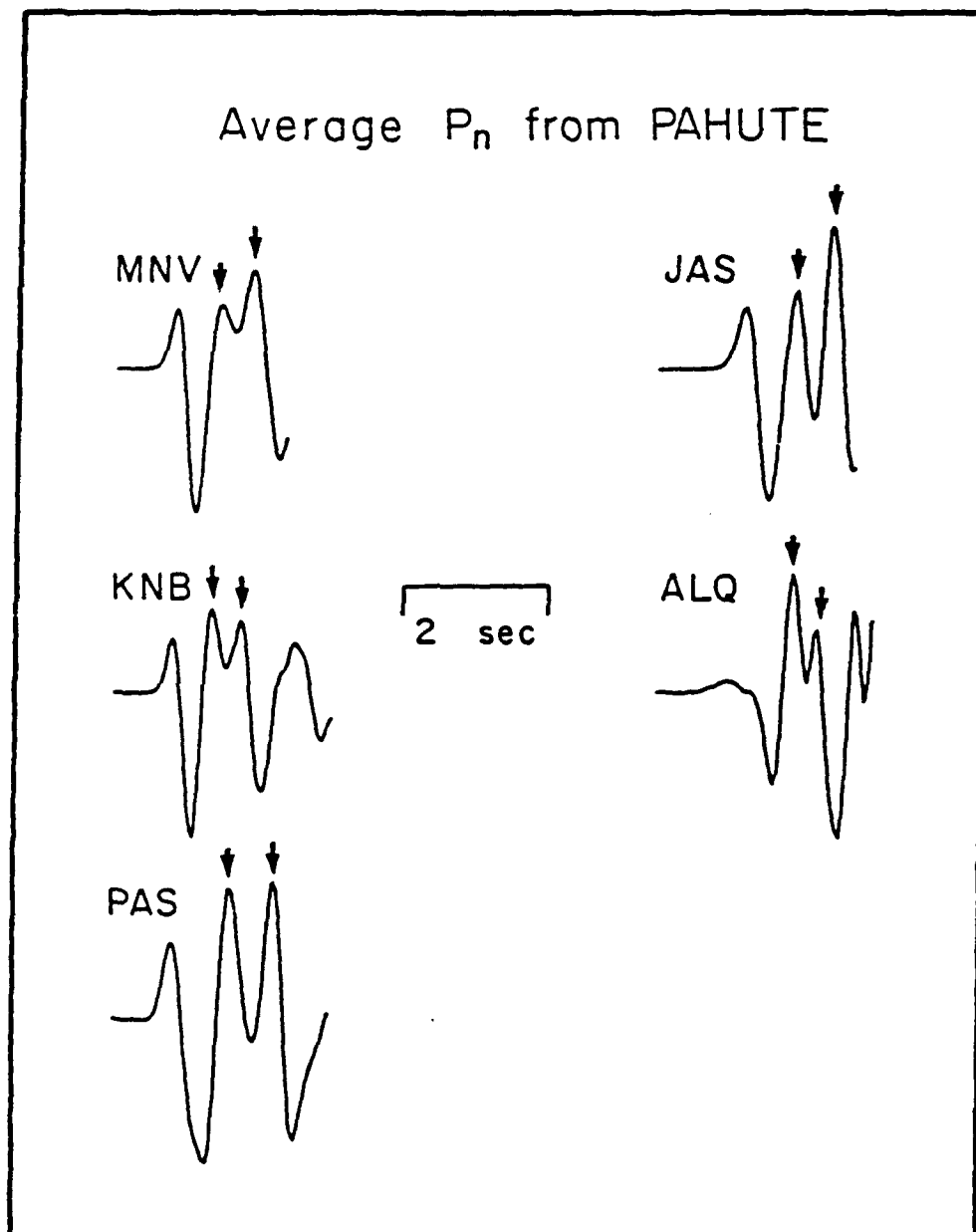


Figure 3. The average P_n waveform for Pahute events observed at stations in the western U.S. digital net. The split third swing is indicated by arrows.

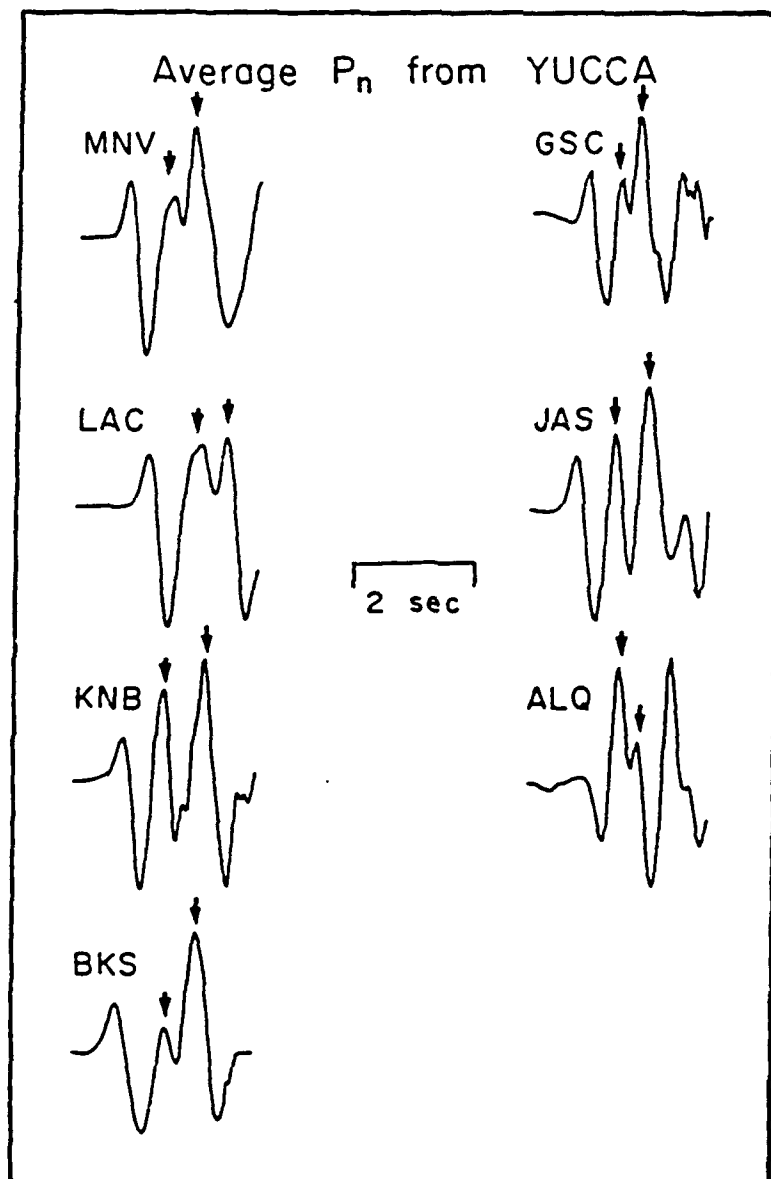


Figure 4. The average P_n waveform for Yucca events observed at stations in the western U.S. digital net. The split third swing is indicated by arrows.

for LAC by averaging signals at ranges prior to the beginning of the triplication. We also show results from two analog stations, BKS and GSC. We hand digitized the data from these stations and then averaged in the same way. Given the stability of the waveforms in the two figures, one would have to conclude that we are seeing a manifestation of a very fundamental property of explosion sources.

We have carried out a modeling study of the broad band records at MNV and KNB. These are the two broad band stations which showed the effects of pP_n most clearly and consistently. Some representative comparisons of observations to synthetics are shown in Figure 5. Since these are broad band stations, we can stably deconvolve out the instrument to obtain ground velocity and we have done so. The synthetics were computed for a realistic plane layered structure using standard matrix propagator techniques. We assumed a Mueller Murphy source and a frequency independent Q operator. The similarity between the observed P_n waveforms in Figures 3 and 4 and the wave shape expected for a turning ray along a high Q path motivated us to examine the possibility that P_n onset is actually energy being turned by a smooth positive gradient in the lid. If a turning ray in the lid is responsible for the P_n waveform, the effect of propagation can be approximated by a delta function at high frequency. If P_n is a head wave on the crust mantle interface, the effect can be approximated by a step. Our modeling study strongly favors the first possibility in that synthetics based on the head wave assumption are always too long in period. If we assume the turning ray model, an appropriate value of t^* appears to be in the range of 0.1 to 0.2 s.

The direct P_n velocity signal for an explosion is a nearly symmetric two sided pulse breaking upward. As indicated by the arrows in Figure 5, the pP_n begins as a downward pulse interfering constructively with the downswing of direct P_n . We found that the observed pP_n was always significantly later than the elastic prediction. For Pahute events, its amplitude is close to elastic, but for Yucca events like those in Figure 5, it generally appears somewhat larger. Its waveform also sometimes differs from the direct arrival. All of these features of pP_n indicate that it is more complex than a simple elastic reflection, and it is probably affected by complex nonlinear processes near the source.

A Triplication Within P_n The idea that the high frequency P_n penetrates the mantle in the western U. S. and is actually associated with a turning ray is significant since many studies have been performed under the assumption that it is a true head wave (Hearn et al., 1984). Variations in the timing of P_n have been mapped exclusively into the velocity variations in the crust and on the upper surface of the mantle. The possibility of a coherent structure within the lid above the low velocity zone has not been investigated. Yet the evidence in the data assembled for this work is clear that there is a triplication within P_n to the south of NTS. Related effects are not present at stations at other azimuths. The structure causing the triplication could thus be related to the tectonic history of the west coast of the United States.

Evidence for the triplication is clear in all three California stations in the digital net, but strongest at LAC. Figure 6 shows the development of the triplication with range. At close ranges, the P_n waveform appears typical. We used records from these ranges to form the average LAC waveform shown in Figure 4. The triplication develops smoothly with range until the second arrival is very clear by 320 km. LAC is obviously at the front end of the triplication. PAS appears to be about in the middle. The waveforms do not appear unusual, but P_n is strongly amplified with respect to P_g . It is presumably reflecting at

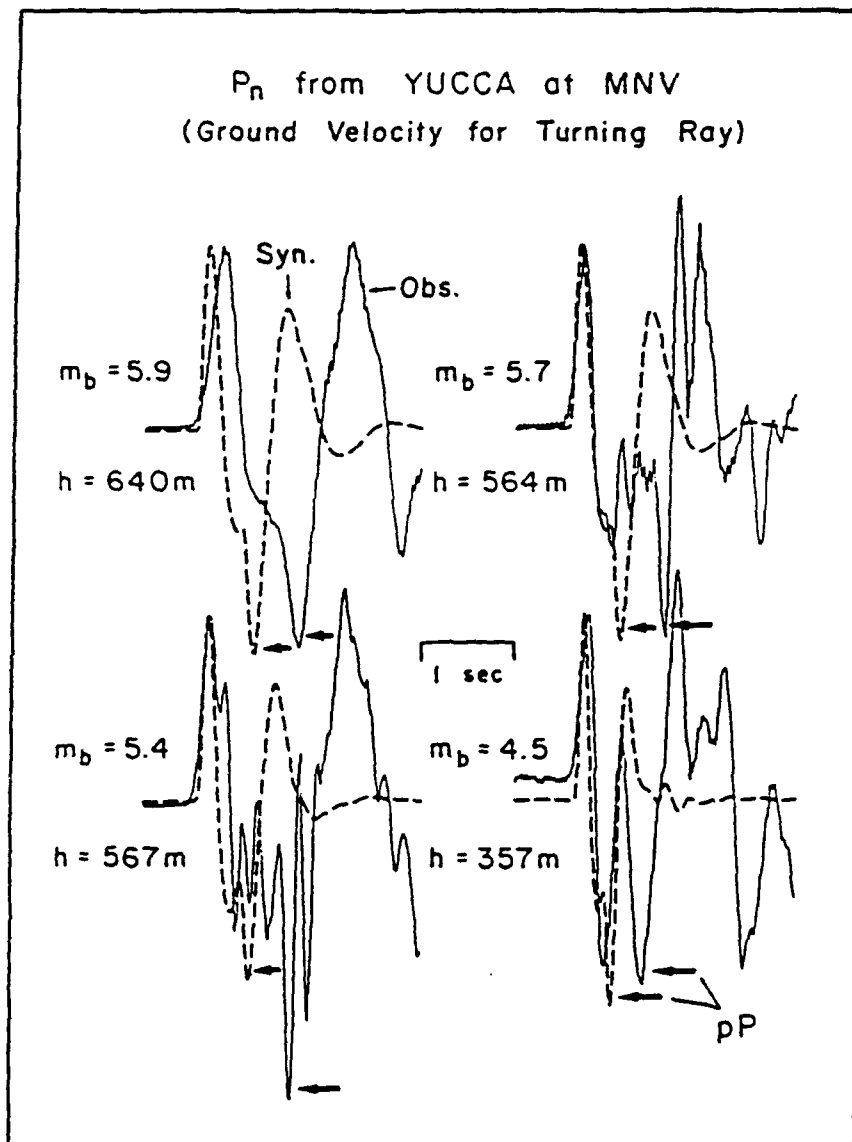


Figure 5. Observed versus synthetic waveforms at MNV for Yucca events. All assumptions are the same as for Figure 15 except for an increase in τ^* from 0.1 to 0.2 s.

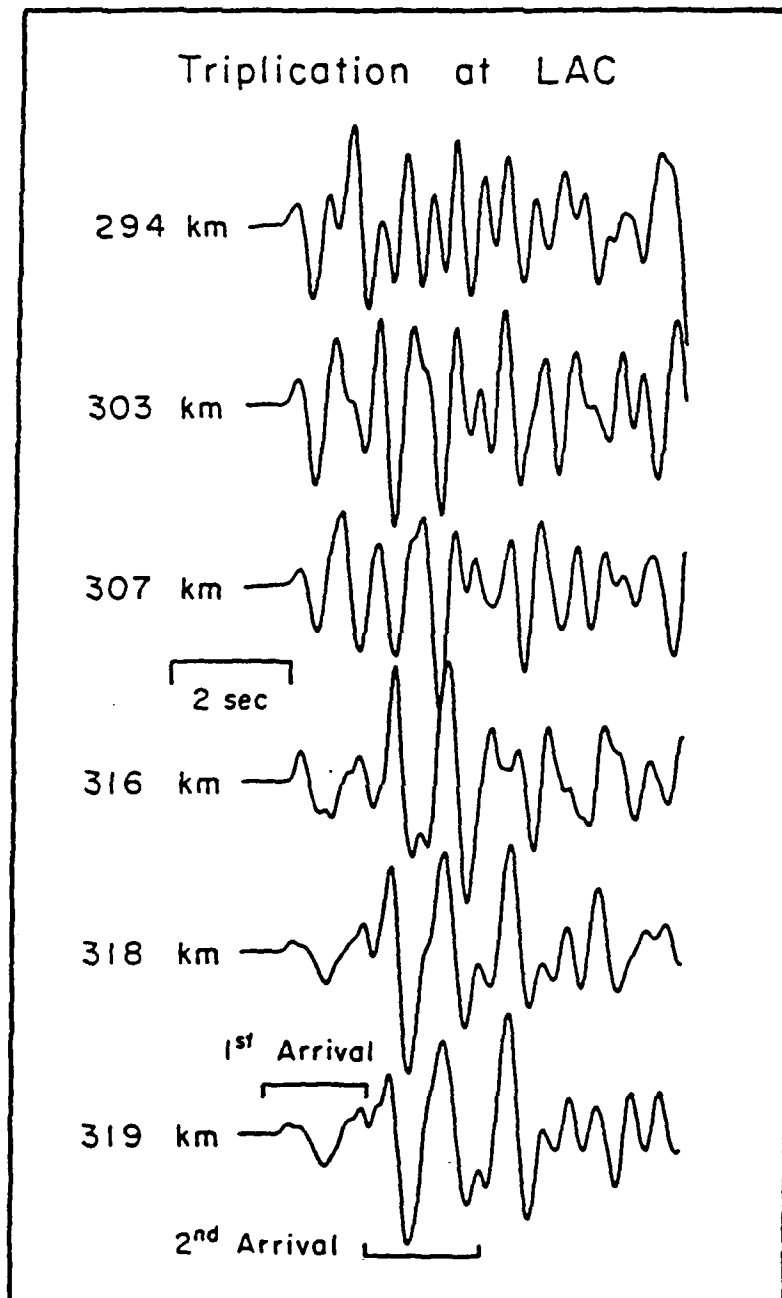


Figure 6. Development of the triplication with range at LAC. At the close ranges, the first energy is the largest and the P_n waveform is similar to that at most stations. At greater ranges, a large second arrival develops and moves toward the front of the record.

critical angle in the lid. PFO, the most distant of the three stations exhibits the reverse of the effects shown in Figure 6. The strength of the effect of the triplication decreases at distances beyond PAS. The discovery of this triplication is significant to the discrimination study if coherent discontinuities in the lid are common features. They probably are not, however, within stable continental interiors both because this one is visible in only one azimuth and because, if they are common, they would have been discovered long before.

Discrimination with the P_n Waveform Figures 3 and 4 demonstrate that the P_n waveform is on average very stable and that it exhibits a distinctive feature a few seconds after onset. The above modeling studies provide a convincing case that this feature is associated with effective pP_n . Since earthquakes uniformly occur much deeper than explosions, it is reasonable to expect that few earthquakes will exhibit a highly similar feature at such short times into the waveform. In a previous report (Burdick et al., 1988), we demonstrated in a quantitative way that this was the case. We collected P_n waveforms from the earthquakes mapped in Figure 1 at stations ALQ and JAS. We windowed out 3 second onset waveforms from both the earthquake and explosion signals and measured their correlation with an analytic norm. This norm attains a maximum value of 1.0 if and only if two waveforms are identical. Figure 7 is taken from that work and shows reasonably efficient separation of explosions from earthquakes. The discrimination of earthquakes from explosions is far from complete. At its current level of efficiency, the P_n waveform discriminant would have to be used simultaneously with other discriminants in a combined analysis. It is also possible that the efficiency could be improved through further study.

The discrimination tests presented in our previous report demonstrated only that explosion P_n waveforms are consistent and stable at regional stations and systematically different than earthquakes. The conditions of the tests are, however, highly idealized. In a realistic situation, signals will be recorded on a regional array from continuously varying azimuths. The discrimination procedure would have to assimilate all of the waveforms from the array and test whether the signals had a feature resembling explosion pP_n on average. The consistency of the P_n waveforms in Figures 3 and 4 indicates that such a procedure should be effective at some level. A simple test as to whether explosion pP_n signals from one station can be used to discriminate between events at another station has been made by correlating the average MNV signal with the JAS data set. The results are shown in Figure 8. The discrimination efficiency is comparable to the level achieved with the JAS waveform proving the feasibility and transportability of the waveform discriminant.

CONCLUSIONS AND RECOMMENDATIONS

It has long been known that the effects of wave propagation on short period P waves at teleseismic distances could be well described by simple ray theory. Accordingly, they have been studied in great detail in efforts to characterize seismic sources. A problem with interpreting them is that they are relatively strongly smoothed by attenuation. An appropriate teleseismic level of t^* is about 1.0 s. If this same ray theory holds for P_n propagation to regional distances, we will have a remarkable new window for addressing the same questions about sources with a t^* level of about 0.1 s; down an order of magnitude in the exponent. The first new avenue research this suggests is to undertake a program of studies directed at answering long standing questions regarding source scaling and pP behavior based on P_n waveforms. A second avenue would of course be to

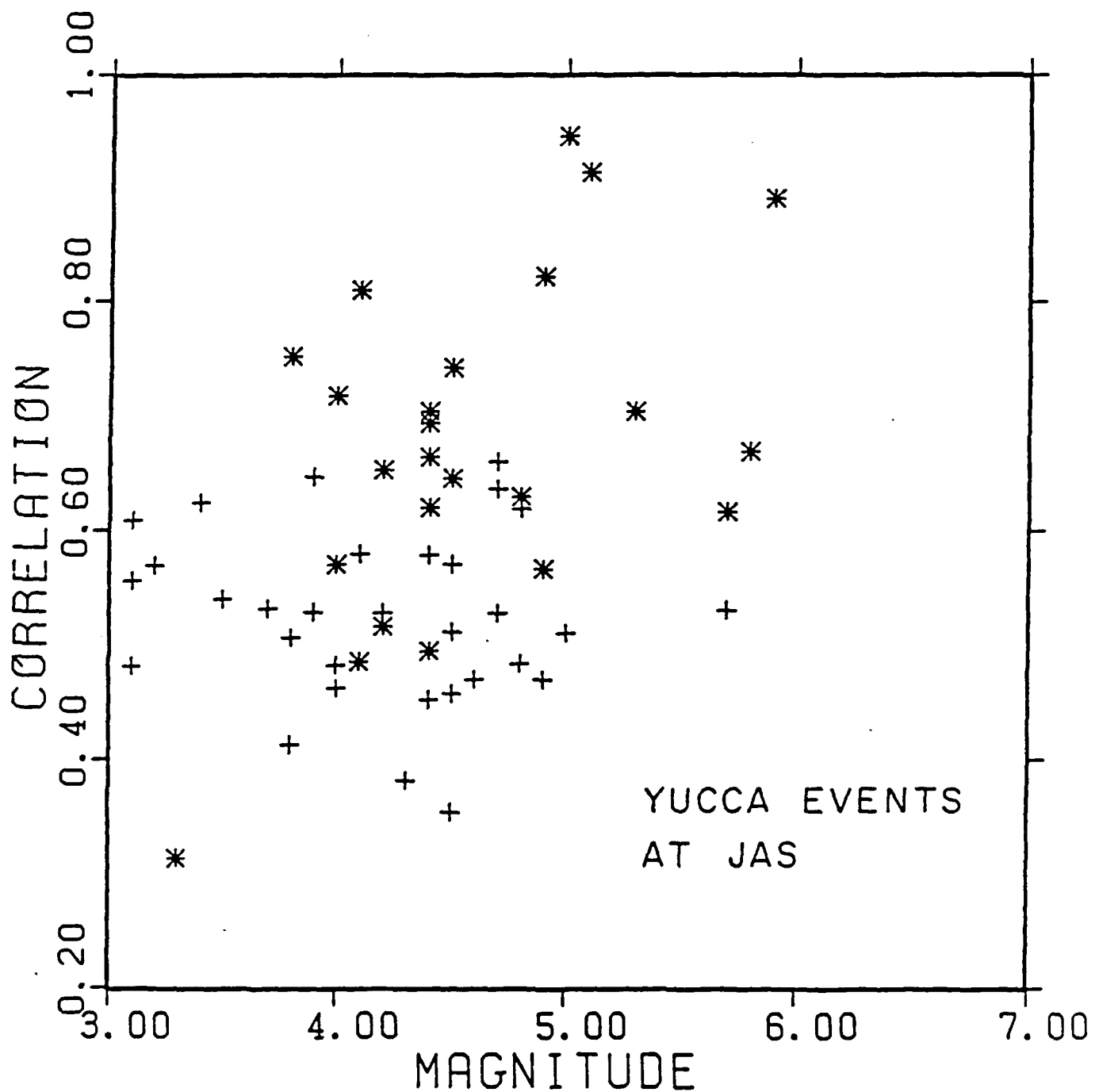


Figure 7. Discrimination of Yucca explosions from earthquakes using correlation with the average P_n waveform at JAS. The explosions are stars and the earthquakes are crosses.

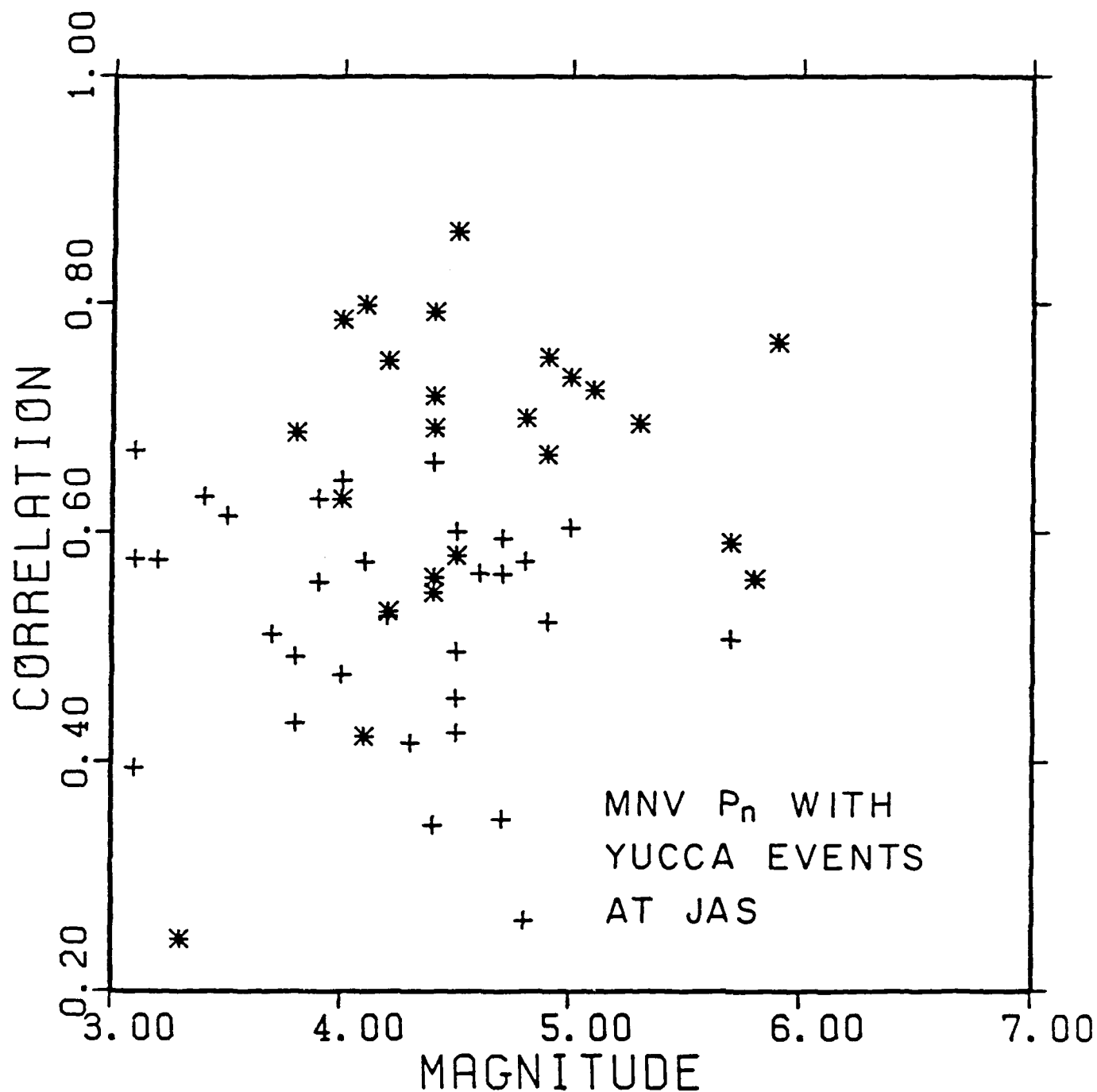


Figure 8. Discrimination of Yucca explosions from earthquakes using the average P_n waveform from MNV and the data base from JAS. Explosions are stars and earthquakes are crosses. The separation of the populations is comparable to that in Figure 26 illustrating the transportability of the discriminant.

to continue to develop a waveform discriminant. Many improvements on its basic design could be tested on it. Its performance and reliability statistics need to be measured and quantified.

REFERENCES

- Aki, K. and P. G. Richards, Quantitative Seismology: Theory and Methods, W. H. Freeman and Company, San Francisco, 1980.
- Burdick, L. J., "Burdick, L. J. and D. V. Helmberger, "Time functions appropriate for nuclear explosions", Bull. Seism. Soc. Am., 69, 957-971, 1979.
- Burdick, L. J., T. C. Wallace and T. X. Lay, "Modeling near field and teleseismic observations from the Amchitka test site", J. Geophys. Res., 89, 4374-4388, 1984.
- Burdick, L. J., C. K. Saikia and N. F. Smith, "Discrimination using P_n and P_g ", AFGL-TR-89-034, 1988.
- Burger, R. W., T. X. Lay and L. J. Burdick, "Average Q and yield estimates from the Pahute Mesa test site", Bull. Seism. Soc. Am., 77, 1274-1294, 1987.
- Hearn, T. H., " P_n travel times in southern California", J. Geophys. Res., 89, 1843-1855, 1984.*
- Murphy, J. R. and T. J. Bennett, "A discrimination analysis of short period regional seismic data recorded at Tonto Forest Observatory", Bull. Seism. Soc. Am., 72, 1351-1366, 1982
- Taylor, S. R., N. W. Sherman and M. D. Denny, "Spectral discrimination between NTS explosions and western United States earthquakes at regional distances", Bull. Seism. Soc. Am., 78, 1563-1579, 1988.

THE EFFECTS OF THREE-DIMENSIONAL STRUCTURE ON CRUSTALLY GUIDED WAVES

B.L.N. Kennett and M.G. Bostock

Research School of Earth Sciences, The Australian National University

GPO Box 4, Canberra ACT 2601

AUSTRALIA

Grant: AFOSR-87-0187

OBJECTIVE

The Lg phase is one of the most prominent features of many regional seismograms in the frequency band from 0.5 to 5 Hz. Although it does not usually exhibit a clear onset it builds to an amplitude maximum at a group velocity close to 3.5 km/s. Lg is commonly the most prominent feature in the later part of a regional seismogram and its size makes it valuable for the detection of small events. However the amplitude of Lg is known to be sensitive to changes in crustal structure and this reduces its utility for discrimination purposes. Given a particular source location it would therefore be very useful to be able to predict the effects of crustal heterogeneity on the characteristics of the Lg propagation.

We present here an approach based on a ray theoretical description of Lg waves which can account for the effects of three dimensional topography at the earth's surface and at the Moho bounding a simple crustal waveguide. This technique is tested on models of oblique Lg propagation across a mountain range and a zone of thinner than normal crust. The method is then used to provide a semiquantitative assessment of the nature of Lg propagation from the Soviet test sites near Semipalatinsk using a crustal model derived from digital topography information.

SUMMARY

The sensitivity of Lg to variation in crustal structure has been widely noted; early studies revealed that as little as 100 km of intervening oceanic crust is sufficient to eliminate Lg propagation across ocean basins (Ewing et al., 1957). The character of Lg propagation across certain continental areas where the crust is known to be complex, most notably central Asia, has been used to constrain structure and provide insight into the operative tectonic processes (Ruzaikan et al., 1977; Ni and Barazangi, 1983; Kadinsky-Cade et al., 1981). These studies have involved the interpretation of short period seismograms to qualitatively characterize broad geographical zones in terms of their amenability to Lg propagation. More quantitative analysis is possible with increased

raypath coverage: Kennett et al. (1985) inverted a comprehensive set of Lg attenuation data over NW Europe to delineate crustal heterogeneity in the North Sea.

Two different descriptions, which are equivalent in the case of a stratified medium, can be made for the physical nature of Lg in a heterogeneous crust: the phase can be considered as a sum of higher mode surface waves trapped in a crustal wave guide, or alternatively, as the result of constructive interference between S-waves multiply reflected between the free surface and the crust-mantle boundary. For heterogeneous zones two methods have evolved to model the propagation of Lg based on the different views of the propagation process.

The coupled mode technique (Kennett, 1984) describes Lg as a sum of modal eigenfunctions, for a reference model, weighted by modal coefficients which vary with position. In two dimensions these coefficients satisfy a system of non-linear differential equations whose solution is, in principle, exact. In practice, however, the method may become computationally intractable in zones of exaggerated heterogeneity ($>5\%$) as consideration of intermode coupling among an increased number of modes becomes necessary. In addition, the coupled mode method is better suited to treating departures in physical properties (elastic moduli and density) from the reference model than changes in position of structural boundaries.

The method of ray diagrams offers a simple means of assessing the propagation of Lg in a qualitative manner: this method relies on the constructive interference of multiple S reflections. A set of rays at fixed slowness is traced through a crustal layer of variable thickness, and the disruption in the pattern of the ray system (or equivalently the reflection points) is used as a measure of modal coupling and scattering. Kennett (1986) by comparing the visually descriptive ray diagrams and coupled mode solutions for simple 2D earth models noted some simple consistent relations between the two and established the validity of the ray based technique.

Our objective here is to extend Kennett's (1986) approach to 3D heterogeneity. After describing the ray diagram method in slightly greater detail and examining what information may be extracted, we examine two, geometrically simple earth models and investigate the effects of oblique incidence on Lg propagation. We then shift our focus to a specific geographical area and assess the likely pattern of Lg propagation by examining ray diagrams for a crudely constructed, real earth model.

THE RAY DIAGRAM METHOD

At a given frequency, a finite number of modes will contribute to the Lg wave train, and each mode, characterized by a particular phase velocity will correspond to an S-wave ray system with associated angle to the vertical. This suggests that the geometrical regularity of a system of rays launched in some systematic fashion may be used as an

indication of the coherence and sustained amplitude of a given mode in addition to a measure of the S-wave constructive interference condition.

At fixed frequency the angle of wave propagation to the vertical increases as the phase velocity decreases. For a given angle to the vertical, determined by the choice of incident mode, the behaviour after interaction with heterogeneity can be conveniently characterized by the spread in propagation angles. Increased angles to the vertical correspond to conversion to lower order modes with the change in angle proportional to the spread in intermode coupling. Similarly steeper propagation corresponds to conversion to higher order modes. In general waves incident with higher phase velocities tend to show a larger variation in ray angle after transmission through the heterogeneity due to increased multiple reflections in the complex zone. In those cases where caustics develop in the ray diagrams the equivalent coupled mode solutions show considerable variation in the amplitudes of the modal coefficients with position.

The models presented in the following analysis exhibit 3D heterogeneity and it is no longer possible to construct ray patterns from a system of plane waves in cross section as in the 2D case. Rather, we have resorted to plan views representing surface/Moho topography via contours and consider a single point source emitting rays at a given angle to the vertical (modal slowness) through a range of azimuths. Regularity in plotted surface/Moho reflection points and the horizontal projection of raypaths provide a measure of the constructive interference condition in a manner analogous to the pattern of 2D ray systems considered by Kennett (1986).

SIMPLE EARTH MODELS

In this section we investigate Lg propagation in 2 simple crustal models and in a reconstruction of the crust in central Asia based on world topography data, using ray diagrams. All of these models are characterized by simple variation in surface and basement (Moho) topography; the physical properties remain constant throughout the crustal waveguide.

Although a more sophisticated analysis incorporating crustal stratification might be implemented with slight modification, this has not been done for several reasons. Ray diagrams are at best semiquantitative and are meant to provide a 'first order' means of assessing Lg propagation through crustal structure. Moreover, although the shape of the crustal waveguide is the dominant factor influencing Lg other factors such as small scale heterogeneity in crustal velocities cannot be entirely ignored. In addition, when we construct a crustal model from just the surface topography we are forced to make a number of assumptions which may not be well founded, and so a very complex model is not warranted.

We have considered two models for which the surface and Moho topography are represented as piecewise smooth surfaces and the zones of variation in waveguide thickness are of limited spatial extent. Shear velocities of 3.5 km/s and 4.6 km/s were chosen to characterize the crust and upper mantle. For a given phase velocity rays were traced away from a point source with multiple reflections at the surface and the Moho. The character of the propagation patterns are indicated in figures 1, 2 by plotting a plan section of the rays and marking the reflection points at the Moho. This display enables the regular character of the Lg wavefront in the homogeneous regions to be compared with the disrupted pattern after passage through the heterogeneity.

Crustal Thickening

The first model (fig 1) is of a linear mountain chain and a section across the model along the profile A-B is shown. Several general features characterize the emergent wavefield for a range of phase velocities. Perpendicular to the axis of the range we note a central corridor marked by a continuous and regular arrangement of bottom reflection points and little variation in ray density with azimuth (even though the angle to the vertical is increased). This corridor is flanked by zones of alternating high and low ray density as the angle between the axis and the wavefront increases. For particular combinations of source location and phase velocity, some zones may exhibit regularity in both ray density and reflection pattern, and, therefore represent windows through which a significant fraction of the initial Lg wave energy can pass. At very large range axis - wavefront angles, rays become trapped within the mountain range and few rays penetrate the structure to the crust outside.

Rays which impinge on the surface at angles to the surface normal less than the critical angle defined by Snell's law will undergo transmission into the upper mantle and are distinguished by filled diamonds marking the Moho reflection points. Kennett (1986) notes that this situation represents a coupling to modes constituting the Sn phase. As observed in the equivalent 2D model (Kennett, 1986), refraction after emergence from the mountain range occurs most prominently near the maximum phase velocity for Lg (above 4.4 km/s). The distribution of these emergent refracted rays is dependent on source location and displays little azimuthal preference.

Crustal Thinning

The second model represents a region of crustal thinning simulating a zone of localized crustal extension and is designed to illustrate the effect of local transverse gradients in topography. In cross section it is characterized by flanks rising from 30 km to 20 km depth to a plateau; its configuration in the horizontal plane is elliptical. Kennett (1986) noted in the analogous 2D model that constriction of the crustal waveguide had a

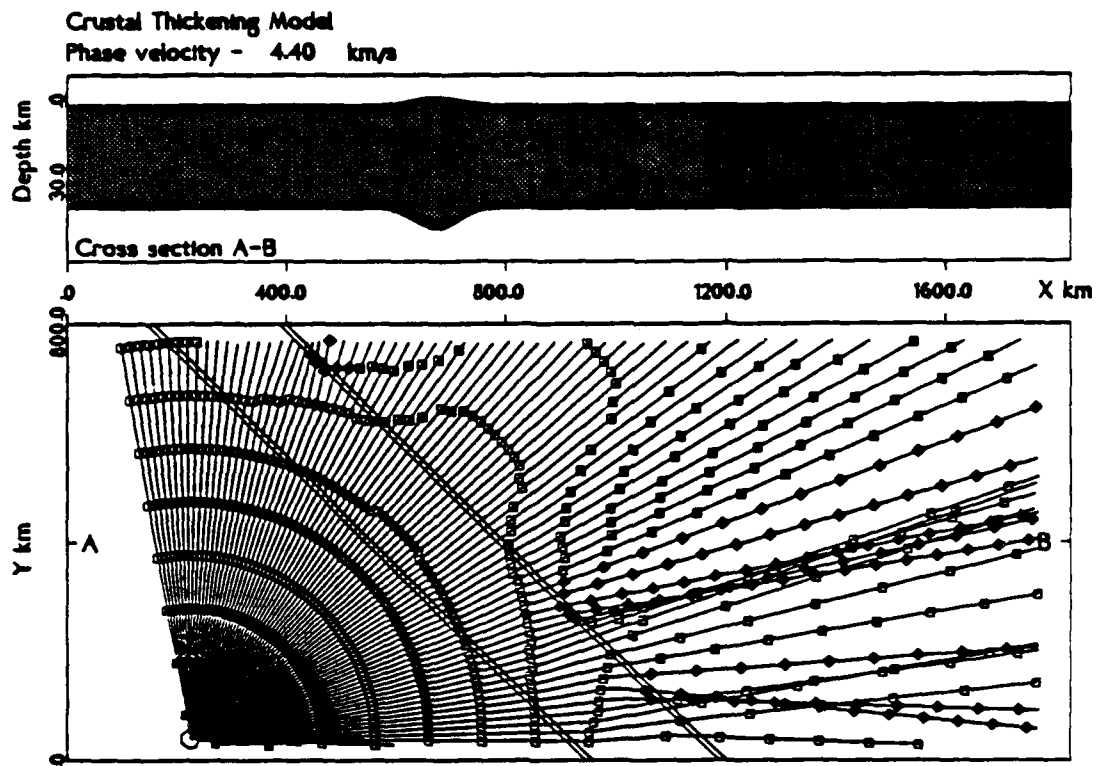


Figure 1. Ray pattern impinging on a linear zone of crustal thickening, simulating a mountain range. Moho reflection points are plotted, filled diamonds indicate leakage out of the crustal waveguide.

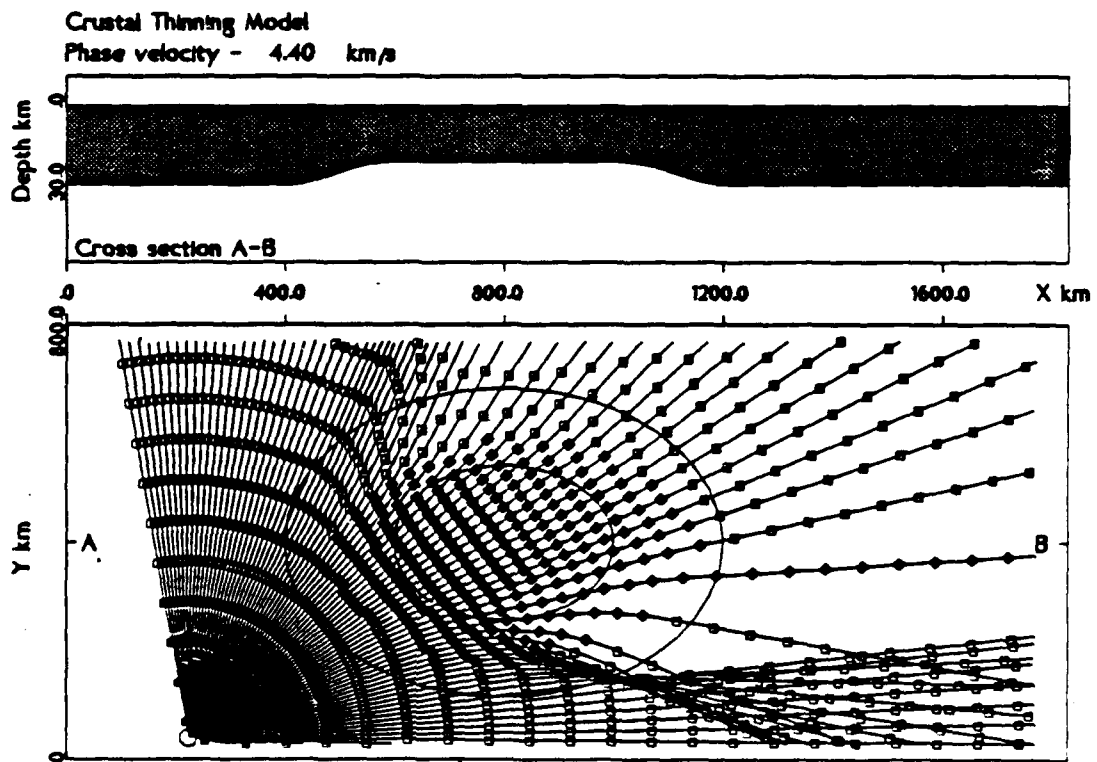


Figure 2. Ray pattern impinging on an elliptical zone of crustal thinning.

more severe effect on transmission of Lg than increase in thickness. This is also apparent in the 3D model where the effect of the crustal thinning is to steer rays away from the angular window defined by the lateral boundaries of the structure and the source position. This is, again, most apparent at higher phase velocities as in the case of figure 2. In this example, we note that rays travelling across the top of the structure are refracted into the mantle, hence the low density of emergent rays is complemented by an additional energy loss through conversion to Sn.

Central Asian Crust

In our final model we examine Lg propagation in the vicinity of the Soviet nuclear test sites located in eastern Kazakhstan, approximately 400 km northeast of Lake Balkhash, near Semipalitinsk. Surface topography was constructed by smoothing digital elevation data supplied at 5' grid intervals from the world topography data base. The depth to the Moho was determined by further smoothing of the surface topography and assuming 80% isostatic compensation. This last assumption, although simplistic, is thought to be reasonable within the limitations of the ray method for a uniform crust.

Rays were traced over a 30° by 20° window with source at Semipalitinsk (see fig 3), for a range of phase velocities between 3.4 and 4.6 km/s. The character of the ray systems can be discussed in terms of three broad geographic zones. To the north, elevation decreases very gradually, consequently the ray patterns are very regular and experience a slight increase in phase velocity with distance from the source. For initial phase velocities above 4.45 km/s, this results in energy loss through conversion to Sn however Lg transmission through this zone for lower phase velocities is likely to be extremely efficient. It is worth noting that Lg recorded at NORSAR would propagate through this region. The general topography in Kazakhstan to the west of the test sites remains relatively constant although there are minor local fluctuations. Ray patterns in this zone are slightly less coherent but still suggest efficient Lg transmission. The Tien Shan and the Altai chains (mountain ranges rising to 7400 m), border the region to the south and east. Changes in relief are extreme and ray patterns are severely distorted especially at higher phase velocities. The character of Lg recorded at stations along these paths beyond the mountain ranges will undoubtedly be very complex; there is likely to be considerable variability with position and significant attenuation due to conversion to Sn and scattering.

As a general note it should be mentioned that the major topographic features in the area exist at a larger lateral scale than those in the two previous models, hence the ray patterns are less dependent on source position.

Lg Rayplot

Semipalitsinsk

PHASE VELOCITY

4.40 km/s

WINDOW

65. - 95. E

40. - 60. N

SOURCE

79. E 50. N

SCALES

Horizontal - km as marked

Vertical - km above msf

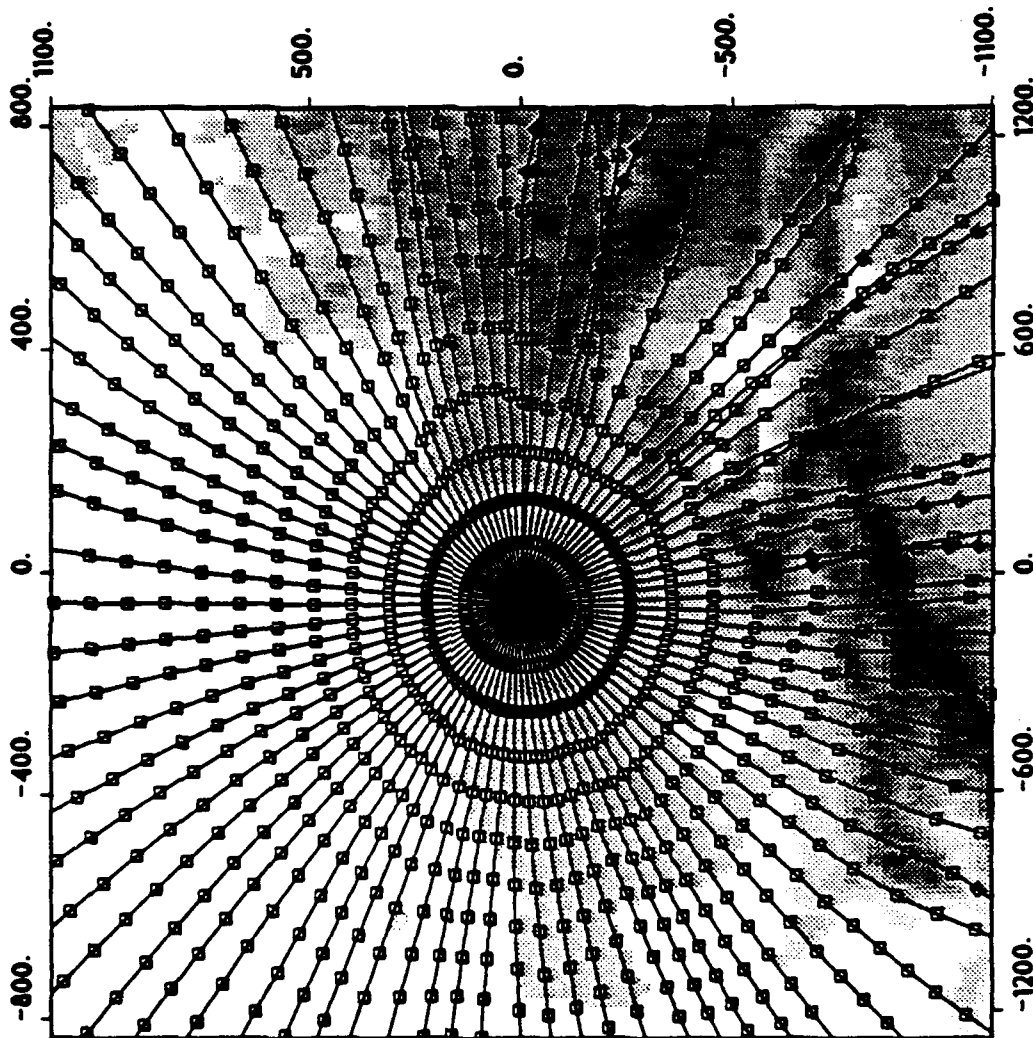


Figure 3. Ray pattern over a 30° by 20° window of central Asia showing topographic relief. Note that there is some systematic distortion in the ray pattern resulting from spherical to rectangular projection.

CONCLUSIONS AND RECOMMENDATIONS

The ray diagram approach to assessing Lg propagation in three-dimensional crustal models provides considerable insight into the nature of the interaction of the Lg phase with heterogeneity. The method is useful for examining the effects of particular types of heterogeneity for plane waves or point sources.

We have been able to show that using simple isostasy assumptions we can build crustal models from digital surface topography which can be used to study Lg propagation from specified locations (e.g. known nuclear test sites). The accuracy of such models can be improved by incorporating detailed information on gravity anomalies and crustal structure where these are available. We are currently in the process of calibrating the ray approach by looking at paths to stations in central Asia using the Lg observations compiled by Ruzaikan et al. (1977), and Ni and Barazangi (1983).

REFERENCES

- Ewing M., Jardetsky W.S. and Press (1957) *Elastic Waves in Layered Media*, McGraw-Hill, New York.
- Kadinsky-Cade K., Barazangi M., Oliver J. and Isacks B. (1981) Lateral variations of high-frequency seismic wave propagation at regional distances across the Turkish and Iranian Plateaus, *J Geophys Res*, **86**, 9377-9396
- Kennett B.L.N. (1984) Guided wave propagation in laterally varying media - I. Theoretical development, *Geophys J R astr Soc*, **79**, 235-255
- Kennett B.L.N. (1986) Lg waves and structural boundaries, *Bull Seism Soc Am*, **76**, 1133-1141
- Kennett B.L.N., Gregersen S., Mykkeltveit S., and Newmark S. (1985) Guided wave propagation in laterally varying media - II. Lg waves in north-western Europe, *Geophys J R Astr Soc*, **79**, 257-267
- Ni J. and Barazangi M. (1983) High frequency seismic wave propagation beneath the Indian shield, Himalayan Arc, Tibetan Plateau, and surrounding regions: high uppermost mantle velocities and efficient Sn propagation beneath Tibet, *Geophys J R astr Soc*, **72**, 655-689
- Ruzaikan A. I., Nersesov I.L., Khalturin V.I. and Molnar P. (1977) Propagation of Lg and lateral variation in crustal structure in Asia, *J Geophys Res*, **82**, 307-316

Optimal Digital Elevation Model Resolution for the Interpretation of Morphotectonics

E J Fielding, T L Gubbels, and B L Isacks
Institute for the Study of the Continents (INSTOC)
Cornell University, Ithaca, NY 14853-1504
(ARPAnet: Fielding@Geology.TN.Cornell.Edu)

Contract number F19628-88-K-0035

Objective

This project has two interrelated objectives. The first is to develop an integrated morphotectonic information system (MIS) that brings together satellite images, digital topography, geology, and seismicity on a single, multiple-window computer screen to be interpreted for the tectonic and geomorphic setting of seismic events and their propagation paths to aid the possible verification of a Comprehensive or Threshold Test Ban Treaty. The second objective is to calibrate the developing system by applying it to the morphotectonic analysis of three tectonically active areas: central Asia, the central Andes, and southern California. Incremental development of the MIS combined with its application to ongoing integrated analysis of key tectonic areas highlights necessary design modifications which are progressively incorporated as research and system development continue.

Morphotectonics is the extraction of tectonic information, such as the character and amount of recent deformation, from geomorphology. Currently available satellite images and digital topographic data are the primary source of regional morphotectonic information. Integration of topographic and image data with teleseismic and local-array seismicity, and other geophysical datasets, will permit the analysis of the tectonic setting of seismic events and their propagation paths. The main objective of our research up to this point has been to investigate the character of available digital topographic data and determine how best to use it for the interpretation of morphotectonics.

Summary

We are developing new methodology for the integration of a wide variety of digital imagery, and geologic, seismic and geomorphic data to efficiently interpret the tectonic settings of remote areas to aid in the verification of possible Nuclear Test Ban Treaties. Both satellite images (e.g., SPOT and Landsat Thematic Mapper—TM) and Digital Elevation Models (DEMs, also called Digital Terrain Elevation Data, DTED, by the DMA) are now available for various parts of the earth at spatial resolutions or grid spacings that vary by about three orders of magnitude, from 10 m to over 10 km. There is a trade-off between the sample spacing and areal coverage of digital topography, with the coarsest resolution (10 km) data available for the entire earth. The effective spatial resolution is not necessarily as high as the grid spacing of the dataset, but depends on the resolution and accuracy of the source (contour maps, airphotos, satellite images, or altimeters), the digitization method used, and the subsequent error correction and resampling. All topographic digitization methods result in varying degrees of degradation of the source spatial resolution. Digitization artifacts introduce errors that must be

quantified in order to effectively interpret the data set. Moreover, the optimal spatial resolution of a DEM or image depends on the scale of the morphotectonic problem being studied. The highest resolution data can be used for local studies, while regional topographic datasets, with wider grid spacings, are useful for orogen-scale analyses (e.g., Isacks, 1988). An optimal MIS must be capable of manipulating multiple resolution datasets to allow the interpretation of various scales of structures.

We have requested digital topography (DTED) from the DMA to cover nearly all the mountainous and seismically active areas of Central Asia (see Fig. 1), and expect to receive the data soon. In the meantime, we have been working with six DTED cells (each 1° by 1°) that cover a 2° by 3° area in the Tadjik SSR including the city of Garm (68°E – 72°E , 38°N – 40°N ; box on Fig. 1, see also Fig. 2) to study the characteristics and utilization of the data. This area has a very high level of seismicity, and is the site of several geologic and seismologic studies (Burman and Gurariy, 1973; Trifonov, 1978; Burtman, 1980; Leith, 1982; Leith and Alvarez, 1985; Leith and Simpson, 1986), and an ongoing seismotectonic study of the Peter I Range (see Fig. 2) by colleagues whom we are cooperating with (USGS-funded study by Hamburger, Pavlis, Eneva, and Sarewitz; Hamburger and others, 1988; Pavlis and others, 1988). The DMA DTED Level 1 (the level available to us) cells, at this latitude, contain 1201×1201 points, an approximate resolution of 100 m.

To investigate the informational content of higher resolution data, we are studying some USGS DEMs from the United States that cover $7.5'$ (0.125°) by $7.5'$ on a 30 m grid. These $7.5'$ DEMs have a higher resolution but are generally only available for limited areas so they cannot be used for regional interpretations. USGS $7.5'$ DEMs are classified as "level 1" DEMs, meaning they have not been corrected to make sure that adjacent maps join correctly, to remove systematic errors, or to make hydrographic features such as rivers, lakes, ridge crests, and islands continuous and correctly located (USGS, 1986; 1987). The DMA DTED is classified by the USGS as "level 3", meaning that adjacent cells will match exactly, systematic errors have been removed, and hydrographic features are correctly portrayed at a scale of 1:250,000 (DMA, 1986; USGS, 1987). Our initial study of the Garm DTED shows that some digitization artifacts remain (Fig. 5).

Conclusions and Recommendations

We have found that the most effective way of displaying digital topography is to use simulated 3D perspective views with synthetic lighting (Figs. 3-5). This "rendering" of the topographic data puts it into a form that is readily interpretable by the human eye. The main drawback of this technique is that it is computationally intensive. We will be working on ways to improve the efficiency of the rendering by taking advantage of the assumptions that can be made about the data, such as the continuity of the surface, and sorting inherent in the regular topographic grid. Existing programs solve the general problem of rendering arbitrary, random collections of 3D polygons. Rendering speeds could be increased by at least an order of magnitude, even with existing hardware. The square nature of the grid of elevation elements, however, means that a factor of ten increase in resolution requires at best a $O(n^2)$ hundredfold increase in computation. Existing algorithms are even worse, requiring something like $O(n^4)$ computations for a grid of n elements on a side.

Preliminary analysis of DEMs has indicated the need for recognizing and possibly correcting for errors or artifacts in the data. Both the original data source and method of digitization contribute to these systematic errors. The most common data source for DEMs is stereo photographs or images. Elevation data can be extracted from a stereo pair of images directly on a regular grid either by human or computer correlation of the surface features, but these techniques are relatively new. Human digitization of stereo photographs or imagery has been commonly done using an automatic-scan stereoplotter. Figures 5 and 6 show the artifacts that are generated by this method of digitization, for the DMA DTED and USGS DEMs, respectively. These systems are set up to automatically scan back and forth across the stereomodel while the operator attempts to keep a "floating dot" on the surface. The inherent time lag in the operator's response to a change in slope, combined with the reversed direction of adjacent scans causes a systematic artifact in the digitized topography visible as a "grain" in the data at full resolution (Figs. 5 and 6).

Study of varying resolutions of DEMs from North and South America and the Garm DMA DTED from Central Asia shows that the minimum spatial resolution necessary for the accurate interpretation of a morphotectonic feature such as a fault-generated mountain block depends on the degree of erosion, the amount of offset, and the along-strike length of the structure. An active, little eroded mountain bounding fault with significant offset and length can be detected on a DEM with an effective spatial resolution as crude as 5–10 points across the width of the uplifted block (about 500 m to 10 km for large structures), while accurate identification of the type and age of the underlying faulting requires data with at least 50–100 points per structure wavelength (25–500 m resolution). This indicates that efficient interpretation of topography for the tectonics and seismic potential of an area will require relatively high resolution DEMs, such as the DMA DTED data (~100 m grid) or higher resolution DEMs derived from stereo SPOT images (10–30 m grid).

References Cited

- Burtman, V.S., 1980, Faults of Middle Asia, *Am. J. Sci.*, v. 280, p. 725–744.
- Burtman, V.S., and G.Z. Gurariy, 1973, Character of folded arcs in the Pamirs and Tien Shan (from the geophysical data), *Geotectonics*, v. 3, p. 90–92.
- D.M.A., 1986, Defense Mapping Agency product specifications for Digital Terrain Elevation Data (DTED), *DMA Aerospace Center, DTED 2nd Ed.*, PS/ICD/200, 32 pp.
- Hamburger, M.W., W. Swanson, and I.L. Neresov, 1988, Seismicity and crustal structure within an active collisional orogen: Results from seismic networks in the Garm region, Soviet Central Asia, *EOS, Trans. AGU*, v. 69, no. 44, p. 1316.
- Isacks, B.L., Uplift of the central Andean plateau and bending of the Bolivian orocline, *J. Geophys. Res.*, v. 93, p. 3211–3231.
- Leith, W., 1982, Rock assemblages in Central Asia and the evolution of the southern Asian margin, *Tectonics*, v. 1, p. 303–318.

- Leith, W., and D.W. Simpson, 1986, Seismic domains within the Gissar-Kokshal seismic zone, Soviet Central Asia, *J. Geophys. Res.*, v. 91, p. 689–697.
- Leith, W., and W. Alvarez, 1985, Structure of the Vakhsh fold and thrust belt, Tadjik SSR: An application of Landsat imagery to continuous-structure mapping, *Geol. Soc. Amer. Bull.*, v. 96, p. 875–885.
- Molnar, P., T. Fitch, and F. Wu, 1973, Fault plane solutions and contemporary tectonics in Asia, *Earth Planet. Sci. Lett.*, v. 9, p. 101–112.
- Ni, J., 1978, Contemporary tectonics in the Tien Shan region, *Earth Planet. Sci. Lett.*, v. 41, p. 347–354.
- Pavlis, G.L., M. Eneva, M.W. Hamburger, and I.L. Neresov, 1988, Aftershock properties in the Garm region, USSR, *EOS, Trans. AGU*, v. 69, no. 44, p. 1316.
- Trifonov, V.G., 1978, Late Quaternary tectonic movements of western and central Asia, *Geol. Soc. Amer. Bull.*, v. 89, p. 1059–1072.
- U.S.G.S., 1986, Standards for digital elevation models, *U.S. Geol. Surv. National Mapping Division, Open-File Report 86-004*, 41 pp.
- U.S.G.S., 1987, Digital elevation models, *U.S. Geol. Surv. National Mapping Program, Technical Instructions, Data Users Guide 5*, 38 pp.

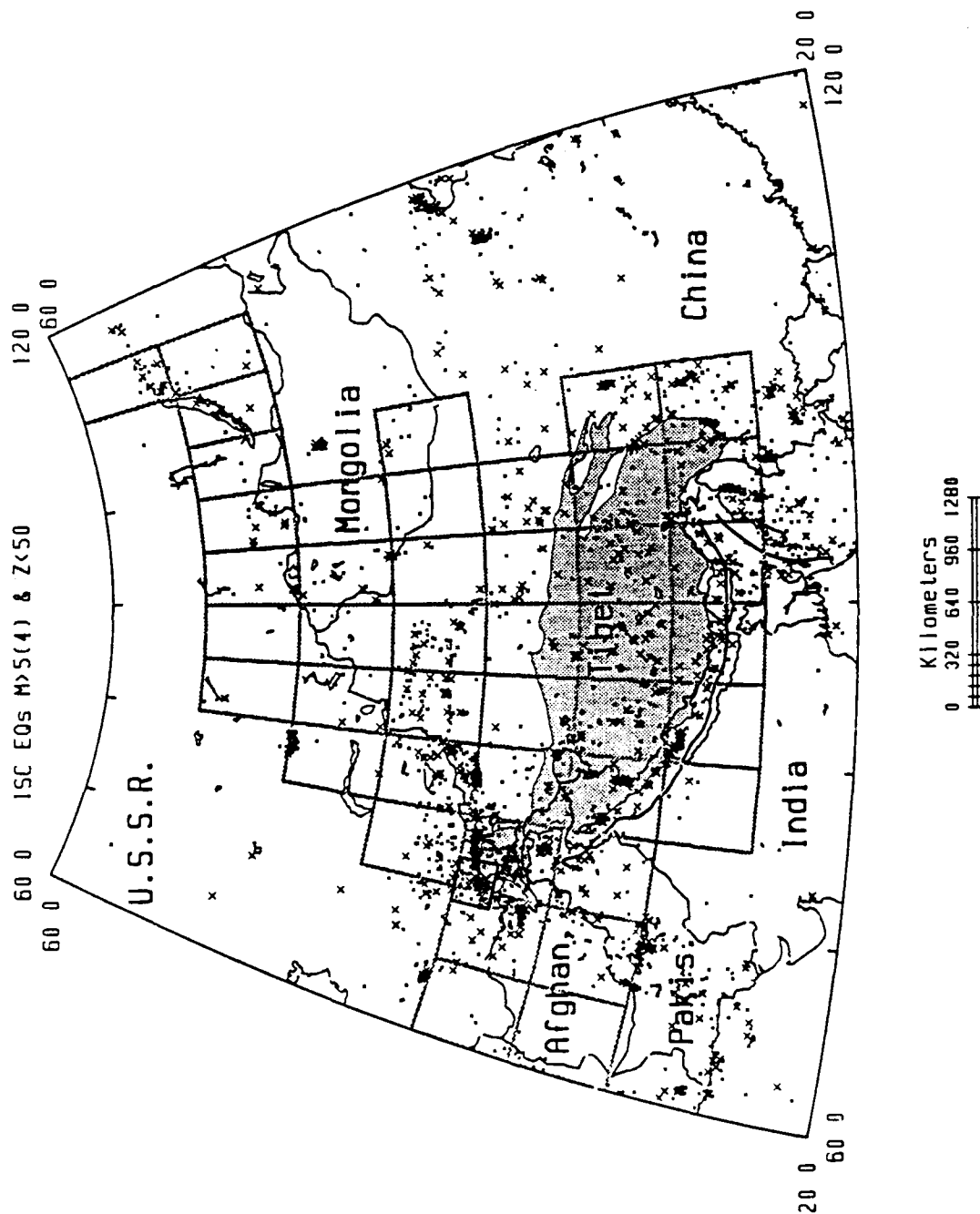


Figure 1: Seismotectonic map of Central Asia, showing area of Tibet and Himalaya orogen above 5 km elevation (gray fill) and shallow earthquakes (<50 km depth) with magnitudes (m_b) greater than 5 (large X's) and greater than 4 (small x's) from the ISC catalog (1964-1982). Thick black line shows thrust front of Himalaya. International boundaries and coastlines of oceans and lakes are shown as thin medium gray lines. Large gray line boxes show area of digital topography requested, Black line box shows digital topography used for preliminary analysis described here (Figs. 3-5), covering area of Tadjik SSR including Garm. Note high seismicity in this region (see also Fig. 2).

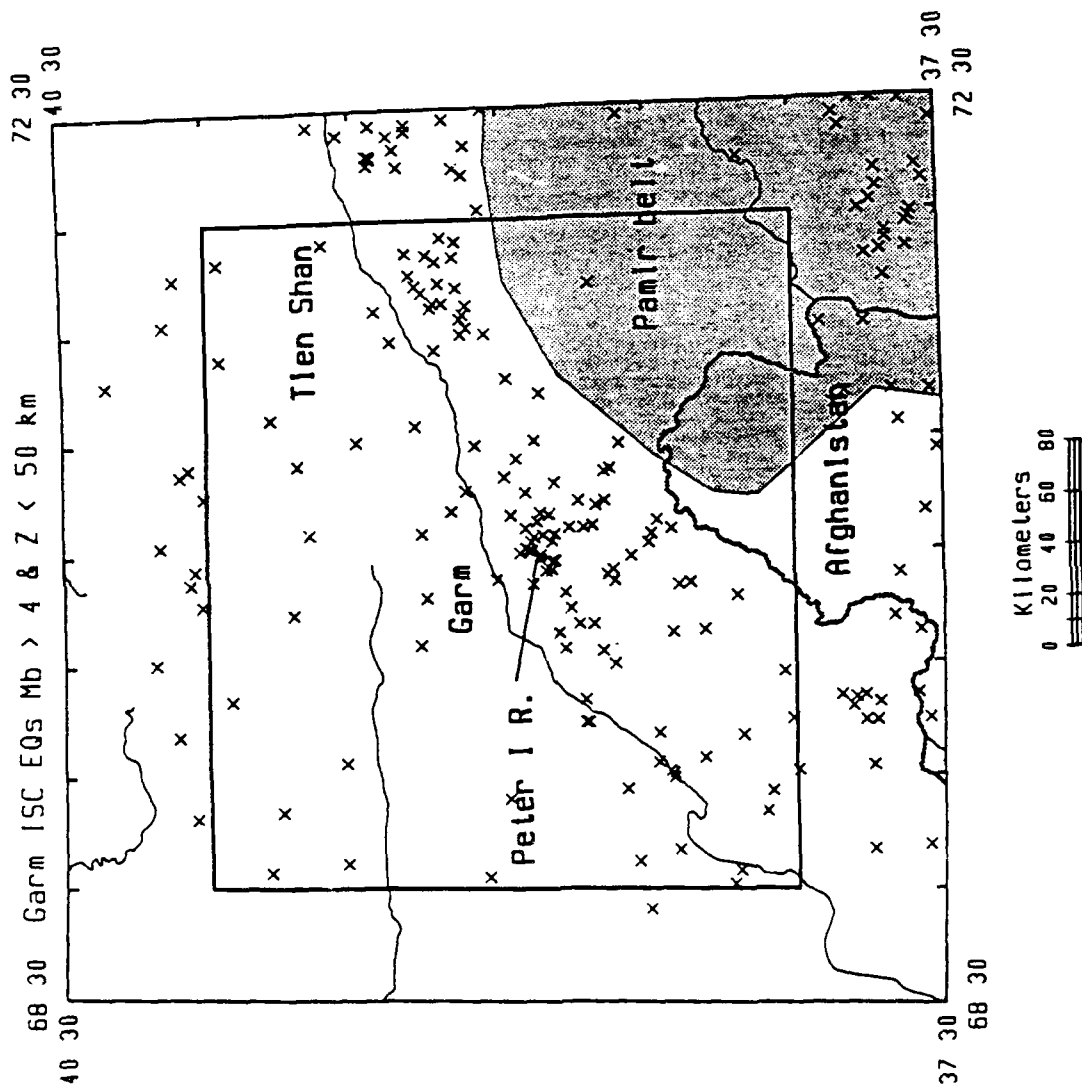


Figure 2: Seismotectonic map of Garm area, showing area of Pamir belt roughly above 5 km elevation (gray fill), and shallow earthquakes with m_b greater than 4 from the ISC catalog (1964-1982) (x's). Thick black line box shows area covered by digital elevation model (DEM) shown in Figs. 3-5. High concentration of seismic events in center of area occur under Peter I Range, part of active Vakhsh thrust belt between Tien Shan and Pamirs. Thin black lines mark rivers.

Vertical Exag. = 1.5
Subsampling = 10
garm_mosaic(1,2400010,1,3600010)



Figure 3: Moderate resolution synthetic 3D perspective view of $2^{\circ} \times 3^{\circ}$ Garm area DEM, viewed from the south looking northward with simulated lighting from the NW. This view is at reduced resolution (~ 1 km), created by taking every 10th point of the full resolution DEM. Note the light colored swath (due to NW facing slopes) running SW-NE across the scene which roughly corresponds to the active Vakhsh thrust belt and seismically active area. Other probably fault-controlled river valleys are visible in the Pamirs (SE corner) and Tien Shan (NW corner).

Vertical Exag. = 1.000000
Subsampling = 1
gara_mosaic(1.100,1.100)



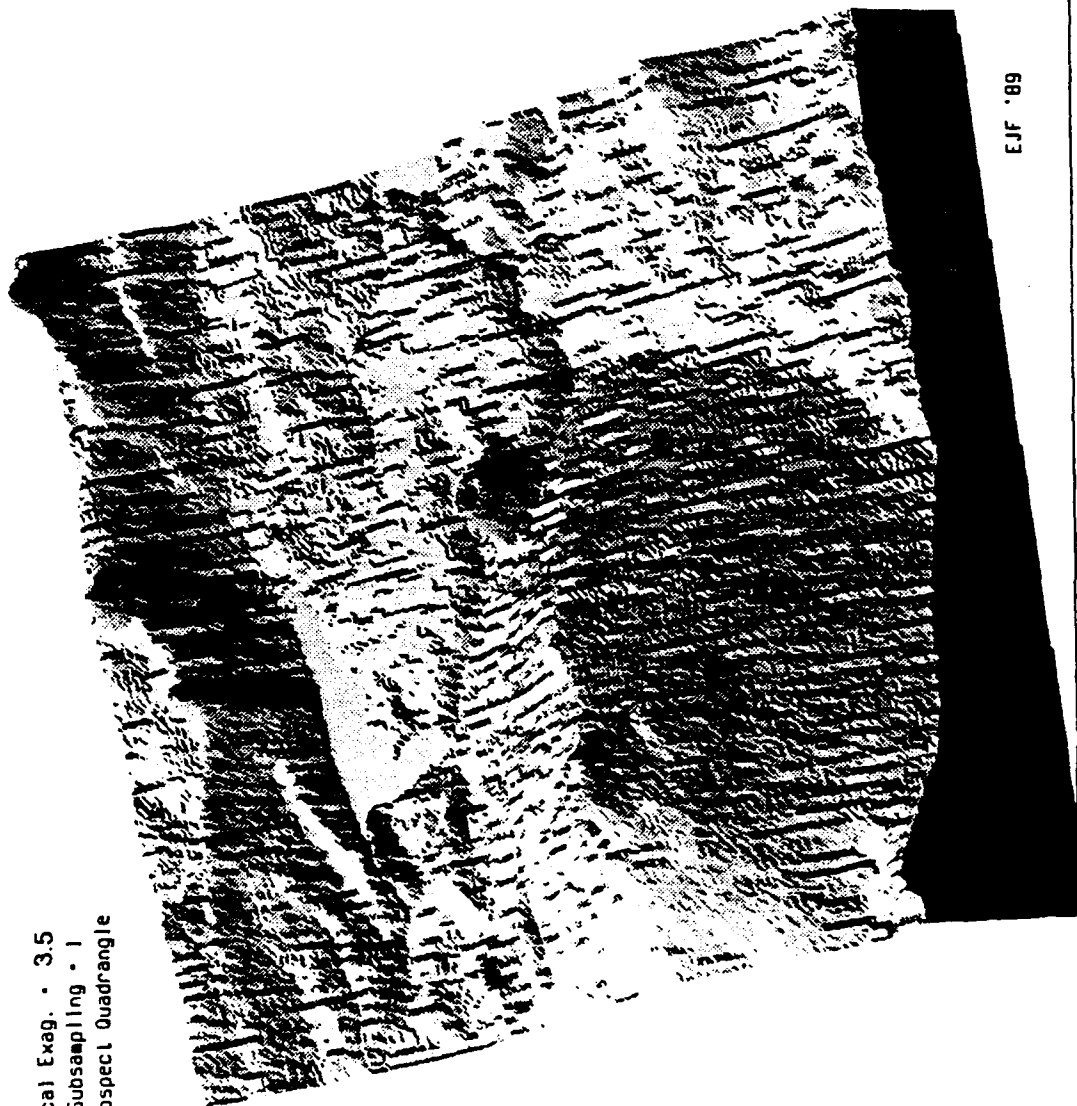
Figure 4: Full resolution synthetic 3D perspective view of area at the SW corner of the Garm area DEM, approximately 10 km on a side. View is from the SSW, with simulated lighting from the SE. This view is at the full resolution of the DMA DTED, approximately 100 m grid. Compare to Fig. 5 which has different rendering parameters for same area. This view enhances the NNE-SSW trending structures (faults and folds) of this area.

Vertical Exag. = 0.500000
 Subsampling = 1
 gamma_sosatc(1,100,1,100)



Figure 5: Full resolution synthetic 3D perspective view of same area as Fig. 4, approximately 10 km square, 100 m resolution. View is from the SSW, with simulated lighting from the NE. Vertical exaggeration is one-half that of Fig. 4. This view enhances the digitization artifacts, visible as a high-frequency grain of small ridges trending roughly E-W especially on the W side of the view.

Vertical Exag. - 3.5
 Subsampling - 1
 Prospect Quadrangle



EJF '89

Figure 6: High resolution synthetic 3D view of USGS DEM from Prospect Peak, CA. This view is from 30 m grid data about 4.5 km wide, viewed from the W with simulated lighting from the NE (upper left of figure). Visible are several volcanic scoria cones and a lake dammed by a lava flow. Note the strong digitization artifacts running E-W across the DEM.

BROAD-BAND STUDIES OF SEISMIC SOURCES AT REGIONAL AND TELESEISMIC DISTANCES USING ADVANCED TIME SERIES ANALYSIS METHODS

by Zoltan A. Der, Doug R. Baumgardt and Robert H. Shumway*

ENSCO Inc, 5400 Port Royal Road, Springfield, VA, 22151.

* Department of Statistics,
University of California at Davis,
Davis, CA.

ABSTRACT

This study involves the application of advanced multichannel signal processing techniques for improving capabilities for explosion source size estimation and discrimination. A multichannel deconvolution technique, developed earlier for extracting pP phases from teleseismic seismograms, is being extended to process regional seismograms. High-resolution array-processing techniques are being applied to short-period seismograms, preprocessed by deconvolution, to "image" explosion and shallow earthquake sources for depth estimation. A similar method is being applied to long-period seismograms from explosions in order to image the tectonic component, if present, and to separate it from the isotropic component of the seismogram. Finally, investigation of regional phases Sn and Lg, recorded regionally and teleseismically in the Soviet Union, have shown that propagation effects (blockages, scattering, anelastic attenuation) must be considered when using Sn and Lg amplitude measurements for discrimination and yield estimation.

INTRODUCTION

The overall goal of this research is to utilize advanced signal processing techniques for improved characterization of seismic sources at both regional and teleseismic distances.

A first major objective is to apply high resolution array processing methods to source imaging for the purpose of estimating depth of focus for shallow events and strain release for explosions. The second objective is to obtain a better understanding of the propagation of high-frequency seismic waves in the Soviet Union, how they are scattered and blocked by geological heterogeneities, and determine how this knowledge can be used to improve our capabilities in regional event identification and yield estimation.

The specific tasks that we will address in this paper include the following:

- (1) Application of multichannel deconvolution regional and combined regional and teleseismic data for the extraction source characteristics.
- (2) Development of source imaging techniques for depth determination and the identification and removal of strain release effects on long-period seismograms.
- (3) Empirical study of regional phase propagation in the Soviet Union, including the investigation of scattering and blockages caused by geological heterogeneities.

MULTICHANNEL DECONVOLUTION

Deconvolution methods belong to the general category of "appraisal" techniques that seek to derive source characteristics using a statistical approach rather than direct modelling. The advantage of such methods is that it is possible to obtain statistical bounds on the accuracy of results while in the case of direct modelling such are not available.

Recent application of such techniques by us and other groups led to a better understanding of the source characteristics of nuclear explosions (Der et al, 1987; McLaughlin et al, 1987). Strong variations in the pP parameters were found for various test sites, often explainable by topography and source depth variations. In this work we are applying these techniques to seismic recordings of nuclear tests at some test sites we have not studied before. These include Amchitka and some of the PNE sites.

Originally the multichannel deconvolution techniques were applied to arrays and test sites both concentrated in a small area. Later work by us and some previous studies by others have shown that the technique may be applied to networks and tests distributed over wider areas such as the RSTN stations. This represents an extension of the applicability of these techniques. Therefore, in this study, we shall do joint deconvolutions of stations over larger areas such as the RSTN and SRO networks. Moreover we shall test the feasibility of joint deconvolutions of regional and teleseismic data. Generally speaking the Green's functions for teleseismic P are simple, while they are extremely complex for regional signals. By doing joint deconvolutions we may be able to extract the same information from regional data as from teleseismic P. Complications will arise because of the fact that the observable frequency ranges of regional and teleseismic data do not completely overlap and because of the takeoff angles of P are different. The deconvolution results can be used as a direct input to the generalized array processors described below.

APPLICATION OF HIGH-RESOLUTION ARRAY PROCESSING TO SEISMIC SOURCE IMAGING

Overall Methodology. The mention of array processing evokes the image of conventional seismic arrays like NORSAR, LASA or NORESS. There has been a lot of research on processing data from such arrays. Generally speaking early work was somewhat disappointing. Major gains in S/N ratio anticipated were not realized and the computer technology was not advanced to a stage where marginal gains could be economically justified. Moreover, the limited understanding of the nature of seismic signals and the background noise was another cause of the failures of these early efforts. We know now that the background noise is strongly non-stationary and the signals are severely modified by site transfer functions leading to "signal loss". Fortunately these transfer functions are deterministic, not random, and can be estimated from the data and incorporated into the array processing.

In the work that we are pursuing we use the term array both in the conventional and generalized sense. A generalized array may be a set of SRO stations or a set of AWRE arrays located at various distances from a source region to be investigated. We shall assume that each array element is convolved with a complex but known "site" transfer function F . Let us examine, for instance, how we can define some "high resolution array beams" for such an array.

We want to minimize the output power P for the filter X (a row vector) that passes the signal with predefined characteristics without any distortion (such as signals of a certain type or coming from a given location of the source region)

$$P = X S X^*,$$

where S is the input power spectral matrix containing all the information about input signals, desired or undesired, and noise, where $*$ denotes conjugate transpose. We impose the constraint that the desired signal is passed undistorted

$$XF = 1,$$

where F is a column vector of complex medium responses and we obtain

$$X = \frac{F^* S^{-1}}{F^* S^{-1} F}.$$

The output power of this filter becomes in the FK analysis case

$$H(\vec{k}) = 1 / [F^* S^{-1} F].$$

This is the well-known Capon (1969) estimator for F-K spectra for the case of a conventional array. It can be modified easily to construct energy countours of the source in space (an image) with the proper choice of the transfer functions F as we shall show below. Moreover the results can be stacked over frequency to form *broad-band images*.

Alternative high resolution "beam" techniques and likely more robust ones are also available for such applications. When modified for the application we have in mind, the estimator of Shumway (1988) has the form

$$H = \frac{\frac{F^* S F}{F^* F}}{(\text{tr} S - \frac{F^* S F}{F^* F})}.$$

Unlike Capon's estimator which is hard to quantify, this estimator has an F distribution, which is eminently suitable for testing the results for statistical significance thus enabling us to explore inversions of seismic data quantitatively, a feature that is much needed in seismology today. This formula also avoids the use of matrix inversion and the necessary addition of a white noise component to the spectral matrix. The numerator in this expression is the normalized conventional (Bartlett) beam and the denominator is the power in the inputs unaccounted for in the beam. Naturally the numerator could be used alone as an estimator, but it has some very undesirable sidelobes.

We now discuss how we are using these estimators for imaging seismic sources.

Source Imaging by Utilizing Body Waves. Let us assume that we have some deconvolved P waves which have been purged of the site effects. For the simplified case of an explosion source, we can write the transfer functions F as

$$F_i(\omega) = G_i(\omega) \exp(j \omega \hat{k}_i \mathbf{x} / c_i),$$

where \hat{k}_i is a unit vector associated with the wavenumber vector, and c_i is the phase velocity both appropriate to the P wave arrival at the station i and \mathbf{x} is a position vector over which we map the output power.

$$G_i(\omega) = 1 - R_i \exp(j \omega \delta t_i).$$

In this expression R_i is the surface reflection coefficient and δt_i is the pP time delay appropriate to pP waves at station i .

In Figure 1 we show broad-band images, constructed using Capon's estimator and stacked over five frequencies, of a hypothetical seismic source region in an elastic half space for simplicity. The images were done for various assumed source depths, where the correct assumed depth was 1.5 km. We can see that the maximum occurs at the correct depth, and we can also obtain some estimate of the resolving capability of the technique. The synthetic P+pP combinations used in deriving these images are shown in Figure 2. The azimuths and phase velocities appropriate to each "station" are shown to the right of this figure. Such methods will obviate the need for visual evaluation of pP "moveout" but would produce a direct estimate of pP parameters and the statistical significances thereof.

Source Imaging by Utilizing Surface Waves. Assume now that we have a collection of surface waves, at various distances and azimuths from a test site. The transfer functions F may be written as

$$F_i(\omega) = P_i(\omega) R_i(\omega) \exp(k \mathbf{x} / c(\omega)),$$

where $P_i(\omega)$ is the path response function, $R_i(\omega)$ is the radiation pattern appropriate to station i for the given source type and $c(\omega)$ is the phase velocity in the source region.

In Figure 3 we show some source images obtained for explosions and a double couple assuming the F transfer functions for each type and thus constructing a "truth table". If we assume the wrong F we get very little output, while with the correct transfer functions we get a spike.

In practical cases the transfer functions can be derived from recordings of an explosion with small strain release, and thus we would be able to extract the same component from all the events in the area. Alternate techniques may also be used to obtain an estimate of the "pure explosion" transfer functions from data. This way it is not necessary to use "path corrections" and the technique can be applied using a few "master events". The distortion of the waveforms due to various positions of the events in the test site is accounted for by the exponential in the formulas above (von Seggern 1972).

We have assembled data from the Shagan test site to test this method. The examples shown use Capon's (1969) technique. We shall implement Shumway's method also. There are

other methods such as that of Brillinger (1985) are also worth considering. Similar techniques are being explored in underwater acoustics (Baggeroer et al 1988). For high noise cases the diagonal reconstruction techniques for spectral matrices can be adopted (Smith et al 1989).

INVESTIGATION OF REGIONAL PHASE PROPAGATION IN EURASIA

This research addresses various aspects of regional phase propagation which have important consequences for seismic testban treaty monitoring, principally in the areas of event identification and yield estimation. The term regional has usually designated phases which propagate primarily in the crust and are most commonly observed at seismic stations at distances of 2000 km or less from seismic sources. The most important regional seismic phases include Pn, Sn, Lg, and Rg. Although these phases are the most important phases at regional distances, they are known to propagate in shield regions at distances much beyond 2000 km.

Lg Propagation. One of the most important phases is Lg, which in some regions has been observed to propagate to distances of 5000 km and beyond (e.g., see Figure 6). Teleseismic Lg has been assessed as a method for estimating precise yields at test sites in the Soviet Union (eg, Baumgardt, 1984; Ringdal and Hokland, 1987; Ringdal and Fyen, 1988). In order to transport an Lg yield curve from one test site to another, propagation effects need to be taken into account.

Many studies have demonstrated that Lg can be partially or completely eliminated by heterogeneities in tectonic and geologic structure. The blockage of Lg to the stations in southern Eurasia have been observed by Ruzaiкин et al (1977), Kadinsky-Cade et al (1981), and Ni and Barazangi (1983) and has been attributed to variations in crustal structure or low Q in the crust. Baumgardt (1985b, 1986) has observed partial and complete blockages of Lg along propagation paths in the northwestern Soviet Union which seem to relate to sudden variations of the sediment thicknesses which Lg encounters as it propagates in and out of sedimentary basins within the Russian platform.

Scattering from tectonic heterogeneities may also affect Lg excitation. Baumgardt (1985a) has suggested that sudden bursts in the pre-Sn coda from Shagan River explosions recorded at NORSAR which may be P waves produced by Lg to P scattering in the Ural Mountains (See Figure 5). Baumgardt (1985b) has studied other Lg propagation paths from PNE explosions. Lg propagation paths which cross the Urals show elevated pre-Sn coda levels and reduction in the Lg level compared to those which do not.

Another possible scattering mechanism is Lg to Sn and Sn to Lg scattering. Studies by Isacks and Stephens (1975), Chinn et al (1980), and Ni and Barazangi (1983) have revealed on regional seismograms so-called "early Lg" phases in the Sn coda, which arrive several seconds ahead of the 3.5 km/sec group-velocity arrival time. In many of these cases, there was no apparent arrival at expected Lg arrival time, which suggested that Lg may have been blocked. Thus, they have concluded that the "early Lg" phases may be Sn-to-Lg mode conversions at geologic discontinuities, such as coastlines.

Figure 4 shows a possible example of Sn-to Lg conversions for a Novaya Zemlya explosion recorded on the intermediate band on the center three-component broadband instrument at NORESS. The arrival times of expected phases, including Sn and Lg are indicated. There are a number of arrivals between Sn and Lg, one of which is probably PcP, as indicated. However, the strong phase labelled E is a shear wave because it has a large transverse component. This phase is too early to be the Lg phase, which, as pointed out by Baumgardt (1987), is weakly recorded at NORESS from Novaya Zemlya. The time delay between the E phase and Sn of 100 seconds is consistent with a Sn-to-Lg conversion point at the coastline of the Kola Peninsula and the Barents Sea, as shown on the map in Figure 4. Baumgardt (1987) has also shown these phases on short-period incoherent beam traces recorded at NORSAR and NORESS from Novaya Zemlya explosions. Also, Baumgardt (1987) has suggested that Lg is weakly recorded at NORSAR and NORESS because of thick sediment accumulations in the Barents Sea.

Another possible example is the strong Sn coda observed from Shagan River explosions at NORSAR, as shown in Figure 5. This coda may have been produced by Sn-to-Lg and/or Lg-to-Sn conversions in the Urals, corresponding to the Lg-to-P conversions proposed by Baumgardt (1985a) to explain the strong pre-Sn coda. The brackets in Figure 5 show the expected arrival times of these phases, which encompass the peak-amplitude portion of the Sn coda.

Propagation Effects on Relative Sn and Lg Amplitudes. The discussion above has shown that Lg amplitudes can be strongly affected by blockages and significant amounts of Sn energy can be converted to Lg. This shows that the relative balance between the Sn and Lg energy observed at a station will be strongly affected by propagation effects. Inasmuch as the relative amount of compressional (Pn, Pg, teleseismic P) and shear (Sn, Lg) wave energy observed on regional seismograms may be used in discrimination of earthquakes and explosions, these effects must be understood and accounted for in discrimination.

In addition to blockages and scattering, anelastic attenuation has been considered to be an important propagation effect on regional phases. Baumgardt (1985b, 1987) studied Lg attenuation in the Russian Platform and concluded that the relative amplitudes of Sn and Lg did not seem to relate closely to Lg Q. The attenuation of Sn was not considered in those studies. However, because Sn likely propagates in the lid above the low-Q zone of the mantle, mantle attenuation may affect Sn more than Lg.

The seismograms in Figure 6 from an earthquake near the Afghanistan-USSR boarder are examples of how the tradeoffs between blockages on Lg and attenuation of Sn can profoundly affect the relative amounts of Sn and Lg energy observed at a station. The top two seismograms, from the SRO stations, KAAO in Afghanistan and SHIO in India, at distances of 1500, and 1890 km, respectively, show poorly recorded Lg waves from the earthquake because of blockages in the Himalayas and the Tibetan Plateau. However, Sn is well recorded at these stations. On the other hand, Lg is clearly observed at the GRFO station in West Germany at the much greater distance of 5400 km, but there are no apparent Sn arrivals. Evidently, Sn is completely attenuated along the path from the earthquake to GRFO, which crosses the northern parts of the Black and Caspian Seas, possibly because of low Q in the upper mantle. However, since Lg propagates efficiently across this path, the crustal Q must be high and there are no major tectonic boundaries which might block or scatter Lg.

In this study, we will attempt to identify the primary tectonic and geological factors which significantly block, scatter, or attenuate shear waves at regional and near regional distances in the Soviet Union. We hope that knowledge of these effects will allow us to calibrate and adjust measurements for these effects so that they can be used in seismic discrimination and yield estimation.

REFERENCES

- Baggeroer, A.B., Kuperman, W.A. and H. Schmidt (1988). Matched field processing: Source localization in correlated noise and optimum parameter estimation problem. *J. Acoust. Soc. Am.*, 83, 571-587.
- Barazangi, M., J. Oliver, and B. Isacks (1977). Relative excitation of the seismic shear waves Sn and Lg as a function of source depth and their propagation from Melanesia and Banda arcs to Australia. *Annali di Geofisica*, 30, 385-407.
- Baumgardt, D.R. (1984). Relative Lg and P-coda magnitude analysis of the largest Shagan River Explosions, SAS-TR-84-03, ENSCO, Inc., Final Report to AFOSR, Springfield, Va.
- Baumgardt, D.R. (1985a). Comparative analysis of teleseismic P and Lg waves from underground nuclear explosions in Eurasia, *Bull. Seism. Soc. Am.*, 71, 1413-1433.

- Baumgardt, D.R. (1985b). Attenuation, blockage, and scattering of teleseismic Lg from underground nuclear explosions in Eurasia, *AFGL-TR-85-0332*, ENSCO, Inc., Springfield, Va.
- Baumgardt, D.R. (1987). Spectral determination of regional and teleseismic Lg attenuation, *AFGL-TR-87-0217*, ENSCO, Inc., Springfield, Va.
- Capon, J. (1969), High resolution frequency-wavenumber analysis. *Proc. IEEE*, 57, 1408-1418.
- Brillinger, D.R. (1985), A maximum likelihood approach to frequency-wavenumber analysis. *IEEE. Trans. ASSSP*, 33, 1076-1085.
- Chinn, D.S., B.L. Isacks, and M. Barazangi (1980), High-frequency seismic wave propagation in western South America along the continental margin, in the Nazca plate and across the Altiplano. *Geophys. J.R. astr. Soc.*, 60, 209-244.
- Der, Z.A. (1970), Some data processing results for a vertical array of triaxial seismometers. *Geophysics*, 35, 337-343.
- Der, Z.A., Shumway, R.H., Lees, A.C. and E. Smart (1985b). Multichannel deconvolution of P waves at seismic arrays, *TGAL-85-4*, Teledyne-Geotech, Alexandria, VA.
- Der, Z.A., R.H. Shumway, and A.C. Lees (1987). Multichannel deconvolution of P waves at seismic arrays, *Bull. Seism. Soc. Am.*, 77, 195-211.
- McLaughlin, K.L., L.M. Anderson, and A.C. Lees (1987). Effects of local geologic structure on Yucca Flats, NTS, explosion waveforms: 2-dimensional finite difference calculations, *Bull. Seism. Soc. Am.*, 77, 1211-1222.
- Ni, J. and M. Barazangi (1983). High-frequency seismic wave propagation beneath the Indian Shield, Himalayan Arc, Tibetan Plateau and surrounding regions: high uppermost mantle velocities and efficient Sn propagation beneath Tibet, *Geophys. J.R. astr. Soc.*, 72 665-689.
- Ringdal, F. and B.Kr. Hokland (1987). Magnitudes of large Semipalatinsk explosions using P coda and Lg measurements at NORSAR, *NORSAR Sci. Rep. No. 1-87/88*, Kjeller, Norway.
- Ringdal, F. and J. Fyen (1988). Analysis of Grafenberg Lg recordings of Semipalatinsk explosions, *NORSAR Scientific Report No. 2-87/88*, Kjeller, Norway.
- Shumway, R.H. and Z.A. Der (1985). Deconvolution of multiple time series, *Technometrics*, 27, 385-393.
- Shumway, P.H. (1987), *Applied Statistical Time Series Analysis*, Prentice Hall.
- Smith, G.B., Feuillade, C., DelBalzo, D.R. and C.L. Byrne (1989), A nonlinear matched-field processor for detection and localization of a quiet source in noisy shallow water environment. *J. Acoust. Soc. Am.*, 85, 1158-1166.
- von Seggern, D.H. (1972), Relative location of seismic events using surface waves. *Geophys. J. R. A. S.*, 26, 499-513.

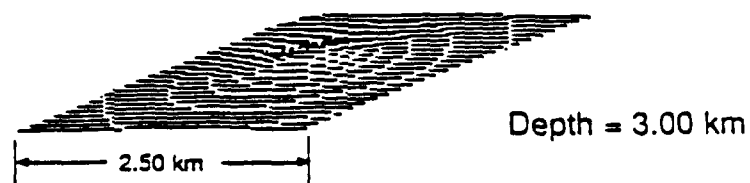
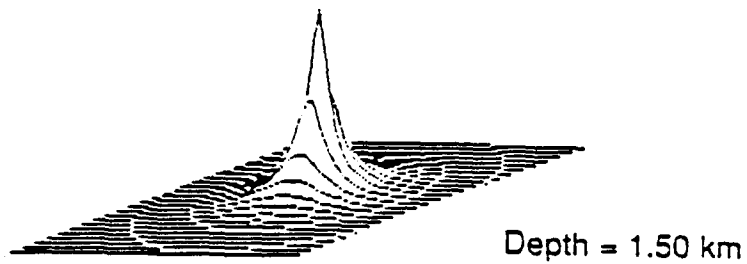
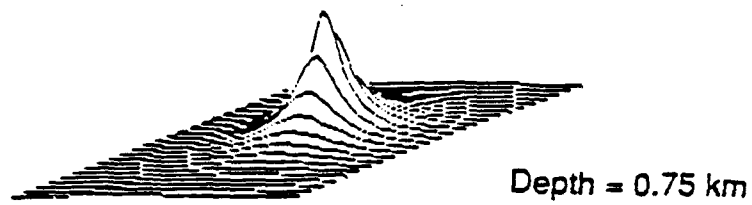


Figure 1 : Depth slices of the broadband image of a compressional source at 1.5 km depth. Each slice of the source region is 2.5 x 2.5 km. The maximum occurs at the proper depth and images do not contain major sidelobes.

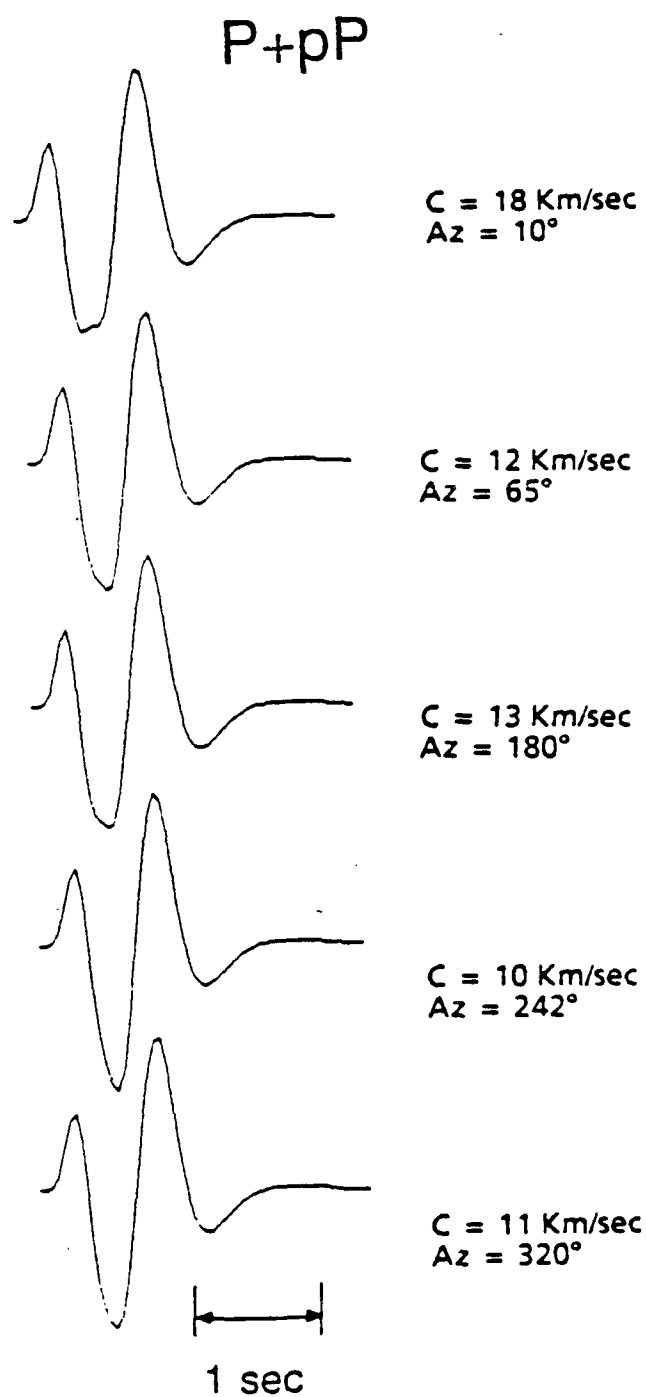


Figure 2: Synthetic P waves for five stations used in the simulations. The azimuths and apparent velocities for each station are shown on the right.

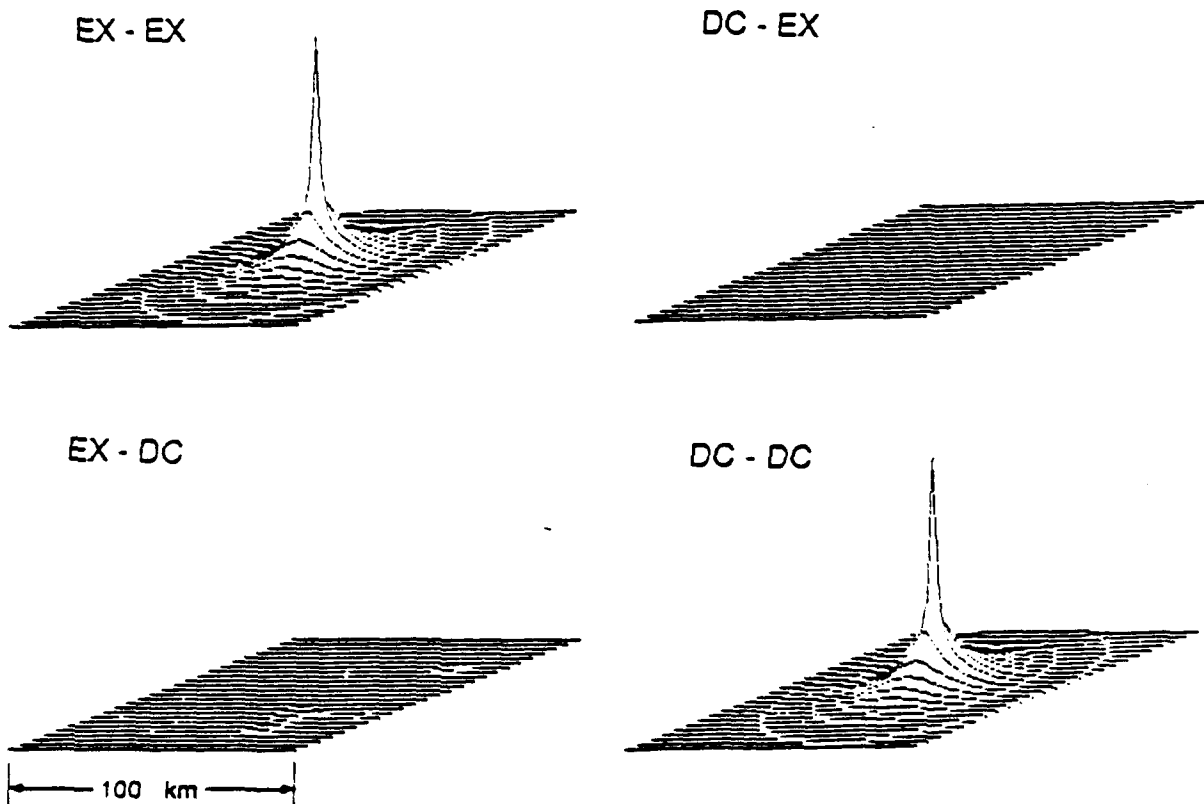


Figure 3: Broadband ambiguity diagrams (images) of sources constructed using surface waves from explosion and a double couple both at 1 km depth. The mismatches (DC-EX and EX-DC) have extremely low power, the matched outputs (EX-EX and DC-DC) are identical.

NOVAYA ZEMLYA EXPLOSION
AUGUST 2, 1987
LAT. = 73.3 N LONG. = 54.6 E

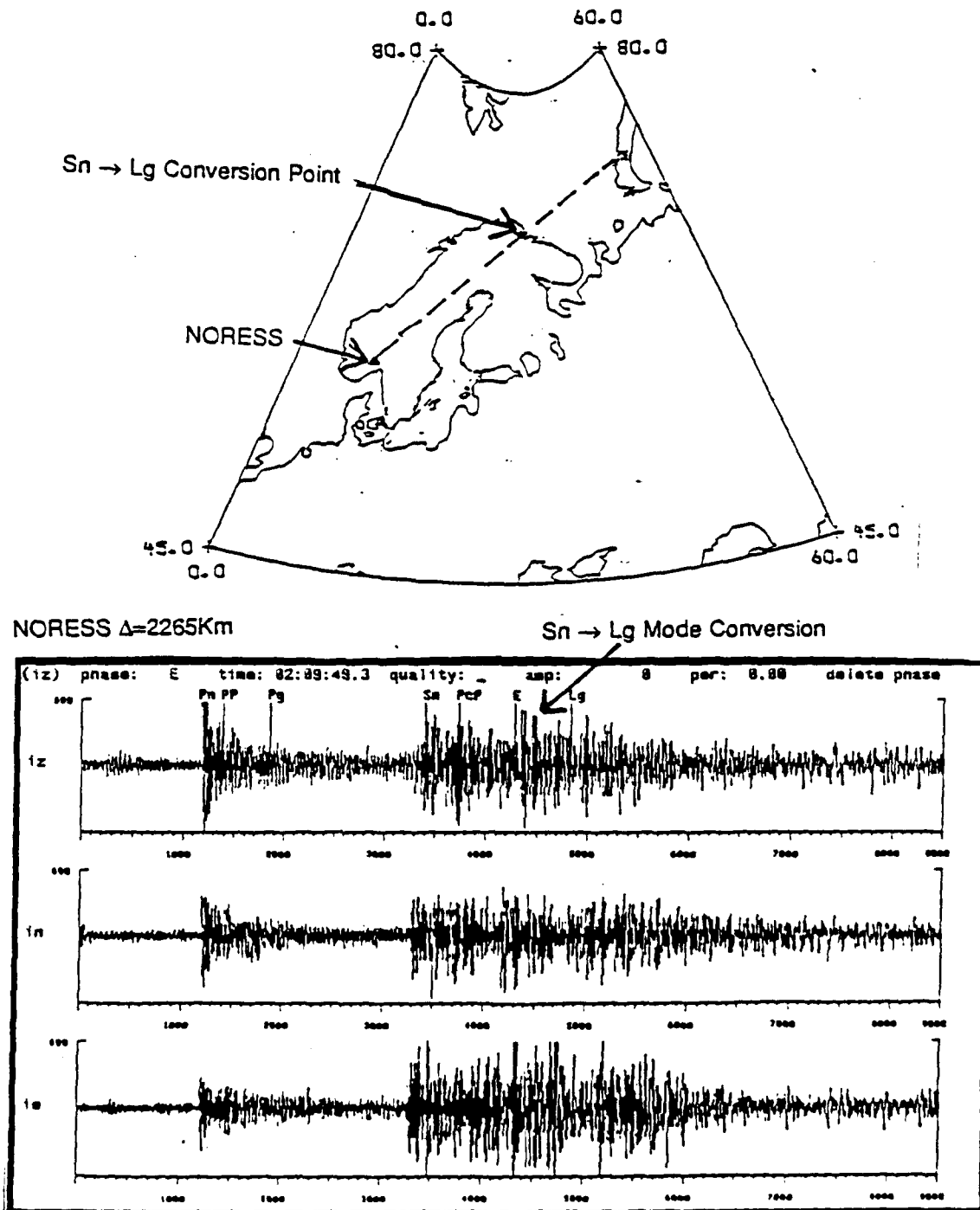


Figure 4: Intermediate band NORESS recordings of Novaya Zemlya explosion. Presumed mode conversion at coastline labeled with "E".

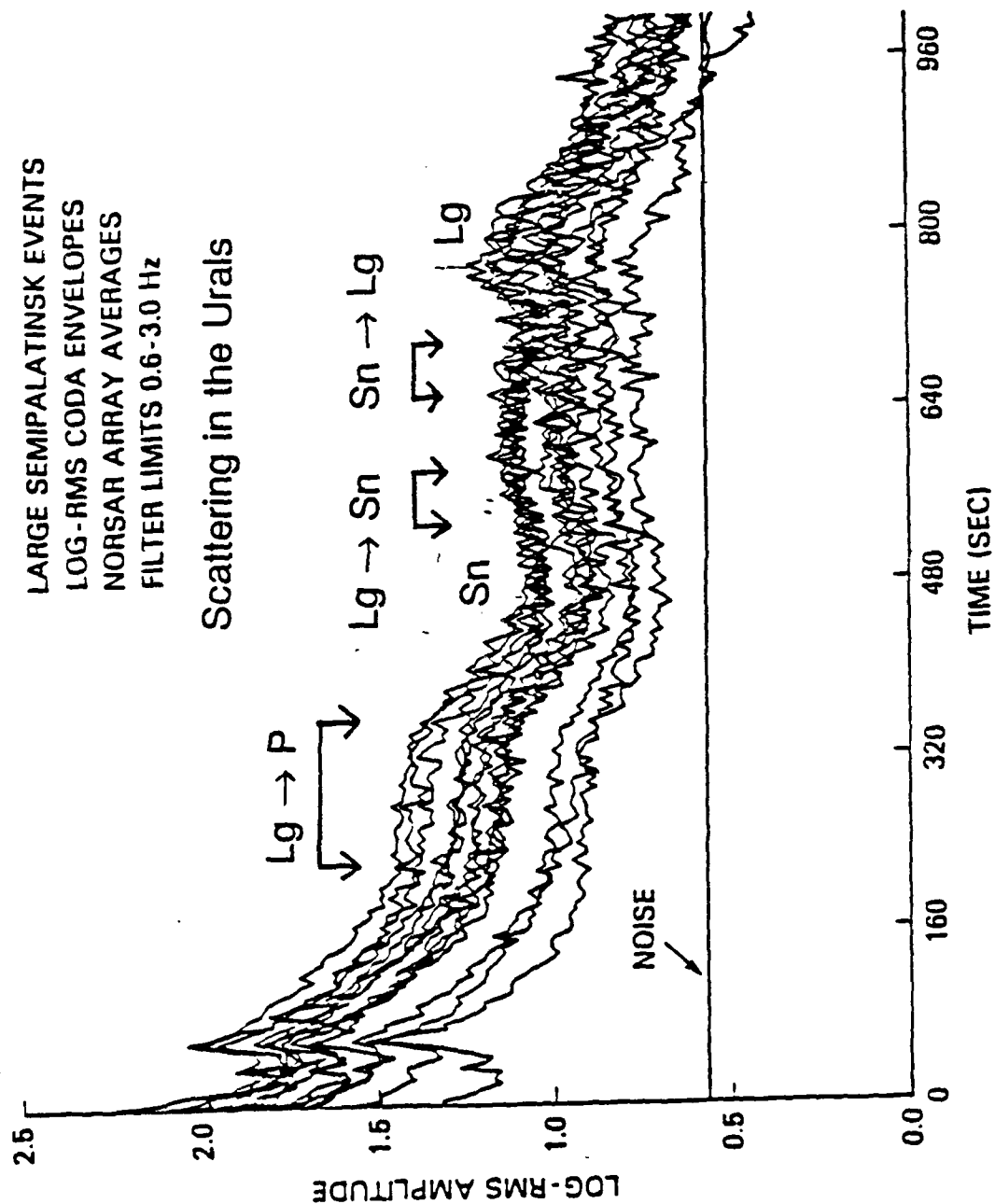


Figure 5: NORSAR incoherent beam envelopes for several Shagan River explosions showing presumed scattered phases from the Urals.

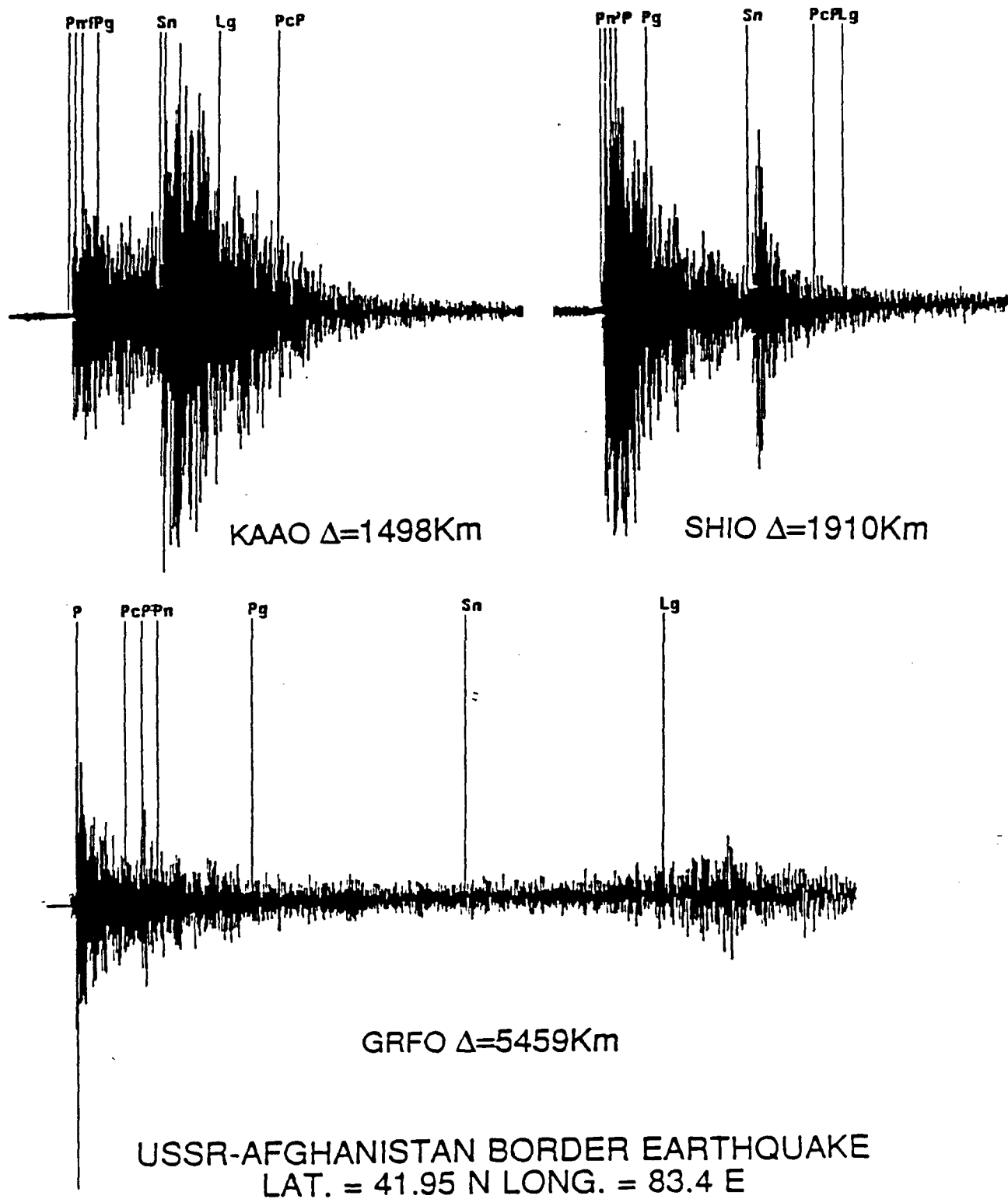


Figure 6: Seismogram for March 29, 1979 USSR - Afghanistan border earthquake. Note weak Lg at KAAO and SHIO, but strong Lg at GRFO.

Strain Amplitude Dependence of Seismic Attenuation and Nonlinearity

Karl B. Coyner
New England Research, Inc.
76 Olcott Drive
White River Junction, VT 05001

Objective

There is a pressing need for experimental stress-strain measurements on rocks in order to understand seismic nonlinearity and attenuation around large strain-amplitude events. Appeals to nonlinearity and a wide range of seismic Q factors are necessary in order to model the near-field displacements and velocities for events in granite, tuff, and salt lithologies (Minster and Day, 1986; McCartor and Wortman, 1988) or to explain the depth dependence of attenuation in the crust (Toksöz et al., 1988). Such appeals can be investigated, or at least bounded, by direct measurements on appropriate samples. The objective of this research is to experimentally and theoretically investigate those factors that affect attenuation in rock: strain amplitude, stress, saturation, lithology, and frequency. In this report the primary emphasis is on strain amplitude effects. In particular, the hysteresis loop technique has been used to measure attenuation as a function of strain amplitude from approximately 10^{-7} strain to almost 10^{-3} strain, clearly revealing the complete transition from linear to nonlinear attenuation, the dramatic increase in attenuation due to friction on cracks, and the limitation of crack closure as an upper bound on maximum attenuation at high strain amplitude.

Summary

Several repeated series of hysteresis loop attenuation measurements were conducted on a cylinder of room dry Sierra White granite approximately 15.2 cm in diameter and 50.8 cm long. The technique involved sinusoidally loading the sample in uniaxial compression with a servo-controlled press. Axial stress and strain were recorded with a precision load cell and a series of three LVDT displacement transducers, respectively (Fig. 1). The large sample size enabled extremely small strains to be measured: small strains over a large distance (approximately 45 cm) and across a large diameter resulted in

reasonably measurable displacements and forces. The sample was exposed to the atmosphere at room temperature and preloaded to 0.1 MPa axial stress. A 0.1 Hz sinusoidal axial force was applied to the sample end with the servo-controller operating in a force-feedback mode. Axial force and strain data were recorded for up to 512 cycles at low strain amplitudes and 16 cycles at high strain amplitudes with a PC-based A/D converter. Measurements were made at different strain amplitudes by varying the voltage of the sinusoidal signal driving the ram. The cycle minima were near zero stress and strain.

Attenuation was calculated from either the phase angle between stress and strain or the area of the hysteresis loops. At low strain amplitudes, the phase angle was calculated from phase spectra of the stress and strain data, where the hysteresis loop area was negligible. At high strain amplitudes, the fractional energy loss per cycle was calculated from the stress-strain data by dividing the area enclosed within the hysteresis loop, which is the energy dissipated during one cycle, by the integrated area beneath the loading section of the cycle, which is the energy introduced into the rock volume. The ratio, divided by two times pi, and corrected by multiplying by a factor of four (Coyner, 1988), is the extensional attenuation, or Q_E^{-1} .

A sequence of stress-strain data for Sierra White granite shows the effect of increasing strain amplitude on gross hysteresis loop shape (Fig 2). Nonlinear attenuation is evident in the nonelliptical loops and by the cusped ends. The shrinking sizes of the hysteresis loops at low strain amplitudes are also easily seen.

Figure 3 contains a summary of the Sierra White granite hysteresis loop attenuation data, in addition to data from resonant bar and ultrasonic experiments (Coyner, 1987), plotted as a function of log strain amplitude. The hysteresis loop measurements cover the broadest range of strain amplitudes, from almost 10^{-7} to 10^{-3} . Three features of the strain amplitude dependence are apparent in the hysteresis loop data: 1) the threshold from linear to nonlinear attenuation occurs at approximately $7 \cdot 10^{-6}$ strain, 2) there is a dramatic increase in attenuation above that threshold, peaking at approximately $200 \cdot 10^{-6}$ strain, and 3) attenuation decreases slightly above that maximum.

The transition from linear to nonlinear attenuation marks the impact of the frictional attenuation mechanism at higher strain amplitudes. The increase in attenuation can be interpreted as frictional loss at grain boundaries and crack surfaces in contact. A similar threshold and portions of the strain amplitude dependence have been previously observed and explained on this basis (Gordon and Davis, 1968; Brennan and Stacey, 1977; Mavko, 1979; Winkler et al., 1979; Johnston and Toksöz, 1980; Stewart et al., 1983; Tittmann, 1984). The present data, however, defines the strain amplitude dependence throughout the entire range in which frictional attenuation operates. The unique feature is the attenuation maximum at 200 microstrain. This peak can be explained by considering that the frictional mechanism is self-limiting. At these strains the cracks which give rise to attenuation are completely closed, and can contribute little more at higher strain amplitudes. This crack closure was directly observed by Batzle et al. (1980) at similar stresses and strains.

The frictional attenuation model requires that attenuation be linearly dependent on strain amplitude (Walsh, 1966; Mavko, 1979; Stewart et al., 1983). In Fig. 4 the hysteresis loops attenuations and the ultrasonic P and S wave attenuations are plotted as a function of strain amplitude on a linear scale. At less than 100 microstrain the relationship does indeed appear linear. The effects of crack closure are seen at higher strains, and the attenuation falls below the extrapolated linear relationship.

The decrease of attenuation above 200×10^{-6} strain in Fig. 3 is a result of the attenuation definition of fractional energy loss. At these large strains any small increase in energy loss is offset by the larger increase in energy stored during the sinusoidal loading, and the attenuation calculated from the ratio actually decreases. This decrease presumably continues with increasing strain amplitude until a large population of new cracks form in conjunction with brittle failure. For Sierra White granite this occurs at around 5000×10^{-6} strain.

The ultrasonic results in Figs. 3 and 4 indicate a similar strain amplitude dependence to the hysteresis loop results although the attenuation is higher. The same frictional mechanism occurs regardless of frequency. The resonant bar results are consistent with the hysteresis loop data at the lower strain amplitudes.

In Fig 5 the low strain amplitude results of these attenuation experiments (hysteresis loop, resonant bar, and ultrasonic pulse), plus the results of others on dry granite are plotted as a function of log frequency from 0.1 Hz to 1 MHz. Previous hysteresis loop measurements were made by Spencer (1981) on vacuum dry Oklahoma granite, and by Liu and Peselnick (1983) on room dry Westerly granite, as corrected by Coyner (1988). Previous resonant bar attenuation measurements were made by Tittmann (1984) and Johnston and Toksöz (1980) on Westerly granite, by Winkler et al. (1979) on Sierra White granite, and by Gordon and Davis (1968) on Tupper Lake granite.

At low frequencies, including the seismic band, room dry granite attenuations cluster between 0.008 and 0.010 (Q 's from 100 to 125). Pressure and crack-healing would decrease these attenuation values, while saturation would substantially increase them (Spencer, 1981). Much lower attenuations are recorded for vacuum dry Oklahoma granite (Spencer, 1981, $Q > 500$), consistent with the effects of volatiles on increasing attenuation (Tittmann, 1977; Clark et al., 1980). The highest attenuation factors are from the ultrasonic attenuation measurements. For room dry rocks, at low strain amplitude, there appears to be a monotonic increase in attenuation with frequency above approximately 50 kHz, although two different experimental techniques (resonant bar and ultrasonic) were used. The attenuation mechanism at these frequencies also includes a large component of scattering.

Conclusions and Recommendations

New opportunities exist for detailed laboratory investigations of rock attenuation through the use of servo-controlled testing machines. Precise stress-strain measurements can be made as a function of strain amplitude, frequency, stress, and saturation in configurations that closely mimic the near-field conditions. In particular, hysteresis loop attenuation measurements provide Q and nonlinearity data for samples subjected to cyclic uniaxial loading.

Experimental results at 0.1 Hz on room dry Sierra White granite indicate that the dependence of attenuation on strain amplitude follows a sigmoidal shaped curve with at least three distinct regions of behavior. Attenuation is linear, or independent of strain amplitude, and corresponds to a Q_r of about 125 at strain amplitudes below approximately $7 \cdot 10^{-6}$.

Above approximately 7×10^{-6} there is a transition into nonlinearity and attenuation is strongly strain amplitude dependent due to friction across crack surfaces. At about 200×10^{-6} the attenuation maximizes at a Q_E of approximately 28. The strain amplitudes are so large that the frictional attenuation mechanism is limited by complete crack closure, preventing any further increase in attenuation. At higher strain amplitudes attenuation actually decreases slightly as the increase in elastic energy stored during one cycle overcomes any additional energy loss. At strain amplitudes around 5000×10^{-6} for Sierra White granite new cracks form as the rock approaches failure, and a new region of nonlinearity and even higher attenuation occurs.

Recommendations include:

- (1) Experimentally investigate the strain amplitude dependence of attenuation in salt and tuff, plus any other appropriate lithologies or analogues.
- (2) Repeat the experiments with water-saturated samples.
- (3) Push the frequency band of the hysteresis loops up towards 100 Hz.

References

Batzle, M.L., G. Simmons, and R.W. Siegfried, Microcrack closure in rocks under stress: direct observation, J. Geophysical Research, 85, 7072-7090, 1980.

Clark, V.A., B.R. Tittmann, and T.W. Spencer, Effect of volatiles on attenuation (Q^{-1}) and velocity in sedimentary rocks, J. Geophys. Res., 85, 5190-5198, 1980.

Coyner, K.B., Attenuation measurements on dry Sierra White granite, dome salt, and Berea sandstone, final report to Lawrence Livermore National Laboratory, Contract #9092405, 1987.

Coyner, K.B., The definition and calculation of Q from phase angle and hysteresis loop attenuation measurements, Scientific Report No. 1 prepared for AFGL Contract No. F19628-87-C-0214, 1988.

Gordon, R.B., and L.A. Davis, Velocity and attenuation of seismic waves in imperfectly elastic rock, J. Geophys. Res., 73, 3917-3935, 1968.

Johnston, D.H., and M.N. Toksöz, Thermal cracking and amplitude dependent attenuation, J. Geophys. Res., 85, 937-942, 1980.

Liu, H.-P., and L. Peselnick, Investigation of internal friction in fused quartz, steel, plexiglass, and Westerly granite from 0.01 to 1.00 Hertz at 10^{-8} to 10^{-7} strain amplitude, J. Geophys. Res., 88, 2367-2379, 1983.

McCartor, G.D., and W.R. Wortman, Nonlinear constitutive relations at moderate strain, Proc. 10th Ann. DARPA/AFGL Res. Symp., 199-204, 1988.

McKavanagh, B., and F.D. Stacey, Mechanical hysteresis in rocks at low strain amplitudes and seismic frequencies, Physics of the Earth and Planetary Interiors, 8, 246-250, 1974.

Minster, J.B., and S.M. Day, Decay of wave fields near an explosive source due to high-strain, nonlinear attenuation, Journal of Geophysical Research, 91, 2113-2122, 1986.

Spencer, J.W., Stress relaxations at low frequencies in fluid-saturated rocks: Attenuation and modulus dispersion, J. Geophys. Res., 86, 1803-1812, 1981.

Stewart, R.R., M.N. Toksöz, and A. Timur, Strain dependent attenuation: observations and a proposed mechanism, J. Geophys. Res., 88, 546-554, 1983.

Tittmann, B.R., Internal friction measurements and their implications in seismic Q structure models of the crust, in The Earth's Crust: Monograph 20, AGU, 197-213, 1977.

Tittmann, B.R., Nonlinear wave propagation study, semi-annual technical report No. 2 for the period December 1, 1983 through May 31, 1984, SC5361.6SAR, Rockwell International Science Center, 1984.

Toksöz, M.N., E. Reiter, and B. Mandal, Seismic attenuation in the crust, Proc. 10th Ann. DARPA/AFGL Res. Symp., 127-134, 1988.

Walsh, J.B., Seismic wave attenuation in rock due to friction, J. Geophys. Res., 71, 2591-2599, 1966.

Winkler, K.W., A. Nur, and M. Gladwin, Friction and seismic attenuation in rocks, Nature, 277, 528-531, 1979.

TABLE 1. Strain amplitude, extensional velocity, resonant frequency, and attenuation of extensional resonant mode in various Nevada tuffs.

SAMPLE	STRAIN (microstrain)	VELOCITY (km/sec)	FREQUENCY (Hz)	ATTENUATION (1000/Q)
SNL WELDED	1.0	3.964	13563	1.10
SNL WEAK	1.0	2.210	5279	5.40
N TUNNEL	1.0	2.241	9337	8.13

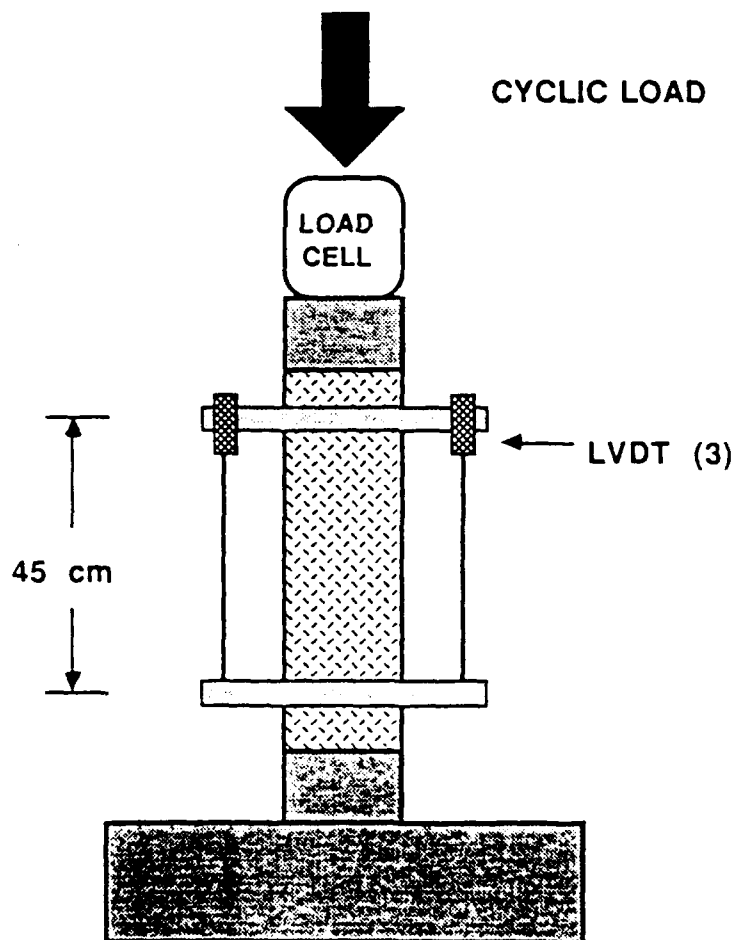


Figure 1. Schematic of experimental arrangement for low frequency hysteresis loop attenuation measurements.

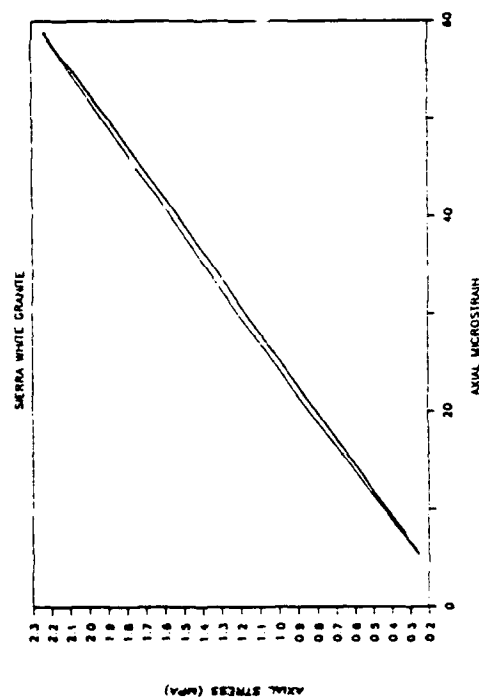
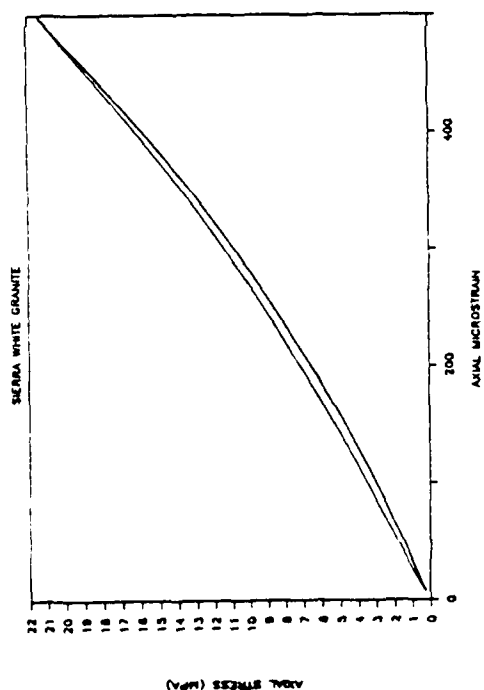
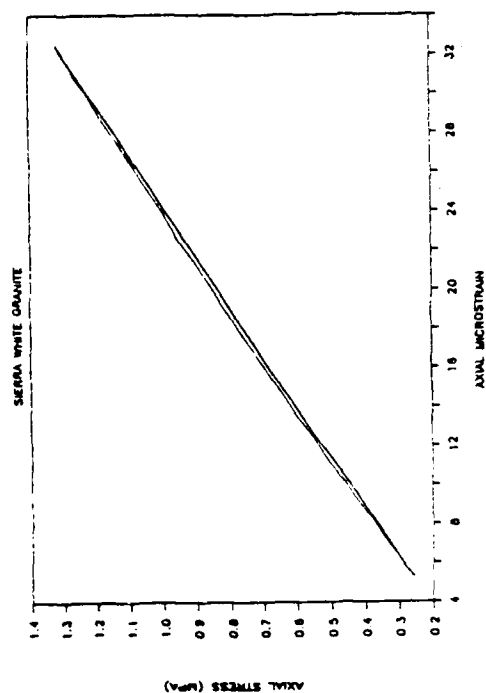
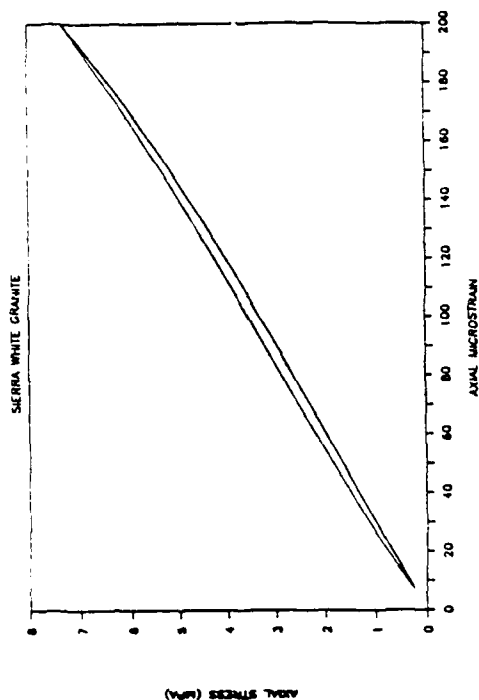


Figure 2. A suite of hysteresis loops for Sierra White granite are plotted as a function of strain amplitude. In the ninety-degree rotated orientation, loop amplitudes decrease from left to right, top to bottom, and correspond to maximum strain amplitudes of 491, 192, 53.5, and 27.2 microstrain.

SIERRA WHITE GRANITE ATTENUATION VERSUS LOG STRAIN AMPLITUDE

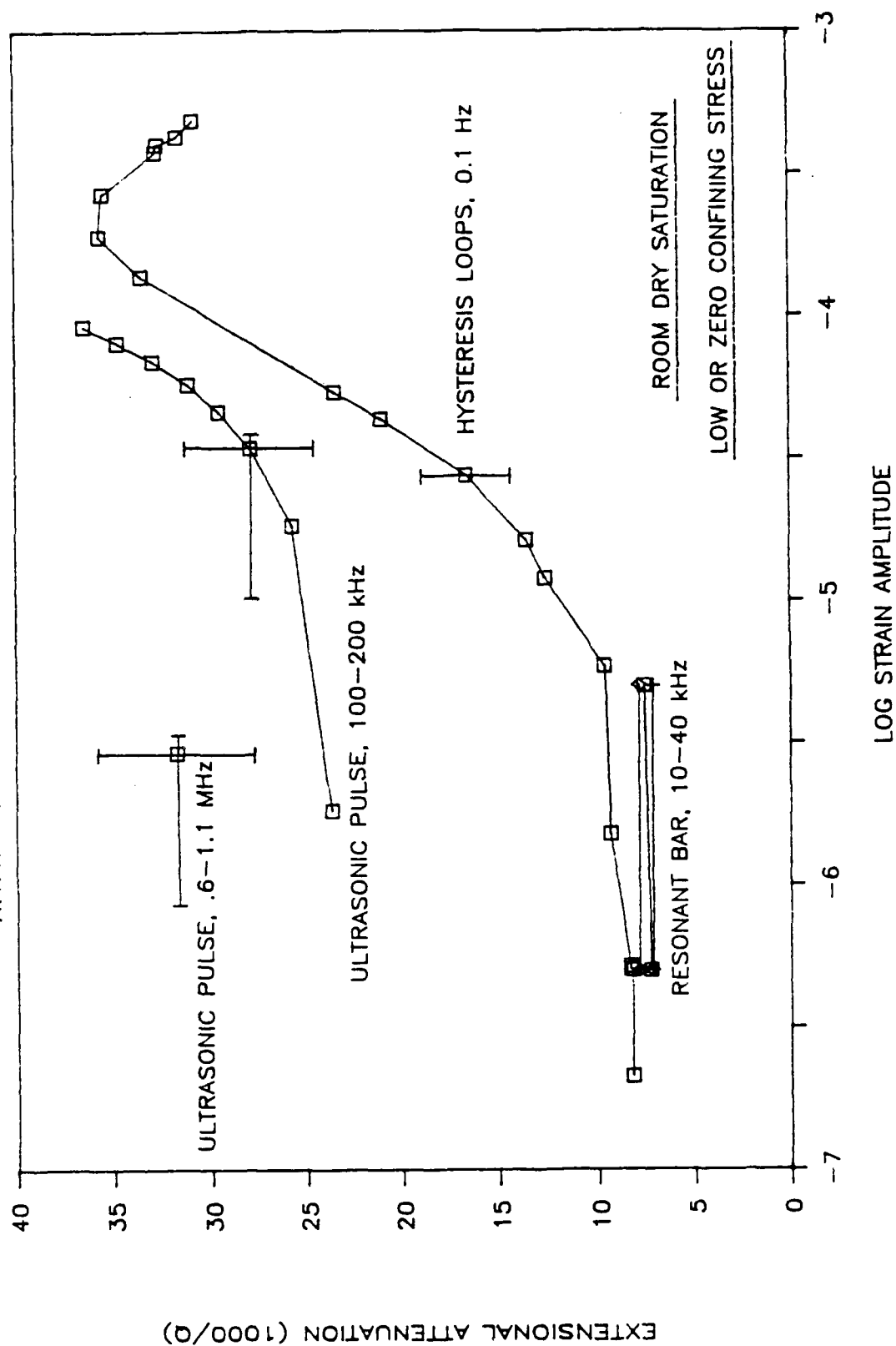


Figure 3. Summary plot of extensional attenuation factors determined with three experimental techniques versus log strain amplitude for room dry Sierra White granite.

SIERRA WHITE GRANITE

ATTENUATION VERSUS STRAIN AMPLITUDE

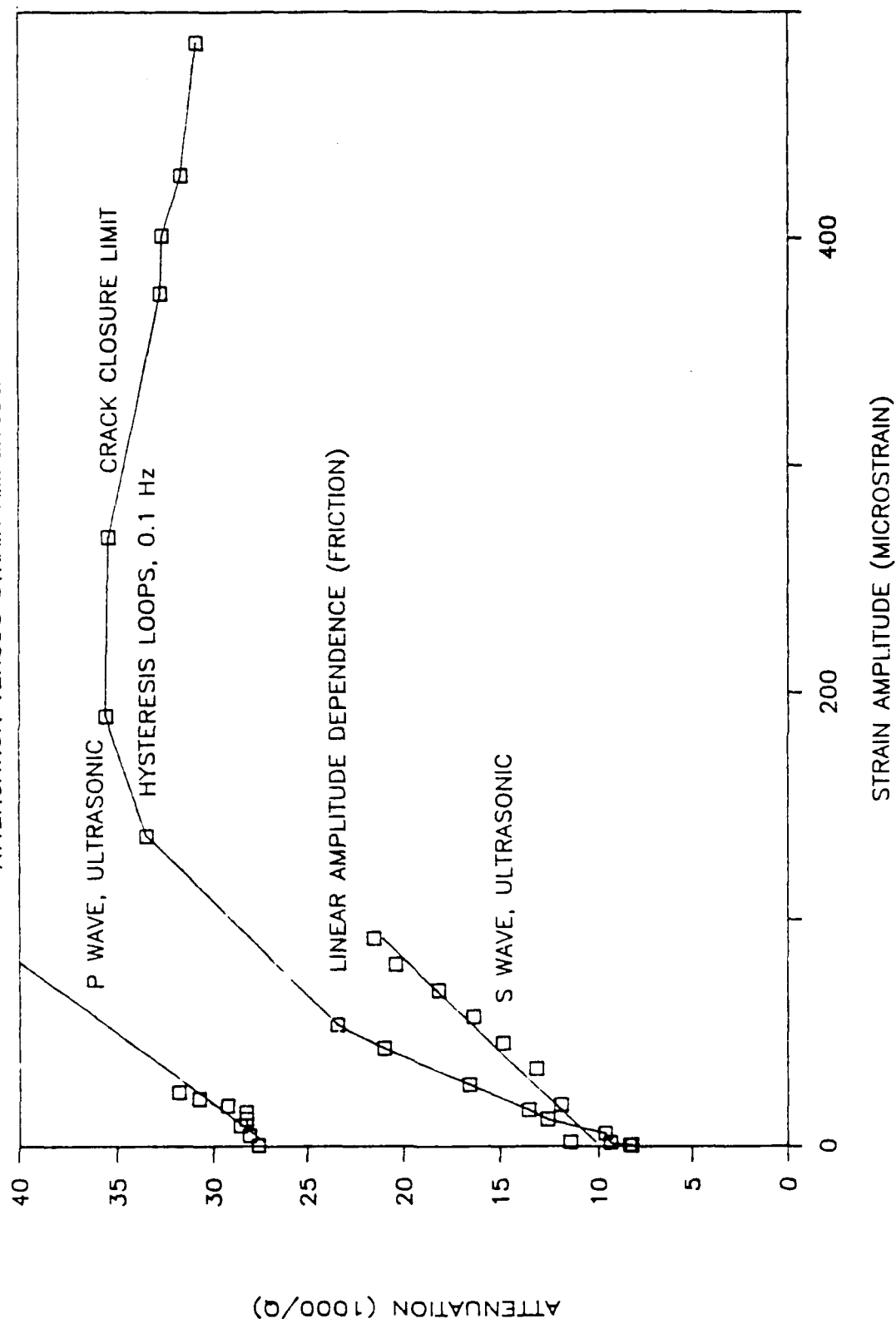


Figure 4. Attenuation factors for Sierra White granite from ultrasonic and hysteresis loop experimental techniques versus strain amplitude.

GRANITES

ATTENUATION VERSUS LOG FREQUENCY

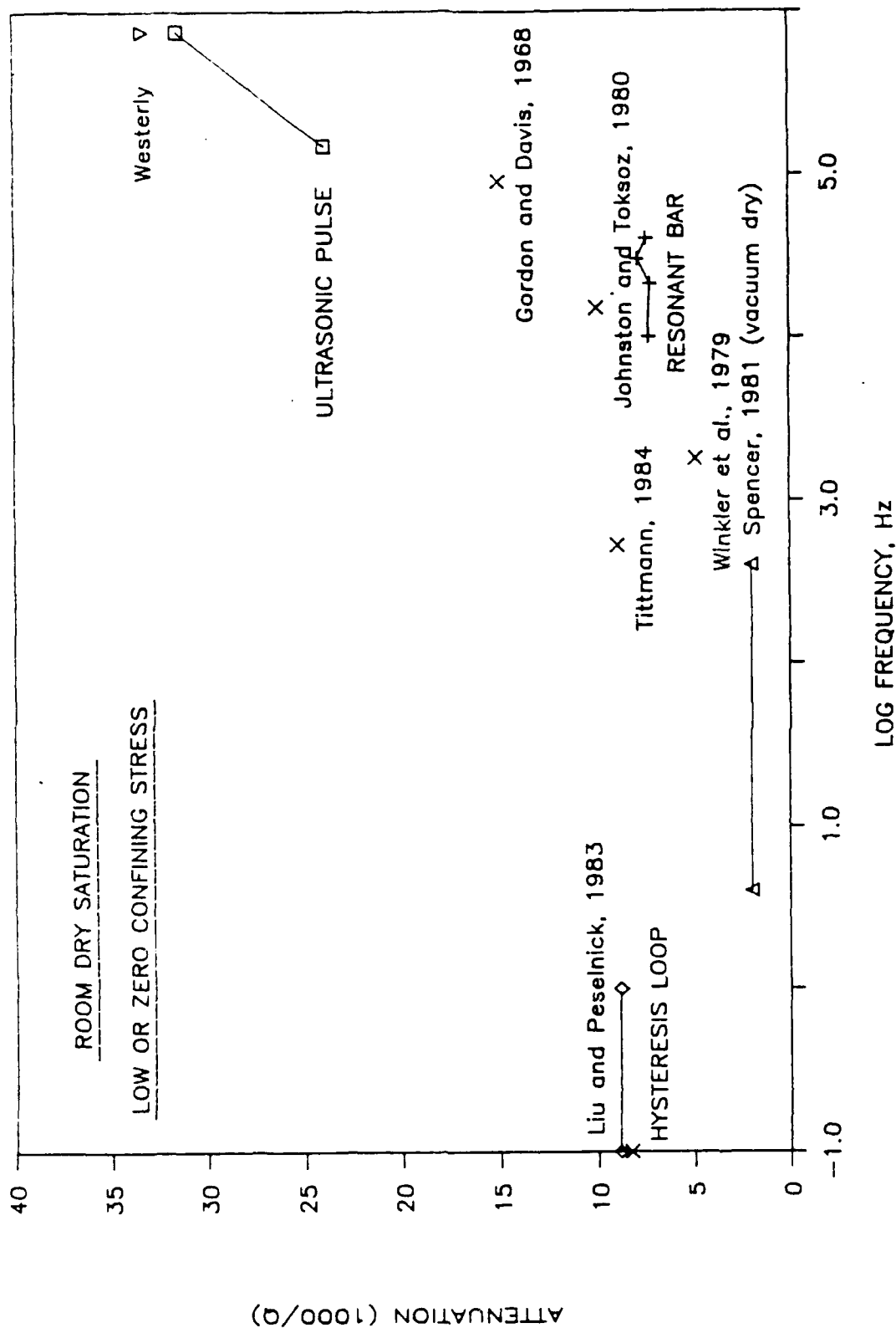


Figure 5. Summary plot of experimental attenuation versus log frequency (Hz) for dry granites at low stress and low strain amplitudes.

OBSERVATIONS OF HIGH-FREQUENCY WAVEFORM COHERENCE IN THE NORTHEASTERN UNITED STATES

Arthur L. Lerner-Lam and William H. Menke

Lamont-Doherty Geological Observatory of Columbia University, Palisades, NY 10964

CONTRACT NO. F19628-88-K-0041

OBJECTIVE

The dependence of seismic waveform coherence on azimuth and epicentral range at local and regional distances helps to constrain the distribution of inhomogeneities in the crust. It also provides information on the spatial variability of ground motion and its impact on yield estimation at regional distances. A controlled source experiment provides the needed sampling in distance and azimuth for rigorous assessment of coherence.

SUMMARY

Buried charges ranging in size from 500 to 6000 lbs were detonated by the USGS at twenty-three sites extending from southeastern Maine through the Adirondacks to southern Ontario (Figure 1). We deployed seventeen three-component digitally recording seismometers sampling at 100 Hz in three small-aperture arrays situated on low-noise hard rock sites in the Adirondacks. Two of the arrays, comprising four and six elements, were very small aperture (<75 m) with nominally linear inter-station offsets of 15-20 m. The third array at Dun Brook Mountain (DBM), shown in Figure 2, comprised seven elements with quasi-logarithmic inter-station offsets ranging from 7 to 710 m, and was situated 11 km from the nearest shot. The system response was flat to velocity above 2 Hz (the seismometer period) and below 30 Hz (the anti-alias corner), providing a relatively broad high-frequency passband. Typical signal-to-noise ratios were about 40 dB.

We have analyzed these data for their spatial coherence. Figure 3 shows a trace-normalized record section of the vertical component from one of the array elements at DBM. Shear-wave propagation and signal levels are excellent out to about 210 km. Inter-station coherence was calculated for 2.5 s time windows successively lagged by 1 second, and the initial phase of one seismogram in each pair in each window is adjusted to maximize coherence in order to minimize the effects of interstation moveout. We then averaged the coherence in the 15 time windows beginning with the direct P arrival, shown as the stippled area in Figure 3. Thus both P- and S-coda are included, though at different ranges. Our observations indicate that the mean coherence of the first 15 s is roughly independent of seismic phase type, epicentral azimuth, and distance. Figure 4 shows the mean coherence for the four smallest inter-station offsets, averaged again over epicentral range. Vertical bars show the observed variation of the time-averaged coherence over epicentral distances ranging from 11 to 209 km. The mean coherences show a strong dependence on frequency and inter-station offset, Δx . The observations can be fit equally well between 5 and 25 Hz by a simple exponential $C = \exp(-a f \Delta x)$ or a Gaussian $C = \exp[-b^2 (f \Delta x)^2]$, shown in Figure 5, with $a = 6.48 \times 10^{-4}$ and $b = 8.48 \times 10^{-4} \text{ m}^{-1} \text{ sec}$. For a sub-array crustal velocity of 5 km sec^{-1} , these values suggest that waveform coherence is small for inter-station offsets only 1/4 to 1/3 of the wavelength of the P energy.

We have also analyzed the particle motion properties of three component waveforms. The onset of P is polarized in a manner expected from source-receiver orientations, but the polarizations of P and S coda are similar to those of random time

series. Moreover, the ratio of transverse energy to vertical energy, shown in Figure 6, is zero for the direct P but rises to near unity within 1-10 cycles.

The simple dependence of coherence on frequency and inter-station offset suggests that in the northeastern United States, scattering processes are governed by the wavelength of seismic energy. A simple model of stochastic wave propagation has been developed (Menke, Lerner-Lam, and Dubendorff, 1989) to explain these coherence observations. The model suggests that scattering of seismic energy is concentrated in the shallowest layers of the crust, with the "scattering layer" being no more than a few kilometers thick.

CONCLUSIONS AND RECOMMENDATIONS

(1) The mean coherence of the first 15 seconds of signal is independent of epicentral range between 11 and 209 km.

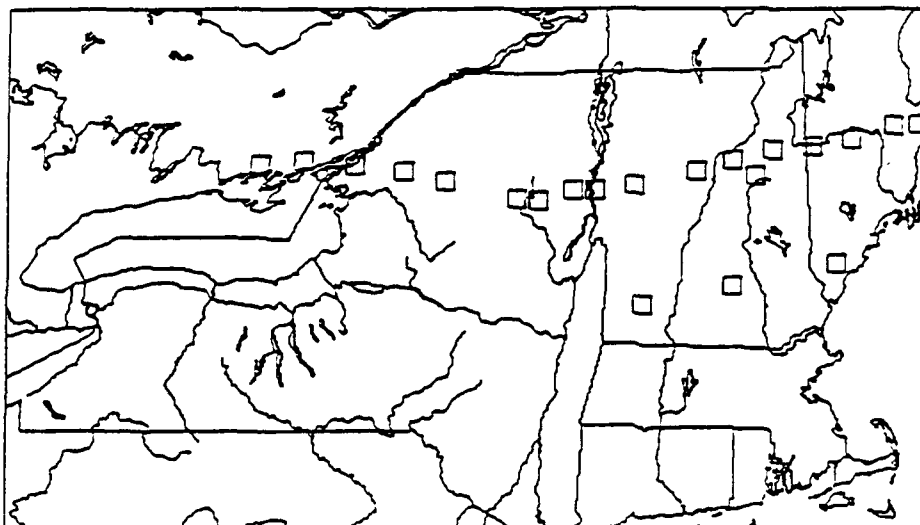
(2) The coherence structure of P and S coda is similar.

(3) The coherence appears to be governed by processes which scale with the wavelength of seismic energy. Between 5 and 25 Hz, coherence falls to $1/e$ when interstation offset is more than $1/4$ to $1/3$ of the wavelength of P energy.

(4) Particle motion observations suggest that the physical mechanism of the waveform distortion is multiple scattering in a heterogeneous crust, rather than propagation through vertically stratified structure. The near receiver structure is probably most important.

(5) A simple model of stochastic wave propagation suggests the presence of a surficial scattering layer several kilometers thick.

Lamont-Doherty Participation in USGS/AFGL
New York - New England Refraction Experiment



I. New Hampshire Tomographic Experiment

II. Waveform Coherence and Attenuation

III. Strong Motion Recording

Figure 1.

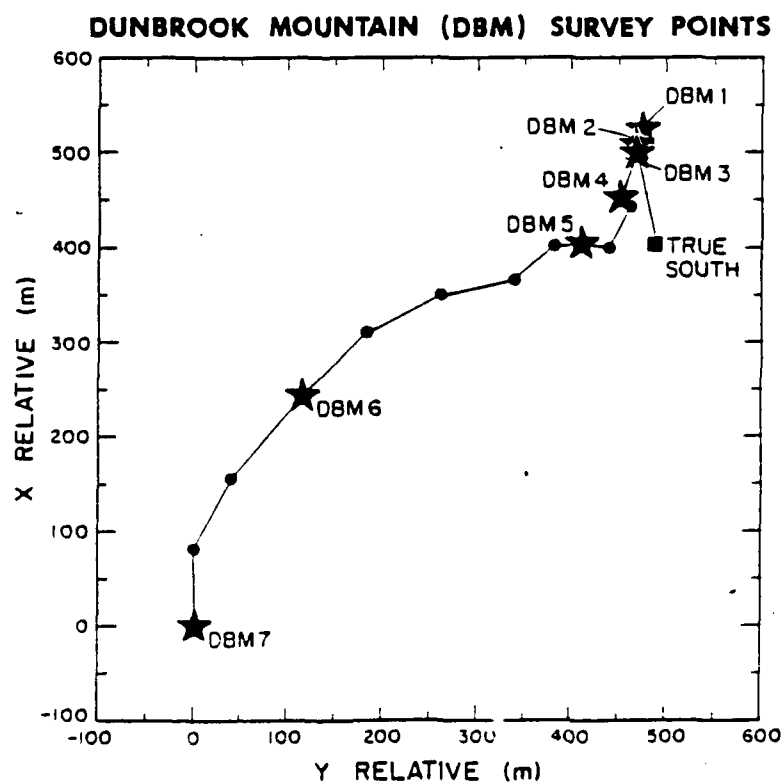


Figure 2.

DUN BROOK MOUNTAIN ARRAY ELEMENT 2

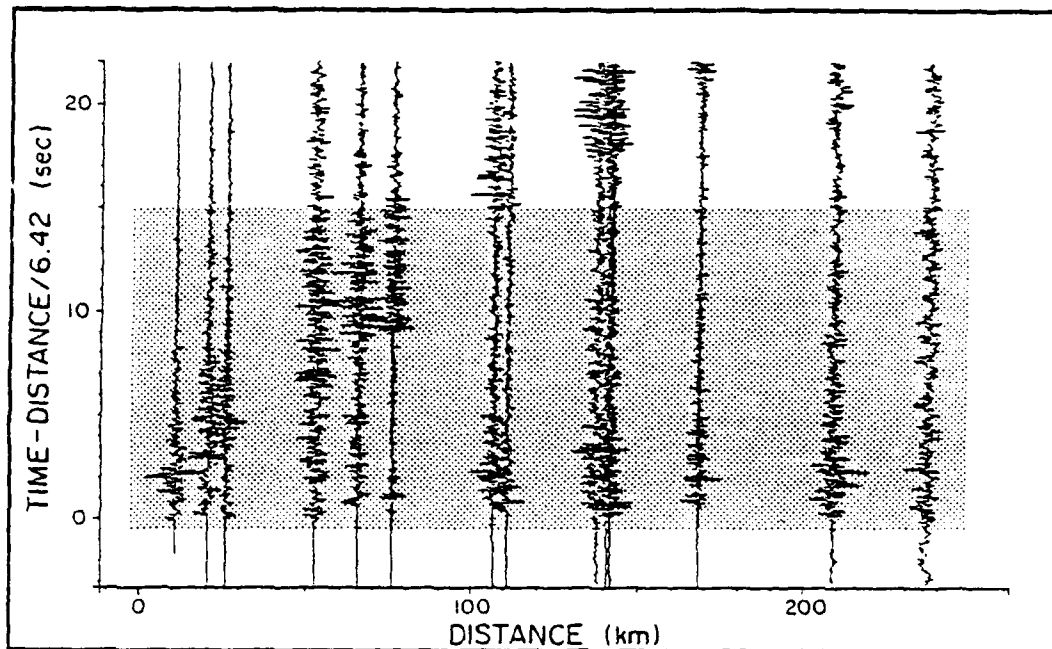


Figure 3.

Mean Coherence 9-50m dbm(11-209), vert

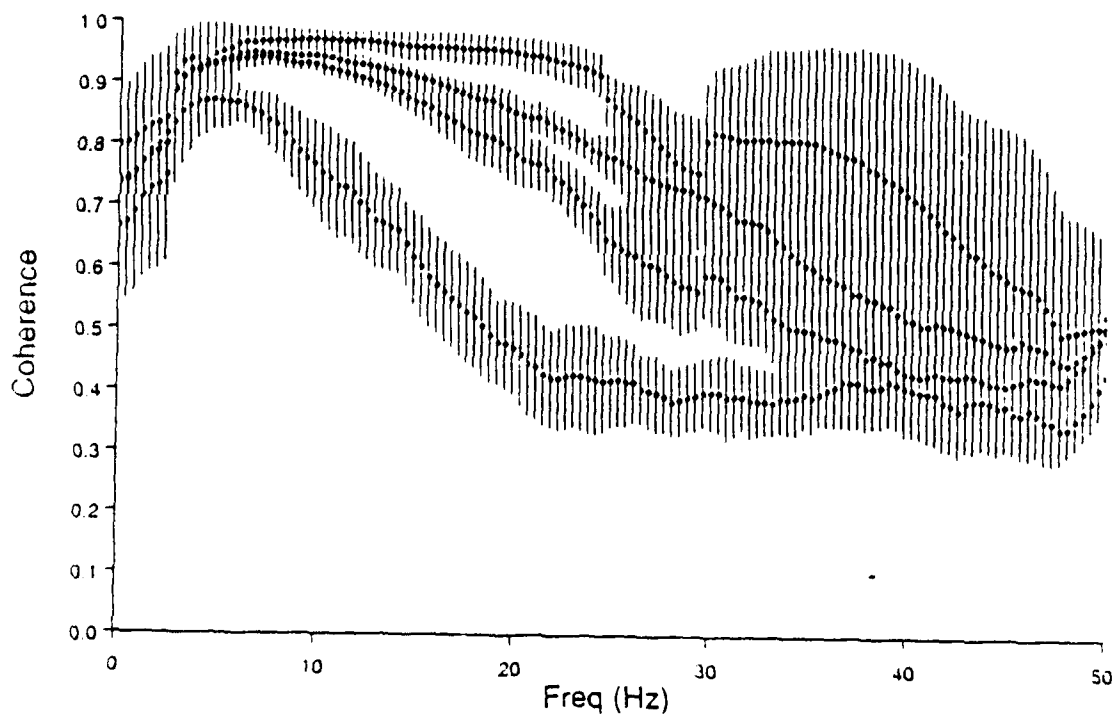


Figure 4.

Dun Brook Mt / NYNEX Experiment

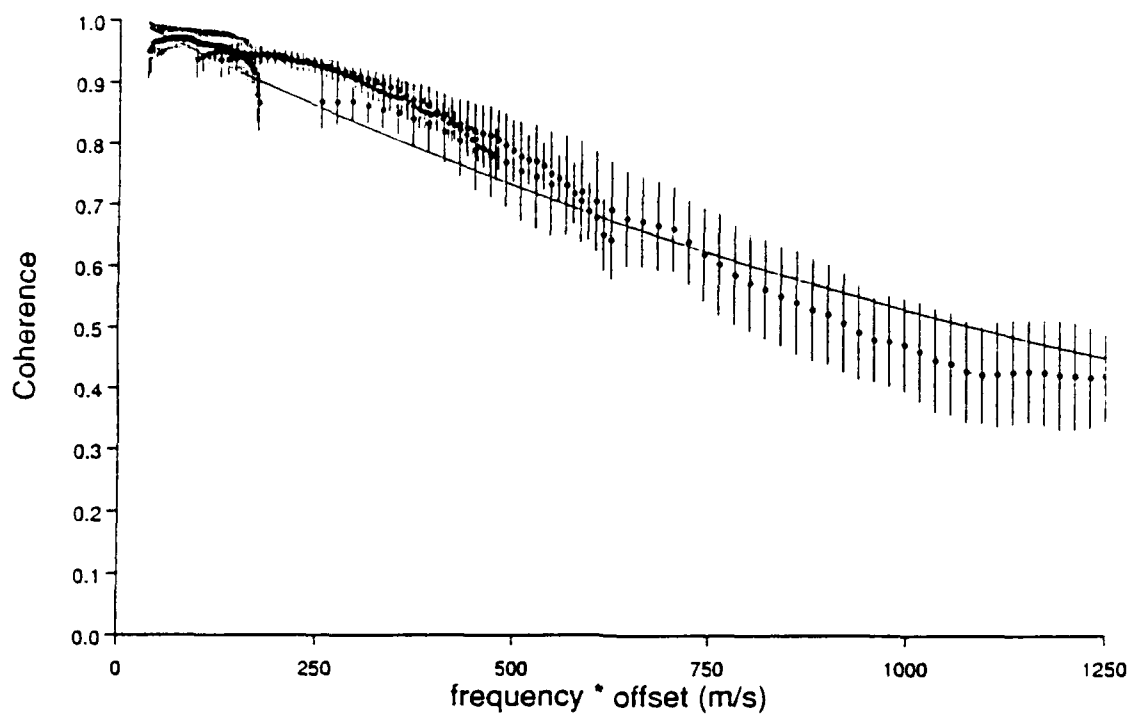


Figure 5.

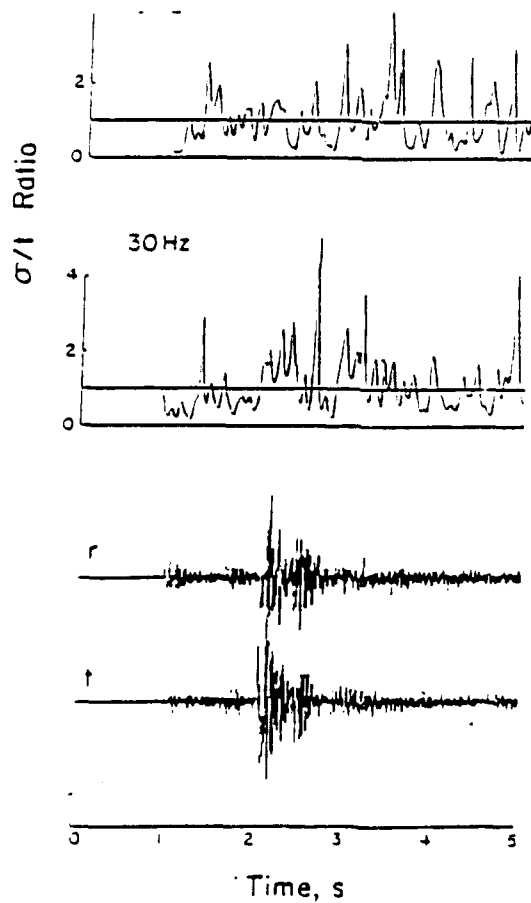


Figure 6.

TITLE: NEAR-SOURCE CONTRIBUTIONS TO TELESEISMIC P WAVE CODA AND REGIONAL PHASES

AUTHOR & AFFILIATION: Thorne Lay, Christopher S. Lynnes (Teledyne)
Department of Geological Sciences, University of Michigan

CONTRACT NO.: F19628-89-K-0011

OBJECTIVE: The objective of this research program is to investigate near-source contributions to the scattered wavefields comprising teleseismic P wave coda and regional phases. The basic approach is to utilize large data sets with good azimuthal and ray parameter coverage to detect event-to-event variations that can reliably be attributed to near-source phenomena, and to then seek a fundamental understanding of the near-source processes that are involved.

SUMMARY: The initial stage of this effort (beginning January, 1989) has involved extension of a previous investigation of teleseismic P coda for NTS explosions. In last year's presentation, the results of applying slant-stacking to a large set of waveforms for Yucca Flat explosions was discussed. The stacking is designed to detect coherent coda energy under the assumption of pseudo-isotropic scattering (i.e. small variation in amplitude pattern over the small cone of angles to teleseismic distances). Some of coherent features were interpreted as the result of topographic scattering of near-field surface and body waves into the teleseismic P field. We have subsequently performed additional numerical simulations that indicate that aliased sampling of a scattered wavefield from a random distribution of point scatterers near the source region may also explain some of the stacking results.

Figure 1 shows the spatial variation associated with coherency in the scattered arrivals for the Yucca Flat suite of events and stations. The grid defines a network of potential scattering locations centered on the source array, and the relief indicates the semblance at each point computed for the moveout velocity that is shown for each case. The moveout velocity and spatial offset for each source-receiver pair determines a time shift which is applied to each seismogram before the entire suite of records is summed. The semblance for a short time gate is computed to assess the coherence of the stacked data set, with higher values reflecting more coherent energy in the first 25 sec of the P coda.

Note that the Yucca Flat data give the largest, albeit low in an absolute sense, semblance values in the center of the grid, which is located in the middle of the source array. A region of moderate semblance values locates off to the northeast of the source array by 10 to 15 km. The results for a stacking velocity of 2.5 km/s are superimposed on a map of the near-source surface topography in Figure 2. The central area, where the semblance

values are largest has no topography; however, the primary outlying region of moderate semblance does correspond to the localized region of topography in the Halfpint Range. This is not the largest topography in the source vicinity, as that is found to the northwest of the sources.

To provide guidance for interpreting the stacking results, we must resort to numerical simulations. Figure 3a shows the semblance surface obtained for a simulation with the same source-receiver combinations as the Yucca Flat data set, with waveforms having direct P arrivals and coda comprised of random noise arrivals in each trace (i.e. no coherent scattering between traces or from event to event). Incoherent noise can result in large semblance values centered near the source array as a result of incomplete suppression of the direct P arrivals and early random arrivals. This may explain some of the higher semblance values found in the data (Figure 3b), given that trace misalignment and true random noise are likely to produce similar phase incoherence. Thus, it is difficult to confidently interpret the larger semblance values in the center of the array.

Many new simulations have been performed to appraise the effect of a complex distribution of scatterers. An example of a random distribution of 70 point scatterers distributed within 10 km of the center of the stacking grid is shown in Figure 3c. The simulated waveforms for this case are fairly realistic approximations to the observed coda in terms of duration and relative amplitude. The semblance surface computed for the correct stacking velocity is shown in Figure 3d. Interference between the arrivals degrades the resolution of individual scatterers, but there is a correlation between most regions of high semblance and relatively dense scatterers. Unlike the noise simulation, this random scatterer calculation has relatively low semblance values in the central area of the array. Note that an localized area of high semblance is found ENE of the array center, similar to the outlying feature in the data. For the simulation, this does not correspond to any dominant subcluster of scatterers, but instead appears to be overemphasized by the characteristics of the source-receiver array geometry. We can thus infer that the corresponding feature in the data need not be the result of topographic scattering from the Halfpint Range, though that possibility cannot yet be ruled out either. The absence of strong semblance for the areas of higher topography toward the northwest does indicate that topographic scattering may not result in coherent arrivals from event to event.

Additional ongoing work in the first few months of this new contract has involved investigation of the frequency dependence of successive time windows in teleseismic P coda. The motivation is to resolve the progressive homogenization of the wavefield due to random scattering contributions, and loss of the pP signature. Preliminary results of this analysis will be presented in a poster session.

RECOMMENDATIONS: Slant-stacking procedures have now been applied to extensive data sets for both Pahute Mesa and Yucca Flat events. It has proven extremely difficult to confidently detect and interpret any coherent scattered arrivals common to the large suites of events and stations. When coherence in the stack has been detected, simulations have demonstrated that it may be the result of incomplete noise suppression or of aliased sampling of a field produced by a complex distribution of scatterers which can not be uniquely interpreted. It appears that energy flux models, which do not require deterministic scattering structures will usually suffice for characterizations of the gross features of the teleseismic P coda. However, it is likely that for individual events it may still prove possible to recognize discrete scatterer contributions to the coda. Analysis of broadband data is vital if one is to attain improved phase stability. It will be very interesting to analyze regional waveform data to ascertain whether coherent scattering structures play a greater role in the substantial waveform variability between shots. This contract will include analysis of that type.

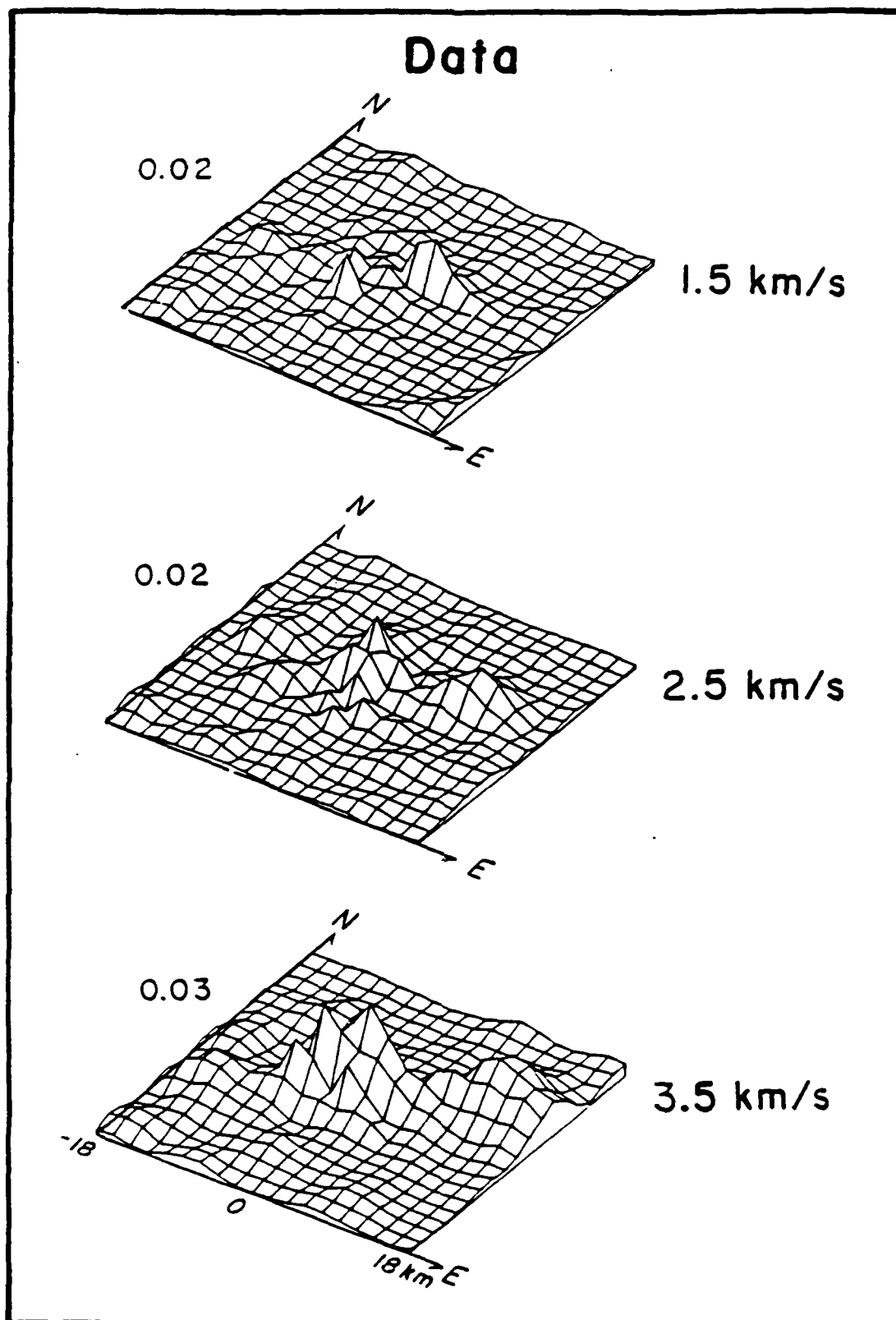


Figure 1. Semblance values calculated at the grid of scattering locations for the Yucca Flat test site, assuming three different scattering velocities. The peak semblance for each surface is shown on the left.

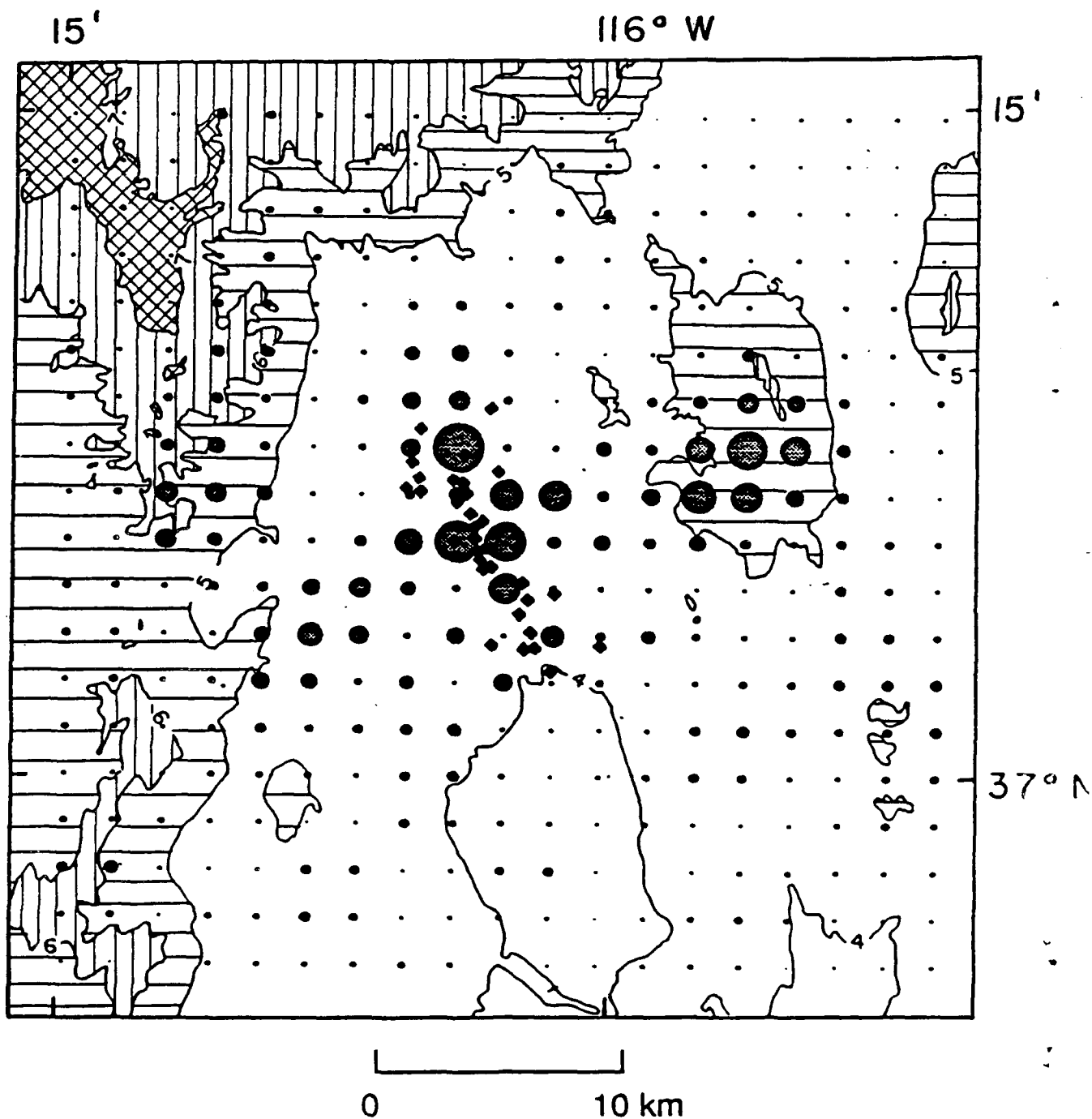
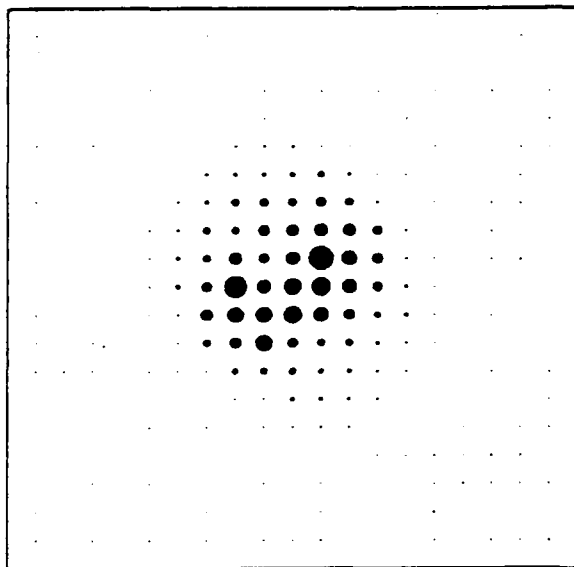


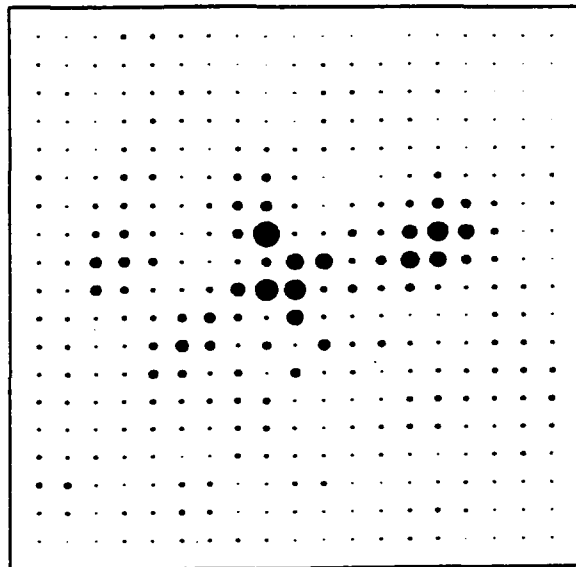
Figure 2. Superposition of the semblance surface for a moveout velocity of 2.5 km/s from Figure 1 on a map of surface topography near the Yucca Flat source region. The contours are in 1000 ft intervals, and the small diamonds indicate the locations of the Yucca Flat events used in the analysis.

a)



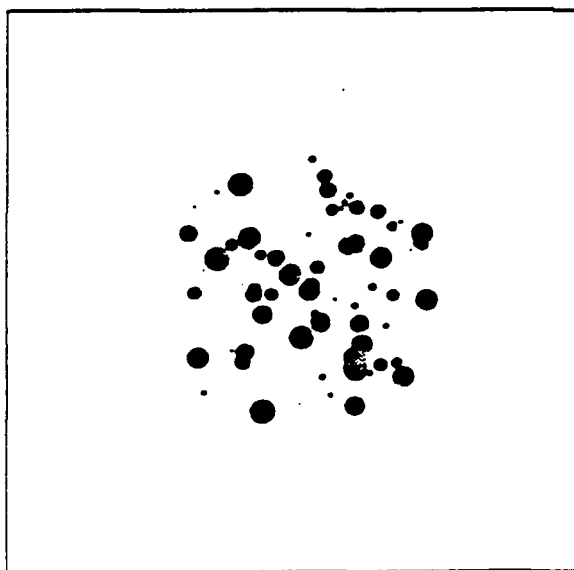
max. semblance=0.11

b)



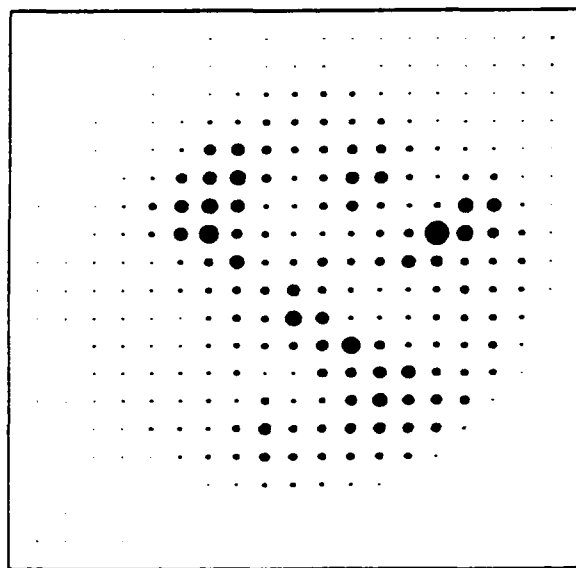
max. semblance=0.04

c)



max. amplitude: 0.2

d)



max. semblance=0.24

Figure 3. (a) Map view of semblances calculated for an incoherent noise simulation. (b) Map view of the semblances for a moveout velocity of 2.5 km/s from Figure 1. (c) Map view of randomly distributed point scatterers used in the simulation described in the text. The relative size of the symbols indicate the relative strengths of the scatterers with a linear scaling. (d) Map view of the semblance surface computed for the simulation with random point scatterers shown in (c).

EFFECTS OF DEPTH OF BURIAL AND TECTONIC RELEASE ON REGIONAL AND TELESEISMIC EXPLOSION WAVEFORMS

K. L. McLaughlin, T. G. Barker, J. L. Stevens, B. Shkoller, and S. M. Day*
S-CUBED, P.O.Box 1620, La Jolla, CA 92038-1620.

*Dept. Geological Sciences, SDSU, San Diego, CA 92182.

CONTRACT # F19628-87-C-0093

INTRODUCTION

Linear elastic point source synthetic seismograms fail to match some important aspects of observed regional seismograms. Figure 1 shows a comparison of two NTS explosions recorded at about 325 Km compared to a synthetic seismogram for an average basin and range structure that properly matches the regional attenuation with distance of Pn, Pg, LR, and Lg at 1 Hz and below. The broadband velocity records (at the top) have been bandpass filtered in selected frequency bands. The general character of the synthetics and observed seismograms are quite good for low frequencies considering that the model is not optimized for the path shown. At high frequencies the P waves are well modeled but the late arriving energy is well below the observations. In particular, the synthetic short period Lg is poorly excited. This shortcoming of synthetics underscores the fact that explosion Lg excitation is a poorly understood phenomenon despite the robust nature of mb(Lg):yield (Nuttli, 1986). Also as expected, coda energy which is clearly due to laterally heterogeneous structure is not properly modeled by a layered Earth structure.

Recently, observations by Murphy and Bennett (1982) and by Taylor et al. (1988) have shown that NTS explosions are lacking in high frequencies (HF) relative to low frequencies (LF) compared to basin and range earthquakes. This possible discriminant has been found to fail for small overburied explosions. In order to investigate whether the HF/LF discriminant is related to scaled depth effects and to better understand the excitation of regional phases such Lg, we have conducted numerical calculations that simulate the excitation of complete regional seismograms by a distributed nonlinear explosion source.

WAVENUMBER INTEGRATION SYNTHETICS WITH 2D NLFD SOURCES

The elastodynamic representation theorem is used to propagate results from axisymmetric nonlinear finite difference (NLFD) calculations. Cylindrically symmetric two dimensional (2D) nonlinear finite difference simulations were performed for three different models, a tuff model intended to simulate the Pahute Mesa NTS structure, a hard brittle rock model (granite) to simulate the Shagan River test site, and a granite model with prestress to simulate the Climax Stock NTS (Piledriver) structure. The displacement and traction time histories from the finite difference calculations are saved on a cylindrical monitoring surface in the linear zone for the duration of the calculation (see Figure 2). The far-field motion may be expressed by use of the elastodynamic representation theorem by an integral over the monitoring surface involving the displacements, tractions, and gradients of the appropriate Green's functions.

Complete regional synthetics are constructed in this manner using Green's functions derived from a wavenumber integration code. Telseismic P waveforms are computed using layered stack propagator Green's functions for the crustal structure. The synthetics include all the effects of a nonlinear distributed source including gravitational forces, spall, nonlinear attenuation, and cracking as well as the complete seismogram for a layered Earth structure. In the case of the calculations done with prestress, the calculations include the effect of tectonic stress release within the nonlinear volume.

PAHUTE MESA SYNTHETICS

Figure 3 shows a comparison of synthetic seismograms for the 2D finite difference source with those for a point explosive source in the same structure. The source was a 125 Kt explosion in the Pahute Mesa tuff model. Three depths of burial are shown. The 2D 200 m depth simulation includes cratering while the 1D model does not. The 690 m and 980 m deep sources are fully contained. The largest differences between the 1D and 2D synthetics are in the modal waves with group velocities below 3 km/sec. These waves propagate in the low velocity surface layers of the Pahute Mesa structure. These waves would not be expected to propagate to large regional distances in the basin and range but may be scattered into Lg or P coda. Comparison of the 2D seismograms with Green's functions for point sources indicate that shallow compensated linear vector dipole (CLVD) point sources could model the principal differences between the 1D and 2D seismograms.

Whole record spectra are shown for the three 2D models in Figure 4. The cratering simulation is reduced in amplitude due to venting. Note that the 680 m depth of burial is enhanced in lower frequencies relative to the 980 m depth of burial while the two sources are virtually identical above 0.8 Hz. Figure 5 shows a comparison of the 680 and 980 m synthetics in three narrow frequency bands centered on 1.25, 2.5 and 4.75 Hz. We see that the two sources excite virtually the same energy in the 1.25 and 2.5 energy bands but that the 980 m source is enriched at 4.75 Hz. The NLFD simulations give qualitative support to the observations that HF/LF ratios are increased for greater scaled depth of burial.

SHAGAN RIVER SYNTHETICS

Synthetics computed for a granite model in an Eastern Kazakhstan crustal structure are shown in Figure 6. In this case a frequency band of 1.25 to 2.0 Hz has been selected to show the principal differences between the explosion point source and the 2D nonlinear source. The Green's functions for a point CLVD at either 680 m or 200 m depth are shown to illustrate that the waves arriving between 30 and 40 seconds may be modeled by a CLVD source above the working point of the explosion. Telseismic P waveforms predicted by the nonlinear source calculations were found to under predict the "pP" compared to observations. Analysis indicates that a larger CLVD component (spall) would increase the apparent "pP" signal and increase Lg excitation.

TECTONIC RELEASE

Synthetic free-field RDP estimates are shown in Figure 7 for the granite simulation with tectonic prestress. In this case, the displacement time history on the monitored surface at the working point level has been integrated to estimate an RDP assuming an elastic whole space. This simulates RDP estimates from free-field seismic recordings. There is some interference from the free surface reflections (pP and pS) but the major feature of the three simulations is clear. The no prestress case shows an overshoot with a stable static level. The 7.5 MPa prestress has nearly zero static level while the 15 MPa prestress reverses the static RDP level.

Synthetics based on these simulations indicate that the long period surface waves are reversed for the 15 MPa prestress, and reduced (nodal) for the 7.5 MPa prestress case. However, as frequency is increased, the differences between the three cases disappear. Figure 8 shows the fundamental mode synthetic seismogram at 100 Km for these three cases, the bottom trace shows all three cases plotted on top of each other. The dispersion of the fundamental mode permits us to compare the excitation as a function of frequency. Note that the long period energy is out of phase and has differing amplitude, while the higher frequency energy is in phase and has the same amplitude for all cases. These observations remain the same if the entire seismogram is considered.

CONCLUSIONS

- Point source explosions in layered structures do not excite enough Lg to match observations.
 - Axisymmetric nonlinear simulations generate more Lg than point explosions however they still did not match observations.
- Axisymmetric nonlinear sources appear as if they have a shallow CLVD component.
 - The CLVD component excites enhanced Lg and Rg with a peaked spectrum compared to the "explosion" spectrum.
 - Frequency of enhancement depends on structure, medium, and depth.
 - The Rg may be subsequently scattered to P and Lg coda.
- Overburied NTS explosions are observed to be HF/LF enhanced with respect to normal buried explosions.
 - Axisymmetric nonlinear simulations give qualitative support to the observations.
 - Overburied simulations show high frequency (HF) enhancement similar Mueller-Murphy to scaling.
 - Normal buried simulations show low frequency (LF) enhancement due to nonlinear free surface interaction.
 - Therefore, HF/LF enhancement for the simulations is a combination of depth scaling (higher confining pressure), increase of material strength with depth, and

the scaled depth of burial effect on the free surface interaction (spall and cracking).

- Teleseismic P waveforms have larger Pmax than predicted by simulations.
 - The teleseismic "pP" phase is too small in the nonlinear axisymmetric simulations indicating that the CLVD of the simulations may not be large enough.
- The tectonic release model for the granite simulations has minimal effect upon the regional seismogram in the short period band.

RECOMMENDATIONS

- Perform calculations for smaller yields with larger overburial.
- Introduce additional layering into the tuff models.
- Introduce axisymmetric lateral heterogeneity into the nonlinear models.
- Improve near-source scattering models to examine the scattering of Rg into Lg.

REFERENCES

- Murphy, J. R., and T. J. Bennett (1982), A Discrimination Analysis of Short-period Regional Seismic Data Recorded at Tonto Forest Observatory, *Bull. Seism. Soc. Am.*, 72, 1351-1366.
- Nuttli, O. (1986), Yield Estimates of Nevada Test Site Explosions Obtained from Seismic Lg Waves, *J. Geophys. Res.*, 91, 2137-2151.
- Taylor, S. R., N. W. Sherman, and M. D. Denny (1988), Spectral Discrimination Between NTS Explosions and Western U.S. Earthquakes at Regional Distances, *Bull. Seism. Soc. Am.*, 78, 1563-1579.

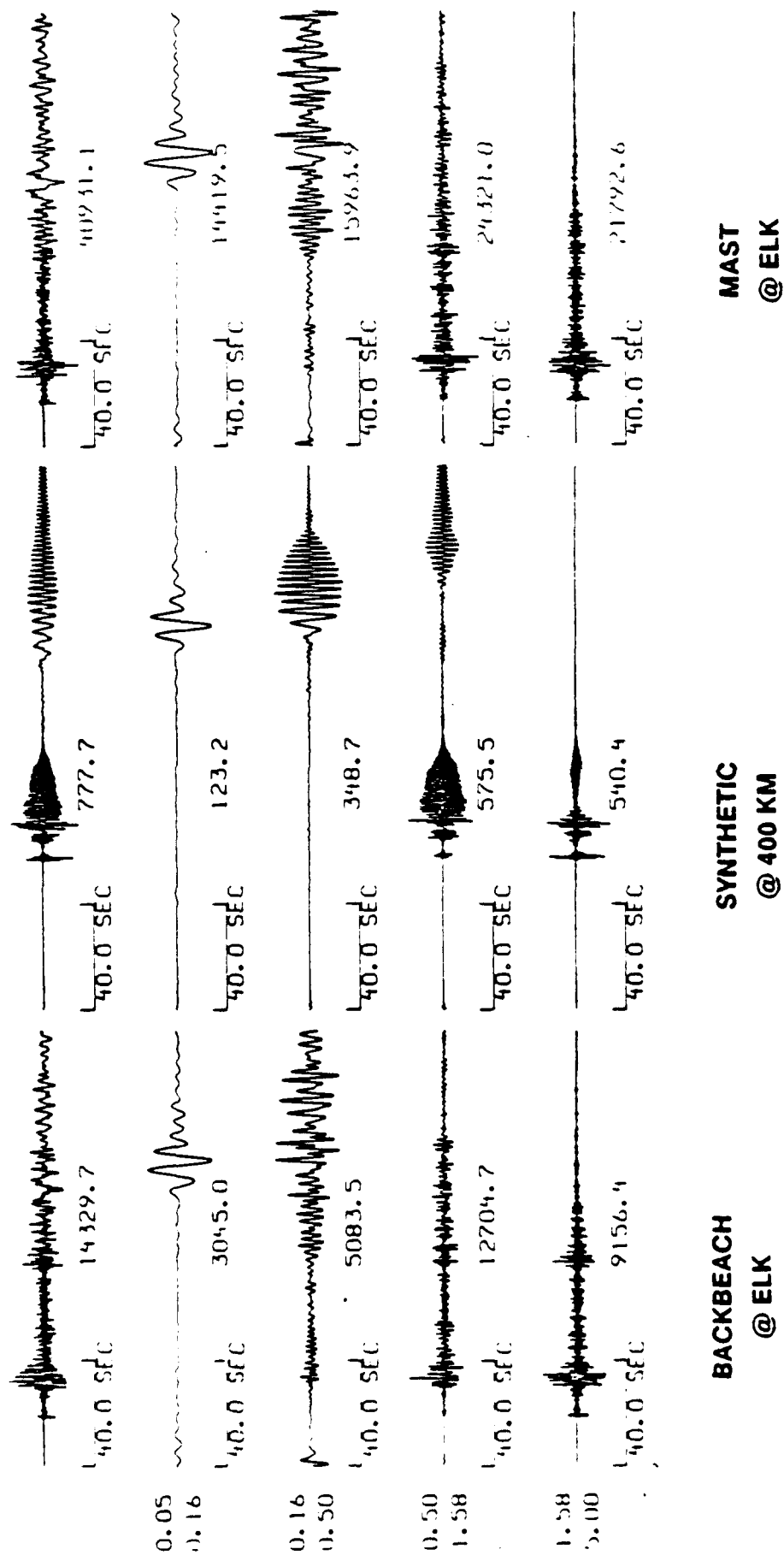


Figure 1. Comparison of bandpass filtered synthetics at 400 km with observations at station ELK: BACKBEACH (right), synthetic (center), and MAST (left).

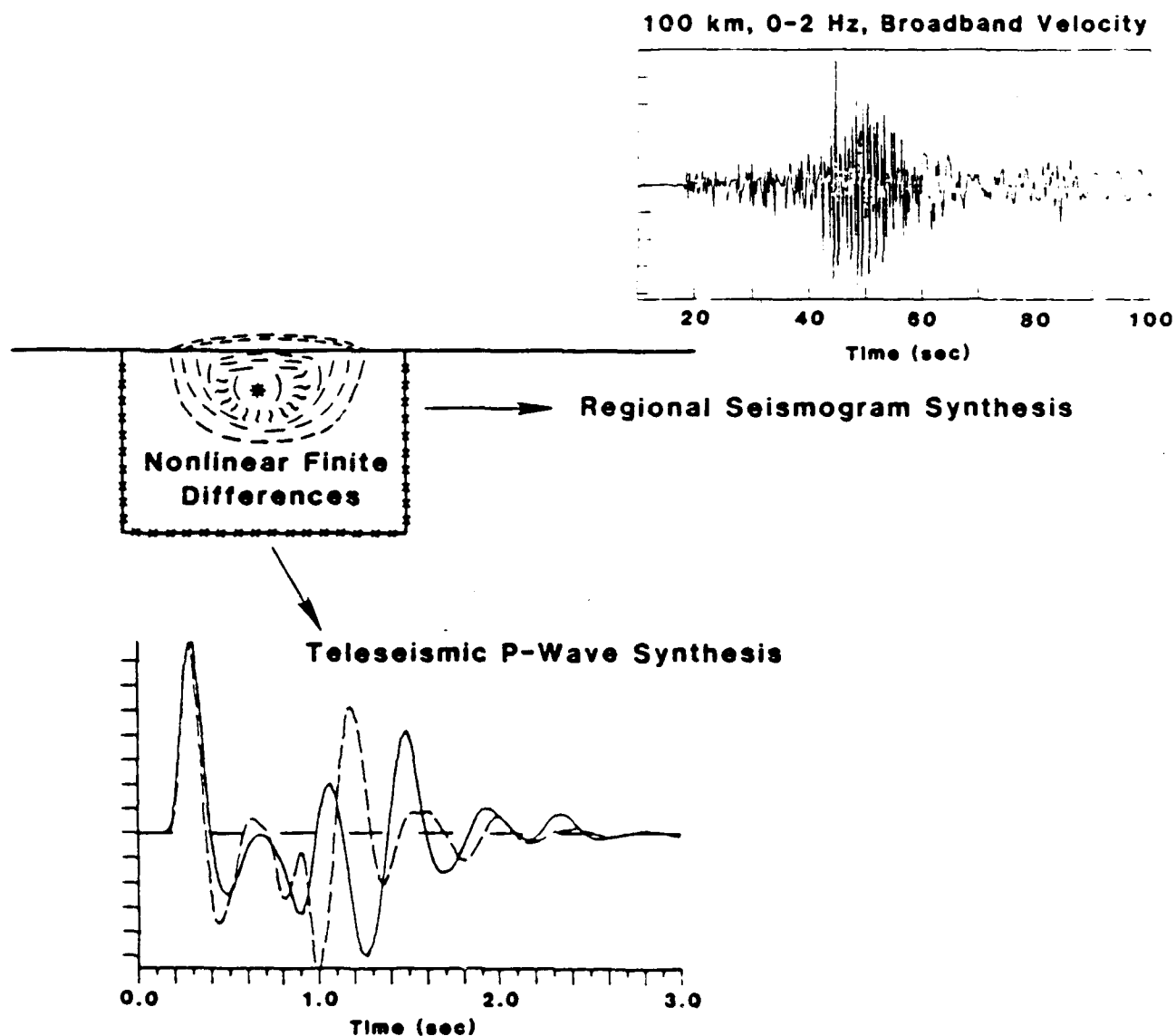


Figure 2.

Two-dimensional finite difference calculations are used to compute displacements and tractions on a monitoring surface outside the nonlinear region surrounding an explosion. Complete regional seismograms and far-field body waves are calculated by using the elastodynamic representation theorem and integrating over the monitoring surface.

PAHUTE MESA

100 km 125KT 0-2 Hz

Radial

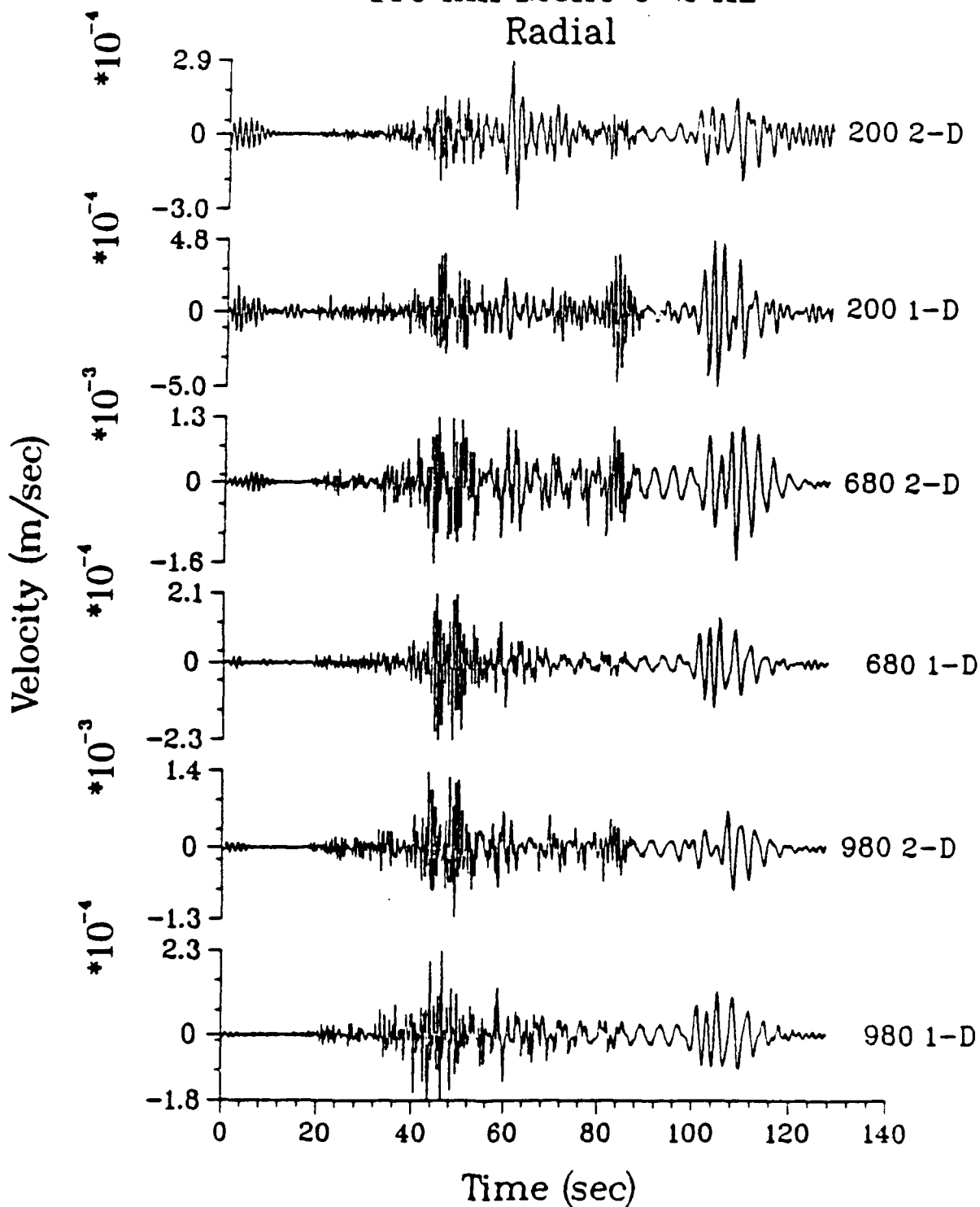


Figure 3.

Comparison of broadband velocity synthetics for the Pahute Mesa tuffs calculations at 100 km. Radial component, 0 to 2 Hz bandwidth.

PAHUTE MESA
100 km 125KT 0-2 Hz
2-D Vertical

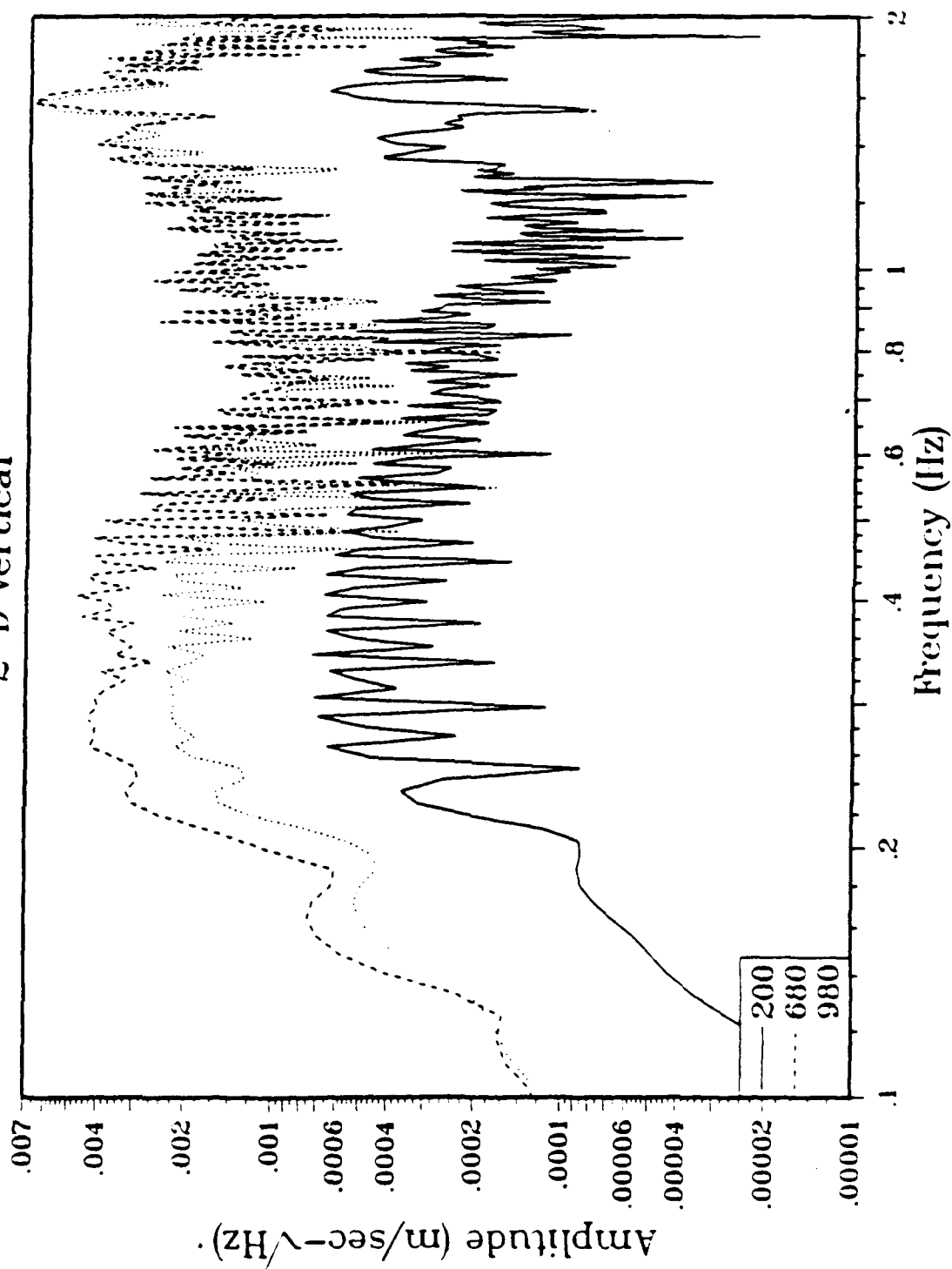


Figure 4. Whole record spectra for the 2D Pahute Mesa tuff synthetics in 5.1a. Note the low-frequency difference between the 680 and 980 meter depth synthetics.

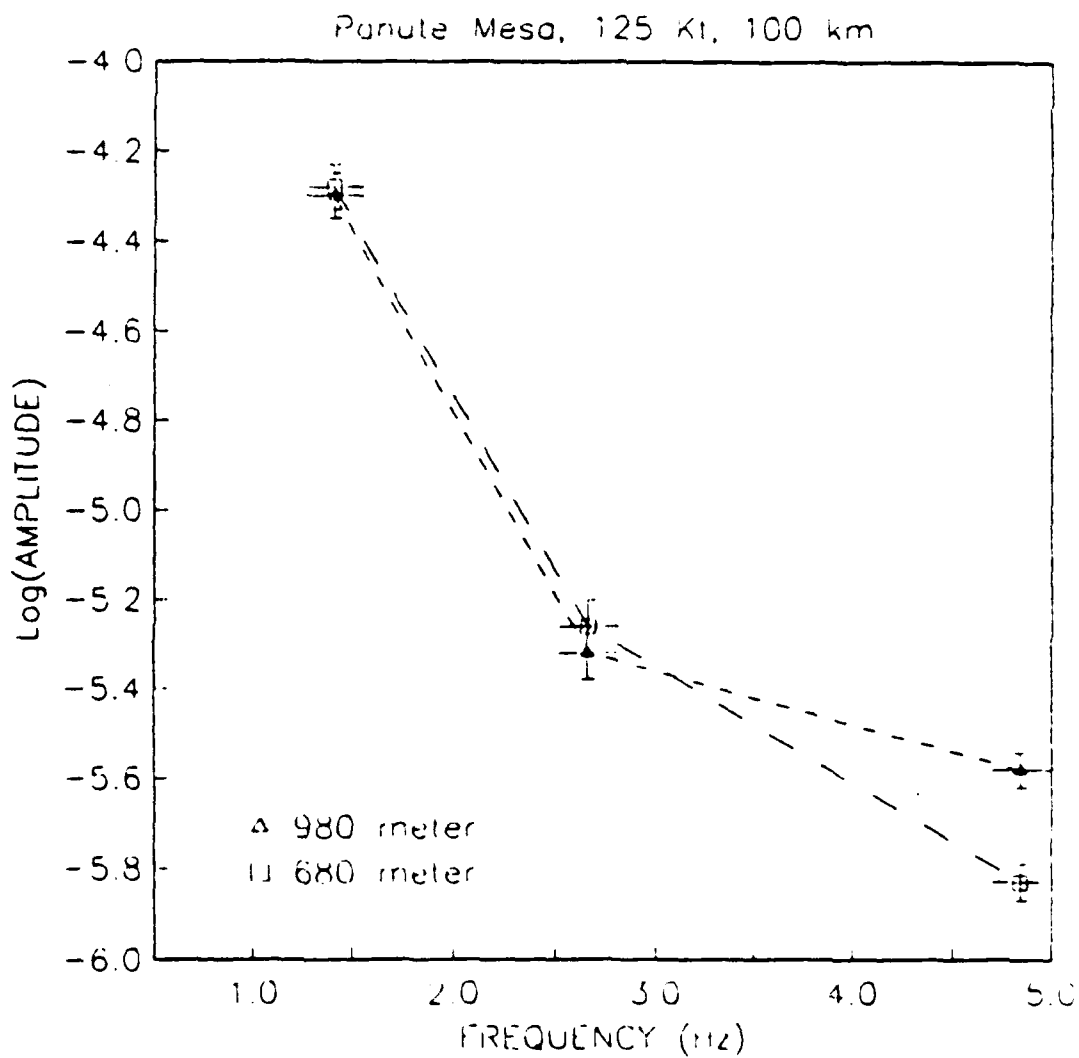


Figure 5.

Average spectral levels of synthetics for 680 and 980 meter depth sources in three frequency bands. The two depths of burial are indistinguishable at 1.4 or 2.5 Hz. The 980 meter synthetic is enriched for frequencies above 4.5 Hz with respect to the 680 meter synthetic.

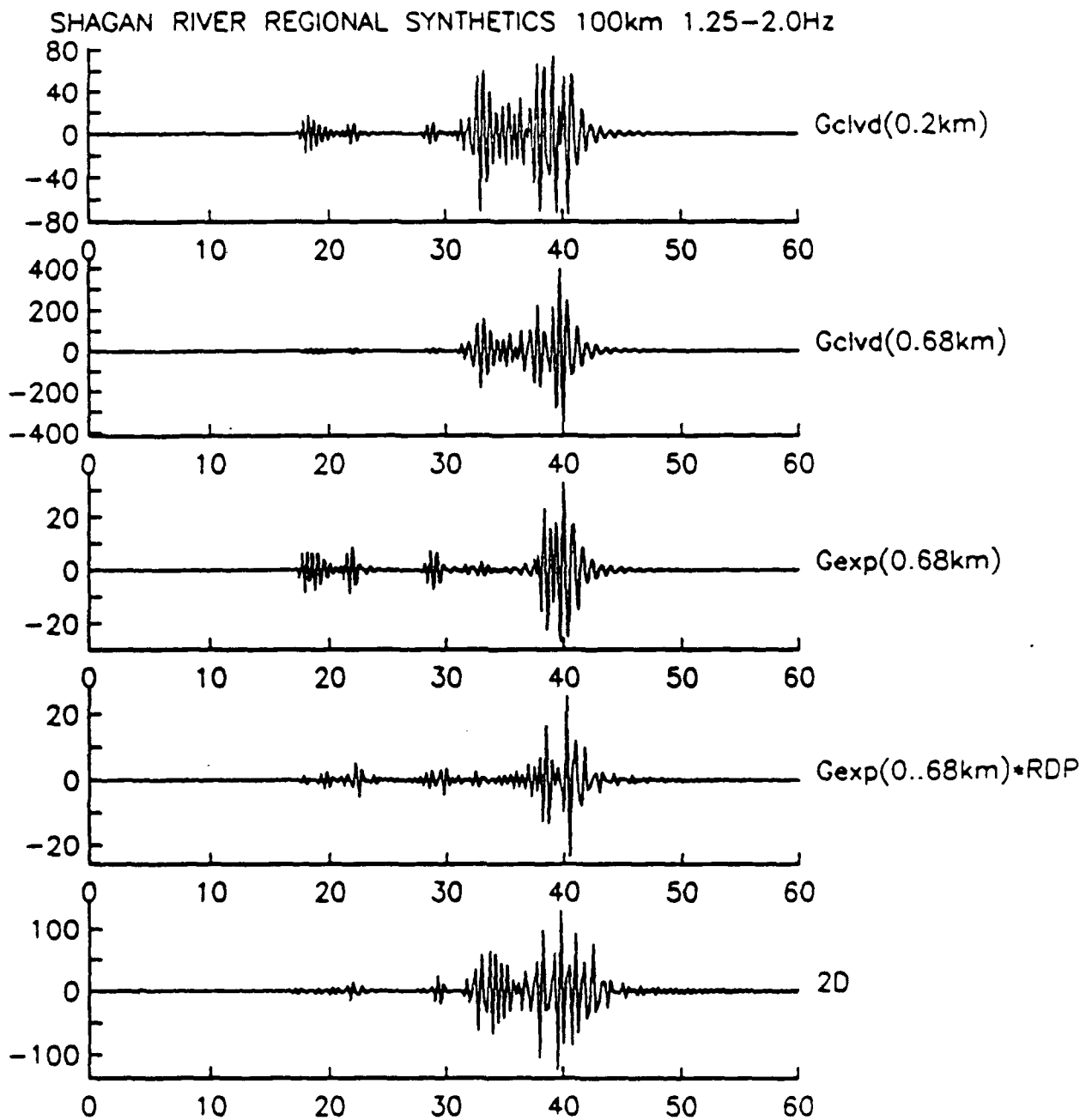


Figure 6. Shagan River 680 meter depth of burial 2D synthetic and several Green's functions in the 1.25-2.0 bandwidth. From bottom to top are: the 680 meter depth 2D synthetic, the 680 meter depth explosion Green's function convolved with the 1D RDP, the 680 meter depth explosion Green's function, the CLVD Green's function at 680 meters depth, and the CLVD Green's function at 200 meters. Note the SV-Lg arrival on the 2D trace that resembles the CLVD Green's function.

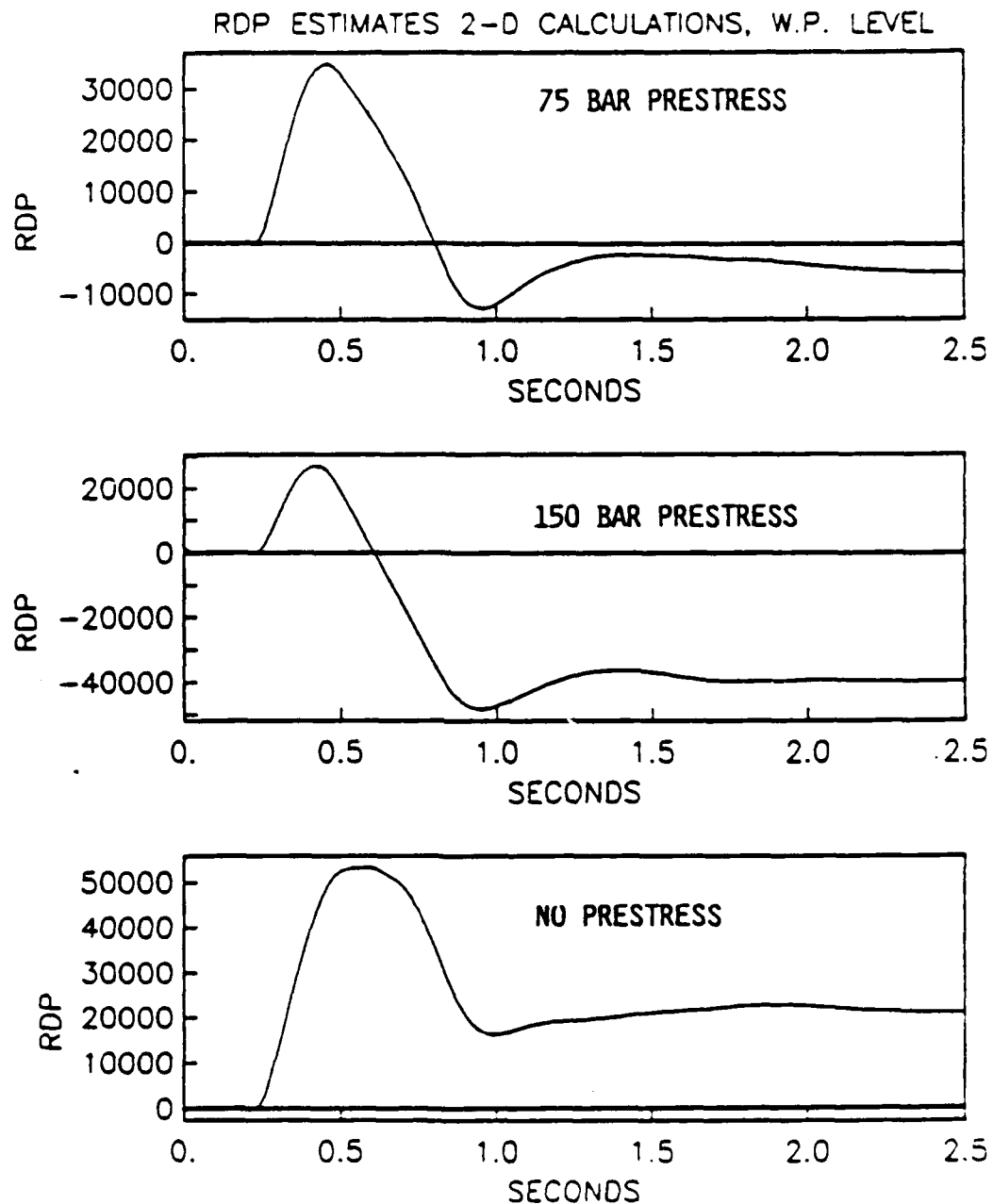


Figure 7.

RDP estimates from the radial displacements of the finite difference calculations at the working point level. No prestress (bottom) shows a typical granite RDP with static level near 20.000 m^3 . 7.5 MPa prestress (top) shows a static level near zero, while the 15 MPa prestress (middle) shows a complete reversal.

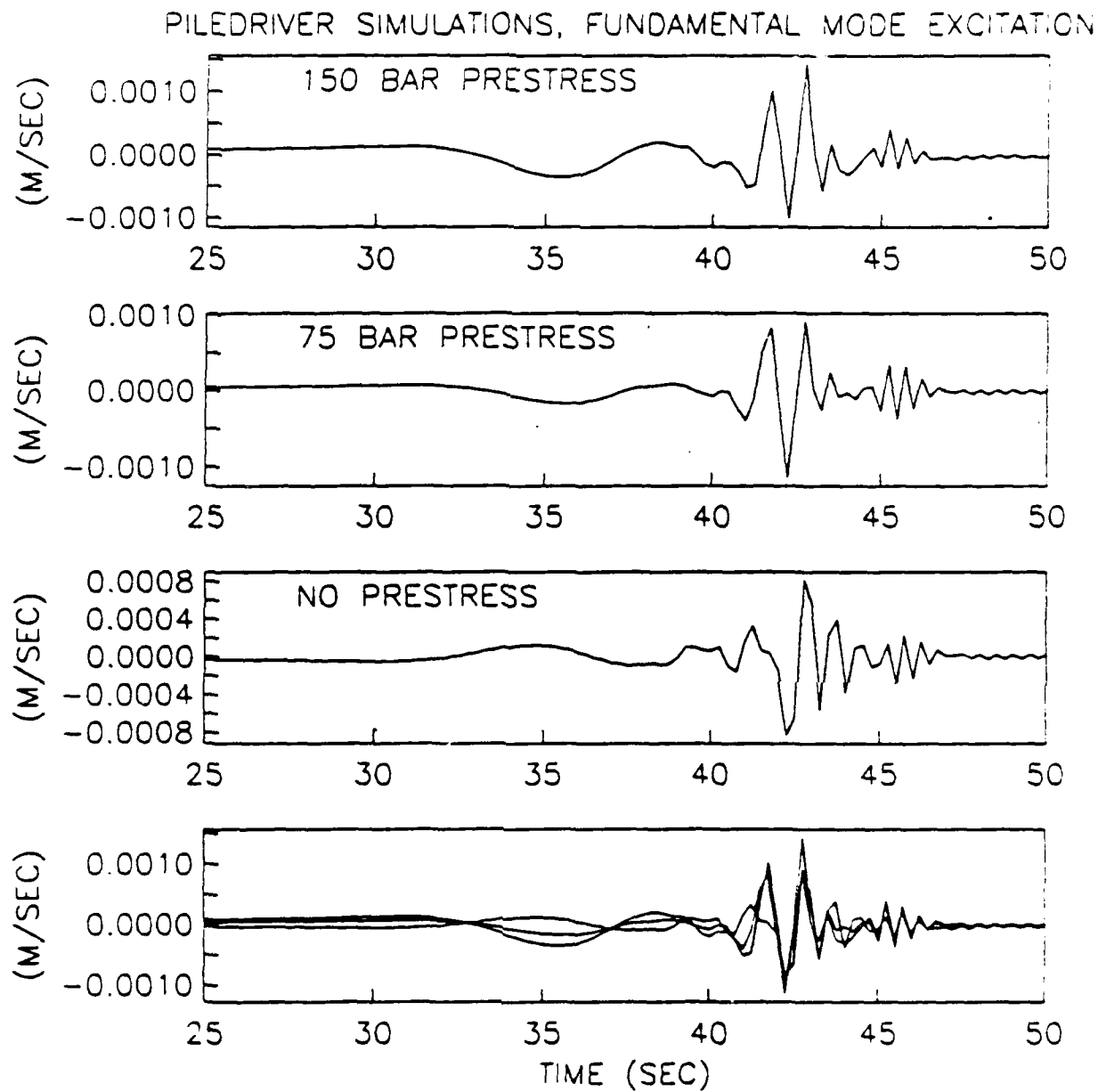


Figure 8.

Fundamental mode excitation for the three 2D PILEDRIIVER simulations. Vertical component, 100 km. 0 to 2 Hz bandwidth. Note that although the 10 second surface waves are reversed for the prestressed cases, the Rayleigh waves are progressively alike with increasing frequency (increasing group velocity).

Summary of a FY89 DARPA Annual Science Review Poster Presentation of:

**Comparative Seismic Observations on a
Downhole Network verses a Vertical Array.**

P.E.Malin
Institute for Crustal Studies
University of California
Santa Barbara, CA 93106

Summary.

Introduction. At the end of the first quarter of calendar year 1989 we were awarded support to use our existing, cooperative UCSB-UCB-USGS Downhole Digital Seismic Network and Varian Vertical Seismic Profiling Array at Parkfield, CA, to study in coordination with UCB the following DARPA related research questions:

1. How near receiver structure, scattering, and intrinsic attenuation distort the high frequency spectra and spectral ratios of P and S phases.
2. How the vertical and horizontal locations of high frequency 3 component stations affect the individual properties of seismic signals, noise, and their ratios (ie. s, n, and s/n).
3. The comparative detection and discrimination characteristics of event-triggered, high-frequency 3-component vertical and horizontal arrays.

The DDSN and Varian Array. The Downhole Digital Seismic Network and Varian Vertical Seismic Profiling Arrays at Parkfield were constructed specifically to detect and record seismic events in the frequency band of 0.5 to 125 Hz with a resolution of 16 bits. The locations of these seismic observatories, along with schematic diagrams of their construction, are shown in Figures 1, 2, and 3. The specifications of the DDSN and Varian Array are as follows:

o The horizontal array consists of 9 geographically separated surface and downhole 3-component, 2 Hz seismometer pairs. The 200 to 950 ft deep downhole instruments are monitored on a full time basis by a radio linked event triggering computer recording system. The sampling rate is 500 Hz and the gains are achieved by 80 db low noise amplifiers. Simultaneous surface and downhole records of different types of seismic events have been obtained from several stations with a matched recording system. (See also Figure 2.)

o The vertical array was cemented into a 5000 ft deep well in Nov 1987. For the purposes of our work for DARPA, we are using a Microvax based event triggering system to monitor the 3-component signals from 4 high-output, 4.5 Hz seismometer packages at 900 ft intervals from 77 ft to 2777 ft underground and 3 high-output 4.5 Hz seismometer packages at 100 ft intervals from 2977 ft to 3177 ft underground. All 21 channels of this vertical seismic profiling network are amplified by 80 db low-noise electronics and sampled at 500 Hz. (See also Figure 3.)

Preliminary Analysis of Observations and Modeling Results. Earthquake and explosion data from the DDSN and Varian Array provide direct control on the effects of near surface structure on the propagation of important P and S type phases relevant to nuclear blast monitoring. Examples of upcoming seismic signals from 2 local earthquakes are shown in Figures 4 and 5.

In both cases, direct visual comparison of, for example, the post S-phase waveforms suggests that significant wave scattering and attenuation occurs above the level of the deepest downhole seismometers. The attenuation can be seen by the clear lack of high frequency waves in the ground level recordings. Such attenuation causes any phase that has reflected from the earth's surface to be a low pass version of the incident wave. The effects of scattering near the earth's surface can be seen from the progressive development of a post S-wave coda with decreasing observation depth. This coda can not be accounted for by multiple reflections of the direct S-wave or other direct type phases since these last only a fraction of a second and are highly damped by the attenuation. Instead, the uphole data show the presence of a nearly 5 second coda at ground level (Figure 5).

We have postulated a simple first order scattering model to account for these observations (Blakeslee and Malin, 1989). As illustrated in Figure 4, the uphole post S-wave seismogram can be modeled as the sum of two parts: a normal lithospheric S-wave to S-wave (body wave to body wave) scattering coda plus a S-wave to Surface-wave (body to surface wave) scattering coda. The latter waves depend on the local velocity and attenuation structure, and give rise to an incoherent low frequency pulse seen several seconds behind the direct S-wave arrival.

Our research approach to further study these effects is to quantify the wave field between the downhole sensors in terms of frequency dependent transfer functions. Subsequently we will use the transfer functions to guide modeling of the observed wave field. We plan to derive a full scattering theory model of the postulated body to surface wave scattering model set forth in Figure 4.

Selected Poster Figures.

Figure 1. Location map of the Parkfield area and the sites of the Downhole Digital Seismic Network Stations and the Varian Vertical Seismic Profiling Array. These two observatories are located on the San Andreas fault in central California, as shown in the inset state map. Each of the DDSN stations is indicated with a solid dot, and there are a total of 9 stations of this type. The Varian VSP array is in the VARIAN A-1 WELL. Other notable locations are the city of Parkfield and the location of the most recent large ($M=6.0$) earthquake.

Figure 2. Schematic diagram of a DDSN station. This cross sectional view of borehole seismometer system shows the gimbaled, 2 Hz 3-component sensor cemented roughly 300 m below ground level. Signals from the sensor are brought to the surface via cable, amplified and digitized at the well head, and telemetered to a central recording system located at Parkfield. As illustrated, simultaneous recording have also been made at ground level at several of the DDSN stations.

Figure 3. Schematic diagram of the Varian VSP array. The vertically oriented sensor string is shown on by the stippled patterns to the side of this Figure. All the sensors were attached to the high pressure tubing for lowering into the well and the entire well was filled with cement to allow coupling of the seismometers to the local rock. Signals from the sensors are brought to ground level by cable and processed by an on site computer controlled event detection system.

Figure 4. a.) Horizontal component seismograms from a Parkfield event recorded on the uphole and downhole sensors at Vineyard Canyon. Note the differences in the post S-wave seismograms and the presence of a large amplitude, low frequency wavelet in the uphole S-wave coda. b.) First order scattering model to account for differences, including the large, low frequency pulse. In this model, the large uphole pulse is interpreted to be an S-wave continuously scattered and trapped near the earth's surface. This phase is not seen in the downhole data, where the dominant portion of the S-wave coda is produced by lithospheric scattering (figure from Blakeslee and Main, 1989).

Figure 5. Vertical component seismograms from a local magnitude 1.9 earthquake as recorded on the high gain seismometers at various depths in the Varian VSP array. The depth at which each seismogram was recorded is shown in ft on the up left hand margin of the trace window. The time ticks are in seconds and the amplitudes are given in digital counts. The depth dependent waveforms clearly demonstrate the validity of the uphole-downhole model shown in Figure 4, as is indicated by the development of the post S-wave coda as the ground surface is approached. At 77 ft below ground level the coda extends several seconds beyond the direct S-wave, a fact that can not be explained by simple multiple reflection of the S-wave by layered structure above the deepest sensor.

FIGURE 1.

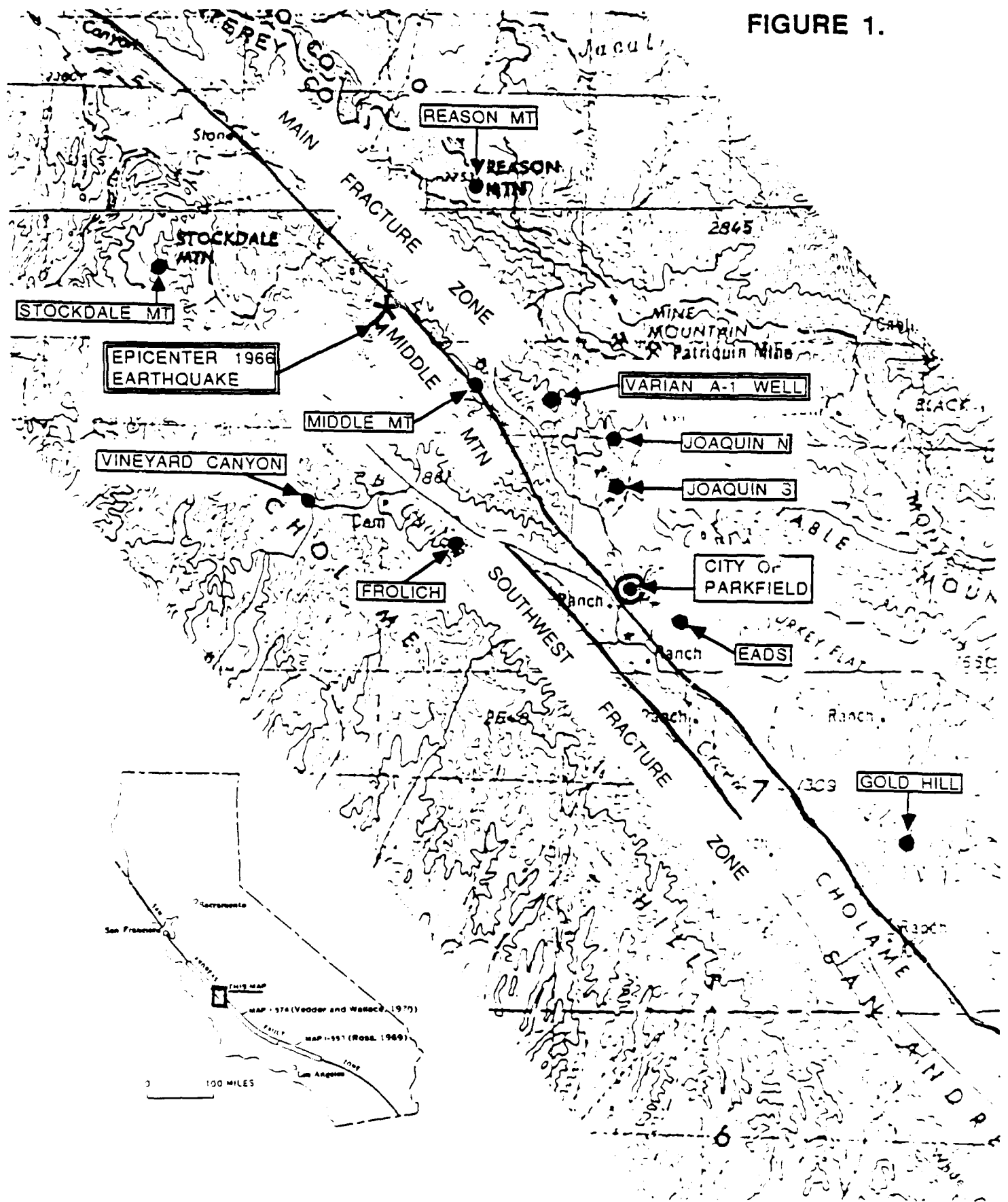


FIGURE 2.

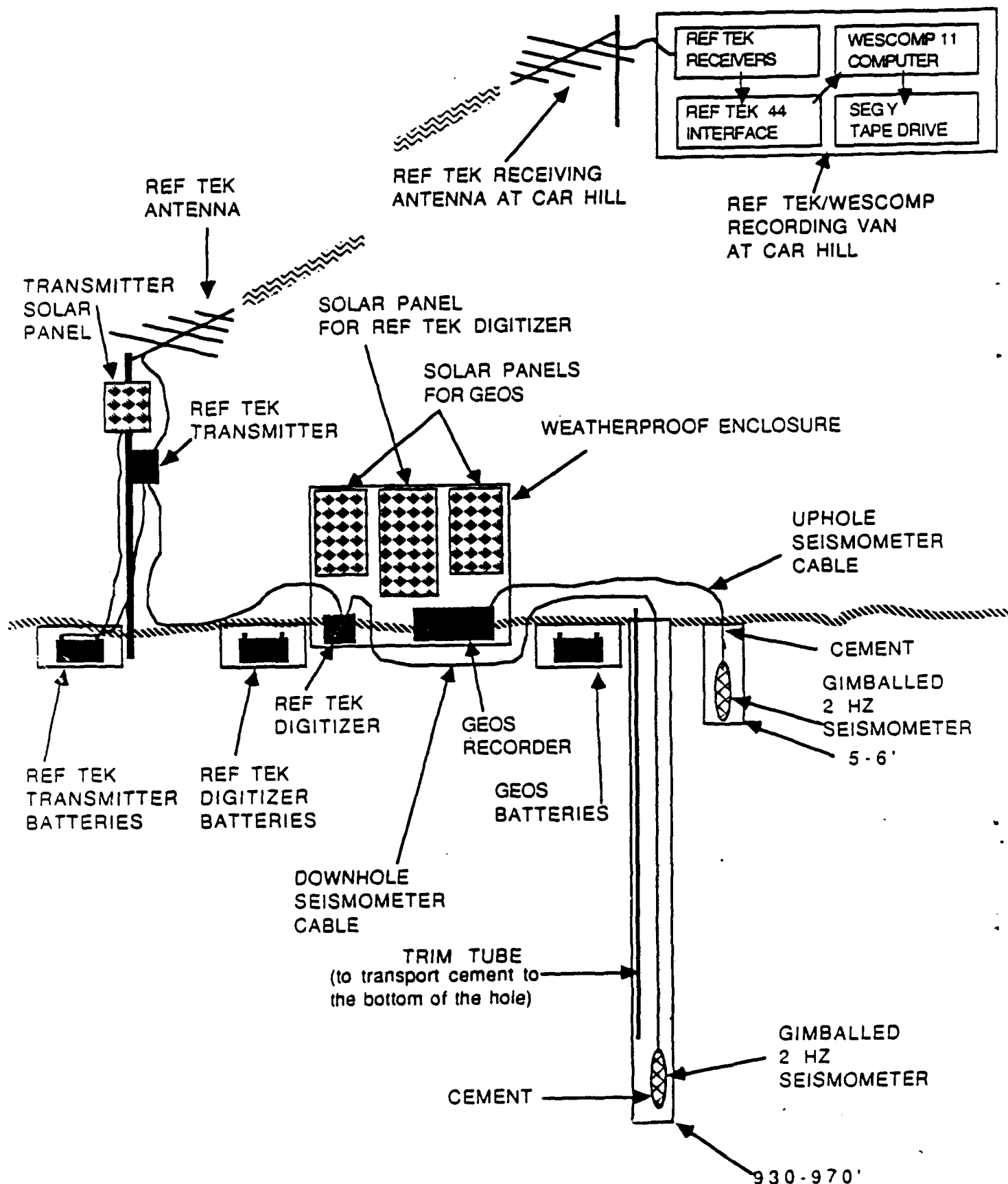


FIGURE 3.

VARIAN A-I SEISMIC OBSERVATORY

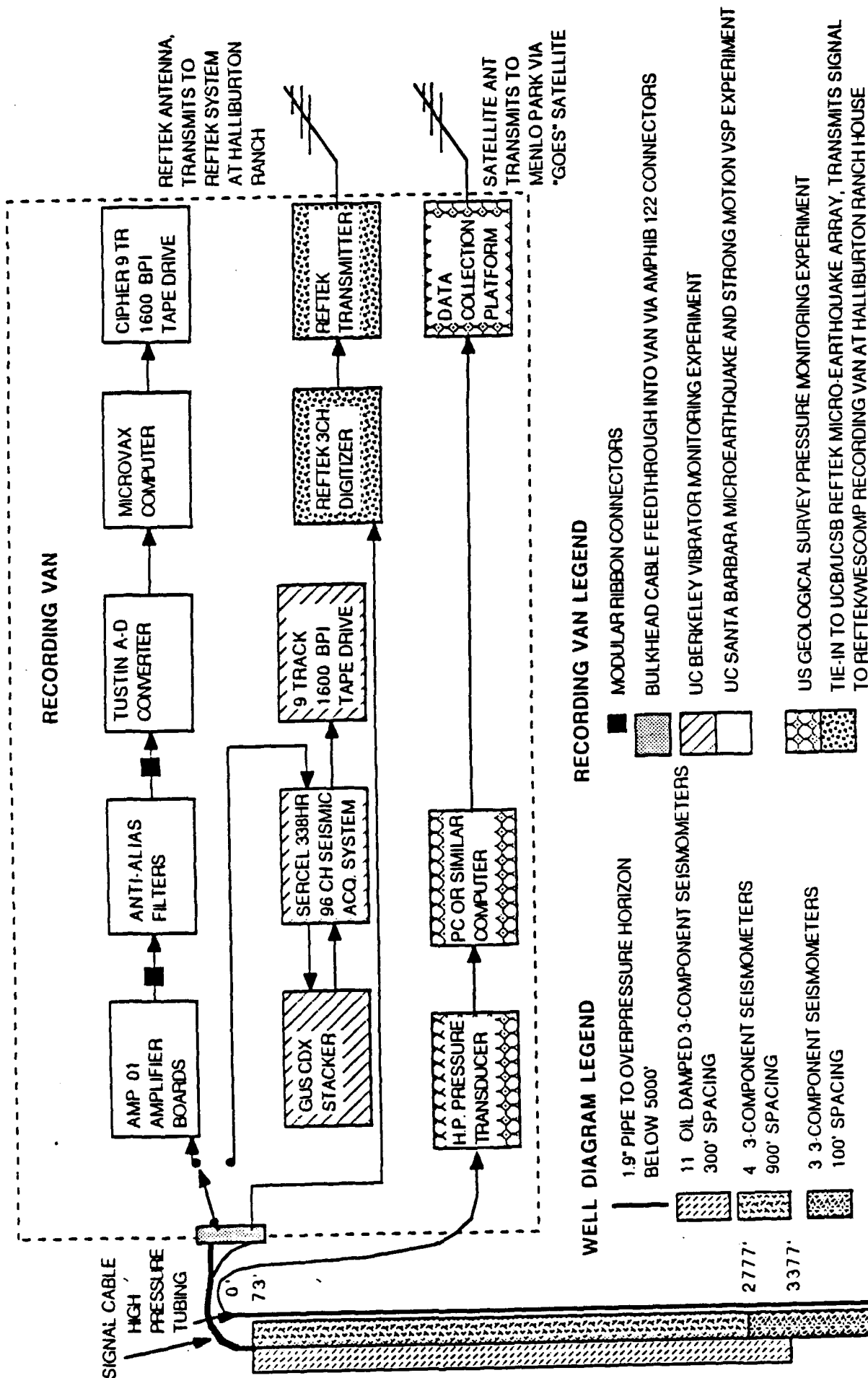
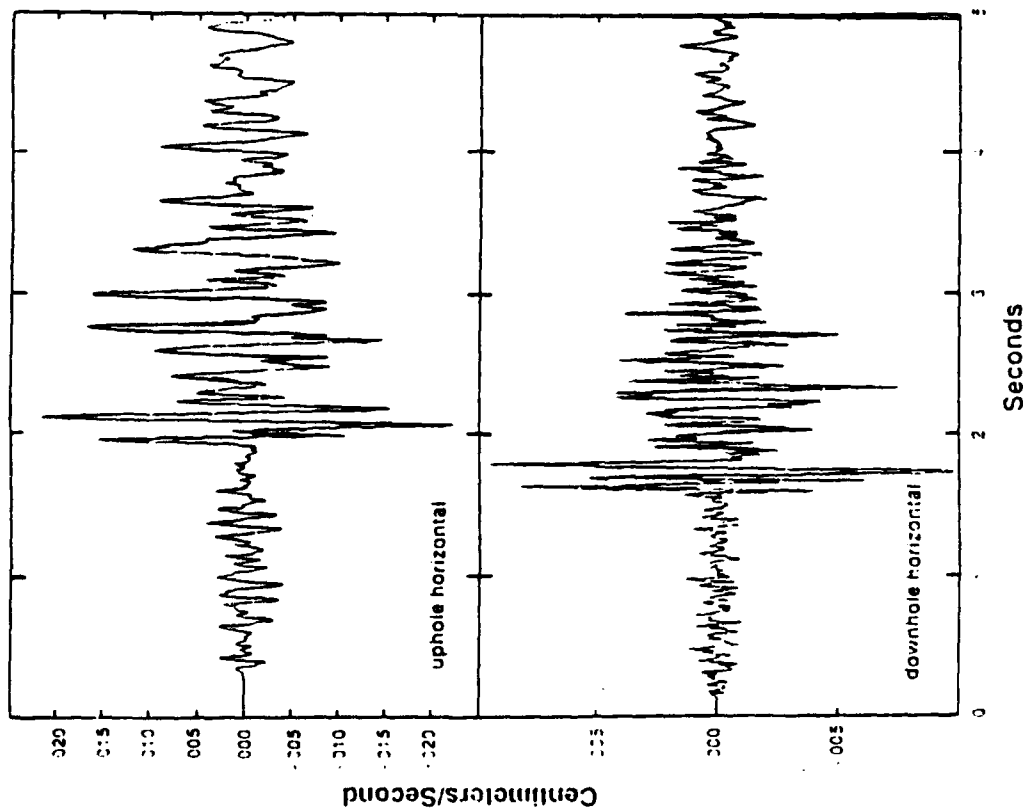


FIGURE 4

A.



B.

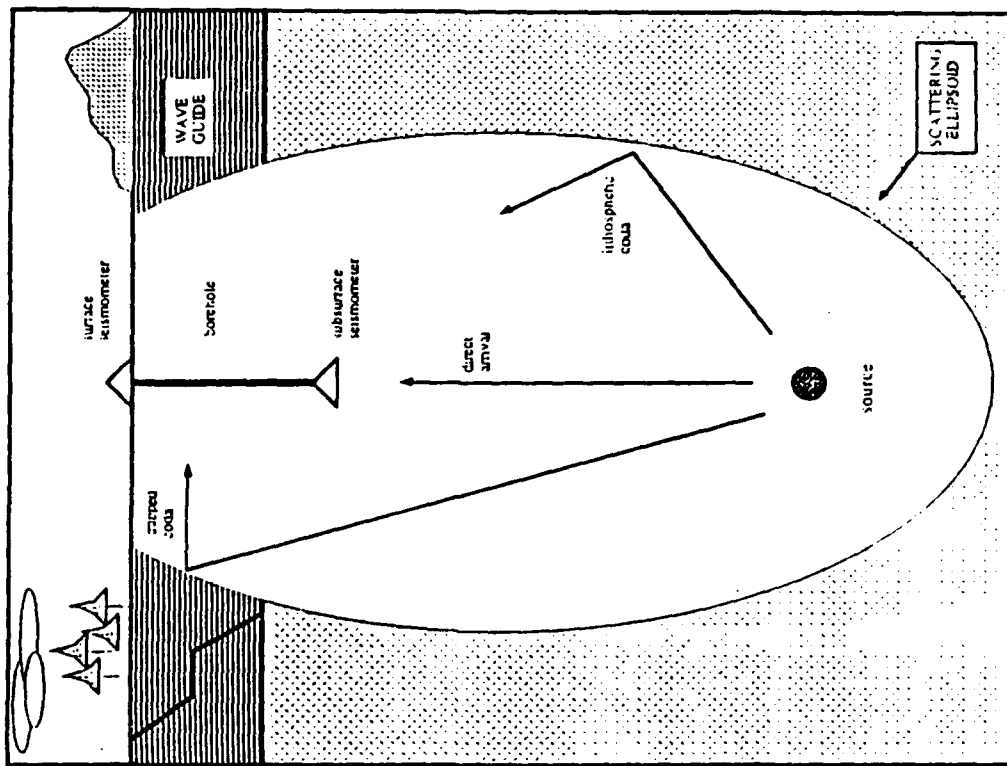
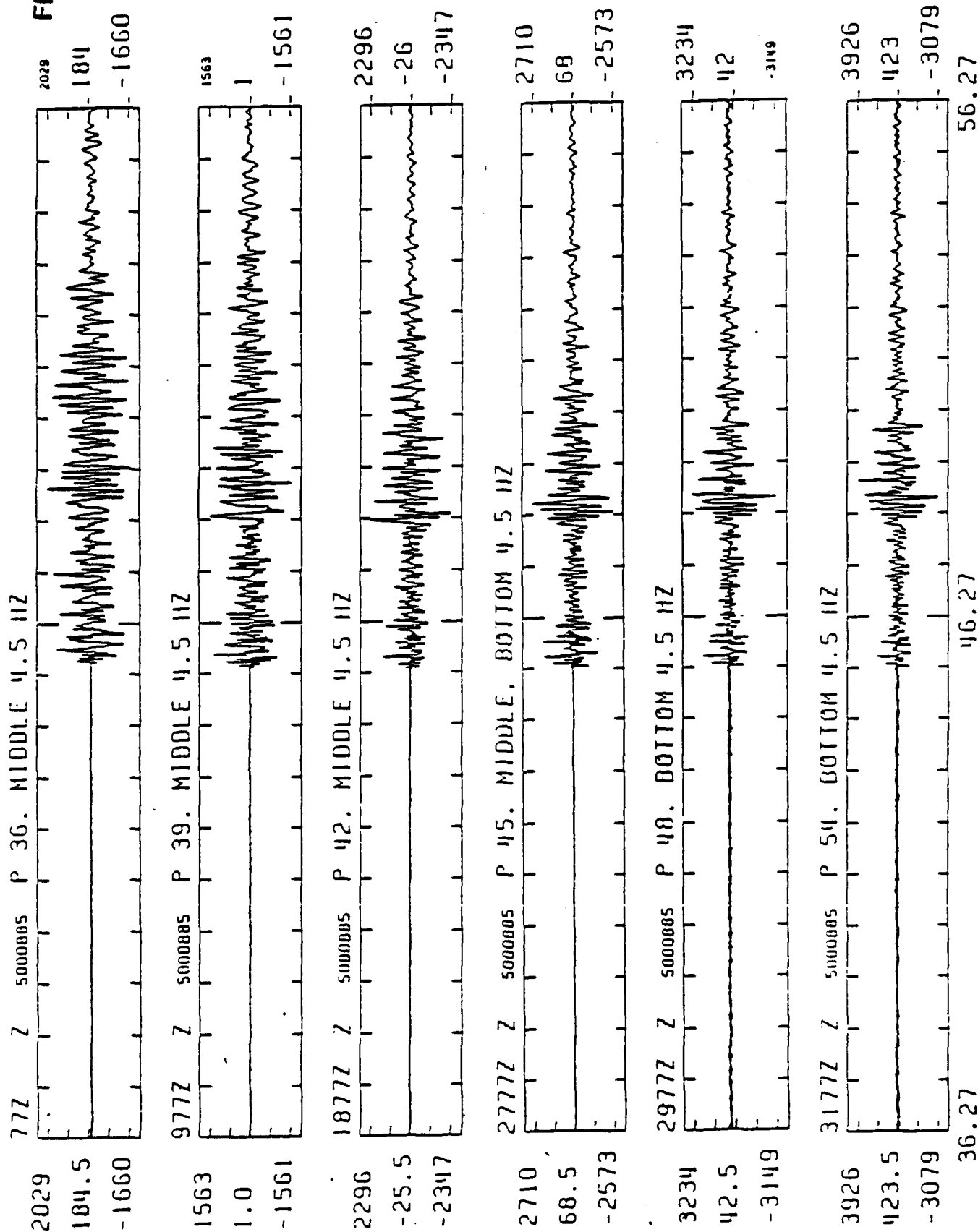


FIGURE 5.



SEC + 1235 25 MAR 1988

46.27

FINITE-DIFFERENCE SIMULATIONS OF SEISMIC WAVE EXCITATION AT SOVIET TEST SITES WITH DETERMINISTIC STRUCTURES

Rong-Song Jih, Wilmer Rivers, and Christopher Lynnes
Teledyne Geotech Alexandria Labs
314 Montgomery Street, Alexandria, VA 22314
(703) 836-3882

CONTRACT NO: F19628-89-C-0063, effective 3 April 1989 (expected)

OBJECTIVE

The long-range objective of this project is to improve the fundamental understanding of how energy from explosion and earthquake sources is partitioned into various seismic wave types due to different geological structures. A better weighting scheme will be derived for combining m_b and M_s in the methodology for yield estimation.

SUMMARY OF RESEARCH PLAN

Due to local structure, explosions at various test sites may produce biased $m_b(P) - m_b(L_g)$ values, since local excitation and scattering may differ markedly among the sites, as indicated by observed data (*e.g.*, Nuttli, 1986; 1987; 1988) and forward modeling (McLaughlin and Jih, 1988; Jih and McLaughlin, 1988a; 1988b). Such biases must be evaluated in the light of TTBT requirements of calibrating magnitude-yield relationships. The research goals of this study are to apply an upgraded 2-D finite-difference method (Levander, 1988; Virieux, 1984; 1986), as well as a 3-D code to be developed, in order to investigate the excitation of various regional phases at several test sites, with emphasis on Soviet test sites, based on detailed geological structure. This approach will provide information directly about the spectral content of seismic waves for different materials and different source depths.

We plan to perform 2-D finite-difference P/SV simulations using East Kazakhstan geological structures (*e.g.*, Leith, 1987) with a suite of incidence angles and different depths. Realistic numerical sources including both explosions and earthquakes (Vidale and Helmberger, 1987) will be used as initial conditions in the separate simulations. Spectra from both source types will be calculated to determine differences in their high-frequency content. The synthetics will be compared to the observed NORSAR and CDSN data as well as to synthetics generated by other techniques (*e.g.*, Lilwall, 1988). These experiments will be repeated for SH (L_g) waves. The finite-difference code will be modified to adapt the topography algorithms used for the P/SV case (Jih *et al.*, 1988) to the SH code. The accuracy of the 2-D code will be improved by coupling the current absorbing boundary conditions with margin-damping techniques.

A 3-D code will be implemented to investigate the seismic problems in a more realistic environment. A 3-D heterogeneous formulation of the wave equation, as well as a 3-D formulation of simple sources, will be implemented. Quasi-transparent boundary conditions and general free-surface boundary conditions (Jih *et al.*, 1988) will be derived for 3-D simulations. We then intend to perform 3-D finite-difference simulations with a suite of incidence angles and different depths, using 3-D geological structures inverted from teleseismic P-wave amplitudes and travel times using the techniques of Aki *et al.* (1976) and Lynnes and Lay (1989). The model parameters of the Soviet test sites will be

refined using results obtained from the Joint Verification Experiment program.

To illustrate some of the approaches that we plan to use once the contract is effective, Figure 1 shows the snapshots of displacement generated by an explosion at depth 3 km in an oversimplified mushroom-shaped intrusion of the crustal structure (Figure 1A) at Karkaralinsk region. The Degelen intrusion is thought to be similarly mushroom-shaped (Leith, 1987). The host rock has P-wave velocity 6.0 km/s, and the intrusion granite has self-similar random velocity with 5% RMS fluctuation (around the mean of 5.5 km/s) and mean autocorrelation distance of 1 km. A simple trapezoidal topography of height 1 km is superimposed on top of the intrusion. Teleseismic P-wave synthetics are computed for a suite of take-off angles and distances with the case of 20° and 5000 km shown in Figure 2. For comparison, the teleseismic synthetics responding to structures without topography and without random variation are also included. The velocity fluctuation of source region excites coda waves which last several seconds after pP. Simulations and analysis with realistic velocity gradient and topographic configuration will be conducted.

REFERENCES

- Aki, K., A. Christofferson, and E. S. Husebye (1976). Three-dimensional seismic structure of the lithosphere under the Montana LASA, *Bull. Seism. Soc. Am.*, 66, 501-524.
- Jih, R.-S., and K. L. McLaughlin (1988a). Investigation of explosion generated SV L_g waves in 2-D heterogeneous crustal models by finite-difference method. *Report AFGL-TR-88-0025 (=TGAL-88-01)*, Teledyne Geotech, Alexandria, VA.
- Jih, R.-S., and K. L. McLaughlin (1988b). Finite-difference modeling of Rayleigh wave scattering and P-SV(L_g) coupling problems (1988). *Report AFGL-TR-88-0093 (=TGAL-88-02)*, Teledyne Geotech, Alexandria, VA.
- Jih, R.-S., K. L. McLaughlin, and Z. A. Der (1988). Free boundary conditions of arbitrary polygonal topography in a 2-D explicit elastic finite-difference scheme. *Geophysics*, 53, 1045-1056.
- Leith, William (1987). Geology of NRDC seismic stations sites in Eastern Kazakhstan, USSR. *Open-File Report 87-597*, U.S. Geological Survey, Reston, VA 22092.
- Levander, A. R. (1988). Fourth-order finite-difference P-SV seismograms, *Geophysics*, 53, 1425-1436.
- Lilwall, R. C. (1988). Regional m_b/M_s, L_g/P_g amplitude ratios and L_g spectral ratios as criteria for distinguishing between earthquakes and explosions: a theoretical study, *Geophys. J.*, 93, 137-147.
- Lynnes, C. S. and T. Lay (1989). Effect of near-source structure on short-period teleseismic P-wave amplitudes, in *Scattering and Attenuation of Seismic Waves*, Vol. 2, Special Issue of *Pure and Applied Geophysics*, (in press).

- McLaughlin, K. L. and R.-S. Jih (1988). Scattering from near-source topography : teleseismic observation and numerical 2-D explosive line source simulations. *Bull. Seism. Soc. Am.* 78, 1399-1414.
- Nuttli, O. W. (1986). Lg magnitudes of selected East Kazakhstan underground explosions. *Bull. Seism. Soc. Am.*, 76, 1241-1251.
- Nuttli, O. W. (1987). Lg magnitudes of Degelen, East Kazakhstan, underground explosions. *Bull. Seism. Soc. Am.*, 77, 679-681.
- Nuttli, O. W. (1988). Lg magnitudes and yield estimates for underground Novaya Zemlya nuclear explosions. *Bull. Seism. Soc. Am.*, 78, 873-884.
- Vidale, J. E., and D. V. Helmberger (1987). Path effects in strong motion seismology, chapter 6 in *Methods of Computational Physics*, 6, 267-319, Academic Press, New York.
- Virieux, J. E. (1984). SH-wave propagation in heterogeneous media: velocity-stress finite-difference method. *Geophysics*, 49, 2247-2249.
- Virieux, J. E. (1986). P/SV-wave propagation in heterogeneous media: velocity-stress finite-difference method. *Geophysics*, 51, 889-901.

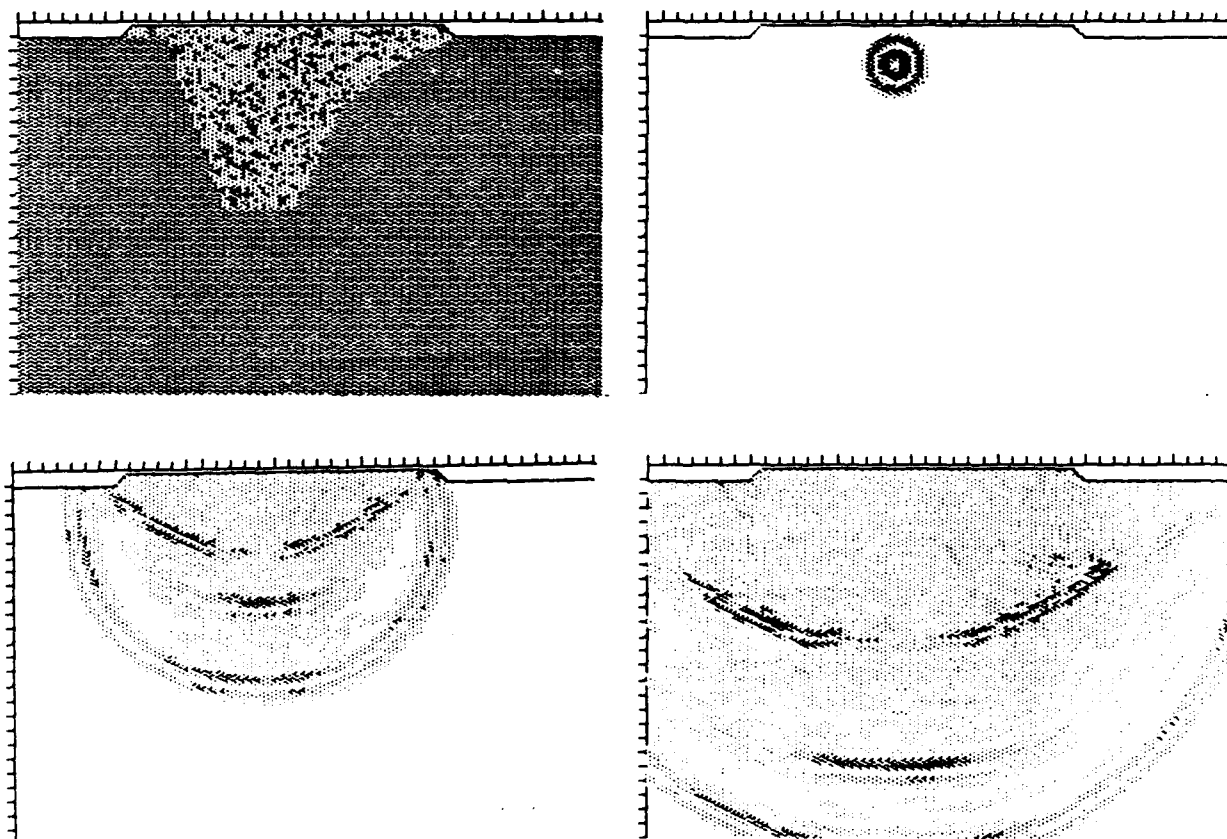


Figure 1. The snapshots of displacement field generated by an explosion at depth 3 km below the trapezoidal topography in an oversimplified mushroom-shaped intrusion of the crustal structure at Karkaralinsk region. The Degelen intrusion is thought to be similarly mushroom-shaped (Leith, 1987). The intrusion granite has self-similar random velocity with 5% RMS fluctuation around the mean of 5.5 km/s, and is embedded in a homogeneous half space with $\alpha = 6$ km.

Teleseismic P-Wave Synthetics With Karkaralinsk Intrusion Model

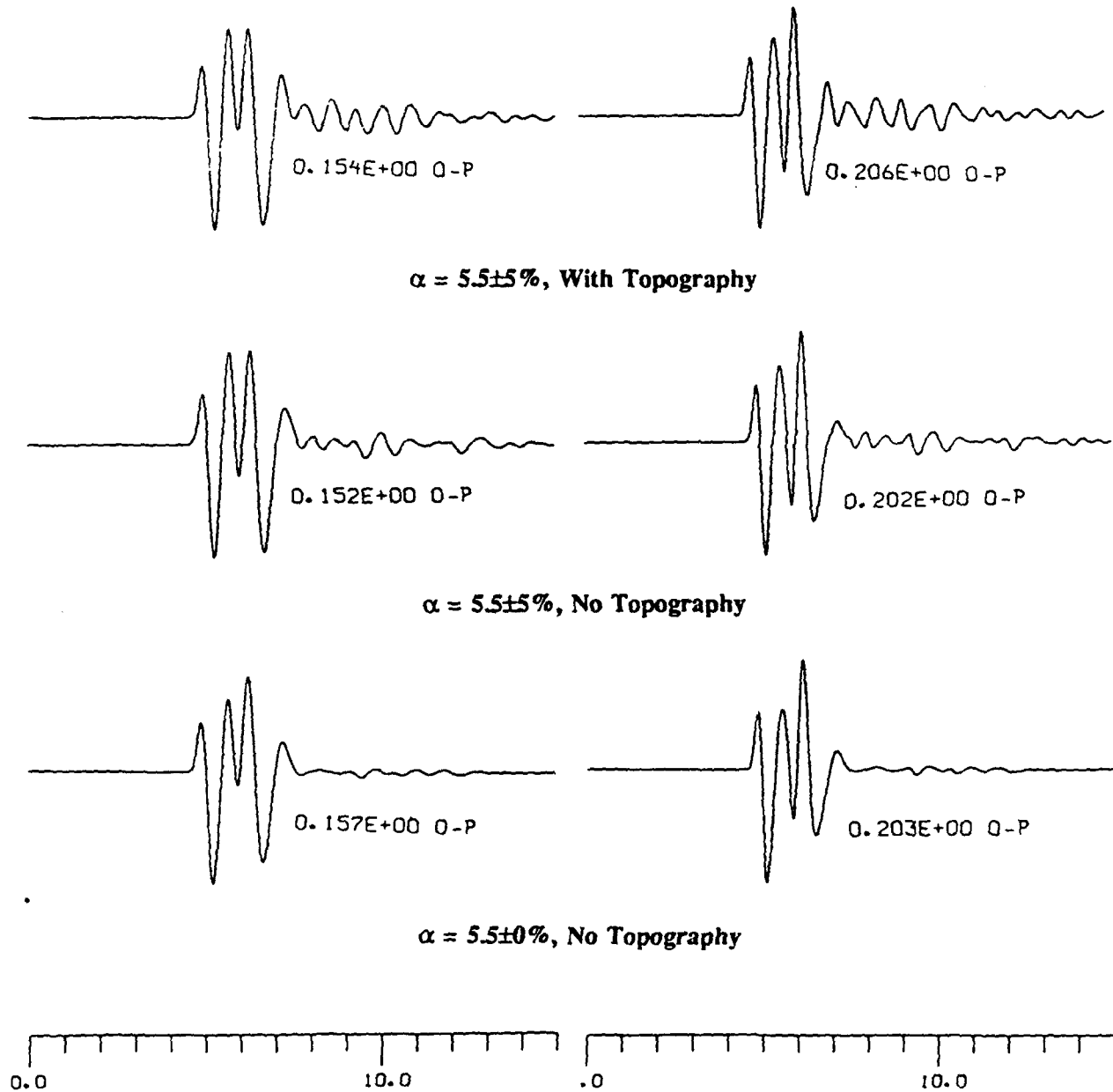


Figure 2. Teleseismic P-wave synthetics of an explosion source derived at take-off angle of 20° and distance of 5000 km with Karkaralinsk granite intrusion model (cf, Figure 1). The explosion source has the burial depth of 3 km. The synthetics have been convolved with Von Seggern and Blandford reduced displacement potential appropriate for 100 kt in granite, an attenuation operator with $t^* = 0.45$ second, and WWSSN SP response (left) or NORSAR response (right). Compared to the results without topography (middle) and without random variation and topography (bottom), the 5% velocity fluctuation of source region excited coda waves which last several seconds after pP.

VARIABILITY OF GROUND MOTION AT FENNOSCANDIAN ARRAYS

M. NAFI TOKSÖZ, EDMOND E. CHARRETTE AND ANTON M. DAINTY¹

EARTH RESOURCES LABORATORY
DEPARTMENT OF EARTH, ATMOSPHERIC, AND PLANETARY SCIENCES
MASSACHUSETTS INSTITUTE OF TECHNOLOGY
CAMBRIDGE MA 02139

CONTRACT NO. F19628-88-K-0036

OBJECTIVE

The primary objective of the research reported here is to study scattering as it affects regional phases. The method of attack is first to calculate the coherency of the wavefield for such phases across closely spaced regional arrays such as NORESS, FINESA and ARCESS as a measure of the effect of scattering. The results are then compared to finite difference computations for a layer over a half space with random perturbations of the velocities and/or the interface between the layer and half space. The coherency for synthetic seismograms from such a model provides the comparison.

SUMMARY OF RESULTS

Introduction

Regional arrays such as NORESS, FINESA and ARCESS provide powerful tools to examine the effect of scattering on seismograms. In previous investigations we have looked at coda, which consists of scattered energy often deviating at large angles from the direct arrivals. In such a situation frequency-wavenumber analysis has proven to be useful because the arrays can resolve the differences in angle clearly. When the effect of scattering on direct phases is considered, however, this method may not produce useful results because unless scattering points are very close to the source or receiver the angle of deviation of the scattered energy will not be resolvable by the array. Flatté and Wu (1988) treat the problem for teleseismic arrivals by examining travel time and amplitude anomalies of 1-3 Hz waves and use an analytic theory to interpret the results in terms of fluctuations in the earth medium. One result of some importance from this work is the short distance (~ 10 km) over which arrivals lose coherence. For regional phases at higher

¹Also NRC Fellow, Air Force Geophysics Laboratory

frequencies even more rapid loss of coherence might be expected. This indicates that information from dense arrays of small aperture is needed, and since travel time and amplitude fluctuations will be smaller new analysis methods are desirable. Accordingly, to evaluate the effect of scattering on direct phases the coherency has been calculated using methods developed for analysis of strong motion array records (Harichandran and Vanmarcke, 1984). The coherency is a frequency domain equivalent of the correlation function used by Bungum *et al.* (1985) and Ingate *et al.* (1985).

The lagged coherency is

$$C(x, \omega) = \frac{S_{ij}(x, \omega)}{[S_{ii}(\omega)S_{jj}(\omega)]^{1/2}} \quad (1)$$

where S_{ij} is the cross spectrum of seismograms $s(x_i)$, $s(x_j)$, lagged to remove time shifts due to travelling wave propagation; the separation $x = x_i - x_j$. S_{ii} and S_{jj} are the autospectra of the two seismograms. To compute the coherency we use methods due to Jenkins and Watts (1969) and Harichandran and Vanmarcke (1984), except that initial estimates of the lag times may be found using frequency-wavenumber analysis (Capon, 1969) to estimate the velocity and azimuth of the mean plane wave and then calculating the lags. The cross correlation and autocorrelations of a shifted pair of seismograms are then windowed with a Hamming window of width 0.5–1 s and the cross spectrum, autospectra and coherency computed. Typical lengths of data in the original seismograms are 3–35 s. This procedure is then repeated for every possible pair of seismograms in the array. In the plots of coherency (strictly, the absolute value of the coherency) and phase lag (the value of the phase of the calculated coherency, a complex quantity), each cross is such a determination. These determinations are then averaged over an appropriate spatial interval and the standard deviations found, using the Fisher Z-transform (Jenkins and Watts, 1969) for the coherency; these averages are plotted as points with error bars. Finally, the phase lag is checked to ensure that the averaged values are close to zero (within $\pm\pi/2$); if they are not a new value of the velocity and/or azimuth is tried until they are. We do not adjust the lags other than through the velocity and azimuth—on occasion, there is residual structure in the phase lags indicating that the signal is not a simple plane wave.

Observations at Fennoscandian Arrays from Quarry Blasts

A quarry blast at 350 km distance recorded at ARCESS and one at 320 km recorded at NORESS are shown with analysis windows in Figure 1. Coherencies as a function of separation at 2, 4 and 6 Hz are shown for the NORESS event in Figure 2. Results at ARCESS and FINESA are similar. The coherency declines with increasing separation and declines faster for higher frequencies. We attribute this decline in coherency to scattering. By looking at different frequencies we have examined different wavelengths. In an attempt to gain an integrated look at the data, Figure 3 plots the spatially averaged coherencies for all frequencies analysed against distance in

wavelengths. Intriguingly, within error limits it appears that the curves of decline of coherency with separation for the different frequencies are all very similar if the separation is scaled to the wavelength. The effect is most dramatic for the NORESS event. The curves for different events appear to be similar; this may reflect the similarity of site/path heterogeneities for these crystalline rock sites. Note that the coherency declines to ~ 0.5 within about one wavelength.

For a preliminary interpretation of these results, we start by noting that in spite of travelling several hundred kilometers through the lithosphere regional seismograms still show distinct phases such as P and Lg, i.e., the effect of scattering is not so strong as to obliterate all features of wave propagation. This suggests the scaling illustrated in Figure 3 must be a propagation effect and indicates that the heterogeneities in the lithosphere must also scale in some manner. This has led us to investigate self-similar models of the crust as discussed in the next section; the appropriate length scales are set by the wavelengths of the waves analysed, which are in the range 0.5–5 km.

Finite Difference Modelling in Highly Heterogenous Media

To analyse the results outlined above, which involve scattering of seismic waves in media with randomly varying velocity fields, we have chosen to use the finite difference method for producing synthetic seismograms. Coherency can then be calculated for a set of synthetic seismograms from a model with specified statistics and compared with the observations. The technique is attractive because it produces a full solution to the elastic wave equation, thus all direct, converted, diffracted and guided waves are accurately modeled. Also, unlike various high frequency approximations, there is no limitation on the ratio of scatterer size to wavelength. This property is essential when modelling waves in a media with self similar velocity fields.

The equations of motion for wave propagation in a two dimensional, elastic, isotropic media can be written in terms of horizontal (u) and vertical (w) particle displacements.

$$\begin{aligned}\rho \frac{\partial^2 u}{\partial t^2} &= \frac{\partial}{\partial x} \left[(\lambda + 2\mu) \frac{\partial u}{\partial x} + \lambda \frac{\partial w}{\partial z} \right] + \frac{\partial}{\partial z} \left[\mu \left(\frac{\partial u}{\partial z} + \frac{\partial w}{\partial x} \right) \right] + F_x \\ (2) \\ \rho \frac{\partial^2 w}{\partial t^2} &= \frac{\partial}{\partial x} \left[\mu \left(\frac{\partial u}{\partial z} + \frac{\partial w}{\partial x} \right) \right] + \frac{\partial}{\partial z} \left[(\lambda + 2\mu) \frac{\partial w}{\partial z} + \lambda \frac{\partial u}{\partial x} \right] + F_z.\end{aligned}$$

In this form Lamé constants λ and μ and density ρ are freely varying functions of position (x, z), and F is the body force term. Unlike earlier finite difference studies in this area, (Frankel and Clayton, 1986), we use a staggered second order finite difference scheme to solve Equation 2. This method is capable of more accurately modelling rapidly varying media, in part because the

effective sampling rate of the velocity field is twice as great as that for a non-staggered grid (Virieux, 1984, 1986). At present we have limited our computations to two dimensional models.

Constructing Random Velocity Perturbations

Random media can be characterized by three basic quantities, their correlation function (or fluctuation spectrum), their probability distribution, and their standard deviation (or spectral amplitude). There are many different correlation functions which can be used to describe a random medium, but in this presentation we will only be concerned with zeroth order Von Karman functions, (Tatarskii, 1961). In two dimensions, the wavenumber domain representation of this class of functions can be written in terms of the correlation length a and the horizontal and vertical wavenumbers k_x and k_z as,

$$\frac{a^2}{1 + a^2(k_x^2 + k_z^2)} \quad (3)$$

The outstanding feature of media with this correlation function is the presence of roughness at all length scales. This property is often seen in nature (Mandelbrot, 1977), and is thought to best reflect the random portion of the earth's velocity field (Wu, 1982; Dainty, 1984; Frankel and Clayton, 1986).

Two dimensional realizations for each of the three material properties, Lamé's parameter, shear modulus, and density, were constructed by inverse Fourier transforming the product of the wavenumber representation of the zeroth order Von Karman function and a random phase term. When transformed back to the space domain, each of the three functions will have the desired autocorrelation function, zero mean and a Gaussian probability distribution.

Example

The effort in finite difference has just begun and so only an example will be presented here. In Figure 4 a model of a layer over a half space with a rough interface and random velocity and density perturbations is shown. For these trial calculations we have limited the size of the model (6.5×25 km) and the frequency content of the seismic signal (1–5 Hz). Synthetic seismograms for the vertical component are shown in Figure 4 with an analysis window for P indicated. P was chosen for analysis because the source is an explosion and the distance travelled is relatively short, about 10 wavelengths. These seismograms were taken for an array between 22 and 24 km distance on the surface of the model and were spaced 125 m apart. The seismograms are lagged

at 4.5 km/s, slower than the P wave velocity of 6 km/s. This indicates scattering to S. Figure 5 shows the coherency at 3 Hz for these synthetic seismograms. Noting that the wavelength at 4.5 km/s and 3 Hz is 1.5 km, we see that the results in Figure 5 agree roughly with Figure 3. This is encouraging and we intend to perform more extensive calculations as discussed below.

CONCLUSIONS AND RECOMMENDATIONS

Coherency declines to ~ 0.5 within about a wavelength for regional phases recorded at the Fennoscandian arrays NORESS, ARCESS and FINESA. Similar effects have been found in synthetic seismograms calculated for models with rough boundaries and self-similar random variations of velocity and density, although the linear dimensions of the models are too small for direct comparison and they are two dimensional rather than three dimensional. Future work will include

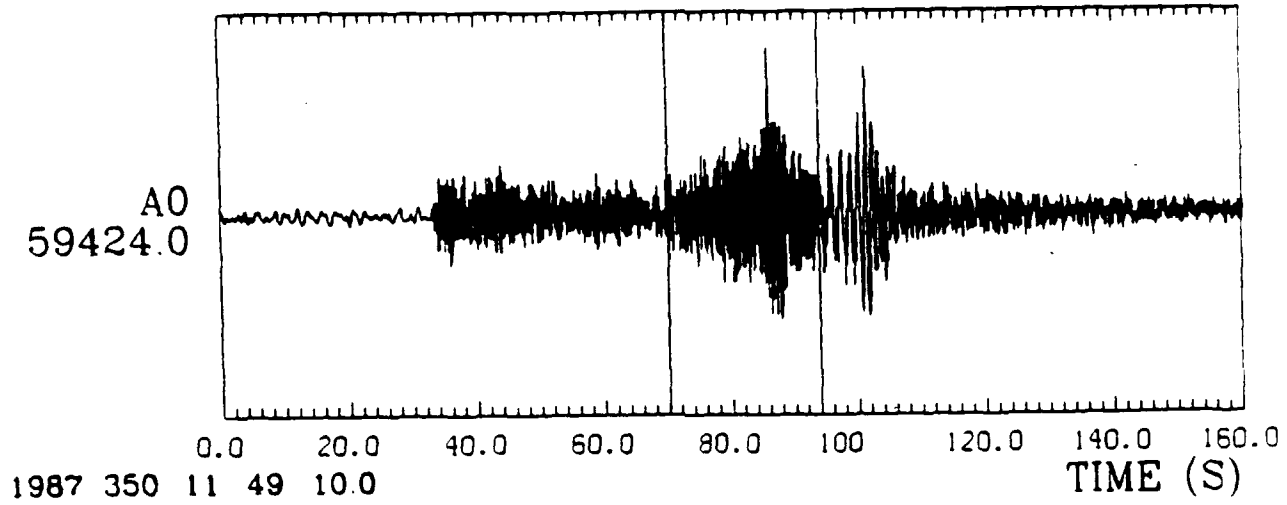
1. Analysis of a larger suite of events of different types from the three arrays in question. Analysis of different phases such as P, P and Lg coda, Sn, Lg and Rg.
2. Computation of larger models including surface topography, more extended frequency bands and possibly three dimensions for better comparisons with synthetic seismograms. Such models will be used to investigate amplitude variation, attenuation and magnitudes as well as coherency.
3. Determine what type of heterogeneity (surface, internal) and what part of the path (near source, main propagation path, near receiver) contribute most to scattering and loss of coherency. This will be carried out by modelling.
4. Use of random simulation of events by perturbing Fourier amplitudes and/or phases between different locations. Preliminary work suggests phase perturbations are much more important than amplitude perturbations.
5. Investigation of other methods of interpreting the data, e.g., methods described in Flatté *et al.* (1979)

REFERENCES

- Bungum, H., S. Mykkeltveit and T. Kværna, Seismic noise in Fennoscandia, with emphasis on high frequencies, *Bull. Seis. Soc. Am.* 75, 1489-1513, 1985.
- Capon, J., High-resolution frequency-wavenumber spectrum analysis, *Proceedings of the IEEE*, 57, 1408-1418, 1969.

- Dainty, A. M., High-frequency acoustic backscattering and seismic attenuation, *Journal of Geophysical Research*, 89, 3172-3176, 1984.
- Flatté, S. M., and R.-S. Wu, Small-scale structure in the lithosphere and asthenosphere deduced from arrival time and amplitude fluctuations at NORSAR, *Journal of Geophysical Research* 93, 6601-6614, 1988.
- Flatté, S. M., R. Dashen, W. H. Munk, K. M. Watson and F. Zachariasen, *Sound Transmission through a Fluctuating Ocean*, Cambridge University Press, New York, 1979.
- Frankel, A. and R. Clayton, Finite difference simulations of seismic scattering: implications for the propagation of short-period seismic waves in the crust and models of crustal heterogeneity, *Journal of Geophysical Research*, 91, 6465-6489, 1986.
- Harichandran, R. S., and E. H. Vanmarcke, Space-time variation of earthquake ground motion, *Department of Civil Engineering Research Report R84-12*, MIT, 1984.
- Ingate, S. F., E. S. Husebye and A. Christoffersson, Regional arrays and processing schemes, *Bull. Seis. Soc. Am.* 75, 1155-1177, 1985.
- Jenkins, G. M., and D. G. Watts, *Spectral Analysis and it's Applications*, Holden-Day, 1969.
- Mandelbrot, B. B., *Fractals*, W. H. Freeman, San Francisco, 1977.
- Tatarskii, V. I., *Wave Propagation in a Turbulent Medium*, McGraw-Hill, New York, 1961.
- Virieux, J., SH-Wave propagation in heterogeneous media: velocity-stress finite-difference method, *Geophysics*, 49, 1933-1957, 1984.
- Virieux, J., P-SV wave propagation in heterogeneous media: velocity-stress finite -difference method, *Geophysics*, 51, 889-901, 1986.
- Wu, R. S., Attenuation of short period seismic waves due to scattering, *Geophys. Res. Lett.* 9, 9-12, 1982.

K87350



N85058

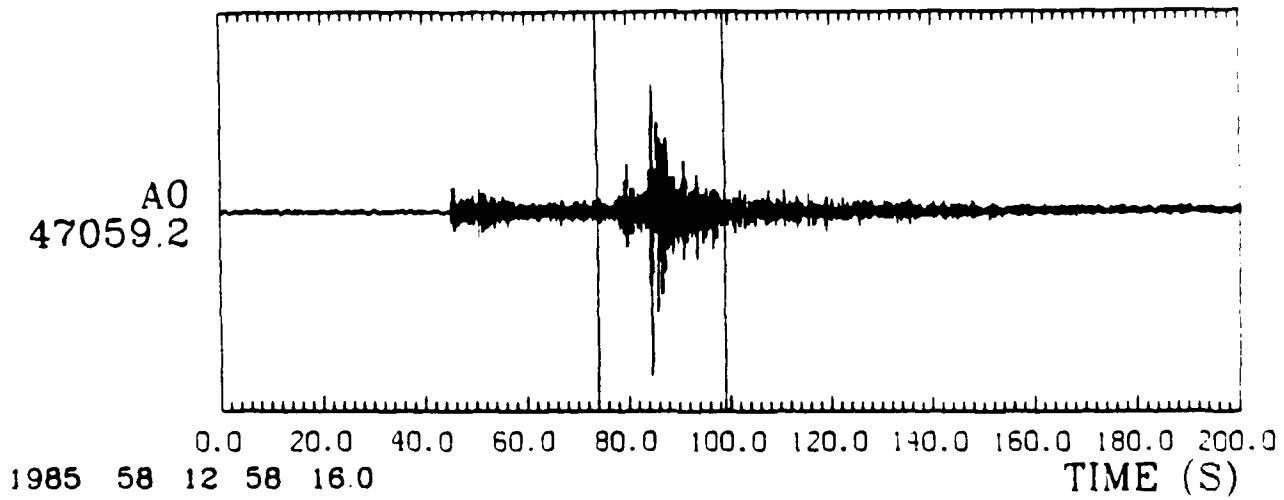


Figure 1: Vertical component seismogram recorded at ARCESS from a quarry blast at 350 km (top) and vertical component seismogram recorded at NORESS from a quarry blast at 320 km (bottom).

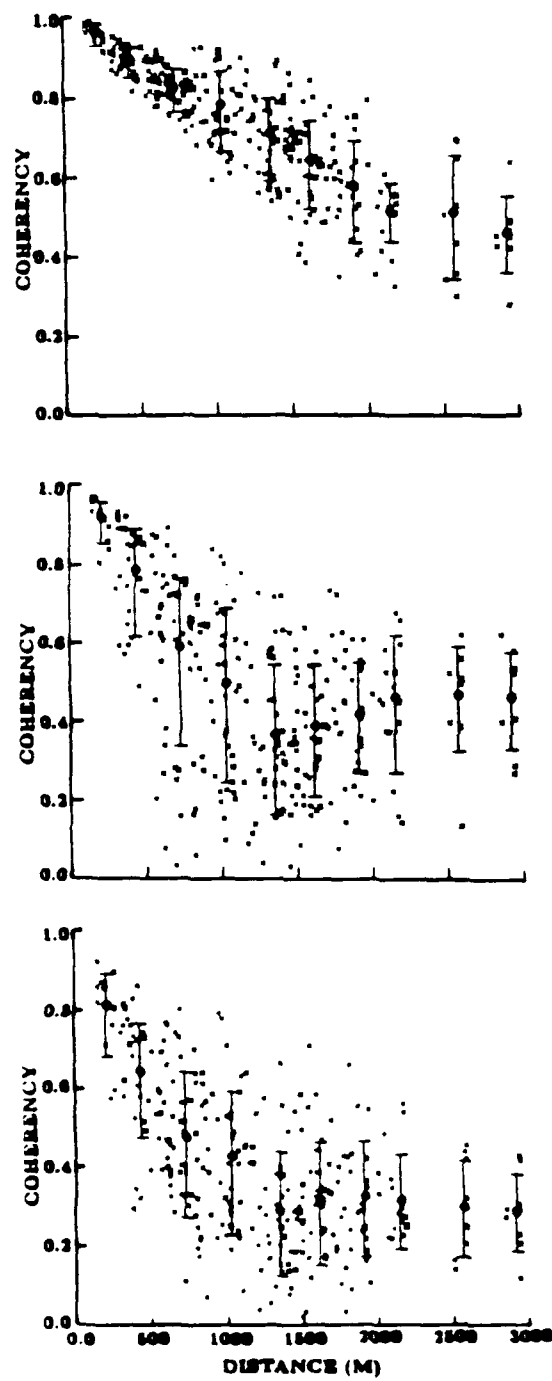


Figure 2: Coherency vs separation at 2 Hz (top), 4 Hz (middle) and 6 Hz (bottom) for the windowed NORESS data in Figure 1.

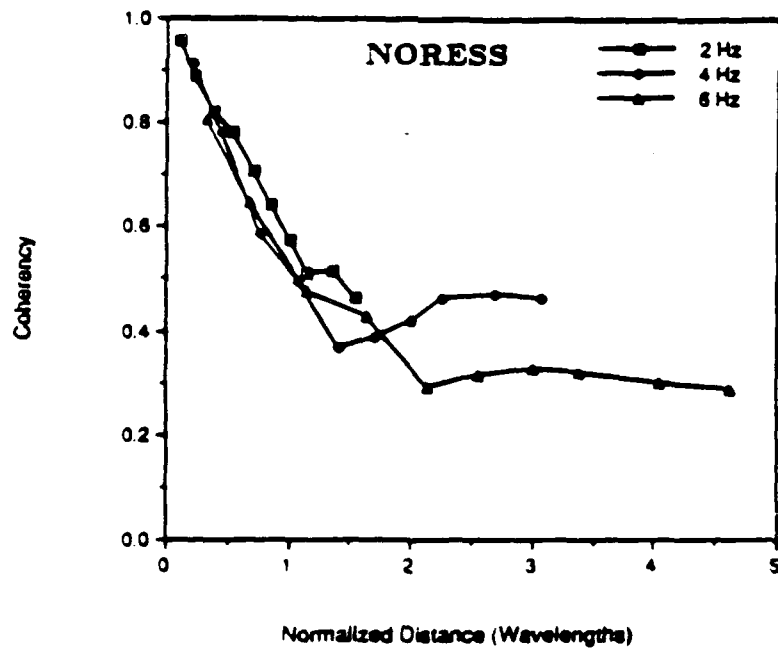
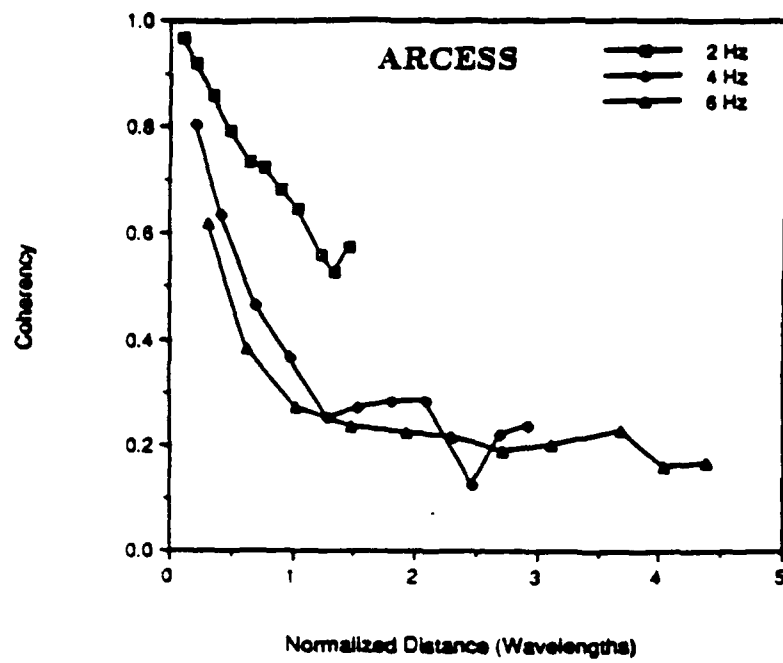


Figure 3: Coherency vs normalized distance for the two events recorded at ARCESS (top) and NORESS (bottom).

Self Similar Model with 15% Perturbations

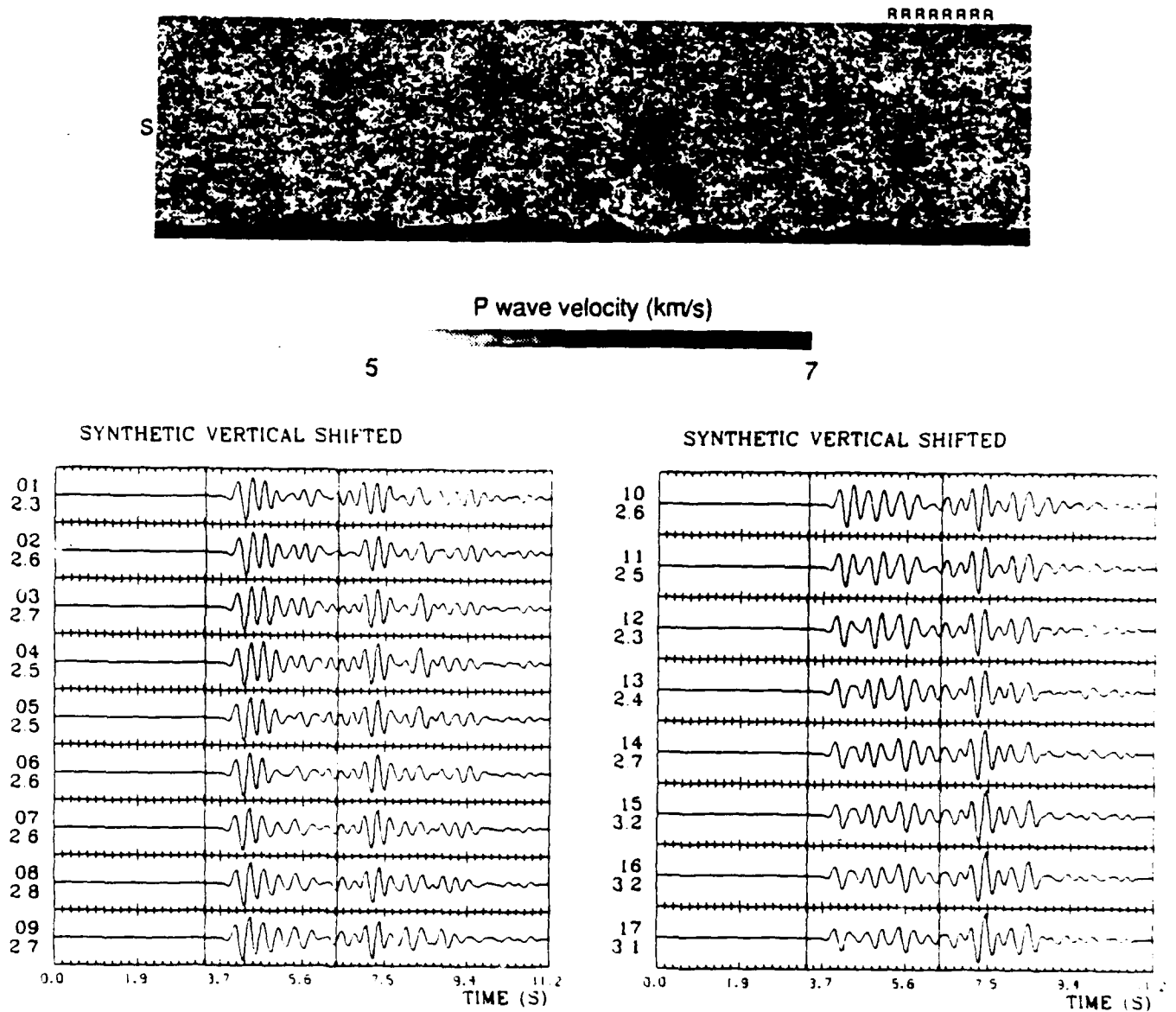


Figure 4: (Top) Model used for synthetic computations. The source is explosive and seismograms are computed for an array 2 km long with a spacing of 125 m. Dimensions of the model are 6.5×25 km; the upper layer has a P velocity of 6 km/s, the lower 7 km/s and Poisson's ratio is 0.25. (Bottom) Vertical seismograms for a wavelet of dominant frequency 3 Hz, lagged at 4.5 km/s and with an analysis window indicated. Top number to right of each trace is the element number (1–22 km, 17–24 km) and the bottom number is the maximum amplitude.

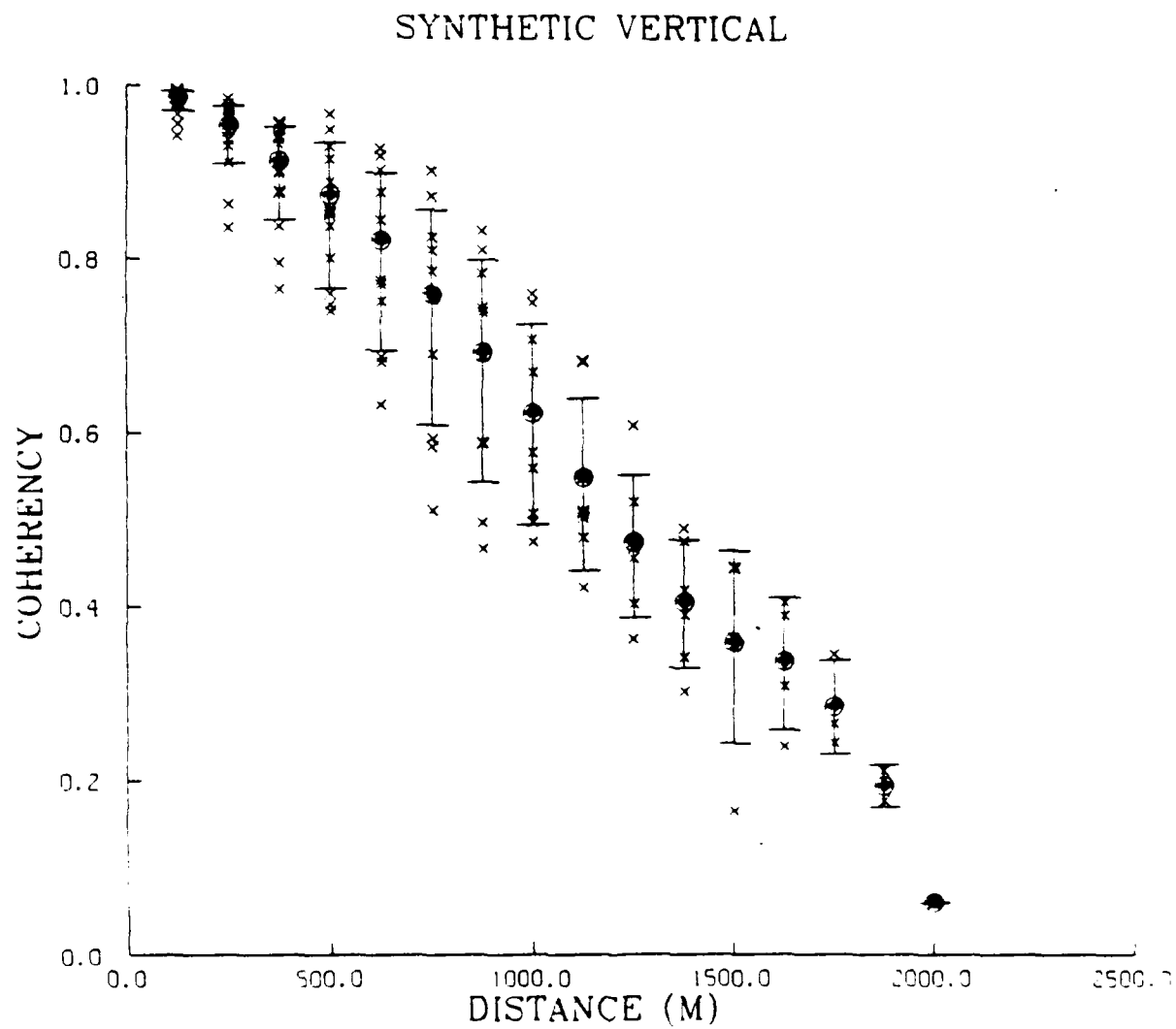


Figure 5: Coherency at 3 Hz for the vertical component synthetic seismograms from the model of Figure 4.

SYNTHETICS SEISMOGRAMS AND RADIATION PATTERNS
FOR AN EXPLOSION IN ANISOTROPIC MEDIA

B. MANDAL AND M. N. TOKSÖZ

EARTH RESOURCES LABORATORY
DEPARTMENT OF EARTH, ATMOSPHERIC, AND PLANETARY SCIENCES
MASSACHUSETTS INSTITUTE OF TECHNOLOGY
CAMBRIDGE, MA 02139

CONTRACT NO. F19628-87-K-0054

OBJECTIVE

The primary objective of this study is to determine the effect of seismic anisotropy on the radiation patterns, calculating the synthetic seismograms for an explosion in an anisotropic medium. Theoretical seismograms show that radiation patterns are strongly affected by the anisotropy. An explosion in an anisotropic medium with horizontal axes of symmetry generates P, SV and Rayleigh waves whose amplitudes vary with azimuth, and significant transverse (SH) waves at certain azimuths.

SUMMARY OF RESULTS

Introduction

The causes of the azimuthal dependence of radiation patterns of P, SV, and Rayleigh waves and the generation of SH and Love waves by underground nuclear explosions have been studied extensively (Kisslinger *et al.*, 1961; Archambeau *et al.*, 1970; Toksöz and Kehler, 1972; Massé, 1981; Wallace *et al.*, 1983; Gupta and Blandford, 1983; Lynnes and Lay, 1988; Johnson, 1988). Various mechanisms, including tectonic strain energy release by relaxation or triggering of an earthquake, dislocation across cracks, spallation and "slapdown" and scattering from heterogeneities have been proposed and found to explain some of the data. No single mechanism has been identified that could satisfactorily explain all the data (Massé, 1981; Gupta and Blandford, 1983; Johnson, 1988.)

In this paper, we will investigate the contribution of the medium anisotropy to the complexity of seismic radiation patterns and the generation of transversely polarized (SH) waves by underground nuclear explosions. The evidence for seismic anisotropy in the earth's crust has

been increasing. Recent observational studies showed that the crust material may have seismic anisotropy due to aligned fractures randomly distributed all over (e.g., Stephen, 1981; Crampin, 1984; Thomsen, 1986; Winterstein, 1986). Several major factors contribute to seismic anisotropy, including: (1) preferred orientation of the minerals due to deposition or metamorphism; (2) geometric effects, such as alternating high and low velocity thin beds (e.g., shales, carbonates); and (3) stress-induced preferred orientation of micro- and macro-fractures at shallow crust. The complete seismogram synthesis in transversely isotropic media with a vertical axis of symmetry (Mandal and Mitchell, 1986) showed that the most simple kind of anisotropy can alter the waveform significantly. Ben-Menahem and Toksöz (1989) showed that the radiation pattern of P waves from an explosion in a transversely isotropic medium was not circular, but depended on the angle from the symmetry axis. Furthermore, the explosion generated a significant amount of S waves, where none would be generated in an isotropic medium. In this paper we compute complete synthetic seismograms from an explosion source in azimuthal anisotropic media. Such a medium can be derived from aligned vertical fractures. We show that anisotropy could have significant effects on radiation patterns of all phases producing a transverse component of P-wave and generating a strong SH-type transverse wave.

Test Models and Synthetic Seismograms

To understand the effects of anisotropy on seismic waves from an explosion source, we use two relatively simple test models: an anisotropic half-space and an anisotropic layer over an isotropic half-space.

1. Half-Space

We chose the anisotropic half-space as our simplest test model. The anisotropy is caused by a parallel set of thin vertical fractures filled by a fluid. The aspect ratio of the fractures is 0.001. The elastic constants are computed by the theory developed by Hudson (1981) and follow theoretical formulations by Crampin (1984). Such a medium is described by a set of five elastic constants with a horizontal symmetry axis. The five elastic constants in terms of velocities are: $\sqrt{\frac{C_{11}}{\rho}} = 5.94$; $\sqrt{\frac{C_{22}}{\rho}} = \sqrt{\frac{C_{33}}{\rho}} = 6.13$; $\sqrt{\frac{C_{44}}{\rho}} = 3.55$; $\sqrt{\frac{C_{55}}{\rho}} = \sqrt{\frac{C_{66}}{\rho}} = 2.85$ and $\sqrt{\frac{C_{12}}{\rho}} = \sqrt{\frac{C_{13}}{\rho}} = 3.43$ km/sec. The density (ρ) is 2.8 gm/cc. An explosion source is placed at a depth 1 km below the surface. The explosion source is generated by three equal diagonal moment tensors (e.g., Mandal and Toksöz, 1989; Fryer and Frazer, 1984). Let us assume the fracture planes are parallel to an east-west direction (i.e., the x - z plane) as shown in Figure 1. We calculate seismograms for five different azimuths ($N0^\circ$, $N22.5^\circ E$, $N45^\circ$, $N67.5^\circ$ and $N90^\circ E$) with stations at

distances 5 and 50 km from the epicenter. The mathematical and numerical formulations are given by Mandal and Toksöz (1989). After the responses are calculated by wavenumber and frequency integration with 0–10 Hz band, the synthetic seismograms are generated by convolving these with a Ricker wavelet-type pulse centered at 1 Hz, 2 Hz, 3 Hz, and 4 Hz. The seismograms are shown in Figures 2–3, respectively, for the five azimuths in the 0° to 90° range. Prominent transverse component motion is observed at azimuths of 22.45 and 67°. At 5 km offset, the arrival times between longitudinal and transverse waves are small. In the high frequency seismograms (4 Hz), wave types can be differentiated by comparing transverse components with vertical or radial components. In this and subsequent figures, the seismograms in the direction of the symmetry axis ($\phi = 90^\circ$) correspond exactly to that of an isotropic medium with appropriate velocities. In an anisotropic medium, the three wave types are: qP (quasi-longitudinal), qSP (transverse wave polarized within the symmetry plane), and qSR (transverse wave polarized perpendicular the symmetry plane). The azimuthal dependence of velocities are affected by the aspect ratio of fractures, fracture density, and properties of materials filling the fractures such as water or air (Hudson, 1981; Shearer and Chapman, 1989).

The seismograms at a distance of 50 km from the source (Figure 3) show that qP waves show a variation of travel times (velocities) and amplitudes as a function of azimuth on both vertical and radial components. There is a small transverse component of P wave at $\phi = 22.5^\circ$, 45° , and 67.5° azimuths. The large pulse in the vertical component is a combination of shear (qSP) and Rayleigh waves. The velocity variation with azimuth is clearly observable. The amplitude also depends on azimuth as seen on both the vertical and radial components. The transverse component seismograms clearly show the large transverse shear wave (qSR) at $\phi = 67.5^\circ$. Also, the shear wave splitting diagnostic of an anisotropic medium is observable.

The frequency dependence of shear and Rayleigh waves may be explained by the free surface effect and azimuthal dependence of elastic constants. In seismograms at 90° azimuth (i.e., the isotropic case), we can see the decrease of the Rayleigh wave amplitude exponentially with frequency. At other azimuths (22.5° , 45° , 67.5°), the qSR and Rayleigh wave amplitude changes rapidly. The phenomena for anisotropic media have some very different features. There is a cusp on shear wave velocity surface (qSP) for fluid-filled fractures (Crampin, 1984; Shearer and Chapman, 1989). The behavior of polarizations of three waves (qP, qSP, qSR) in such a medium has been studied by Shearer and Chapman (1989). The complexity of reflection and transmission properties in an anisotropic medium have been reported by Rokhlin *et al.* (1986). Frequency dependence of Rayleigh waves come from a complicated velocity surface of the shear wave.

The generation of transverse components by an explosion in an anisotropic half-space are due to the azimuthal variation of elastic constants which results in non-spherical displacements at the source. Although we construct the explosion source using three equal orthogonal moment tensors, the final source vector is a product of the moment tensor matrix and the system matrix

whose components contain medium elastic constants (C_{ijkl}), density and phase slownesses.

II. Layer Over Half-Space

This model consists of a 2 km thick anisotropic layer over an isotropic half-space. The source is an explosion at 1 km depth in the anisotropic layer as shown in Figure 4. The anisotropic layer contains aligned, vertical, fluid-filled fractures with an aspect ratio of 0.001 and crack density of 0.2, the same as the previous model. The five elastic constants in terms of velocities are : $\sqrt{\frac{C_{11}}{\rho}} = 5.35$; $\sqrt{\frac{C_{22}}{\rho}} = \sqrt{\frac{C_{33}}{\rho}} = 5.47$; $\sqrt{\frac{C_{44}}{\rho}} = 3.00$; $\sqrt{\frac{C_{55}}{\rho}} = \sqrt{\frac{C_{66}}{\rho}} = 2.42$ and $\sqrt{\frac{C_{12}}{\rho}} = \sqrt{\frac{C_{13}}{\rho}} = 3.40$ km/sec. The density (ρ) is 2.7 gm/cc. The isotropic half-space has the P- and S-wave velocities of: $V_p = 6.2$ and $V_s = 3.5$ km/sec. The density is 2.8 gm/cc. Synthetic seismograms are calculated for the same source and receivers arrangements, as in the previous example. Figures 5 and 6 show the synthetic seismograms at distances 5 km and 50 km, respectively. The time offset for 50 km distance is 6.25 sec (8 km reduced velocity). The transverse motion due to anisotropy is very prominent. The multiples are also observed in transverse motion. The explanation of frequency dependence may be explained as one did in a half-space model.

CONCLUSIONS

An explosion in an anisotropic medium has a non-uniform radiation pattern and generates significant transverse motion at certain azimuths because: (1) A spherical explosion in an anisotropic medium becomes a non-spherical source due to the directional dependence of elastic compliance. (2) The reflection (especially at free surface) and conversion of seismic waves propagating in an anisotropic medium further complicate the seismograms and their frequency dependence. These examples show that anisotropy may be a significant factor in contributing to the generation of transverse waves by explosions.

REFERENCES

- Archambeau, C.G. and C. Sammis, 1970, Seismic radiation from explosions in prestressed media and the measurement of tectonic stress in the Earth, *Rev. Geophys.*, 6, 241-288.
- Ben-Menahem, A. and M.N. Toksöz, 1989, Radiation patterns from explosions in anisotropic media, in press.

- Crampin, S., 1984, Effective elastic constants for wave propagation through cracked solids, *Geophys. J. R. astr. Soc.*, 76, 135-145.
- Fryer, G.J. and N. Frazer, 1984, Seismic waves in stratified anisotropic media, *Geophys. J. R. astr. Soc.*, 78, 691-710.
- Gupta, I.N. and R.R. Blandford, 1983, A mechanism for generation of short-period transverse motion from explosions, *Bull. Seism. Soc. Am.*, 73, 571-591.
- Hudson, J.A., 1981, Wave speeds and attenuation of elastic waves in material containing cracks, *Geophys. J. Roy. astr. Soc.*, 64, 133-150.
- Johnson, L.R., 1988, Source characteristics of two underground nuclear explosions, *Geophys. J.*, 95, 15-30.
- Kisslinger, C., E.J. Mateker, Jr., and T.V. McEvilly, 1961, SH motion from explosions in soil, *J. of Geophys. Res.*, 66, 3487-3496.
- Lynnes, C.S. and T. Lay, 1988, Analysis of amplitude and travel-time anomalies for short-period P-waves from NTS explosions, *Geophys. J.*, 92, 431-443.
- Mandal, B. and B.J. Mitchell, 1986, Complete seismogram synthesis for transversely isotropic media, *J. Geophys.*, 59, 149-156.
- Mandal, B. and M.N. Toksöz, 1989, Computation of complete waveforms in general anisotropic media -I. Algorithm, submitted to *Geophys. J.*.
- Massé, B.P., 1981, Review of seismic source models for underground nuclear explosions, *Bull. Seism. Soc. Am.*, 71, 1249-1268.
- Rokhlin, S.I., T.K. Bolland, and L. Adler, 1986, Reflection and refraction of elastic waves on a plane interface between two generally anisotropic media, *J. Acoust. Soc. Am.*, 79, 906-918.
- Shearer, P.M. and C.H. Chapman, 1989, Ray tracing in azimuthally anisotropic media-I. Results for models of aligned cracks in the upper crust, *Geophys. J.*, 96, 51-64.
- Stephen, R.A., 1981, Seismic anisotropy observed in upper oceanic crust, *Geophys. Res. Lett.*, 8, 865-868.
- Thomsen, L., 1986, Weak elastic anisotropy, *Geophysics*, 51, 1954-1966.

Toksöz, M.N. and H.H. Kehrler, 1972, Tectonic strain release by underground nuclear explosions and its effect on seismic discrimination, *Geophys. J. R. astr. Soc.*, 31, 141-161.

Wallace, T.C., D.V. Helmberger, and G.R. Engen, 1983, Evidence of tectonic release from underground nuclear explosions in long-period *P* waves, Vol. 73, 593-613.

Winterstein, D.F., 1986, Anisotropy effects in *P*-wave and *SH*-wave stacking velocities contain information on lithology, *Geophysics*, 51, 661-672.

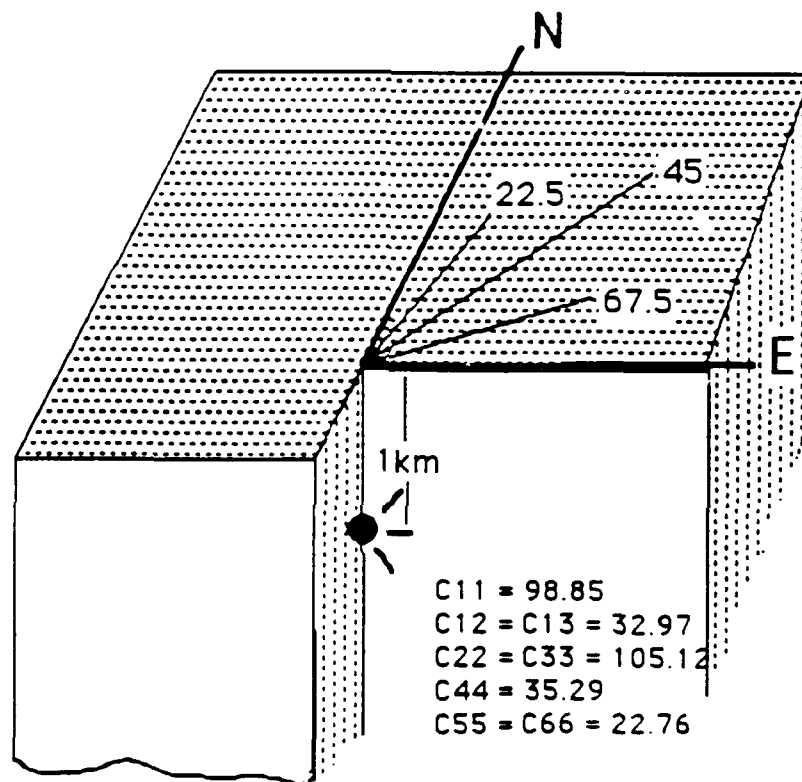


Figure 1: The schematic diagram of an anisotropic half-space model. Dashed lines represent fractures.

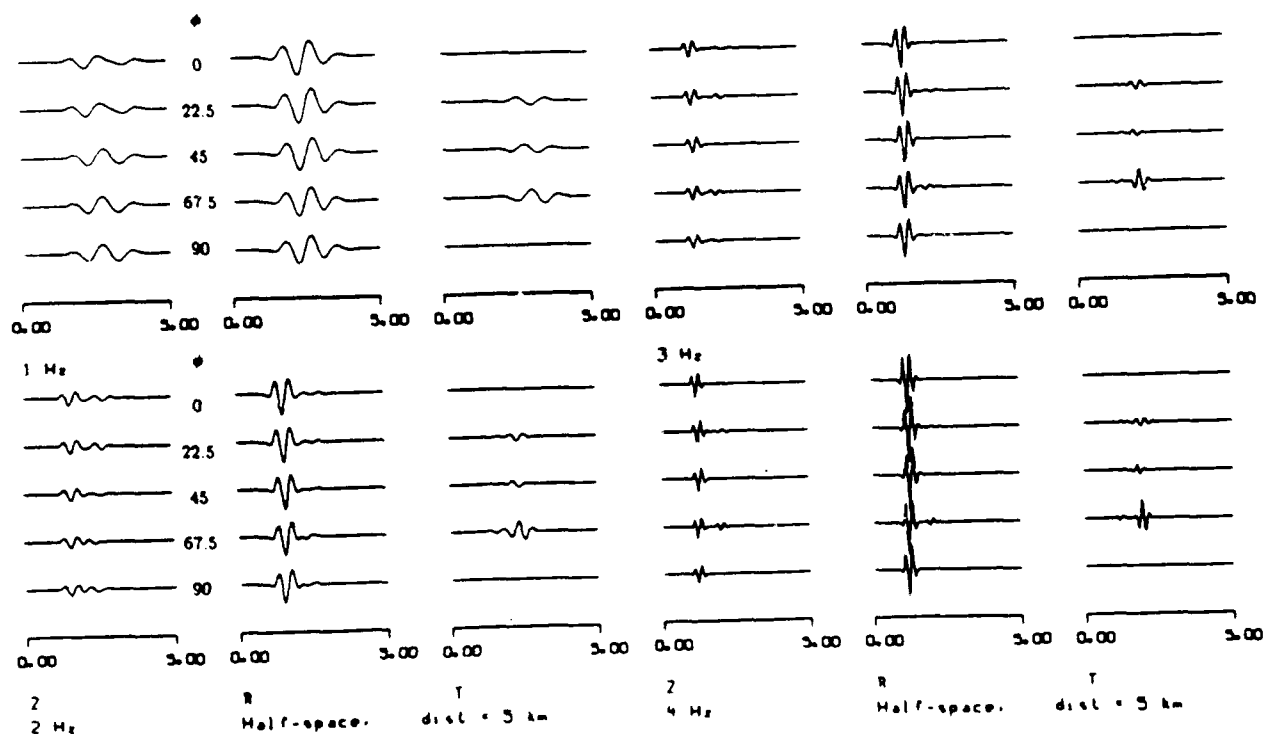


Figure 2: Three-component synthetic seismograms at 5 km epicentral distance, for five azimuths and frequencies of 1, 2, 3, and 4 Hz. The seismograms at $\phi = 90^\circ$ are equivalent to those of an isotropic reference medium.

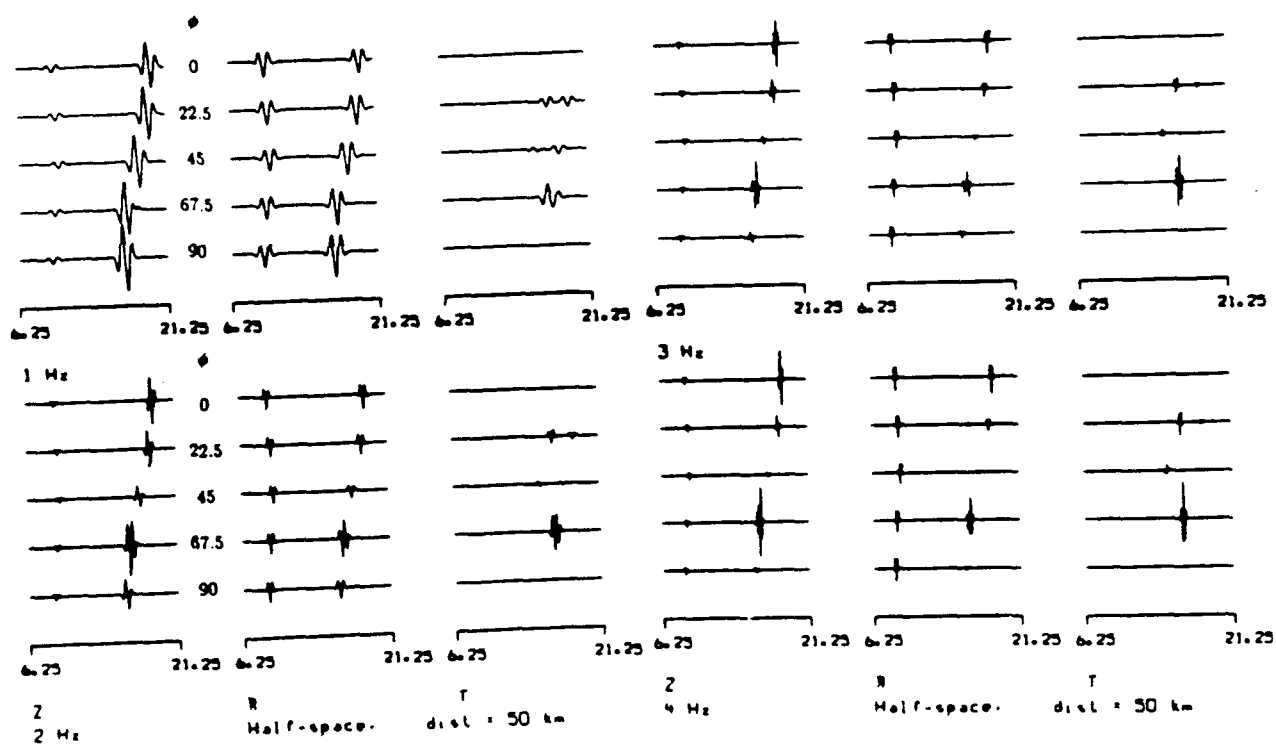


Figure 3: Three-component synthetic seismograms at 50 km epicentral distance, for five azimuths and frequencies of 1, 2, 3, and 4 Hz. The seismograms at $\phi = 90^\circ$ are equivalent to those of an isotropic reference medium.

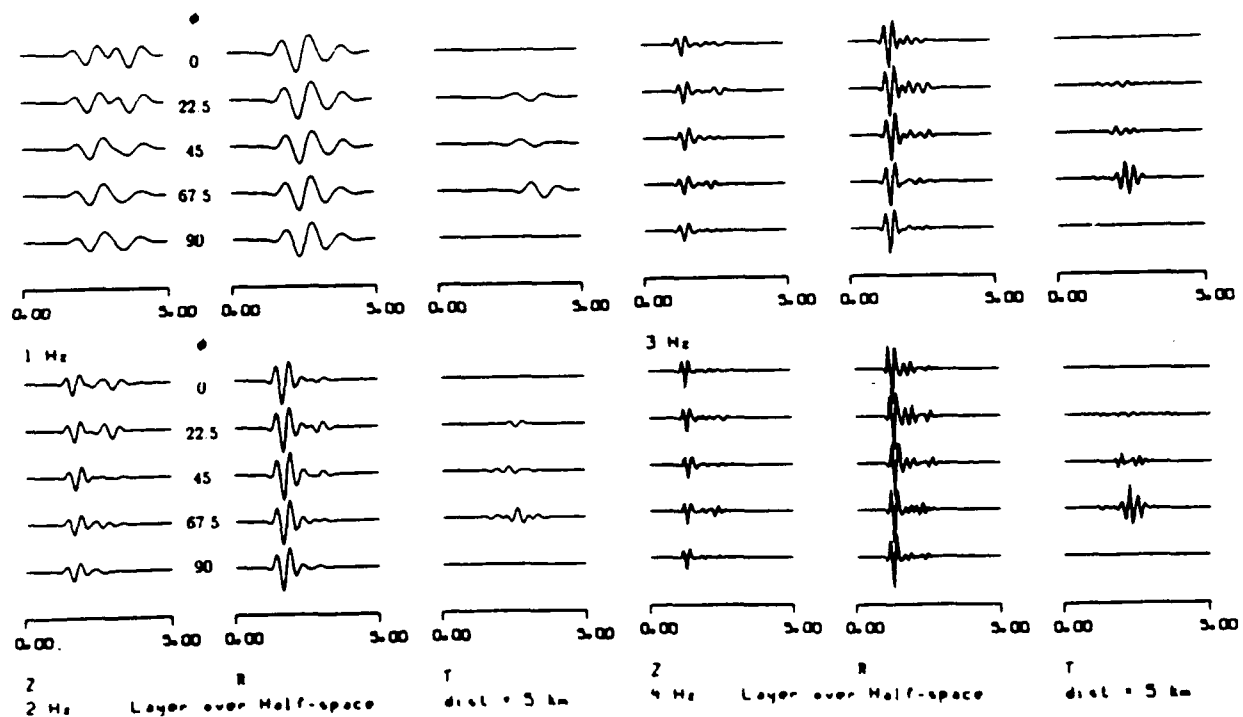


Figure 5: Three-component synthetic seismograms for layer over half-space at 5 km epicentral distance, for five azimuths and frequencies of 1, 2, 3, and 4 Hz. The seismograms at $\phi = 90^\circ$ are equivalent to those of an isotropic reference medium.

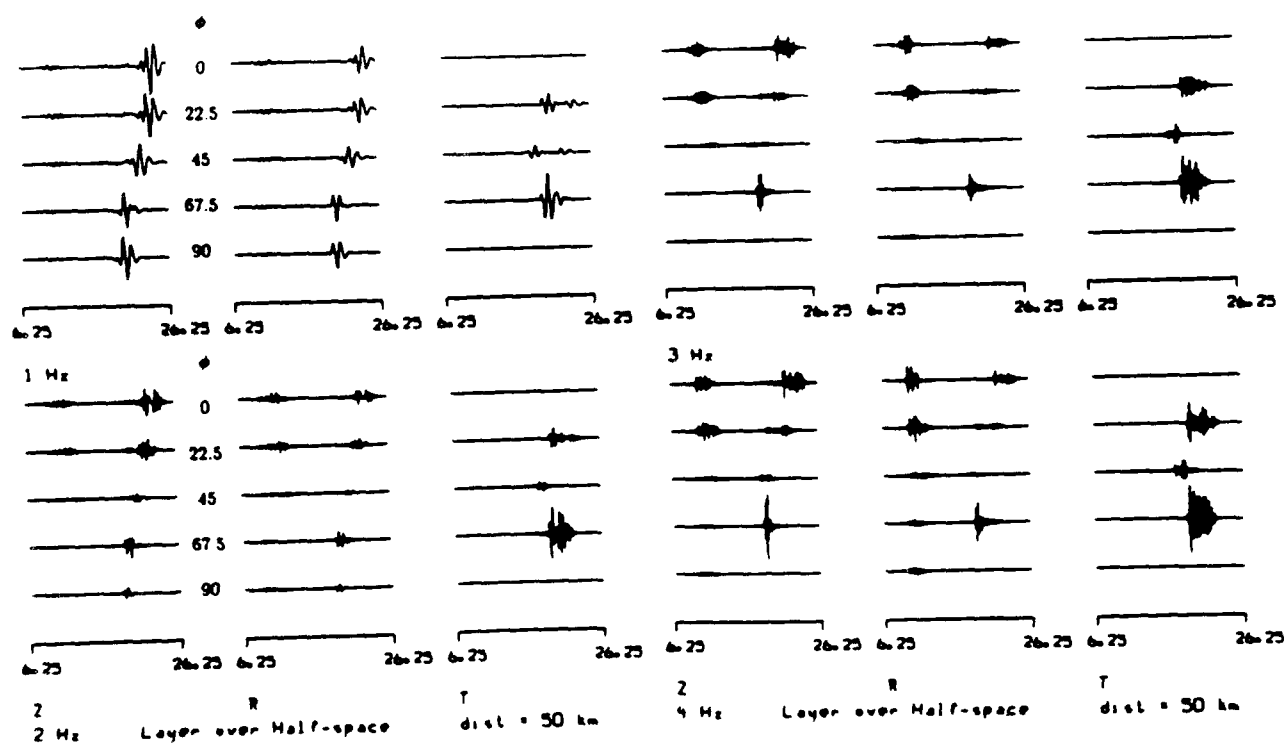


Figure 6: Three-component synthetic seismograms for layer over half-space at 50 km epicentral distance, for five azimuths and frequencies of 1, 2, 3, and 4 Hz. The seismograms at $\phi = 90^\circ$ are equivalent to those of an isotropic reference medium.

ENERGY FLUX MODELS FOR SEISMIC WAVE PROPAGATION IN A SCATTERING LAYER

Charles A. Langston

Dept. of Geosciences
Pennsylvania State University
University Park, Pennsylvania 16802

Contract No. F19628-87-K-0024

Objective:

The general objective of this research is to understand the factors important in shaping the seismic signature of small events recorded at local and regional distances. Specific objectives of this contract are 1) the identification of deterministic aspects of the wavefield from small earthquakes and explosions to allow the inference of source depth and other source parameters, and 2) to understand the effects of scattering and lithospheric heterogeneity on the propagation of high frequency regional phases. The combined analysis of "deterministic" and "stochastic" wave propagation effects is required to unravel the complexity of regional phases for the purposes of event discrimination.

In this paper, I examine a series of scattering models in an attempt to investigate characteristics of teleseismic P wave coda and the coda of long-period Rayleigh waves. Both codas, although produced by distinctly different wave types, are intimately related since previous studies have suggested that P coda, in particular, contains scattered P-to-Rayleigh conversions. The mechanisms which give rise to P-to-Rayleigh conversions probably are also important in the reciprocal problem of Rayleigh-to-body wave scattering. The objective of this study is to develop a self-consistent theory of coda formation using an energy flux model and to parameterize the level and decay of coda seen in P and Rayleigh waves. The parameterization allows the investigation of several plausible mechanisms which cause coda.

Summary:

The results of a previous study of teleseismic P wave coda recorded at Pasadena, California (Langston, 1989), showed that the single scattering model of coda Q was inappropriate when applied to levels and decay of teleseismic P coda. In particular, it was found that although the exponential slope of coda decay was related to the degree of heterogeneity beneath a receiver a slower decay implied greater heterogeneity rather than less heterogeneity. Through the use of simple plane wave synthetic seismograms for plane layered media, it was shown that coda slope was sensitive to the degree of heterogeneity in a scattering layer and to the efficiency by which energy can be trapped in the layer before radiating out into the lower structure. Empirically, one-dimensional plane layered heterogeneity produced coda which decayed exponentially. Structure which produced little scattering allowed body waves to radiate into the mantle quickly causing fast (or "low Q") coda decay but high levels of coda with very slow decay (or "high Q") were produced with highly heterogeneous structures. These observations are contrary to the strict interpretation of genesis of coda by the single scattering model.

An energy flux model can be constructed to parameterize coda decay caused by the entrapment of energy by a scattering layer and its diffusion into the lower halfspace. Making the assumptions that coda energy is homogeneously distributed throughout the layer and follows a diffusion law for energy flow out of the layer we obtain:

$$A_c = \sqrt{\frac{I_D}{t_d}} e^{\frac{-\omega t_d}{2Q}} (1 - e^{\frac{-\omega t_d}{2Q}})^{\frac{1}{2}} e^{\frac{-\gamma t_d}{2}} \quad (1)$$

where,

A_c = coda amplitude

t_d = travel time of P wave through the layer

Q_s = scattering Q parameter

I_D = integral of the squared velocity of the direct wave

ω = circular frequency

γ = power diffusivity constant for the layer

An implicit assumption in the construction of this equation is that there are no mode conversions, i.e., the wave propagation involves scalar waves. This is obviously violated even in the case of scattering of teleseismic P waves near a receiver. Analysis of the high level of horizontal component displacements relative to vertical component displacements in the data from Pasadena suggested that much of the coda was composed of low group velocity surface waves scattered by random 3D heterogeneity. These scattering mechanisms must be modeled more realistically before the parameters of an equation like (1) or the coda Q of the single scattering model can be safely interpreted.

A study of the stability of parameters determined by equation (1) was performed using digital data obtained from three stations of the Berkeley seismic network in Central California (Figure 1). Taking teleseisms which were simultaneously recorded by two or more stations, Q_s and γ , were determined from coda envelopes of the three component data for a 1.5 hz bandpass. It was found that the scattering Q parameter, Q_s , was relatively unstable but that the slope of the log coda envelope was generally very consistent between stations and between events of similar source depth. Furthermore, it was found that shallow teleseisms had a coda decay rate one half as fast as deep teleseisms suggesting that scattering near the source serves to contribute as much coda as near-receiver scattering. Figure 2 shows a typical determination of coda parameters from a deep and shallow source showing the difference in coda decay.

Coda decay and level for long-period Rayleigh waves were investigated for explosions at NTS recorded in Western North America (Figure 3). Several working assumptions were used in an effort to discriminate between various scattering and anelastic mechanisms. The single scattering model, an energy flux model with anelasticity, and an energy flux model with Rayleigh to body wave scattering out of a scattering layer were examined. The data were bandpass filtered at center frequencies of 0.2 and 0.1 hz and processed to obtain coda envelopes. Some low noise Rayleigh data enabled the determination of coda envelopes at 0.05 hz. Figure 4 shows an example of filtered Rayleigh waves at Corvallis, Oregon.

The first basic result of this study of Rayleigh waves was that observed coda followed the characteristics of coda for teleseismic P waves and local short-period S waves. That is, coda level decayed exponentially away from the direct Rayleigh arrival. Figures 5 and 6 show the observed log coda curves at 0.1 and 0.2 hz, respectively, with straight line fits determined using a least-squares procedure and the single scattering model. The second major result of the study was that it was impossible to discriminate between scattering models based on the data fits.

The first scattering model examined was the single scattering model which has become a standard for data interpretation (Aki, 1969). This is given by:

$$A_c(\omega, t) = C \frac{e^{-\frac{\omega}{2Q_c}}}{\sqrt{t}} \quad (2)$$

where Q_c is the coda Q parameter. Q_c determined from the data was generally consistent for all stations for the two frequency bands suggesting that Rayleigh coda consisted of homogeneously scattered waves all over Western North America (Figure 7). It is interesting to note that the average values of 100 to 200 are consistent with previously determined anelastic Q's by Mitchell and his co-workers using amplitude decay of the direct Rayleigh wave (Hwang and Mitchell, 1987).

An energy flux model was constructed in an effort to separate the effects of anelastic Q and scattering Q as suggested by Frankel and Wennerberg (1987) and Wu (1985). Summarizing the development, coda amplitude is given by:

$$A_c(\omega, t) = \frac{\sqrt{2I_D t_d}}{t} e^{-\frac{\omega}{2} \left[\frac{1}{Q_s} + \frac{1}{Q_l} \right]} \left(1 - e^{-\frac{\omega}{2Q_l}} \right)^{\frac{1}{2}} e^{-\frac{\omega}{2Q_l}} \quad (3)$$

where Q_s is the scattering Q and Q_l is the anelastic Q. Inversion of the data yielded the same quality of fit as found using the single scattering model with results shown in Figures 8 and 9. Q_l was sensitive to the slope of the log coda data which is obvious from the form of equation (3) and attained similar values as coda Q. It is interesting to note the large scattering Q's obtained in comparison to anelastic Q. This may suggest that anelastic Q controls the development of coda as well as the amplitude decay of the direct Rayleigh wave.

Unfortunately, if the model for attenuation found for teleseismic body waves is applied to the Rayleigh wave data, then it is possible to explain the decay of coda purely by scattering of Rayleigh waves into body waves which then radiate into the mantle. This is given by a hybrid energy flux - radiative diffusion model:

$$A_c(\omega, t) = \sqrt{\frac{2I_D t_d}{t}} e^{-\frac{\omega}{2Q_l}} \left(1 - e^{-\frac{\omega}{2} \left[\frac{1}{Q_s} - \frac{1}{Q_R} \right]} \right) e^{-\frac{\omega}{2Q_R}} \quad (4)$$

where the replacement:

$$\gamma = \frac{\omega}{Q_R}$$

has been made to define the "radiative Q", Q_R . This parameterizes the scattering of body waves from the incident Rayleigh wave in the way seen for the behavior of teleseismic body wave coda given in equation (1). In a fundamental sense, both Q_s and Q_R become measures of the scattering efficiency of the medium. The scattering Q removes energy from the direct wave into the coda but the radiative Q removes coda and direct wave energy directly from the layer. Results (Figures 10 and 11) show that Q_R now controls coda decay in the same way as Q_l and Q_c did in the previous models. The quality of fit to the data was the same as the other two coda models.

Summary and Recommendations:

The formation of coda for teleseismic body waves follows mechanisms which are interpreted in ways opposite of the standard single scattering model. Slow coda decay and high coda levels are indicative of highly scattering media. Apparently low coda Q's (fast decay) are controlled by the transparency of the local crust which allows scattered body waves to quickly propagate back into the mantle. Thus, there is little real attenuation of the primary body wave

involved.

Analysis of teleseismic coda recorded by the Berkeley network supports a simple model of coda formation in structure near the seismic source and in structure near the receiver. Deep events are observed to have relatively lower coda levels with faster decay than shallow events.

Long-period Rayleigh waves are seen to have coda similar in characteristics to other short-period data sets. The analysis of the coda decay for Rayleigh waves which scatter over Western North America suggest that it is very difficult to separate the effects of anelastic attenuation and scattering.

Seismic experiments which combine several different data sets for scattering in an isolated lithospheric volume should be attempted to produce a self-consistent scattering model based on numerical wave equation solutions. Simple coda theories can shed light on the trade-offs involved in disparate assumptions but are too simple to adequately address the real scattering mechanisms involved in the wave propagation.

References:

- Aki, K.(1969). Analysis of seismic coda of local earthquakes as scattered waves, Jour. Geophys. Res., **74**, 615-631.
- Frankel, A., and L. Wennerberg(1987). Energy-flux model of seismic coda: separation of scattering and intrinsic attenuation, Bull. Seism. Soc. Am., **77**, 1223-1251.
- Langston, C.A.(1989). Scattering of teleseismic body waves under Pasadena, California, Jour. Geophys. Res., **94**, 1935-1951.
- Hwang, H.-J., and B.J. Mitchell(1987). Shear velocities, Q , and the frequency dependence of Q in stable and tectonically active regions from surface wave observations, Geophys. J. R. astr. Soc., **90**, 575-613.
- Wu, R.S.(1985). Multiple scattering and energy transfer of seismic waves - separation of scattering effect from intrinsic attenuation - I. Theoretical modelling, Geophys. J. R. astr. Soc., **82**, 57-80.

Figure Captions:

- Figure 1: Location of broad-band digital stations of the Berkeley seismic network used in the teleseismic P-wave coda study.
- Figure 2: Example of log coda envelopes from a shallow and deep event recorded at MHC. Deep events typical have faster coda decay and lower levels of coda compared to shallow events.
- Figure 3: Map of western North America showing WWSSN and Canadian network stations used for the study of Rayleigh coda from nine underground nuclear explosions at NTS. Also shown are the great circle paths between NTS and the stations.
- Figure 4: Long-period vertical component at COR (Corvallis, Oregon) showing the fundamental mode Rayleigh wave and coda for the 9/06/79 explosion. Below the top data trace are three different bandpass filtered traces showing the development of coda at frequencies of 0.05, 0.1 and 0.2 Hz. Amplitudes for the filtered traces have been normalized.

Figure 5: Stacked coda envelopes (0.1 hz) for each station with the fit for the single scattering approximation model. Coda envelopes were shifted in amplitude in each graph by a factor of 10 for plotting purposes. Stations have been grouped by distance. The peak in each envelope corresponds to the direct Rayleigh arrival. Note that the envelope slopes are comparable for all stations.

Figure 6: Stacked coda envelopes (0.2 hz) with coda fits. Same scheme as Figure 5.

Figure 7: Inferred Q_c values for the single scattering model. Error bars show one standard deviation in the parameter estimate from the inversion algorithm. Triangles are for 0.1 hz coda. Circles are for 0.2 hz coda. Note the clustering of Q_c values between 100 and 200.

Figure 8: Q_i and Q_s determinations for 0.1 hz coda using the energy flux model, equation (3). Note the change in scale for Q_s . Scattering Q 's are one to two orders of magnitude greater than anelastic Q 's. Anelastic Q clusters around 100.

Figure 9: Q_i and Q_s determinations for 0.2 hz coda for the energy flux model. Results are similar to those at 0.1 hz.

Figure 10: Scattering Q , Q_s , and "radiative" Q , Q_R , for 0.1 hz coda inferred using equation (4). In this case, radiative diffusion of Rayleigh-to-body wave conversions out of the crustal waveguide mimics the effect of anelasticity.

Figure 11: Radiative diffusion model results for 0.2 hz coda. Same scheme as Figure 10. Note that Q_s and Q_R are nearly the same for all cases.

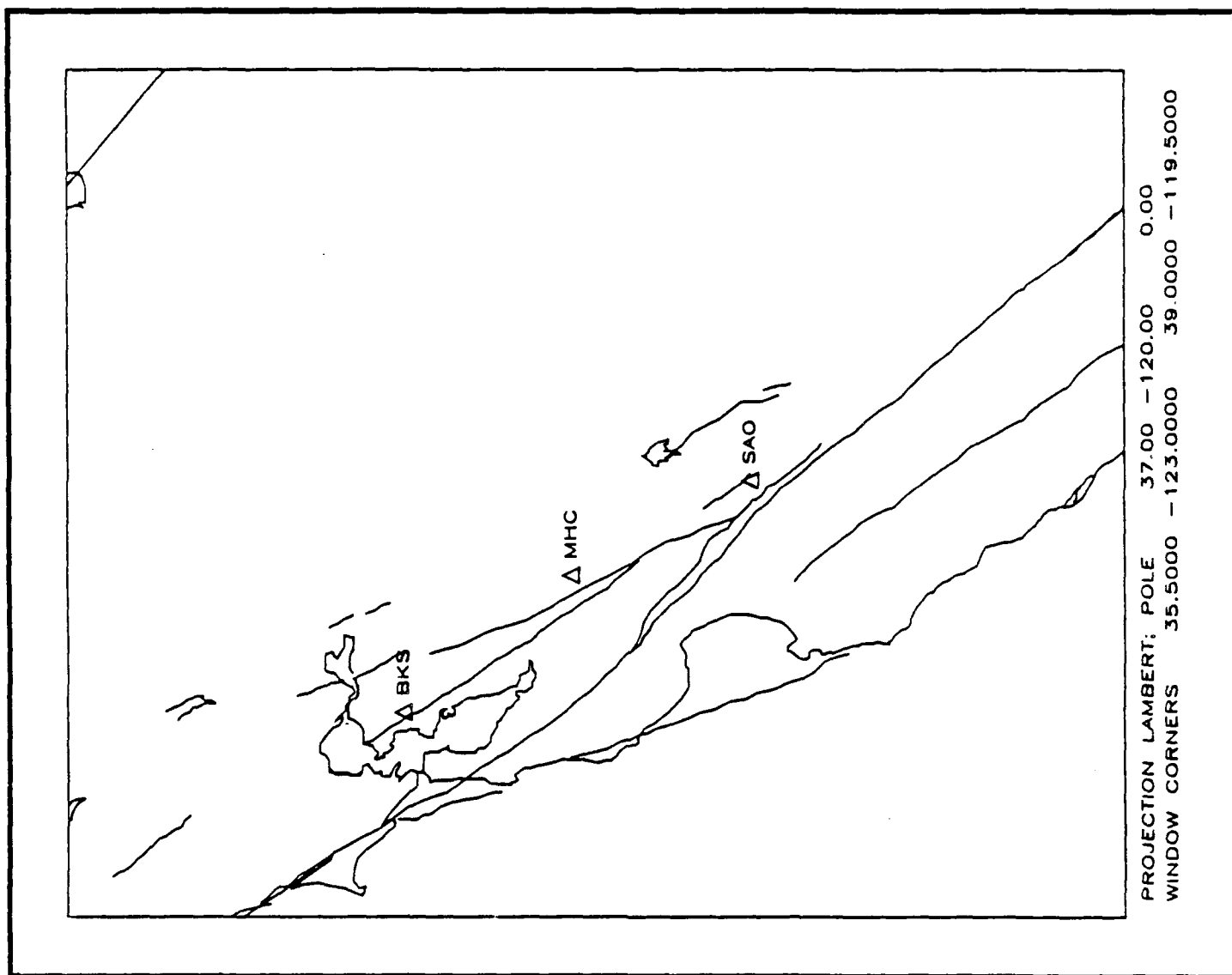


Figure 1

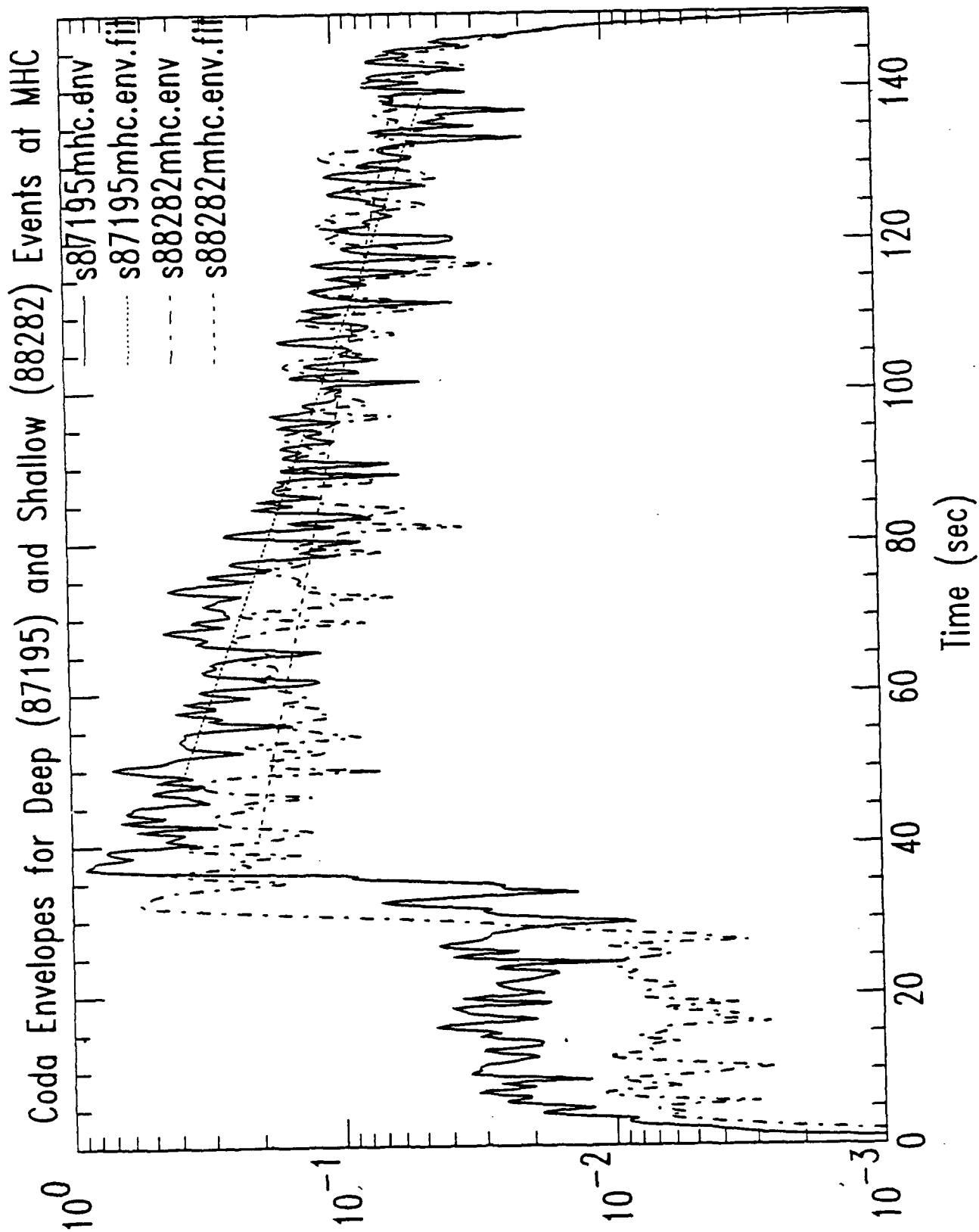


Figure 2

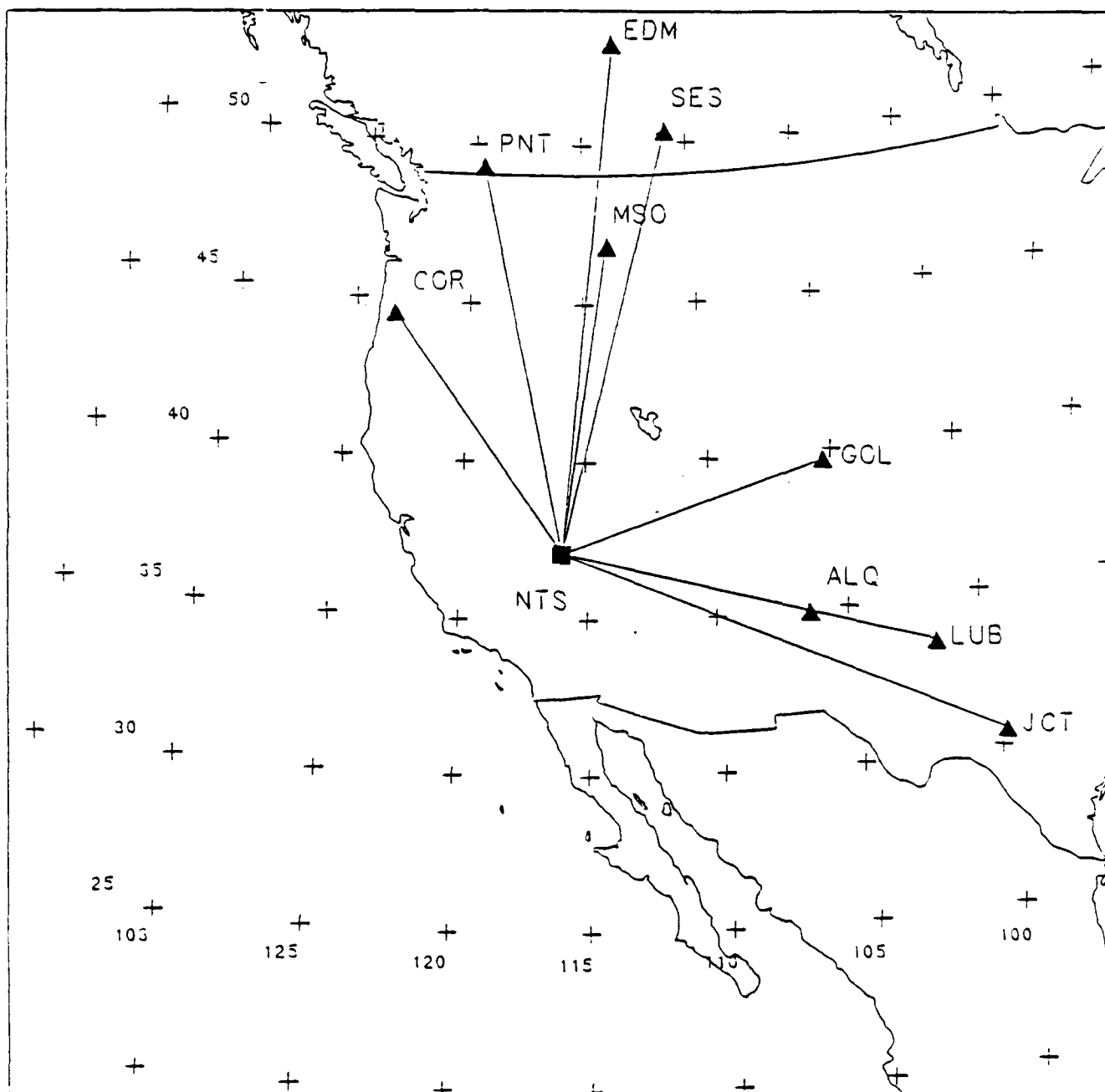


Figure 3

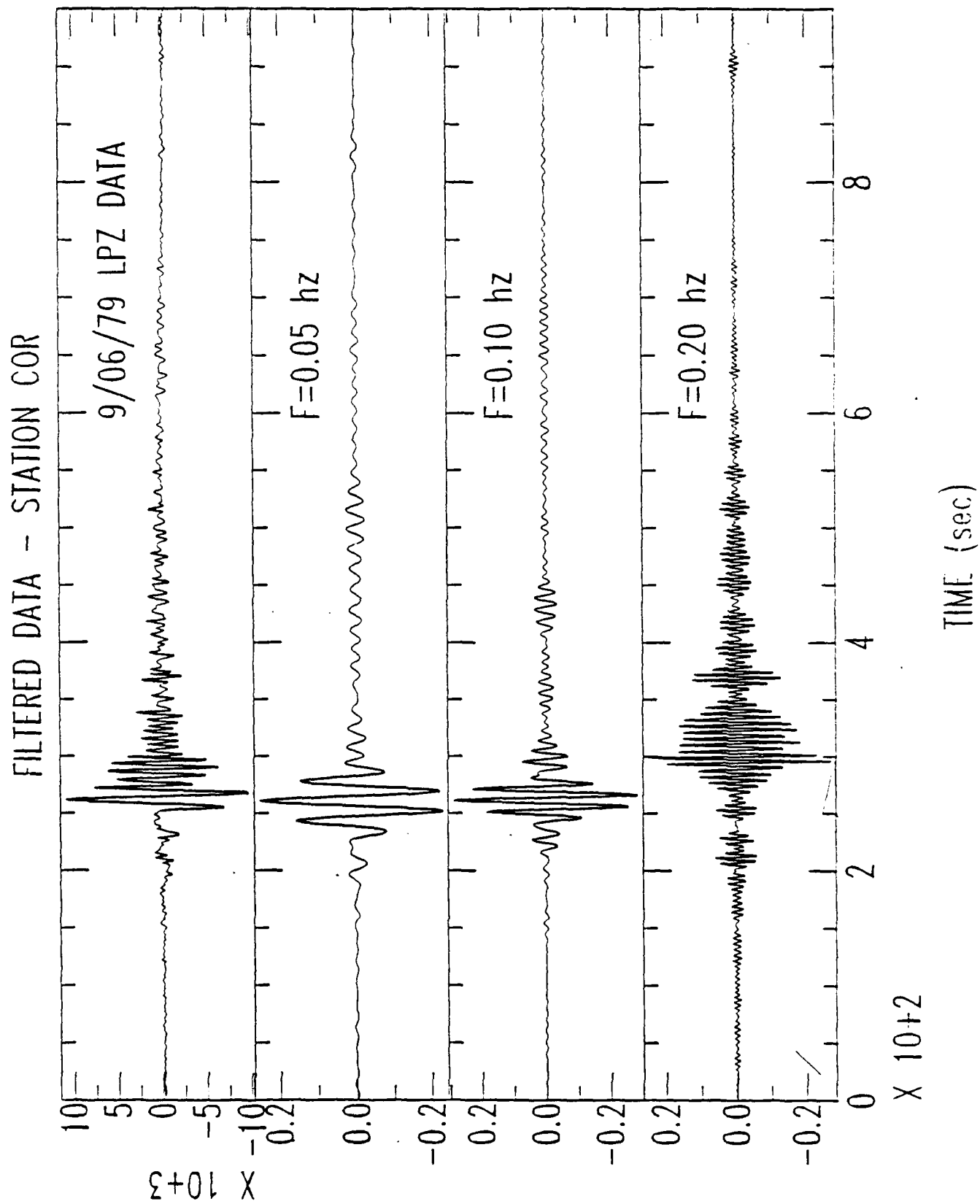


Figure 4

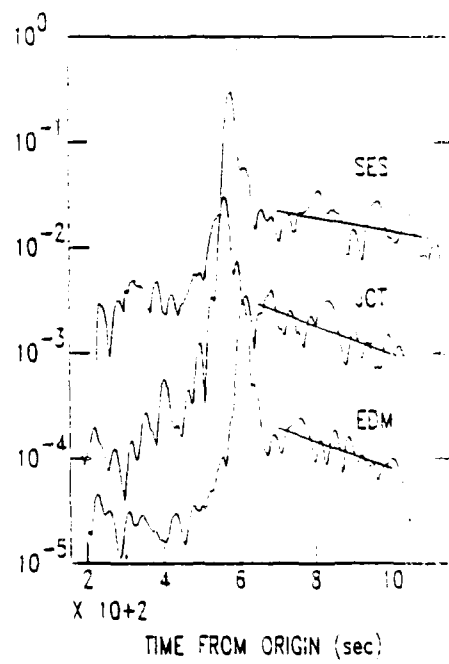
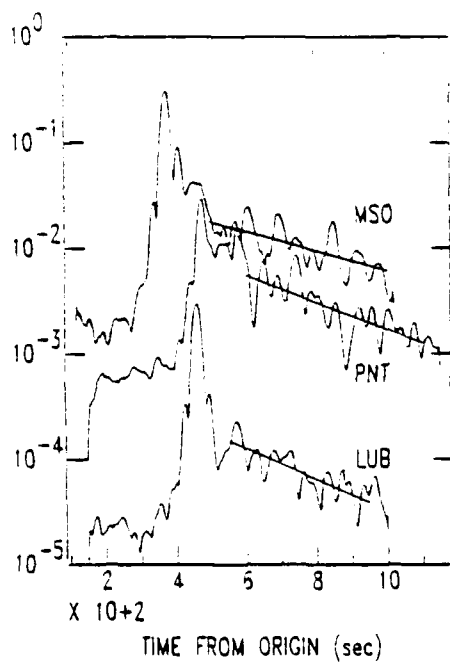
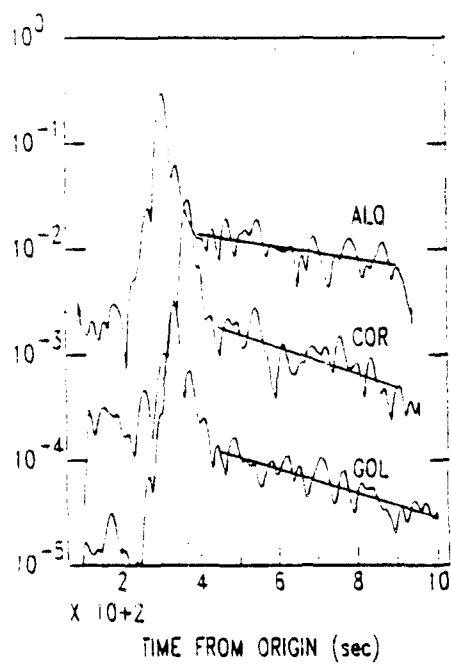


Figure 5

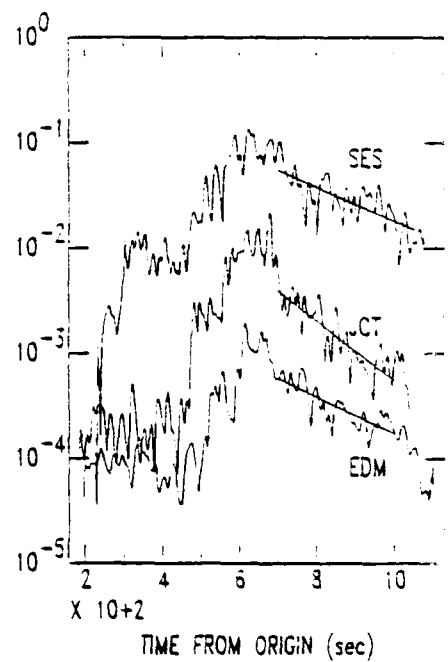
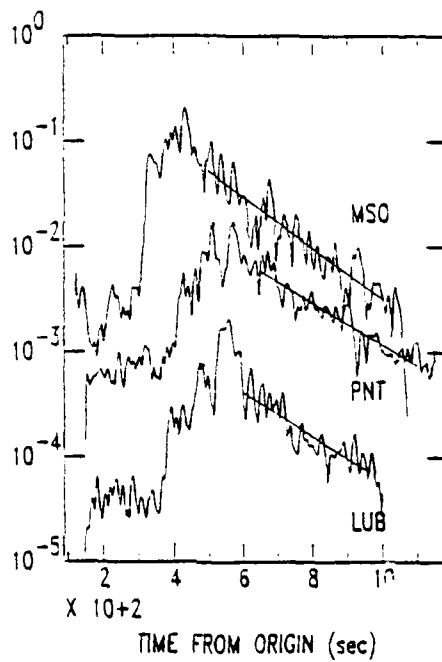
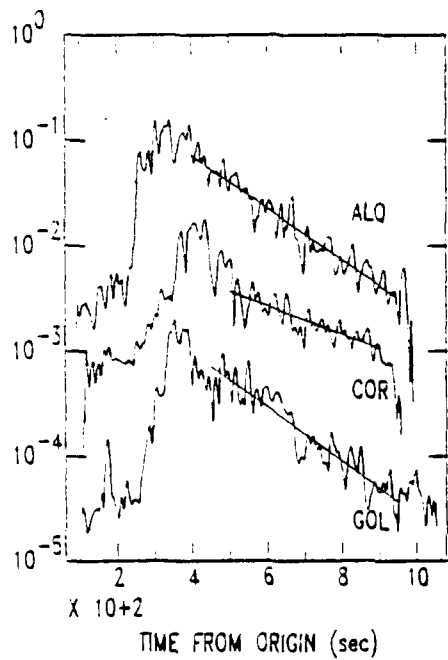


Figure 6

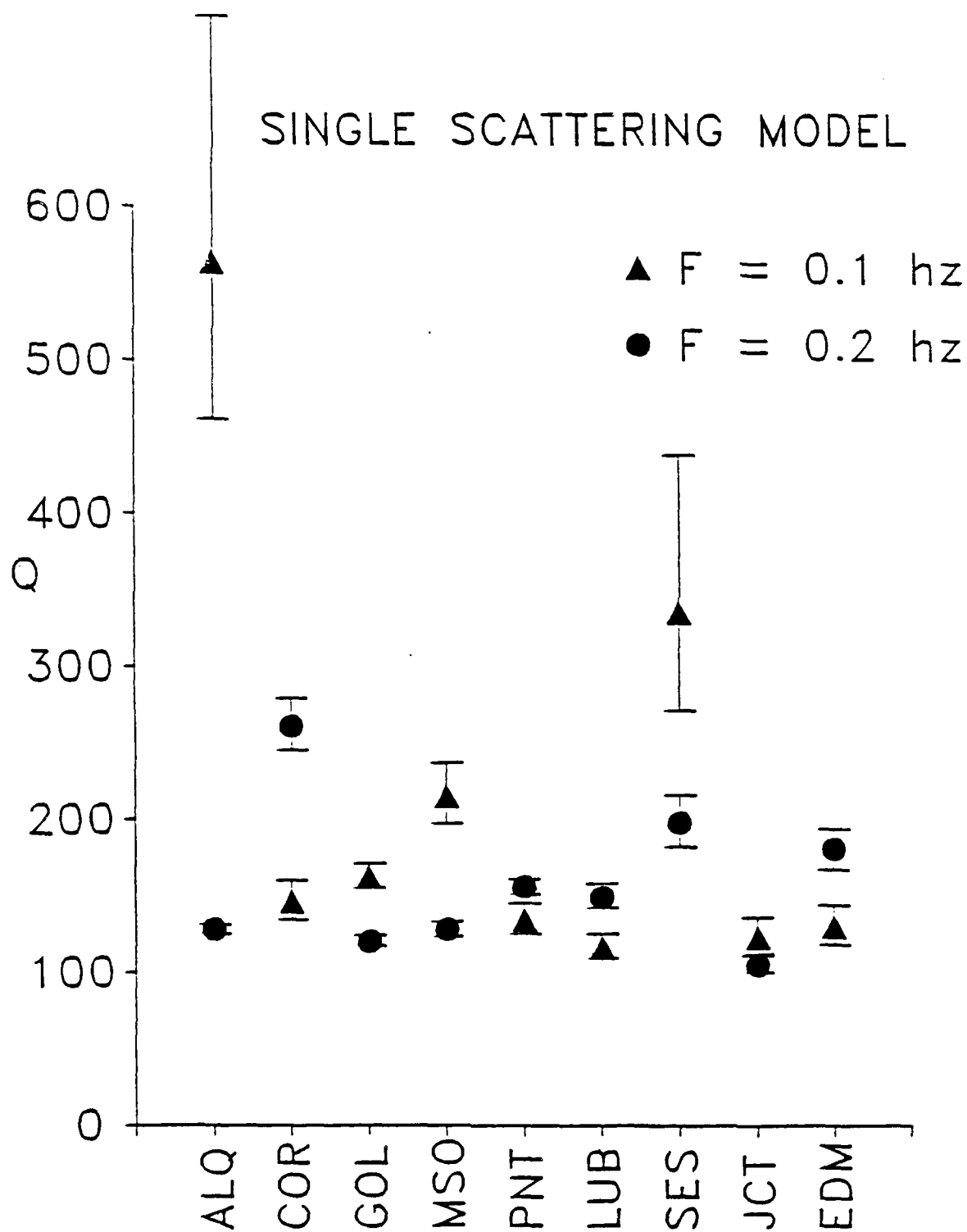


Figure 7

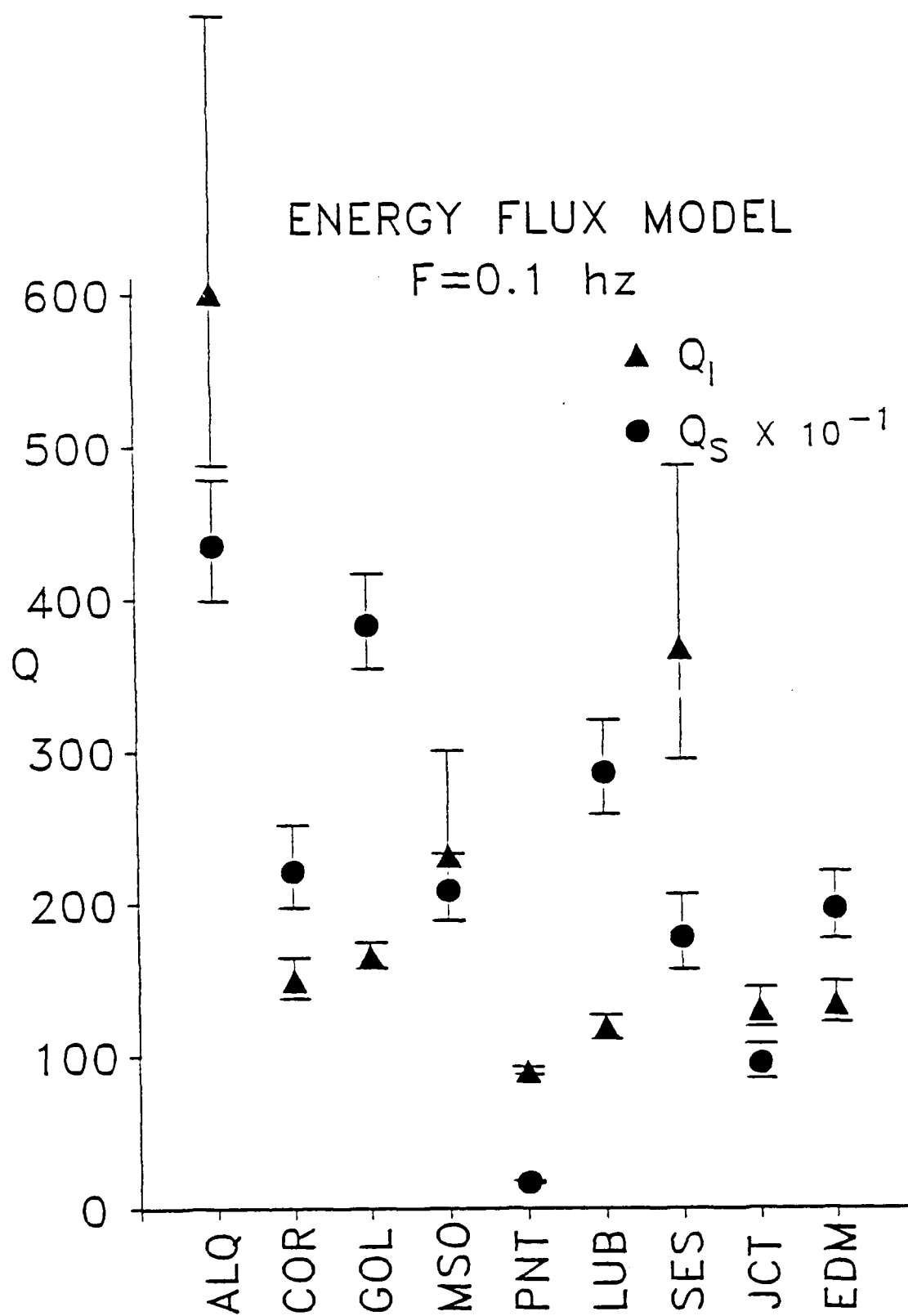


Figure 8

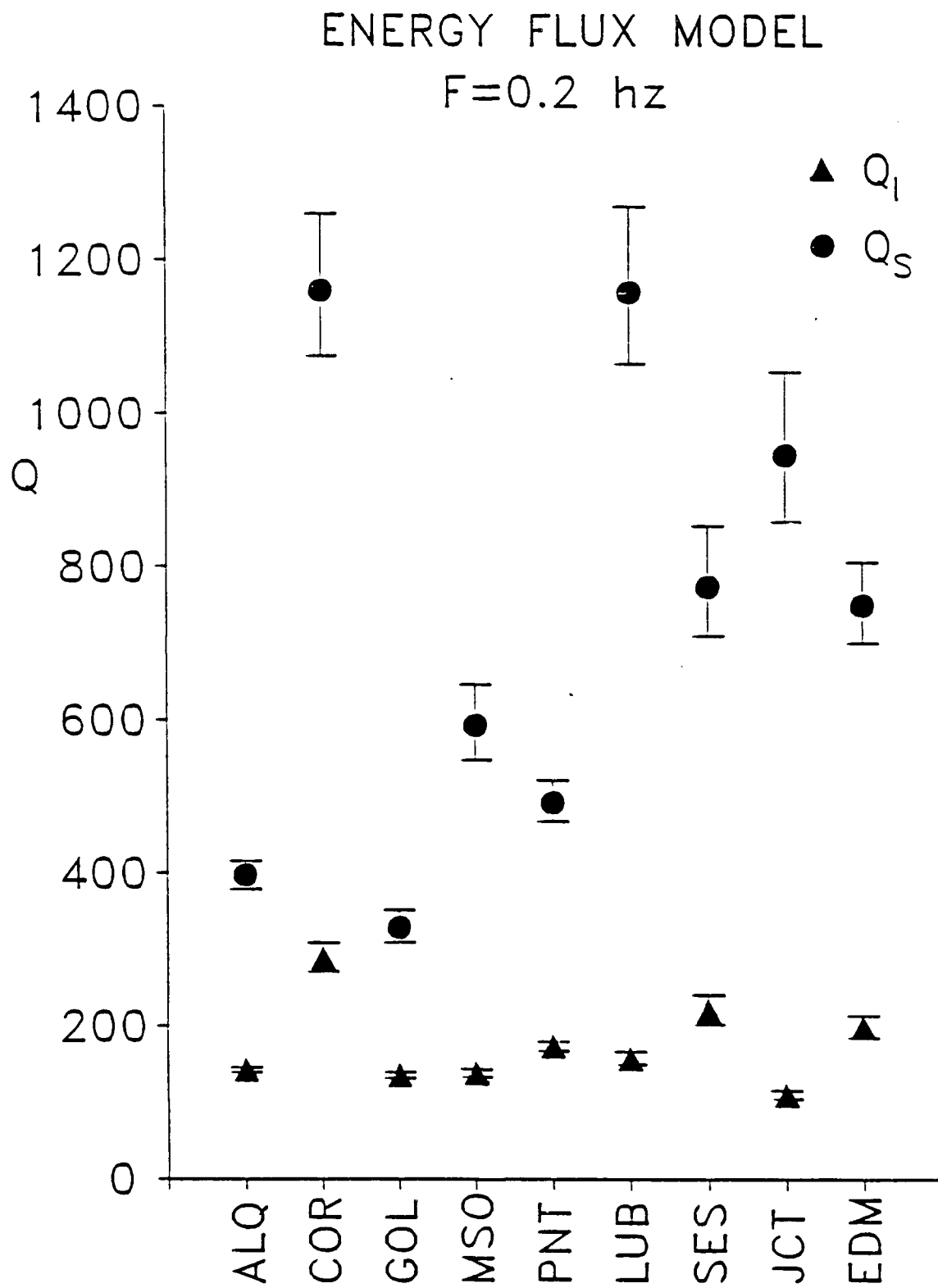


Figure 9

RADIATIVE DIFFUSION MODEL

$F=0.1 \text{ hz}$

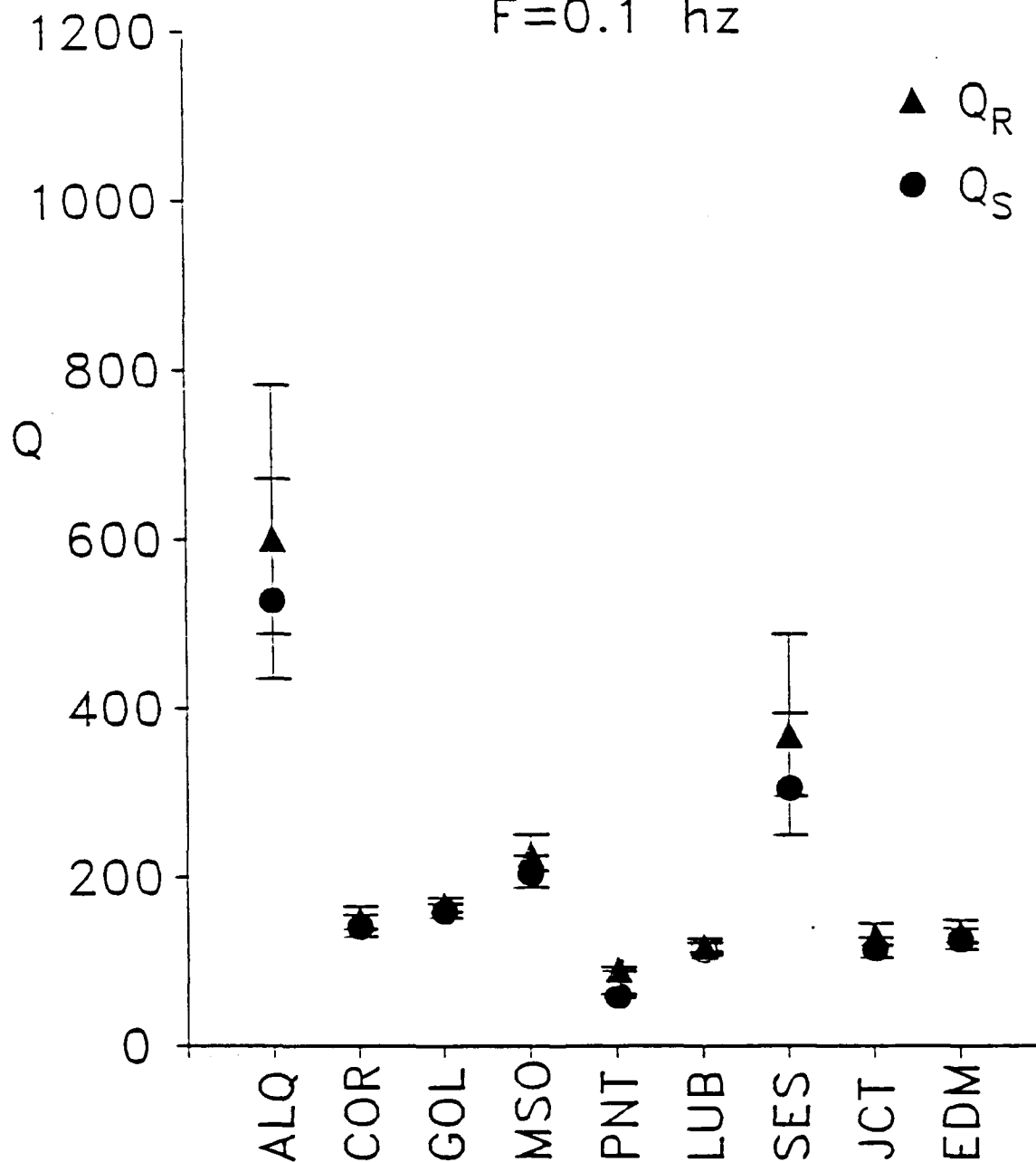


Figure 10

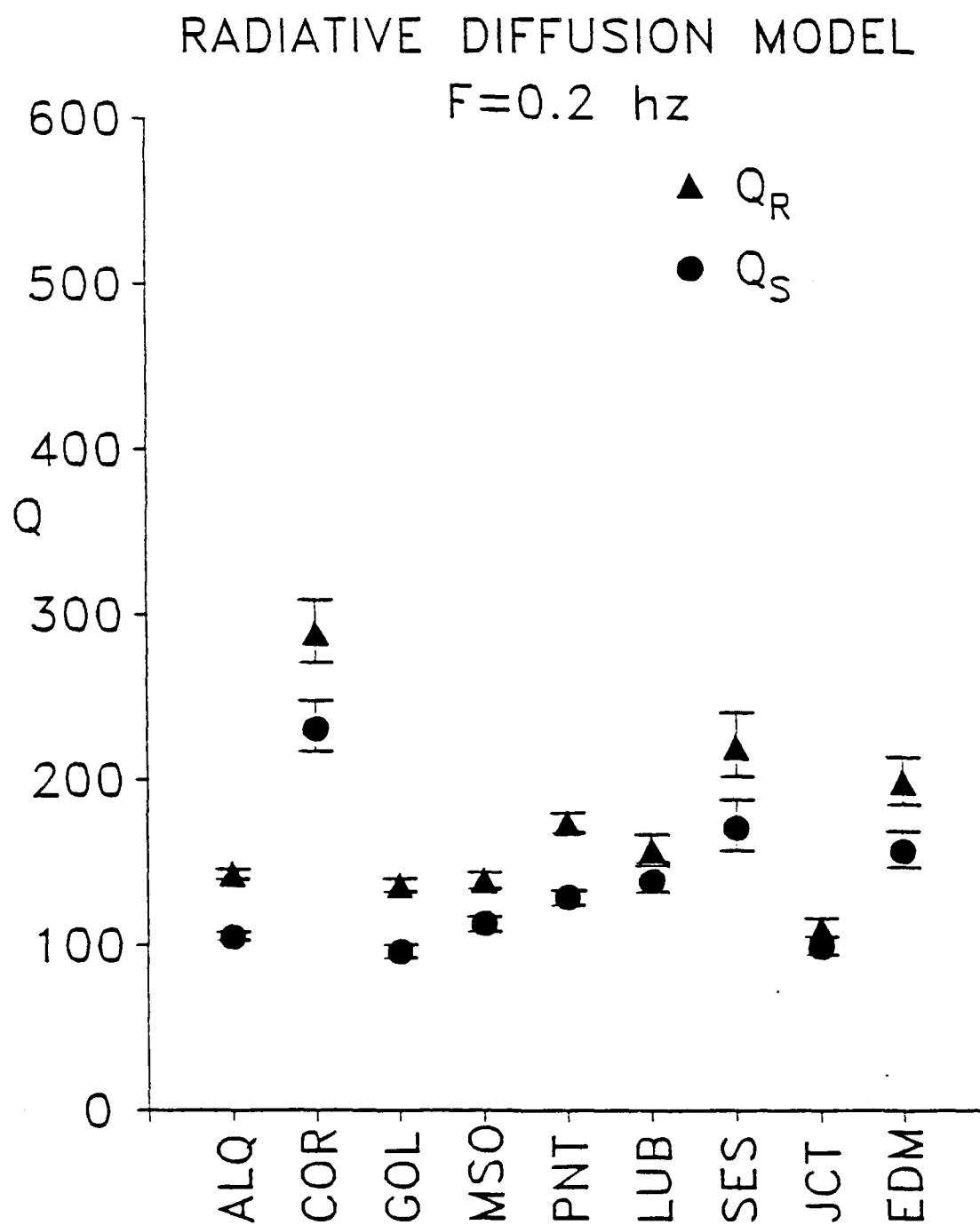


Figure 11

STOCHASTIC GEOLOGIC EFFECTS ON NEAR-FIELD GROUND MOTIONS

R. E. Reinke
K. R. Anderson
R. V. Goerke
J. A. Leverette

Geological Response Section
Civil Engineering Research Division
Air Force Weapons Laboratory
Kirtland AFB, N.M. 87117-6008

M. A. Bogaards
B. W. Stump

Department of Geological Sciences
Southern Methodist University
Dallas, Texas 75275

STOCHASTIC GEOLOGIC EFFECTS ON NEAR-FIELD GROUND MOTIONS

Over the course of the past few years the Air Force Weapons Laboratory has conducted a series of small scale high explosive field experiments in an effort to better understand the seismic source function. One of the lessons learned from these experiments is that random geologic variations have a significant influence on the results of these experiments and that any attempt to model these experiments must take into account these stochastic effects. Several of the tests, ranging in size from 5 to 100 pounds, were designed specifically to study the effects of random geologic inhomogeneity upon small scale spatial variability in ground motion. This paper will discuss the results of these tests and the implications of random geologic variability for the interpretation of near-field ground motions.

One of the early experiments which we performed was the Array Test Series (ARTS). The objective of these tests, which were all 5 pounds in yield, was to study the effects, in the recorded ground motion field, of the superposition of multiple charges in various patterns. Our initial plan was to analyze the data in a totally deterministic fashion - i.e. assume that the difference in waveforms from one azimuth to another would be relatively small. As a test of this assumption a single charge experiment, ART 2 (Figure 1.), which included measurements at multiple azimuths at the 20 meter range was performed. When the data were compared from one azimuth to another, variations as large as a factor of 10 were found above the 30 Hz region (Figure 2.) Another experiment (a "Huddle Test" in which the accelerometers were placed in a closely spaced group) was then conducted to verify that the instrumentation was not at fault. An additional set of experiments in which 5 five pound charges were detonated in sequence on the same test bed utilizing the same gage array provided convincing evidence that scattering by geologic inhomogeneities and not source irregularity was responsible for a significant portion of the variability.

Additional tests were conducted to further study the influence of spatial variability on ground motion. This test series, nicknamed CRAPS for Coherence for Range and Array Parameters, consisted of four 100 pound detonations fired in sequence on the same test bed using the same gage array (Figure 3.). An extensive subsurface exploration effort was conducted in

conjunction with this test series. This work, which included high resolution seismic surveys, cone penetrometer testing and drilling and sampling, was designed to obtain a statistical characterization of the random variability in the subsurface geology. The primary goal of the test series was to model the observed variability in ground motion in terms of the statistical characterization of the subsurface.

The ground motion data set from the CRAPS experiments has been analyzed to determine the repeatability of the seismic source function. The ground motions were recorded by accelerometers placed at ranges of 10, 20 and 30 meters. The sets of amplitude spectra of the ground motion records at each of these azimuths were treated as ensembles and mean spectra computed for each of the four tests so that one event could be compared to another. Subtle variations do exist between the first test (detonated in in situ material) and the following tests (fired in the backfilled crater pits). For the backfill detonations observed at the ten meter range there is less than a 20 percent variation out to frequencies of 400 Hz. At the ten meter range the first test has 40 percent higher amplitudes at the long (< 20 Hz) periods. The high (> 20 Hz) frequency amplitudes for the in situ detonation are reduced by as much as a factor of 2 over the following tests. These differences may result from the in situ cratering process compared to the backfill cratering process although the exact physical mechanisms remain to be identified. Overall, this spectral comparison shows that the variations in the mean spectra from shot to shot are much smaller than the azimuthal variability from a single shot which was found to be as high as a factor of 5. (Figure 4.)

Prior to the CRAPS test series a high resolution seismic refraction survey was conducted on the same test bed utilizing the CRAPS ground zero as the shotpoint. The refraction survey consisted of eight radial lines of geophones extending out from the ground zero. Geophones in each line were spaced at 1 meter intervals out to a range of 72 meters yielding a total of 576 recording locations. An eight gage shotgun was used as the seismic source. In an effort to separate the deterministic and stochastic portions of the wavefield, a number of different analysis techniques were applied to the data set obtained from this recording array. In one analysis technique amplitude spectra were computed for the waveforms for each azimuth and each range from the source. The set of amplitude spectra from a particular

range was then treated as a statistical ensemble and the mean and standard deviation computed. The standard deviation was then normalized with respect to the mean to obtain the coefficient of variation. The coefficient of variation for the 20 meter range is plotted in Figure 5. Also plotted in Figure 5. is the coefficient of variation for the 20 meter range obtained from the full scale CRAPS I explosion. There is good agreement between the seismic survey results and the full scale explosion out to the 70 Hz region indicating that similar wave propagation phenomena are affecting both experiments.

The results of these experiments demonstrate the need for the separation of stochastic and deterministic wave propagation effects when interpreting the results of small scale field tests. Similar degrees of spatial variability in ground motion have been found at other sites. McLaughlin *et al* (1983) discuss the station to station waveform coherence for near-field explosion accelerograms recorded on a nine element array at Pahute Mesa, Nevada Test Site. For this array, at a range of 6 km from a 5.6 M_L underground explosion with an interstation spacing of 100 meters, strong incoherent signals were found above 5 Hz on all components. This incoherence was attributed to scattering. Vernon *et al* (1985) discuss earthquake seismogram coherence for a nine station array with an interstation spacing of 50 meters located near the Pinon Flat observatory in California. Several events with magnitudes between 3.0 and 4.2 and hypocentral distances ranging from 10 to 50 km were analyzed. For this data set, P waves were found to be coherent up to the 25 to 35 Hz region, with S waves coherent to about 15 Hz. The results discussed here raise questions about the appropriateness of using single-station point measurements of the ground motion field for the inversion of seismic source functions. Additional work is needed to define the spatial variability present at other sites of interest. Small scale experiments conducted to define the degree of variability could place limitations on the interpretation of near-source, regional, and teleseismic measurements of earthquakes and explosions made at a single point. These surveys could also be useful in explaining the lack of coherence between individual station pairs in small seismic arrays, such as the Pinon Flat array.

REFERENCES

McLaughlin, K., L. Johnson, and T. McEvelly (1983). Two-dimensional array measurements of near-source ground accelerations, Bull. Seism. Soc. Am. 73, 349-376.

Vernon, F., J. Fletcher, L. Haar, T. Bolswick, E. Sembera, and J. Brune (1985). Spatial coherence of body waves from local earthquakes recorded on a small aperture array (abstract), EOS, Trans. Am. Geophys. Union 66, 954.

ACKNOWLEDGEMENTS

Funding for these experiments was provided by the Air Force Weapons Laboratory Independent Research Program under Projects ILIR8207, ILIR8414, and ILIR8711. Additional support was provided by The Air Force Office of Scientific Research through Grant AFOSR-84-0016 to Southern Methodist University.

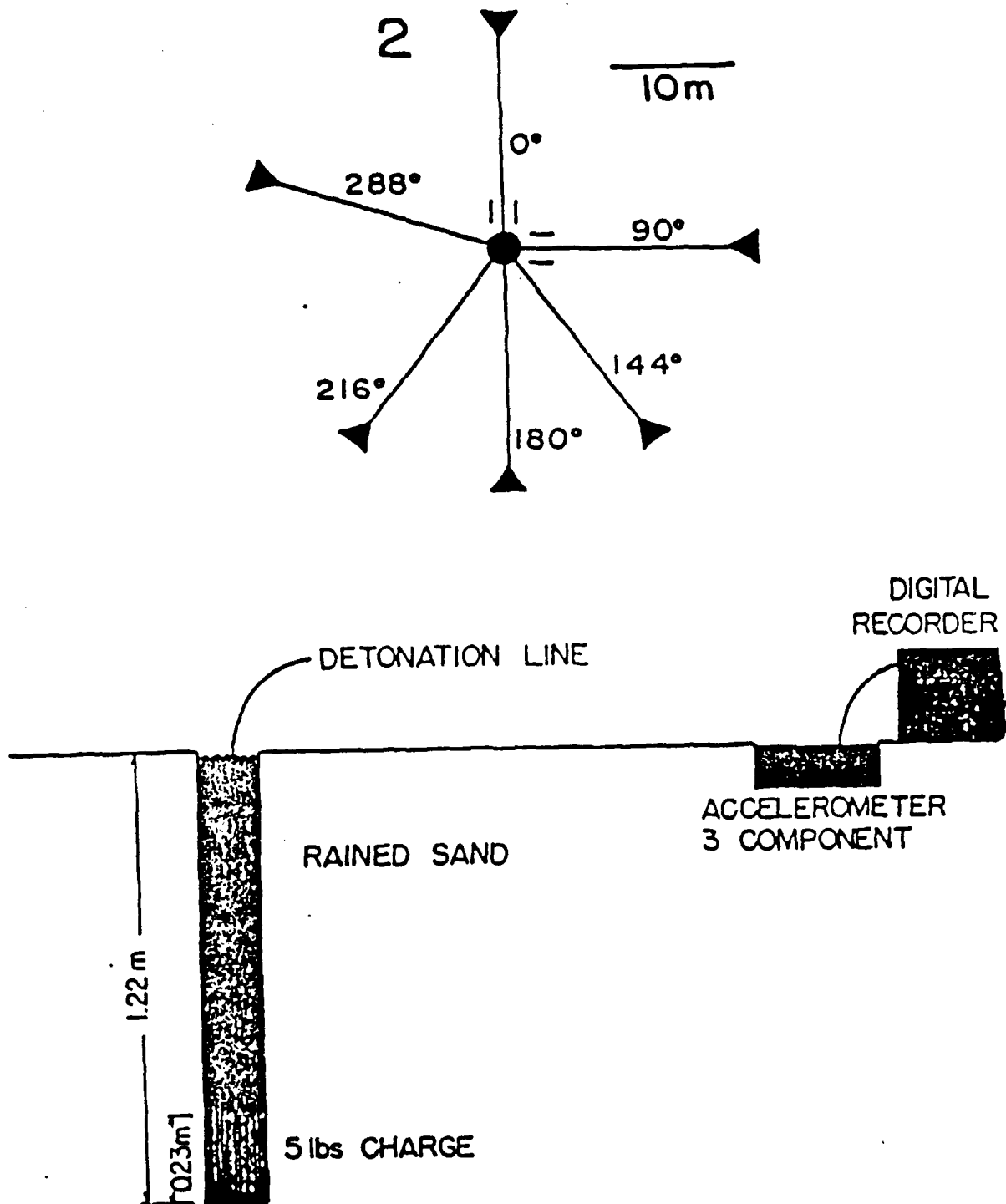


Figure 1. Experimental layout for the ART 2 Test Event.

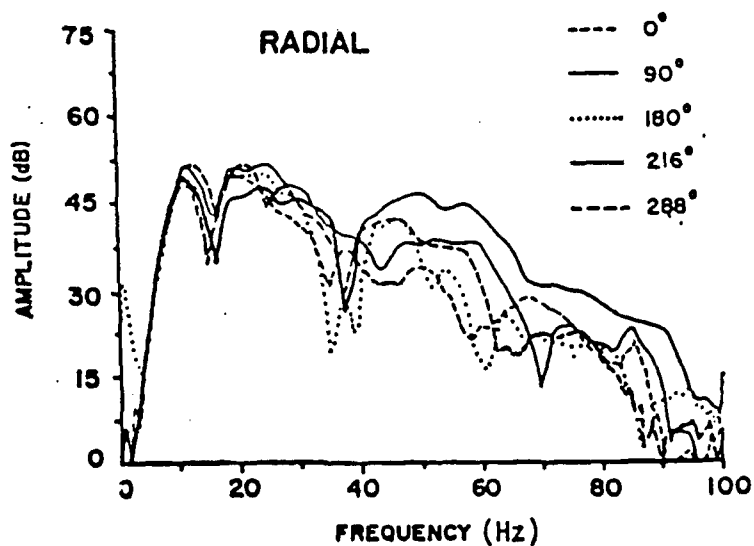
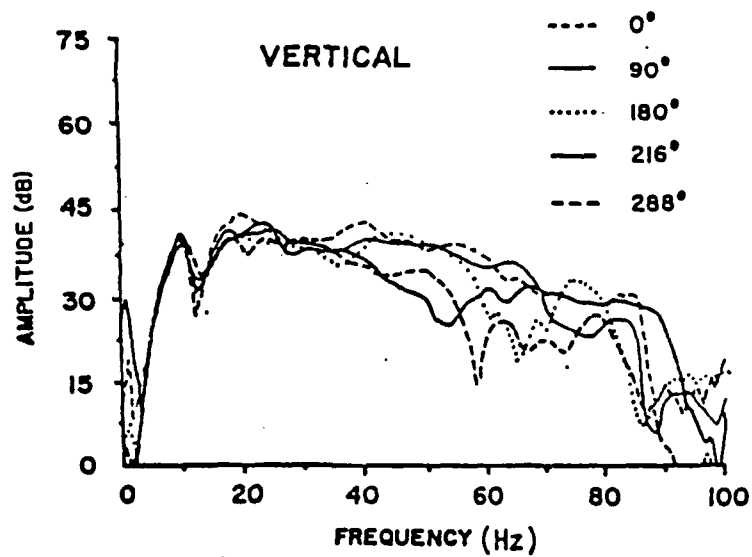


Figure 2. Vertical and radial acceleration spectra for ART 2.

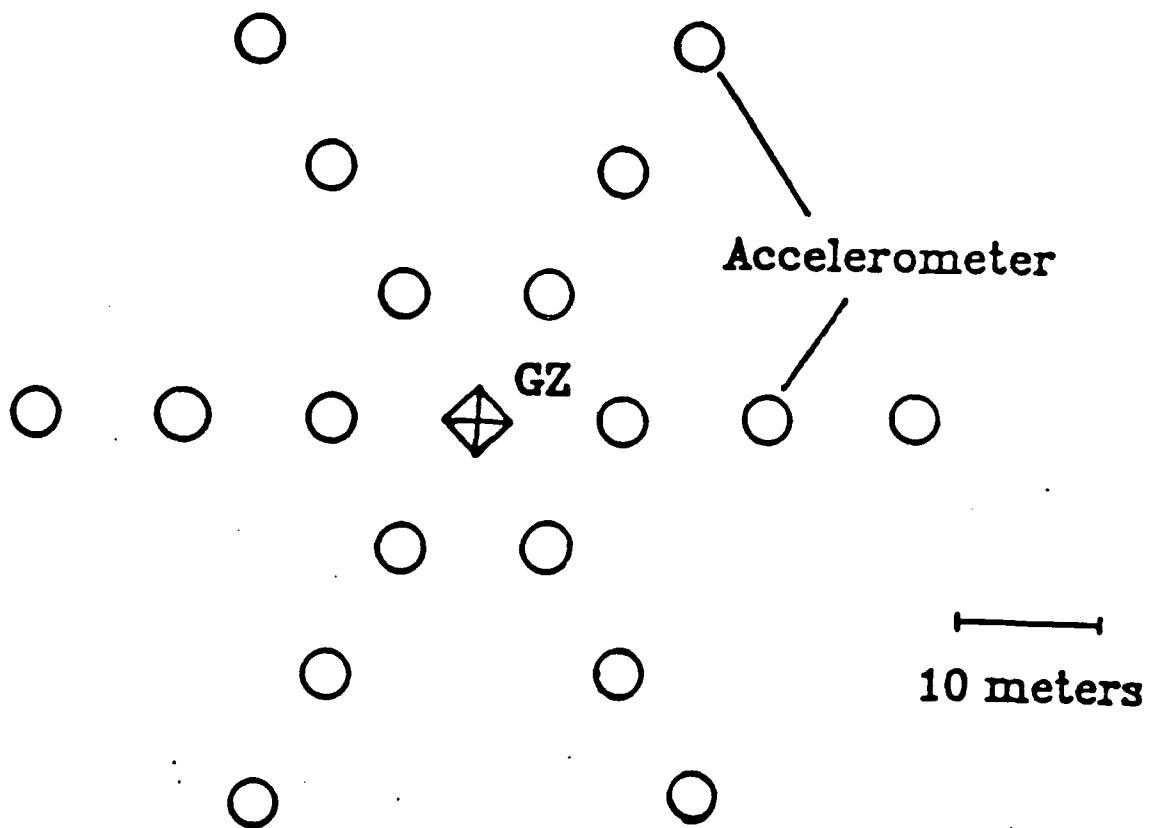
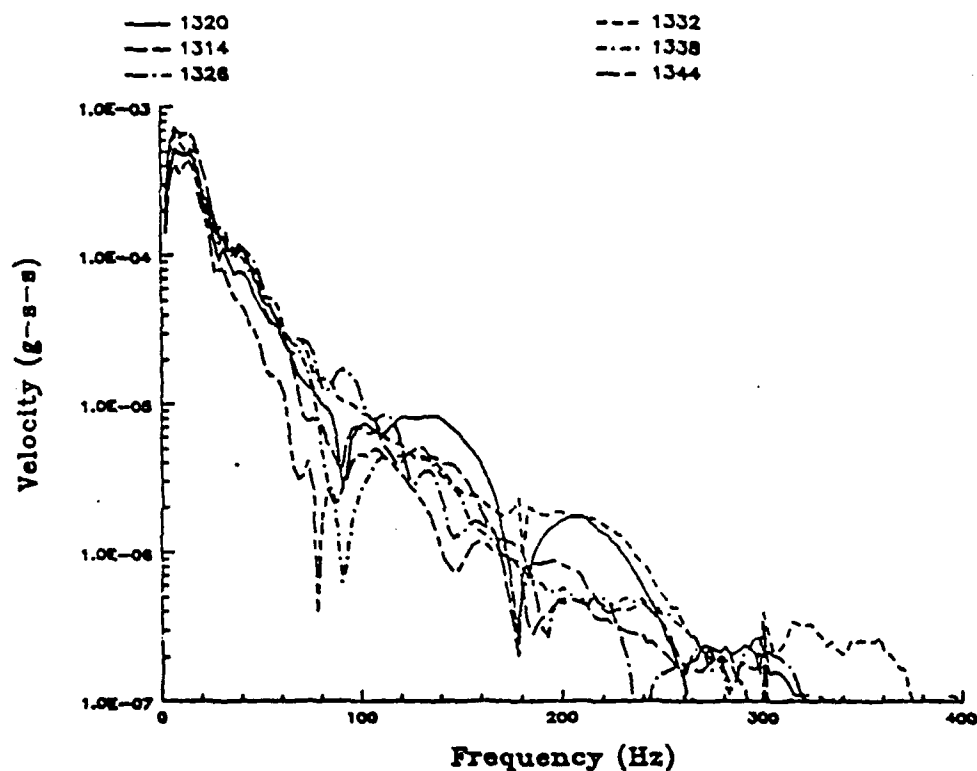


Figure 3. Plan view of CRAPS test bed.

CRAPS II COMPARISON 10m 1m RADIAL



CRAPS MEAN SPECTRAL COMPARISON

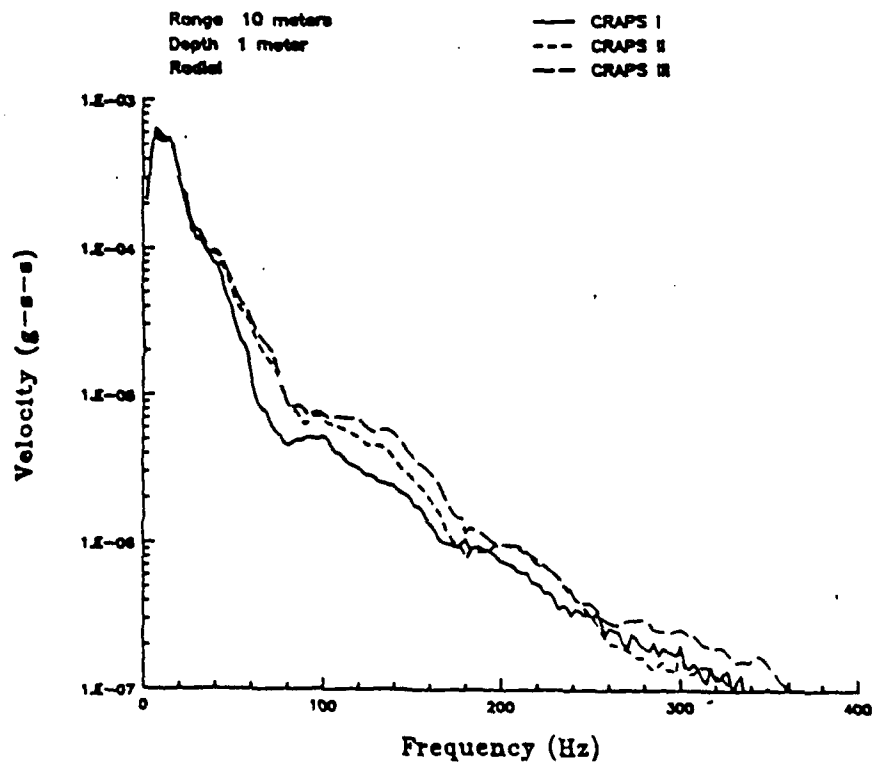


Figure 4. Comparison of azimuthal variability with mean spectra.

CRAPS I CV 20m 0m Vel Vertical

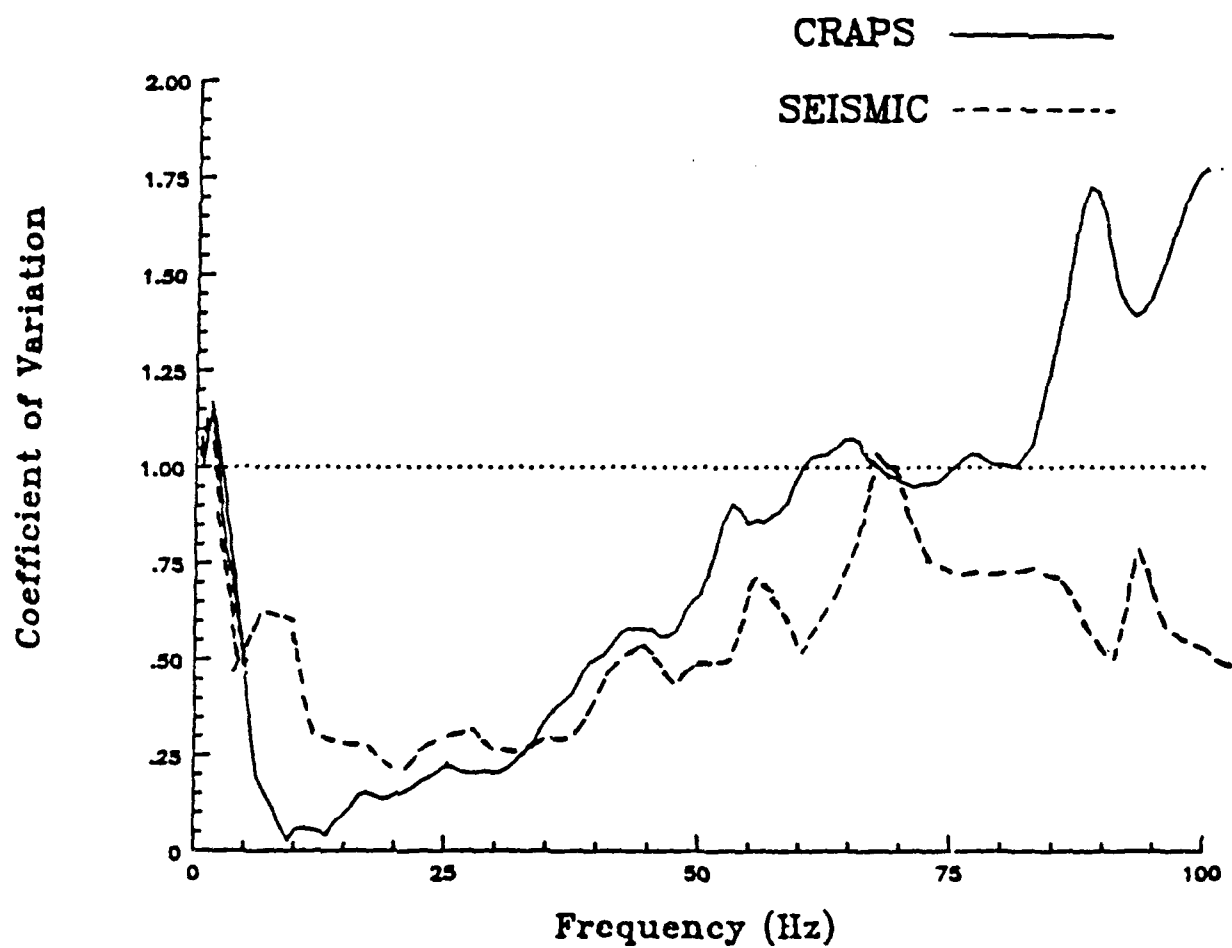


Figure 5. Comparison of CRAPS and seismic coefficient of variation for 20 meter range.

THE DAMAGE MECHANICS OF POROUS ROCK

Charles G. Sammis
Department of Geological Sciences
University of Southern California
Los Angeles, CA 90089-0740

and

Michael F. Ashby
Engineering Department
Cambridge University
Trumpington Street
Cambridge, CB2 1PZ, England

Contract # F19628-89-K-0008

OBJECTIVE

The overall objective of this line of research is to develop a damage mechanics for the compressive failure of rock which can be used as the constitutive relation in the numerical codes which simulate underground explosions. This work is motivated by the observation that elastic nonlinearities associated with the active fracturing of rock in the source region of underground explosions can effect the near-field seismic pulse shape. Toward this end, Ashby and Sammis (1989) modeled the growth and interaction of fractures which nucleate a preexisting cracks within the rock, and used the results to formulate a damage mechanics for the compressive failure of low-porosity crystalline rock (like granite). One immediate result of this work has been to emphasize the importance of scaling when applying rock mechanics laboratory results to field-scale underground explosions.

The objectives of the work described below has been 1) to extend the damage mechanics to porous rock (like sandstone and tuff) and 2) to develop a laboratory testing program to guide the theoretical development. Recent theoretical results include analysis of the initiation and propagation of damage at a void contained within a brittle cracked matrix. In the laboratory we are exploring the feasibility of using CaSO_4 (plaster of Paris) as a model material for porous rock. These lab studies have highlighted the importance of pore collapse as a failure mechanism under conditions of high confining pressure.

SUMMARY

The Damage Mechanics of Porous Cracked Rock

Many sedimentary rocks and man-made materials like cement and plaster, contain pores or holes, together with a population of finer cracks. In simple compression these material fail in a way which usually involves dilatation; but under triaxial compression, the volume can decrease - that is, the material densifies. In particular, a pure hydrostatic compression, if sufficiently large, can collapse the porosity, giving a sort of failure.

Consider a dual population of defects consisting of N_p large spherical pores per unit volume each of radius a_p and N_c smaller randomly oriented cracks (per unit volume) each having a length $2a_c$ as illustrated in Figure 1. When such a material is loaded in triaxial compression, stress concentrations in the vicinity of the pores produces extension of the smaller cracks within the matrix.

When the confining pressure is small, a region of tensile stress is developed at the poles of pores. Small cracks which are oriented parallel to σ_{11} may extend in mode I as shown in Figure 2. Sammis and Ashby (1986) analyzed the initiation of such tensile cracks for the case where they intersect the pore and found the initiation condition

$$\sigma_{11} = 3.42 \sigma_{33} + \frac{1.6 K_{Ic}}{\sqrt{2 \pi a_c}} \quad (1)$$

In this expression K_{Ic} is the critical stress intensity factor for mode I, and we have assumed a worst case scenario in which the full length of a small crack is parallel to σ_{11} and just intersects a pore. Note that nucleation becomes increasingly difficult as the confining stress σ_{33} is increased.

It is convenient to write eqn. (1) in dimensionless form by defining $s_{ij} = \sigma_{ij} \sqrt{\pi a_c} / K_{Ic}$ which gives

$$s_{11} = 3.4 s_{33} + 1.13 \quad (2)$$

By defining $\lambda = \sigma_{33}/\sigma_{11} = s_{33}/s_{11}$, eqn. (2) may be written

$$s_{11} = \frac{1.13}{1 - 3.42 \lambda} \quad (3)$$

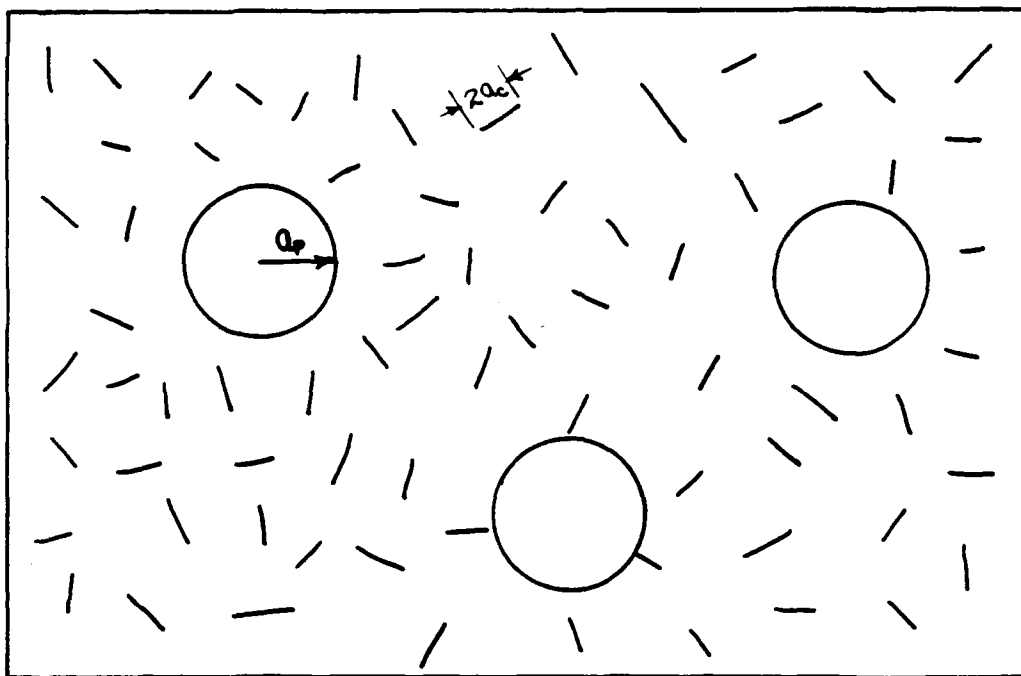


Figure 1. Pores of radius a_p in a matrix containing smaller cracks of length $2a_c$.

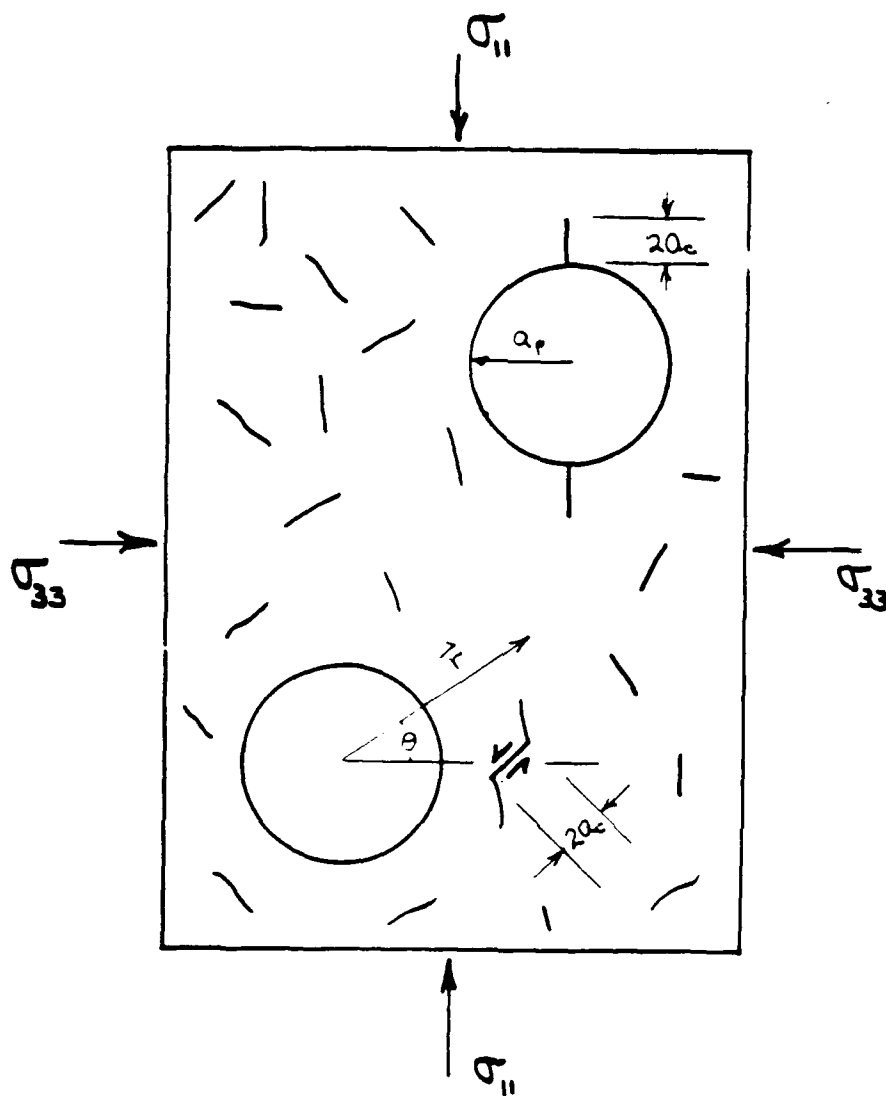


Figure 2. Top right pore illustrates the worst-case scenario for the nucleation of crack growth in the tensile field at the pole of a pore. Lower left pore illustrates the nucleation of "wing cracks" in the compressive field in the equatorial plane of a pore. The worst-case scenario is when $\theta = 0$ and $r = a_p + \sqrt{2} a_c$.

It is also possible to nucleate tensile cracking in the equatorial plane of a pore. Although this is a region of compressive stress concentration $\sigma_{\theta\theta}$, the maximum shear stress $[(\sigma_{\theta\theta} - \sigma_{rr}) \text{ or } (\sigma_{\theta\theta} - \sigma_{\phi\phi})]$ may be large enough to nucleate "wing crack" growth from suitably oriented small cracks as illustrated in Figure 2. Ashby and Hallam (1986) and Ashby and Sammis (1989) investigated the nucleation of such wing cracks arriving at the following criterion:

$$\sigma_{\max} = 3 \sigma_{\min} + \frac{3.1 K_{Ic}}{\sqrt{\pi a_c}} \quad (4)$$

where a_c is the half-length of the inclined starter crack. In this case σ_{\max} is the largest principal stress and σ_{\min} is the smallest principal stress of the local stress field.

The nucleation condition in eqn. (4) may be written in the same form as eqn.(3):

$$s_{11} = \frac{D}{1 - C \lambda} \quad (5)$$

where

$$C = \frac{3 (B_r - A_r) + A_\theta - B_\theta}{A_\theta - 3 A_r}$$

$$D = \frac{3.1}{A_\theta - 3 A_r} \quad (6)$$

and

$$A_\theta = 1 + \frac{1}{23} \left(\frac{a_p}{r} \right)^3 \left[\frac{11}{2} + 18 \left(\frac{a_p}{r} \right)^2 \right]$$

$$B_\theta = 1 + \frac{1}{2} \left(\frac{a_p}{r} \right)^3$$

$$A_r = \frac{24}{23} \left(\frac{a_p}{r} \right)^3 \left[1 - \left(\frac{a_p}{r} \right)^2 \right]$$

$$B_r = 1 - \left(\frac{a_p}{r} \right)^3 \quad (7)$$

For the case when $\sigma_{\min} = \sigma_{\phi\phi}$, the coefficients A_r and B_r in eqn. (6) are replaced by

$$A_\phi = \frac{3}{23} \left(\frac{a_p}{r} \right)^3 \left[2 \left(\frac{a_p}{r} \right)^2 - \frac{3}{2} \right]$$

$$B_\phi = B_\theta \quad (8)$$

The A_α and B_α coefficients in eqns. (7) and (8) depend on the distance from the pore (a_p/r). Since we have assumed the worst-case scenario for nucleation at the poles (see Fig. 2), we have also assumed the worst-case for nucleation at the equator. This occurs when the inclined crack just touches the pore and $r = a_p + \beta a_c$ with $\beta = 1/\sqrt{2}$. In this case equations (7) and (8) are evaluated using

$$\left(\frac{a_p}{r} \right) = \frac{1}{1 + \beta \left(\frac{a_c}{a_p} \right)} \quad (9)$$

Equation (4) for nucleation at the equator is compared with eqn. (3) for nucleation at the pole in Fig. 3 for the case $a_c/a_p = 0.1$. Two cases have been evaluated for eqn. (4); one assumes $\sigma_{\min} = \sigma_{\phi\phi}$ while the other assumes $\sigma_{\min} = \sigma_{rr}$. At relatively low values of the confining pressure (small λ) cracks nucleate first at the poles. However, with increased confining pressure a critical value λ_c is reached above which cracks first nucleate in the equatorial plane.

An expression for the critical stress ratio λ_c can be found by equating (3) and (5)

$$\lambda_c = \frac{D - 1.13}{3.42 D - 1.13 C} \quad (10)$$

where C and D are given by eqns. (6) and must be evaluated for crack opening in both the r and ϕ directions to see which gives the minimum λ_c . Note that λ_c depends only on (a_c/a_p) as illustrated in Figure 4. When a_c/a_p is small, λ_c is smallest for cracks opening in the r direction. When $a_c/a_p > 0.23$, λ_c is smallest for cracks opening in the ϕ direction.

As we discovered in the experiments described below, two failure modes are also possible in porous solids. The first is the usual dilatant shear failure which results from the interaction of cracks

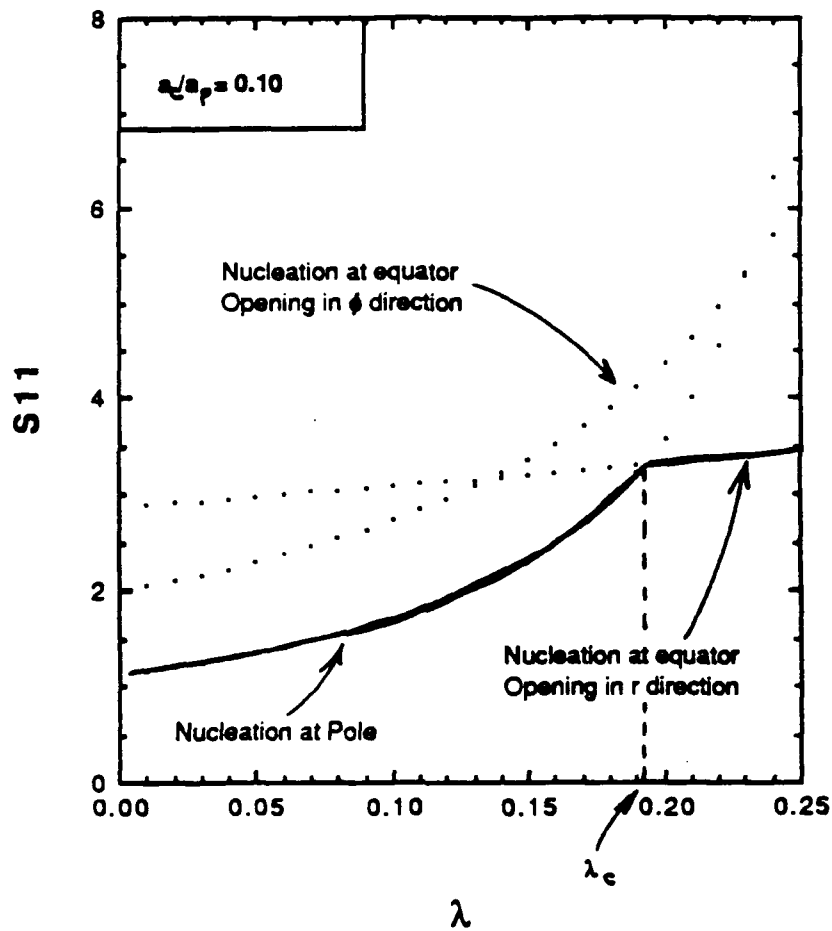


Figure 3. Comparison of the stress, s_{11} , required to nucleate damage at the poles with that required to nucleate in the equatorial plane. λ_c is the critical stress ratio σ_{33}/σ_{11} below which damage nucleated at the poles and above which damage nucleated in the equatorial plane.

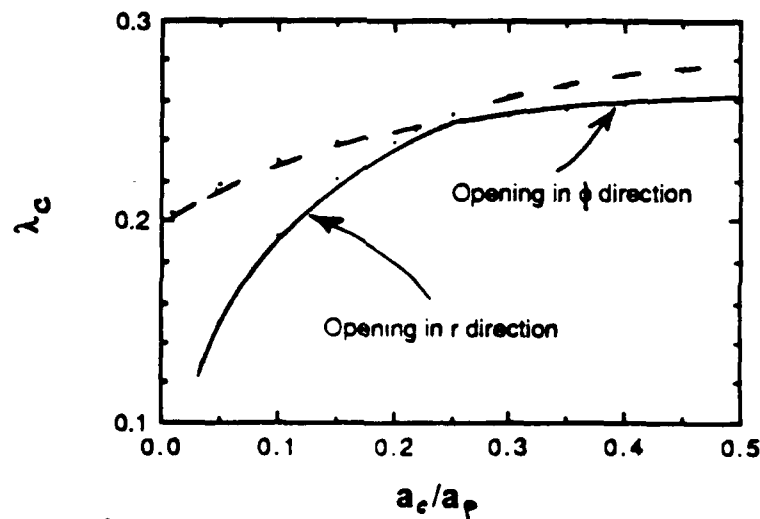


Figure 4. The critical stress ratio λ_c as a function of the size of the cracks relative to the pores (a_c/a_p).

growing from the poles of the pores. However, a second failure mode appears to be associated with the accumulation of damage in the equatorial plane and involves a collapse of the porosity. We are currently investigating these failure modes.

An Experimental Study of the Failure Characteristics of a Model Porous Rock

In order to study the failure mechanisms of porous rock under compression, it was decided to study a low-strength model porous material that could be easily fabricated with a controlled range of initial damage. The motivation behind this line of action was the need to investigate the effects the flaw distribution on the compressive failure characteristics in a controlled way in order to guide the damage mechanics development described above.

A number of considerations were taken into account in deciding the material to be used for these studies:

- a. It should be easy to manufacture to various densities,
- b. It should be easily allow the incorporation of a controlled density and distribution of flaws.
- c. It should not display microplasticity up to the fracture load.
- d. It should have a low enough strength to enable measurement at easily accessible loads under various stress states.

A material that appears to incorporate the above properties is Plaster of Paris. Plaster of Paris is essentially Calcium Sulphate Hemihydrate, $\text{CaSO}_4 \cdot 2\text{H}_2\text{O}$ and is made by heating gypsum between $120^\circ - 160^\circ \text{C}$.



When plaster of Paris is mixed with water the reverse reaction takes place: water is reabsorbed with the formation of gypsum. The matrix of the "as-cast" material consists of interlocking grains of gypsum with an average size of approx. $2\text{-}3\mu\text{m} \times 10\text{-}15\mu\text{m}$. In addition, the samples contain small numbers of approximately spherical pores probably due to water trapped during casting. The average size of such pores is $212 \pm 18 \mu\text{m}$. These pores were found to be the main source of failure in the material.

Specimens of higher density than that of the as-cast plaster were obtained by forcing some of the water out of the mould immediately after casting. The resultant increase in density was associated with a decrease in the average diameter of the spherical pores shown in Fig 5. Due to the sensitivity of the elastic and mechanical properties of the material to the various processing parameters and environmental factors, and the scarcity of any reliable information in the literature, it was decided to measure the elastic and the mechanical properties of the material as functions of the relative density and associated pore size prior to investigating its failure characteristics. The properties measured included: the Young's modulus, the modulus of rupture, the fracture toughness, K_{Ic} , the uniaxial tensile strength and the uniaxial compressive strength. In addition, the compressive strength under purely hydrostatic conditions was also measured, in order to construct the failure surface of the material and compare with theoretical predictions. The results for the as-cast material are summarized in Table 1. The effects of material density on the various parameters are given in Figs. 6 - 9. The uniaxial compression data is given in Figs. 10 and 11 while the hydrostatic compression results are in Figs 12 and 13. Note that a collapse type of failure occurs under hydrostatic loading. The uniaxial and hydrostatic data are used to construct a fracture initiation surface in Fig. 14 and a failure surface in Fig 15. We are currently setting up triaxial experiments to further explore these surfaces.

CONCLUSIONS AND RECOMMENDATIONS

There appear to be two modes of failure in porous rock corresponding to the two modes of damage initiation. When cracks nucleate at the poles and grow parallel to σ_{11} , the interaction between cracks from different pores leads to an instability of the type discussed by Sammis and Ashby (1986) and Ashby and Sammis (1989). The interaction model developed by Ashby and Sammis (1989) for damage initiated at inclined cracks cannot be directly applied to the case of pores. The bending beam interaction developed by Sammis and Ashby (1986) is too cumbersome. We are currently working to develop a new failure criterion more suited to the case of porous solids. When cracks nucleate in the equatorial plane, failure in this plane is also possible. This type of failure involves spalling material into the pore and is characterized by a collapse of the porosity. Since this type of failure involves small-scale shear failure of the cracked matrix (caused by the stress

Table 1 Summary of the properties of the as-cast material

<u>Processing parameters.</u>	
Ratio of powder to water, by weight	100:62.5
Curing time, minimum, days	7
Curing temperature, °C	20 ± 5
Relative humidity during curing, %	60 ± 20
<u>Physical properties</u>	
Theoretical density, g/cm ³	2.35
Density, g/cm ³	1.17 ± 0.03
Total porosity content, %	51 ± 2
Mean diameter of spherical macropores, μm	212 ± 18
Mean diameter of micropores, μm	2 ± 1
Mean grain size, μm	3 × 15
<u>Elastic and Mechanical properties.</u>	
Young's modulus, GPa (bending)	4.5 ± 0.1
Young's modulus, GPa (uniaxial compression)	4.6 ± 0.3
Modulus of rupture (3-point bending, 75% water), MPa	5.5 ± 0.7
Modulus of Rupture (4-point bending), MPa	5.8 ± 0.6
Weibull modulus,	6.2
Fracture toughness (SENB), MPa ^{1/2}	0.14 ± 0.015
Uniaxial compressive strength, MPa	14.6 ± 0.9
Hydrostatic compressive strength, MPa	19.2 ± 1.4
Uniaxial tensile strength, MPa	3.2 ± 0.6

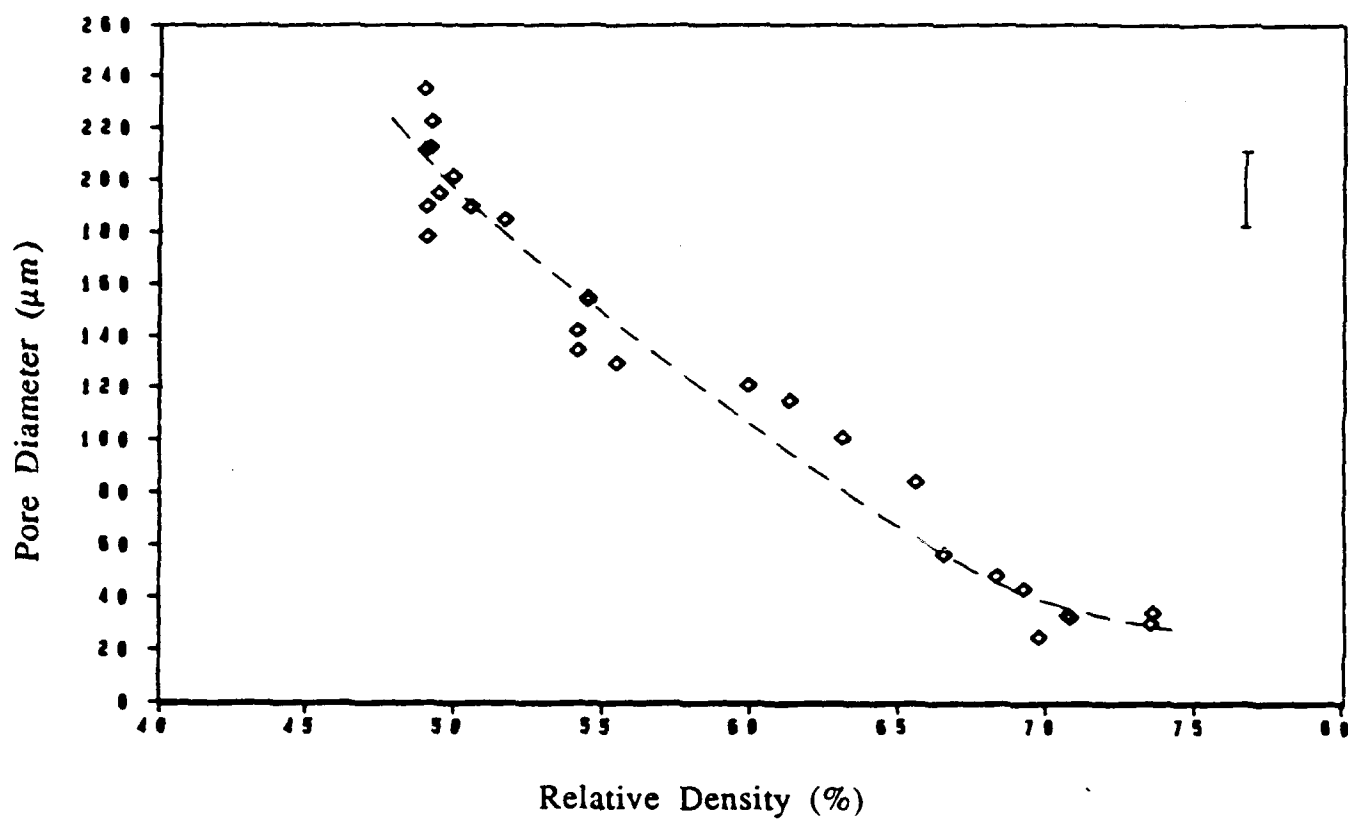


Figure 5. Macropore diameter as a function of relative density of hydrated Plaster of Paris.

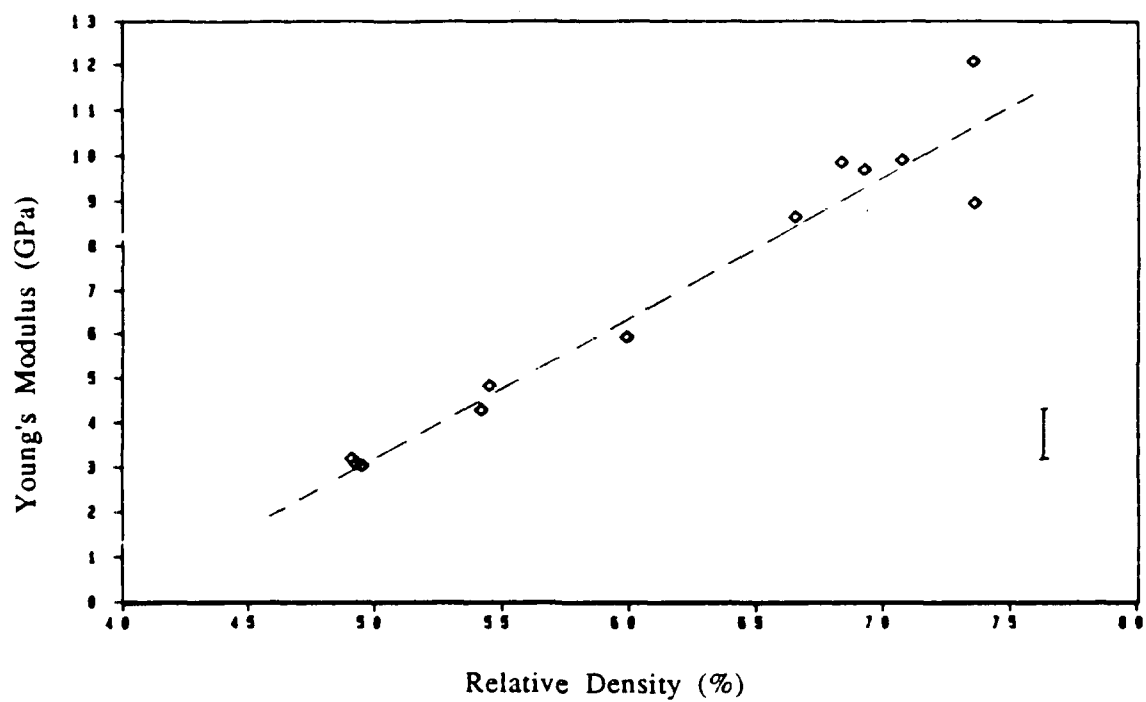


Figure 6. Young's Modulus in uniaxial compression as a function of relative density.

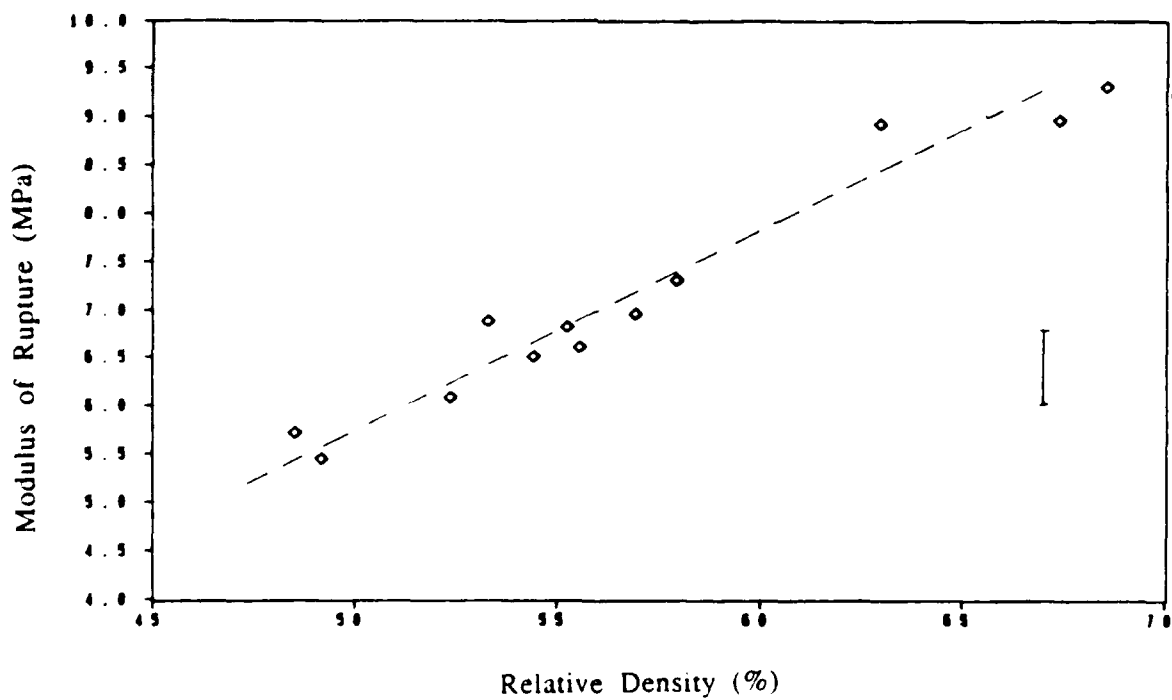


Figure 7. Modulus of Rupture in 4-point bending as a function of relative density of hydrated Plaster of Paris.

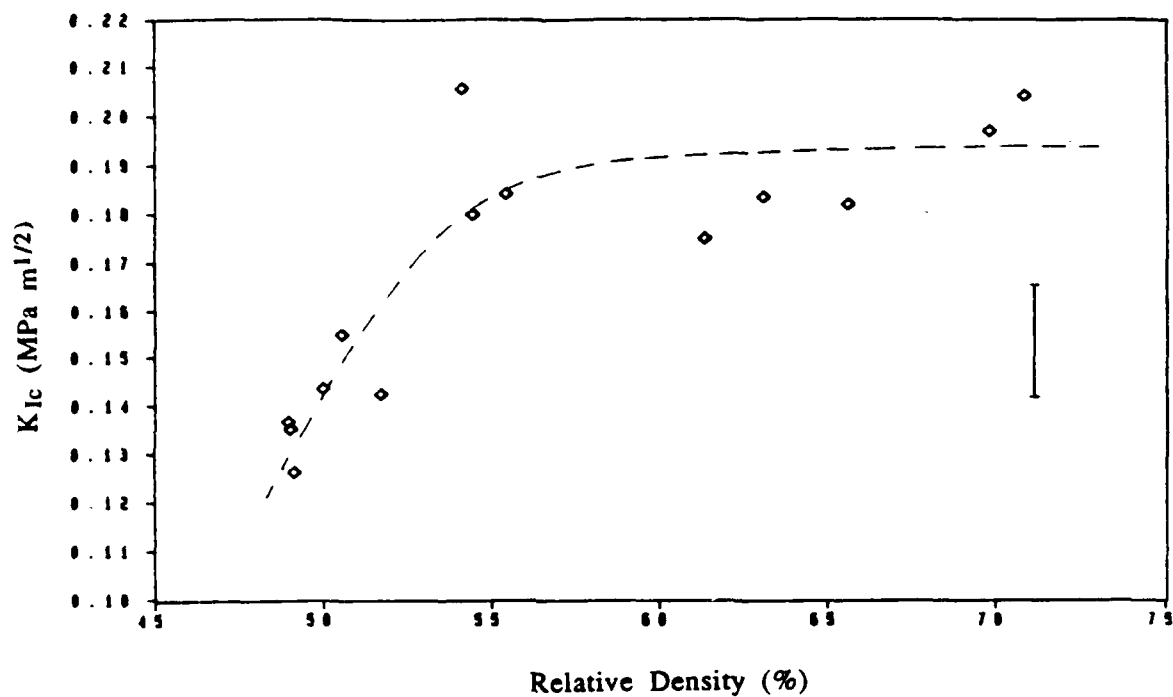


Figure 8. Fracture Toughness, K_{Ic} , as a function of relative density of hydrated Plaster of Paris.

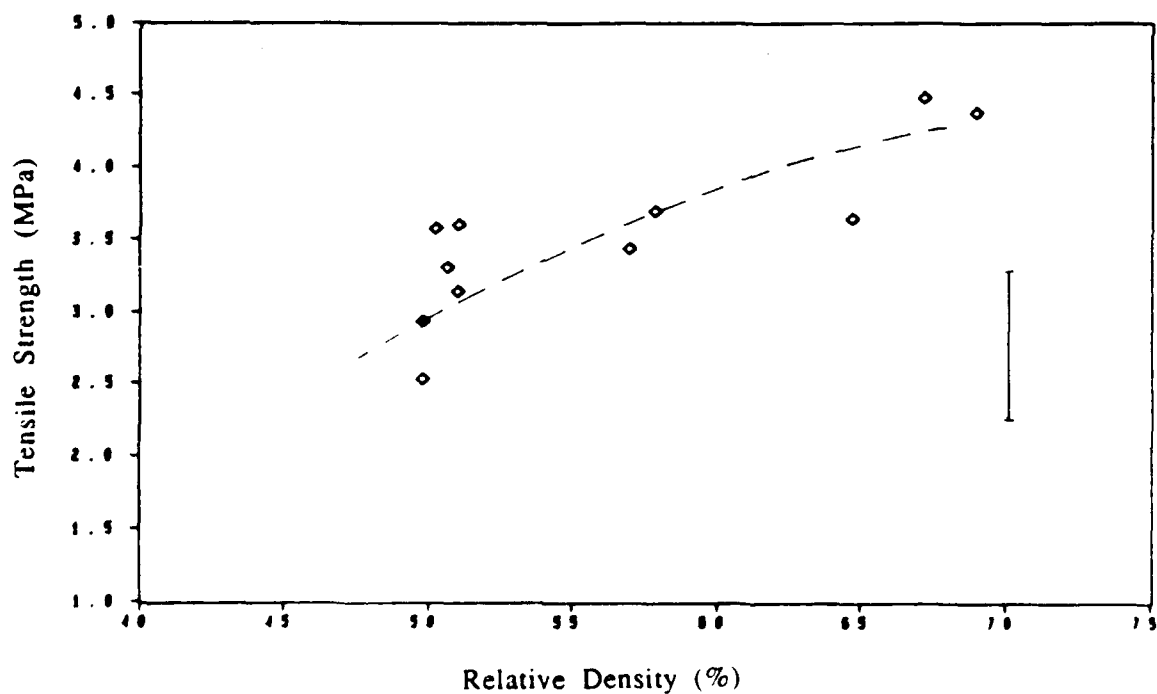


Figure 9. Tensile Strength as a function of relative density of hydrated Plaster of Paris.

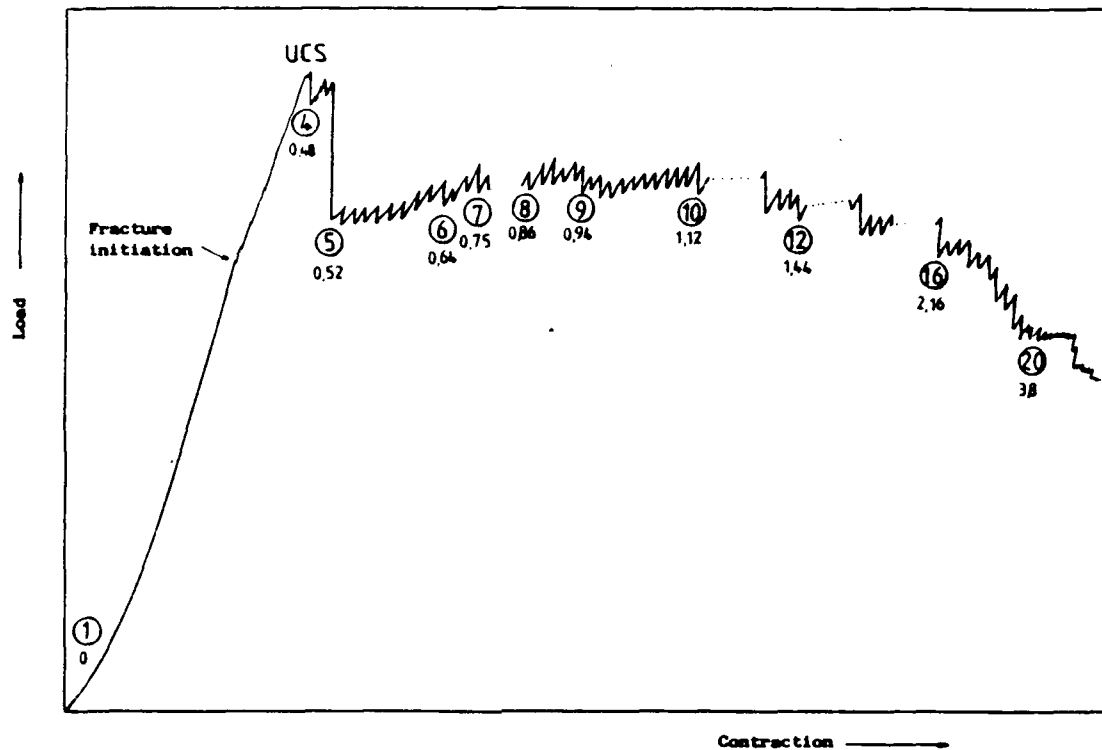


Figure 10. Load-contraction curve for a specimen tested in uniaxial compression.

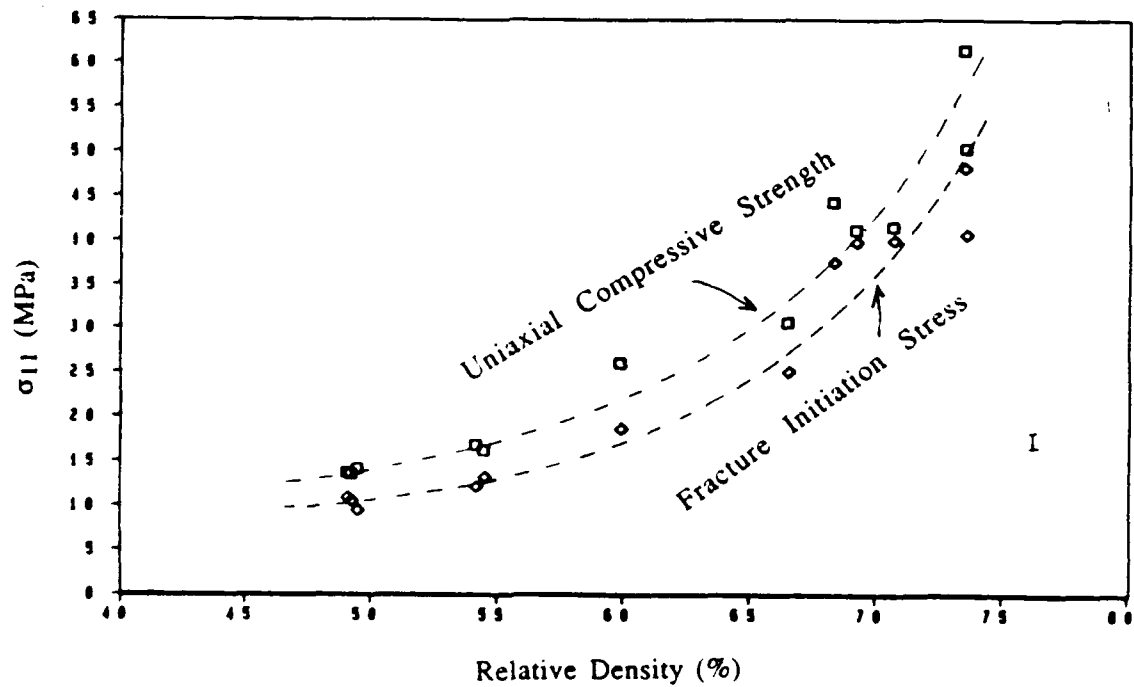


Figure 11. Uniaxial compressive strength and fracture initiation stress (first non-linearity of the σ - ϵ curve) as a function of relative density of hydrated Plaster of Paris.

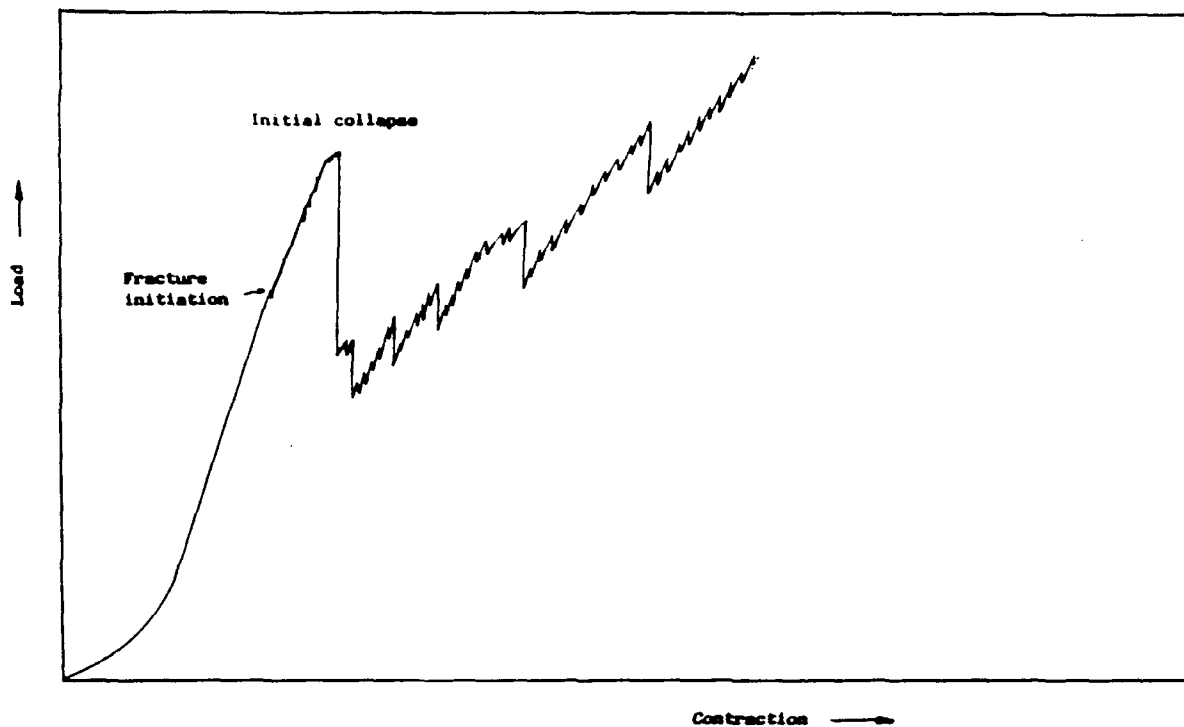


Figure 12. Load-contraction curve for a specimen tested in hydrostatic compression.

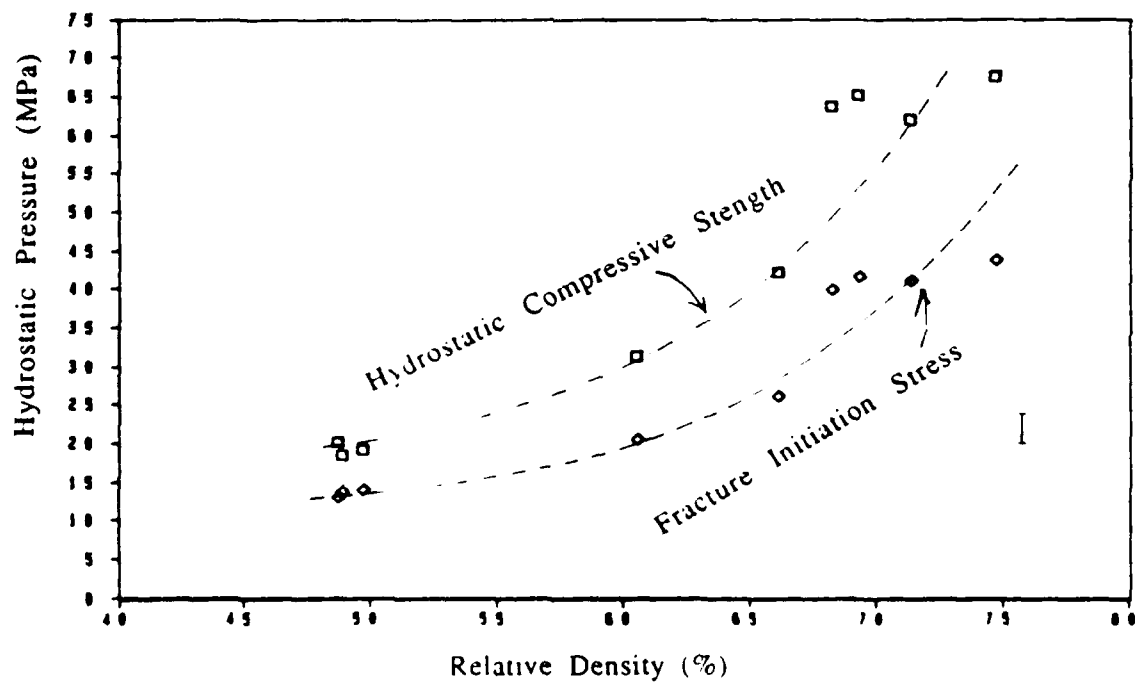


Figure 13. Ultimate hydrostatic compressive strength and fracture initiation stress as a function of relative density of hydrated Plaster of Paris.

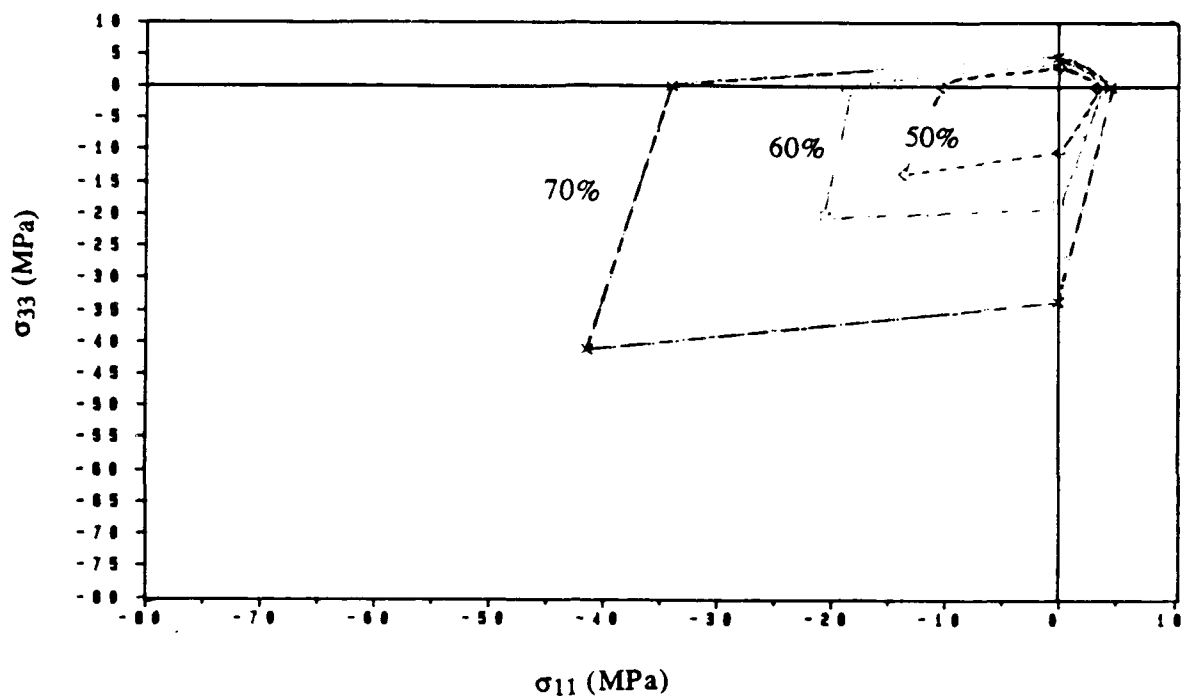


Figure 14. Fracture initiation stress surfaces for Plaster of Paris for three densities.

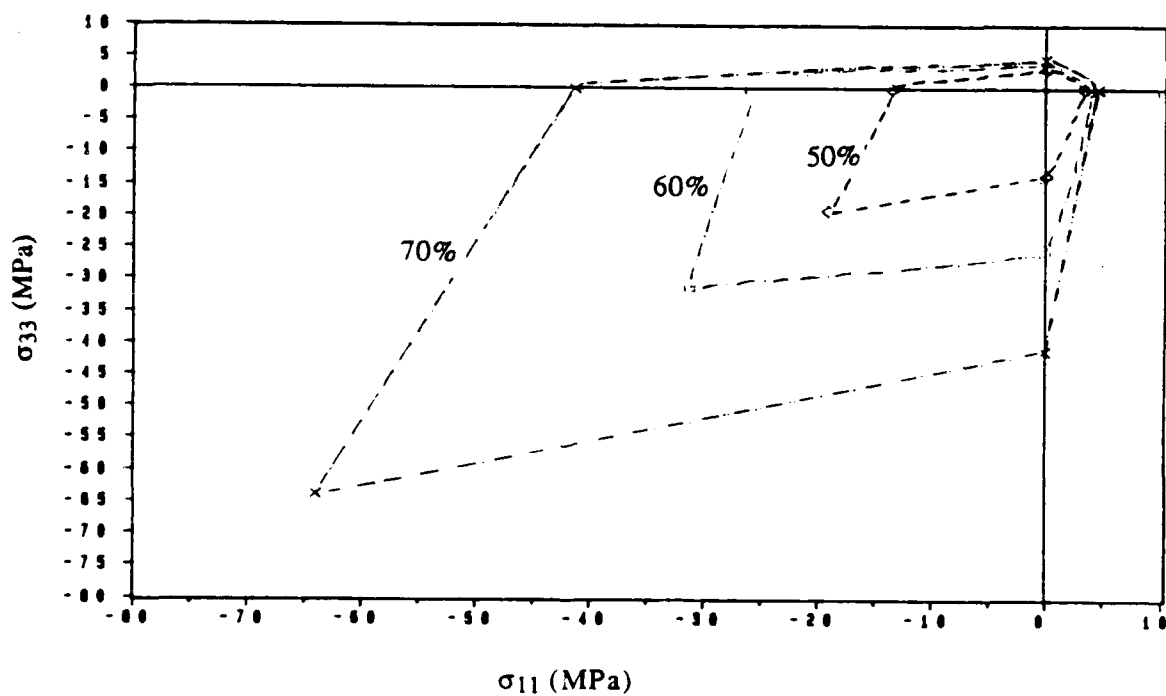


Figure 15. Final Failure stress surfaces for Plaster of Paris for three densities.

concentration of the pores) it may be modeled using the damage mechanics for cracks developed by Ashby and Sammis (1989). We are currently working on this analysis. The experimental program is being extended to explore the failure mode of plaster of Paris over a range of triaxial stress states $\sigma_{11} > \sigma_{33}$. A third ongoing theoretical effort involves simplifying the Ashby and Sammis (1989) damage mechanics for low porosity crystalline rock into a form which can be incorporated into numerical simulations.

REFERENCES

- Ashby, M.F., and S.D. Hallam, The failure of brittle solids containing small cracks under compressive stress states, *Acta metall.*, 34, 497-510, 1986.
- Ashby, M.F., and C.G. Sammis, The damage mechanics of brittle solids in compression, submitted to *PAGEOPH*, 1989.
- Sammis, C.G. and M.F. Ashby, The failure of brittle porous solids under compressive stress states, *Acta metall.*, 34, 511-526, 1986.

NONLINEAR ATTENUATION IN SALT AT MODERATE STRAIN

Gary McCartor and William Wortman
Mission Research Corporation
Contract No. F19628-87-C-0240

OBJECTIVE

In order to characterize a distant seismic pulse according to the energy which generated it, a source function is needed which can be used to initiate the seismic signal at sufficient range from the event that the subsequent propagation can be described in *linear* terms according to the properties of the earth. Thus an observed seismic signal implies a source function which may be compared with known functions for discrimination and yield estimation. Therefore, the properties of such source functions must be known to use this technique. Near-field in situ data from various events have been taken. The smallest strains observed, due to practical free field instrument placement selection, are typically no less than 10^{-5} and are often much greater. If the pulse at this extreme range undergoes no further significant nonlinear modification, its characterization can supply the needed source function. However, if any additional nonlinear changes are important, a useful source function cannot be determined. Consequently, it is important to characterize any possible nonlinear attenuation of moderate strain pulses, preferably through methods which allow generalization to all placement media of interest. It is our ultimate objective to define source functions outside the region where significant nonlinear attenuation takes place.

SUMMARY

The gross nonlinear effects of vaporization, crushing, cracking and plastic behavior induced by strains much greater than 10^{-3} must be taken into account to obtain an understanding of such data. Complex equations of state or constitutive relations including effective stress and porosity are needed. These methods generally apply for strains greater than 10^{-3} ; at lesser strains linear behavior is assumed. However, it seems clear that some residual nonlinear effects continue out to strains less than 10^{-5} . One would like to have a physically based model of any nonlinear effects in order to use existing near field data to define a more distant linear source function or at least to determine what effect, if any, the nonlinearities over the moderate strain range have on the linear source function.

We are attempting to develop nonlinear constitutive relations for the mildly nonlinear attenuation in the moderate strain regime (scaled ranges of 10^2 m/kT^{1/3} to 10^4 m/kT^{1/3} or strains from 10^{-3} to 10^{-6}) for explosively generated seismic pulses. The relations are to be used to determine the character of seismic pulses in the linear low-strain regime (beyond 10^4 m/kT^{1/3}) which may then serve as source functions for regional or teleseismic propagation. A linear source function can be found by numerical propagation of an experimentally known initial pulse through the moderate strain range to account for mild residual nonlinear attenuation.

Moderate strain attenuation data in a salt medium from Salmon,¹⁻⁶ Cowboy,⁷⁻⁹ Livermore small scale explosions,¹⁰ Rockwell damped oscillation experiments¹¹ and New England Research ultrasonic pulse attenuation,¹² with one exception, are fairly consistent internally. The first three provide a detailed indication of the change of amplitude and shape of explosively driven pulses. Proposed constitutive relations must reproduce these data. The data from the wide range of yields in salt indicate that yield^{1/3} scaling applies with a remarkable precision; if all times and distances are scaled by yield^{1/3}, the scaled amplitudes and shapes of pulses from all experiments are nearly the same.¹³ Thus the initial pulse on entering the moderate strain regime must scale at some small scaled range and the subsequent attenuation must result from constitutive relations which have no time or space scales which are fixed by the medium. This provides a significant reduction in the domain of allowable nonlinear behavior.

Substantial attenuation data, over the range of moderate strains, exists for salt. Larson's laboratory data were taken from the effects of a series of small chemical explosives in blocks of pressed salt. Velocity data were taken at several gauges such that the totality of the examples from all shots covered peak velocity to compressional velocities, which is approximately the peak strain, of 10^{-1} to 10^{-3} . Using a triplet of records from a single shot, it was estimated that over peak strains of 1.4×10^{-3} , 7.0×10^{-4} and 4.6×10^{-4} , the Q changes from 12.5 to 24.9. The corner frequency for this experiment was about 5×10^4 Hertz.

The Salmon data were generated by a 5.3 kT nuclear explosion in salt. The work by McCartor and Wortman³ as well as McLaughlin and Gupta⁴ shows that the high quality data clearly indicate a high level of attenuation. It is estimated that for peak strains from 4×10^{-3} to 3×10^{-4} , the effective Q is to order of 10 or less at a corner frequency of about 6 Hertz. This Q appears nearly constant,³ perhaps increasing mildly with range,⁴ over the order of magnitude strain range available. However, in view of the fact that small strain data from other experiments, including the decoupled event Sterling⁴ which used the Salmon cavity, indicate a much larger

Q, it seems likely that there are residual nonlinearities at the extreme range of the Salmon data.

Tittmann¹¹ has studied the attenuation of flexural and torsional harmonic oscillations of salt samples. It has been found that the attenuation, expressed in terms of Q^{-1} as a function of strain amplitude, tends to be nearly constant for strains from 10^{-8} to 10^{-6} , then increase for greater strains. The attenuation is a decreasing function of confining pressure with an average Q of approximately 200 at 10^{-6} strain at a frequency of 400 Hertz for confinement consistent with the explosions.

The regime covered by the Cowboy experiments overlaps that for Salmon, by beginning at strains of about 5×10^{-3} and extending out to 10^{-5} . The Cowboy experiments consisted of a series of shots over a range of yields, both coupled and uncoupled, such that the individual events generally had only a few instruments in operation. Several authors have combined these data by invoking the experimentally compelling evidence for simple scaling, which suggests that the velocity pulse data from various yields can be equated by scaling all times and distances by the cube root of the yield.

Trulio⁶ analyzed the scaling-combined Cowboy data to estimate Q as dictated by decrease in peak displacement with range by using one decade at a time in the frequency domain. He found that attenuation decreases as range increases in a fashion inconsistent with linearity expressed as dispersive harmonic potential waves. If the coupled Cowboy data are fit assuming a Q independent of range, Q must be a function of frequency ranging from about 5 at low frequencies (1 Hz at Salmon scale) to nearly 100 at high frequencies (32 Hz at Salmon scale). However, simple scaling is inconsistent with this fit since scaling requires linearity coupled with a Q independent of frequency. At fixed frequency, the attenuation expressed in terms of Q, is dependent upon range. Since it is assumed that the medium is approximately homogeneous, the implication is clear that the attenuation must be amplitude dependent and so nonlinear.

Minster and Day⁸ have used the scaled peak velocity data for Cowboy to determine if these data require an amplitude (nonlinear) or frequency dependent Q for consistency. They determined that a Q^{-1} which consists of a small constant (consistent with small strain data from Tittmann) plus a term proportional to the peak strain provides a good fit to the data. The observed attenuation effects do not firmly indicate the need for a frequency dependent Q but indicate that an amplitude dependent Q provides a more convincing fit than a constant Q. It is concluded that there must be nonlinear attenuation in the Cowboy strain regime.

New England Research¹² has carried out a series of laboratory experiments for which compressional and shear ultrasonic pulses consisting of about two cycles at 100-200 kHz were propagated through a sample. Attenuations were calculated using a spectral ratio technique. Variation of the attenuation with peak strain amplitude and confining pressure were determined. For the dome salt it was found that over a strain range of 5×10^{-7} to 3×10^{-5} and for a confining load range of 0.1 to 1 MPa, the P-wave attenuation is nearly constant and can be described by a Q of about 20. There is no particular evidence of nonlinearity in these data alone.

In summary, the salt data appear to support the hypothesis that explosively generated pulses encounter nonlinear attenuation for strains much greater than 10^{-6} . No detailed knowledge of the attenuation mechanism currently exists but there does appear to be a consistency in that the explosively generated pulses closely obey simple scaling which suggests that the mechanism must be rate independent. The *effective* Q for this process increases with increasing frequency and increases with decreasing strain.

The Salmon data have an "elastic precursor" feature which may be useful in understanding some nonlinear effects of attenuation. Each of the pulses experimentally observed at six sensors at ranges from 166 meters to 660 meters exhibit a discontinuity in the slope upon the initial steep rise in pulse velocity, as seen in Figure 1. This appears as a toe-like behavior in the leading edge of the velocity profile which has been described by Perret¹ as an "elastic precursor" to the main pulse. The absolute amplitude of the toe remains approximately constant with range, at a particle velocity of about 0.5 m/s, while its amplitude relative to the peak increases with range. This precursor amplitude corresponds to a compressional strain level of $\epsilon \approx 10^{-4}$. The leading edge of the pulses propagates at a speed of 4.7 km/sec while the pulse peaks propagate at a speed of 3.7 km/sec. The elastic compressional speed of in this medium is typically about 4.6 km/sec. This indicates that the precursor signal seen in the Salmon data is due to elastic behavior while the subsequent pulse suffers a lower propagation speed due to some relaxation or plastic behavior.

Perret suggests that the precursor may develop in the observation region based on moderate strain plastic behavior. In order to account for the precursor data in Salmon, the equation of state would have to provide linear behavior up to a threshold (of about 5 bars) and through some deformation of the material, relax the modulus abruptly to a value which provides a compressional propagation speed about 20% less than for infinitesimal strains in undisturbed material.

Consider a medium for which the shear modulus permanently decreases upon having a critical strain threshold exceeded; the compressional modulus before

and after exceeding the strain threshold reflects the compressional speeds at the beginning and peak of the Salmon pulses. This will be referred to as a shear failure model. In this discussion, the compressional speed decreases to 80% of its original value. Taking the Lamé constants λ and μ to have a ratio of 2, a decrease of the compressional speed of 20% corresponds to reducing the shear modulus to about 38% of its elastic value. The reduction of modulus at a fixed strain is consistent with scaling since the strain is a unitless quantity and there is no rate dependence. The scaling restriction does require that the relaxation time of the modulus change be short compared with any representative time scale of the data; we take the transition to be instantaneous.

The elastic threshold was taken at a compressional strain of 10^{-4} ; the resulting pulse sequence at the ranges to observation stations for Salmon is as shown in Figure 2. The character of the calculated precursor is much like that seen experimentally, in that the leading feature is drawn out, the transition to the main pulse takes place at a constant amplitude and the peak moves at a significantly lower speed. Still the amplitude of the main peak does not decrease as quickly as the data indicate.

When the modulus decreases, the elastic energy in the pulse decreases. This energy is lost to heating the medium. For the parameter used, over a full cycle for which most of the pulse exceeds the critical strain, approximately one-third of the original elastic energy will be lost. This corresponds to an effective Q of about 13 for peak strains well in excess of 10^{-4} . This value of Q is far less than that expected for very small strains but it is still more than the 5 to 10 seen for Salmon attenuation.

The attenuation from partial shear failure does not produce an amplitude for the pulse at 660 meters which is as small as that seen experimentally. More attenuation has been added to attempt to match better the data by employing a linear Q of 10 in an absorption band from 1 to 100 Hertz.

A range of thresholds for the shear failure was added. The model has been altered to produce a variation of failure threshold values of compressional strain over a range of 30% with a constant probability about the 10^{-4} value. The set of pulses at the Salmon instrument ranges then calculated using the additional linear Q and spread out shear failure is given in Figure 3.

CONCLUSIONS AND RECOMMENDATIONS

This work indicates that the "elastic precursor" seen in Salmon near-field, moderate strain, velocity data is reproduced rather well with the hypothesis of partial shear failure which is activated for the duration of the pulse when the compressional

strain exceeds 10^{-4} . This also gives an attenuation mechanism which accounts for much of the energy loss seen in the decay of pulses from Salmon with range. However, the overall attenuation produced is not adequate to account for that seen in the data. The addition of a linear absorption band attenuation, which is active over much of the significant frequency range appropriate to Salmon and which has a Q of 10, then provides a propagation model which nearly reproduces the signals at ranges beyond 166 meters when the observed signal at this range is used as the source. Furthermore, this threshold mechanism provides a transition to more modest attenuation at small strains which is required to be consistent with Cowboy data.

The fact that the reduction in compressional wave speed is attributed to shear failure, rather than alteration of some other material property, is largely a matter of consistency with past thinking on modes of material behavior; there is no direct experimental link to shear properties. The general agreement with data which results here could just as well have been produced by any method which reduces the compressional modulus in the required amount.

The use of a Q description for attenuation which is clearly nonlinear is probably not useful, except as a crude estimate of the degree of amplitude reduction. In fact, the use of Q in nonlinear cases can provide very deceptive results since the frequency and range dependence are generally mixed. It would be best to describe the attenuation mechanism directly in terms of an equation of state. This will allow the application to different experiments. The result of a nonlinear attenuation for a propagation experiment can always be used to find an effective Q by, say, use of spectral ratios but the same mechanism will produce a different effective Q if the character of the initial waveform is changed. The effective Q is not a robust quantity for nonlinear attenuation.

We expect to use the finite difference propagation code, which was developed as a tool for our current work on Salmon, as a testbed for development of nonlinear constitutive relations. This avoids the use of Q and concentrates directly on the physical mechanisms which produce attenuation. Ideally one would like to express a constitutive relation in terms of parameters known to be important, such as porosity, effective stress, crack density, crack growth, etc., in order to allow a model which can be generalized to different media.

REFERENCES

1. Perret, W.R., *Free-Field Particle Motion from A Nuclear Explosion in Salt, Part I, Project Dribble, Salmon Event*, VUF-3012, Sandia, 1967.
2. Rogers, L.A., *Free-Field Motion Near a Nuclear Explosion in Salt: Project Salmon*, J. Geophys. Res. 71, 3425 (1966).
3. McCartor, G., and W. Wortman, *Experimental and Analytic Characterization of Nonlinear Seismic Attenuation*, MRC-R-900, Mission Research Corp., March 1985.
4. McLaughlin, K.L. and I.N. Gupta, *Strain and Frequency Dependent Attenuation Estimates in Salt from Salmon and Sterling Near-Field Data*, Teledyne Geotech, to be submitted to Geophysical Research Letters, 1986.
5. Murphy, J.R., *A Review of Available Free-Field Seismic Data from Underground Nuclear Explosives in Salt and Granite*, CSC-TR-78-0003, Computer Sciences Corporation, September 1978.
6. Trulio, J., Applied Theory, Inc., private communications, 1986.
7. Murphey, B.F., *Particle Motions Near Explosions in Halite*, J. Geophys. Res. 66, 947 (1961).
8. Minster, J.B. and S.M. Day, *Decay of Wave Fields Near an Explosive Source Due to High-Strain Nonlinear Attenuation*, J. Geophys. Res. 91, 2113 (1986).
9. Wortman, W. and G. McCartor, *Nonlinear Seismic Attenuation from Cowboy and Other Explosive Sources*, MRC-R-1107, Mission Research Corp., September 1987.
10. Larson, D.B., *Inelastic Wave Propagation in Sodium Chloride*, Bull. Seism. Soc. Am. 72, 2107 (1982).
11. Tittmann, B.R., *Non-Linear Wave Propagation Study*, SC5361.3SAR, Rockwell International Science Center, 1983.
12. Coyner, K.B., *Attenuation Measurements on Dry Sierra White Granite, Dome Salt and Berea Sandstone*, New England Research, September 1987.
13. Trulio, J., *Simple Scaling and Nuclear Monitoring*, ATR-78-45-1, Applied Theory, Inc., 1978.

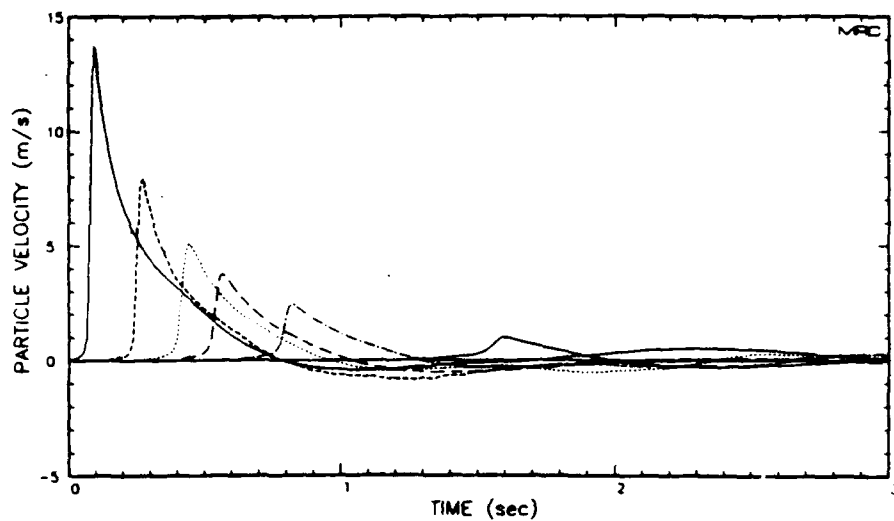


Figure 1. Salmon radial velocity pulses seen at 166, 225, 276, 318, 402 and 660 meters range (0.036 seconds offset).

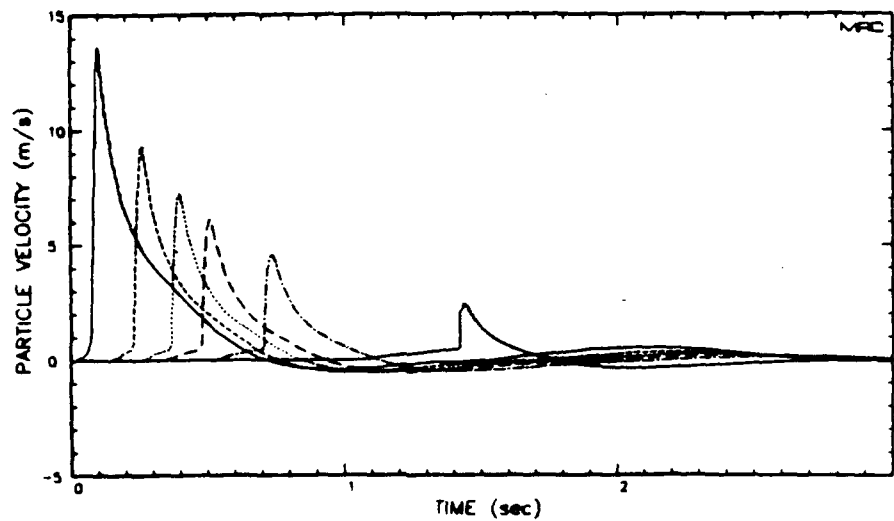


Figure 2. Calculated pulse with shear failure.

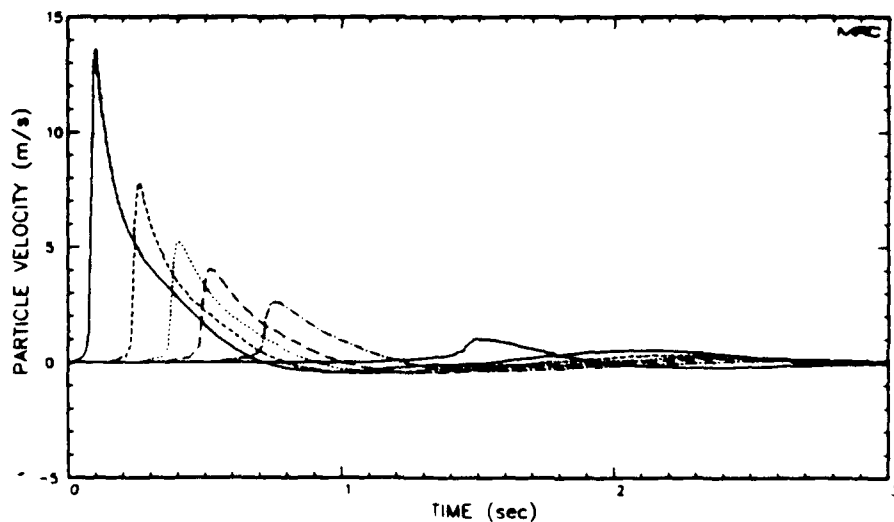


Figure 3. Calculated pulses with smoothed shear failure and an absorption band Q of 10.

NONLINEAR FINITE DIFFERENCE SIMULATIONS OF CAVITY DECOUPLED EXPLOSIONS IN SALT AND TUFF

J. L. Stevens, J. R. Murphy, and N. Rimer
S-CUBED, P.O. Box 1620, La Jolla, CA 92038-1620

Contract No. F19628-87-C-0093

OBJECTIVE

The objective of this project is to develop an improved understanding of the high frequency character of the seismic source function of decoupled, underdecoupled and overdecoupled explosions. This is accomplished by performing a suite of one-dimensional finite difference simulations of explosions in air-filled cavities in salt and tuff emplacement media. The range of yields used in these calculations spans the range from underdecoupling to overdecoupling.

SUMMARY

The long period seismic source function of a decoupled explosion is reduced in amplitude by an amount that depends on the tamped coupling efficiency, the shear modulus of the emplacement material, the detailed nonlinear behavior of the emplacement material, and the physical characteristics of the air inside the cavity. The high frequency decoupled source function also depends on these factors, but the decoupling effect is reduced, and the effect of air is much more pronounced than on the long period source function.

In this study, we have performed a series of calculations to model both the long period and short period character of the seismic source function of decoupled, underdecoupled, and overdecoupled explosions. The material properties used in this set of calculations were chosen to be similar to the Mill Yard and Sterling experiments. The Mill Yard explosion was detonated in an 11 meter unsaturated tuff cavity, while the Sterling explosion was detonated in a 17 meter salt cavity. The latter decoupling criterion (the theoretical explosion yield above which nonlinear material behavior begins to occur), is 21 tons for the Mill Yard tuff case and 220 tons for the Sterling salt model. The range of yields used in the calculations was 5 to 160 tons for the tuff simulations and 95 to 1520 tons for the salt simulations. For comparison purposes, additional calculations were run using a linear material model, and also using a step pressure source in place of the detailed air shock model.

The theoretical long period decoupling factor for fully decoupled explosions can be calculated from the results of a tamped calculation and the relation for the reduced velocity potential for a pressurized cavity. The long period limit ψ_{∞} is given by

$$\psi_{\infty} = \frac{3}{16\pi\mu} (\gamma - 1) W$$

where W is the explosion yield, μ is the shear modulus of the material, and γ is the

adiabatic expansion constant for the air inside the cavity. Note that for a decoupled explosion, ψ_{∞} depends quite strongly on the shear modulus of the external medium. Substituting the appropriate values, we find $\psi_{\infty} \approx 14.0W$ for a decoupled explosion in tuff, and $\psi_{\infty} \approx 3.45W$ for a decoupled explosion in salt where W is the yield in kilotons and ψ_{∞} is in m^3 . Dividing the results of a tamped calculation by these numbers, we find the theoretical long period decoupling factors $D_{tuff} \approx 23$ and $D_{salt} \approx 93$.

In Table 1, we list the results from the tuff calculations for an explosion in an air-filled cavity as described above. The columns in the table give the yield of the simulation, ψ_{∞} , the peak value of the time domain reduced displacement potential, the decoupling ratio, the elastic radius (radius to limit of plastic yielding), and the radius to the limit of pore crushing. As can be seen from the table, the nonlinear material behavior is too complex to be accurately described by a single decoupling threshold criterion. Yielding begins with an explosion yield of between 20 and 40 tons, however pore crushup begins with explosion yields as small as 5 tons. The effect of pore crushup is to remove energy from the outgoing seismic wave, so it has the effect of increasing decoupling. As a result, the maximum low frequency decoupling factor of 44 is achieved with a yield of 20 tons, which exceeds the decoupling factor of 23 predicted with a linear material model. With higher explosion yields, the decoupling effectiveness decreases as yielding becomes the dominant effect. At 160 tons, the decoupling factor decreases to less than that for a linear model.

Table 1. Explosion in 11 Meter Air-Filled Tuff Cavity					
Yield kt	ψ_{∞} m^3	ψ_{peak} m^3	$\psi_{tamped}/\psi_{\infty}$	R_e m	R_c m
0.005	0.061	0.105	26.7	11.30	13.36
0.010	0.099	0.153	32.9	11.30	17.74
0.020	0.149	0.246	43.7	11.30	22.39
0.040	0.364	0.530	35.8	12.38	27.11
0.060	0.618	0.840	31.6	13.14	29.86
0.080	0.913	1.212	28.5	14.42	32.11
0.160	2.802	3.335	18.6	20.25	43.36

In Figure 1, we show the reduced velocity potentials for all seven yields for the tuff calculations. All of the calculations show a high frequency peak corresponding to cavity reverberations. For the smallest yield of 5 tons, the air shock reverberations dominate the spectrum. The dominant frequency of this peak increases with yield, ranging from 100 Hz for the 5 ton calculation to 600 Hz for the 160 ton calculation. This result indicates that the high frequency enhancement due to cavity reverberations is more likely to be observed from an overdecoupled explosion than from a fully decoupled or partially decoupled explosion.

In Figure 2, we show the decoupling factors for the tuff simulations, plotted as a function of frequency. These decoupling factors were determined by cube-root scaling the tamped explosion spectrum to the same yield as the cavity simulation, and then

taking the ratio of tamped to cavity spectra. At high frequencies the cavity reverberations dominate the spectrum. The cavity reverberations are nearly independent of the material properties of the external medium. Because of this there is little difference in the seismic source function at high frequencies between simulations using linear and nonlinear models of the external material. Because the cavity reverberations generate a substantial amount of high frequency energy, the high frequency decoupling factors are significantly lower for the air-filled cavity simulations than for the step pressure calculations. Because the nonlinear effects cause attenuation of high frequencies in the tamped case, however, the decoupling factors drop off rapidly at high frequency, and are reduced to less than one at sufficiently high frequency in all cases.

In Table 2, we summarize the results of the salt calculations. The columns in the table have the same meanings as in Table 1, but the crush radius is omitted because the salt is modeled as a nonporous material. As can be seen from the table, yielding begins at slightly less than 190 tons in good agreement with the latter decoupling criterion. The decoupling factor, however, remains about the same over a large range of explosion yields, and decreases by only a factor of 2 at 1520 tons, even though the elastic radius has increased to 33 meters.

Yield kt	Ψ_{∞} m^3	Ψ_{peak} m^3	$\Psi_{tamped}/\Psi_{\infty}$	R_e m
0.095	0.297	0.413	101.7	17.00
0.138	0.453	0.613	96.9	17.00
0.190	0.732	0.904	82.6	17.94
0.276	1.151	1.397	76.3	18.53
0.380	1.683	2.003	71.8	19.49
0.570	2.909	3.339	62.3	20.82
0.760	4.135	4.723	58.5	22.01
1.520	10.375	11.545	46.6	33.27

In Figure 3, we show the reduced velocity potentials for the eight yields used in the simulations. As with the tuff models, all of the calculations containing an airshock show a high frequency peak corresponding to cavity reverberations. Again, the frequency of the peak increases with yield, ranging from just over 100 Hz for the 95 ton simulation, to about 600 Hz for the 1520 ton simulation. In the 1520 ton simulation, nonlinear effects are sufficiently large to reduce the amplitude of the reverberation peak. In all other cases, there is little difference between the linear and nonlinear simulations at high frequencies.

In Figure 4, we show the decoupling ratio for the salt simulations. The results are very similar to the tuff simulations. The air-filled cavity simulations have lower decoupling ratios than the step pressure simulations at high frequencies, particularly for overdecoupled explosions. Again, the decoupling ratio is reduced to less than one at sufficiently high frequencies.

CONCLUSIONS AND RECOMMENDATIONS

The results of this set of simulations of decoupled explosions in salt and tuff indicate that:

1. Explosions in decoupled cavities generate significantly more high frequency energy than would be predicted from a simple step in pressure on the cavity wall. The decoupling factor decreases to less than one at sufficiently high frequencies. High frequency decoupling factors are larger for overdecoupled explosions than for "fully" decoupled explosions at the same frequency with the same cavity geometry.
2. At high frequencies, there is little difference between the source functions predicted by linear theory and those predicted by a nonlinear external material model. This happens because the high frequency spectra are dominated by cavity reverberations. This remains true for overdecoupled and partially decoupled explosions.
3. Explosions in cavities in unsaturated tuff decouple more than would be predicted based on linear theory. This happens because the dominant nonlinear mechanism which is operating at low stress levels is pore crushing which attenuates the outgoing wave. At sufficiently high explosion yields, about a factor of five higher than the Latter criterion, plastic flow becomes the dominant mechanism, and decoupling decreases to less than predicted by elastic theory.
4. In salt cavities, plastic flow begins at about the yield predicted by the Latter criterion. The amount of decoupling, however, decreases very slowly with explosion yield. Low frequency decoupling is reduced by only a factor of two at an explosion yield 7 times the Latter criterion.

11 Meter Air Filled Tuff Cavity Simulations

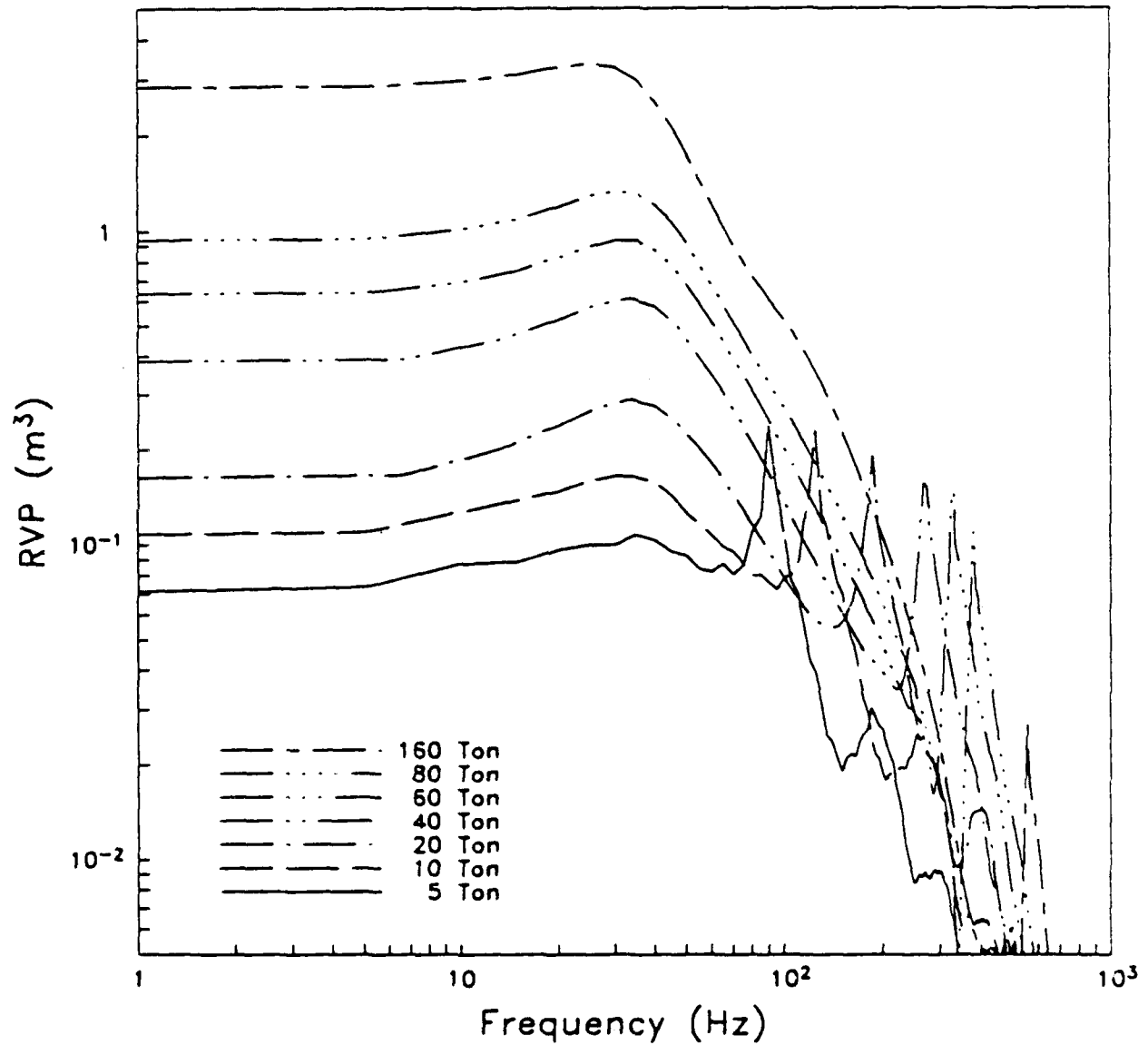


Figure 1. Reduced velocity potential for 7 different yields for an air filled cavity inside a medium with a nonlinear tuff material model.

11 Meter Air Filled Tuff Cavity Simulations

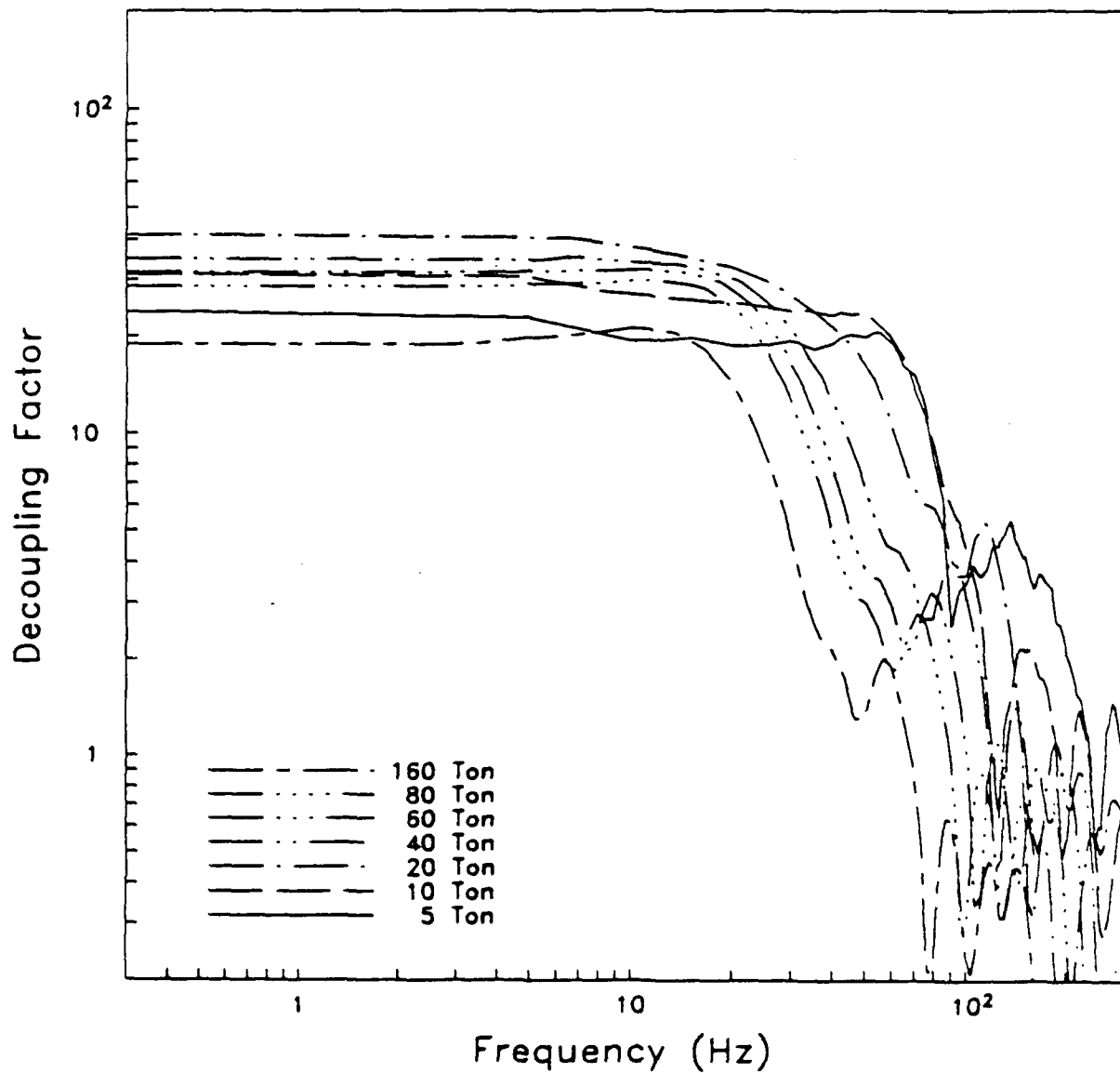


Figure 2. Frequency dependent decoupling factor for 7 different yields for an air filled cavity inside a medium with a nonlinear tuff material model.

17 Meter Air Filled Salt Cavity Linear Simulations

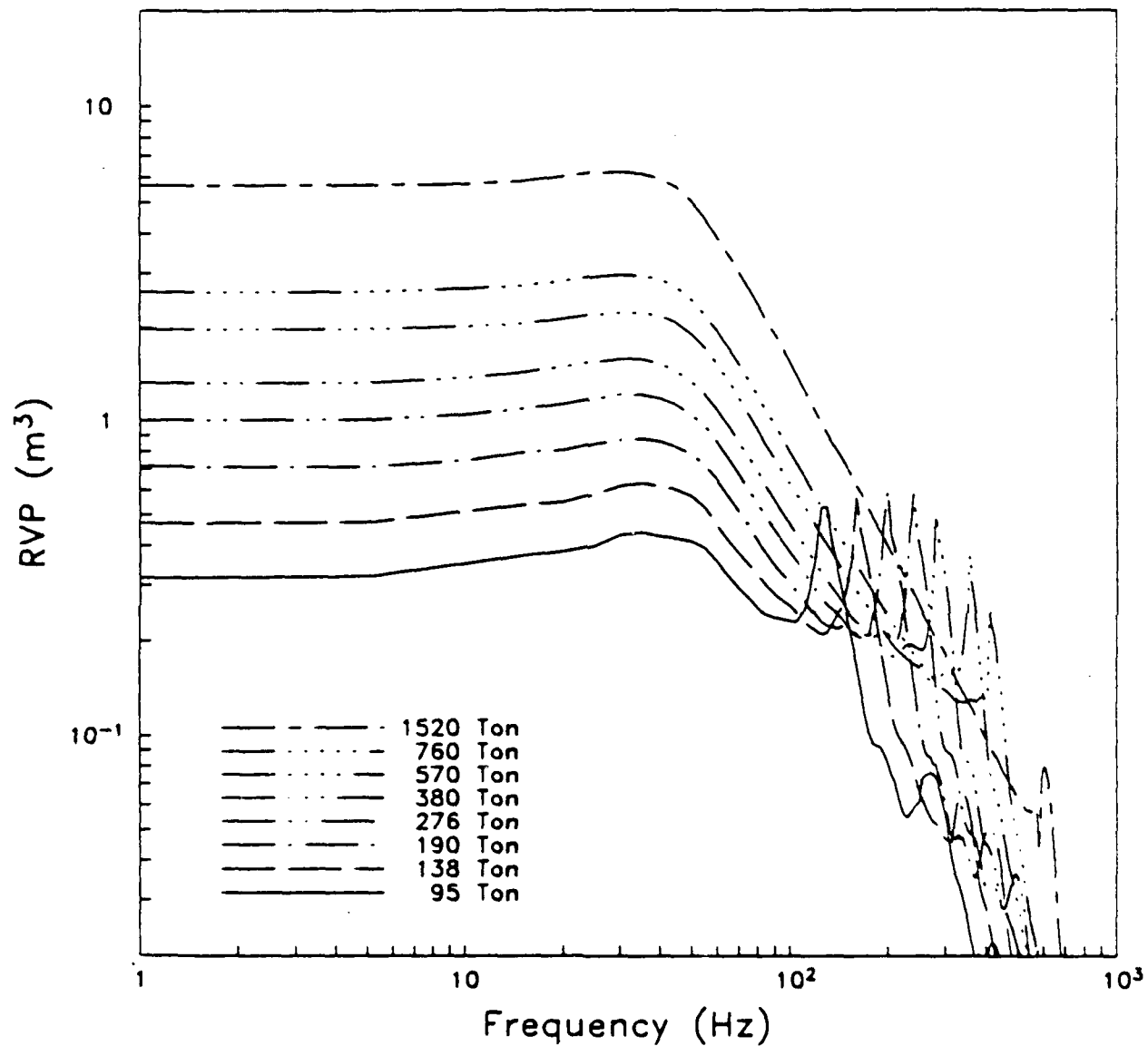


Figure 3. Reduced velocity potential for 8 different yields for an air filled cavity inside a medium with a nonlinear salt material model.

17 Meter Air Filled Salt Cavity Simulations

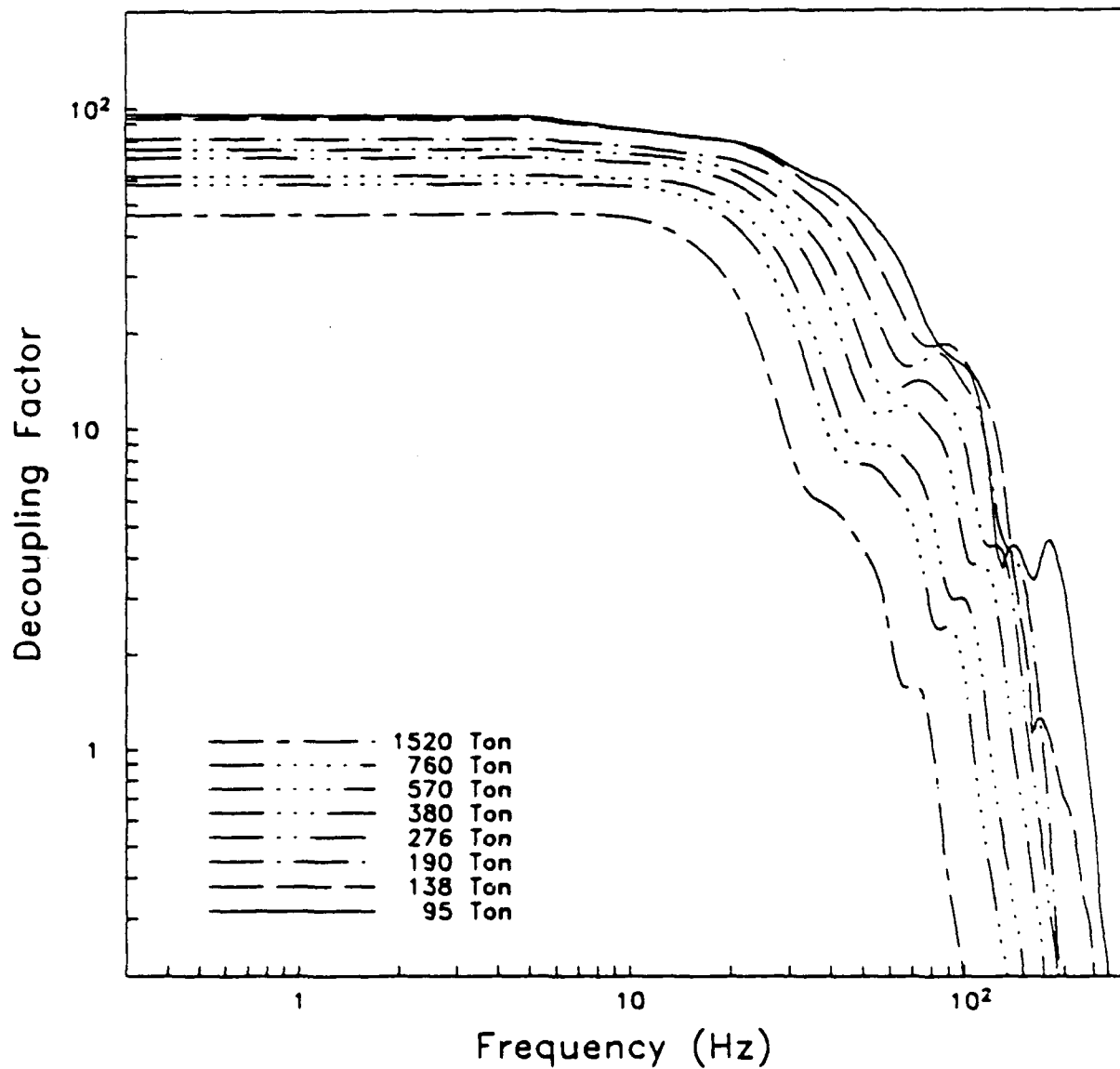


Figure 4. Frequency dependent decoupling factor for 8 different yields for an air filled cavity inside a medium with a nonlinear salt material model.

STRUCTURE EFFECTS ON REGIONAL WAVEFORMS

Terry C. Wallace
William E. Holt

Department of Geosciences
University of Arizona
Tucson, Arizona 85721

Contract No.: F19628-87-K-0046

OBJECTIVE

Regional distance seismology has been the focus of research in recent years for nuclear explosion detection, location, discrimination, and yield determination. The emphasis on regional data serves a twofold purpose: (1) regional stations can significantly reduce the detection threshold, and (2) regional data appear to provide a stable and precise estimate of the yield of underground nuclear explosions. In order to use regional distance phases for discrimination and yield determination, it is necessary to better understand propagation effects and how source properties, such as density, seismic velocity and depth of burial, affect the excitation of phases such as Pn, Pg, Sn and Lg.

The objective of this research is to study the path effects and develop crustal models which will accurately predict regional phases. We have completed the calibration and regionalization of crustal structure for China and Indoburma. It is particularly important to relate blockage of Lg and Pg to geologic processes. Further, certain tectonic environments tend to transmit Pg efficiently in comparison to Pn.

SUMMARY

Regional phases Pg and Lg show a very strong dependence on travel path. In terms of rays, it is possible to think of Pg and Lg as S or P waves trapped in a crustal waveguide. Although scattering is apparently a very strong excitation mechanism (in the case of explosions, the departure from plane layered structure is thought to contribute significantly to the generation of Lg), the "continuity" of the waveguide is extremely important to the efficiency of Pg and Lg propagation. Kennett et al. (1985) suggest that Lg may actually be blocked by certain geologic structures such as grabens or mountain ranges due to velocity structure which departs from horizontal stratification. This is largely due to seismic energy being transferred between crustal and mantle propagation (Lg to Sn or Pg to Pn) or back reflection of the energy to reduce the amplitude. Both Lg and Pg show considerable promise as yield predictors, but the path effects must be calibrated.

In Eurasia a number of investigators have noted path irregularities for Lg. Ruzaiкин et al. (1977) noted that the Tibetan Plateau was inefficient in terms of propagating Lg. Bennett et al. (1989) and Baumgardt (1984) also show that the northern Caspian Sea is a barrier to Lg, and suggest that crustal thinning may be the cause. We have studied Pn and Pg in western China and Tibet and found that Pg blockage correlates with rapid changes in crustal thickness. In an effort to "map" the blockage effects, we have investigated the crustal thickness in Eurasia.

We have used the procedure of Wallace (1986) to invert the long-period regional distance body waves to determine crustal thickness and upper mantle velocity in Eurasia. Our observations consist of the long-period P_{nl} waveforms recorded at WWSSN stations. A total of 78 earthquakes with known source parameters in the Hindu Kush, Tibet, southwest China and Burma, which were recorded at one or more WWSSN stations at regional distances were used as a data base. This provided us with a total of 130 regional distance paths. Figure 1 shows the location of the 78 sources along with the 130 paths superimposed on the smoothed topography of the collision zone (contour interval is 1 km). Individual P_{nl} waveforms were inverted for the crustal thickness that the long-period energy sampled along the entire path. The corresponding upper mantle Pn velocity was then determined using the absolute travel time.

The study area was divided into a set of regionalized blocks. The blocks were partitioned on the basis of topography and geology. The size of the blocks was limited primarily by the path coverage. Figure 2 shows the regionalized block model superimposed on the smoothed topography. Figure 3 shows the path coverage through the blocks. The five disperse paths in Block 1 traverse some fairly high topography in western Pakistan, but also cover some lower elevation regions of the southern USSR and eastern Iran. Block 2 covers portions of the Tien Shan and Hindu Kush-Pamir. Blocks 4, 6, and 9 encompass the western Karakoram, central Tibet and eastern Tibet regions, respectively. Blocks 5, 7 and 10 cover the transition zone from low to high topography, or the Himalayan mountain front. Portions of northern and eastern India are within blocks 3 and 8, and block 11 includes the Indoburma ranges and northern Burma Arc. The Yunnan Grabens and Panxi Rift regions are within blocks 12 and 13, and block 14 includes southern China.

The inversion results for the regionalized block models are shown in figures 4 and 5. The standard deviation is a formal estimate from the model variance covariance matrix after the weighted least squares inversion. The results for crustal thickness are shown in Figure 4. Blocks 2 and 4 which include the Hindu Kush, Pamir, and Karakoram regions, have crustal thicknesses which varie from 63-67 km. Many workers have noted thick crust in this region. Roecker (1982) determined that the Moho was at 70 ± 5 km beneath the Pamir-Hindu Kush regions. Brandon and Romanowicz (1986), using pure path phase velocity measurements, estimated a 70-km-thick crust beneath the Hindu Kush, and Karakoram. Gravity data suggest a thick crust of 70 km beneath the Karakoram and around 66 km beneath the Hindu Kush (Mishra, 1981). There appears to be considerable Moho topography between the Karakoram and Hindu Kush (Mishra, 1981; Finetti et al., 1979) where the Moho upwarps to shallower levels of 58 km. It must be remembered that the long-period regional distance (P_n) energy essentially "averages" the structure along the travel path. Although crustal thicknesses may in places exceed 65 km beneath the Karakoram and Pamir-Hindu Kush, the thickness values obtained for blocks 2 and 4 (67, and 63 km) are a reasonable average for the region.

The thick crust for blocks 6 and 9 (central and eastern Tibet) are in agreement with results from numerous authors (Gupta and Narin, 1967; Bird and Toksöz, 1977; Chun and Yoshi, 1977; Patton, 1980; Chen and Molnar, 1981) of a 65- to 72-km-thick crust. Blocks 5, 7 and 10 include portions of the Himalayan mountain front, up to the edge of the Tibetan plateau and have thicknesses that range from 43-49 km. Kono (1974) examined the Bouguer gravity in eastern Nepal and found that the crust under the Himalayas is much thinner than would be expected if the range was in isostatic compensation (see also Lyon-Caen and Molnar, 1984; Karner and Watts, 1983 for more information on gravity in the Himalaya). The model of Kono (1974) suggests that a smooth inclined north dipping Moho exists beneath the Himalayas. The value of crustal thicknesses for blocks 5, 7, and 10 are perhaps representative of the average thickness along the inclined Moho beneath the high topography of the Himalayas. Wide angle reflection work by Hirn et al. (1984b), however, does not support a smooth incline of the lithosphere beneath the Himalayas but rather is consistent with a 45-55 km deep, relatively flat, Moho underneath the ranges. This Moho takes a 15 km step just to the north of the High Himalayas. The crustal thickness values for blocks 3 and 8 are in agreement with other thicknesses observed for northern India and Pakistan (Brune and Singh, 1986; Zong-Ji, 1987).

Block 11 corresponds to the location of the Indoburman ranges, the eastern extent of the collision and mountain-building zone. Thickness values in the region just outside of block 11 to the east are around 30 km. The northern Indoburma reach elevations as high as 3 km. However, given the low average smoothed topography in this region, the thick crust for this block (48 km) may indicate that the Indoburman ranges are overcompensated. Le Dain et al. (1984) noted the large negative gravity anomaly over the Indoburman ranges (Verma et al., 1976; Warsi and Molnar, 1977) and suggested that the negative buoyancy of the subducting slab may be a mechanism that keeps the region out of isostatic balance. Other estimates of crustal thickness beneath the Indoburman ranges, inferred from gravity data, range from 35-45 km (Zhang and Zang, 1986). Moho depths computed from gravity also indicate a 10 kilometer deep root beneath the Indoburman ranges with total depths extending to 46 kilometers (Zong-Ji, 1987). The results from this study indicate a root around 13-18 km deep beneath the Indoburman ranges. The thickness values for blocks 12, 13, and 14 are all in agreement with crustal thicknesses computed from gravity and seismics (Zong-Ji, 1987).

The inversion results for upper mantle P_n velocities are shown in Figure 5. P_n velocities in northern India range between 8.1 and 8.2 km/s. These values are consistent with upper mantle

velocities in old continental lithosphere. The most interesting result shown in Figure 5 is the high Pn velocity beneath the Tibetan Plateau, Karakoram and Pamir-Hindu Kush (Blocks 4, 6, and 9, respectively). High Pn velocities beneath the Tibetan Plateau, Karakoram and Pamir-Hindu Kush have been noted by other workers (Menke and Jacob, 1976; Barazangi and Ni, 1982; Hirn et al., 1984a). Moreover, high shear wave velocities beneath the Plateau have been detected from surface wave dispersion studies (Chen and Molnar, 1981; Romanowicz, 1982; Jobert et al., 1985). Barazangi and Ni (1982) found high Pn and Sn velocity values of 8.43 and 4.73 km/s respectively beneath the Tibetan plateau. Hirn et al. (1984a) observed very high Pn velocities of 8.7 km/s on a reversed refraction profile in southern Tibet between the high Himalayas and the Yarlung Zangbo Jiang suture. They attributed the anomalously high velocity to anisotropy in an E-W direction in the upper most mantle.

Upper mantle velocities in blocks 12 and 13 are lower than most of the adjacent blocks. Blocks 12 and 13 include regions such as the Yunnan Grabens and Panxi Rift zones where both active strike-slip and normal faulting are prevalent. Low upper mantle velocities of 7.6-7.9 km/s have also been detected beneath the Yunnan region by Zong-Ji (1987). The normal faulting in Yunnan is a feature of pull-apart basins produced by right stepping right-lateral strike-slip movement (Guangxun et al., 1986; Holt et al., 1989). A Cenozoic back-arc setting with associated volcanics, along with numerous present-day hydrothermal springs (Zhijie and Guoying, 1985) is consistent with the low upper mantle velocities in the Yunnan, China, and eastern Burma regions.

The high Pn velocity obtained for block 11 probably reflects the presence of Indian lithosphere beneath the Indoburman ranges. This Indian lithosphere (block 11) is cold and has high velocities in contrast to the Asian lithosphere to the east. Block 14 (southern China) is beyond the significant influence of subduction, and collision, and thus Pn velocities are higher in comparison to block 13 to the west.

CONCLUSIONS AND RECOMMENDATIONS

The crustal thickness has a strong effect on the character of short-period regional phases. With the improved models developed for crustal and upper mantle structure presented here, short-period synthetics need to be computed and compared to the observations. Preliminary comparisons with our structure map and Ruzaijin et al.'s (1977) blockage map indicates that change in crustal thickness is not the only contributing factor to blockage.

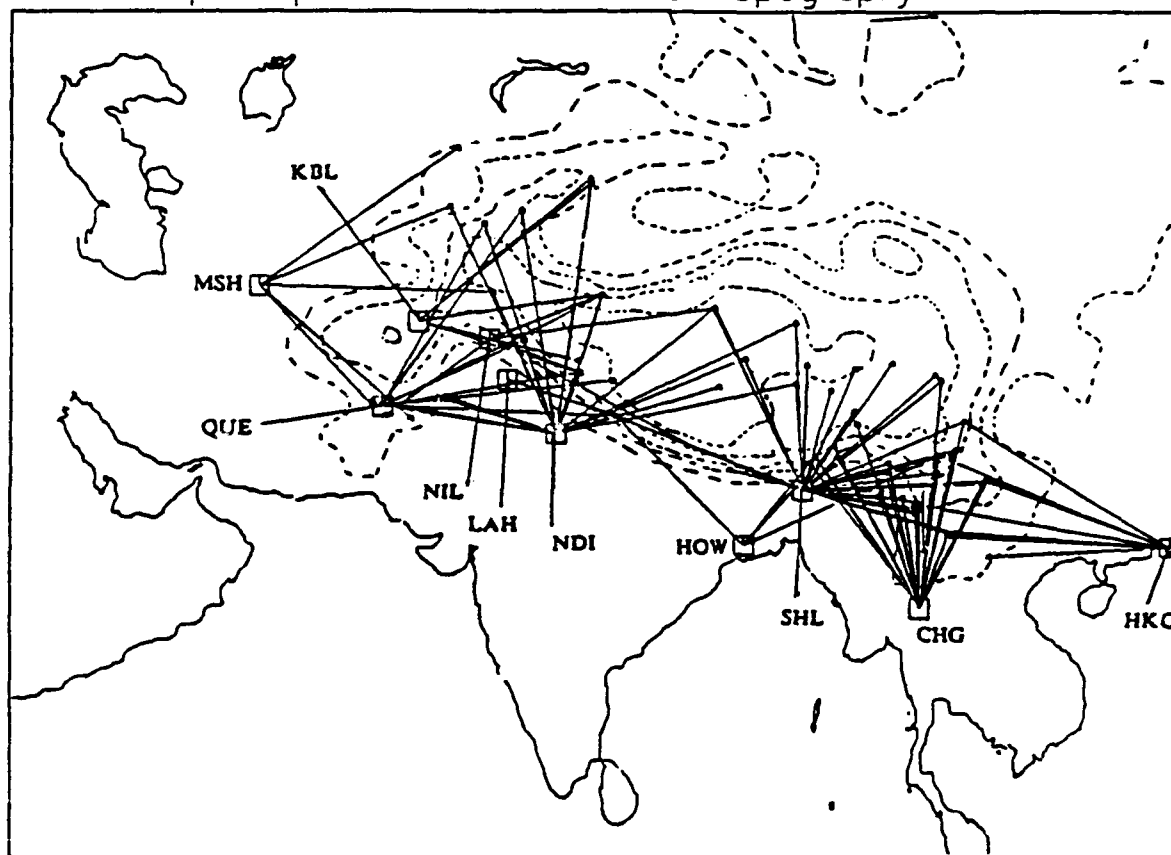
In the future we will utilize the new digital stations in the Soviet Union to refine the crustal regionalization. In particular, we need to concentrate on Lg efficiency.

REFERENCES

- Barazangi, M., and J. Ni, Velocities and propagation characteristics of Pn and Sn beneath the Himalayan arc and Tibetan Plateau: Possible evidence for underthrusting of Indian continental lithosphere beneath Tibet, *Geology*, 10, 179-185, 1982.
- Bird, P., Initiation of Intra-continental subduction in the Himalaya, *J. Geophys. Res.*, 83, 4975-4987, 1978.
- Bird, P., and M.N. Toksoz, Strong attenuation of Rayleigh waves in Tibet, *Nature*, 266, 161-163, 1977.
- Brandon, C., and B. Romanowicz, A "No-Lid" zone in the central Chang-Thang platform of Tibet: evidence from pure path phase velocity measurements of long-period Rayleigh waves, *J. Geophys. Res.*, 91, 6547-6564, 1986.
- Brune, J.N., and D.D. Singh, Continent-like crustal thickness beneath the Bay of Bengal sediments, *Bull. Seis. Soc. Am.*, 76, 191-203, 1986.
- Chen, W.P., and P. Molnar, Short-period Rayleigh wave dispersion across the Tibetan Plateau, *Bull. Seis. Soc. Am.*, 65, 1051-1057, 1975.
- Chun, K. Y., and T. Yoshi, Crustal structure of the Tibetan Plateau: A surface-wave analysis, *Bull. Seis. Soc. Am.*, 67, 735-750, 1977.
- Finetti, I., F. Giorgetti, and G. Poretti, The Pakistani segment of the DSS profile Nanga Parbat-Karakul, *Boll. Geof. Teor. App.*, 21, 159-171, 1979.

- Guangxun, L., L. Fangquan, L. Guirong, Active tectonics and state of stress in seismic region of north-west Yunnan Province, China, *Seismology and Geology*, 8, 12-14, 1986.
- Gupta, H.K., and H. Narain, Crustal structure in the Himalayan and Tibet Plateau region from surface-wave dispersion, *Bull. Seis. Soc. Am.*, 57, 235-248.
- Hirn, A.G., G. Jobert, G. Wittlinger, Z. Xu and G. Yuan, Main features of the upper lithosphere in the unit between the high Himalayas and the Yarlung Tsangbo Jiang suture, *Ann. Geophys.*, 2, 113-118, 1984a.
- Hirn, A., J.C. Lepine, G. Jobert, M. Sapin, G. Wittlinger, X.Z. Xin, G. E. Yuan, W.X. Jing, T.J. Wen, X.S. Bai, M.R. Pandey and J.M. Tater, Crustal structure and variability of the Himalayan border of Tibet, *Nature*, 307, 23-25, 1984b.
- Holt, W.E., T.C. Wallace, J.F. Ni, and M. Guzman-Speziale, The active tectonics in the eastern Himalayan syntaxis and surrounding regions, in Prep., 1989.
- Jobert, N., B. Journet, G. Jobert, A. Hirn, and S. Ke Zhong, Deep structure of southern Tibet inferred from the dispersion of Rayleigh waves through a long-period seismic network, *Nature*, 313, 386-388, 1985.
- Kono, M., Gravity anomalies in east Nepal and their implications to the crustal structure of the Himalayas, *Geophys. J.*, 17, 369-403, 1974.
- LeDain, A.Y., P. Tapponnier, and P. Molnar, Active faulting and Tectonics of Burma and surrounding regions, *J. Geophys. Res.*, 89, 453-472, 1984.
- Menke, W.H., and K.H. Jacob, Seismicity Patterns in Pakistan and northwestern India associated with continental collision, *Bull. Seis. Soc. Am.*, 66, 1695-1711, 1976.
- Mishra, D.C., Crustal structure and dynamics under Himalaya and Pamir ranges, *Earth and Planetary Science Letters*, 57, 415-420, 1982.
- Patton, H., Crust and upper mantle structure of the Eurasian continent from the phase velocity measurements and Q of surface waves, *Rev. Geophys.*, 18, 605-625, 1980.
- Roecker, S.W., Velocity structure of the Pamir-Hindu Kush region: possible evidence of subducted crust, *J. Geophys. Res.*, 87, 945-959, 1982.
- Romanowicz, B. A., Constraints on the structure of the Tibet Plateau from pure path phase velocities of Love and Rayleigh waves, *J. Geophys. Res.*, 87, 6865-6883, 1982.
- Ruzaikin, A. I., I. L. Nersesor, V. I. Khalturin and P. Molnar, Propagation of Lg and lateral variations in crustal structure in Asia, *J. Geophys. Res.*, 82, 307-316, 1977.
- Verma, R.K., M. Mukhopadhyay, and M.S. Ahluwalia, Seismicity, gravity and tectonics of northeast India and northern Burma, *Bull. Seis. Soc. Amer.*, 66, 1683-1694, 1976.
- Wallace, T.C., Inversion of long-period regional body waves for crustal structure, *Geophys. Res. Lett.*, 13, 749-752, 1986.
- Warsi W.E.K., and P. Molnar, Gravity anomalies and plate tectonics in the Himalaya, *Ecologie et geologie de l'Himalaya, Colloques internationaux du C.N.R.S.*, 268, 1977.
- Zhang, J., and S. Zang, Characteristics of earthquake distribution and the mechanism of earthquakes in the boundary area between Burma, India, and China, *Acta Seismological sinica*, 8, 1986.
- Zhijie, L., and G. Guoying, Geology of the Tengchong geothermal field and surrounding area, West Yunnan, China,
- Zong-Ji, C., Geodynamics and tectonic evolution of the Panxi rift, *Tectonophysics*, 133, 287-304, 1987.

Paths Superimposed On Smoothed Topography



 WSSN Station
 Earthquake Source

Figure 1: Eurasian region of study. Smooth topography (1 km contour) is shown with dashed line. Earthquake epicenters (stars), stations (boxes) and ray paths used in the study are also shown.

Regionalized Block Model With Smoothed Topography

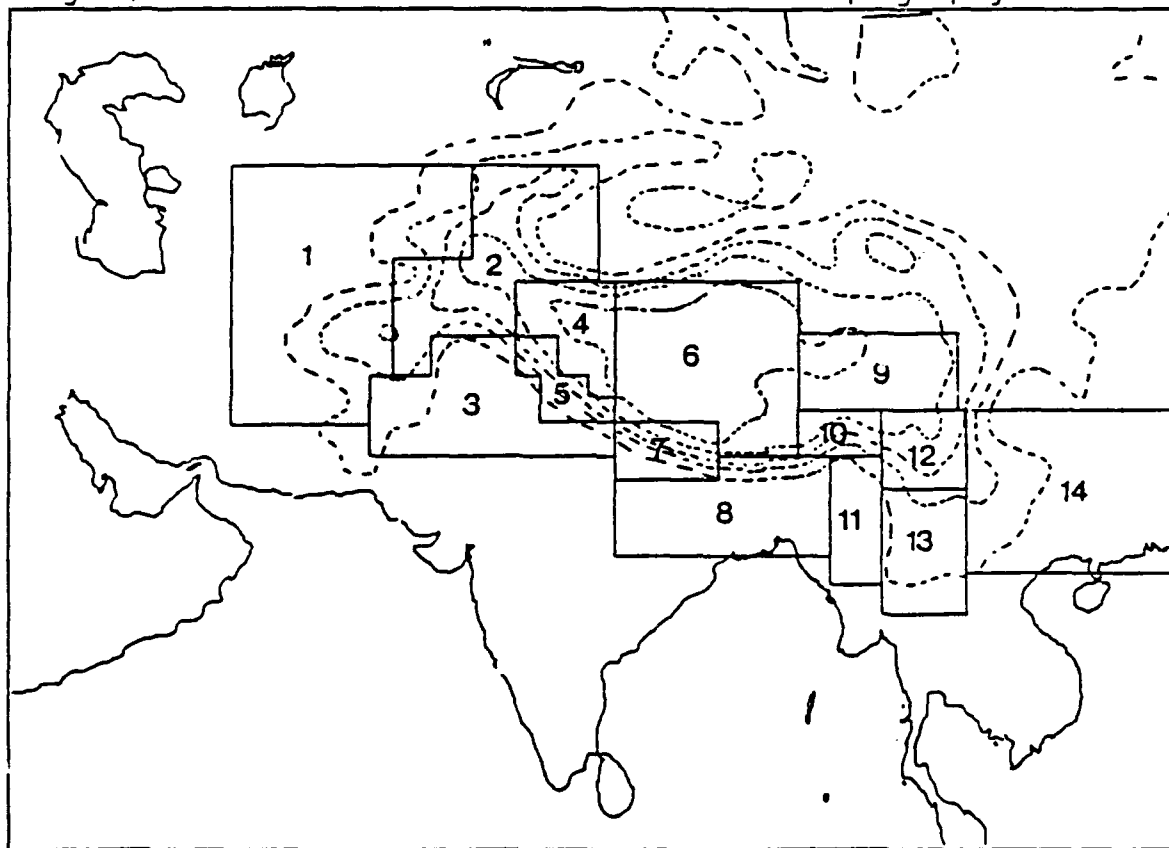


Figure 2: Regionalized block model. Numbers on block are referred to in text.

Regionalized Block Model with Path Coverage

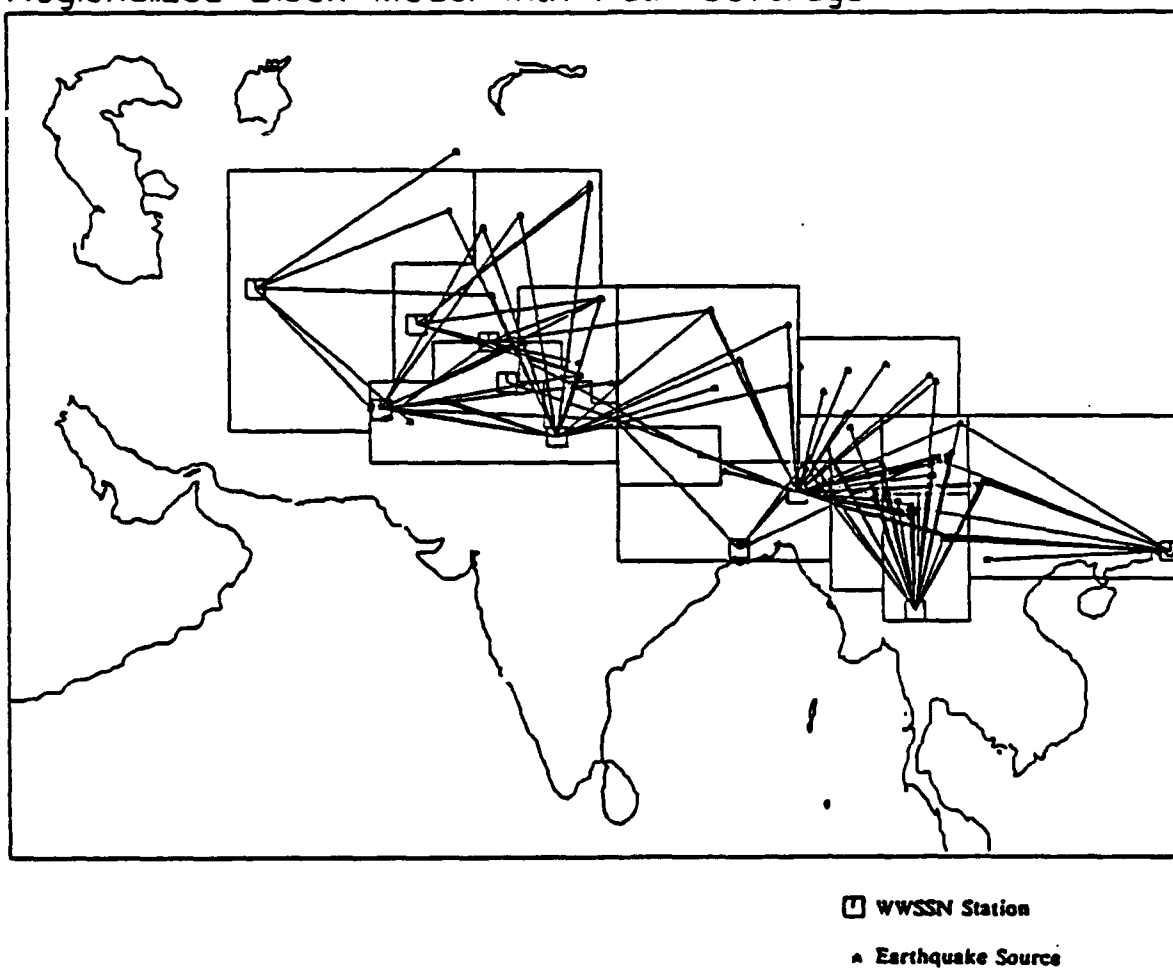


Figure 3: Path coverage of the block model.

Crustal Thickness

Regionalized Block Model

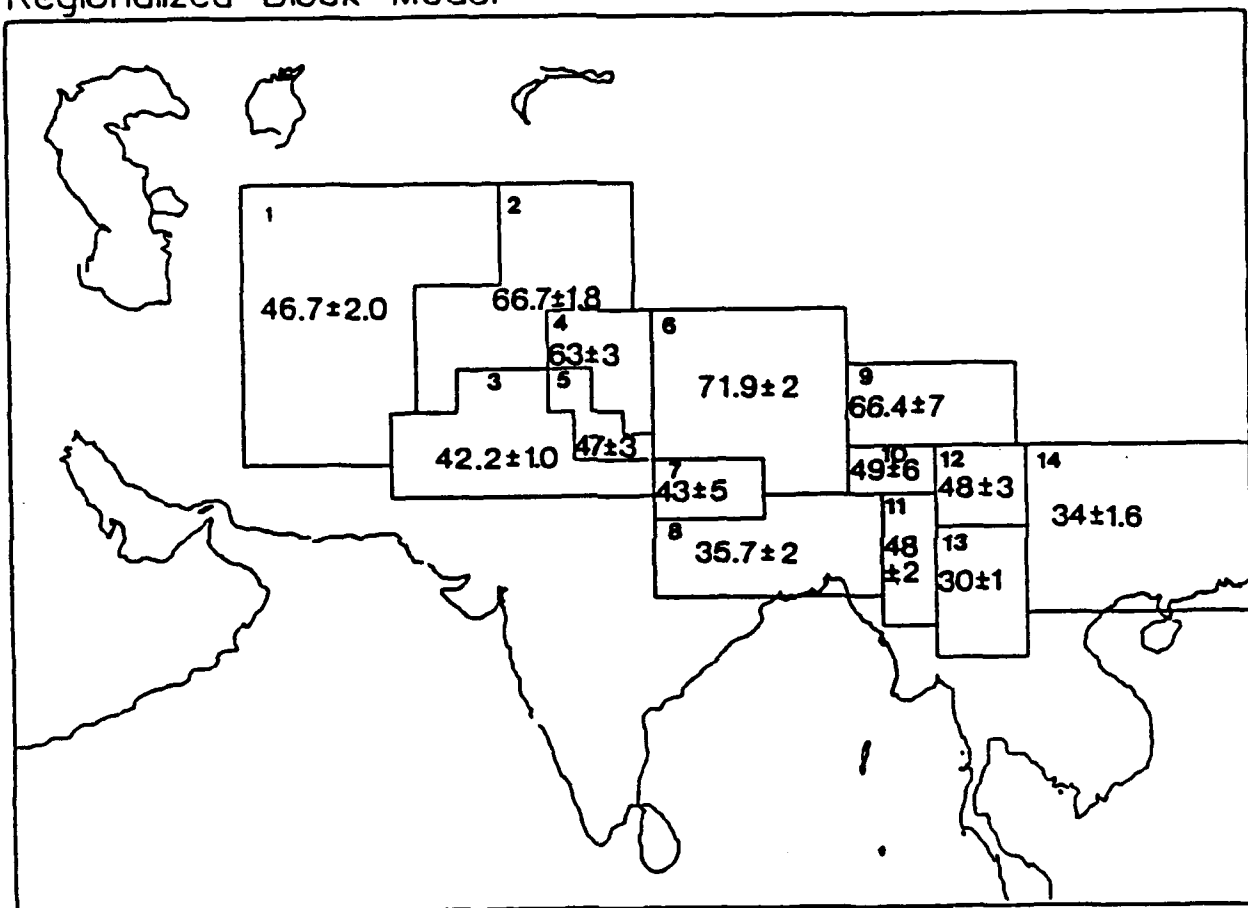


Figure 4: Model parameter estimates for crustal thickness in the regionalized model. Standard deviation is a formal estimate from model variance-covariance matrix.

Upper Mantle (Pn) Velocity

Regionalized Block Model

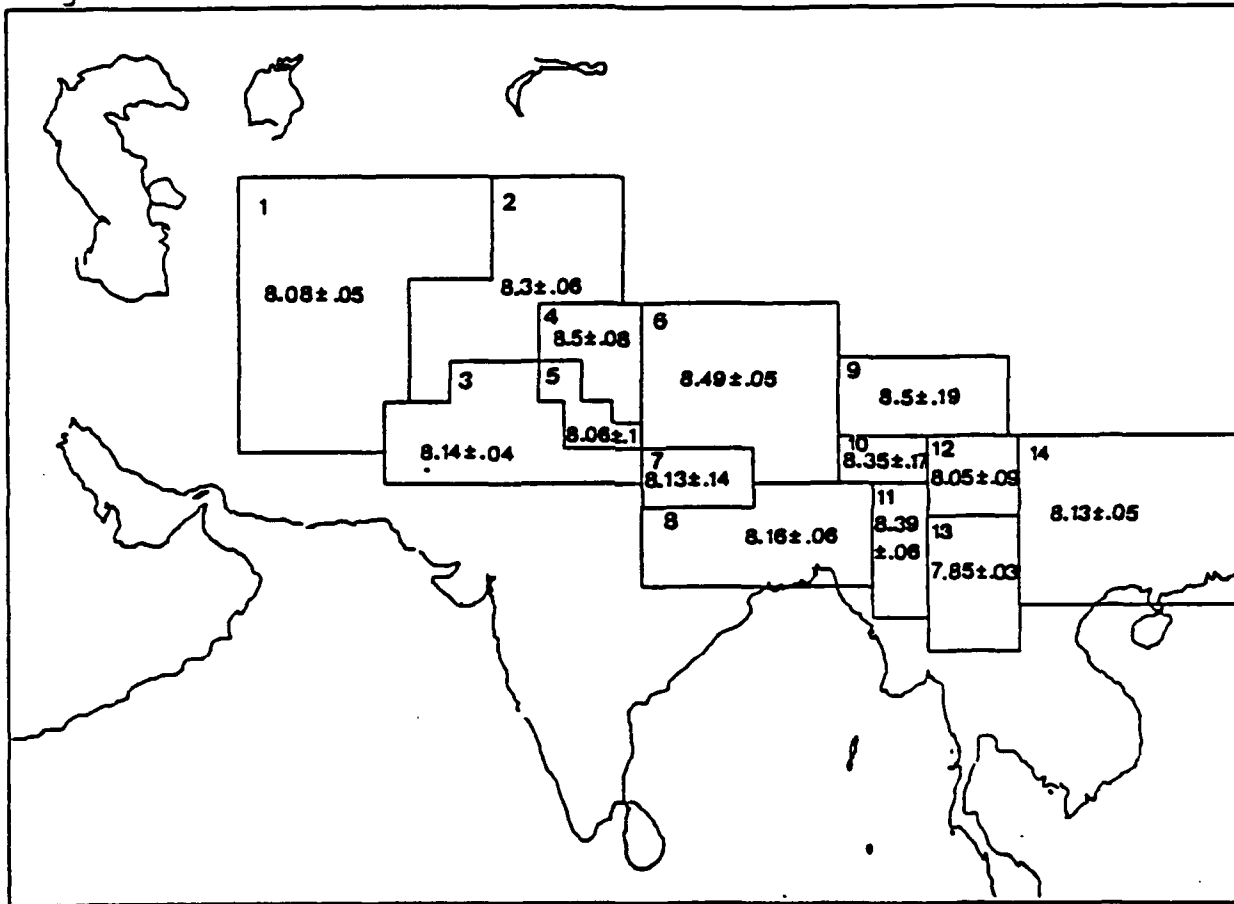


Figure 5: Model parameter estimates (Pn velocity) for the regionalized model.

HIGH-FREQUENCY REGIONAL DISCRIMINATION STUDIES USING NRDC AND CDSN SEISMIC NETWORKS

W. Winston Chan , Robert K. Cessaro, and Richard Baumstark
Teledyne Geotech Alexandria Laboratories
314 Montgomery Street,
Alexandria, VA 22314

Contract Number F19628-88C-0051

OBJECTIVE

To improve detection and the ability to discriminate between quarry blasts, earthquakes, and nuclear explosions, and to provide better seismic yield estimates through further understanding of high frequency regional seismic signals. Digital seismic data from the Natural Resources Defense Council network (NRDC) and China Digital Seismic Network (CDSN) are utilized to study the regional propagation of high-frequency seismic phases in Eurasia at relatively close-in distances. Evaluation will be made on the capability of these networks in the detection and discrimination of quarry blasts, earthquakes, and nuclear explosions using regional phases consisting of P_n , L_g , S_n , and P_g . The excitation and propagation parameters of the regional crustal phases will be quantified for both the tectonic and stable regions of Eurasia. Geological assessments of the varying geology of the regions of interest will be performed to better interpret the regional variations of crustal propagation characteristics.

SUMMARY

To further exploit the capability of regional seismic phases, P_n , P_g , S_n , and L_g , in discrimination problems, it is important to understand fully the excitation and propagation of these phases across a wide variation of tectonic and geological regions for quarry blasts, earthquakes and nuclear explosions. Discriminants and yield estimation corrections may not be applied uniformly without regional constraints, owing to the effect of varying site geologies and propagation paths. In addition to reflecting the source characteristics, the discriminants may also be affected by regional variations in attenuation properties and crustal structure between each seismic source and the various receivers. The path attenuation effects are crucial in seismic yield estimation, since the amplitudes are heavily dependent on the efficiency of the propagation of the high-frequency regional phases.

Propagation of regional phases generated by seismic events has been widely studied to measure their attenuation properties for corrections to yield estimates. In particular, L_g is most commonly used to investigate various regions of the world due to its efficient propagation at regional distances (*e.g.*, Nuttli, 1973, 1980; Gupta and Burnett, 1980; Hasegawa, 1985; Campillo *et al.*, 1985). In most of these studies, the attenuation effects have been estimated by assuming some preferred forms of the geometrical spreading-dispersion effect and fitting $Q(f)$. In recent studies by Nuttli (1986a,b), very different attenuation corrections are required for estimating the yields of NTS and East Kazakh events from regional data.

In general, there is little agreement among the various investigators as to the value of the relative amplitudes and frequency contents of the crustal arrivals for discriminating between earthquakes, quarry blasts and nuclear explosions. The dominant phase velocities of *Lg* have been found to depend on the source depth (Barley, 1979), and *Lg* excitation is observed to decrease with increasing source depth compared to *P* (Noponen and Burnett, 1980). Murphy and Bennett (1982) claim that at UBO explosion spectra have less high frequency content than earthquakes. Recently, the implications of high-frequency regional propagation characteristics of various crustal phases with regards to detectability and discrimination capability for decoupled nuclear explosions by a hypothetical internal network in the USSR were discussed by Evernden *et al.* (1986). Their study was based on certain assumptions of the frequency dependence of *Q* and assumptions of the source spectral slope, and it may therefore be limited in bandwidth and geographical coverage. A broadband analysis of regional phases for various tectonic and stable regions is therefore necessary to resolve the issues raised in the Evernden *et al.* (1986) study.

The deployment of the NRDC and CDSN networks have made it possible to study the propagation of regional phases in Eurasia at distances of less than 15° (Fig. 1). The proximity of these stations to the test sites in the Soviet Union and China has provided data with well recorded *Pn*, *Sn*, *Lg*, and *Pg* at regional distances. These data constitute an excellent database for research towards understanding the underlying properties governing the excitation and propagation of seismic waves in the stable and tectonic regions of Eurasia, and so these two networks will be the principal source of data analyzed in this project. The database contains local quarry blasts which are identified with the aid of satellite imagery (Thurber *et al.*, 1989). An analysis in both the frequency and time domains of these sources will lead to effective discriminants as well as better understanding of their excitations.

Seismic event discrimination based on the spectral signatures have been applied to regional data recorded at network stations of the Natural Resource Defense Council (NRDC) and the Chinese Digital Seismic Network (CDSN) during 1987. The data base consists of 190 quarry blasts, earthquakes, and explosions recorded at the NRDC stations and 73 events recorded at the station WMQ of the CDSN with paths traversing the East Kazakh and Tien Shan regions. In this phase of the study, we concentrate on the analysis of data from the NRDC network. Various regional phases, *Pn*, *Pg*, *Sn*, and *Lg*, are emphasized in the analysis. Data are retrieved from the vertical component of the short-period channel of the NRDC stations. In order to study the frequency distribution of the various phases, we have performed a band-pass filtering of the data. Due to the high sampling rate of the NRDC stations (250 samples per second), we have used an infinite impulse response 3-pole butterworth filter in order to be able to band-pass the entire waveform. The filtered short-period data indicate that there are *Pg*-phase signals above the noise level at a pass-band of as high as 32-64 Hz while *Lg*-phase signals are observed up to the 8-16 Hz pass-band (Fig. 2a) for quarry blasts and much lower frequency energy for earthquakes (Fig. 2b).

Guided by the band-pass filtering analysis which indicates the broad-band characteristics of the seismic signals, we are able to design the frequency bands to be used in performing a spectral ratio discrimination study in the E. Kazakh/Tien Shan region. For the NRDC stations, we are able to examine spectral ratios between widely spaced frequency bands of 1.6-2.5 Hz and 16.0-25.0 Hz using the short-period data. First order spectral ratio vs distance relationships are obtained for each of the phases by performing linear fits to the

EURASIA

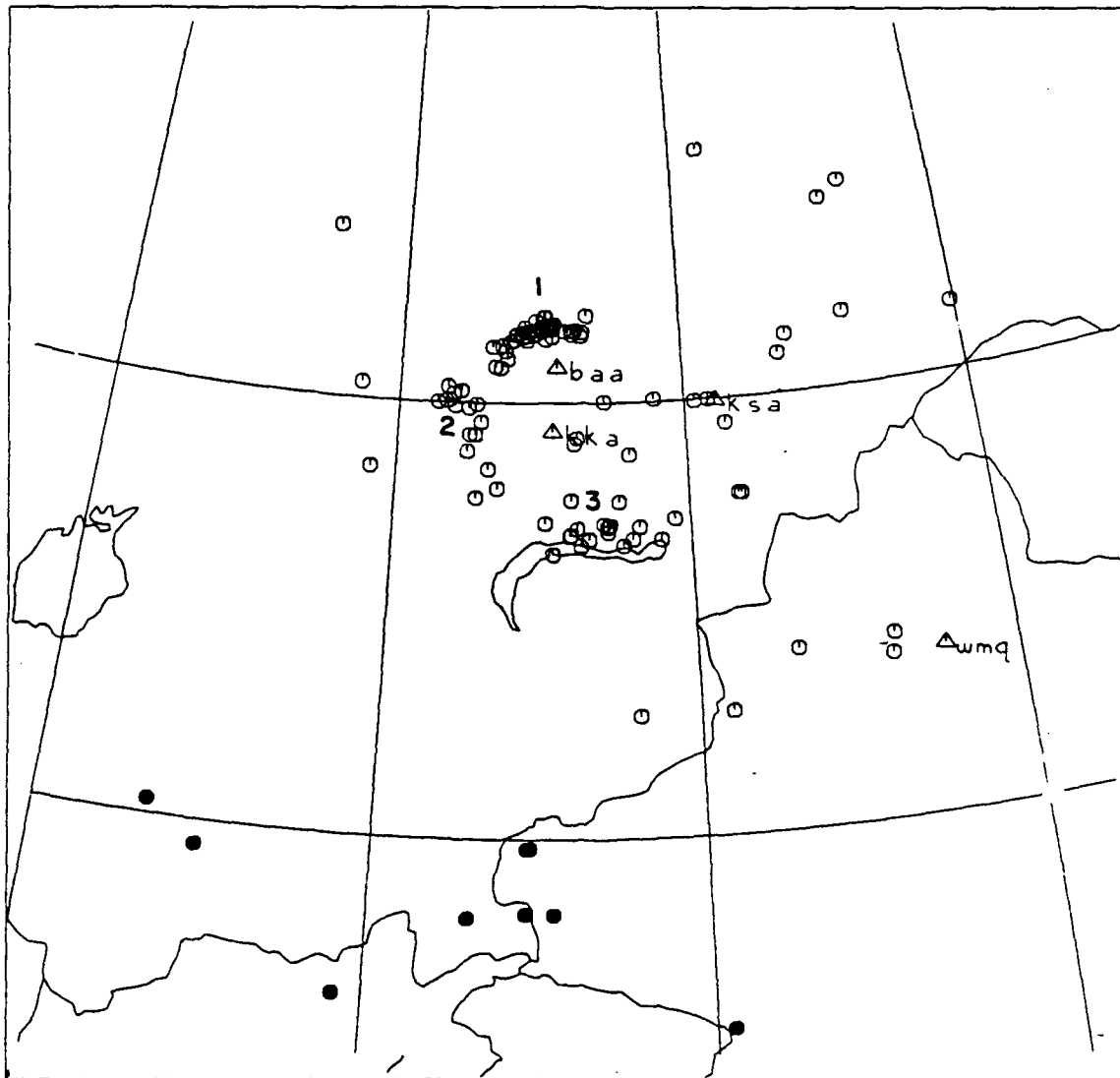


Fig. 1. Map indicating the locations of the seismic events in the E. Kazakh region. The solid circles denote events that are likely to be earthquakes. The groups of events indicated by 1, 2, and 3 are likely to be mine blasts.

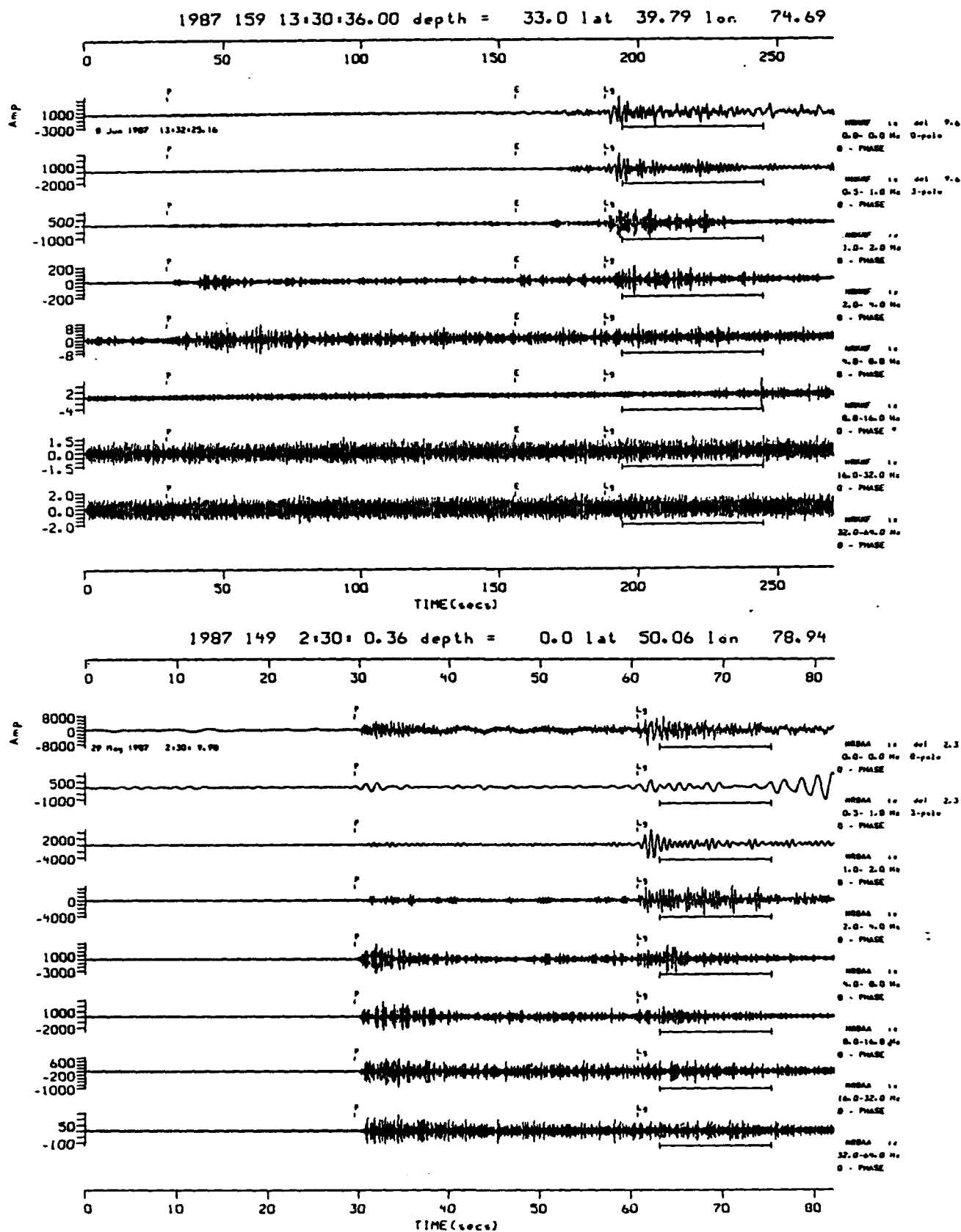


Fig. 2. Bandpassed filtering of a presumed earthquake (top) and explosion (bottom) in the E. Kazakh region indicating the frequency content of each. The explosive P-wave is rich in high frequency energy even up to the 32.0-64.0 Hz passband.

log of the spectral ratios as a function of distance as indicated in Fig. 3 (Taylor *et al.*, 1988). The scatter in the spectral ratios is reduced by normalizing the earthquake and explosion data by distance. The m_{bLg} magnitudes for the events are estimated using Nuttli (1986a) magnitude relationship for the Shagan region. The attenuation values are obtained from Bennett *et al.* (1988). As an example, the preliminary results are presented in Fig. 4 where the spectral ratios of Lg and Pg between 1.6-2.5 Hz and 16.0-25.0 Hz are plotted against the m_{bLg} magnitudes for station KKL. Even though there are indications that the earthquakes might have a lower amplitude ratios than explosions, further analysis of the large number of events of unknown source is required in order to access the applicability of the spectral discriminant in the E. Kazakh region.

CONCLUSIONS AND RECOMMENDATIONS

The preliminary results presented in this study indicate that there may be signs that the spectral ratio method can discriminate between earthquakes and explosions, the main obstacle remains to be the lack of ground truth information on the classification of the seismic events in the test case. In order to evaluate the applicability of the spectral ratio method to discriminate between seismic events in the East Kazakh region, better constraints are required on the identification of the source of the seismic event as input to the experiment. Expanding the data base to include data from the CDSN stations will provide significant constraints to this study.

The narrow bandpass filtering scheme provides a full characterization of each seismic signal in the time and frequency domains. If the same event is observed at several stations, then we shall have some descriptions of the distance dependence of the wavetrain as well. The data characterizing the events will consist of descriptions of the absolute and relative amplitudes of the arrivals in various frequency bands and their time domain envelopes (including that of their codas as well). With the collected data, we shall also compile information that may be useful for providing physical explanations for the empirical results. Such information will include, but not be limited to, source depths, types of blasts, path characterization, and source mechanisms. Additional emphasis will be placed upon paths that may have anomalously efficient propagation of the regional phases.

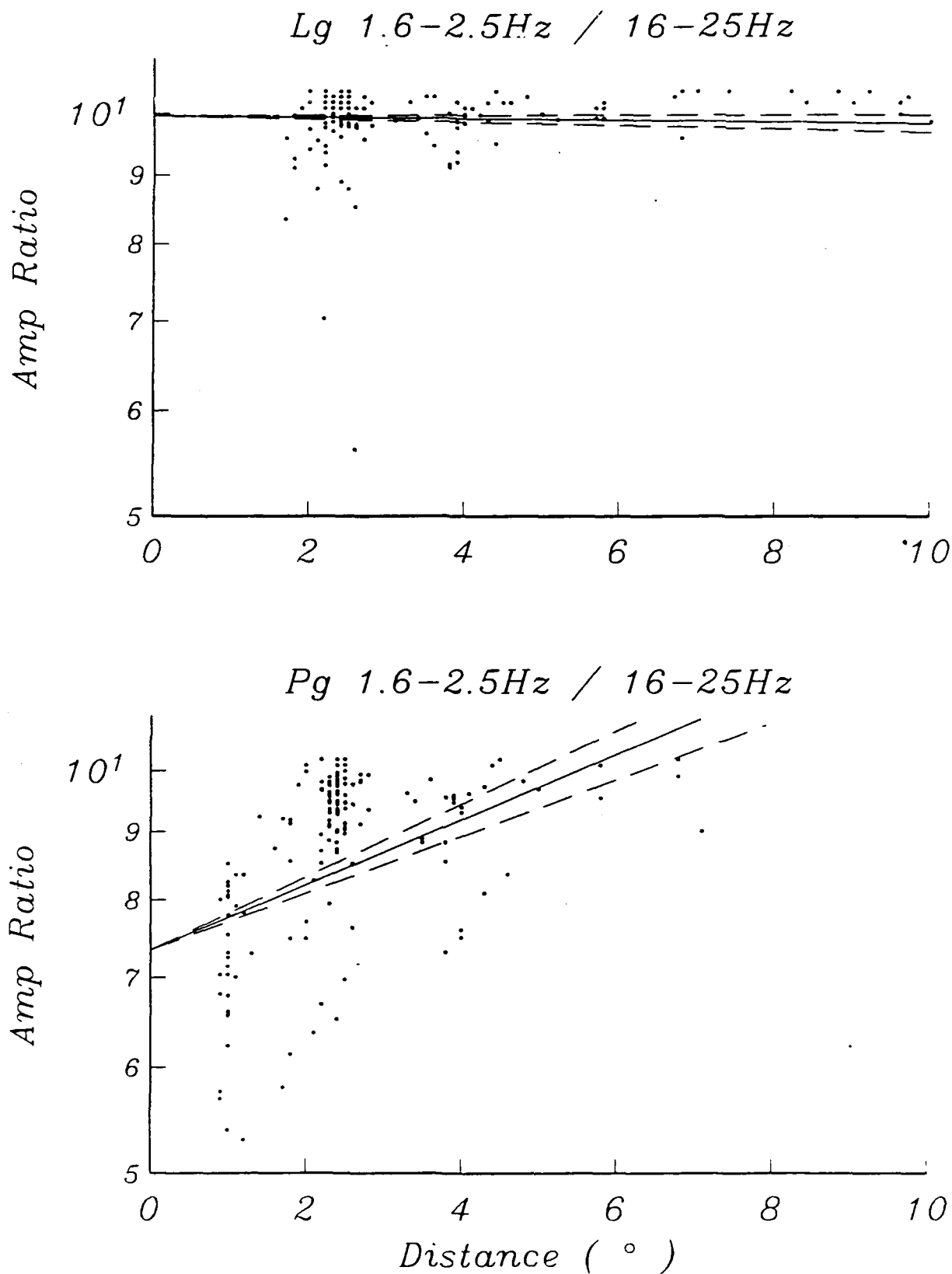


Fig. 3. Distance-amplitude ratio relationship for Pg and Lg phase. The least squares-fitted slope is used as a first order distance correction to the spectral ratios for each individual phase.

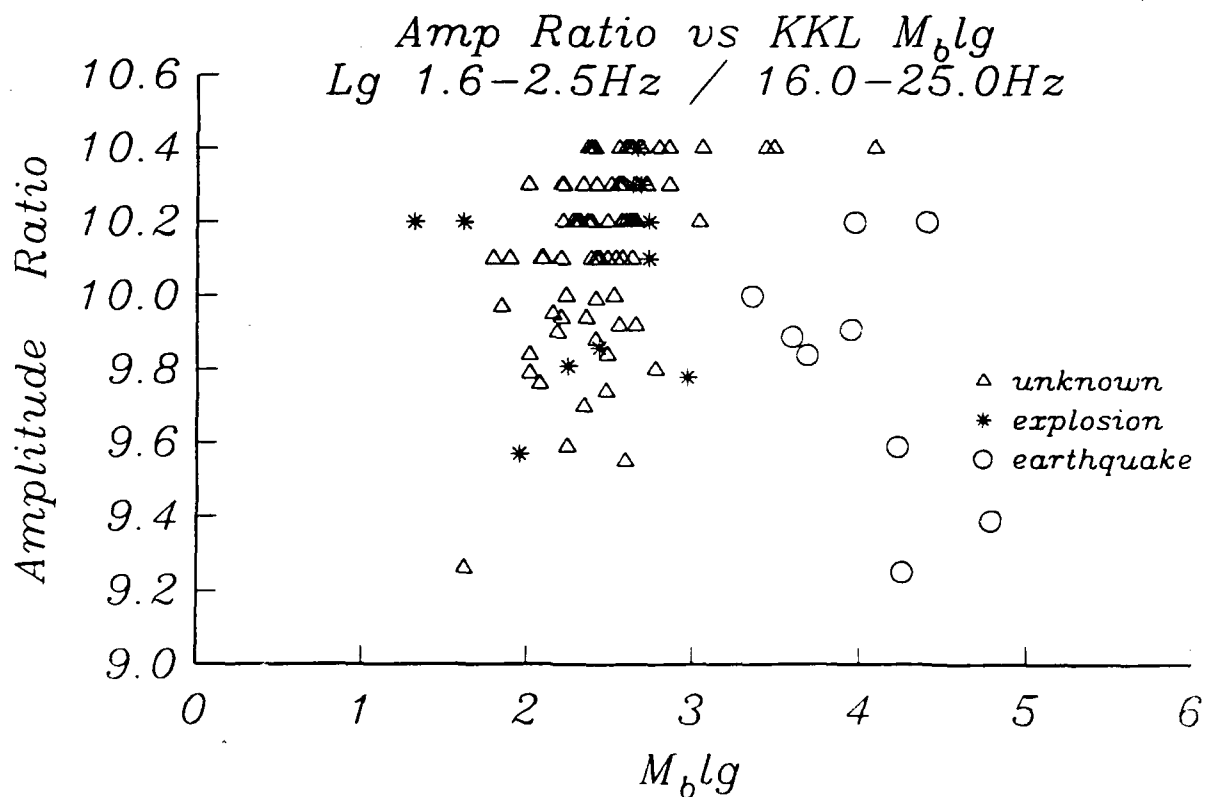
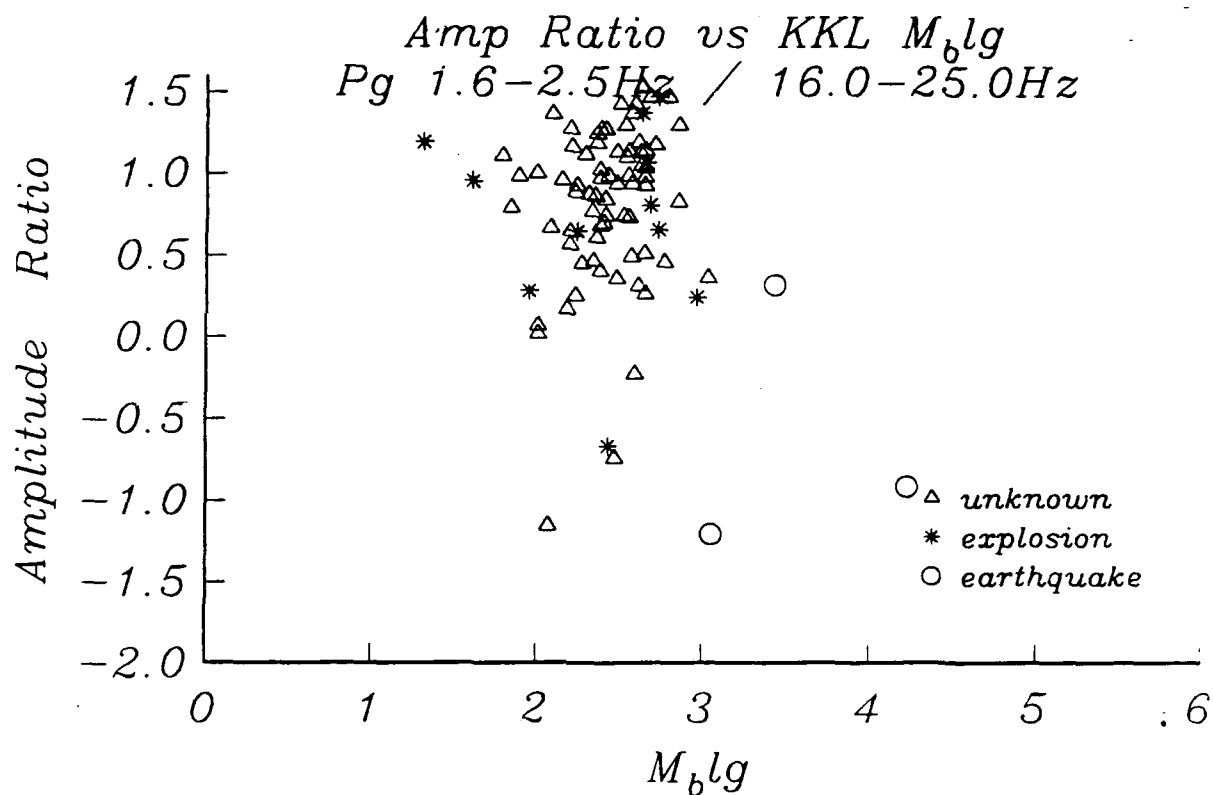


Fig. 4. Pg and Lg amplitude ratios (1.6-2.5/16.0-25.0) plotted against m_{bLg} for station KKL. The large number of events of unknown source prevents a conclusion to be drawn on the applicability of the spectral discrimination method in E. Kazakh.

REFERENCES

- Barley, B. J. (1979). On the use of seismometer arrays to locate sources of higher mode Rayleigh waves, AWRE Report No. 054/78, Atomic Weapons Research Establishment, Aldermaston, England.
- Bennett, T. J., B. W. Barker, and J. R. Murphy (1988). Regional phases from East Kazakh seismic events, *Seism. Res. Letts.*, **59**, 151.
- Campillo, M., J. Plantet, and M. Bouchon, (1985). Frequency dependent attenuation in the crust beneath central France from Lg waves: data analysis and numerical modeling, *Bull. Seism. Soc. Am.*, **75**, 1395-1411.
- Evernden, J. F., C. B. Archambeau, and E. Cranswick, (1986). An evaluation of seismic decoupling and underground nuclear test monitoring using high-frequency seismic data, *Rev. Geophys.*, **24**, 143-215.
- Goncz, J. H., W. C. Dean, Z. A. Der, A. C. Lees, K. L. McLaughlin, T. W. McElfresh and M. E. Marshall (1987). Propagation and excitation of Lg, Sn, and P-Pn waves from Eastern United States earthquakes by regression analysis of RSTN data, TGAL-86-7, Teledyne Geotech, Alexandria, Virginia.
- Gupta, I. N. and J. A. Burnetti (1980), Amplitude-distance relationships for regional phases in shield regions, *SDAC-TR-80-7a*, Teledyne Geotech, Alexandria, Virginia.
- Gupta, I. N., K. L. McLaughlin, and R. A. Wagner (1987). Attenuation of ground motion in the eastern North America, report for the Electric Power Research Institute, Teledyne Geotech, Alexandria, Virginia.
- Hasegawa, H. S. (1985). Attenuation of Lg waves in the Canadian shield, *Bull. Seism. Soc. Am.*, **75**, 1569-1582.
- Mechler, P., M. Nicolas, A. Chaouch, and B. Massinon (1980). Seismic crustal and subcrustal phases propagation, Final report, Laboratoire de Geophysique Appliquee, Universite Pierre et Marie Curie, Paris, France.
- Murphy, J. R., and T. J. Bennett (1982). A discrimination analysis of short-period regional seismic data recorded at Tonto Forest Observatory, *Bull. Seism. Soc. Am.*, **75**, 1077-1086.
- Noponen, I. and J. Burnetti (1980). Alaskan regional data analysis. In "Studies of Seismic Wave Characteristics at Regional Distances", *AL-80-1*, Teledyne Geotech, Alexandria, Virginia.
- Nuttli, O. W. (1973). Seismic wave attenuation and magnitude relations for eastern North America, *J. Geophys. Res.*, **78**, 876-885.
- Nuttli, O. W. (1980). The excitation and attenuation of seismic crustal phases in Iran, *Bull. Seism. Soc. Am.*, **70**, 469-485.
- Nuttli, O. W. (1986a). Lg magnitudes of selected East Kazakhstan underground explosions, *Bull. Seism. Soc. Am.*, **76**, 1241-1252.
- Nuttli, O. W. (1986b). Yield estimates of Nevada Test Site explosions obtained from seismic Lg waves, *J. Geophys. Res.*, **91**, 2137-2152.
- Taylor, S. R., N. W. Sherman, and M. D. Denny (1988). Spectral discrimination between NTS explosions and western United States earthquakes at regional distances, *Bull. Seism. Soc. Am.*, **78**, 1563-1579.

A STUDY OF TELESEISMIC P AND P CODA FROM U.S. AND SOVIET NUCLEAR EXPLOSIONS

I. N. Gupta, C. S. Lynnes, R. S. Jili, and R. A. Wagner
Teledyne Geotech
314 Montgomery Street
Alexandria, Virginia 22314

CONTRACT No. F19628-88-C-0051

OBJECTIVE

Study teleseismic P and P coda from U. S. and Soviet nuclear explosions. Investigate the usefulness of multichannel data for estimating yields and the presence of prominent phases in P coda due to near-source and near-receiver scattering. Examine the origin of large arrivals immediately following P and pP on records of NTS shots.

SUMMARY

Multichannel NORSAR data for 21 NTS (8 Pahute Mesa and 13 Yucca Flat) explosions (Figure 1) were used to obtain P and P coda amplitudes integrated within the frequency range of 0.5 to 3.0 Hz. The P and P coda windows are 12.8 and 25.6 sec long with the P window starting 4 sec before the first P. The spectral amplitudes, corrected for instrument response, t^* and approximate source spectrum, are obtained by following the same procedure as in our earlier study (Gupta et al., 1985a). Least-squares inversion for source and receiver terms was applied separately to P and P coda spectral amplitudes derived from all available channels. Figure 2a shows the derived source terms for P and P coda plotted versus yield, on log-log scale. When a slope of unity is forced through the data points, the standard deviation of residuals (single observation) is only 0.12 and 0.09 magnitude unit (m.u.) for P and P coda, respectively. In comparison, when spectral amplitudes from the single channel NAO are used, the standard deviation of residuals is 0.15 and 0.17 m.u. for P and P coda, respectively (Figure 2b). It seems therefore that the use of multichannel data for both P and P coda can significantly improve the yield estimates. Note that the mean P and P coda regression lines in Figure 1 are separated by 0.56 m.u. or a factor of about 3.6.

The magnitude residuals for P (i.e. source term, in log units, minus log yield) for the same 21 NTS shots are plotted in Figure 3a (after the mean value has been removed). The magnitude residuals, spread over the range 0.22 to -0.31 m.u., are either negative or small for most shots in the Pahute Mesa and northern Yucca Flat regions and positive for shots in southern Yucca Flat. It is interesting to note that Patton (1988) observed a similar pattern for magnitude residuals based on Lg. For P coda, the magnitude residuals are considerably smaller (Figure 3b) except for PORTMANTEAU which has a large negative residual, probably due to its position at the edge of Yucca Basin (Lynnes and Lay, 1988; Stead and Helmberger, 1988). The difference between P and P coda magnitude residuals (equivalent to amplitude ratio P/Pcoda in magnitude unit), shown in Figure 3c, is significantly larger for the Pahute Mesa shots than for the Yucca Flat explosions. Since P coda amplitudes are less variable than P, this means that P spectral amplitudes (within the P window) for Yucca Flat shots are generally much larger than for Pahute Mesa shots.

High-resolution frequency-wavenumber (f-k) spectra methods were applied to NORESS records of several underground nuclear explosions. The results are expressed in terms of frequency-slowness spectral estimates of the signal at specified times. We first analyzed the NORESS data for the Kazakh explosion of 16 December 1984 ($\Delta \approx 38^\circ$ and $m_b = 6.1$). Using Parzen-tapered 3.2 sec long windows, the results for windows centered on P, P + 4 sec, P + 5 sec, P + 8 sec, P + 9 sec, and P + 10 sec are

shown in Figure 4 for three different frequency passbands as indicated. The first arrival in each figure is a P wave with phase velocity of about 17 km/sec and arriving from the expected source azimuthal direction. The broadband results in Figure 4a show evidence for secondary sources of energy arriving about 4 and 8 sec after the first P from azimuthal directions approximately due east and south-west of the array. The phase velocities for both arrivals are rather low (less than 3 km/sec), suggesting them to be due to scattering of teleseismic P to S (or Rg) near the array location. Fairly similar results for the two secondary sources are observed in Figures 4b and 4c.

Results of f-k analysis applied to the Pahute Mesa shot of 24 September 1987 ($\Delta \approx 73^\circ$, $m_b \approx 5.7$) are shown in Figure 5 for three different passbands. The source azimuth for this source is quite different from that for the Kazakh shot. Results are shown for the six time windows P, P + 4.0 sec, P + 4.5 sec, P + 5.0 sec, P + 5.5 sec, and P + 6.0 sec. Since S/N on the spectra of this explosion recorded at NORESS was good only for frequencies less than about 4 Hz, results for much higher frequencies were not obtained. These three figures also provide evidence of scatterers approximately due east and south-west of the array. The derived locations of the two scatterers are also nearly the same as suggested earlier by analysis of the Kazakh shot data.

Theoretical and experimental studies indicate that a large amount of ground surface motion in the vicinity of a shallow explosion is contained in surface waves. Greenfield (1971) suggested that a significant portion of arrivals in P coda (taken to be between 10 and 40 sec after first P) may be due to near-surface scattering of explosion-generated Rayleigh waves into teleseismic P. Gupta et al. (1985b) proposed that near-source scattering of fundamental-mode Rayleigh waves (Rg) into teleseismic P (referred to as Rg→P hereafter) may be responsible for the large arrivals immediately following P and pP on NORSAR records of NTS shots. Gupta and Blandford (1987) also found evidence for "secondary arrivals due to surface interaction phenomena" which showed greater dependence on shot medium velocity than the earlier teleseismic arrivals of P and pP. Several other investigators (e.g. Frasier, 1972; Bakun and Johnson, 1973) suggested this later arrival to be the slapdown phase associated with near surface spallation. Two-dimensional linear finite-difference simulations of explosion sources in the Yucca Flats (NTS) by McLaughlin et al. (1987) indicated the presence of large secondary arrivals (within the first 5 sec of P) due to scattering of surface waves mainly at offsets in the basement structure and at the sides of the valley. Numerical modeling of explosions within the laterally varying Yucca Flats geological structure by Stead and Helmberger (1988) also showed the locally scattered Rayleigh waves to generate large arrivals following P and pP. It is important to understand the generation of these large but later arrivals, especially because they are often larger than the first P and may, therefore, be used for estimating m_b .

We examined short-period, vertical component teleseismic P arrivals at NORSAR from 14 Pahute Mesa (NTS) shots (the same as used in an earlier study, Gupta and Blandford, 1987). Knowing the shot depth, d and the overburden velocity (average shot-point to surface compressional wave velocity), α , the time interval between pP and P arrivals is approximately given by the delay time, $t_d = 2d/\alpha$. Using a window length of 12.8 sec, beginning 4 sec before the onset of P, and applying a Parzen taper, Fourier spectra were obtained for the 14 shots recorded at the center element of NORSAR subarray 1A; these will be referred to as P(12.8 sec) spectra. This window is long enough to contain several seconds of secondary arrivals following P and pP since t_d for all shots used in this study is no larger than about 1 sec. By using a 6.4 sec window starting 2 sec before the onset of direct P, P(6.4 sec) spectra were also obtained for all explosions. The time window beyond about $2t_d$ after the beginning of direct P should perhaps contain mostly the secondary arrivals due to scattering near the source and the receiver. We therefore also selected a window 6.4 sec long and delayed by $2t_d$ with respect to the window used for the P(6.4 sec) spectra (an example is shown in Gupta and Blandford, 1987); the spectra of these will be referred to as R→P(6.4 sec) spectra.

For an explosion source with source function $S(f)$ within a homogeneous half space, the fundamental-mode Rayleigh wave amplitude $R(f)$ is given by the expression (Hudson and Douglas, 1975):

$$R(f) = \frac{C S(f)}{r^{0.5} \rho \alpha^{3.5}} f^{1.5} 10^{-2.18 t_d f} \quad (1)$$

where a Poisson's ratio of 0.25 is assumed, ρ is the density, r is the epicentral distance and C is a numerical constant. If the scattering function (which converts R to teleseismic P) does not change much with frequency over a small frequency range (such as 0.5 to 2.0 Hz), equation (1) shows that a plot of the spectral ratio $\log (R_g \rightarrow P/P)$ versus frequency should have a slope of about -2.18.

Using the single layer model based on the shot depth and average overburden velocity, synthetic seismograms for all 14 shots were computed by using the Haskell-Thompson matrix method. The von Seggern and Blandford (1972) source function scaling (granite RDP with $k = 16.8$ and $B = 2.04$), NORSAR instrument, and a t^* of 0.45 (Der et al., 1937) were used. Spectral ratios for the observed/synthetic seismograms were obtained by using the $P(12.8 \text{ sec})$, $P(6.4 \text{ sec})$, and $R \rightarrow P(6.4 \text{ sec})$ windows, and the mean spectral slopes, corrected for noise, were computed for various frequency ranges. Results for 0.5-2.0 Hz frequency range are shown in Figure 6 in which, considering the simplicity of our model, agreement between theory and observation seems good, especially for the deeper shots (in terms of wavelength, i.e. those with larger t_d values); the mean slope values are all close to -2.2, in agreement with equation 1.

The maximum-likelihood multichannel deconvolution method of Shumway and Der (1985) was applied to the P wave data from 9 Pahute Mesa shots recorded at both NORSAR and EKA. Results from spectral ratios based on the deconvolved source functions are shown in Figure 7. Once again, the mean slope values, similar to those in Figure 6a, are in agreement with the theoretically expected values.

CONCLUSIONS AND RECOMMENDATIONS

Least-squares inversion for source and receiver terms, applied to NORSAR multichannel P and P coda spectral amplitudes for 21 NTS shots, indicates magnitude versus yield relationships with standard deviation of residuals of only 0.12 and 0.09 m.u. for P and P coda, respectively. High-resolution f - k spectral analysis of the NORESS data at several frequencies and from various shots (along significantly different azimuthal directions) persistently indicates the presence of two local scatterers that are near the surface and approximately due east and south-west of the array. Near-source scattering of fundamental-mode Rayleigh-to- P ($R \rightarrow P$) appears to be responsible for the large arrivals immediately following P and pP on many NORSAR records of NTS shots. The usefulness of P coda for estimating yields should be tested for stations other than NORSAR. Similarly, the role of $R \rightarrow P$ should be explored for NTS shots at several stations (other than NORSAR and EKA) and for Soviet shots at several recording sites.

REFERENCES

- Bakun, W. H. and L. R. Johnson (1973). The deconvolution of teleseismic P waves from explosions MILROW and CANNIKIN, *Geophys. J.* 34, 321-342.
- Der, Z. A., R. H. Shumway, and A. C. Lees (1987). Multichannel deconvolution of P waves at seismic arrays, *Bull. Seism. Soc. Am.* 77, 195-211.
- Frasier, C. W. (1972). Observations of pP in the short-period phases of NTS explosions recorded at Norway, *Geophys. J.* 31, 99-109.
- Greenfield, R. J. (1971). Short-period P-wave generation by Rayleigh-wave scattering at Novaya Zemlya, *J. Geophys. Res.* 76,
- Gupta, I. N. and R. R. Blandford (1987). A study of P waves from Nevada Test Site explosions: Near-source information from teleseismic observations? *Bull. Seism. Soc. Am.*, 77, 1041-1056.
- Gupta, I. N., R. R. Blandford, R. A. Wagner, J. A. Burnett, and T. W. McElfresh (1985a). Use of P coda for determination of yield of nuclear explosions, *Geophys. J.* 83, 541-553.
- Gupta, I. N., R. R. Blandford, R. A. Wagner, and J. A. Burne (1985b). Use of P coda for explosion medium and improved yield determination, in *The Vela Program*, A. U. Kerr, Editor, Executive Graphic Services, Virginia, 711-720.
- Hudson, J. A. and A. Douglas (1975). On the amplitudes of seismic waves, *Geophys. J.* 42, 1039-1044.
- Lynnes, C. S. and T. Lay (1988). Observations of teleseismic P wave coda for underground explosions, *PAGEOPH* 128, Nos. 1/2, 231-249.
- McLaughlin, K. L., L. M. Anderson, and A. C. Lees (1987). Effects of local geologic structure on Yucca Flats, Nevada Test Site, explosion waveforms: two-dimensional linear finite-difference simulations, *Bull. Seism. Soc. Am.* 77, 1211-1222.
- Patton, H. J. (1988). Application of Nuttli's method to estimate yield of Nevada Test Site explosions recorded on Lawrence Livermore National Laboratory's digital seismic system, *Bull. Seism. Soc. Am.* 78, 1759-1772.
- Shumway, R. H. and Z. A. Der (1985). Deconvolution of multiple time series, *Technometrics* 27, 385-393.
- Stead, R. J. and D. V. Helmberger (1988). Numerical-analytical interfacing in two dimensions with applications to modeling NTS seismograms, *PAGEOPH* 128, Nos. 1/2, 157-193.
- von Seggern, D. H. and R. R. Blandford (1972). Source time functions and spectra for underground nuclear explosions, *Geophys. J.* 31, 83-97.

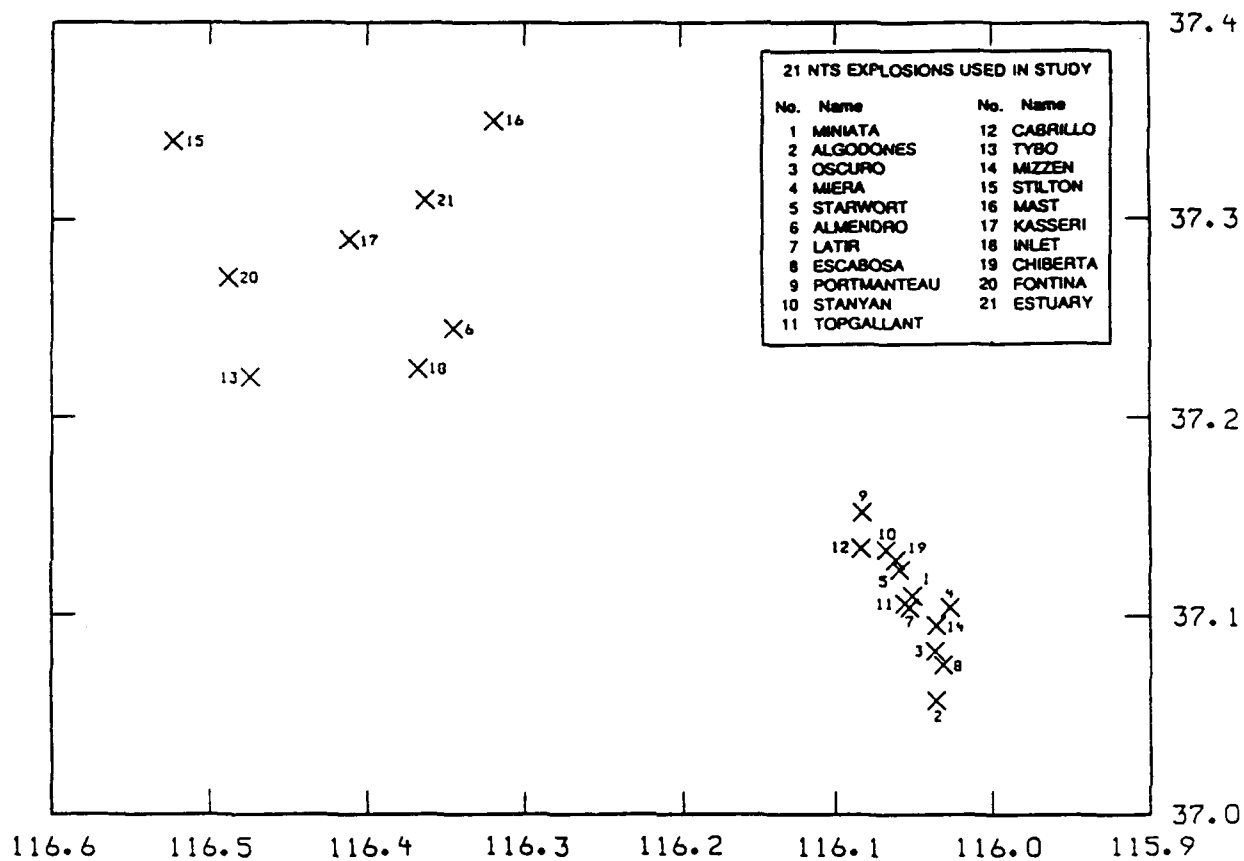


Figure 1. Location of 21 NTS explosions used in the study of P and P coda at NORSAR.

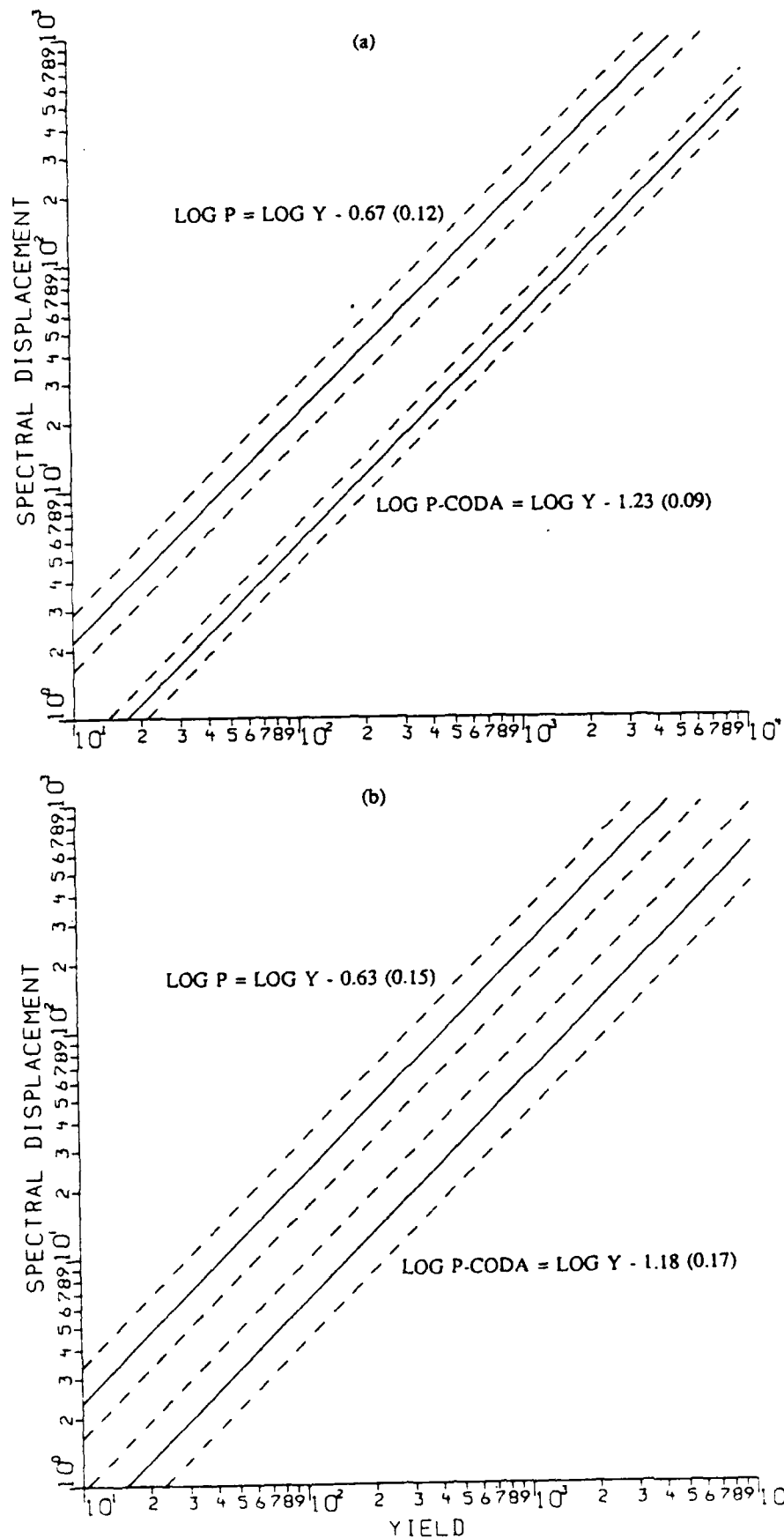


Figure 2. Spectral displacement for P and P coda versus yield based on (a) NOR SAR multichannel data for 21 NTS shots and (b) single channel of NA0 for 19 shots. The standard deviation of residuals is the least for P coda based on entire NOR SAR array data.

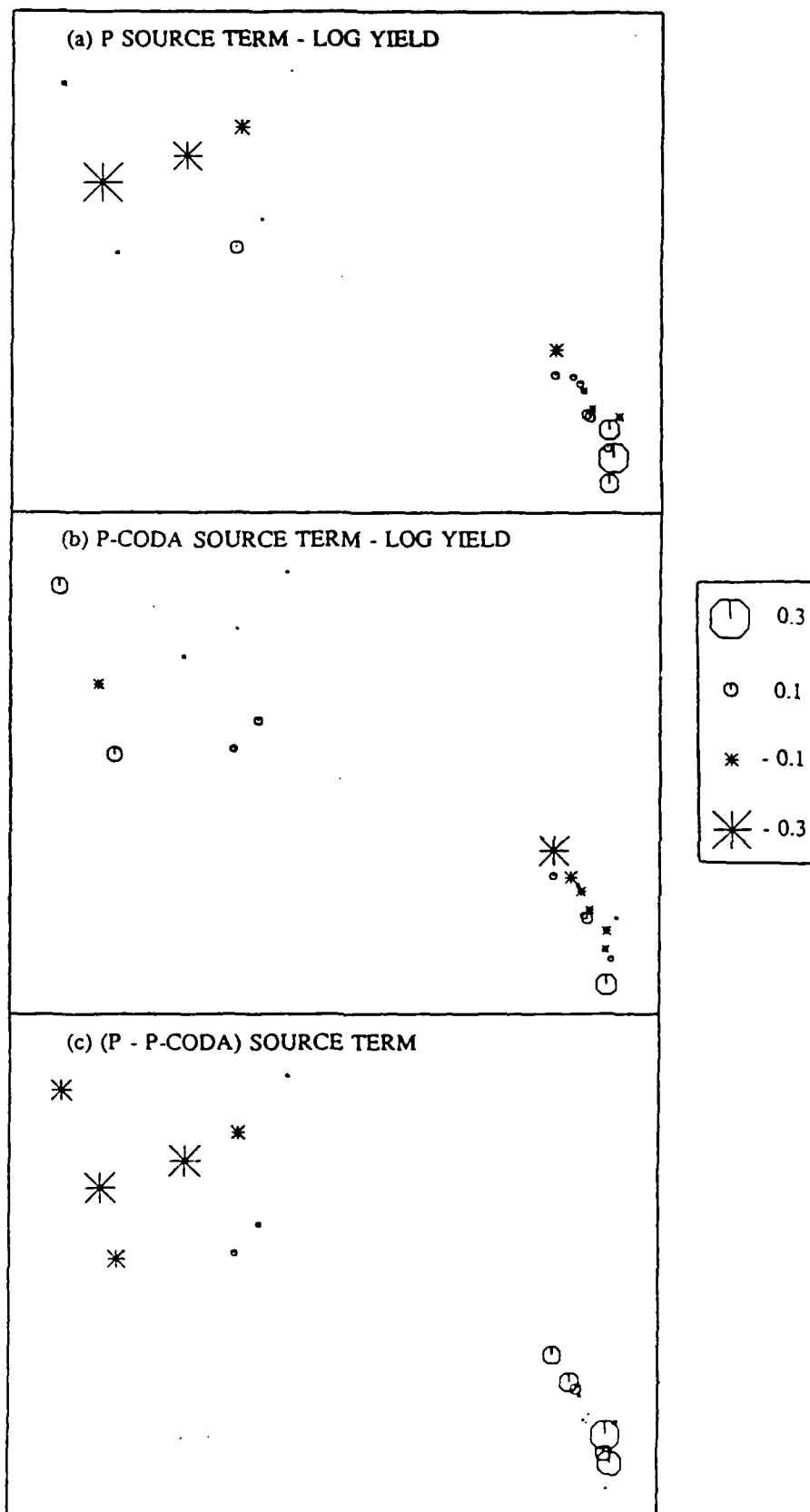


Figure 3. Magnitude residuals for 21 NTS shots based on (a) P and (b) P coda, showing that the P coda residuals are much smaller than P residuals. (c) Difference between P and P coda magnitude residuals indicating the spectral amplitude ratio P/P-coda to be generally larger for Yucca Flat shots than for Pahute Mesa shots.

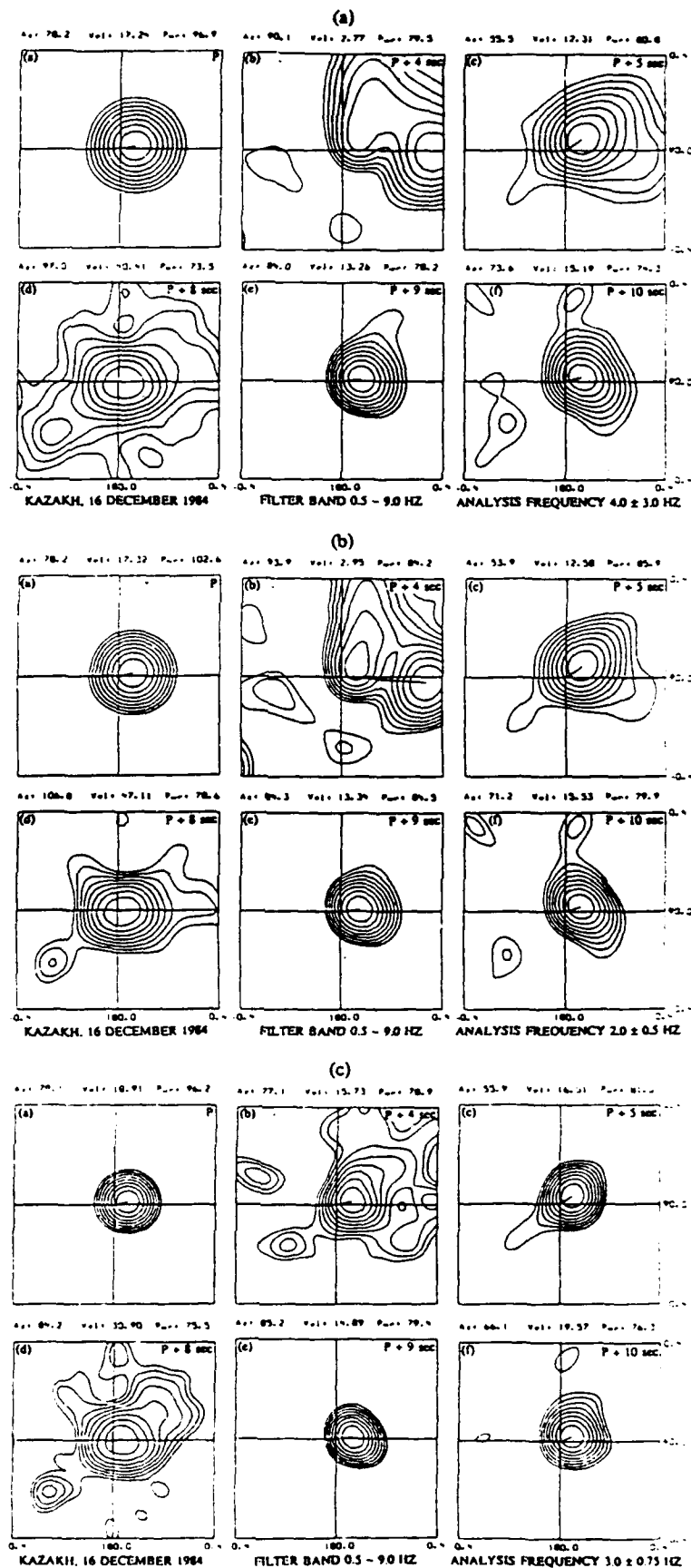


Figure 4. Frequency-slowness spectral estimates for six different time windows for the Kazakh explosion of 16 December 1984, for (a) broadband (4.0 ± 3.0 Hz), (b) the narrow 2.0 ± 0.5 Hz passband, and (c) the narrow 3.0 ± 0.75 Hz passband data. The numbers on top of each plot indicate azimuth (deg), phase velocity (km/sec), and signal power (dB), respectively. Note the low phase velocity, secondary arrivals in the P + 4 sec (approximately due east) and P + 8 sec (approximately due south-west) windows. 396

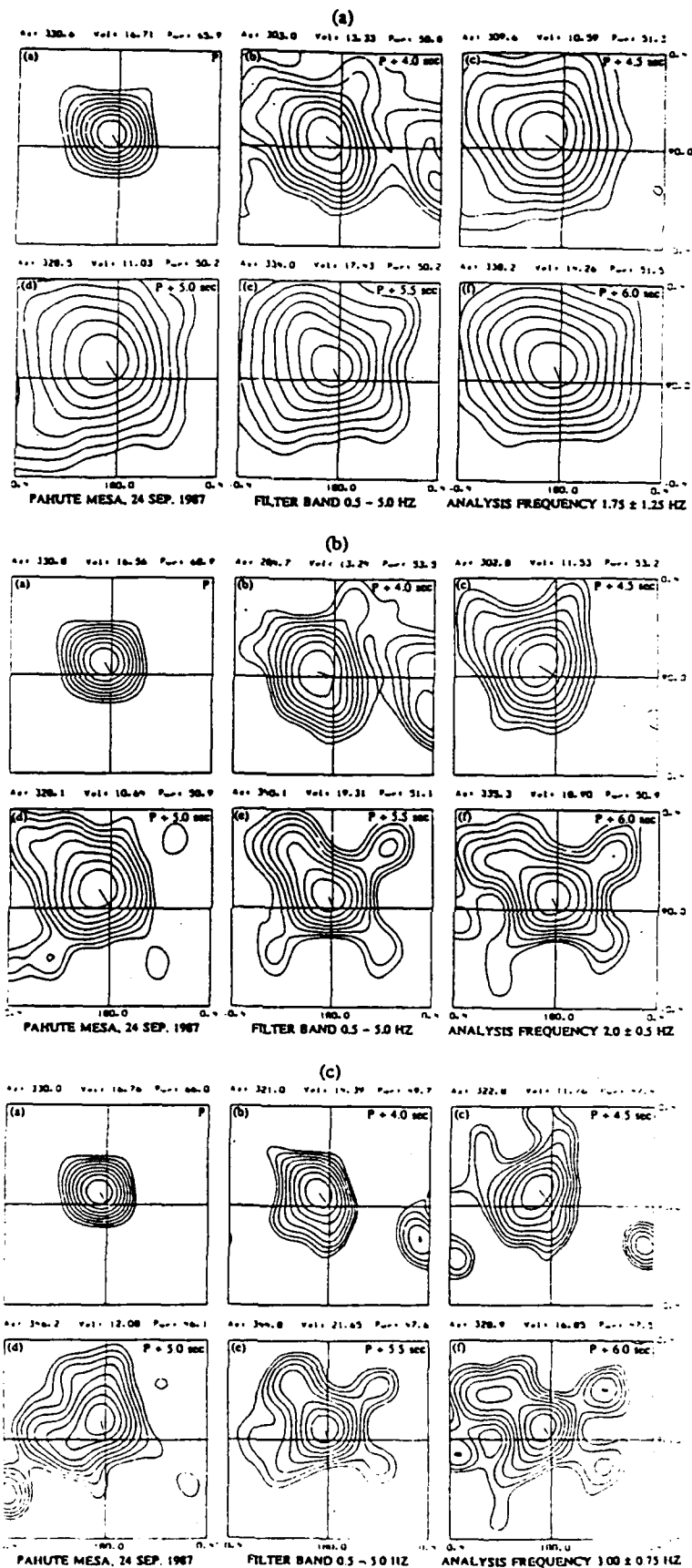


Figure 5. Similar to Figure 4 for the Pahute Mesa shot of 24 September 1987 for (a) broadband (1.75 ± 1.25 Hz), the narrow 2.0 ± 0.5 Hz passband, and (c) the narrow 3.0 ± 0.75 Hz passband data.

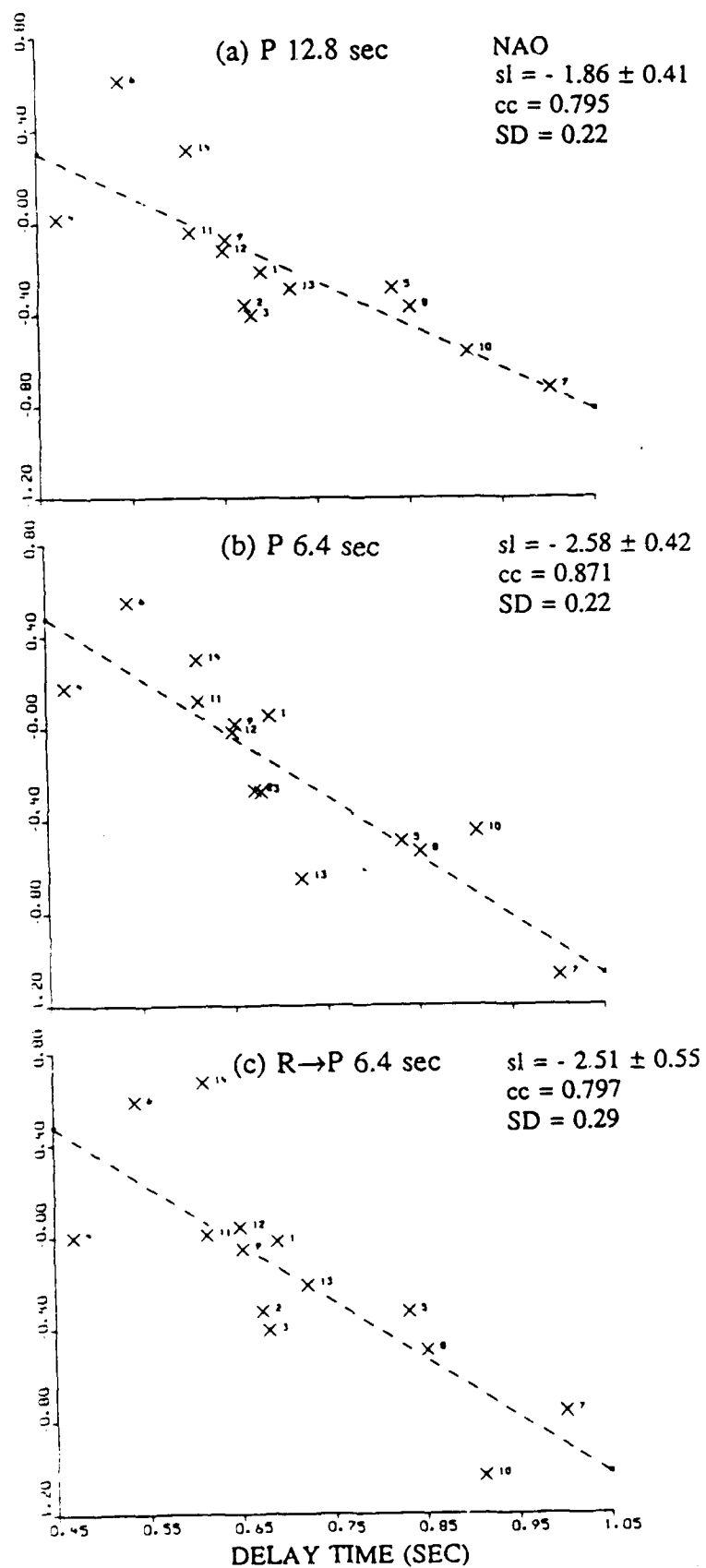


Figure 6. Mean observed/synthetic spectral ratio slopes over the frequency range of 0.5 to 2.0 Hz versus t_d for 14 Pahute Mesa shots recorded at NORSAR. Results for three different time windows are shown. The abbreviations sl, cc, and SD denote the mean slope (with one standard deviation value), the correlation coefficient value, and one standard deviation of the residuals, respectively.

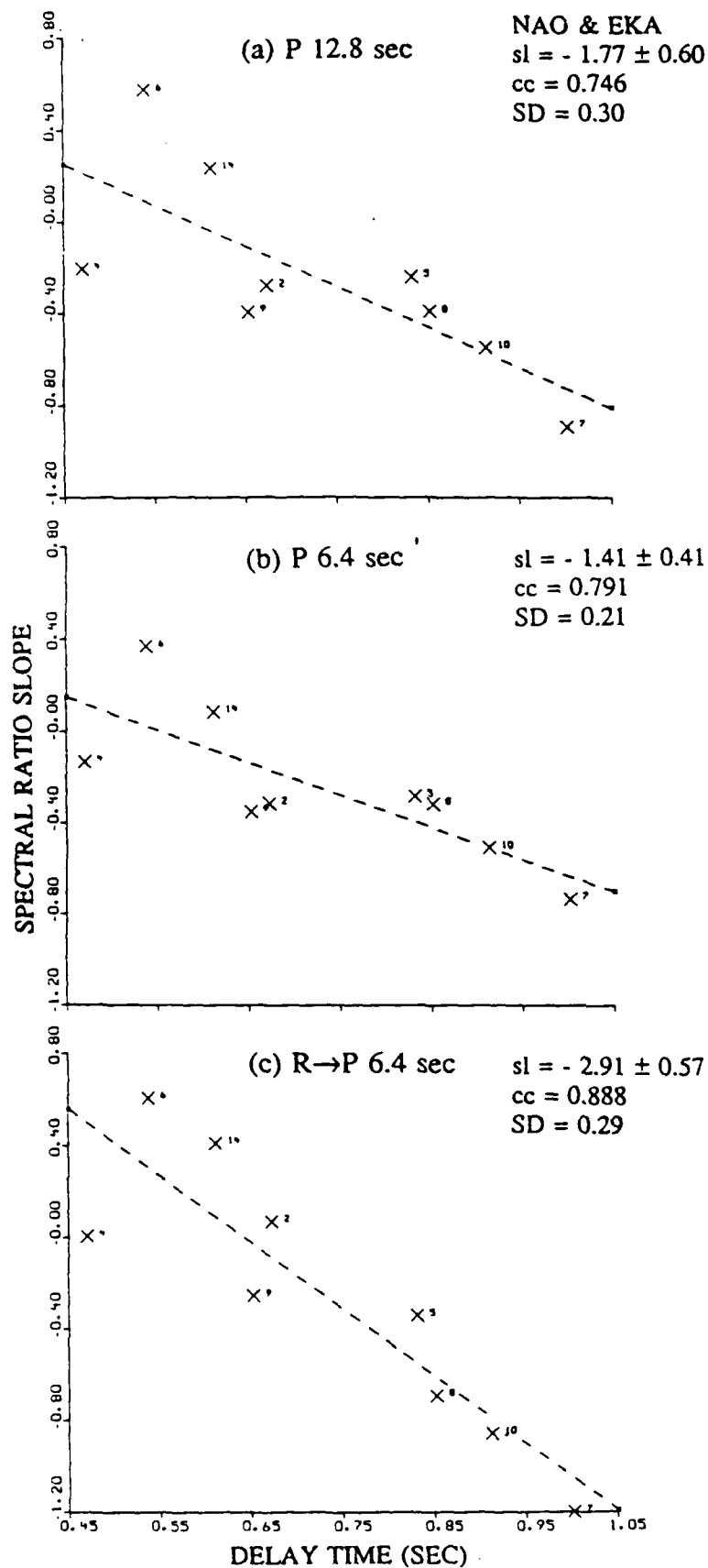


Figure 7. Similar to Figure 6 for 9 Pahute Mesa shots based on the deconvolved source terms derived by using both NORSAR and EKA data.

Siting Survey and Configuration Optimization of a New Regional Array in the Federal Republic of Germany

Hans-Peter Harjes
Institute of Geophysics, Ruhr-University, Bochum, FRG.
Contract No. F 49620-88-C-0045

Abstract.

The project is aiming at a siting survey for an advanced seismic array in the Federal Republic of Germany which could be used in a multi-array network jointly with arrays in Scandinavia to detect and identify seismic events especially at regional distances.

In order to assess the eventual capabilities of a new high-frequency array in the FRG, it was necessary to conduct a noise survey and to evaluate signal characteristics, both in the high-frequency band up to 50 Hz.

It was found that the Bavarian Forest (BF) in the southeastern part of the FRG at the border to Austria and Czechoslovakia is principally suited for such an array installation.

Continuous field work has been carried out in this area from April 4 to July 9 1988. This time period covered winter conditions with heavy snow in April to summer conditions including farming activities. A portable digital data acquisition system recorded more than 500 seismic events, about half of them occurred at local or regional distances.

Representative noise power spectra were calculated for 10 sites in the BF-area. The most favourable ones show values slightly lower than $1 \text{ nm}^2/\text{Hz}$ at 1 Hz and a smooth decay proportional to f^{-4} per decade up to 40 Hz, leading to a value of $10^{-4} \text{ nm}^2/\text{Hz}$ at 10 Hz and $10^{-5} \text{ nm}^2/\text{Hz}$ at 20 Hz.

For comparison a noise sample was taken at NORESS and analyzed with the same procedure. The NORESS power spectrum at 1 Hz is about $10 \text{ nm}^2/\text{Hz}$ and shows a steep slope proportional to f^{-5} at low frequencies due to the influence of microseisms. It crosses the BF-spectra at 2 Hz. At frequencies above 5 Hz the NORESS spectrum also follows the f^{-4} slope with absolute values a factor of 2-3 lower than the BF-sites ($5 \cdot 10^{-5} \text{ nm}^2/\text{Hz}$ at 10 Hz and $3 \cdot 10^{-6} \text{ nm}^2/\text{Hz}$ at 20 Hz).

1. Introduction

Since the establishment of the Graefenberg (GRF) array in 1980, considerable efforts have been made in the Federal Republic of Germany to use array data for seismic monitoring of underground nuclear explosions. Research was focused on discrimination studies using the broadband characteristic of seismic signals. From the very beginning it became obvious that for detection purposes this installation - built for general seismological research - should be amended by a special short-period array. The broadband instruments with a high-cut filter at 5 Hz are not optimal for detection of weak events, especially at regional distances. High frequency signals which seem to be extremely important for the identification of small underground explosions at regional distances are not detectable on records of the broadband array. On the other hand, initial results from a small-size (3 km diameter) 25-element short-period array in Norway (NORESS) have been very encouraging, as the array has proven capable of taking advantage of the very efficient propagation of high-frequency seismic phases in Eurasia. Together with a similar recently installed array in Northern

Norway (ARCESS), the proposed array in Southern Germany (tentatively named GERESS = German Experimental Seismic System) would build a north-south profile of roughly 2000 km length.

Unlike NORESS it was not possible to collocate the new short-period array with an existing GRF subarray because the latter is built on a sedimentary column which strongly attenuates high frequencies.

The Bavarian Forest at the southeast border of the FRG to Austria and Czechoslovakia represents the largest outcropping crystalline complex - as part of the Bohemian Massif - in Central Europe. This region is principally suited for an array installation of the proposed kind as has been demonstrated by the excellent detection capabilities of conventional seismic stations in the CSSR and Austria. But in the FRG the environment has to be carefully investigated due to human and industrial noise sources. Apart from these local noise conditions, sufficient seismic signals from various azimuths should be recorded and evaluated to assess the propagation of high-frequency signals, especially across geological boundaries like the one between the Russian Platform and Western Europe or the influence of the Alps on signals originating from the Mediterranean earthquake region.

2. Field Work

During phase I of the project the siting survey was completed and final results of the noise analysis are now available. Measurements have been carried out initially in October 1987 and from April 5 to July 9 1988 continuously. Some additional data have been collected later in 1988 to prove the long-term variability of noise conditions and to calibrate the results with data from well-defined events (e.g. JVE-experiment).

The measurements concentrated on an area in the Bavarian Forest (Bayrischer Wald) in the southeastern edge of the FRG (figure 1). The advantage of this area is its geological setting (crystalline outcropping rocks from the Bohemian Massif) and the low population density. The landscape is mostly mountainous up to 1200 m elevation. Nearly all sites were situated in extensive forest areas to minimize cultural noise and instruments were installed on granite or gneiss rocks to record high frequencies, especially from events at regional distances. By this temporary surface installation the seismometers were quite sensitive to wind noise but for technical and financial reasons no other arrangement was feasible. Detection capabilities derived from noise estimates of these data should represent conservative values.

For survey purposes three portacorders with direct recording were used. In case of favourable places one of three digital data acquisition systems was installed for a time period of several weeks.

Each system was equipped with three vertical short-period seismometers (1 Hz Geotech S-13) which were installed at distances between 100 m and 300 m to avoid false alarms by coincidence triggering. The survey concentrated on three areas within the Bavarian forest

- a. the southern region (south of the city of Hauzenberg)
- b. the northern region (northeast and southwest of Frauenau)
- c. the central region (east of the city of Freyung).

Very soon the site survey concentrated on the central area which is closest to the CSSR border. Very few roads, low population density, and extensive woodland offered adequate pre-conditions for seismic installations. The first station near Haidmuehle (HAID) was established in April. It was placed on weathered granite. Later, two other stations at Gr.Lichtenberg (GRLB)

and Kiesberg (KIBG) were established on gneiss. During the JVE-experiment an additional station was installed at Sulzberg (SULZ). Portacorder records showed a generally low noise background and especially a small day-to-night variation. The only obvious disadvantage appeared to be some saw-mills which generated monochromatic seismic noise during working hours.

For comparison some noise samples have been taken at the Graefenberg array (station B5) which confirmed earlier measurements showing relatively high cultural noise levels.

Finally during a short trip to Norway in October 1988, some recordings were made at NORESS to get a direct comparison of noise values by using the same data acquisition system and - more important - the same processing procedure as for data from the area under investigation in Germany.

3. Noise Analysis.

The processing of field data included several steps. At the beginning the field tapes had to be converted to standard 9-track IBM-compatible format. Then an appropriate file system was established on the SUN computing system of the Institute of Geophysics in Bochum. The CSS-format was used for this and also for the waveform data file. In this way the data could also easily be transferred to DARPA's analysis centre in Washington.

Having recorded the field data in event mode the pre-event window can be used for noise evaluation.

In this report the following procedure was applied: Altogether 20 seconds of the pre-event window were divided into 19 blocks of 2 seconds length each with an overlap of one second. Each data block was padded with zeros to get a transformation length of 2^{10} for FFT reminding that the original sampling frequency of the field data was 250 Hz. The 19 raw Fourier spectra were averaged to lower the variance without affecting stationary noise peaks. The final step includes an average of 12 noise spectra from each station and a plot of the mean values and their standard deviation.

The noise spectra (figure 2a-f) are calculated separately for day and night. They cover the whole time period during which the corresponding station was operating. By that procedure, working hours, weekends, and different weather conditions are included in the noise estimate.

In the central area Haidmuehle (HAID) was the station which was installed at the beginning of the survey. Its noise estimate (figure 2a) includes data from times when the ground was covered with snow and also from summer times. In the individual spectra no significant difference could be observed. The spectrum shows a continuous slope with a small variance and even the 2 Hz peak can only be recognized during night times. The day spectrum is dominated by a noise maximum at 4-5 Hz which is supposed to originate from a saw mill at a distance of a few kilometers in the village of Haidmuehle.

The spectra of the second station in that region, GRLB, show the smallest day/night variation we observed (figure 2b). The only difference remains the influence of the already mentioned saw mill. Its distance from GRLB and HAID is about the same. Apart from this peak, the noise spectrum at GRLB shows a smooth decay proportional to f^{-4} from 1 Hz to 30 Hz and a small standard deviation. Taking into account that the recording time covered nearly a period of one month, this area seemed to be quite promising as a candidate for an array installation.

To secure this suggestion, two other sites were explored in the vicinity. Indeed, the spectra at Kiesberg (KIBG), situated approximately 2.5 km south of GRLB look very similar (figure 2c). The only difference can be seen at 2 Hz where we identify the well-known noise peak. Because the

data at both stations have been collected at different time periods we have to expect this noise influence at every station during a more permanent operation.

Later in 1988 (September and October), some additional data were collected at Sulzberg (SULZ), approximately 1.5 km northwest of GRLB.

This fourth station (figure 2d) in the central area of the survey confirmed the favorable opinion about the area and provisions were started to establish a multi-element array during phase II of the contract.

To put our noise results from the Bavarian Forest into proper place, additional data were collected at the Graefenberg array and at NORESS. GRF can be regarded as a typical European site whereas NORESS is well known for its excellent noise conditions being situated on the Scandinavian shield.

At day the GRF-spectrum (figure 2e) shows much larger values than any of the BF-spectra. The influence of industry and traffic is especially pronounced in the large variation. The night-spectrum at GRF looks similar to the BF-spectra between 1 Hz and 8 Hz. For higher frequencies the different geological setting (sediments) causes still higher noise values. From this direct comparison we can conclude that the BF-area exceeds most other places in the FRG - and certainly GRF - as a potential site for an establishment of a high-frequency array.

More interesting is the comparison of the proposed Bavarian area with NORESS. The spectra shown in figure 2f were calculated from a 24 hour noise sample analyzed with the same procedure as described above. There are remarkable differences in the noise spectra. For low frequencies around 1 Hz NORESS clearly suffers from the influence of the coast which results in an order of magnitude higher PSD-values compared to the Bavarian Forest area ($10 \text{ nm}^2/\text{Hz}$ to less than $1 \text{ nm}^2/\text{Hz}$). Apparently this high microseisms lead to a steep slope of the spectrum proportional to f^{-5} up to frequencies of 2-5 Hz. For higher frequencies this slope is flattened and comparable to the f^{-4} fall-off at the BF-area. The absolute noise values at 10 Hz and 20 Hz are certainly lower at NORESS but interestingly some influence of industrial noise between 5 Hz and 8 Hz can be identified in the spectrum at day and at night as well. Whether the sharp noise peak at 30 Hz was only occasional during the short period of data acquisition cannot be decided from this noise sample.

In concluding the comparison between NORESS and the BF-area we found a factor of 10 higher noise values at NORESS for frequencies around 1 Hz and a factor of 2-3 higher noise values at the BF-site for frequencies between 2 Hz and 20 Hz. The consequence of this difference in terms of detection capabilities can only be evaluated in comparison with commonly recorded events.

4. Event Recordings

During the noise survey the data acquisition system principally operated in detection mode as outlined in chapter 2. A conventional STA/LTA-detector algorithm was applied. Using an updating LTA the recording length was variable but generally the complete interval between Pn-waves and Lg-waves was recorded.

After inspection of the detection times which were compared with various bulletins, i.e. PDE for teleseismic events, NORSAR and EMSC (European Mediterranean Seismic Centre) for regional seismicity and the GRF-monthly bulletin for local events, the corresponding waveforms were extracted from the original data.

Although the whole field campaign lasted for a time period of more than three months, the actual recording time covered only 60 days. The remaining time was needed for setting up stations, changing batteries, and preparing new sites.

During the 60 days 504 events were detected and evaluated. About half of these events (265) were found to be teleseismic, 93 occurred at regional distances (150 km - 2000 km), and 146 events were classified as local seismicity.

4a. Global Detection Capability.

Data from a field survey with a recording time of 60 days can only give a rough estimate of the global detection capability of the investigated site. A permanent seismometer installation in a vault will certainly diminish the influence of wind noise. On the other hand, even a preliminary evaluation should show a correspondence between the detection threshold which can be inferred from the noise level and that from actual data.

In figure 3 a magnitude-frequency histogram is shown which includes all detected events with epicentral distances larger than 2000 km. From this diagram we derive an overall teleseismic detection threshold at about $m_b = 4.5$. A simple calculation yields a corresponding noise level of 2-4 nm at 1 Hz assuming an S/N-ratio of 2 for detection. This value is comparable to the power spectral estimates found in the area.

A peculiarity of the Bavarian Forest area with regard to teleseismic detection capabilities is certainly the large number of PKP-phases. 88 events - or roughly one third of the total 265 teleseismic detections - were PKP-detections originating from the Pacific. In fact, all detected teleseismic events with magnitudes less than $m_b = 3.6$ were identified as PKP-events. This result clearly demonstrates the potential of arrays on the Northern Hemisphere for monitoring special sites on the Southern Hemisphere as can be shown for the French test site at Mururoa. Figure 4 demonstrates the excellent detection capability for this distance by the record of a presumed explosion on 16.6.1988 which was only reported by the seismological agency in New Zealand.

4b. Regional Event Recordings.

As the planned array in the Bavarian Forest area is specifically aiming at high-frequency seismology, particular emphasis was given to recordings of regional events. During the field campaign, 93 events were recorded in a distance range of about 150 km to 2000 km. These events cover all azimuths although the majority of events are incident from east or southeast directions.

The Polish copper mines near Lubin and the coal mines in Upper Silesia contribute 19 events to the whole data set. Epicentral distance is 338 km and 411 km, respectively from the central area (GRLB).

The spectral behaviour is quite different. Whereas the seismograms from Lubin copper mine show a very consistent picture with distinct Pn-, Pg-, and Lg-phases and relatively high frequencies (figure 5), the seismograms from Upper Silesia coal mines are more complex (figure 6), high frequencies are missing and often no clear Pn-onset can be defined. Several times the detector triggered on Lg-amplitudes for these coal-mining induced events, in contrast the detector never missed the Pn-arrival for Lubin events of comparable size.

Apart from these differences which are presumably related to the source process, variations of regional phases merely come from crustal differences on the wave path. To the north and west of the investigated site, there are thick sedimentary layers which should attenuate high frequencies. The seismicity of these regions (central and northern Germany, France) is relatively low, but we recorded one $m_l = 2.3$ event from Eisenach/GDR, epicentral distance 328 km to the north (fig.7) and a magnitude $m_l = 2.5$ event from France at a distance of 506 km to the west (figure 8).

To the east several quarries in Czechoslovakia produce seismic signals. Many of these are at distances less than 150 km and contribute to the 146 detected local events which also originate

from quarries in southern Germany and from a few earthquakes in the Austrian Alps. Figure 9 shows an example of a recording of a CSSR event at 340 km distance. Remarkably large amplitudes can be seen in the 5 Hz - 20 Hz bandpass-filtered trace.

To the southeast of the BF-site the activity of the Eurasian earthquake belt is monitored. In ascending distance we recorded earthquakes from Yugoslavia (distance = 330 km), the Adriatic Sea (distance = 750 km), Greece (distance = 1300 km) and Turkey (distance = 1450 km).

At distances of 1000 km and more the waveforms from earthquakes in Greece and Turkey as well as from Southern Italy and Northern Africa are very complex, no significant signal energy can be recognized above 10 Hz. Whether this observation generally depends on the heterogeneous wave path or whether it results from our limited data set, needs further investigation.

5. Future Work.

As a consequence of the noise survey the most promising area for an array installation was found to be the central region of the Bavarian Forest east of the city of Freyung. This area was selected to establish a provisional 9-element array.

Data from this installation will be used to study the coherence of signal and noise which is needed for the array design.

In late 1988 the seismometer vaults were prepared. It is planned to collect data until May 1989 and after evaluating these data and depending on the results, accurate seismometer sites for a possible regional array will be defined.

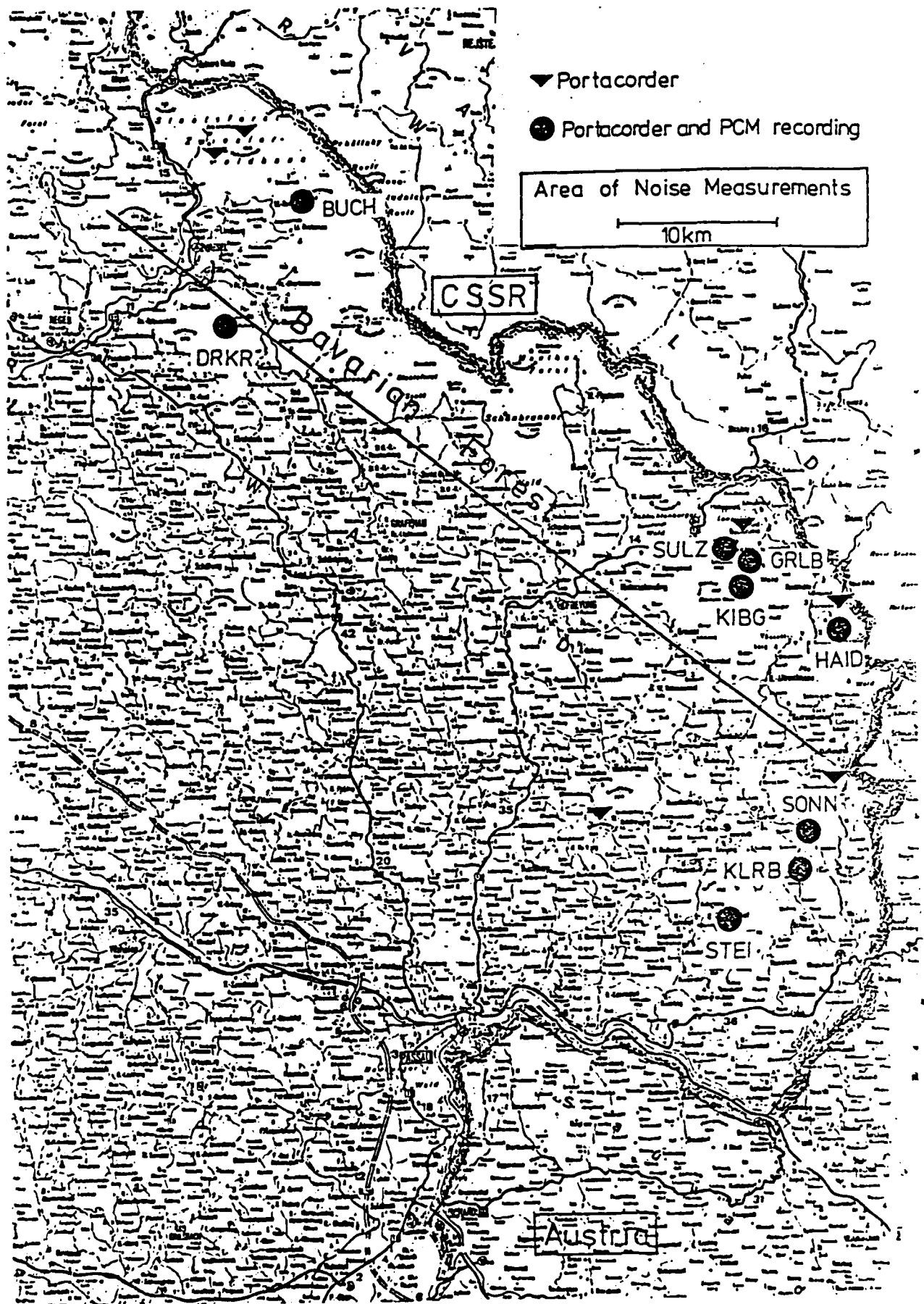


Fig. 1: Location of Field Sites for Noise Measurements

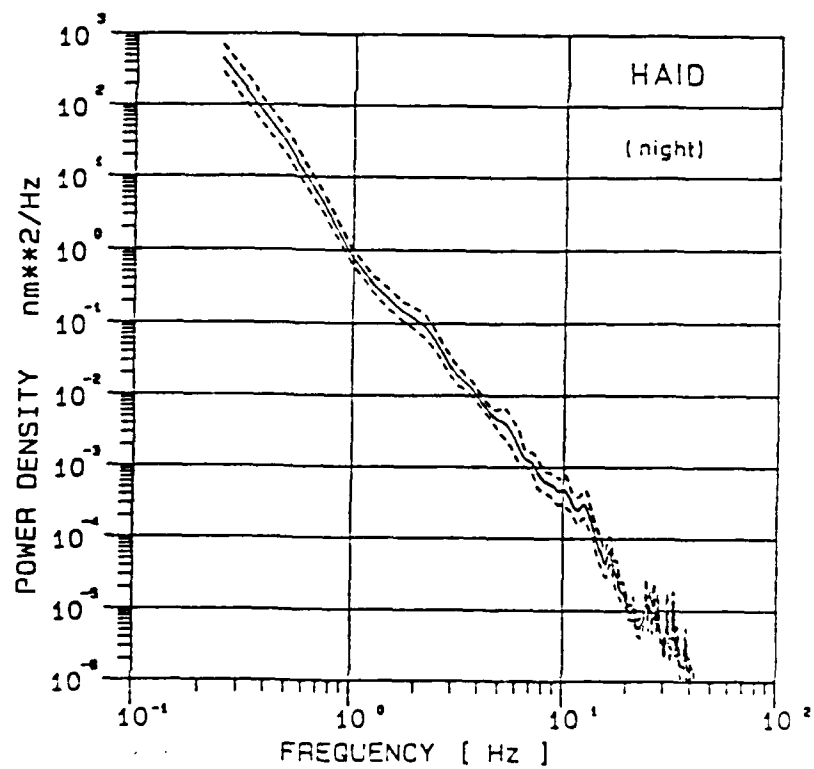
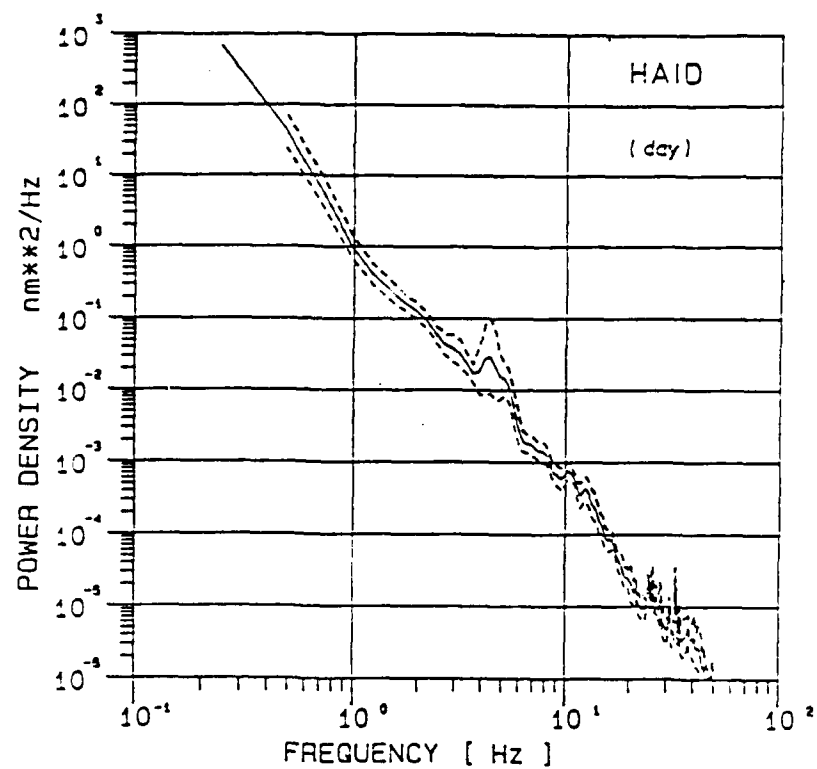


Fig. 2a: Spectral Power Density Estimates of Noise
(mean and standard deviation) for Station HAIDMUEHLE

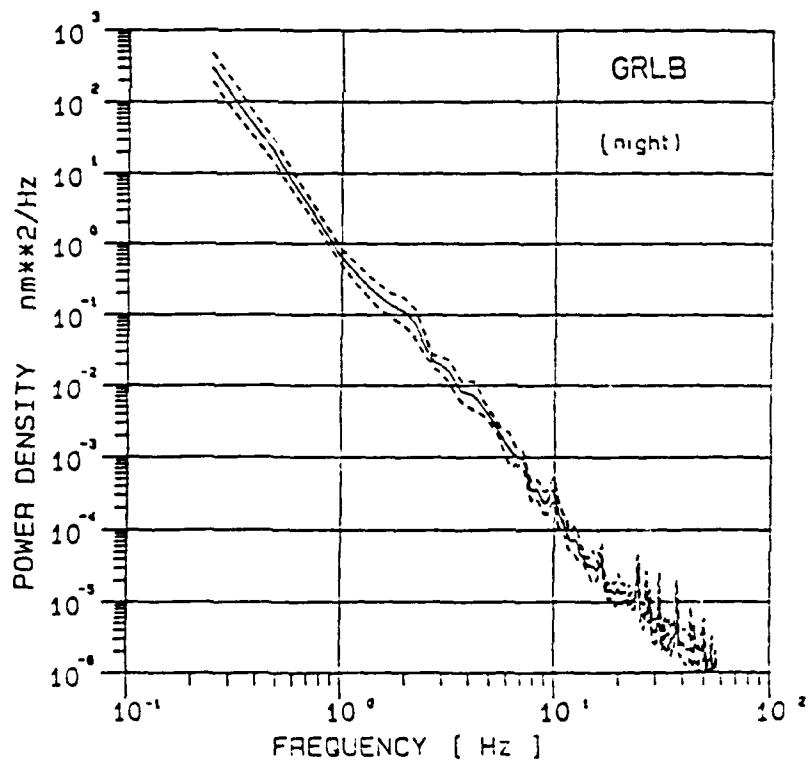
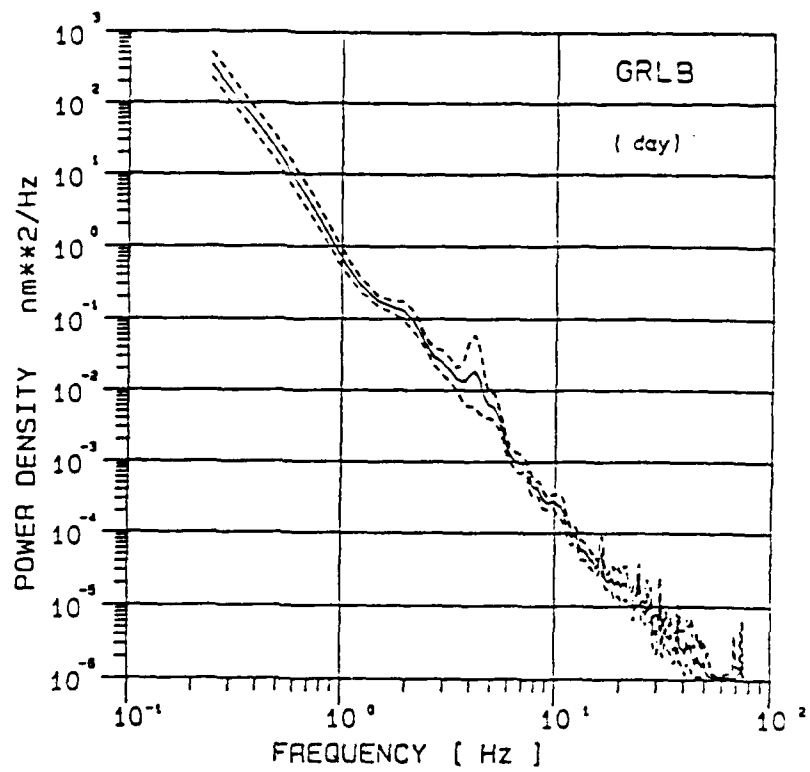


Fig. 2b: Spectral Power Density Estimates of Noise
(mean and standard deviation) for Station GROSS-LICHTENBERG

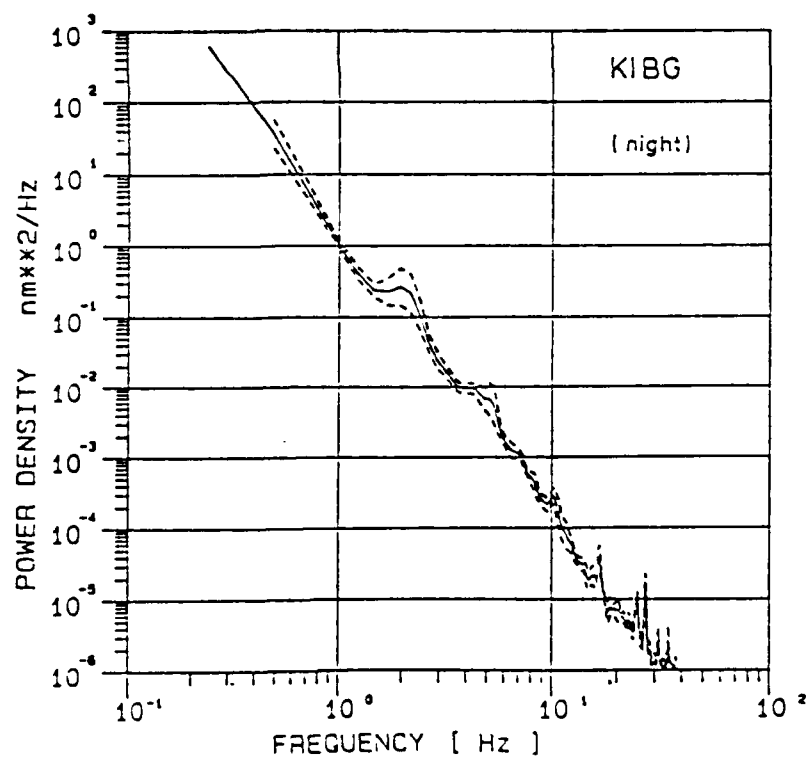
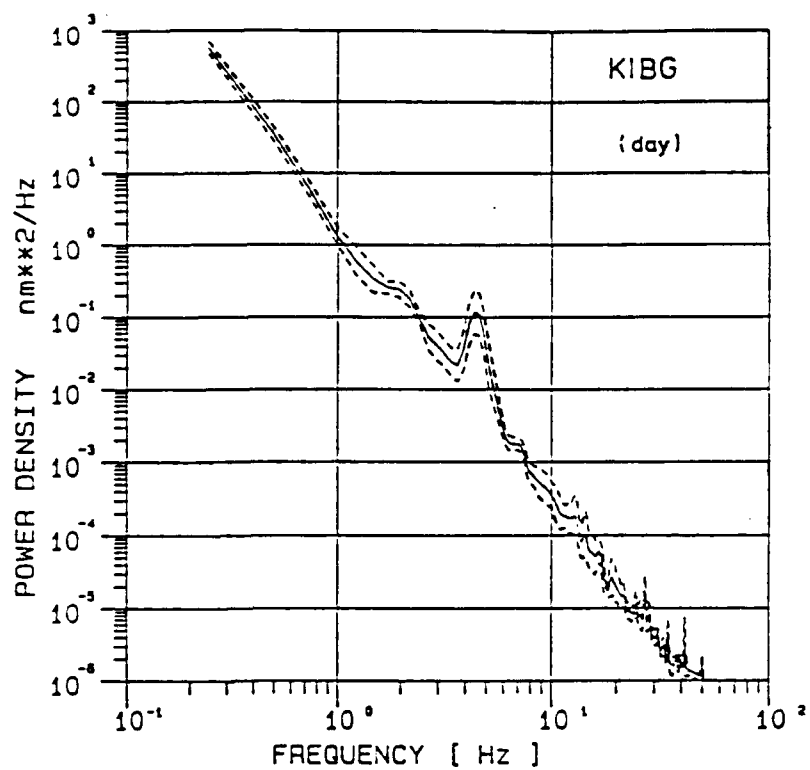


Fig. 2c: Spectral Power Density Estimates of Noise
(mean and standard deviation) for Station KIESBERG

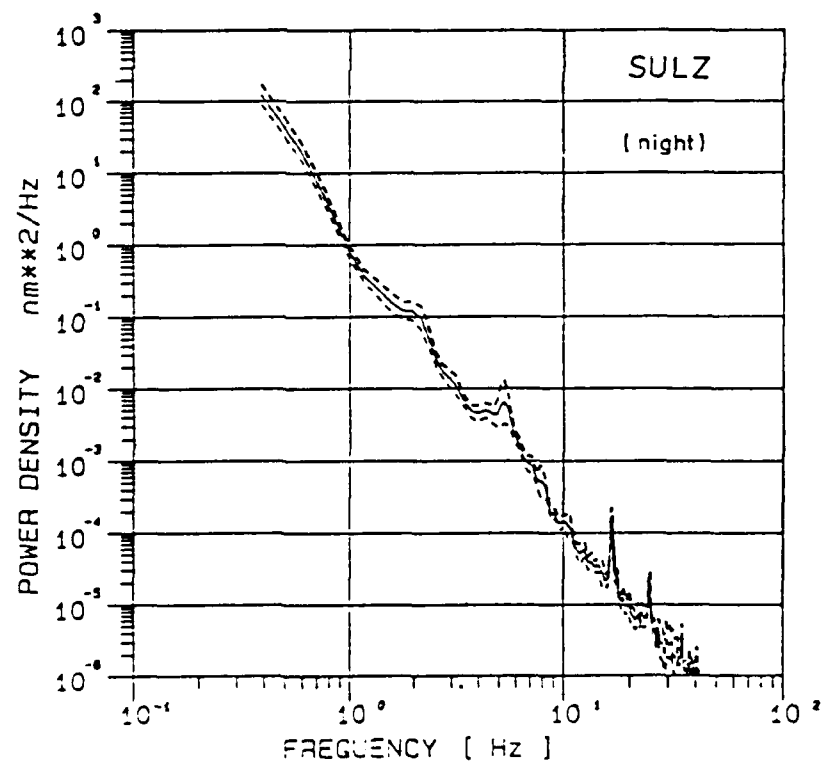
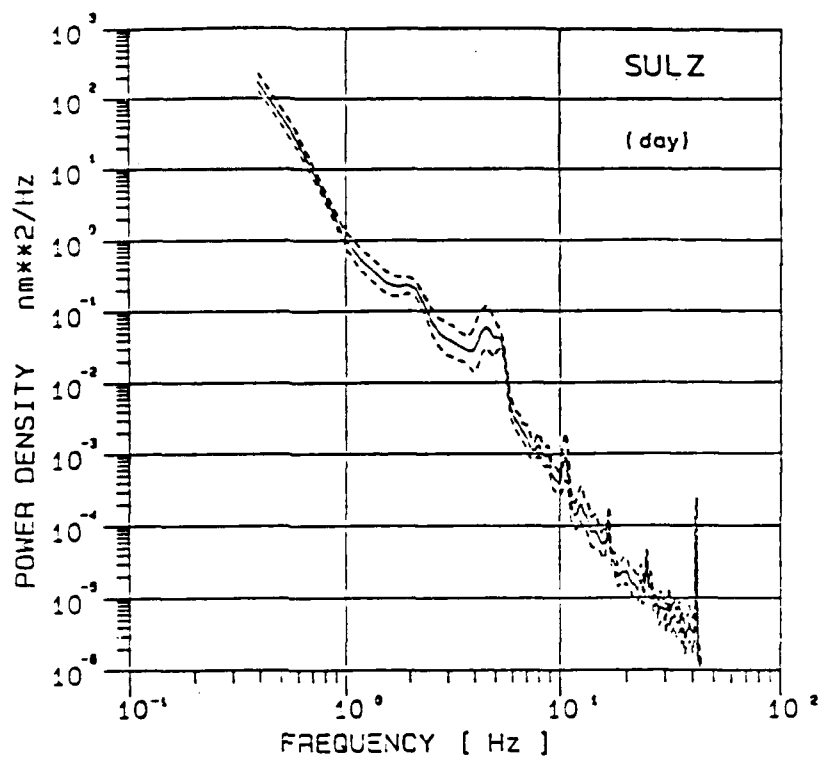


Fig. 2d: Spectral Power Density Estimates of Noise
(mean and standard deviation) for Station SULZBERG

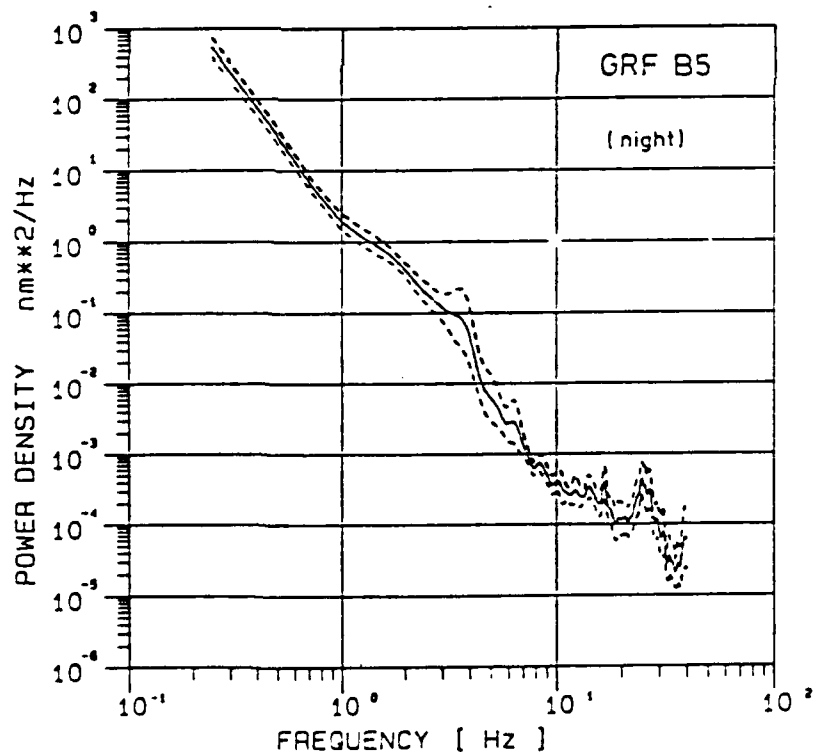
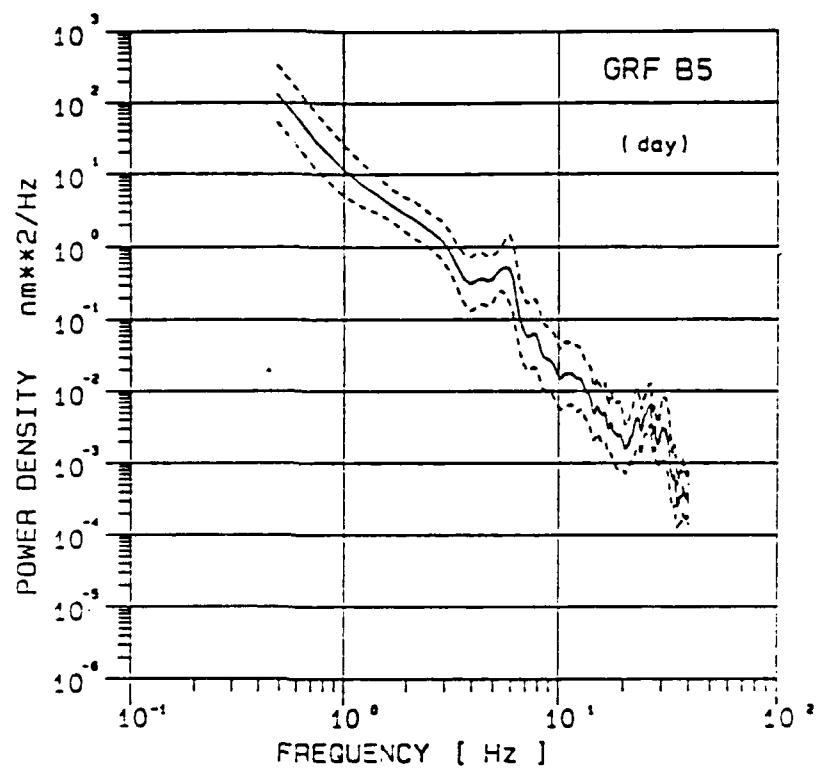


Fig. 2e: Spectral Power Density Estimates of Noise
(mean and standard deviation) for Station GRAEFENBERG

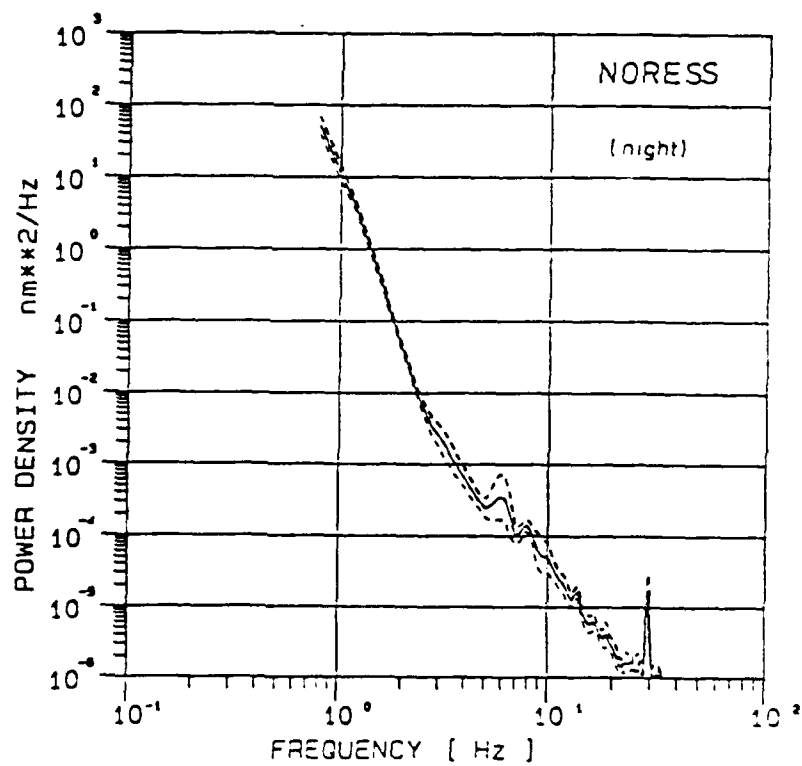
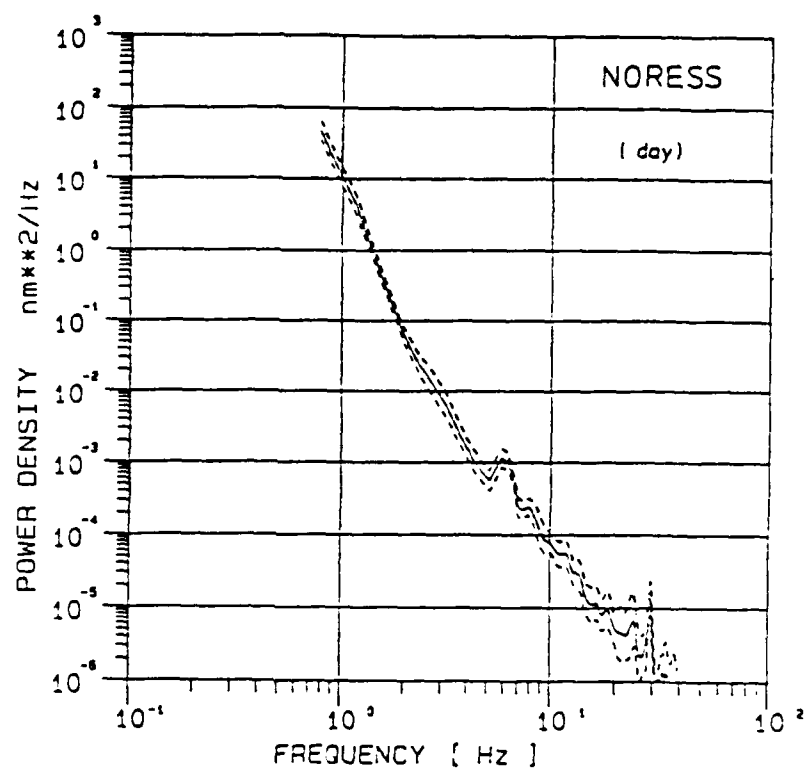


Fig. 2f: Spectral Power Density Estimates of Noise
(mean and standard deviation) for Station NORESS

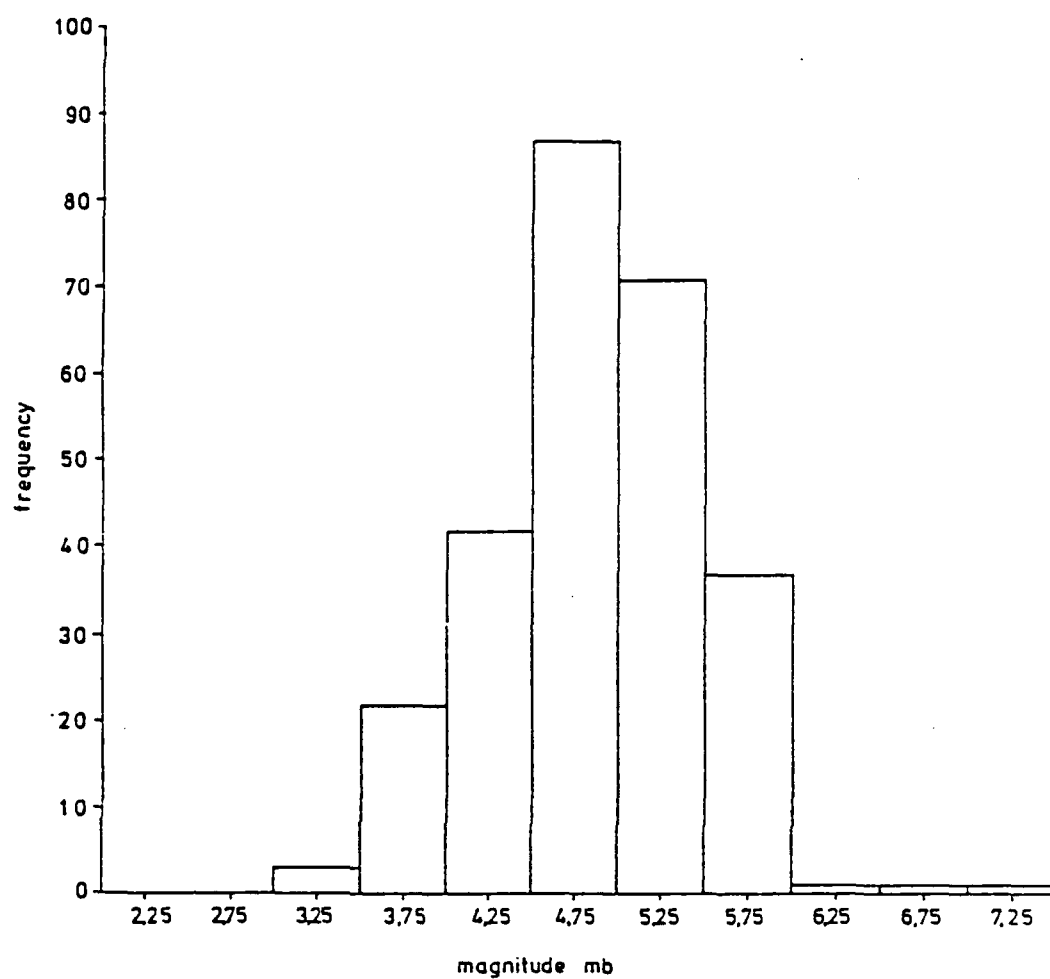


Fig. 3: Magnitude-Frequency Histogram
of Detected Teleseismic ($\Delta > 2000$ km) Events

DATA 16.05.38 17:34:12.875

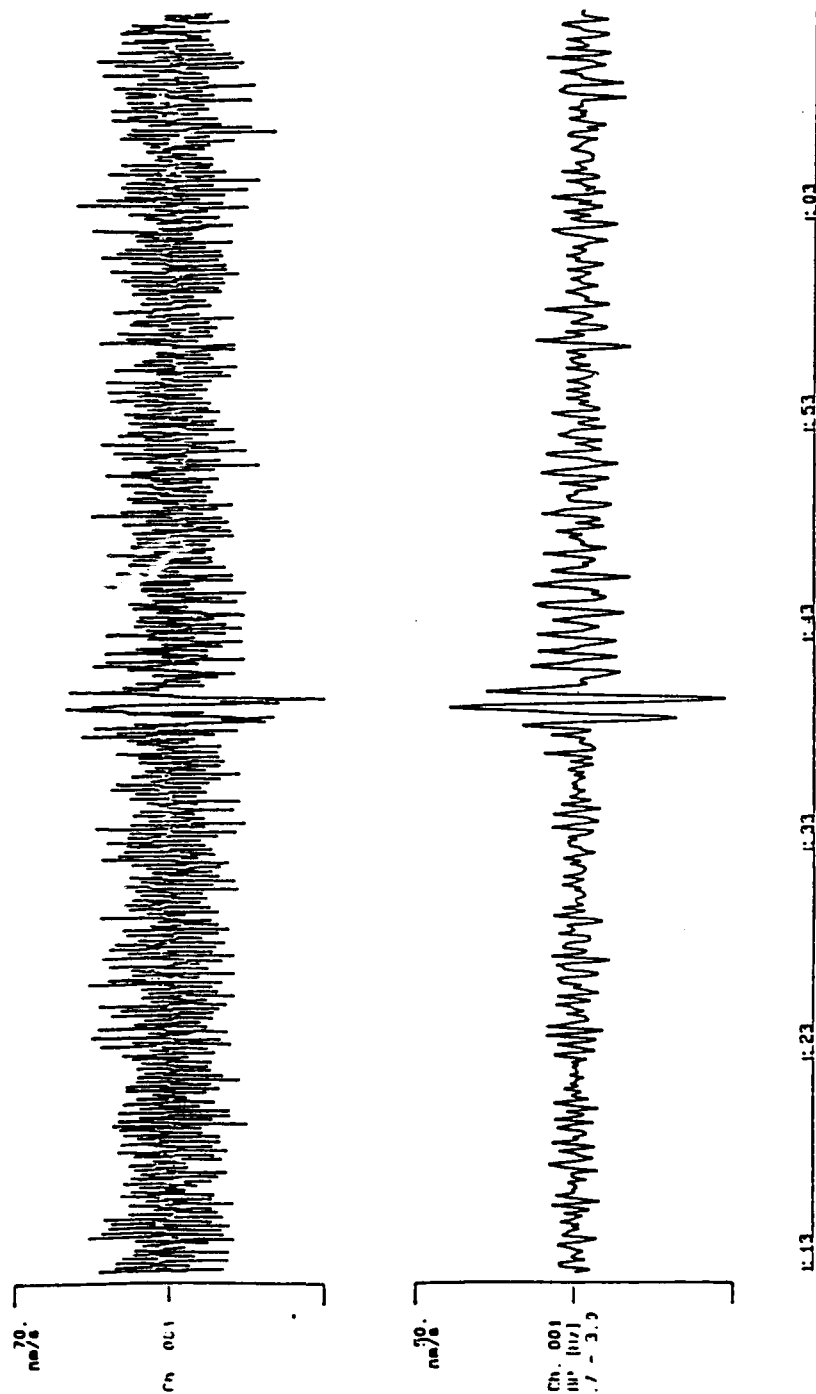


Fig. 4: PkP-Recording of Small Mururoa Explosion : $\Delta = 145.5^\circ$, $A = 9\text{nm}$, $T = 0.9\text{ sec}$

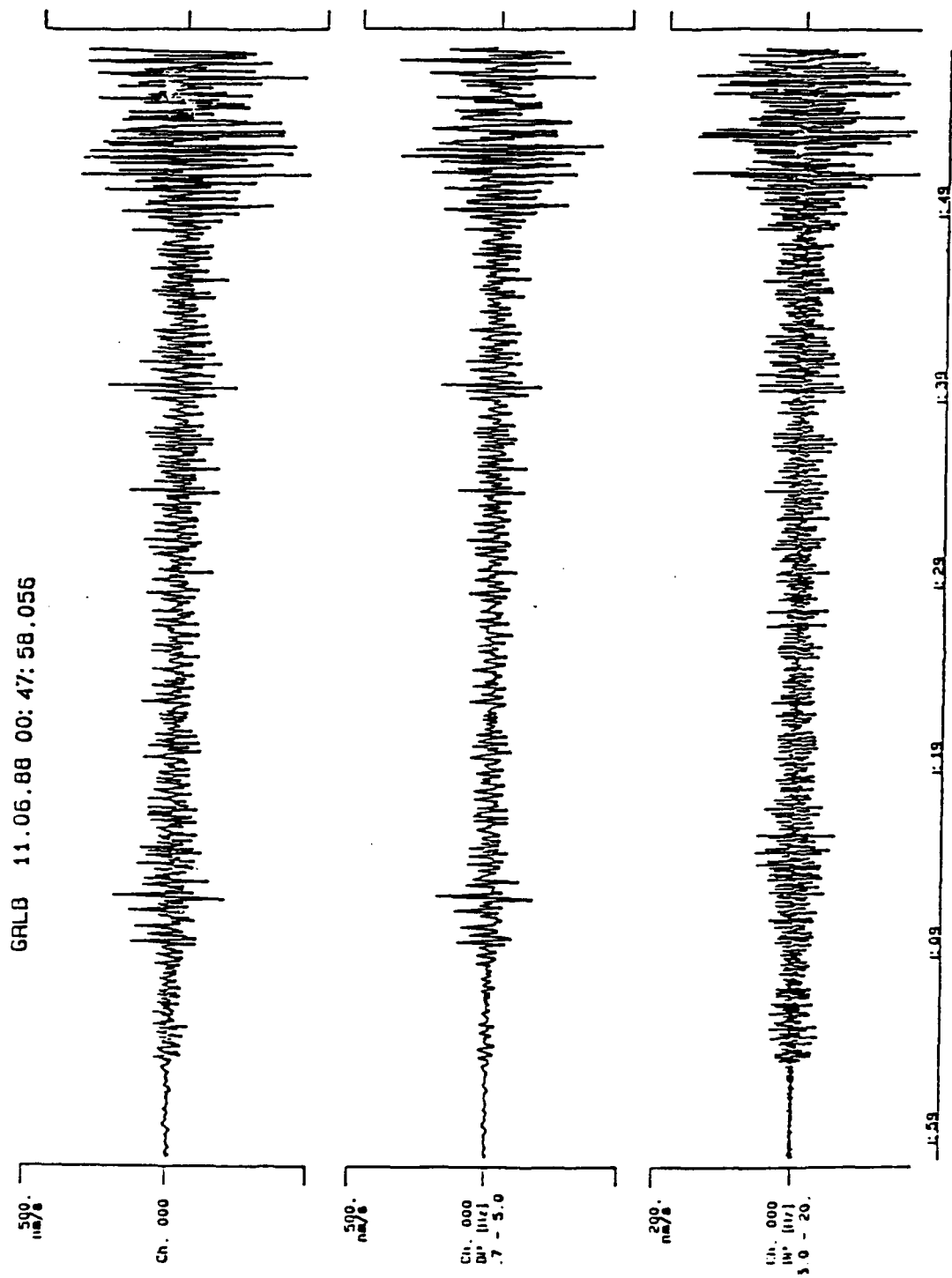


Fig. 5: Lubin (Copper Mine) Event : $M_L = 3.6$, $\Delta = 338$ km
Original Recording (top), Lowpass (middle) and Highpass (bottom) Filtered Trace

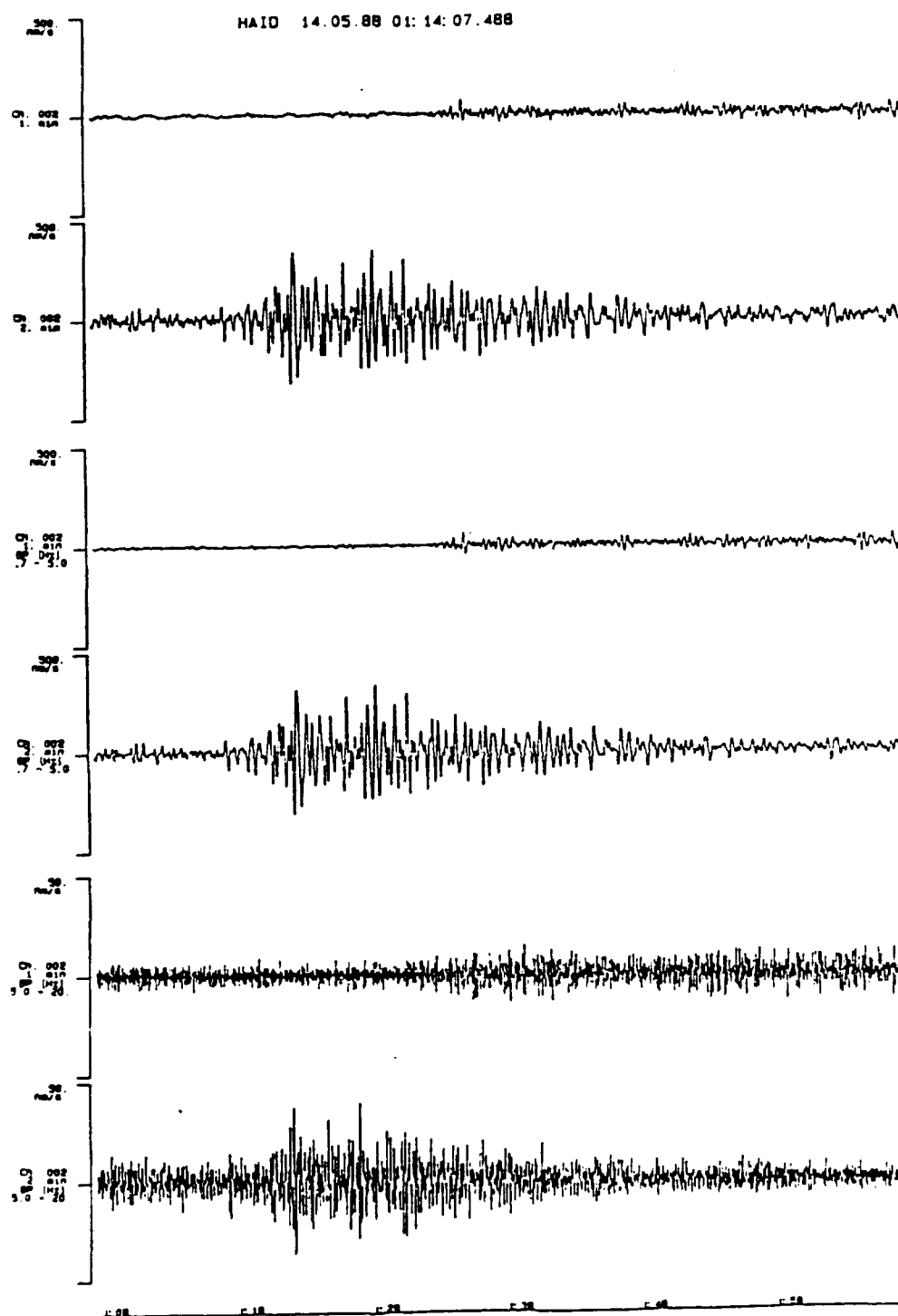


Fig. 6: Upper Silesia (Coal Mine) Event, $M_L = 3.1$, $\Delta = 411$ km
Original Recording (upper traces), Lowpass (middle)
and Highpass (bottom traces) Filtered Seismograms

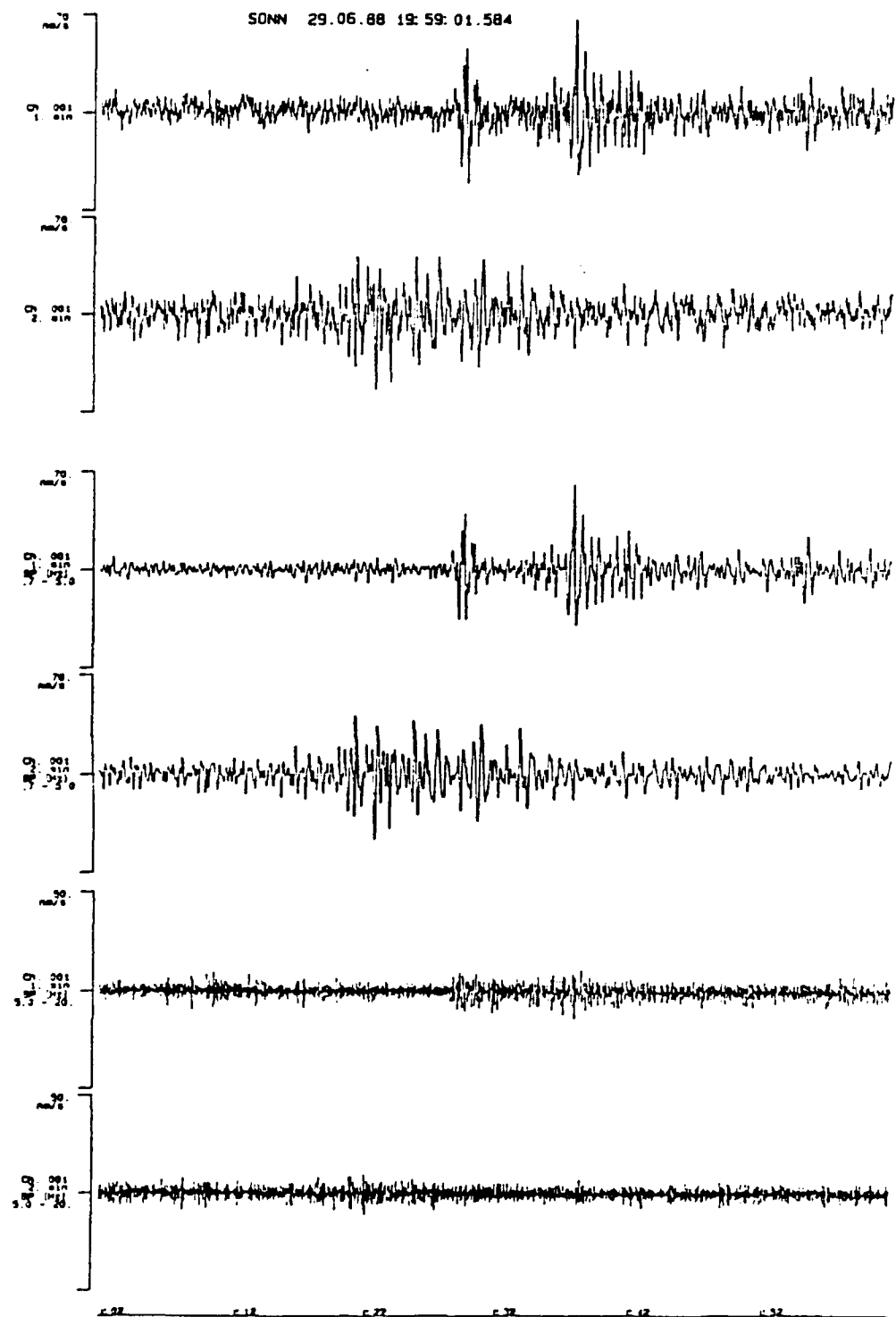


Fig. 7: Earthquake near Eisenach / GDR : $M_L = 2.3$, $\Delta = 328$ km
Original Recording (upper two lines), Lowpass (middle)
and Highpass (bottom traces) Filtered Seismograms

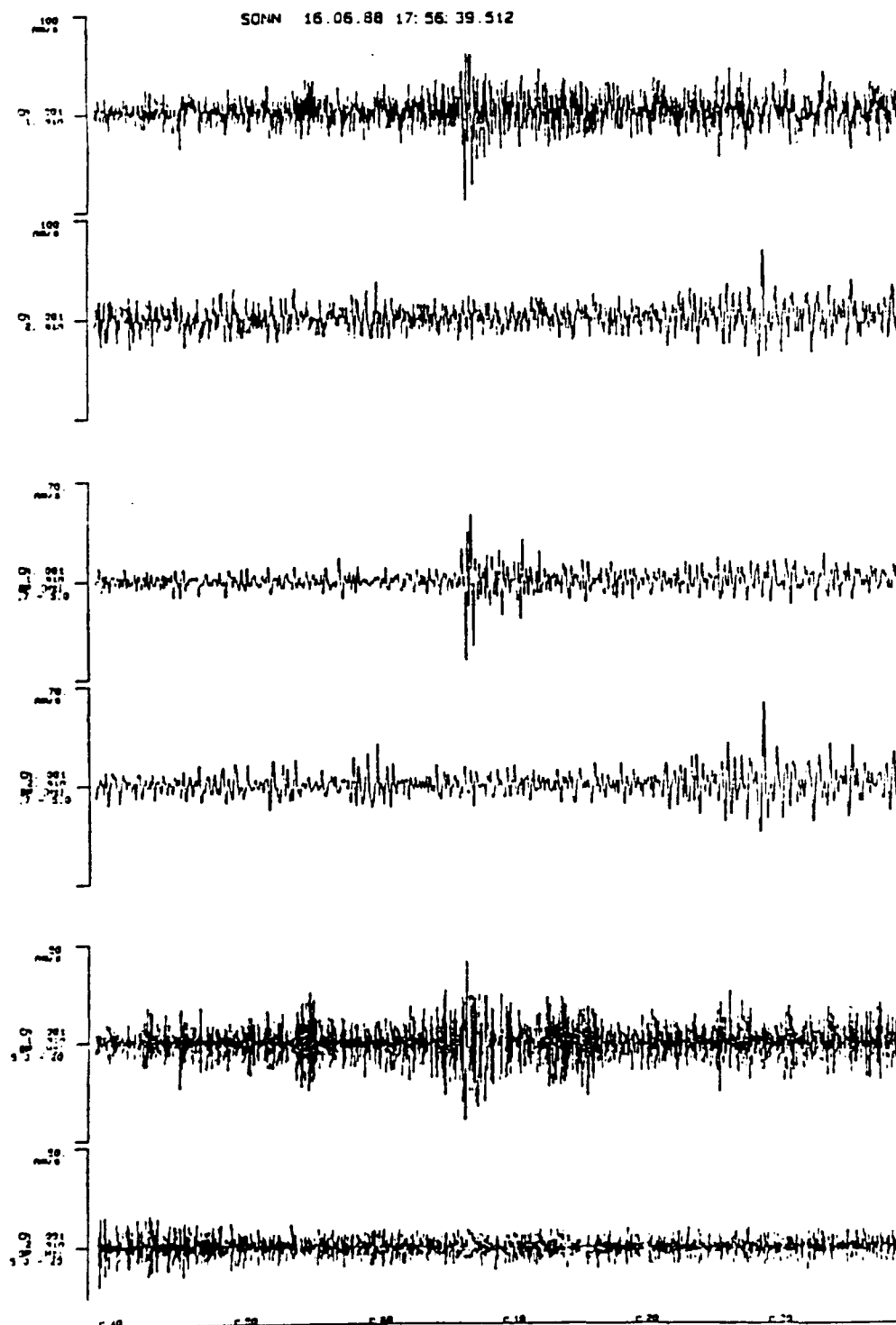


Fig. 8: Earthquake in France : $M_L = 2.5$, $\Delta = 506$ km
Original Recording (upper two lines), Lowpass (middle)
and Highpass (bottom traces) Filtered Seismograms

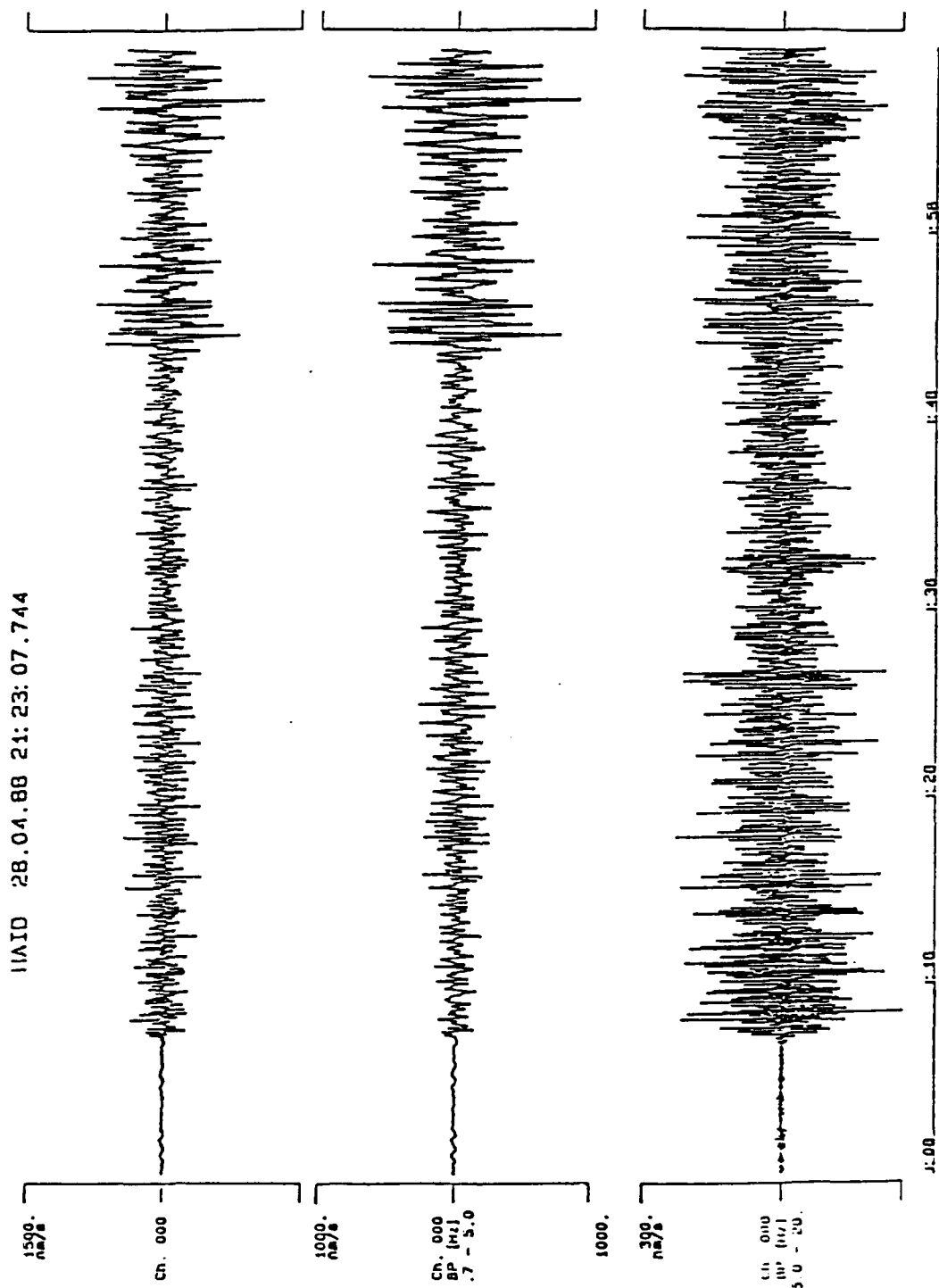


Fig. 9: CSSR (quarry ?) Event in the West Carpatians : $M_L = 3.3$, $\Delta = 340$ km
Original (top), Lowpass (middle) and Highpass (bottom) Filtered Recording

SYSTEMATIC ANALYSIS OF VERTICAL- AND THREE-COMPONENT HIGH FREQUENCY PHASE-RATIO REGIONAL DISCRIMINATION

Christopher Lynnes, W. Winston Chan, and Robert K. Cessaro
Teledyne Geotech Alexandria Laboratories
314 Montgomery Street, Alexandria, VA 22314
(703) 836-3882

Contract Number: F19628-89-C-0063

Objectives

The primary objective is to improve the ability to discriminate between quarry blasts, earthquakes, and nuclear explosions, and further the understanding of the physical basis for high-frequency regional discrimination using vertical- and three-component digital network and array data. In order to improve our understanding of high-frequency discriminants based on the ratios of regional phases such as P_n , L_g , S_n , P_g and L_g , a large database from digital seismic networks and arrays will be utilized to study the regional propagation of high-frequency regional crustal phases. The excitation and propagation parameters of regional crustal phases, will be quantified for the tectonic and stable areas in North America. The impact of propagation effects on the efficiency and magnitude threshold of discrimination will be assessed.

Summary

Recently proposed high-frequency discriminants based on P_n/S_n and P_n/L_g ratios have proven successful for events recorded at the NORESS array (Dysart and Pulli, 1987). However, the application of these discriminants at intermediate frequencies was unsuccessful (Dysart and Pulli, 1988). Furthermore, the success of similar discriminants based on P/L_g ratios has been limited for events in the western U. S. [WUS] (Hutchenson and Kraft, 1986; Taylor *et al.*, 1988). Since the latter studies used actual and/or simulated WWSSN instrument responses, which peak at about 1 Hz, the reasons for the failure of the discriminant may lie either in the lower frequency range considered or in the different propagation characteristics between the WUS and Scandinavia. However, Bennett and Murphy (1986) also found poor performance by a P_g/L_g discriminant for the WUS, suggesting that propagation may be a crucial factor.

To exploit further the capability of regional seismic phases such as P_n , P_g , S_n , and L_g in discrimination problems, it is important to understand fully the excitation and propagation of these phases across a wide variety of tectonic and geological regions for quarry blasts, earthquakes and nuclear explosions. Discriminants may also be strongly affected by regional variations in attenuation properties and crustal structure between each seismic source and the various receivers. One problem is that some regional phases that are prominent along certain paths may be absent along others. For instance, L_g and P_g are often easily observable in tectonically active areas such as

the Western U. S. (Nuttli, 1980), whereas S_n is largely absent in the same region (Molnar and Oliver, 1969). At the same time, P_g is small in eastern North America whereas S_n is prominent, especially at high frequencies. Kennett *et al.* (1985) have reported L_g being observed for some paths to NORESS and not others. A study by Goncz *et al.* (1987) showed a wide variation in the crustal phase characterization expressed in terms of the relative amplitudes and frequency contents of the various arrivals in North America. In addition to the discrimination implications, the propagation of regional phases generated by seismic events is also important to the attenuation corrections used for yield estimates, and to the assessment of detection capabilities.

One reason that the causes of the failures of P/S discriminants are enigmatic is that the reasons for their success are still unknown. Perhaps the most straightforward explanation is that explosions generate less shear energy than do earthquakes (Dysart and Pulli, 1987). This explanation requires that source-generated shear energy dominate over the shear energy generated by scattering. This would also suggest that the failure of the discriminant at intermediate frequencies may be due to scattering by a characteristic scale length heterogeneity or to P-SV modes associated with a characteristic layering, which may produce enough shear energy to give an ambiguous event identification.

However, even a completely isotropic source in a spherical earth will generate some SV energy via $P \rightarrow S$ conversions at the free surface and discontinuities in the lithosphere. Consequently, the above explanation for the success of the P/S discriminant can be tested by applying the discriminant to three-component data, e.g., P_n/S_n . In this case, the shear parameter will measure only the energy generated by the source and by scattering due to lateral heterogeneity. If the relative excitation of shear energy by explosions and earthquakes is the dominant factor in the success of the P/S discriminant, it should provide an improved discrimination capability over purely vertical-component data at high frequencies. Furthermore, since it reduces the contributions to the shear phase from $P \rightarrow SV$ scattering and conversions, it should also improve the discriminant in the intermediate frequency range. The three-component arrays at NORESS and ARCESS may be used for further testing the above hypothesis for the breakdown at intermediate frequencies: three-component array processing (Jurkevics, 1986) should reduce the contribution from near-receiver scattering, which is expected to be a significant portion of the scattered energy.

Conclusions and Recommendations

In order to study the effects of propagation on high-frequency regional discriminants, a database of short and intermediate period seismic data from digital networks and arrays, (regional USGS and NRC networks, the ECTN, the LRSM network and arrays, the RSTN network, and the YKA and LASA arrays), to study the propagation characteristics of regional phases across stable and tectonic provinces of North America (Fig. 1). The variations of spectral ratios between pairs of phases, i.e., P_n/S_n , P_n/L_g , S_n/L_g , and P_g/L_g , at different frequency bands up to 15 Hz will be established. Event characteristics for all types of sources and propagation paths will be compared. Narrow bandpass filters (Goncz *et al.*, 1987) will be applied to each regional phase to

obtain a full characterization of the frequency content in time and frequency domain (Fig. 2). Distribution of the high-frequency content of these phases will be compiled for detection purposes. Spectra of the individual phases will also be computed, and estimates will be made of the scaling law and source spectra.

Events that are observable at several stations are expected to shed light on the distance dependence of the wavetrain as well. The data characterizing the events will consist of descriptions of the absolute and relative amplitudes of the arrivals in various frequency bands and their time domain envelopes (including coda). Ancillary information that may be useful for providing physical explanations for the empirical results (e.g., source depths, types of blasts, path characterization, and source mechanisms) will also be incorporated.

In order to determine the reason for the success of the high-frequency P/S discriminants, as well as possible reasons for their failure at intermediate frequencies, high and intermediate frequency three-component LRSM and RSTN data will be used to test P/S discriminants for regional phases (P_n , P_g , S_n , S_g , L_g) using the rotated transverse component for the shear waves and the radial and/or vertical components for the compressional waves. The same P/S discriminants will be computed for the vertical component as well for comparison. Both high-frequency and intermediate-frequency ratios will be computed, and the relative efficiency of the vertical component and three-component methods will be assessed. NORESS and ARCESS three-component array data will be examined to see if three-component array analysis improves the P/S discriminant at intermediate frequencies by subduing the contribution from near-receiver scattering.

REFERENCES

- Bennett, T. J. and J. R. Murphy (1986). Analysis of seismic discrimination capabilities using regional data from western United States events, *Bull. Seism. Soc. Am.*, **76**, 1069-1086.
- Chun, K.-Y., G. F. West, R. J. Kokoski, and C. Samson (1987). A novel technique for measuring L_g attenuation results from Eastern Canada between 1 to 10 Hz, *Bull. Seism. Soc. Am.*, **77**, 398-419.
- Dysart, P. and J. Pulli (1987). Spectral study of regional earthquakes and chemical explosions recorded at the NORESS array, in *Technical Report C87-03*, Center for Seismic Studies, Arlington, Virginia.
- Dysart, P. and J. Pulli, (1988). Spectral study of regional earthquakes and chemical explosions recorded at the NORESS array, in *Technical Report C88-01*, Center for Seismic Studies, Arlington, Virginia.

- Gonczi J. H., W. C. Dean, Z. A. Der, A. C. Lees, K. L. McLaughlin, T. W. McElfresh and M. E. Marshall (1987). Propagation and excitation of L_g , S_n , and $P-P_n$ waves from Eastern United States earthquakes by regression analysis of RSTN data, *Technical Report TGAL-86-7*, Teledyne Geotech, Alexandria, Virginia.
- Hutchenson, K. and G. Kraft (1986). Maximum likelihood magnitudes and discrimination of regional phases, *Final Report DCS-SFR-86-01*, ENSCO, Springfield, Virginia.
- Jurkevics, A. (1986). Polarization analysis using an array of three-component sensors, in *Technical Report C86-07*, Center for Seismic Studies, Arlington, Virginia.
- Kennett, B. L. N., S. Gregersen, S. Mykkeltveit, and R. Newmark (1985). Mapping of crustal heterogeneity in the North Sea basin via the propagation of L_g -waves, *Geophys. J. R. Astr. Soc.*, **83**, 299-306.
- Molnar, P. and J. Oliver (1969), Lateral variations of attenuation in the upper mantle and discontinuities in the lithosphere, *J. Geophys. Res.*, **74**, 2648-2682.
- Nuttli, O. W. (1980), The excitation and attenuation of seismic crustal phases in Iran, *Bull. Seism. Soc. Am.*, **70**, 469-485.
- Nuttli, O. W. (1986a), L_g magnitudes of selected East Kazakhstan underground explosions, *Bull. Seism. Soc. Am.*, **76**, 1241-1252.
- Nuttli, O. W. (1986b), Yield estimates of Nevada Test Site explosions obtained from seismic L_g waves, *J. Geophys. Res.*, **91**, 2137-2152.
- Taylor, S. R., M. Denny, E. S. Vergino, and R. E. Glaser (1988), Regional discrimination between NTS explosions and western U. S. explosions, *Bull. Seism. Soc. Am.*, (submitted).

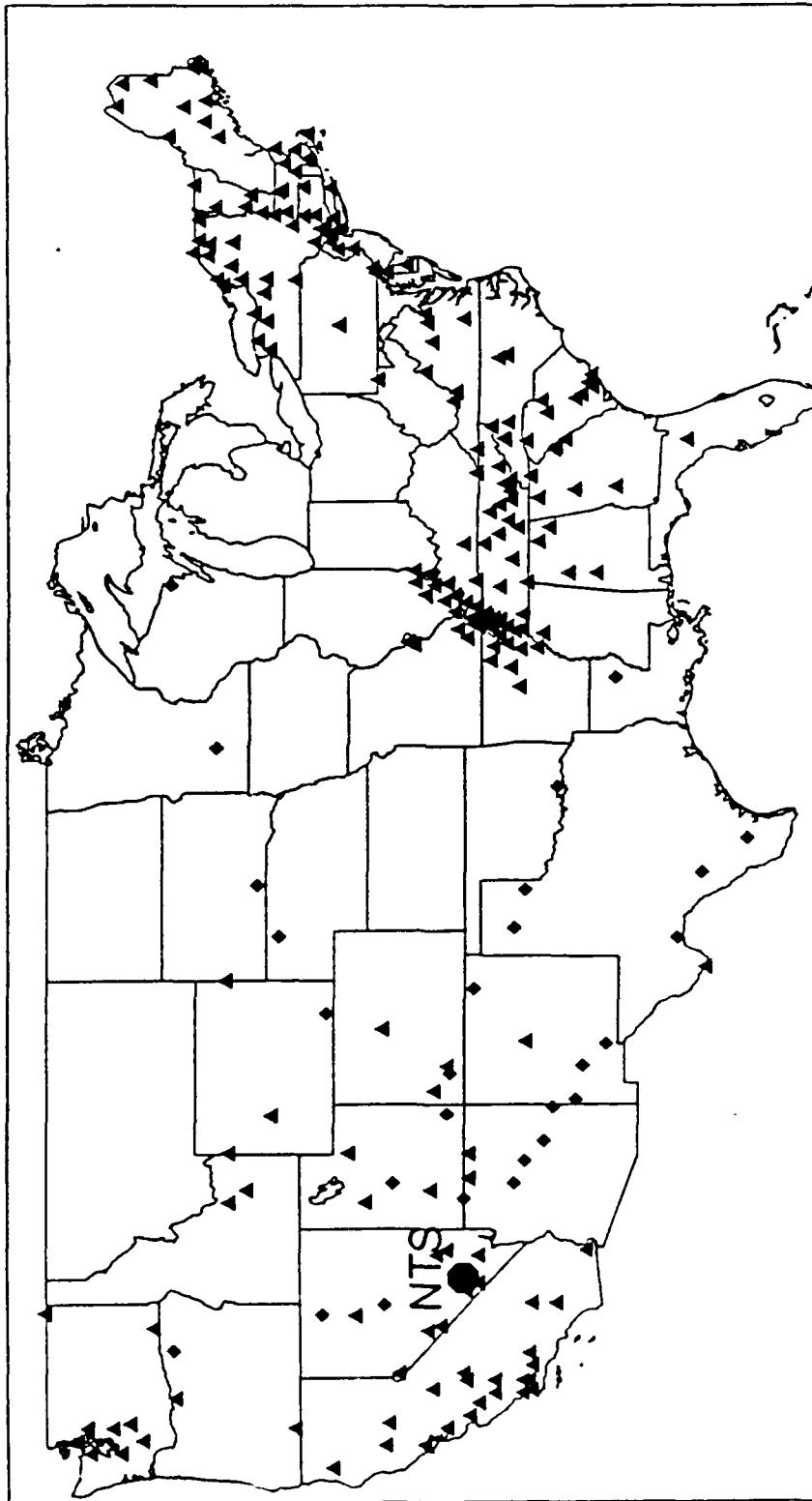


Figure 1. Map of USGS- and NRC-supported regional networks (triangles) and selected linear deployments of LRSM stations (diamonds).

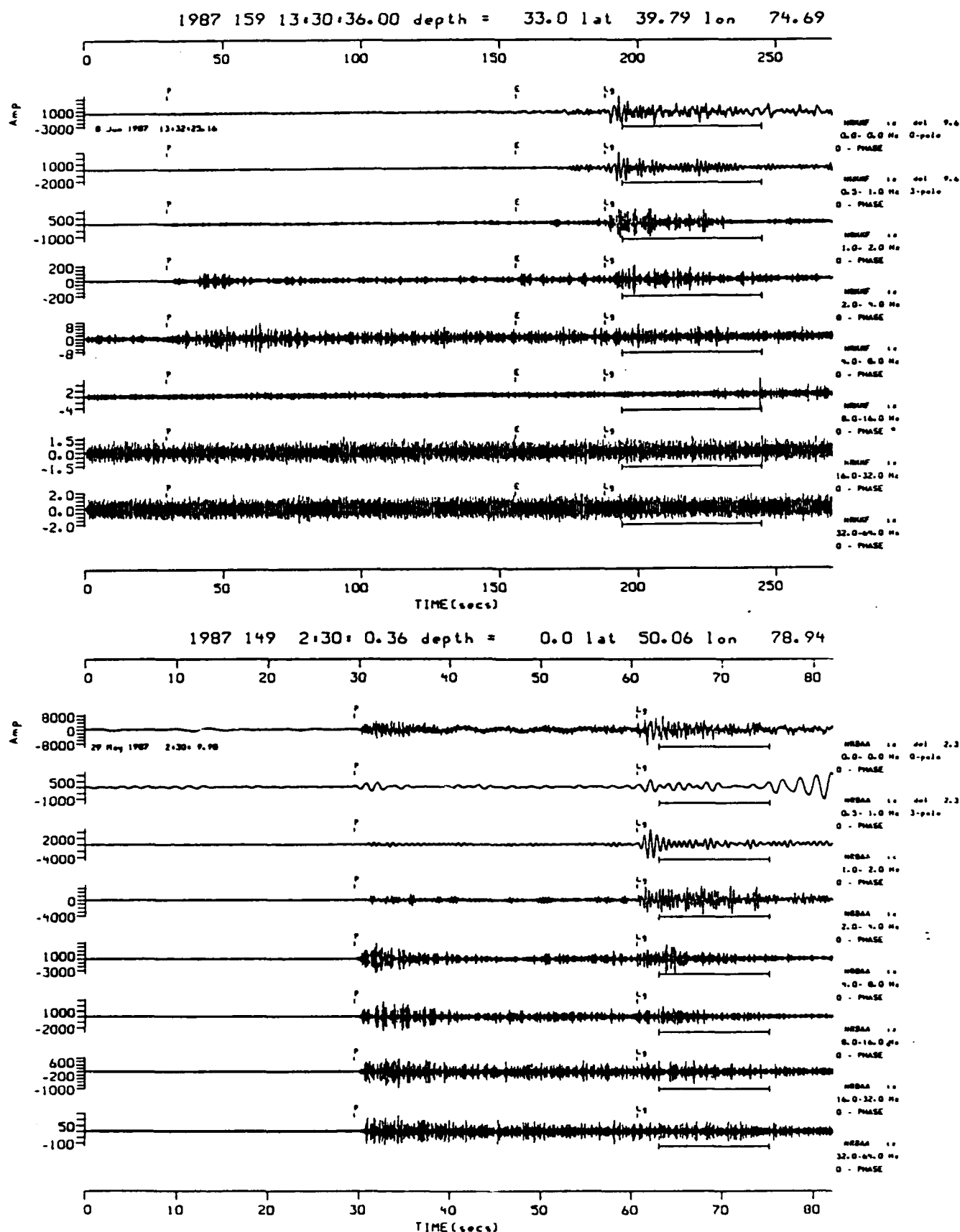


Fig. 2. Bandpassed filtering of a presumed earthquake (top) and explosion (bottom) in the E. Kazakh region indicating the frequency content of each. The explosive P-wave is rich in high frequency energy even up to the 32.0-64.0 Hz passband.

Compressional- and Shear-Wave Polarizations at the Anza Seismic Array

R. Aster, P. Shearer, B. Minster, J. Berger
IGPP, U. C. San Diego A-025, La Jolla, CA 92093

Contract No.: F196628-88-K-0044

Objectives

The proposed use of high-frequency seismic stations for improved seismic monitoring capabilities raises the issue of the effect of near-station structure on the interpretation of high-frequency three-component seismograms. We investigate the polarization behavior of P- and S-wave arrivals between 2 and 60 Hz using local earthquakes recorded by the three-component Anza array. We use a quantitative time domain measure of the linear polarization to address the question of whether seismic polarizations can be modeled in terms of scattering, or whether seismic anisotropy is required.

Summary of Results

We have analyzed earthquakes recorded by the Anza array (Figure 1; Berger, et al., 1982), a three component seismic array located astride the San Jacinto fault zone where it intersects the Southern California Batholith. We observe consistent alignments in initial P- and S-wave particle motions recorded from near-vertically incident energy at stations KNW and WMC throughout the period of operation (Figure 2). To measure the degree and duration of this alignment polarization in an unbiased and automated manner, we form the *normalized data variance tensor* (the covariance matrix, e.g., Kanasewich (1975)).

$$\hat{V} = \langle \hat{x} \hat{x}^T \rangle, \quad (1)$$

where the unit vector sequence $\{\hat{x}\}$ is obtained from the three component data sequence $\{\vec{x}\}$ by

$$\hat{x} = \frac{\vec{x}}{|\vec{x}|}. \quad (2)$$

We use (1) instead of the data variance tensor itself

$$V = \langle \vec{x} \vec{x}^T \rangle \quad (3)$$

because we wish to evaluate a moving window measure of polarization that is unbiased by the sudden changes of amplitude associated with phase arrivals. Such biases are not easily quantifiable and take the form of a time shift of the polarization history as large as half the window length. Using the normalized data variance tensor results in each sample having equal weight and eliminates this source of bias, at a cost of producing a less sharp estimate of when polarization changes occur.

\hat{V} is decomposed to obtain eigenvectors, \hat{e}_i , and associated eigenvalues, l_i , that define an ellipsoid with semi-axes in the \hat{e}_i directions with corresponding lengths $l_i^{1/2}$. The l_i are normalized

$$\lambda_i = \frac{l_i}{l_1 + l_2 + l_3} \quad (4)$$

and the \hat{e}_i and the λ_i are sorted so that

$$\lambda_1 \geq \lambda_2 \geq \lambda_3. \quad (5)$$

The λ_i are physically interpretable as the mean energy in the \hat{e}_i directions for the windowed subsequence. The inequality (5) defines a triangular section T of the plane, P , defined by

$$\lambda_1 + \lambda_2 + \lambda_3 = 1 \quad (6)$$

in $(\lambda_1, \lambda_2, \lambda_3)$ space. The apices of T correspond to the canonical forms:

$$\text{line: } \lambda_1 = 1, \lambda_2 = \lambda_3 = 0 \quad (7)$$

$$\text{circle: } \lambda_1 = \lambda_2 = 1/2, \lambda_3 = 0 \quad (8)$$

$$\text{sphere: } \lambda_1 = \lambda_2 = \lambda_3 = 1/3. \quad (9)$$

Because observed initial polarizations at Anza tend to be linear (Figure 2), we seek a measure of how closely subsequent polarizations agree with this initial direction. Thus, we evaluate a moving-window linearity coefficient, the *directed linearity*, d , where

$$d = l(\hat{a} \cdot \hat{e}_1)^2. \quad (10)$$

l is the *linearity*, a normalized linear function of the eigenvalues that has values near 1 and near 0 for variance tensors that define highly linear and highly oblate ellipsoids, respectively

$$l = \lambda_1 - \lambda_2 \quad (11)$$

\hat{a} is the initial direction of the particle motion following the phase pick, adaptively evaluated for each event (Figures 3a, 3b), and \hat{e}_1 is the eigenvector for the windowed subsequence that has the largest associated eigenvalue, λ_1 . Geometrically, l corresponds to 1 minus the normalized distance along the triangle altitude from the apex of T corresponding to perfectly linear motion (7) (Figure 4a). $(\hat{a} \cdot \hat{e}_1)^2$ thus corresponds to the proportion of \hat{e}_1 power in the \hat{a} direction. d is a quantitative measure of the linearity in the \hat{a} direction from which the degree and duration of linear motion may be measured (Figure 4b). d is plotted as a function of time for the two stations in Figures 5a, 5b, 5c and 5d.

Applying this linearity measure to seismograms from stations KNW and WMC, we make the following general observations for these near-vertically incident arrivals:

- The horizontal projection of the P-wave arrival particle motion does not generally indicate the azimuth to the event (Figure 2).
- The P-wave arrivals at WMC are distinctly linear, while those at KNW show only a weak linear polarization (Figures 3a, 5a).
- The S-wave arrivals have a strong alignment at both stations (more so for KNW) (Figures 2, 3a, 3b). These alignments are significantly different.
- The weak polarization of the P-wave at KNW persists into the P-coda much more so than at WMC (Figures 5a, 5b).
- The duration of linear motion for S-waves is approximately twice as long at WMC than at KNW (Figures 5c, 5d).

Composite compressional first motions from Anza and SCSN are shown in upper-hemisphere stereographic projections in Figure 6. The general tendency (not surprisingly) is for the motions to agree with seismic radiation from right-lateral strike-slip faulting typical of the San Andreas fault system. The far-field S-wave

radiation pattern expected from this double couple source fits the alignment of the initial S-wave polarizations at KNW, but not at WMC (Figure 2).

Conclusions and Recommendations

Based on the above observations, we conclude that shear-wave splitting due to seismic anisotropy is not required to explain the S-wave alignments at KNW, (although the KNW observations unfortunately cover only slightly more than 1/4 of the azimuthal range), because the observed alignments are well-modeled by source radiation and ray tracing. The S-wave alignments at WMC, while not as intense as at KNW, cannot be modeled by source radiation from right-lateral strike-slip faulting, and thus may be influenced by appreciable crustal anisotropy. The alignments in the horizontal plane for the P-arrivals for both stations (which is much more intense at KNW) cannot be explained by simple models of anisotropy, which do not predict this type of behavior for compressional waves, or by source radiation patterns, and must be due to scattering from local inhomogeneities and/or topography. Perhaps significantly, KNW is located on a NE-SW trending ridge that is approximately parallel to the observed alignment, while WMC is located on a flat plain. The decay in the linear motion of the S-wave is also likely to be controlled by scattering at both stations; the arrival of a slower, orthogonally polarized S-wave would not produce the appreciable motion observed on the vertical component and would be expected to result in a more consistent linear interval following the phase arrival. Further study will extend this analysis to the remaining stations of the Anza array and to other high-frequency 3-component data sets.

References

- Berger, J., Baker, L.N., Brune, J.N., Fletcher, F.B., Hanks, T.C., Vernon, F.L., 1982. The Anza array: a high dynamic-range, broad-band, digitally recorded, radio-telemetered seismic array, *Bull. Seism. Soc. Am.* 74,
- Fletcher, J., Haar, L., Hanks, T., Baker, L., 1987. The digital array at Anza, California: Processing and Initial Interpretation of Source Parameters, *J. Geophys. Res.*, 92, No. B1, 369-382.
- Kanasewich, E.R., 1975. Time Sequence Analysis in Geophysics, Univ. of Alberta Press, Edmonton.
- Scott, J.S., Masters, T.G., Berger, J., 1988. Three-dimensional structure of the San Jacinto Fault Zone near Anza, California, *EOS Trans. AGU*, 69.

Earthquakes Recorded by the Anza Array (10/1/82 - 11/24/88)

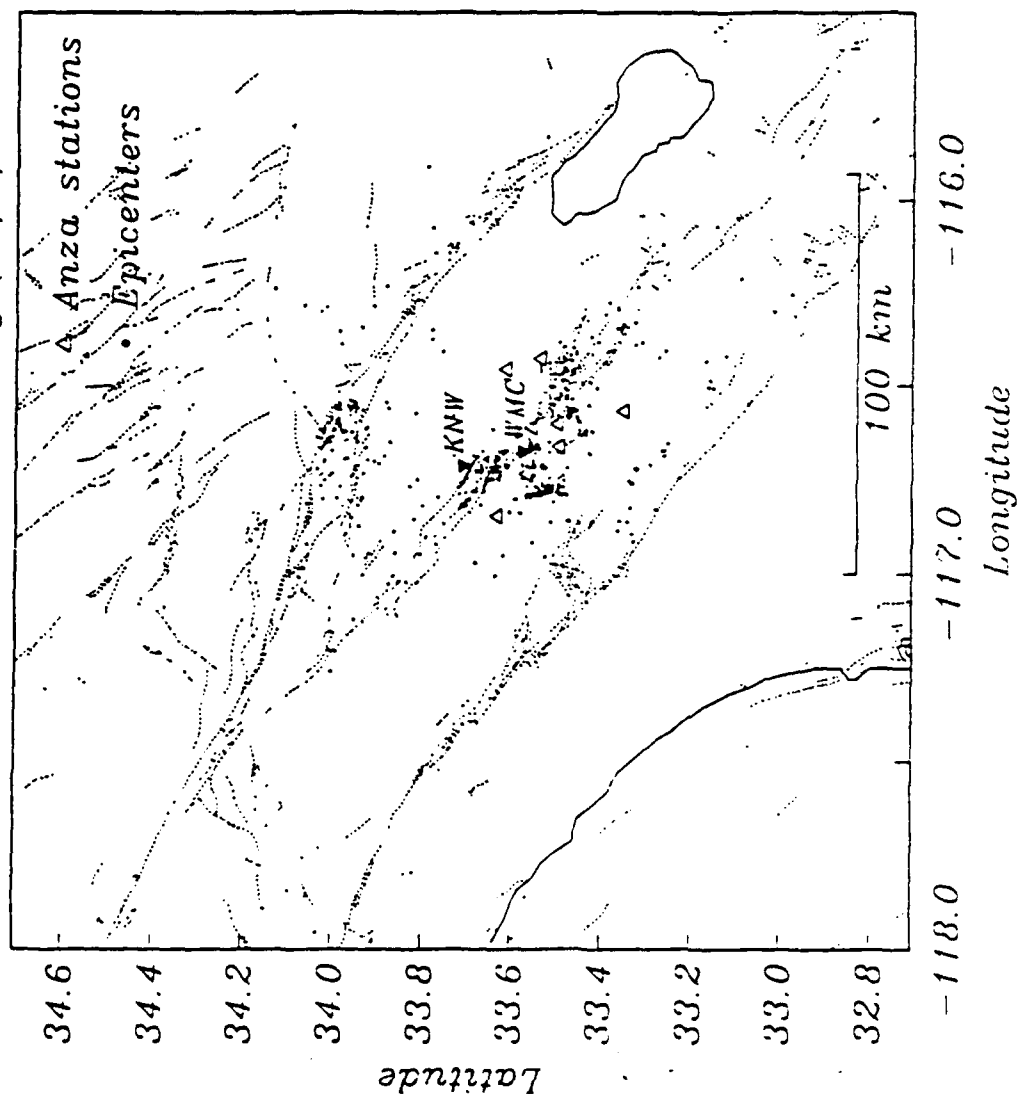


Figure 1. Earthquakes recorded by the Anza array up to 24 November, 1988. Prominent surface faults are shown as well as the Pacific and Salton Sea coastlines. Arrival times from 13 USGS-California Institute of Technology Southern California Seismic Network (SCSN) were used along with readings from the 10 Anza stations to obtain these locations. The 1-dimensional velocity model of Scott et al. (1988) was used. KNIW and WMC, stations discussed in the text, are noted. The three prominent parallel NW to SE fault zones indicated are (from W to E) the Elsinore, San Jacinto and San Andreas.

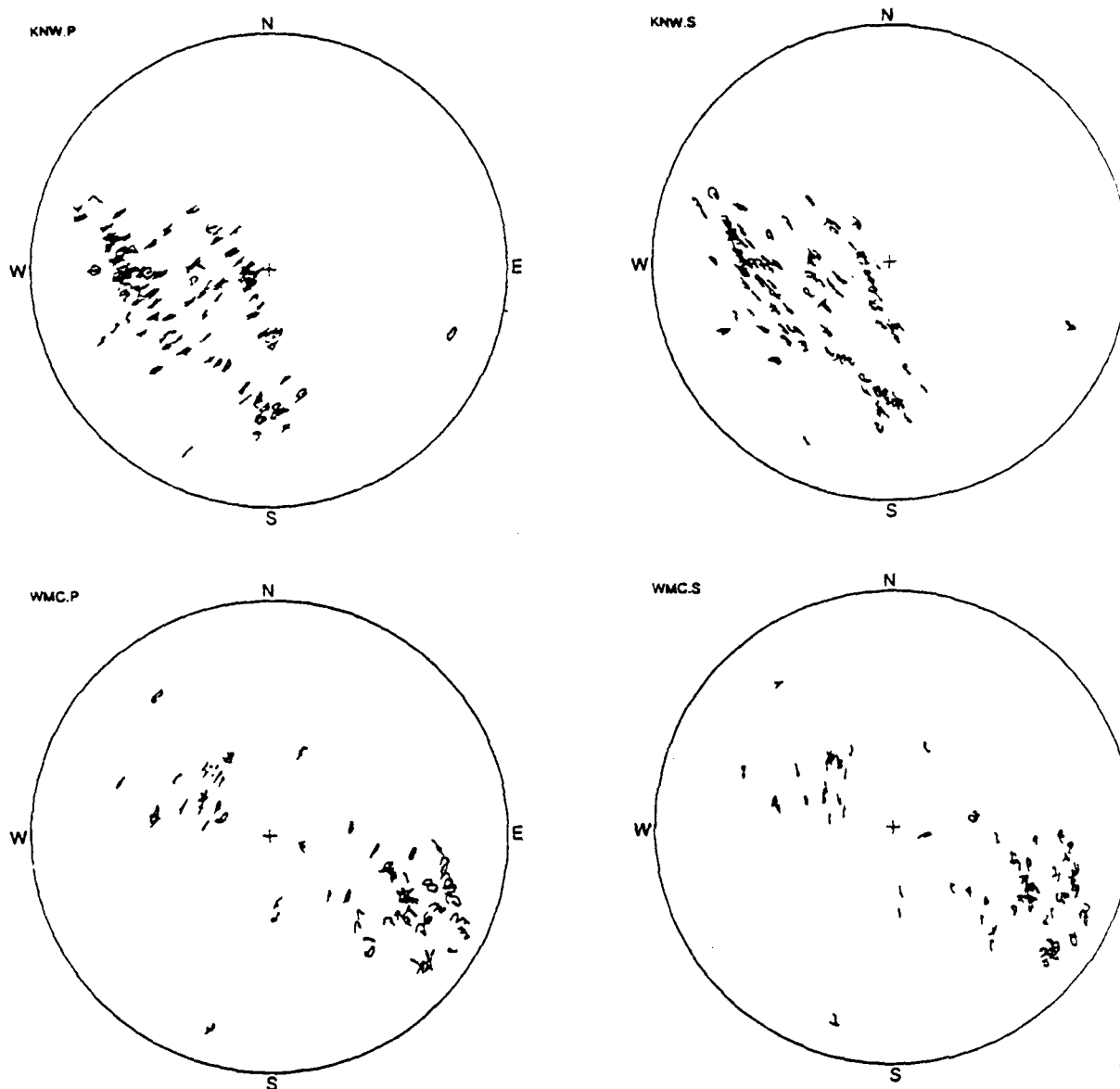


Figure 2. Initial (20 samples (.08 s) after the pick time) particle motions in the horizontal plane for earthquakes recorded at the Anza array stations KNW (127 events) and WMC (80 events) between October, 1982 and November, 1987. To minimize the contamination of phases by S to P and P to S conversions at the free surface and at any underlying horizontal interfaces, these events were chosen to have straight-line station-to-hypocenter angles of less than or equal to 45° from vertical. The self-scaled horizontal projection of the particle motions are plotted on a polar projection, where the plot azimuth is equal to the event azimuth relative to the station and the plot radius is proportional to the dip angle. The perimeter corresponds to a dip angle of 45° . Note the general alignment in initial motion for both P and S arrivals, and especially that the P particle motions at both stations do not lie in the idealized SV plane and hence do not indicate the earthquake azimuth.

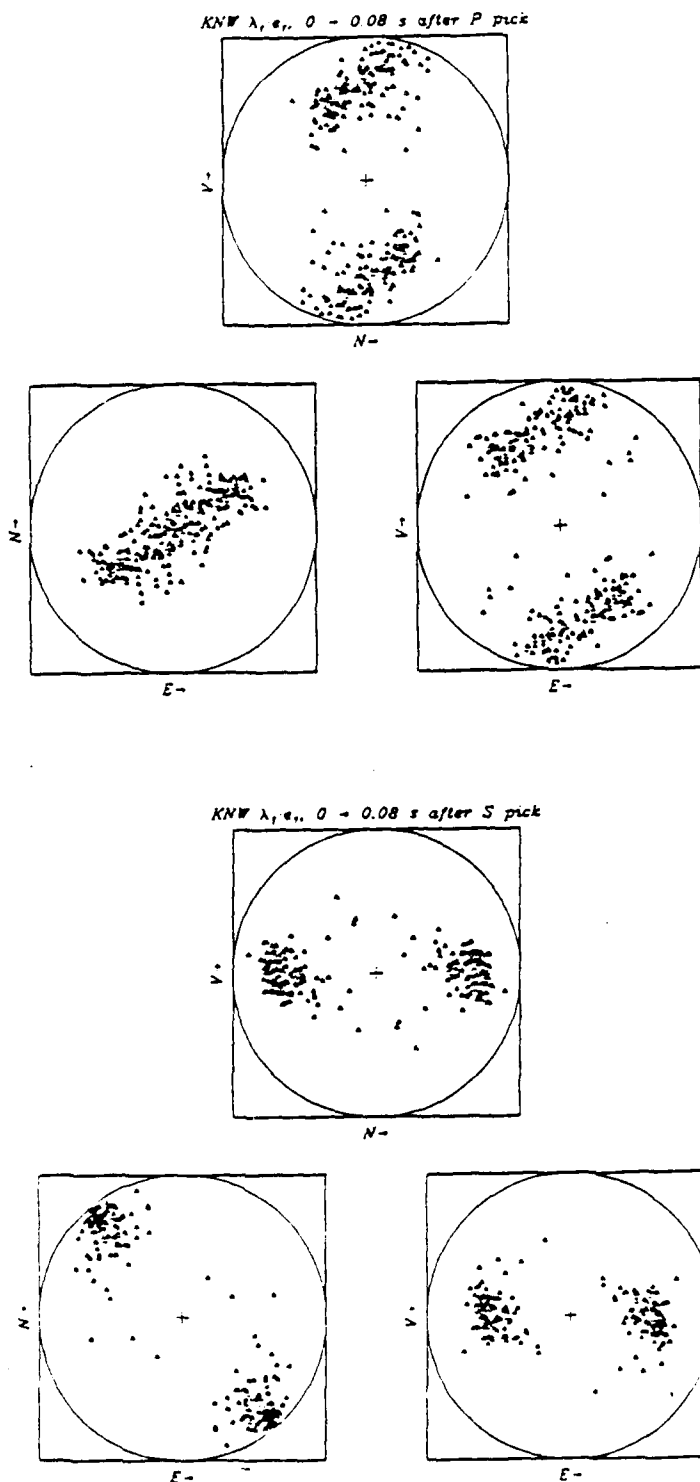


Figure 3a. Scaled eigenvectors, $\lambda_1 \hat{e}_1$, corresponding to the largest eigenvalues from the eigenvector-eigenvalue decomposition of the data variance tensor (3) for P- and S wave arrivals for the 127 KNW events shown in Figure 2. Two origin-symmetric points are plotted for each eigenvector, indicative of the 180° ambiguity in the semiaxes of the ellipsoidal variance tensor. The vectors are displayed in three orthogonal views, with the limb of the unit sphere indicated in each case. The window used was 20 samples (.08 s) beginning at the USGS S-pick. Note the highly oriented S-wave arrivals relative to the P-wave arrivals. We use (3) instead of (1) here because we are interested only in measuring the eigenvector direction and not in timing polarization changes.

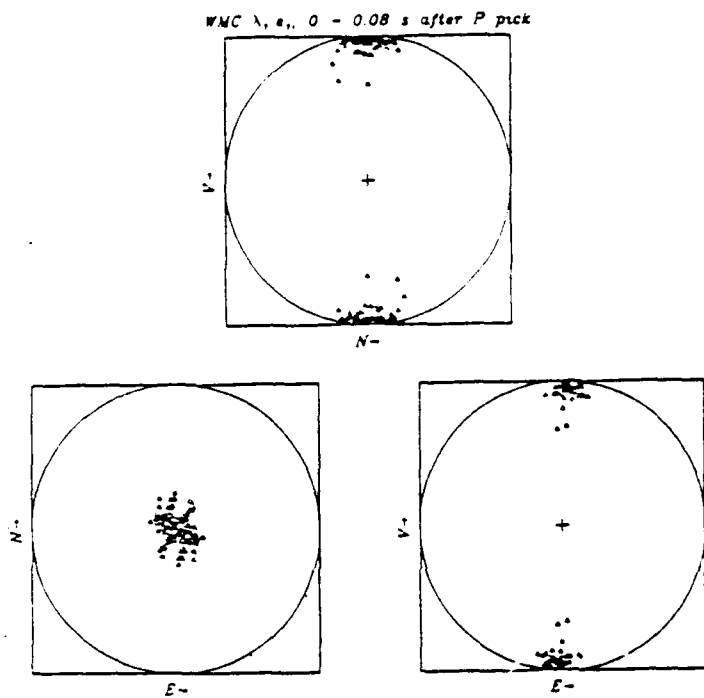
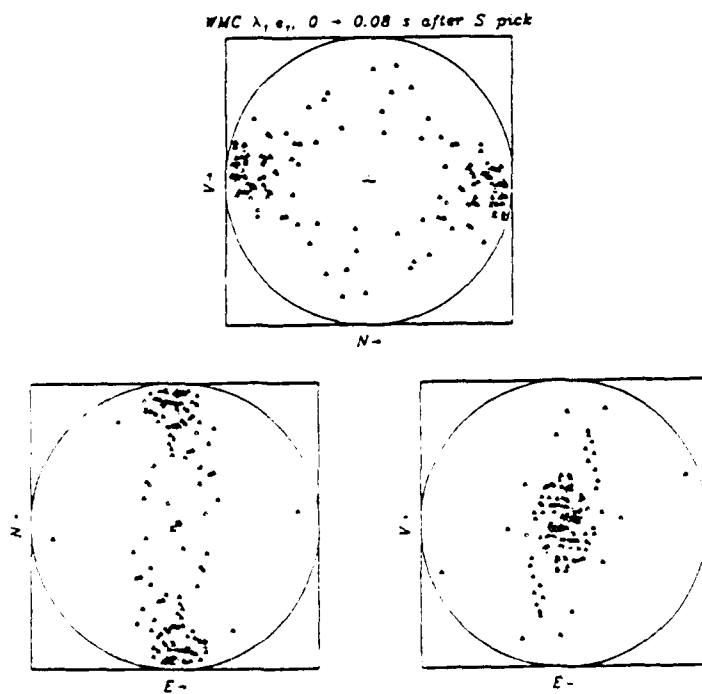


Figure 3b. Scaled eigenvectors, $\lambda_1 \hat{e}_1$, for P- and S-wave arrivals for the 80 WMC events shown in Figure 2. The window used was 20 samples (.08 s) beginning at the USGS S-pick.



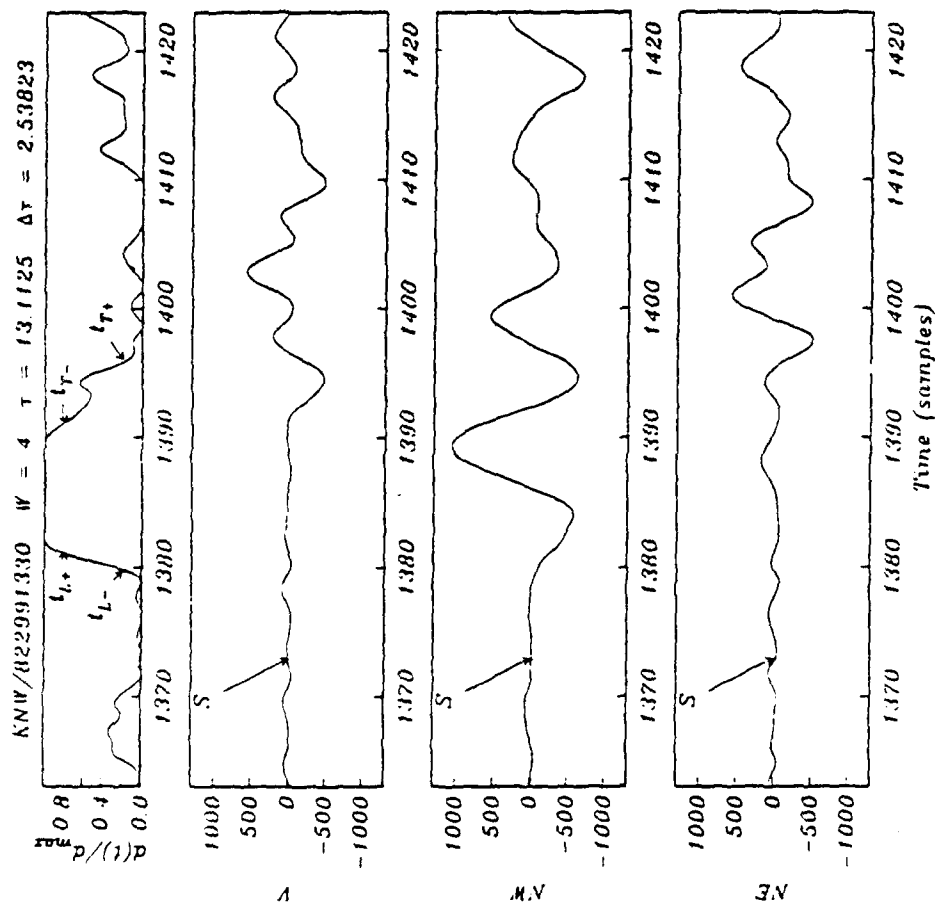
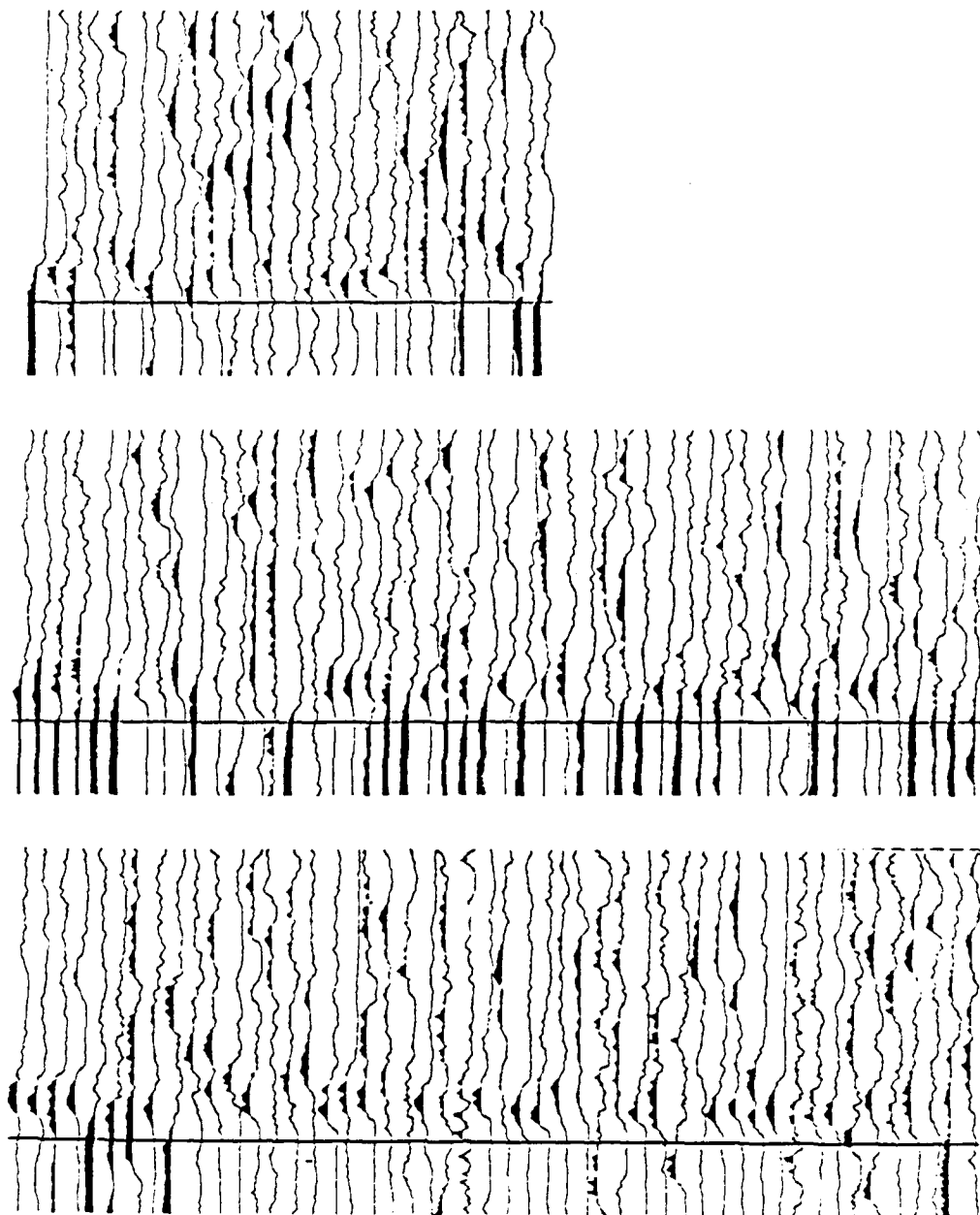


Figure 4b. The directed linearity, d , normalized by its maximum value, for a S-wave recorded at station KNW. The window length used was 4 samples. The leading and trailing edges of the linear particle motion period have been estimated with error bars by locating the 20% and 80% of maximum levels on the leading and trailing edges. Note that the leading edge provides a better estimate of the S arrival time than the indicated USGS pick. The components plotted are those deployed in the Anza array (Vertical, NW (parallel to the San Jacinto fault), NE (perpendicular to the San Jacinto fault)) (Figure 1). The NW component also corresponds approximately to the mean direction of initial S-wave motion for this station (Figure 2, Figure 3a). The decay of the linear portion of the S-wave is due to energy in the vertical direction as well as in the horizontal plane. We have found this to be typical for events at both stations.

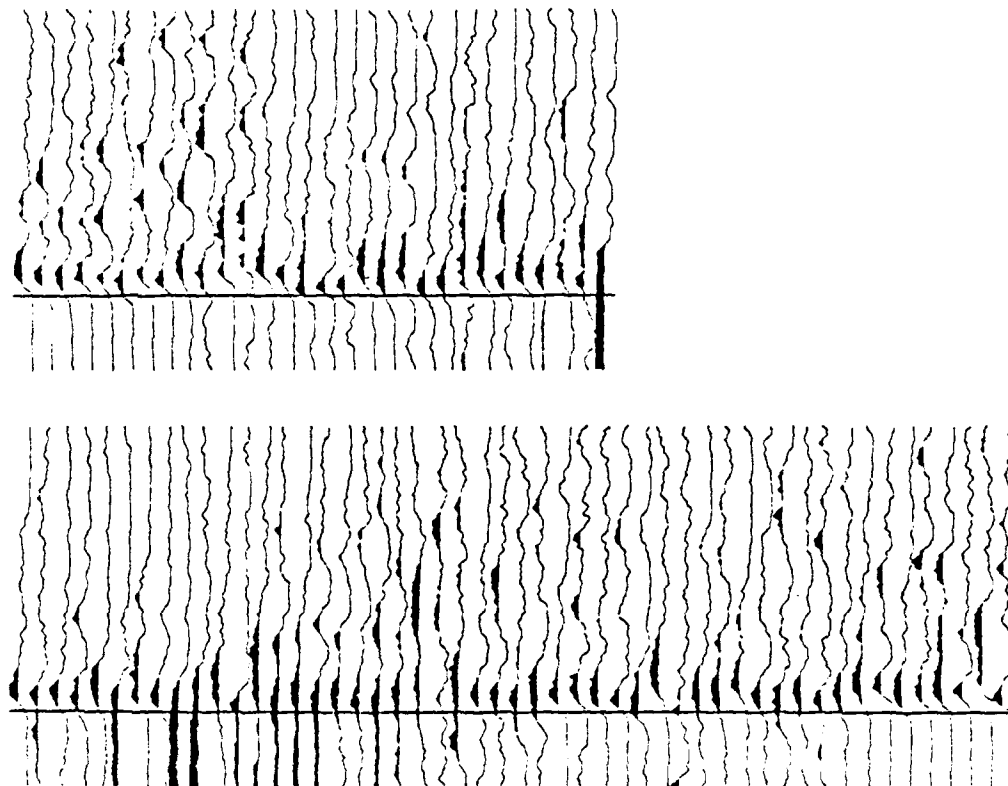
KNW P-wave Directed Linearity (127 events)



1 second

Figure 5a. d/d_{\max} from a 20 sample (.08 s), zero lag moving window in the vicinity of the P-wave for 127 events recorded at KNW. The total trace length is 250 samples (1 s). The vertical line indicates the USGS P-wave pick (Fletcher et al., 1987) and values above 0.5 have been filled. The polarization of these arrivals is quite weak; in several cases the prearrival noise is significantly more polarized than the P-arrival due to slightly higher noise on one component. Note that the weak polarization persists into the P-wave coda somewhat longer than at WMC (Figure 5b).

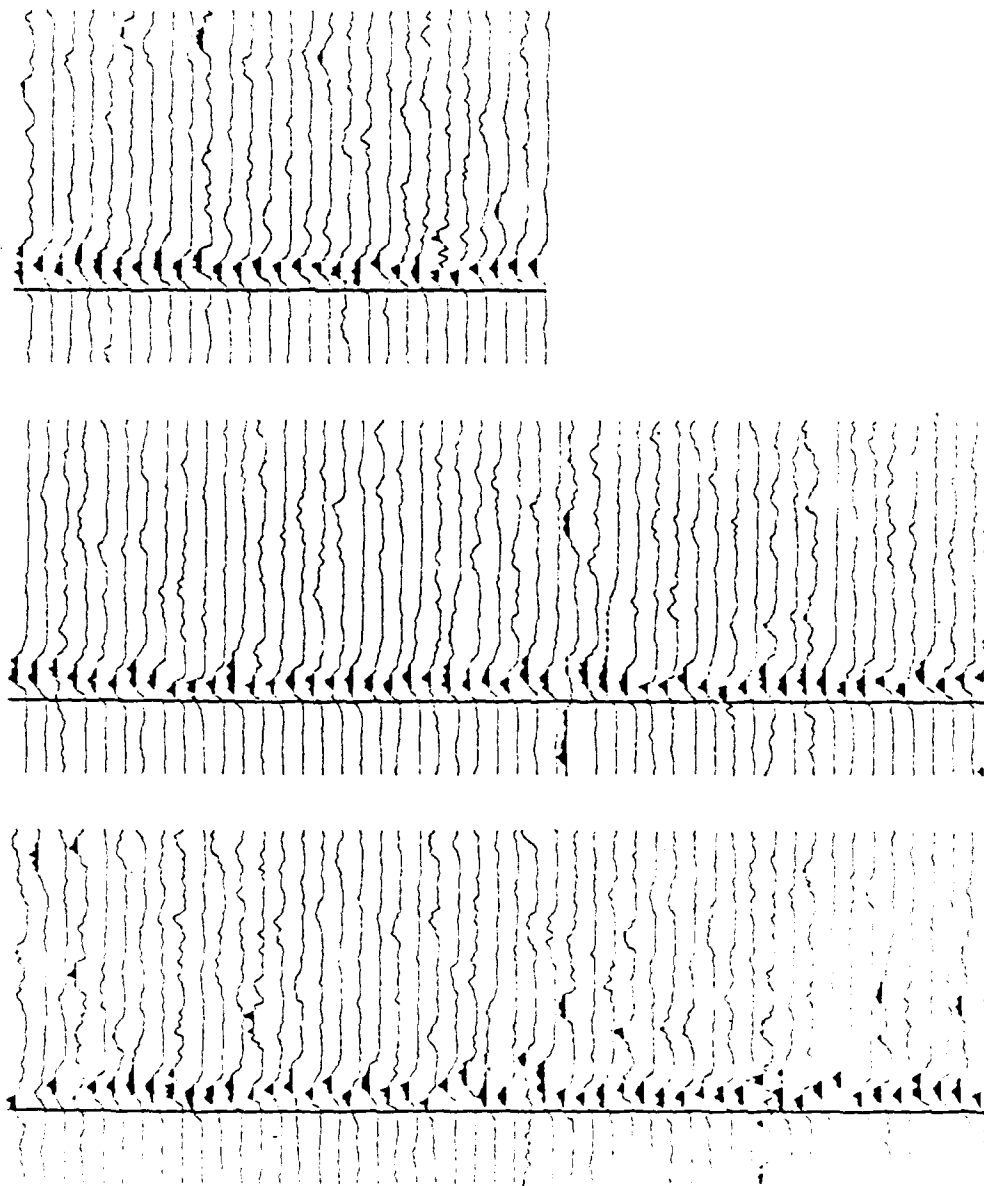
WMC P-wave Directed Linearity (80 events)



1 second

Figure 5b. d/d_{max} from a 20 sample (.08 s), zero lag moving window in the vicinity of the P-wave for 80 events recorded at WMC. The total trace length is 250 samples (1 s). The vertical line indicates the USGS P-wave pick (Fletcher et al., 1987) and values above 0.5 have been filled.

KNW S-wave Directed Linearity (127 events)



1 second

Figure 5c. d/d_{max} from a 20 sample (.08 s), zero lag moving window in the vicinity of the S-wave for 127 events recorded at KNW. The total trace length is 250 samples (1 s). The vertical line indicates the USGS S-wave pick (Fletcher et al., 1987) and values above 0.5 have been filled. Note the highly linear first arrivals for the majority of the events. The initial linear motion (as measured in Figure 4) persists for approximately 10 - 25 samples (.04 - .10 s).

WMC S-wave Directed Linearity (80 events)

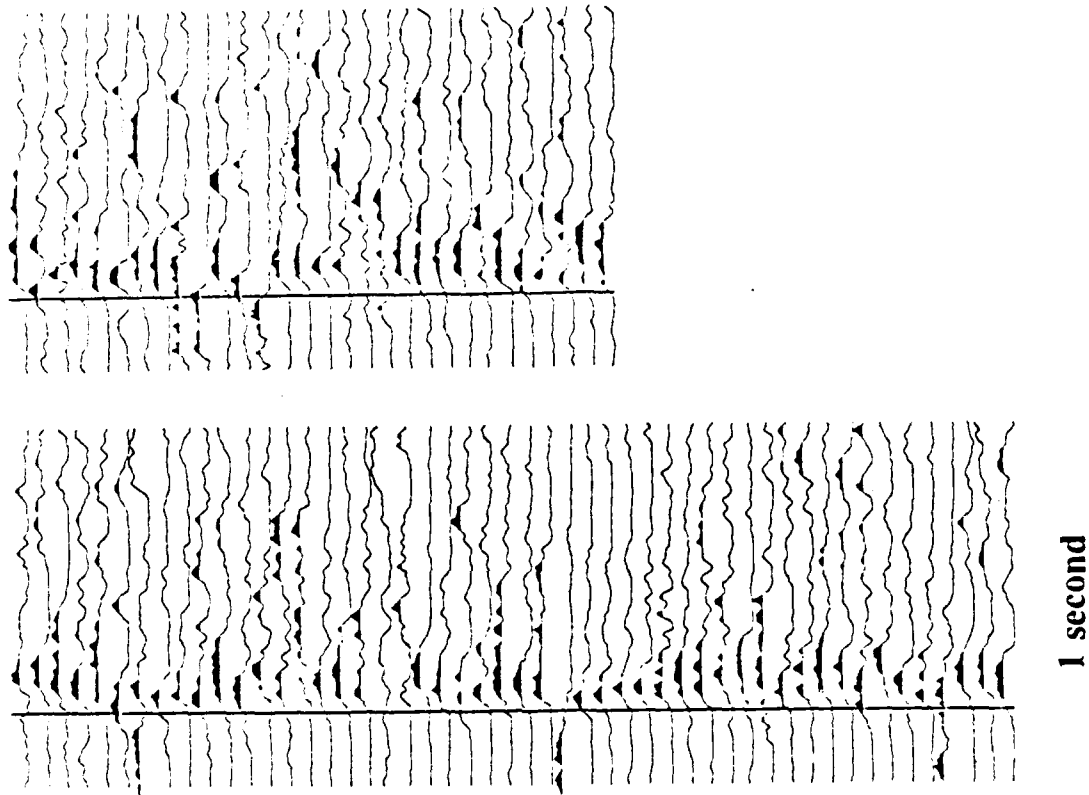


Figure 5d. d/d_{\max} from a 20 sample (.08 s), zero lag moving window in the vicinity of the S-wave for 80 events recorded at WMC. The total trace length is 250 samples (1 s). The vertical line indicates the USGS S-wave pick (Fletcher et al., 1987) and values above 0.5 have been filled. The linear motion is much less pronounced compared to KNW (Figure 5c) and is more persistent. The initial linear motion (as measured in Figure 4) persists for approximately 15 - 50 samples (.06 - .20 s).

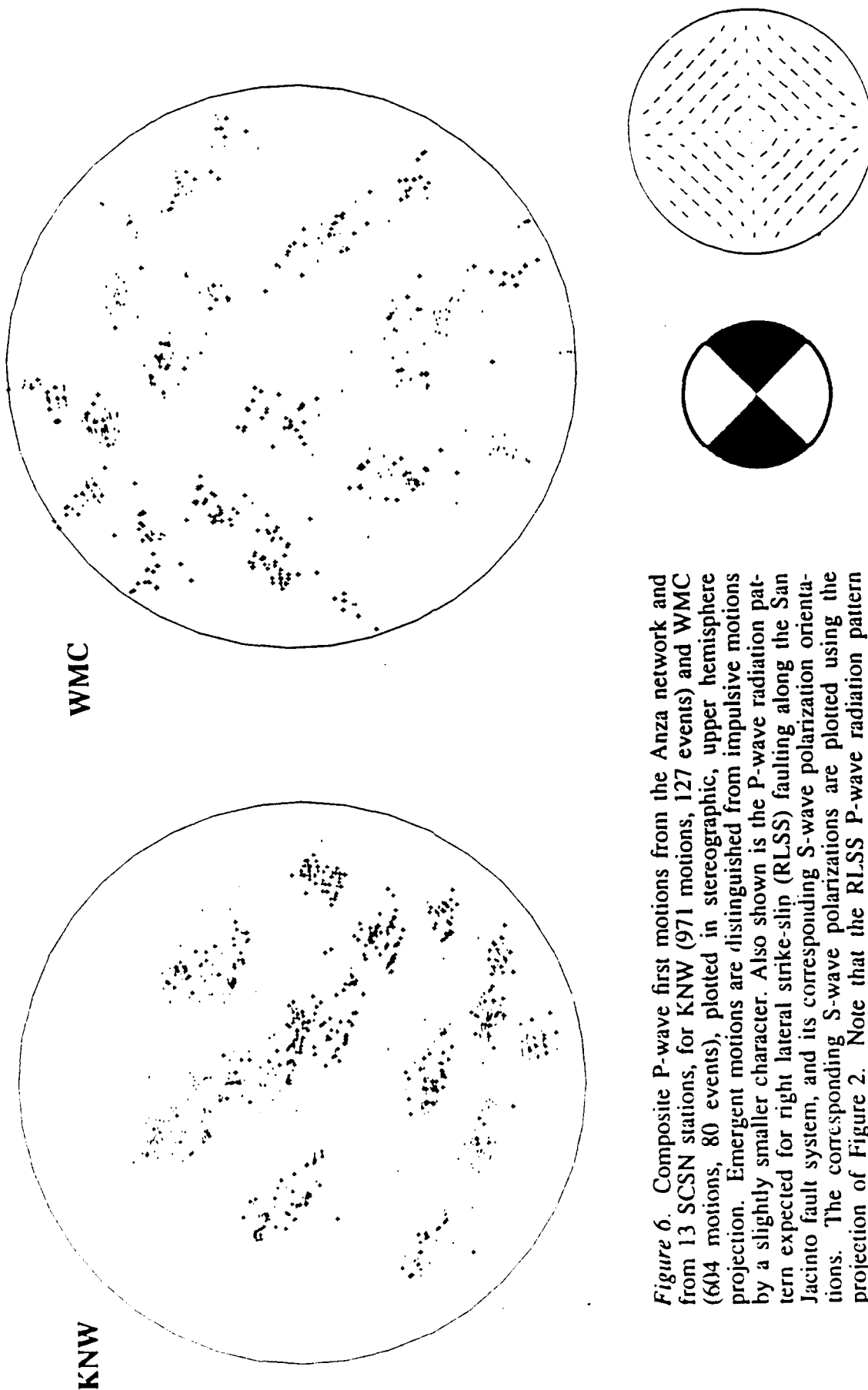


Figure 6. Composite P-wave first motions from the Anza network and from 13 SCSN stations, for KNW (971 motions, 127 events) and WMC (604 motions, 80 events), plotted in stereographic, upper hemisphere projection. Emergent motions are distinguished from impulsive motions by a slightly smaller character. Also shown is the P-wave radiation pattern expected for right lateral strike-slip (RLSS) faulting along the San Jacinto fault system, and its corresponding S-wave polarization orientations. The corresponding S-wave polarizations are plotted using the projection of Figure 2. Note that the RLSS P-wave radiation pattern agrees approximately with the observed P-wave first motions for both stations (42 events are common to both stations) and fits the observed S-wave polarizations for KNW (Figure 2). The RLSS S-wave polarization orientations do not, however, predict the alignments seen in the initial S-wave motions at WMC (Figure 2). (Figures 2, 3a and 3b).

A GENERALIZED BEAMFORMING APPROACH TO REAL TIME
NETWORK DETECTION AND PHASE ASSOCIATION

Frode Ringdal and Tormod Kværna

NTNF/NORSAR, P.O. Box 51, N-2007 Kjeller, Norway

Contract No. F49620-89-C-0038

Objective

The objective of this study is to investigate methods for multi-array detection, phase association and location, using as primary data sources the three regional arrays (NORESS, ARCESS, FINESA) in Fenno-scandia. The emphasis is on approaches which are suitable for incorporation in an expert system environment. As part of this effort, the problem of continuously monitoring the regional seismic noise field is also addressed, with the purpose to obtain a quantitative assessment of the upper limit of magnitudes of seismic events that would go undetected by such a network.

Summary

General approach

In the processing of seismic network data, individual phase detections corresponding to the same seismic event must be properly associated and grouped together. This is today usually done starting with an initial trial epicenter and then applying various search strategies supplemented by combinational techniques.

This paper presents, and gives examples of application of, a method for associating phase detections from a network of stations, which is analogous to the conventional delay-and-sum beamforming commonly applied in array detection processing. A number of beams are steered to a predefined grid of aiming points in a geographical space. Each beam has an associated set of time delays, where each delay corresponds to the predicted travel time for a given phase at a given station.

We assume that the data of each network station is initially subjected to a detection processing procedure, whereby a list of phase detections and attributes is generated. The beamforming process, for a given beam, at time T , can be described as looking for a pattern of detections/non-detections that matches the predicted pattern for a hypothetical event with origin time T and location within the beam region. The actual beam value is derived from probabilistic considerations, and in essence describes how well the observed pattern matches the prediction. By moving along the time axis, we thus obtain a beam trace that can be subjected to standard threshold algorithms for detection. The process can be supplemented by various individual "quality of fit" measures calculated at each time point.

After processing individual beams as described above, a grouping/ reduction process is applied to the set of all beam detections to eliminate side lobe detections. This then results in an event list, comprising origin times, locations and a list of associated phases. Further refinement can then be achieved by standard techniques for accurate hypocenter determination, magnitude computation, final consistency check, etc.

The generalized beamforming approach also provides a convenient tool to monitor continuously the seismic noise field associated with a given beam. An application of particular interest in a monitoring situation would be to calculate, at each step in time, upper confidence limits for the magnitude of non-detected events for each beam. This would be useful to obtain a realistic assessment of actual network detection capabilities, at any given point in time. The paper presents an example of practical application of this approach.

Regional phase association

The method has been applied to a data base comprising 24 hours of recordings from the regional arrays NORESS, ARCESS and FINESA, with a beam deployment covering Fennoscandia and adjacent areas.

A RONAPP-type detector was first applied to each array individually, using the broad-band F-K method to obtain phase velocity and azimuth for each detected phase. The resulting detection lists then provided the input to the network processor.

The beam grid used for network processing is shown in Figure 1, and comprises altogether 121 aiming points, approximately equally spaced. Typical distance between aiming points is 150 km.

In the network beamforming process, a simple model of assigning 0/1 probabilities to individual phases at each station was used. We required that estimated phase velocities, azimuth, dominant frequency and arrival times fall within predefined ranges for a phase detection to be accepted for a given beam. These tolerance ranges are specified in Table 1. Note in particular that only very general criteria are applied, and we have made no attempt to optimize performance by regionalization.

With this simplified model, the network beamforming process in practice was reduced to, for each beam and each time T, counting the number of phase matches for a hypothetical event located in the beam region and having origin time T. The detection threshold was set equal to 2. Thus, all occurrences of two or more matching phase detections were flagged as potential events. A typical beam trace is shown in Figure 2.

A grouping procedure was then applied to the overall beam detection list. This was done by successively linking together entries in the beam detection list in such a way that a new entry would be linked if it had at least one individual phase detection in common with a previous entry in the group. The maximum allowable duration of a group was set to 10 minutes (in practice, the longest duration was 7 minutes for this data set). In order to resolve obvious multiple events, groups were split up if two P-detections from the same array occurred with more than 30 seconds arrival time difference.

The results are summarized in Table 2. It is important to note that the total of 91 groups comprise all possible events that could be associated, given the station detection lists. Also, a scrutiny of the data shows that only 3 of these groups contain multiple events, all of these being small presumed mining explosions seen by one array only.

Some of the entries in Table 2, e.g., those generated from two secondary phases, are probably questionable seismic events, and even if real, many be impossible to locate accurately. An upper magnitude limit could be estimated for such events, in order to determine whether further detailed analysis is desirable. However, the large majority of the entries appear to correspond to real seismic events, and the grouping procedure facilitates the subsequent detailed analysis of the associated phases.

The network beamforming procedure gives an initial estimate of event location by selecting the "best beam" in each group. This is defined as the beam with the greatest number of associated phase detections, and if equality, the smallest average time residual of the detected phases. Since the initial beam grid is very coarse, we applied a beampacking algorithm for each detection group, using a grid spacing of 20 km in order to improve the location estimate.

The results of this automatic procedure are shown in Table 3 for those events for which independent location estimates were available. We note that the estimates are very consistent (median difference 40 km), and thus the beam results can be used as a reasonable first estimate of event location. For more accurate results, available techniques for accurate hypocenter location (e.g., TTAZLOC) should be used.

Continuous monitoring of upper event magnitude limits

As a second application of the generalized beamforming procedure, we now address the problem of monitoring the noise levels on each beam, and use this information to assess the size of events that might go undetected.

In formulating the approach, we consider a given geographical location, and a given "origin time" of a hypothetical event. Assume that N seismic phases are considered (there might be several stations and several phases per station).

For each phase, we have an estimate S_i of the signal (or noise) level at the predicted arrival time. For P-phases, S_i might be the maximum STA value (1 second integration window) within ± 5 seconds of the predicted time. For Lg, S_i might be the average STA value over a 10-20 seconds window.

We assume that the network has been calibrated (or alternatively that standard attenuation values are available), so that magnitude correction factors (b_i) are available for all phases. Thus, if a detectable signal is present:

$$m_i = \log (S_i) + b_i \quad (i = 1, 2, \dots, N)$$

Here, m_i are estimates of the event magnitude m . Statistically, we can consider each m_i as sampled from a normal distribution (m, σ). (A standard value of $\sigma = 0.2$ seems reasonable for a small epicentral area.)

Let us now assume a "noise situation", i.e., that there are no phase detections corresponding to events at the given location for the given origin time.

We then have a set of "noise" observations a_i , where

$$a_i = \log(S_i) + b_i \quad (i = 1, 2, \dots, N)$$

If a hypothetical event of magnitude m were present, it would have phase magnitudes m_i normally distributed around m . We know that for each phase,

$$m_i \leq a_i \quad (i = 1, 2, \dots, N)$$

Let us look at the function

$$f(m) = \text{Prob}(\text{all } m_i \leq a_i \text{ / event magnitude } m)$$

For each phase

$$f_i(m) = \text{Prob}(m_i \leq a_i / m) = 1 - \Phi\left(\frac{m - a_i}{\sigma}\right)$$

where Φ is the standard (0,1) normal distribution.

Thus, assuming independence,

$$f(m) = \prod_{i=1}^N f_i(m)$$

The 90 per cent upper limit is then defined as the solution of the equation $f(m) = 1 - 0.90$

It is important to interpret the 90 per cent limit defined above in the proper way. Thus, it should not be considered as a 90 per cent network detection threshold since we have made no allowance for a signal-to-noise ratio which would be required in order to detect an event, given the noise levels. Rather, the computed level is tied to the actually observed noise values, and to the fact that any hypothetical signal must lie below these values. Our 90 per cent limit represents the largest magnitude of a possible hidden event, in the sense that above this limit, there is at least a 90 per cent probability that one or more of the observed noise values would be exceeded by the signals of such an event.

As an application of the method, we selected an area as shown in Figure 3 situated at similar distance from the three arrays. For each of the three arrays, one Pn beam and one Lg beam were steered to this location. The beam traces were filtered using the frequency bands 3-5 Hz (Pn) and 2-4 Hz (Lg). Magnitude calibration values (b_i) were obtained by processing previously recorded events of known magnitude (M_L) and at similar distance ranges, and then determining b_i values independently for Pn and Lg.

Based on these input traces from the three arrays, a network beam was then formed, using time delays for each phase that corresponded to the given location. Arrival time tolerances were set to ± 5 seconds for P-phases and ± 10 seconds for secondary phases. This is roughly consistent with a beam radius of 50 km as shown on the figure.

We chose to analyze a 3 1/2 hour interval during which four regional seismic events of $M_L > 2.0$ were reported in the Helsinki bulletin. No events were reported near the beam area in this period. Figure 4 shows 90 per cent upper magnitude limits as previously defined, plotted as a function of time. In this figure, only the Pn phase has been used, and the three arrays are shown individually and in combination (bottom trace).

It is clear from Figure 4 that when considering individual arrays only, there are several possible time intervals when relatively large events ($M_L \sim 2.0-3.0$) might go undetected because of signals from interfering events. However, when the Pn phases are combined, these instances occur much more seldom.

Figure 5 shows a similar plot, but this time including both the Pn and the Lg phase for each array. Even on an individual array basis, this causes substantial reduction in the upper magnitude limits. For the combined plot (bottom trace of Figure 5), which takes into account all 6 Pn and Lg phases from the three arrays, we see that the upper limit is well below $M_L = 2.0$ for the entire time interval. Thus, we may conclude that, at the specified level of confidence, no event of $M_L = 2.0$ or higher occurred in the beam region during the time period considered.

Conclusions

With regard to phase association, the generalized beamforming technique provides an effective method to group all combinations of individual phase detections that could possibly correspond to the same seismic event. At the same time, preliminary estimates of epicenter and origin time are obtained.

The primary importance of this would be to obtain a starting point for subsequent detailed interactive analysis aimed at precise determination of source parameters. In particular, expert system approaches (either script-based or rule-based) could be invoked at this stage. The advantage of applying the generalized beamforming as the first step is to reduce the amount of combinational processing that would be necessary otherwise. It is here noteworthy that the processing load when applying generalized beamforming increases in a linear fashion when the number of individual phase detections increase, whereas combinational possibilities tend to increase exponentially. While we have in this paper used only a three-array network, the extension to larger networks is clearly straightforward.

The application of the method to provide continuous monitoring of upper magnitude limits at specified beam locations provides a useful supplement to standard statistical network capability studies. In particular, this application would give a way to assess the possible magnitude of non-detected events during the coda of large earthquakes. In such situations, it would be appropriate to use global network data and include as many relevant phases as possible for each network station. For example, while an expected P phase at a given station may be obscured by the earthquake coda, later phases such as

PcP or PP may be less influenced, and the noise level at their respective expected arrival times would therefore provide important information as to the size of possible undetected events.

As a final comment, we note that the approach presented here to upper limit magnitude calculation could be applied to extend the utility of various discriminants, such as $M_s:m_b$. For small explosions, surface waves frequently are too weak to be observed at any station of the recording network. Obtaining reliable upper bound on M_s in such cases would expand the range of usefulness of this discriminant. In practice, an "upper bound" for single-station measurements has often been given as the "noise magnitude" at that station, i.e., the M_s value that corresponds to the actually observed noise level at the expected time of Rayleigh wave arrival. The proposed procedure will include this as a special case of a more general network formulation.

In future studies, we plan to investigate the application of more sophisticated probabilistic models in the generation of beam traces and the continuous extraction of features associated with the individual beams. Application to larger networks, including teleseismic monitoring using global network data, will also be considered.

	Phase Type				
	Pn	Pg	Sn	Lg	Rg
Distance interval ¹⁾ (km) for which a phase is accepted	160-3000	0-600	160-3000	0-2000	0-400
Maximum allowable deviation from predicted arrival time (s)	15	20	30	35	40
Maximum allowable azimuth deviation (degrees)	20	20	20	20	20
Acceptance limits for apparent phase velocity (km/s)	5.8-14	5.8-10	3.2-5.8	3.0-5.0	2.5-3.7
Acceptance limits ²⁾ for dominant frequency (Hz)	0.5-20	0.5-20	0.5-20	0.5-20	0.5-20

1) For NORESS, the Rg phase is not included in the phase table

2) For FINESA, a lower frequency limit of 0.9 Hz is used for all phases.

Table 1. Acceptance limits for parameters used in the network beamforming process.

Number of phase groups:		Number of phases for best beam in each group						
		2	3	4	5	6	7	8
NORESS only	18	13	4	1	0	0	0	0
ARCESS only	34	19	10	4	1	0	0	0
FINESA only	14	13	1	0	0	0	0	0
Two arrays	17	9	4	3	0	1	0	0
Three arrays	8	0	0	2	0	1	3	2
Totals	91	54	19	10	1	2	3	2

Table 2. Phase groups associated by the network beamforming procedure for a 24-hour interval.

Event No.	Date	Time	Network		Mag. M _L	No. of phases	No. of arrays	Beamforming		'Error' (km)
			Lat.	Lon.				Lat.	Lon.	
1	88/03/17	08.40.25.0	57.73	11.03	2.5	7	3	57.9	10.4	39
2	"	08.46.18.7	58.07	11.36	2.6	6	2	57.9	10.8	36
3	"	09.07.10.3	58.08	11.43	2.7	8	3	57.8	10.8	47
4	"	10.21.23.0	69.6	29.9	2.9	8	3	69.6	30.5	23
5	"	10.27.20.0	59.2	27.6	2.3	4	2	59.5	27.5	34
6	"	10.46.21.0	59.2	27.6	<2	2	1	59.8	28.7	90
7	"	11.18.48.0	59.3	27.2	2.3	5	3	58.9	26.7	52
8	"	11.54.41.0	65.8	24.7	<2	5	1	66.6	24.4	89
9	"	11.57.57.9	60.57	8.36	1.8	2	1	60.6	8.1	14
10	"	12.02.36.0	59.4	28.5	2.1	3	2	59.5	28.2	20
11	"	12.42.22.9	59.78	10.76	2.3	3	1	59.5	10.0	52
12	"	14.13.14.0	58.33	6.28	2.4	4	1	58.0	6.1	38
13	"	14.21.08.0	60.9	29.4	2.3	3	2	61.3	29.1	47
14	"	14.33.58.3	59.06	5.88	2.2	2	1	58.9	3.3	144
15	"	18.58.08.1	59.68	5.57	3.2	7	3	60.0	5.7	36

Table 3. Location estimates obtained automatically from the beampacking procedure compared with independent network locations from the Helsinki and Bergen bulletins. Note the good consistency, especially for events with more than one detecting array.

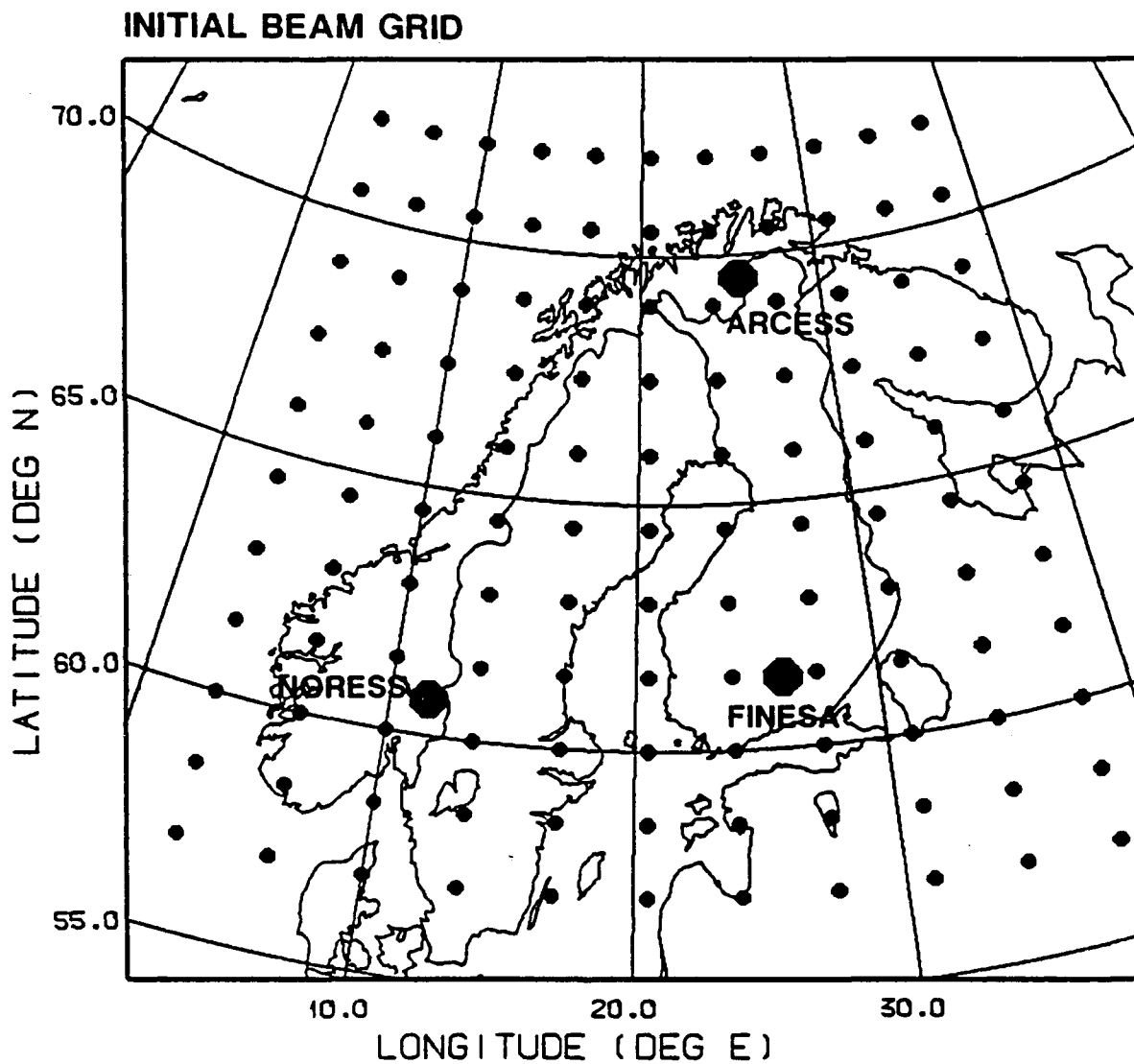


Fig. 1. Beam grid used in the generalized beamforming procedure for the purpose of associating regional phases from NORESS, ARCESS and FINESA. The location of the three arrays is shown on the map.

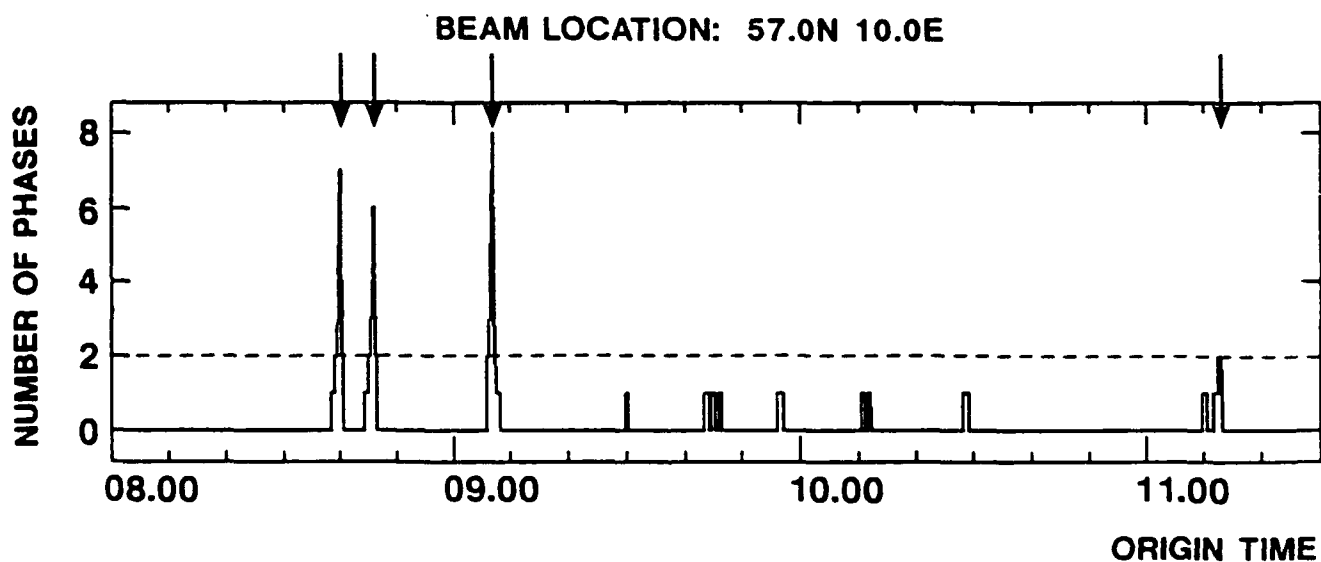


Fig. 2. Example of typical output trace for one network beam (steered to 57°N, 10°E). In the 3 1/2 hour interval shown, there were 4 confirmed seismic events located in the beam region. These were all correctly detected (arrows), and no false phase associations occurred during the interval.

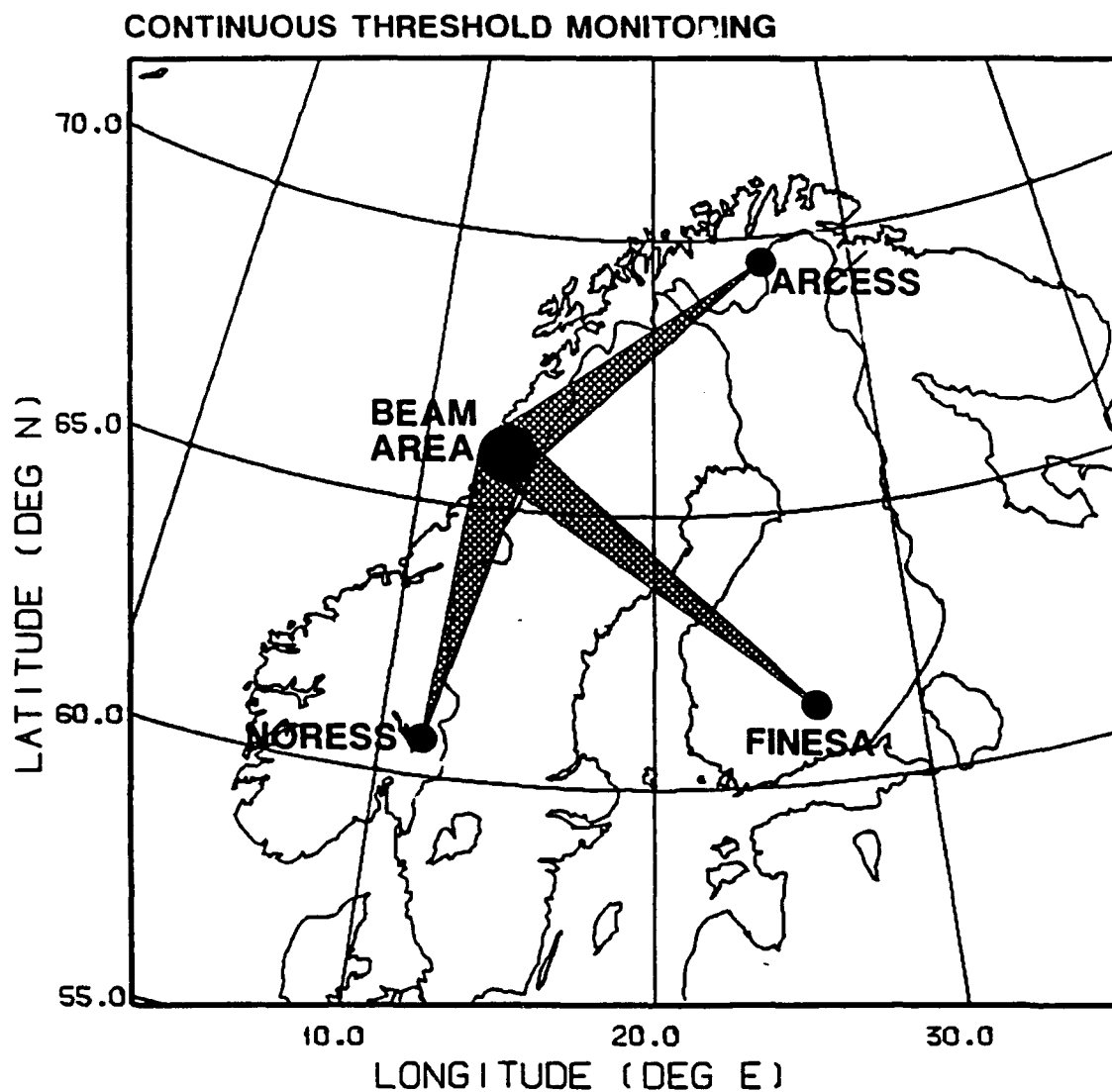


Fig. 3. Location of the beam area used in the example of continuous monitoring of upper magnitude limits on non-detected events. The area covers a circle of approximately 50 km radius, and is situated at similar distances from the three arrays.

CONTINUOUS THRESHOLD MONITORING - PN PHASE

90% PROBABILITY

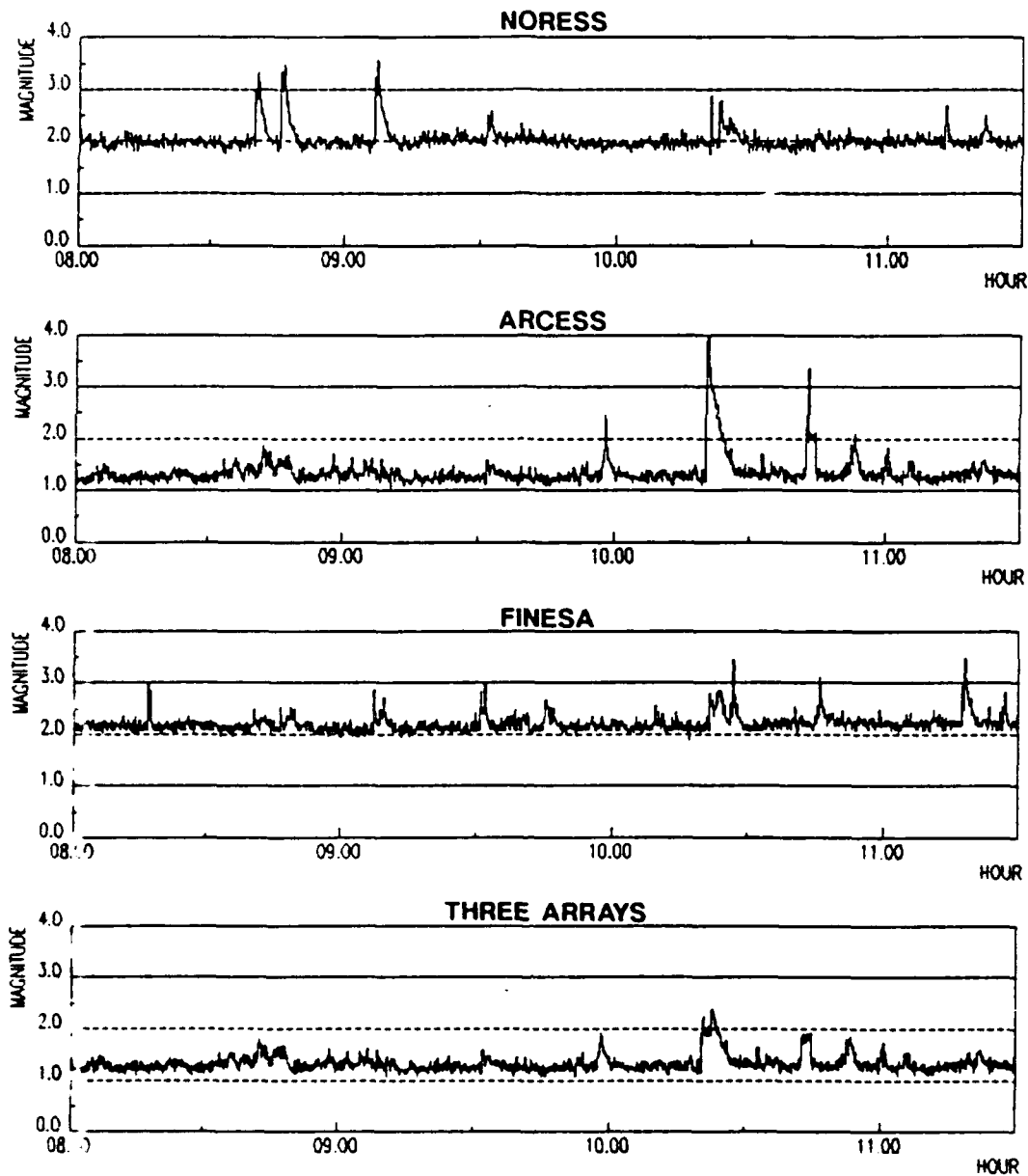


Fig. 4. Results from the continuous threshold monitoring of the area shown in Figure 3 for a 3 1/2 hour period, using Pn phases only. The top three traces show, for each array, the largest magnitude of a possible non-detected event (confidence 90 per cent) as a function of time. The bottom trace shows the result of combining the observations from all three arrays (Pn phase only) as described in the text.

CONTINUOUS THRESHOLD MONITORING - PN AND LG PHASES

90% PROBABILITY

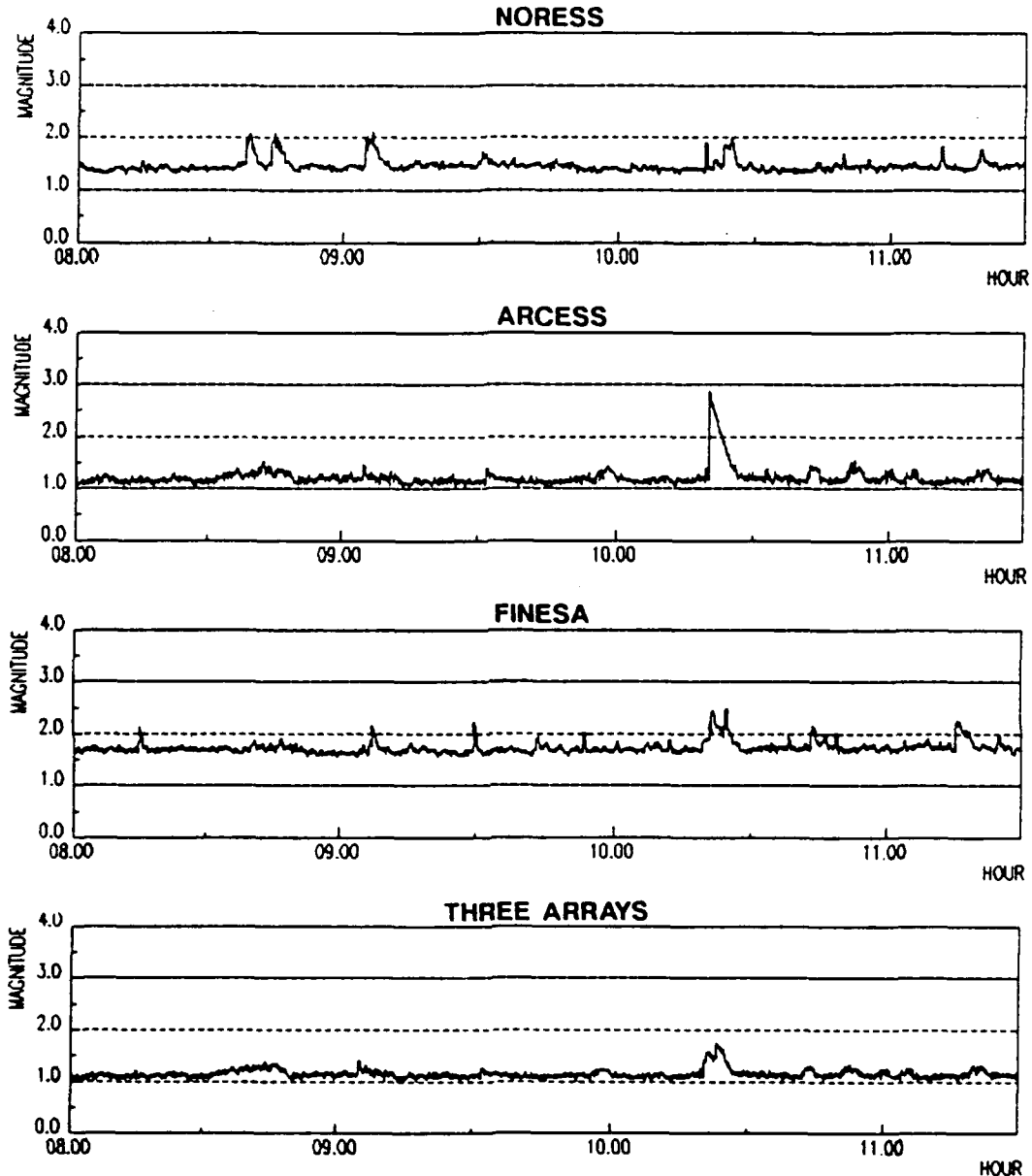


Fig. 5. Same as Figure 4, but using both the Pn and Lg phases for the upper magnitude limit calculations. Comparing with Figure 4, we note that this serves to lower the thresholds, both for each individual array (top three traces) and for the combined results (bottom trace).

PROCESSING OF REGIONAL EVENTS RECORDED
ON THE NORESS/ARCESS/FINESA ARRAYS

Svein Mykkeltveit, Jan Fyen, Tormod Kværna and Roger A. Hansen

NTNF/NORSAR, Post Box 51, N-2007 Kjeller, Norway

Contract No. F49620-89-C-0038

Objective

One of the objectives of NORSAR's regional array program is to record continuous data for use in seismological verification research. The program currently focuses on the evaluation of the capabilities of a network of regional arrays in detecting and identifying low-magnitude regional events. The data used in this research are from the two arrays NORESS and ARCESS in Norway and the FINESA array in Finland.

This paper comprises three separate investigations related to analysis of data from these arrays. The first investigation reports on statistics on regional phases, derived from the complete NORESS detection lists for the period 1985-88. The second investigation is an evaluation of the performance of the recently upgraded FINESA array, whereas the third investigation utilizes data recorded simultaneously on all three arrays in producing joint event locations.

Summary

Statistics on regional phase attributes

The NORESS detection lists for the period 1985 to 1988 contain more than 200,000 entries, comprising teleseismic, regional and local phase arrivals. The network bulletins for this four-year period published by the University of Bergen, Norway, and the University of Helsinki, Finland, contain altogether 16,000 events that are local or regional to the NORESS array. For each of these 16,000 events, we calculated the expected arrival times at NORESS for the regional phases Pn, Pg, Sn and Lg, and then searched the detection lists to see whether the theoretical arrival times matched those of actual phase arrivals detected on the NORESS array. Certain criteria were established in this regard, and, e.g., for the Pn phase these were that the arrival times should not deviate by more than 6 seconds from the predicted ones, the phase velocity (routinely determined by frequency-wavenumber analysis for each detected signal) should be within the interval 6-15 km/s, and the arrival azimuths (also determined by frequency-wavenumber analysis) should be within 30° of the predicted values.

This process of merging of the network bulletins with the NORESS detection lists produces a wealth of information on attributes like phase velocities, arrival time residuals and arrival azimuth residuals relative to the network locations. The results may also be used as a basis for compiling data bases of interesting events from specific source regions.

Some results from this study for the Pn phase are shown in Figs. 1 and 2. Fig. 1 (top) shows the number of Pn phases detected at NORESS during 1985-88 from the various regions. The corresponding events are grouped within $1^\circ \times 2^\circ$ blocks (North-South and East-West, respectively). Fig. 1 (bottom) also shows the average Pn phase velocity for events within each block. The high Pn velocities (averaging more than 10 km/s) for events in the Estonian region of the USSR stand out clearly in the map. Arrival azimuth residuals are shown in Fig. 2. It is seen that the Estonian region also exhibits a rather complex pattern of azimuth residuals.

An evaluation of the performance of the upgraded FINESA array

In early 1988, the geometry of the FINESA array was expanded by adding five elements to the array, as shown in Fig. 3. The FINESA array geometry currently comprises 15 vertical only seismometers within an aperture of 2 km.

FINESA data are recorded on magnetic tape at the array site, and the tape recording is normally event triggered by a built-in voting detector. In order, however, to properly evaluate the performance of the upgraded FINESA array, data were recorded continuously for a 14-day period during March 8-21 of 1988. The tapes were played back and checked at NORSAR, and approximately 55% of the data for this period could be recovered and were hence subjected to detection processing.

A beam deployment comprising 72 beams (66 coherent, 6 incoherent) was used for the detection processing of the continuous FINESA data. The beam deployment used is in agreement with the recommendations by Kvärna et al (1987) and Kvärna (1988). The detection processing results in lists with attributes for each detected signal, like detection time, signal frequency, phase velocity and arrival azimuth. These lists were compared against the Helsinki bulletin. Only those bulletin events occurring when the FINESA array was operating properly were considered, and there were altogether 103 such events.

Signals detected on FINESA were associated to the Helsinki bulletin events by requiring a reasonable match of FINESA detection parameters (arrival time, phase type from velocity, and arrival azimuth) with the corresponding ones predicted from the information in the Helsinki bulletin. It was found that out of the 103 reference events, 99 had at least one detected P- or S-phase, i.e., 96 per cent. Two of the four events that were not detected, occurred at the Lahnaslampi mine in Finland (64.2°N , 28.0°E), at a distance of 322 km from FINESA. Most blasts at Lahnaslampi are quite small, and are not detected by FINESA. The two remaining events were both small ones (magnitude less than 2 for one event; magnitude not given for the other) at ranges more than 700 km from FINESA.

These results for the upgraded FINESA array are quite encouraging. An investigation based on 14 days of continuous FINESA data from 1986 (with the original array geometry) concluded that 84 per cent of the regional events listed in the Helsinki bulletin were detected by the array (Korhonen et al, 1987). The addition of the five extra sensors to

the array geometry thus resulted in a considerable improvement of the array's capability to detect small regional events.

Joint event locations from three-array data

Data recorded at FINESA were used together with NORESS and ARCESS data in assessing the capabilities of this three-array network in locating events in the Fennoscandian region. A set of 10 events, for which there was at least one detected phase for each array, was selected for an event location experiment. The events are listed in Table 1 and shown in Fig. 4. The event magnitudes range from less than 2.0 to 3.2. The origin times and geographical coordinates for the 10 events are taken from the Helsinki bulletin.

The continuous processing of data recorded at each of the three regional arrays in Fennoscandia provides estimates of arrival times and azimuths. These parameters together with the associated uncertainties were used as input to the TTAZLOC program developed by Bratt and Bache (1988). TTAZLOC incorporates the arrival time and azimuth data into a generalized-inverse location estimation scheme, and can be applied to both single-array and multiple-array data.

Figs. 5a, b and c show ARCESS, NORESS and FINESA data, respectively, for event 3 in Table 1. The panels show on top three optimally steered P-wave beams for three different frequency bands. The three lower traces of the panels show data for a single channel, also for three different frequency bands. The detection times for the phases used in the location experiment are marked by arrows. The figures show that this event is recorded with a high SNR ratio at the closest array (FINESA), whereas it is marginal at the two other arrays, but is detected due to the SNR gain that is achieved through beamforming. Very simple rules based on phase velocity and relative arrival times and amplitudes are used in the phase assignment, and Pn, Sn and Lg phases are considered.

Table 1 gives the results of the location experiment. On the average, the joint three-array locations deviate from the network locations published in the Helsinki bulletin by 16 km. Two-array and one-array locations were computed for all combinations of events and array sub-networks, also using the TTAZLOC algorithm. The resulting average deviations from the network solutions are 26 and 68 km, respectively.

Conclusions and recommendations

The merging of the complete NORESS detection lists with the regional network bulletins results in a large amount of statistical information on characteristics of regional phases in Fennoscandia and adjacent areas. Similar information will result from merging with the ARCESS and FINESA detection lists. The knowledge gained from this exercise will be of relevance and importance to the Intelligent Array Processing System (IAS), and it is anticipated that this knowledge will be represented in IAS's knowledge base.

Our evaluation of the upgraded FINESA shows that this array in its current configuration represents a valuable addition to the network of regional arrays in Fennoscandia. To fully exploit the FINESA data, however, it will be necessary to upgrade the on-site data acquisition system and also provide a communications link. This will allow real time transmission of FINESA data to the NORSAR data processing center at Kjeller for processing jointly with NORESS and ARCESS data. According to current plans, such upgrade and the installation of a communications link will be completed by the summer of 1989, as a cooperative effort between NORSAR and the University of Helsinki.

The results from our three-array location experiment show that the improvement in the location accuracy when invoking data from three arrays rather than one or two is significant, and we consider the results reported here as quite promising, when taking the following into account: The arrival times used were those determined automatically by the online processing. It is conceivable that human intervention for adjustment of arrival times and/or refinement of the automatic procedure would improve the location estimates. Only standard travel time tables for the phases Pn, Sn and Lg were used. The introduction of regionalized travel time tables is likely to result in improvements. Finally, master event location schemes of various kinds hold considerable promise and are expected to further enhance the capabilities of accurately locating regional events.

References

- Bratt, S.B. and T.C. Bache (1988): Locating events with a sparse network of regional events. Bull. Seism. Soc. Am., 78, 780-798.
- Korhonen, H., S. Pirhonen, F. Ringdal, S. Mykkeltveit, T. Kværna, P.W. Larsen and R. Paulsen (1987): The Finesa array and preliminary results of data analysis. Univ. of Helsinki, Inst. of Seismology, Report S-16.
- Kværna, T. (1988): On exploitation of small-aperture NORESS type arrays for enhanced P-wave detectability. Semiannual Tech. Summary, 1 Oct 1987 - 31 Mar 1988, NORSAR Sci. Rep. 2-87/88, Kjeller, Norway.
- Kværna, T., S. Kibsgaard, S. Mykkeltveit and F. Ringdal (1987): Towards an optimum beam deployment for NORESS; experiments with a North Sea/Western Norway data base. Semiannual Tech. Summary, 1 Apr - 30 Sep 1987, NORSAR Sci. Rep. 1-87/88, Kjeller, Norway.

Event No.	Date	Time	Network		Mag. ML	No. of phases used	3-array error (km)	Average 2-array error (km)	Average 1-array error (km)
			Lat.	Lon.					
1	88/03/12	14.15.38	67.1	20.6	<2	5	19	31	36
2	88/03/15	11.34.36	59.5	26.5	2.5	8	9	8	39
3	88/03/15	14.20.49.5	60.93	29.19	2.4	6	34	34	34
4	88/03/15	14.39.35	59.5	25.0	2.3	8	8	23	95
5	88/03/16	11.45.36	63.2	27.8	2.5	6	32	31	41
6	88/03/17	09.07.13.2	58.33	10.93	2.7	7	16	24	44
7	88/03/17	10.21.17	69.6	29.9	2.9	8	4	13	45
8	88/03/17	11.18.48	59.3	27.2	2.3	5	15	36	108
9	88/03/17	18.58.07.1	59.72	5.62	3.2	6	9	51	179
10	88/03/18	05.16.20	69.2	34.7	2.6	5	15	12	57
Average over 10 events							16	26	68

Table 1. Results from TTAZLOC location experiments using data from NORESS, ARCESS and FINESA. Epicentral location estimates are given as reported by the Helsinki bulletin for a set of ten regional events. The table gives the deviation from these reference locations, as inferred from the TTAZLOC experiments described in the text.

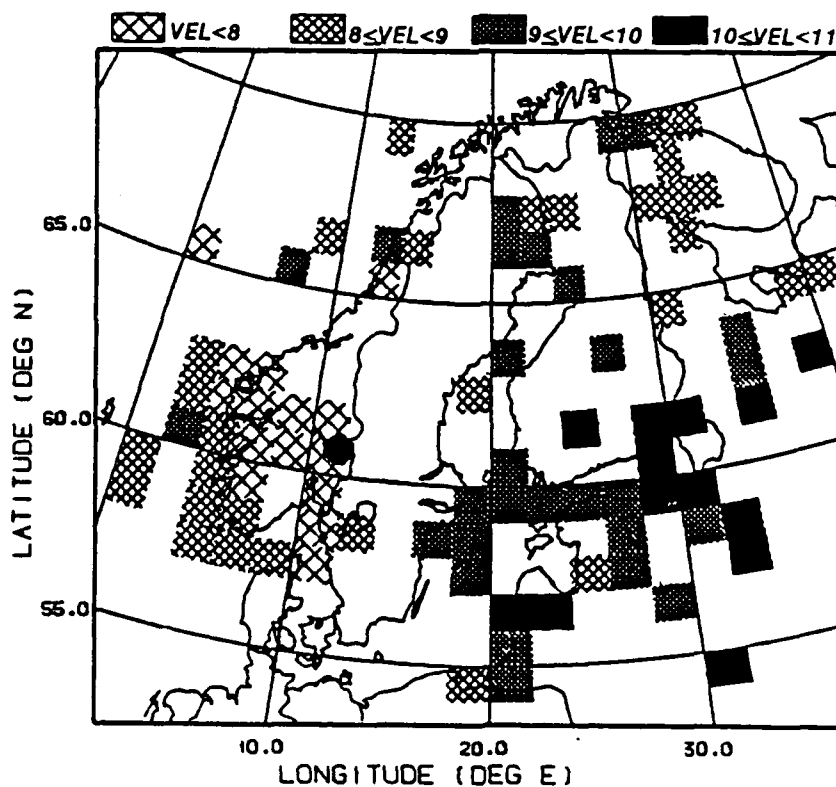
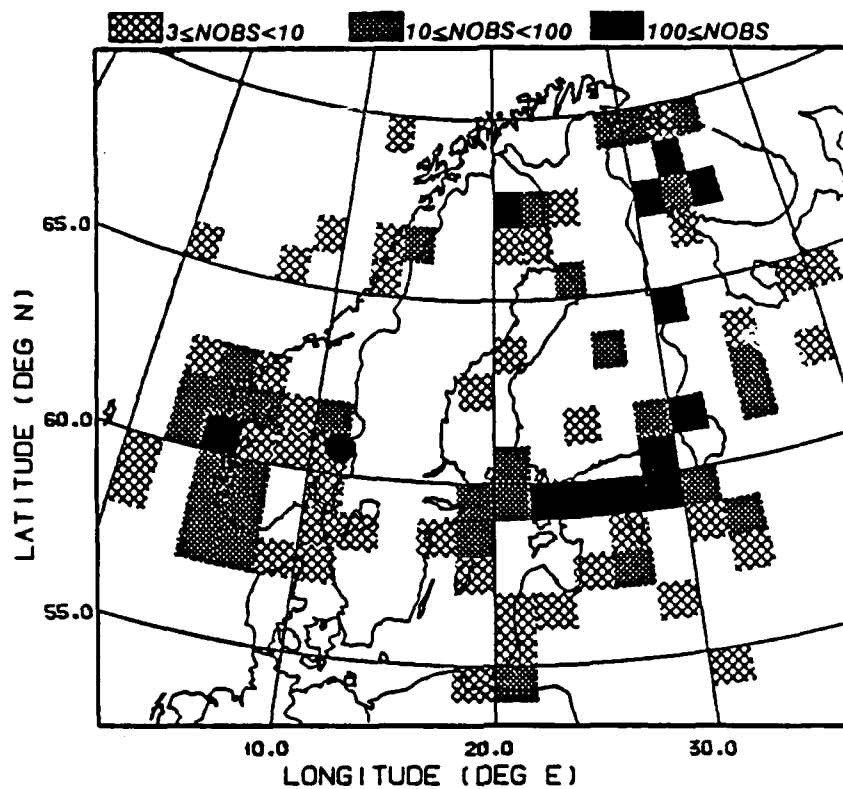
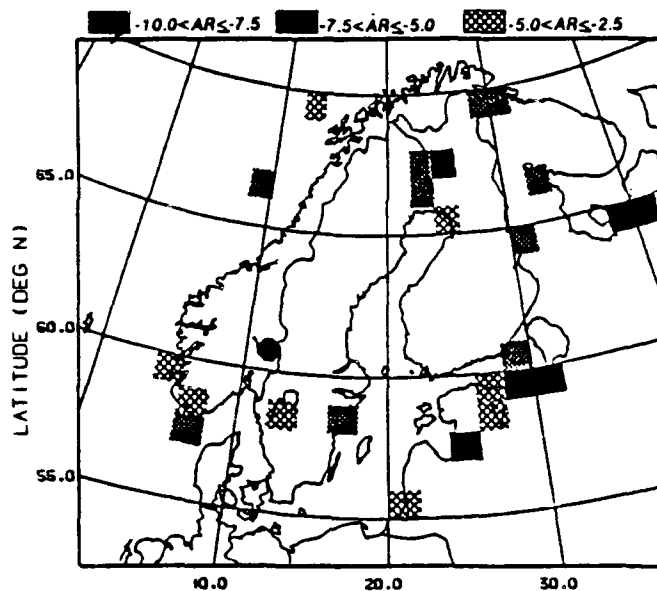
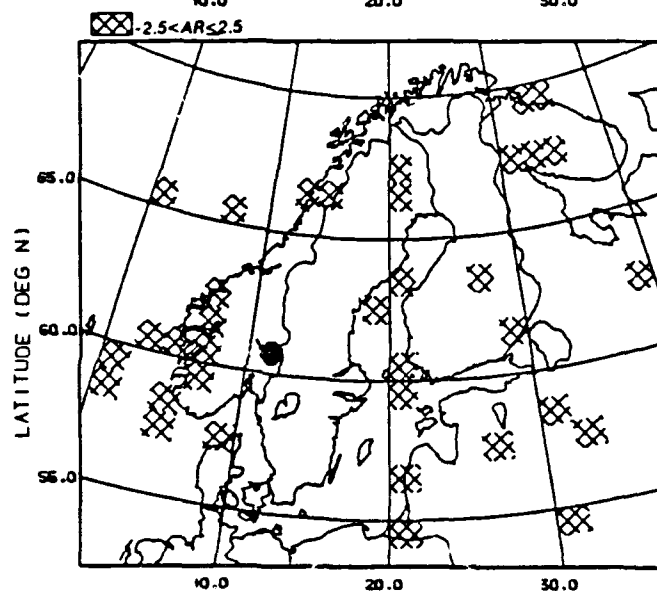


Fig. 1. Top: Number of Pn phases detected at NORESS (NOBS) from the various source areas. Bottom: Corresponding average Pn velocities (VEL). NORESS is indicated by a special symbol.

Negative
azimuth
residuals



Azimuths
within
2.5 degrees
of 'true' values



Positive
azimuth
residuals

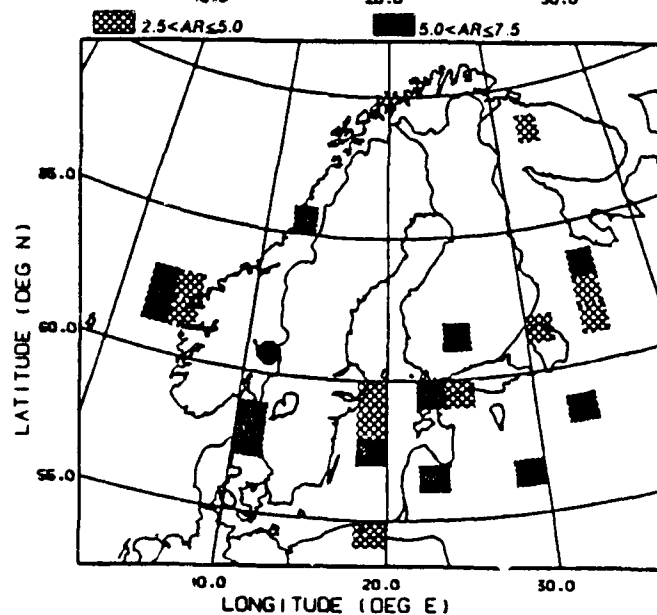
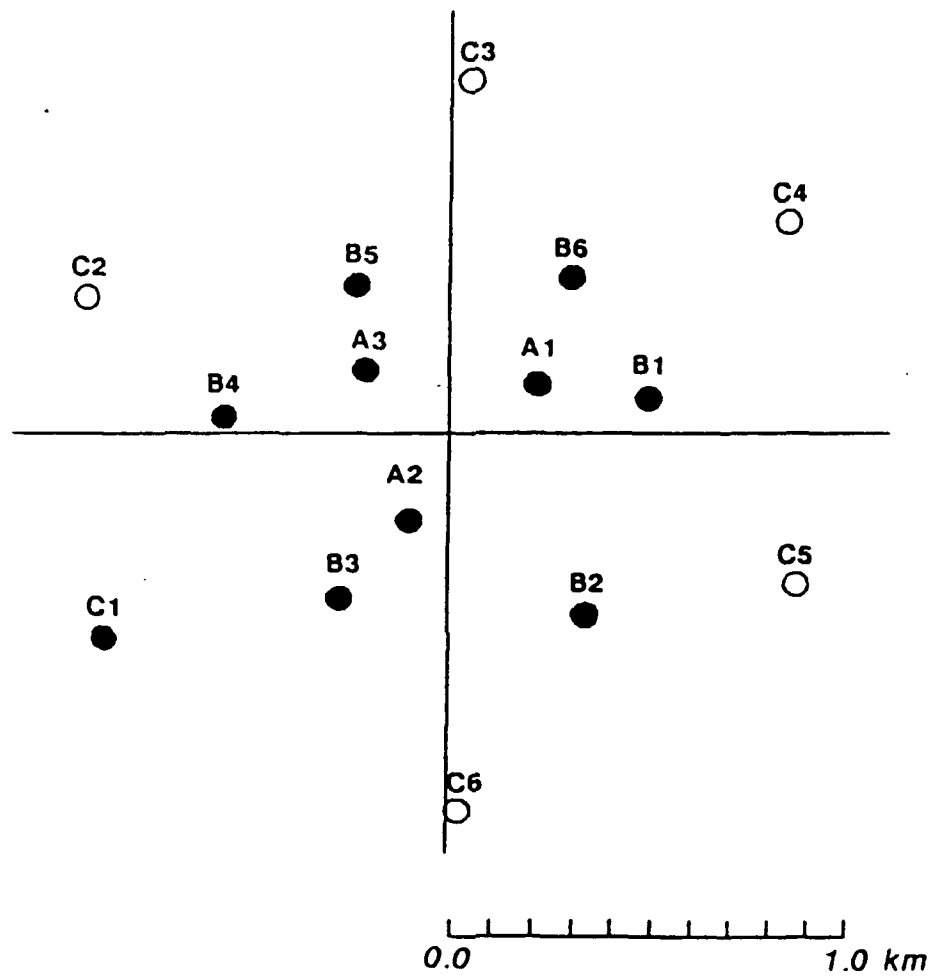


Fig. 2. Azimuth residuals (AR - estimated azimuth minus "true" azimuth, in degrees) for Pn phases detected at NORESS.

FINESA



○ Array elements added in 1988

Fig. 3. The geometry of the FINESA array in Finland. Open circles denote array elements that were added in 1988.

Events for joint 3-array location

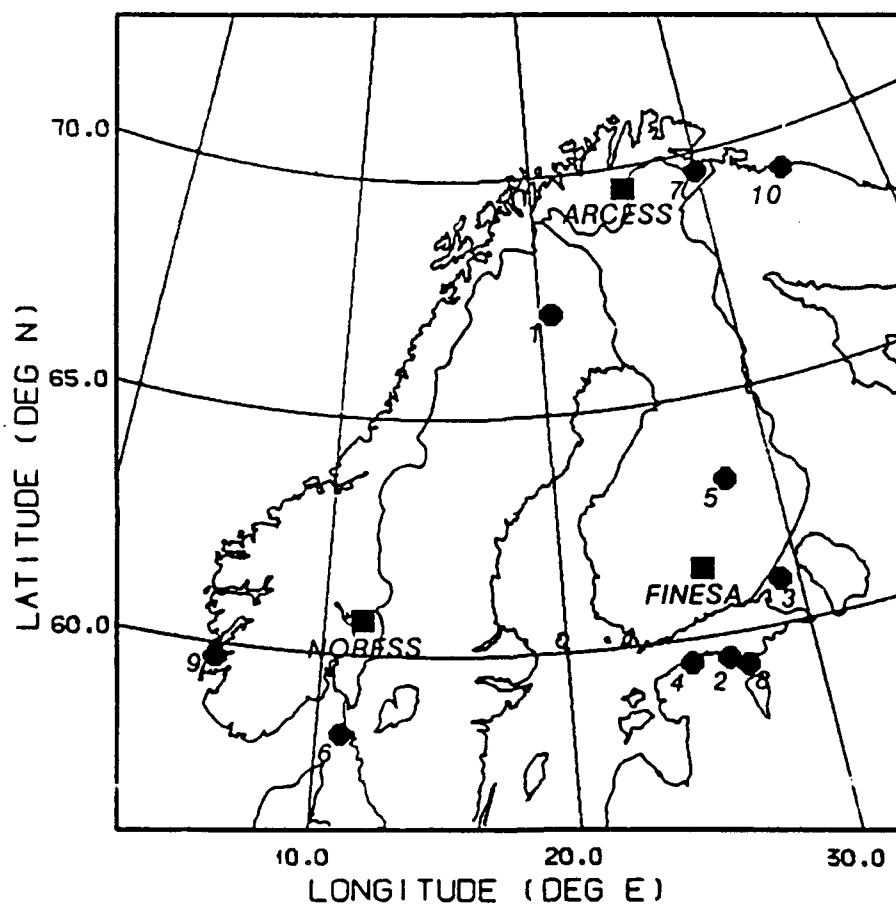


Fig. 4. The map shows the location of the three regional arrays NORESS, ARCESS and FINESA, as well as the location of ten events used in the TTAZLOC location estimation experiment.

Event 3 at ARCESS

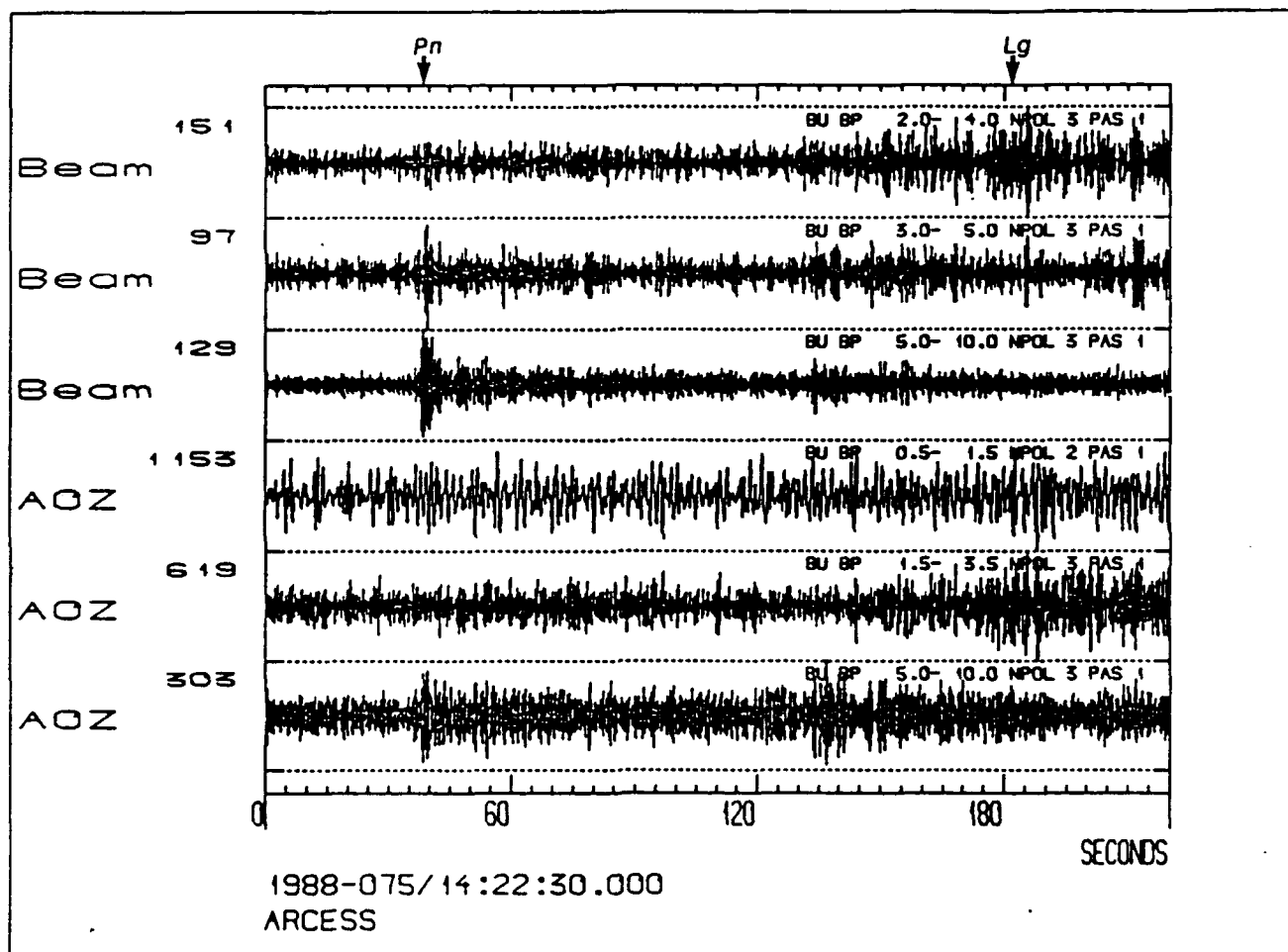


Fig. 5a. ARCESS data for event 3 in Table 1. The panel shows on top three P-beams steered towards the epicenter, for three different filter bands. The three bottom traces correspond to three different filters applied to the vertical sensor at site A0. The detection times (by the automatic online processor) for the phases Pn and Lg are indicated by arrows.

Event 3 at NORESS

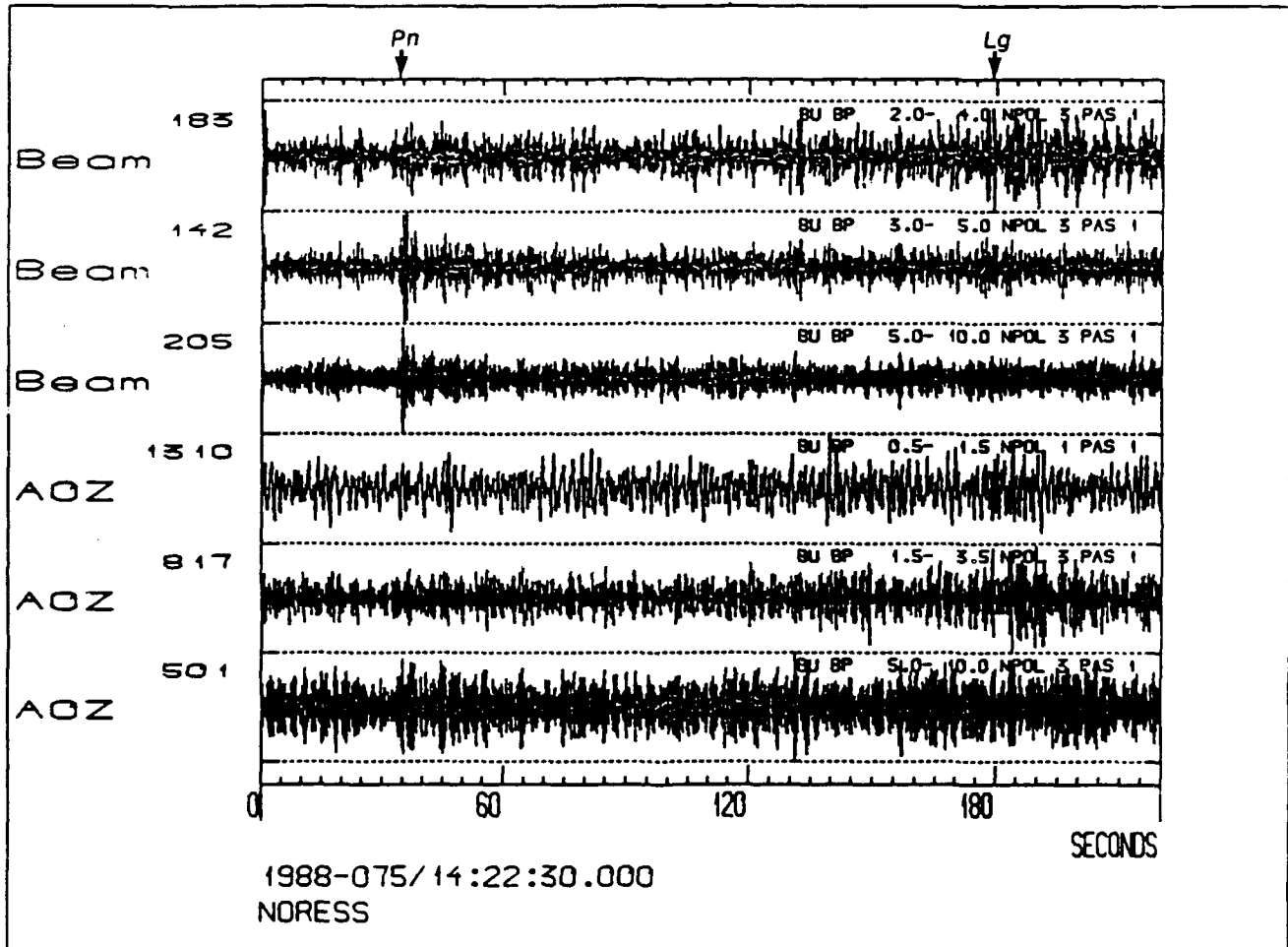


Fig. 5b. Same as Fig. 5a, but for NORESS data.

Event 3 at FINESA

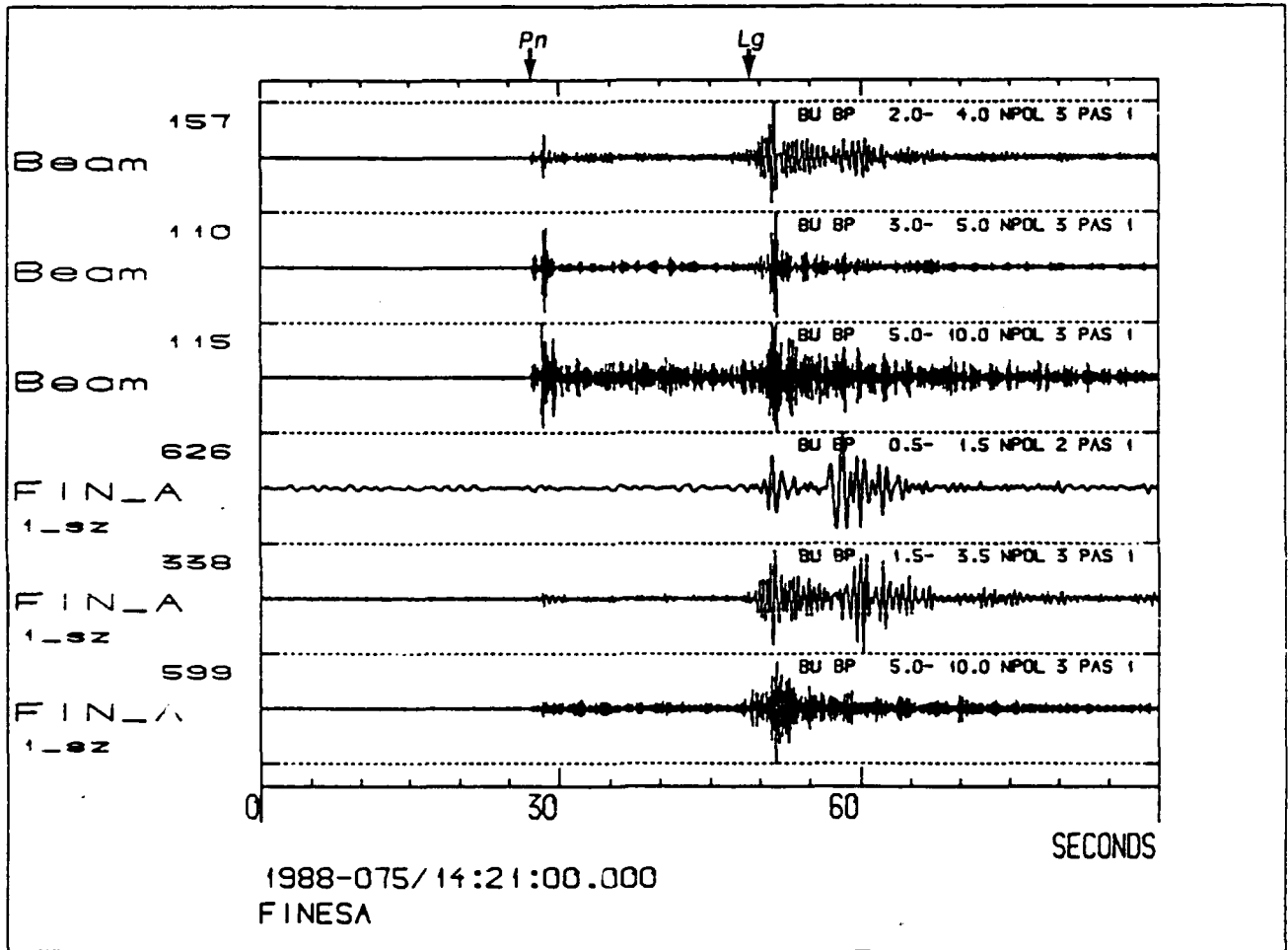


Fig. 5c. Same as Fig. 5a, but for FINESA data. The single channel data are taken from the sensor at site A1 (see Fig. 3).

Multiple Crustal Phases from Regional EVENTS

Recorded at NORESS

Kristin S. Vogfjord
Charles A. Langston

Department of Geosciences
Pennsylvania State University
University Park, PA 16802

Contract NO: F19628-87-K-0024

Objective

The objective of this study is to understand the dominating factors shaping the seismic signals from small regional events. We want to determine how much of the energy on a regional seismogram can be explained by successive arrivals of multiply reflected and converted crustal phases and how much energy is incoherent, due to scattering from inhomogeneities along the travel path. That pursuit requires studying the effects of wave propagation through a layered structure to identify the phases in the seismic records that are set up by the structure. When the structural effects have been accounted for, the remaining discriminatory source effects can be deduced.

Procedure

Shape and arrival times of wavelets on a regional seismogram are determined primarily by the underlying crustal structure and any attempt to determine discriminatory depth effects requires understanding of the propagation effects. The most prominent arrivals are generally reflections from first order discontinuities, or turning waves from sharp gradients in velocity with depth. The less prominent arrivals in individual seismograms are usually obscured by scattered waves. Array data can be used to identify these smaller phases in regional seismograms, thus providing tighter constraints on the possible crustal models and allowing for identification of possible depth phases.

The events studied so far are shown in Figure 1. They range in distance from about 90 - 250 km. Frequency-wavenumber analysis is performed on each event to search for coherent arrivals within the seismograms and, if found, determine their phase velocities. In the closest events, clear reflections from a mid-crustal interface, P_cP are seen, and in the events further away P_s and S_s head-waves or turning waves, and single and double reflections off the Moho, $P_M P$, $(P_M P)^2$, $S_M S$, and $(S_M S)^2$, as well as mode

conversions, P_{MS} , are recognizable.

Figure 2 shows a part of the record section for event 88137, at 93 km distance. The seismograms have been low-pass filtered to highlight the two small phases following the reflections off Cd and off the Moho. The phase velocities of these coherent phases determine the incidence angle and can thus constrain the travel path of each wavelet. For the four arrivals shown, the velocities are 6.8 km/s (P_{CdP}), 8.2 km/s (P_{MP}), 8.4 km/s ($P_{CdPPCdS}$?) and 8.8 km/s (P_{MS} ?). The relative amplitudes, arrival times and phase velocities of these phases should be able to determine the earth structure responsible for this wave pattern.

An enhanced seismogram is obtained for each event by piece-wise slant-stacking of the various phases with the appropriate phase velocity, as determined from the f-k analysis. This improved signal is then used for comparison with synthetic seismograms to determine earth structure. Figure 3 shows four of the enhanced seismograms as a function of distance from the array. The distance for each event is that given by the NORESS bulletin, which we have found can be off by as much as 50 km. For example location of events in the same mine as event 88133, with identical waveforms, ranges in distance from 125 km to 175 km. The final distance determination for each event must be made on the basis of relative arrival times, amplitudes and phase velocities within each improved seismogram.

Identification of the phases in the enhanced seismograms is made from simple traveltime calculations, and from comparison with synthetic seismograms, obtained by wavenumber integration, assuming plane layered velocity structure. Figure 4, shows a synthetic cross section calculated from the model obtained by Sellevoll and Warrick (1971) for the Flora-Asnes profile, with a 1 km thick, $V_p=5.2$ km/s surface layer. The synthetics are obtained by integration over wavenumbers, representing all significant P-waves leaving the source, and assuming a .05 sec triangular time function. The main features in the synthetics appear similar to those in the enhanced seismograms, but the timing of Moho reflections from this structure do not match the observed ones and it therefore needs to be modified further. A variation in Moho thickness with distance appears to be necessary to match the arrival times in all events.

An attempt is made to estimate the amount of incoherent energy in the seismograms, by subtracting the envelope of the enhanced seismogram from a piece-wise slant stack of envelopes with the appropriate phase velocities, which is used as an estimate of the total energy in each event. The difference between the two, gives an estimate of the amount incoherent energy. This is shown in Figure 5 for events 88137 and 88147. In the waveform stacking process coherent energy traveling with the stacking velocity is enhanced, but incoherent energy, and coherent energy sweeping across the

array at a different speed, are diminished. In the envelope stacking, energy from coherent arrivals with phase velocities different from the stacking velocities, in each time window, are smeared out and thus somewhat attenuated. As expected this approach indicates increased incoherent arrivals with distance. However, the more distant seismograms are complex combinations of many more phases than the closer ones, and interference of multiple arrivals may therefore add to the incoherency.

Summary

With the use of array data in regional waveform studies, more obscure arrivals can be extracted from the data and phase velocities of all coherent arrivals can be determined, thus placing tighter constraints on the underlying structure and allowing a more reliable depth determination.

Future work will include more events at these same azimuths, but different distances in order to get cross sections of the crust. Compare them to obtain differences in crustal structure and thickness between azimuths, and search for earthquakes to determine the characteristics of depth phases.

References

- Sellevoll, M. A. and R. E. Warrick, (1971). Refraction study of the crustal structure in Southern Norway, B.S.S.A., 61, 457-471.

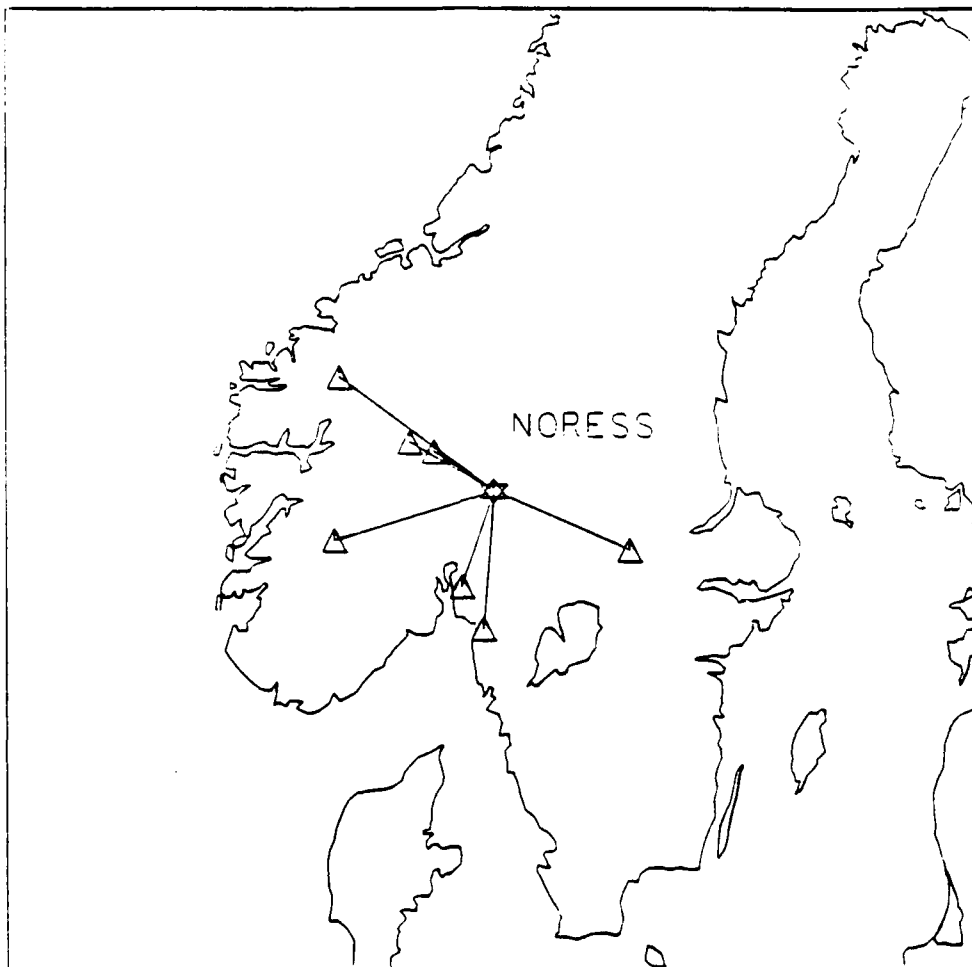


Figure 1 - Map showing the location of NORESS (star) and the events under study (triangles).

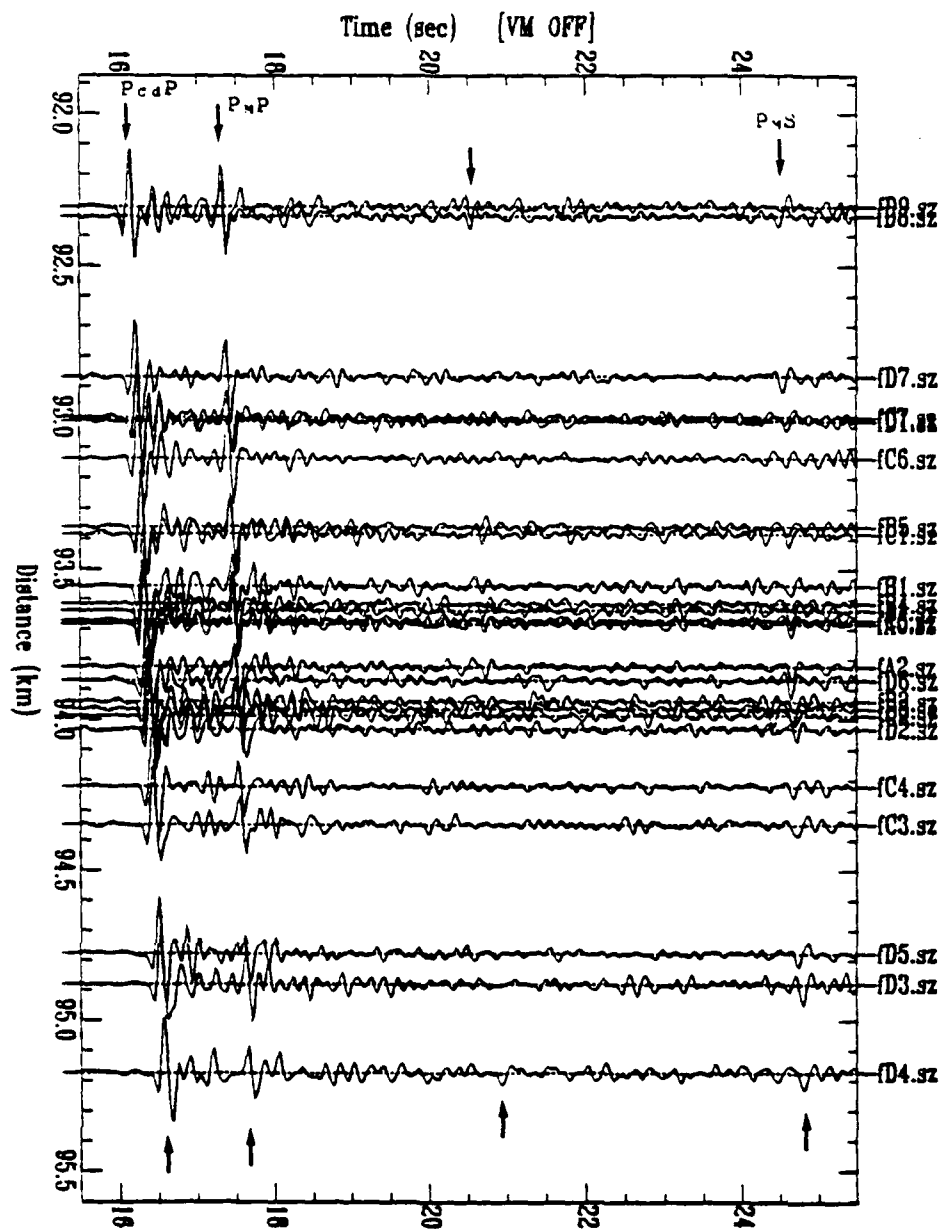


Figure 2 - Record section of the vertical components from event 88137, at 93 km distance, projected along the great circle path between the source and NORESS. The data has been low-pass filtered with $c_f = 6$. Hz. The detectable coherent arrivals have phase velocities: 6.8 km/s, P_{cP} ; 8.2 km/s, P_{nP} ; 8.4 km/s, $P_{cP}P_{cS}$?; 8.8 km/s, P_{nS} ?.

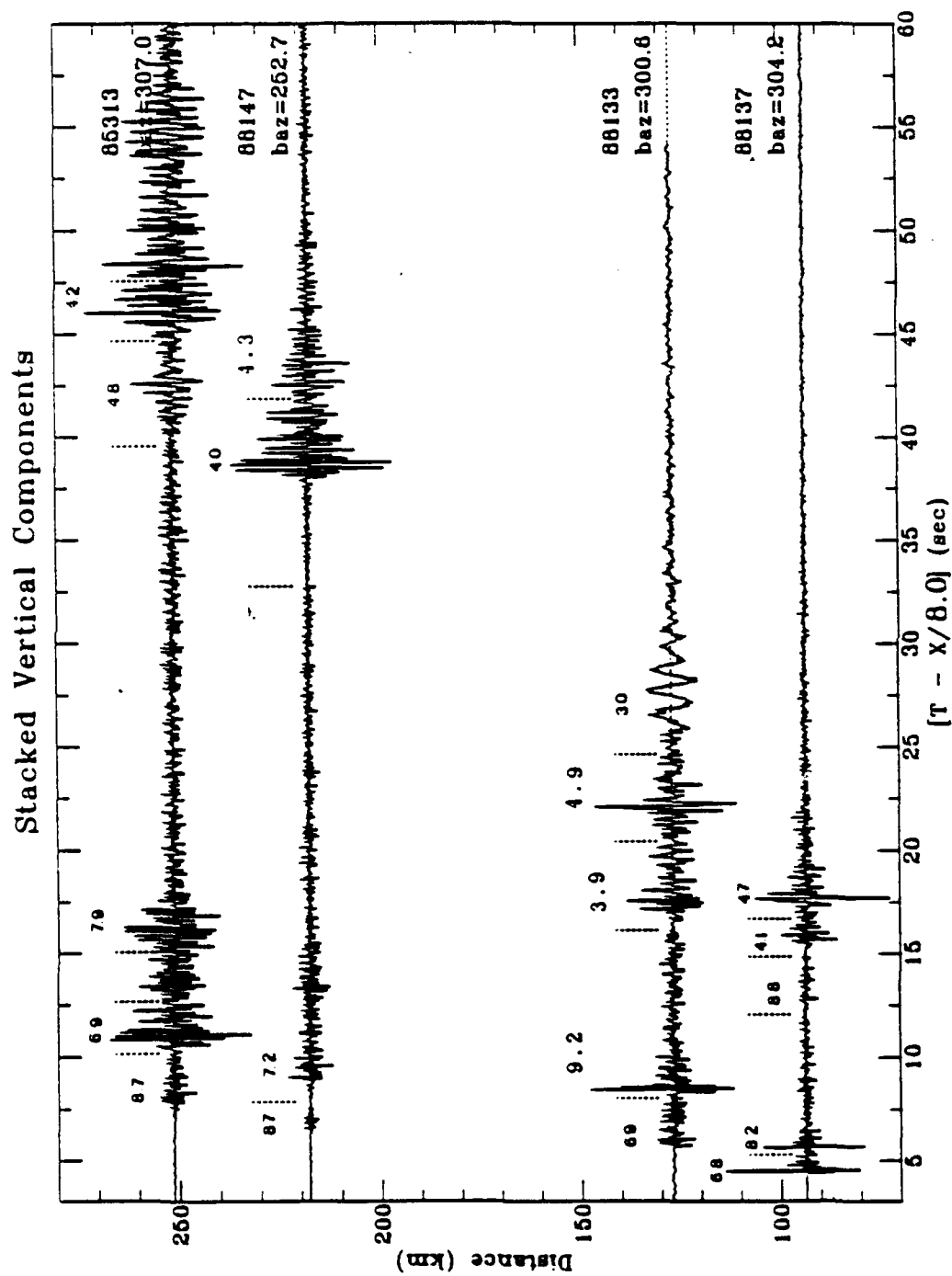


Figure 3 - Enhanced vertical seismograms, normalized to maximum amplitude, plotted as a function of distance. The stacking velocity within each slant-stack time window is indicated.

Synthetics - Explosion source

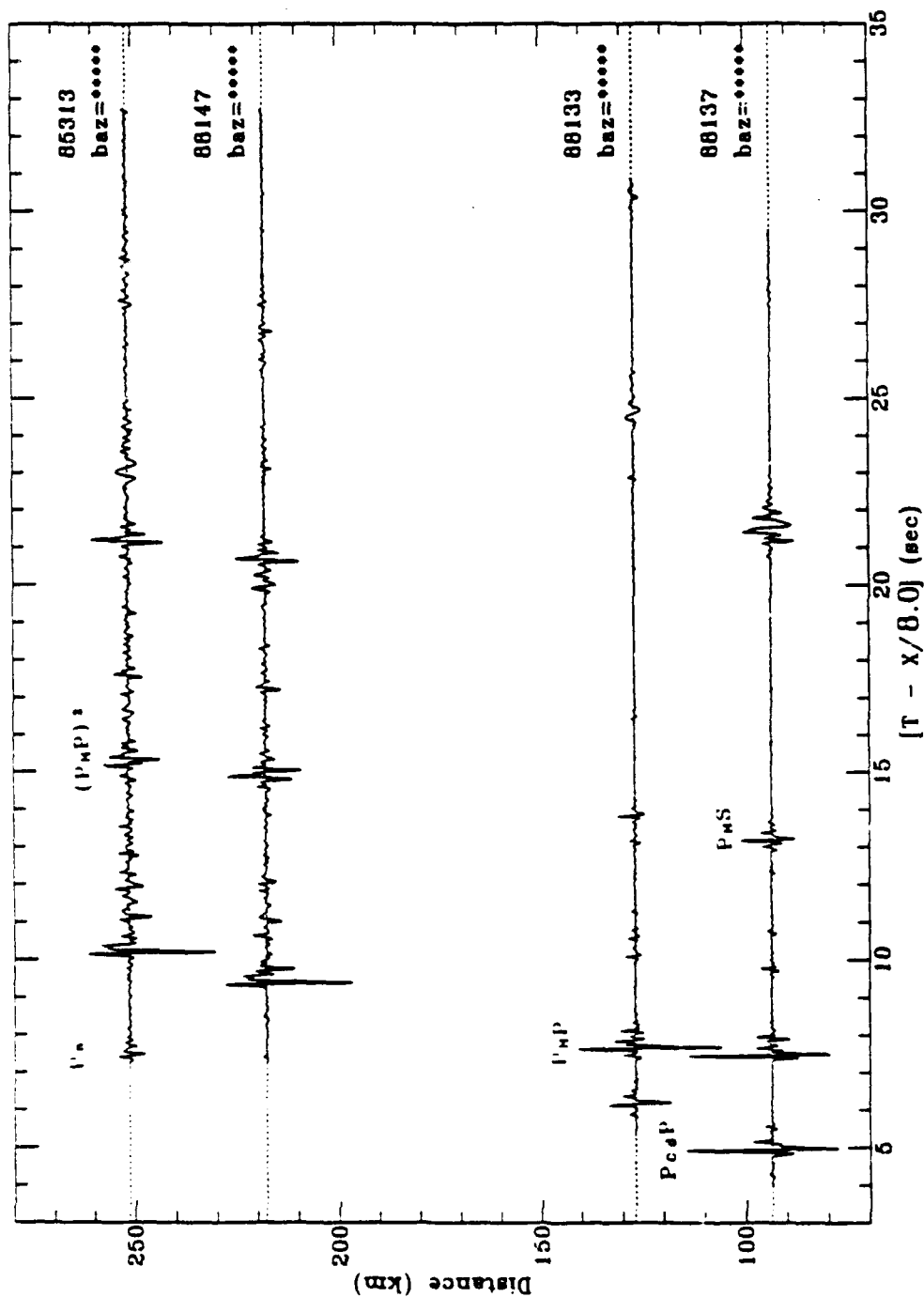


Figure 4 - Vertical synthetic seismograms from an explosion source, normalized to maximum amplitude. Calculated from the velocity model of Sellevoll and Warrick (1971) and assuming a triangular source time function of .05 sec duration. Major arrivals are indicated.

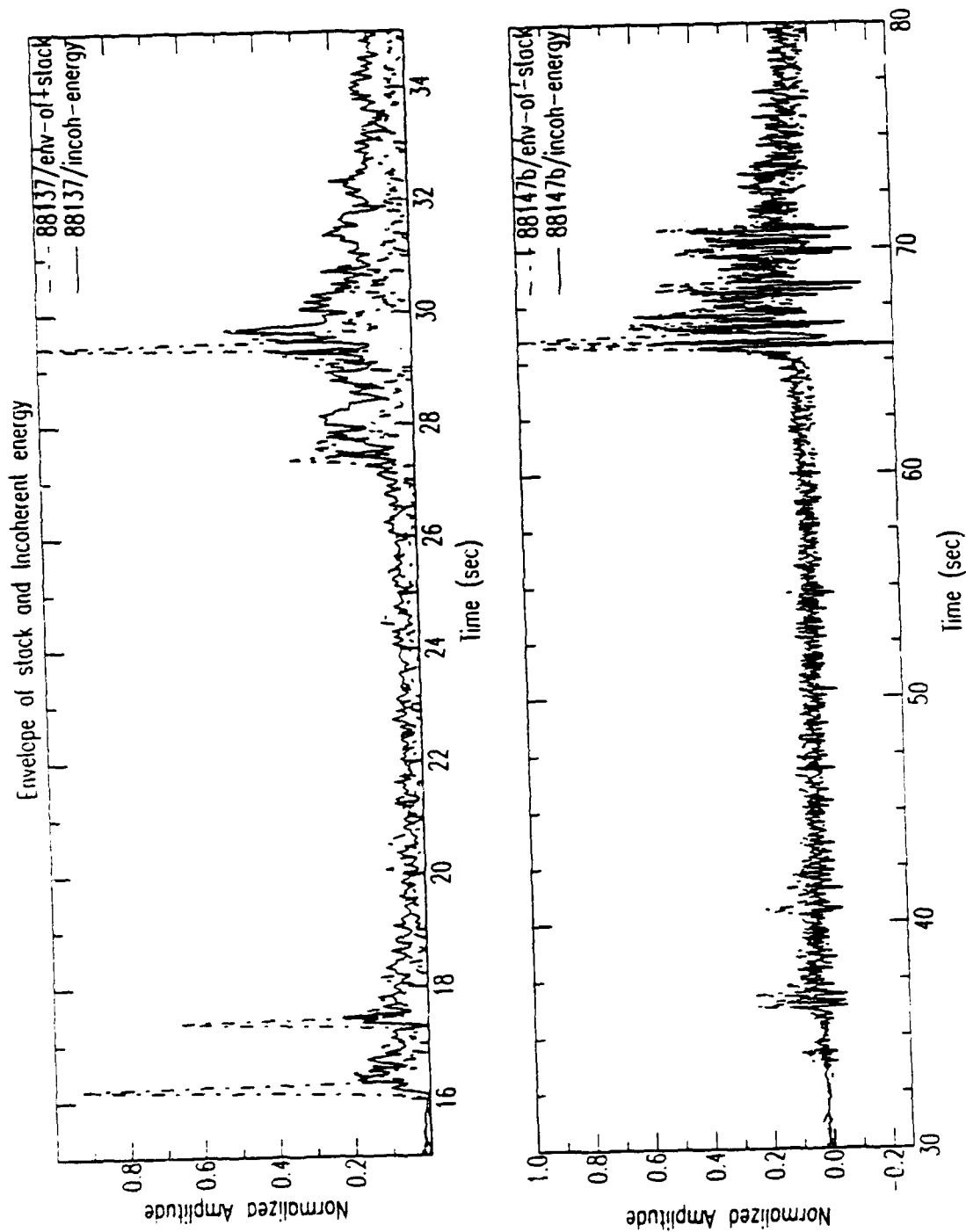


Figure 5 - Normalized envelope of the enhanced seismograms (---) and incoherent energy (—) in events 88137 and 88147.

Effects of source positions on the diffracted field at short distances

S. Gaffet and M. Bouchon

Radiomana - 27, rue Claude Bernard - 75005 Paris - France

ABSTRACT

The generation of surface waves by explosions located inside and below sediment-filled valleys is studied using the discrete wavenumber-boundary integral equation method. In a case of a long and flat basin we show that the fundamental mode and the first mode of the Rayleigh wave are clearly generated and reflected at the edges of the valley. We find an increase of the first mode amplitude when the explosion occurs below the valley compared to the amplitude obtained when the explosion occurs inside the valley. The interface shape has also a great influence on the diffracted field. Flat interface can generate surface waves send out the valley with stationary frequency and long duration while irregular interface can generate surface waves with dispersed phase velocities.

INTRODUCTION

We extend our previous study (Gaffet S. and M. Bouchon, 1989) concerning the effect of topography on surface motion to the understanding of the different ground motions generated by an explosive source located in a two dimensional laterally heterogeneous medium. We have formulated the discrete wavenumber-boundary integral equation method (Bouchon M., 1985; Campillo M. and M. Bouchon, 1985; Campillo M., 1987; Bouchon M., M. Campillo, and S. Gaffet, 1989) in the case of in-plane P-SV motions in sediment valleys.

Test of the method

In order to test the validity of the method we have first verified the reciprocity theorem (Fig. 1). This figure compares the different horizontal and vertical displacements computed in the four following configurations, *i.e.* horizontal force - horizontal displacement (Fig. 1a), vertical force - vertical displacement (Fig. 1b), horizontal force - vertical displacement (Fig. 1c), vertical

force - horizontal displacement (Fig. 1d). The calculations have been made in the case of a valley and the four sets of results obtained satisfy the reciprocity theorem. The similarity of each set of results can be made as precise as desired by increasing the number of wavenumber used in the wave field representation.

Ground motions in a sediment-filled valley

We have first considered the geometrical type of valley defined by the interface shape equation (Bard P.-Y., 1980):

$$\begin{aligned} s(x) &= h & |x| < d_1 \\ &= \frac{h}{2} \left(1 + \cos \frac{\pi (x - d_1)}{d_2} \right) & d_1 < |x| < d_1 + d_2, \text{ with } \frac{d_2}{d_1} = \frac{1}{4} \\ &= 0 & |x| > d_1 + d_2 \end{aligned}$$

with the medium elastic parameters and stations location as displayed Figure 2. Two explosive sources are considered: The first one is located in the center of the valley at 0.4 km depth (case A), the second explosion is located in the center and below the valley at 0.6 km depth (case B). The corresponding surface displacement fields are showed Figures 3 and 4 in a contour map form. Each contour line represents the amplitude level interpolated in time and space. The source time function is a Ricker wavelet having a time dependence in displacement

$$f(t) = (b - 0.5) \exp(-b), \text{ with } b = [\pi (t - t_s) / t_p]^2,$$

where t_s and t_p are respectively the time of maximum amplitude and the period of the pulse that we choose to be $t_p = 1.16$ sec.

Besides the direct field visible in the lower part of the contour diagrams one can see distinct laterally propagating phases generated at the edges of the valley. In the case B (*i.e.* explosion below the basin, Fig. 4) two distinct phases are simultaneously generated at the edges and propagate accross the valley with two different phase velocities of about 1.1 km/s and 2.0 km/s. The predominant displacement component is vertical for the slower phase while it is horizontal for the second phase. These laterally propagating disturbances are the fundamental mode ($c = 1.1$ km/s) and the first mode ($c = 2.0$ km/s) of the

Rayleigh wave. In the case A (*i.e.* explosion inside the valley, Fig. 3) the first mode has a smaller amplitude than in the case B and the displacement field is composed mainly of the fundamental mode of the Rayleigh wave.

Influence of the interface shape

Two interfaces are now considered with the configurations described Figure 5. For each case the explosive sources are located at the same depth (*i.e.* 0.4 km) at the right of the valley. For the irregular basin the source is placed straight above the deeper part of the basin. The seismograms obtained are displayed Figure 6 in a three dimensional representation which is here more suitable to emphasise the behaviour of the surface waves send out the valley. In the case of the flat basin the generated surface wave is made up of a long duration wave packet having a stationary frequency of about 1.4 Hz. In the case of the irregular basin we observe a such surface wave (*i.e.* the fundamental mode) with a smaller duration and varying frequency content. The first mode of the Rayleigh wave is also generated and appears on the horizontal component between the two first pulses of the surface wave.

CONCLUSIONS

We have formulated the discrete wavenumber-boundary integral equation method and applied it to the case of sediment-filled valleys with explosive source in the aim to describe the influence of the source position and of the valley geometry on the shape of the diffracted fields at short distances. We have showed at the frequencies studied (*i.e.* around 1.0 Hz) that the fundamental mode and the first mode of the Rayleigh wave can be strongly generated by an explosion located in the vicinity of a valley. The excitation of each mode depends on the source position, the first mode has a greater amplitude when the source is below the basin than when it is inside the basin. We also observe in the case of an irregular interface geometry a broadening of the first Rayleigh wave mode outside the basin.

The next step of this work is to study the importance of interface geometry and source position effects at teleseismic distances.

References

- BARD, P.-Y. and M. BOUCHON (1980). *The seismic response of sediment-filled valley. Part 2. The case of incident P and SV waves*, Bull. Seismol. Soc. Am. 70, pp 1921-1941
- BOUCHON, M. (1985). *A simple complete numerical solution to the problem of diffraction of SH waves by an irregular interface*, J. Acoust. Soc. Am. 77, pp 1-5
- BOUCHON, M., M. CAMPILLO, and S. GAFFET (1989). *A boundary integral equation-discrete wavenumber representation method to study wave propagation in multilayered media having irregular interfaces*, Geophysics in press
- CAMPILLO, M. and M. BOUCHON (1985). *Synthetic SH-seismograms in a laterally varying medium by the discrete wavenumber method*, Geophys. J. Roy. Astr. Soc. 82, pp 307-317
- GAFFET, S. and M. BOUCHON (1989). *Effects of two-dimensional topographies using the discrete wavenumber-boundary integral equation method in P-SV cases*, J. Acoust. Soc. Am. in press

Figure captions

FIG. 1. Application of the reciprocity theorem in the case of a cosine valley geometry. The figure compares the displacements obtained when exchanging force and displacement in the four cases displayed in A, B, C, and D.

FIG. 2. Geometry configuration and geological elastic parameters used for the synthetic seismograms displayed Figures 3 and 4.

FIG. 3. Seismograms obtained in the case A (top configuration of Figure 2) are presented in a contour map form. The left part shows the horizontal component, the right part shows the vertical component. The time window (vertical axis) is 15.0 s. The station location offsets are presented on the horizontal axis. We have indicated different characteristic phases with the marks "d" (direct field), "a" (fundamental Rayleigh wave mode), and "b" (first Rayleigh wave mode). The period of the source function is $t_p = 1.16$ s.

FIG. 4. Same as Figure 3 for the case B (bottom configuration of Figure 2).

FIG. 5. Geometry of the valley and geological parameters used to compute the seismograms displayed Figure 6.

FIG. 6. Three dimensional representation of the ground motions obtained in the two configurations displayed Figure 5. The period of the source function is $t_p = 1.0$ s. The horizontal component of the motion is presented on the left hand side of the figure for the irregular basin (top) and for the flat basin (bottom). The right hand side presents the vertical ground motion components. The time window is 7.0 s. The notation "b" indicates the appearance of the first Rayleigh wave mode on the horizontal component in the case of the irregular valley geometry.

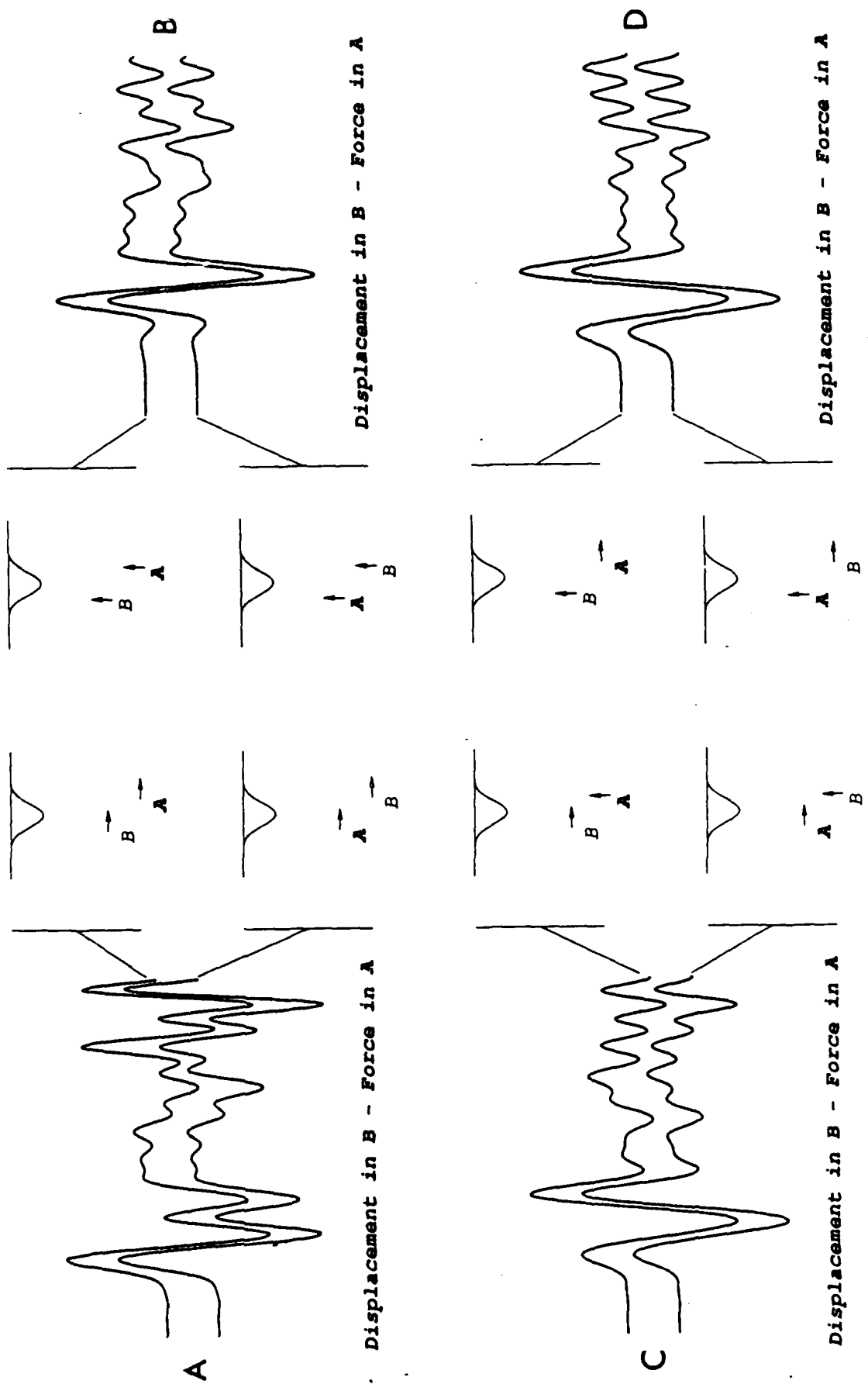
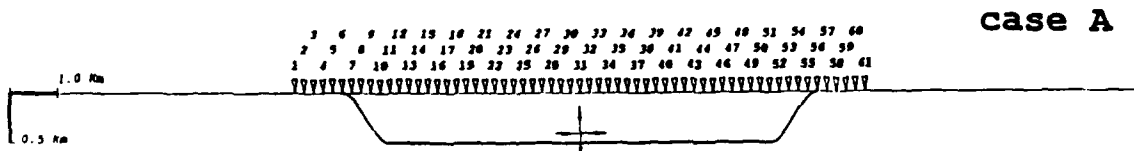


Figure 1

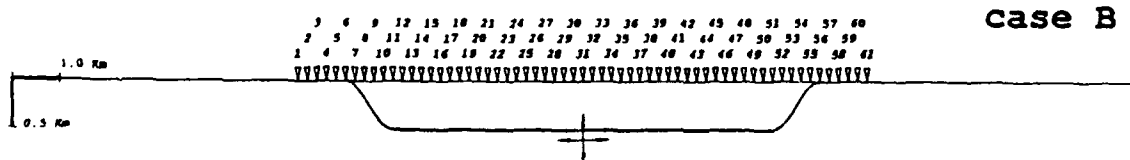


Middle	α (km/s)	β (km/s)	ρ (g/cm ³)	γ
1	2.000	1.100	2.200	0.28
2	5.000	2.800	2.800	0.27

Number of stations: 61

Source: Explosion

Time window: 15.00 sec.



Middle	α (km/s)	β (km/s)	ρ (g/cm ³)	γ
1	2.000	1.100	2.200	0.28
2	5.000	2.800	2.800	0.27

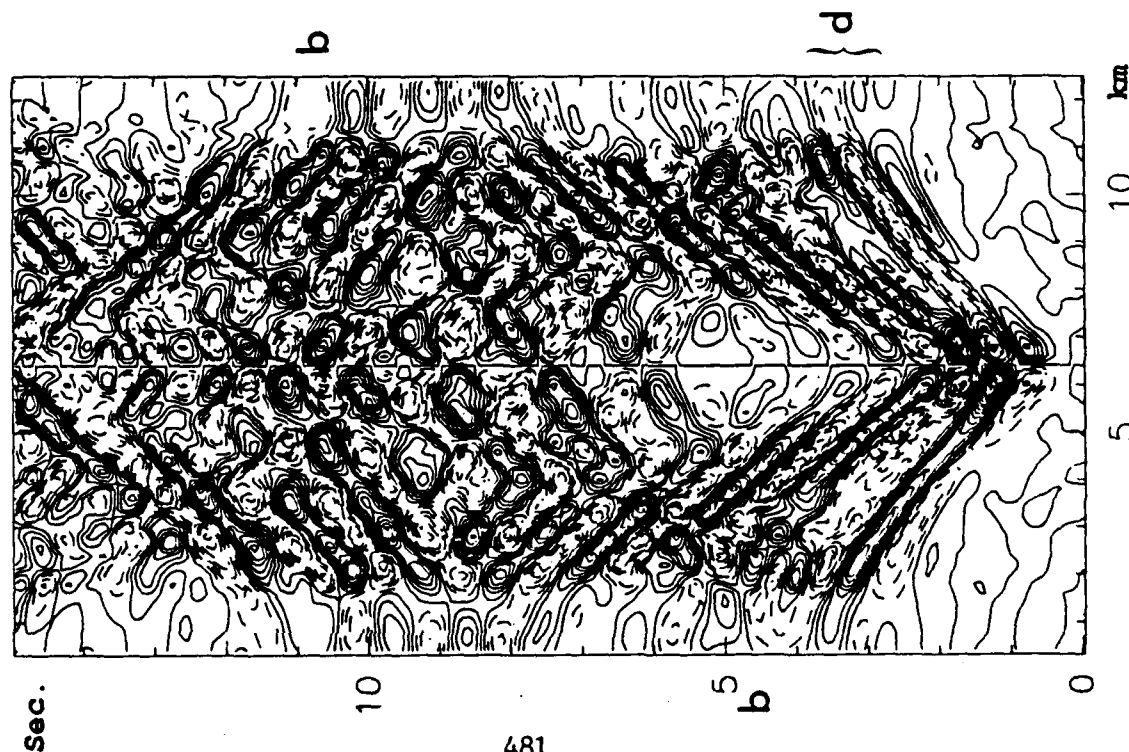
Number of stations: 61

Source: Explosion

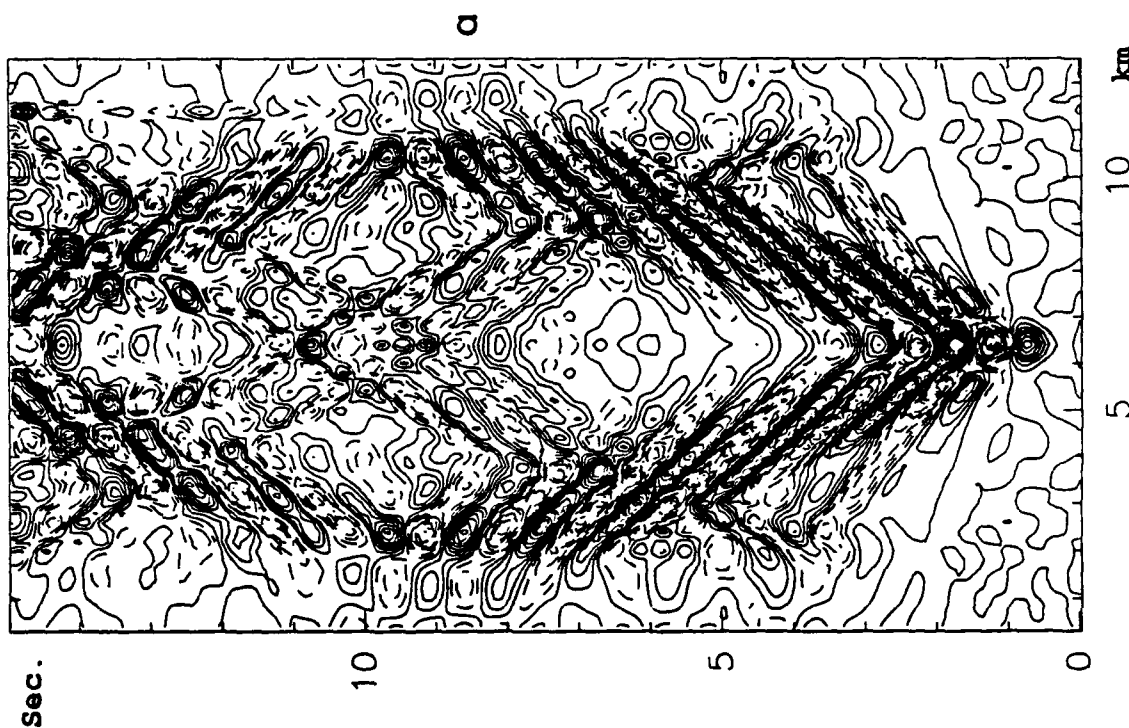
Time window: 15.00 sec.

Figure 2

-- Explosion -- A -- Type II valley -- Low velocity contrast --



Horizontal component



Vertical component

Figure 3

--- Explosion - B --- Type II valley - Low velocity contrast ---

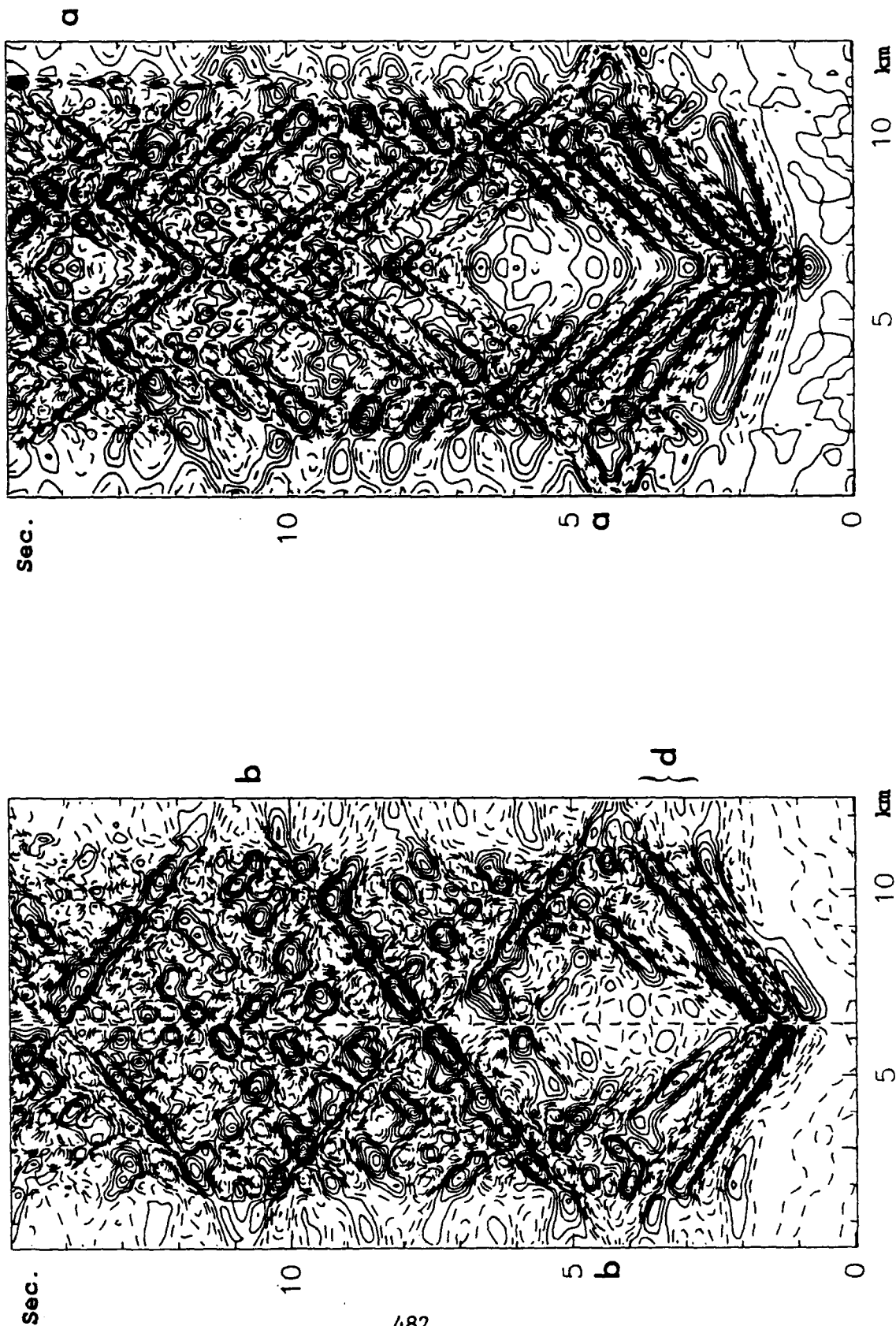
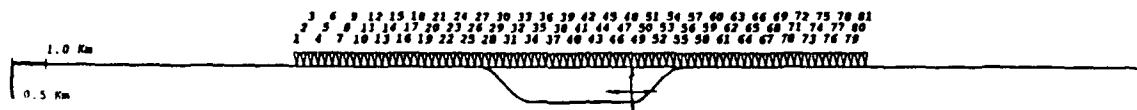


Figure 4



Middle	α (km/s)	β (km/s)	ρ (g/cm ³)	γ
1	3.287	1.742	2.010	0.30
2	6.200	3.623	2.970	0.24

Number of stations: 81

Source: Explosion

Time window: 8.00 sec.



Middle	α (km/s)	β (km/s)	ρ (g/cm ³)	γ
1	3.287	1.742	2.010	0.30
2	6.200	3.623	2.970	0.24

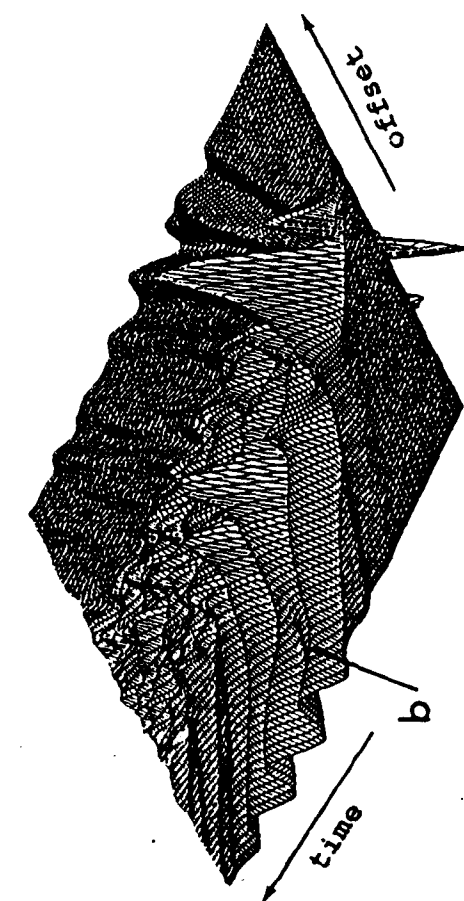
Number of stations: 81

Source: Explosion

Time window: 8.00 sec.

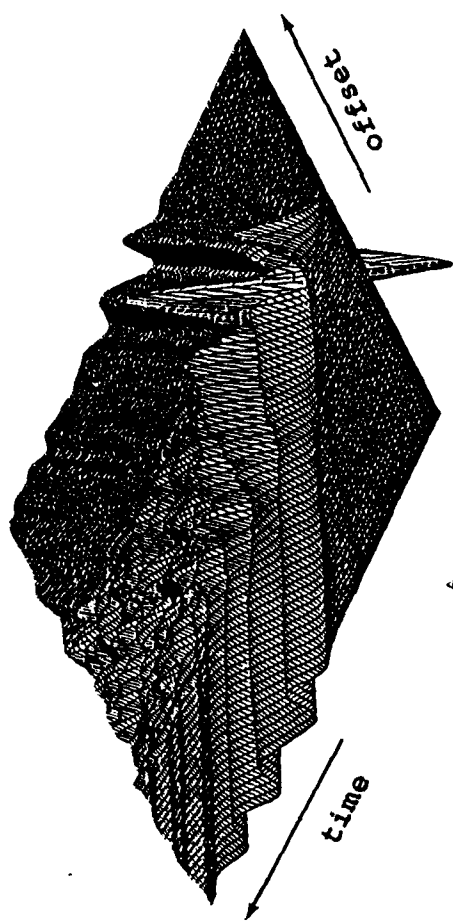
Figure 5

Irregular basin



Horizontal component

484



Vertical component

Flat basin

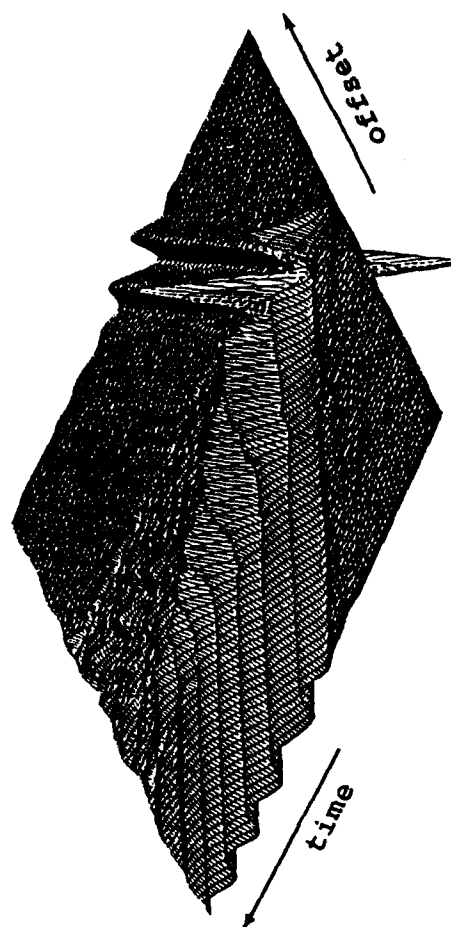
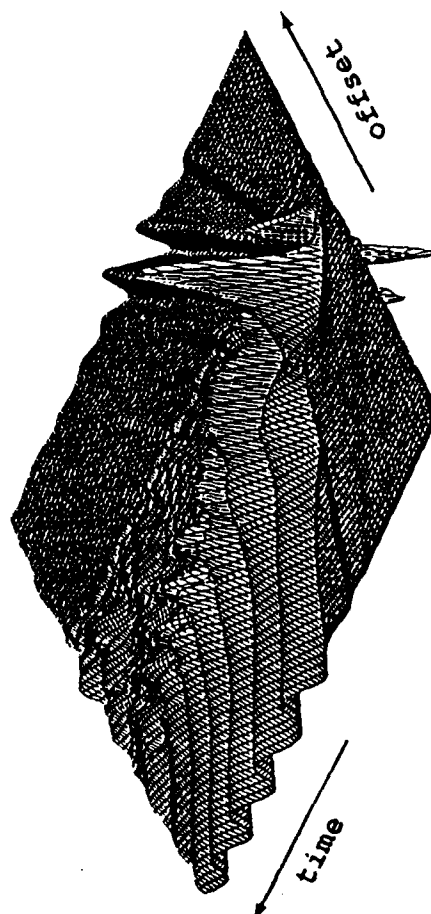


Figure 6

REGIONAL SEISMIC EVENT LOCATION IN KAZAKHSTAN, U.S.S.R.

Clifford H. Thurber, S.U.N.Y. at Stony Brook

Contract #F19628-88-K-0037

OBJECTIVE: Three-component data from a sparse three-station seismic network in eastern Kazakhstan, surrounding the Soviet nuclear test site, have been analyzed to determine location estimates for regional events recorded by two or three stations. Our primary objective is to demonstrate the capability of a sparse network of three-component stations to locate regional events even when as few as two stations record a given event. From the catalog of event triggers from the NRDC network, we have identified a suite of 20 regional events recorded by at least two stations for analysis. These events occurred between May and September 1987. Included among them are the three chemical explosions detonated in September 1987 as part of the cooperative NRDC-Soviet Academy program. Analysis of "before-and-after" satellite images in the areas of clusters of events helps to identify specific active mining sites.

SUMMARY: Three-component data from a sparse three-station seismic network in eastern Kazakhstan, surrounding the Soviet nuclear test site, have been analyzed to determine location estimates for regional events recorded by two or three stations. Included among these events are the September 1987 chemical explosions whose locations are known (Figure 1). Locations are calculated using arrival times of P and S phases and arrival azimuths from first P. Location uncertainties are estimated using a combination of *a priori* and *a posteriori* data uncertainties. A layered P-wave velocity model adapted from Soviet Deep Seismic Sounding surveys is employed for calculating travel times, and two S models are tried.

Location results for the chemical explosions are excellent, even if only two stations are used: absolute location errors are less than 10 km, and estimated 90% confidence uncertainties are only a few km (Table 1; Figure 2). The data are also adequate to correctly determine their depth (i.e., focus at the surface).

The other regional events include numerous suspected mine blasts, and two earthquakes from the Tien Shan. The calculated locations of the latter events agree well with a teleseismic location for one of them, falling within a belt of regular seismic activity. Nearly all of the presumed blasts can be associated with mapped mines, and we have been able to identify the source areas for two sets of blasts in high-resolution satellite images. "Before and after" photographs allow us to identify specific active mines. Our location estimates agree quite well with the observed active mines (Figures 3 and 4).

CONCLUSIONS AND RECOMMENDATIONS: We have demonstrated the capability of the three-station NRDC-Soviet Academy of Sciences network in Kazakhstan to locate regional events accurately over a wide area. Locations are determined using arrival times and arrival azimuths of observed phases, in most cases with data from only 2 stations. The September 1987 chemical explosions can be located with reasonable precision and accuracy either with data from all three network stations or using just two (BAY and KKL). Furthermore, the data are sufficient to correctly determine the depths of the chemical explosions (i.e., surface focus). We have also derived a well-constrained epicenter for an event in the Tien Shan at a distance of 700 km from the nearest station that agrees well with the published PDE location. Many other events are located in areas of mining activity identified in satellite photos and/or navigational charts, and the spectral characteristics of many indicate that they are ripple-fired explosions (Hedlin et al., 1989), but the precise location of each individual event cannot be unambiguously determined. Analysis of before-and-after satellite photo images in these areas

helps to identify specific active mining sites, and the success in locating events at or near these active sites adds confidence in our ability to accurately locate regional events with data from as few as two stations.

There are several extensions to the present work that we intend to pursue. One is the use of relative event location techniques, including waveform correlation to determine precise arrival time differences. This can be applied to clusters of events such as at Ekibastuz, where it might be possible to match the pattern of relative event locations to the distribution of active mines observed in the satellite images. In this way it should also be possible to verify whether or not other events from the same general vicinity (events h, j, and m) were from distinct sites. At the same time, additional satellite images will be examined to seek potential alternative sites of explosions. Finally, one of the most pressing issues is the routine determination of source depth. Ruud et al. (1988) claim that depths can be constrained using data from a single station. Analysis of the chemical explosion data indicates depth can be constrained if multiple secondary arrivals (such as P_g and S_n) are available. Our future work will include further testing of this claim for the data from other regional events in Kazakhstan, as well as an examination of the problem on a theoretical basis.

References

- Hedlin, M. A. H., J. B. Minster, and J. A. Orcutt, The time-frequency characteristics of quarry blasts and calibration explosions recorded in Kazakhstan, U.S.S.R., *Geophys. J.*, in press, 1989.
- Ruud, B. O., E. S. Husebye, S. F. Ingate, and A. Christoffersson, Event location at any distance using seismic data from a single, three-component station, *Bull. Seismol. Soc. Am.*, 78, 308-325, 1988.

Table 1

Catalog of 1987 two- and three-station event locations

ID	O.T. (d-h-m-s)		Latitude	Longitude	Error ellipse	Type	Area
a	1340936	16.4	50.190	74.157	26 x 3 @ -85°	blast	Karaganda
b	1350908	35.2	51.709	75.514	8 x 4 @ +74°	blast	Ekibastuz
c	1351035	0.3	49.304	72.712	3 x 2 @ +53°	blast	Karaganda
d	1410916	43.3	50.744	73.279	2 x 2 @ -80°	blast	Karaganda
e	1430849	22.7	49.275	75.738	5 x 2 @ -34°	blast	Karagayly
f	1450926	43.7	51.670	75.454	12 x 3 @ +84°	blast	Ekibastuz
g	1450956	40.9	51.743	75.316	10 x 2 @ +74°	blast	Ekibastuz
h	1460531	4.8	51.819	74.797	6 x 4 @ -85°	blast	Ekibastuz
i	1460833	26.5	51.760	75.571	15 x 6 @ -83°	blast	Ekibastuz
j	1621241	4.9	51.454	75.488	7 x 5 @ +16°	blast	Ekibastuz
k	1621250	34.3	51.677	75.525	17 x 7 @ +88°	blast	Ekibastuz
l	2340021	50.7	44.129	85.363	12 x 6 @ -69°	quake	Tien Shan
m	2390852	53.0	51.213	74.302	13 x 5 @ -26°	blast	Ekibastuz
n	2390937	34.8	46.900	77.389	6 x 3 @ +23°	blast	Balkash
o	2440344	38.8	43.808	85.948	6 x 5 @ +14°	quake	Tien Shan
p	2440908	52.0	46.924	77.241	14 x 5 @ +15°	blast	Balkash
q	2450802	10.2	51.639	75.481	12 x 6 @ -69°	blast	Ekibastuz

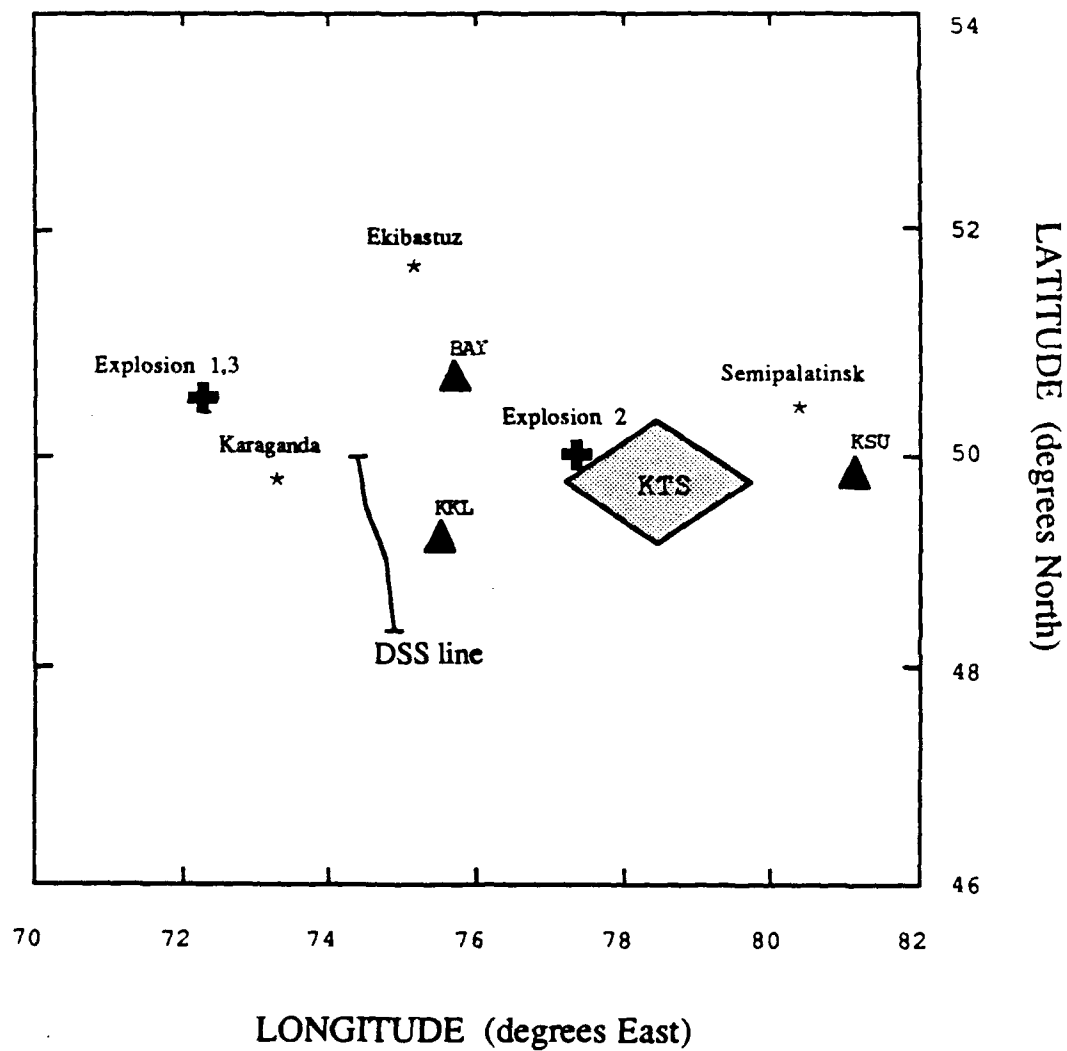


Figure 1. Configuration of the NRDC-Soviet Academy seismic network, located near the Kazakhstan Test Site (KTS) on the steppes of Central Asia. Stations BAY, KKL, and KSU are indicated by the solid triangles. Also shown are the sites of the September 1987 chemical explosions (+) and the location of a Deep-Seismic-Sounding profile (DSS).

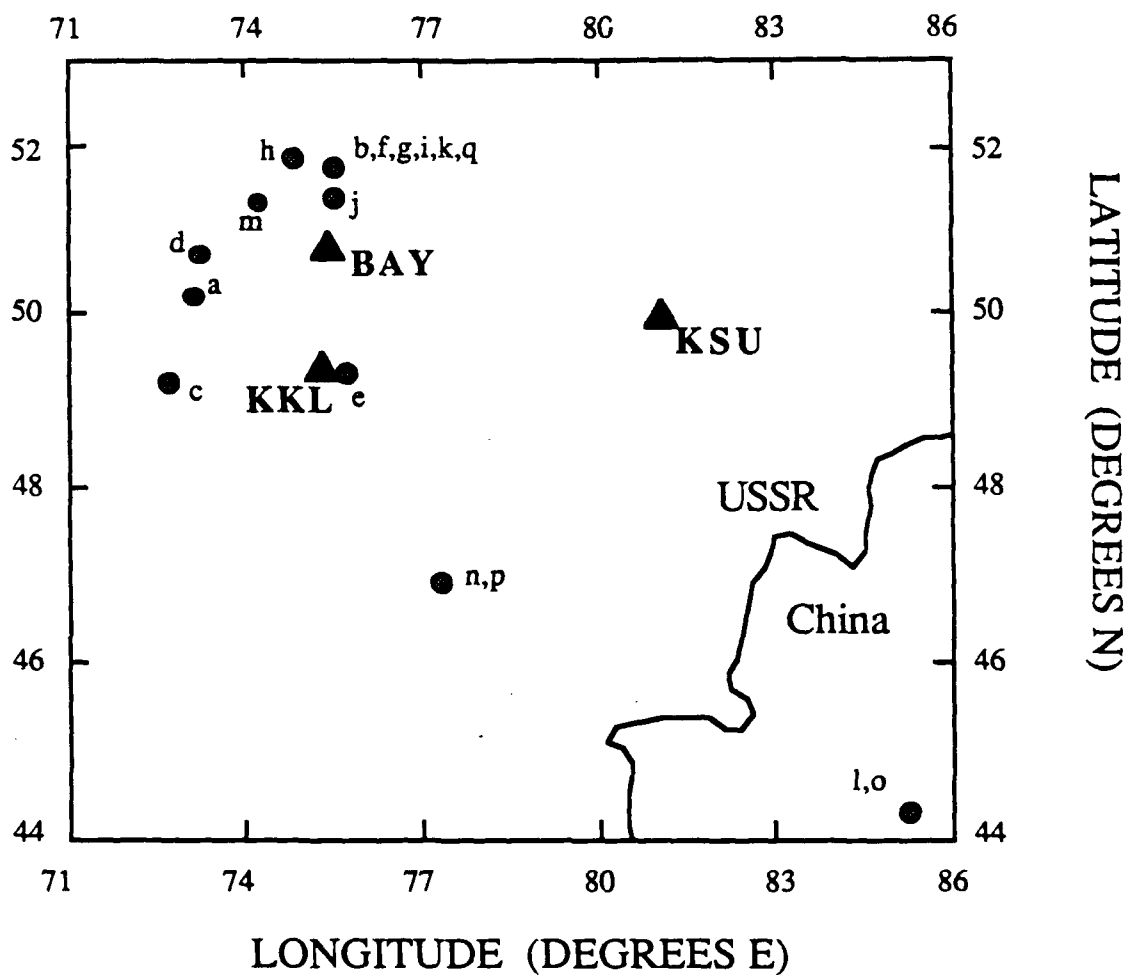


Figure 2. Map of two- and three-station locations for regional events in the time period May to September, 1987. See Table 4 for a list of the locations and their uncertainties.

51°52'N 75°17'E

51°48'N 75°44'E



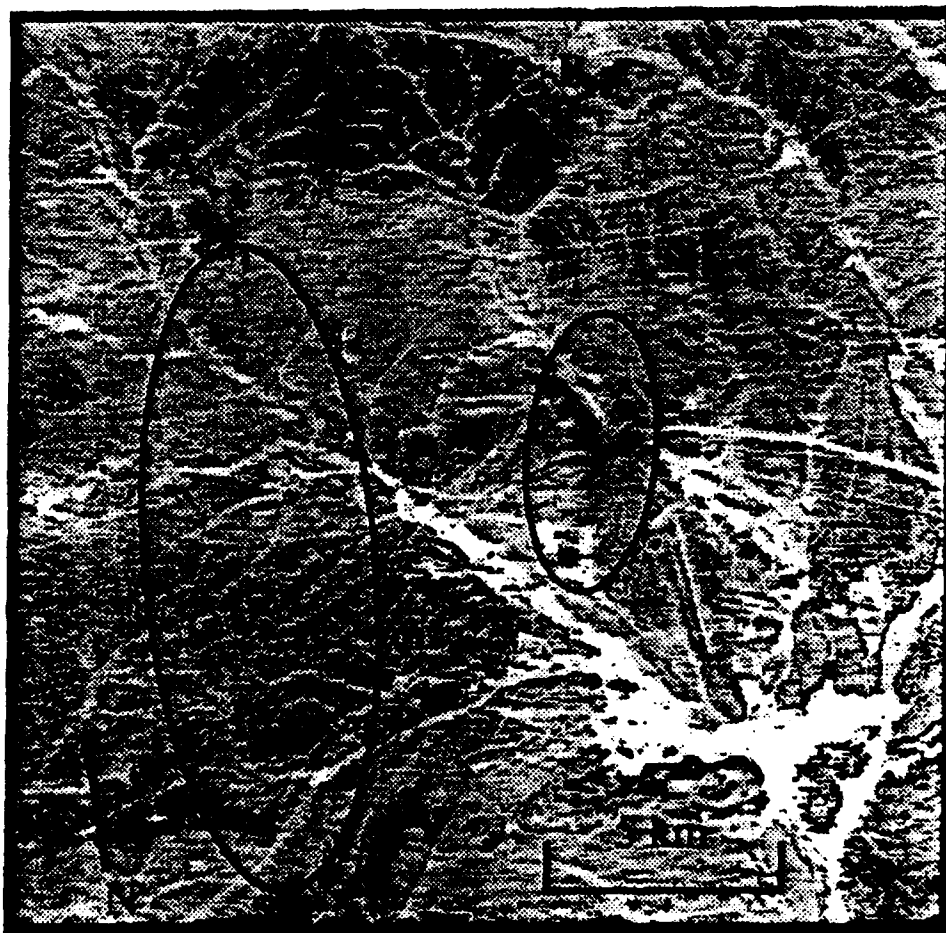
51°36'N 75°08'E

51°31'N 75°35'E

Figure 3. Reproduction of a 35 km square portion from a SPOT satellite image around the town of Ekibastuz (at left center) showing obvious mining activity. Seven individual mines in a partial ring around the town are marked A through G. The largest mine (A) is about 5 km across. Also indicated are the epicenters and 90% confidence ellipses for events b, f, g, i, k, and q. Base photo Copyright 1986, SPOT Image Corporation.

47° 03' N 77° 13' E

47° 00' N 77° 31' E



46° 50' N 77° 09' E

46° 47' N 77° 27' E

Figure 4. Reproduction of a 21 km square portion from a SPOT satellite image north of Lake Balkash. The Sayak air field is visible in the lower right. Two mine areas are marked A and B. Also indicated are the epicenters and 90% confidence ellipses for events n and p. Base photo Copyright 1986, SPOT Image Corporation.

NUCLEAR MONITORING RESEARCH AND DEVELOPMENT SYSTEM (NMRD)

by

Thomas C. Bache

Science Applications International Corporation
10260 Campus Point Drive
San Diego, California 92121

INTRODUCTION

The overall objective of the DARPA program in seismology is to develop new technology to improve U.S. capability to monitor underground nuclear explosion testing. The Center for Seismic Studies (the *Center*) is supported by DARPA to provide a testbed to develop, test, evaluate, and demonstrate new seismic monitoring technology. The first-generation system now operated at the *Center* includes a network of computers, a large database, database access and seismological processing software, data services (to assemble selected data sets), and communication services (providing external access to *Center* resources). The new NMRD system will replace this first-generation system and provide greatly expanded capabilities in each of these areas. It is being developed by SAIC and several subcontractors including Inference Corporation and Teledyne Geotech.

The major elements of the new NMRD system include the following:

- Near real-time acquisition of data from a large number of seismic stations (including many new stations specifically designed for the seismic monitoring problem).
- Automated processing systems that provide a realistic environment for testing and evaluating new monitoring techniques.
- A database management system for archiving the relevant seismic data.
- Software tools for convenient data retrieval
- Software tools that provide the data retrieval, data manipulation, automated processing, and interactive processing infrastructure needed to allow seismologists to focus on the evaluation of new techniques.
- A network of computers with ample capacity for seismic data processing tasks.
- A communications capability to provide access to *Center* resources by external users

The NMRD system includes five semi-independent subsystems (*WASHIDC*, *US/INDC*, *Integrated Processing*, *Database Management System*, and *R&D Testbed*). These are shown as the five major boxes inside the cross-hatched region in Figure 1. This figure also shows the primary data sources for each subsystem. In subsequent sections each of the NMRD subsystems is described briefly, and this is followed with an overview of the NMRD software and hardware architecture. Finally, the major elements of new (to seismic monitoring) technology incorporated into NMRD are highlighted, and the schedule for the development is summarized.

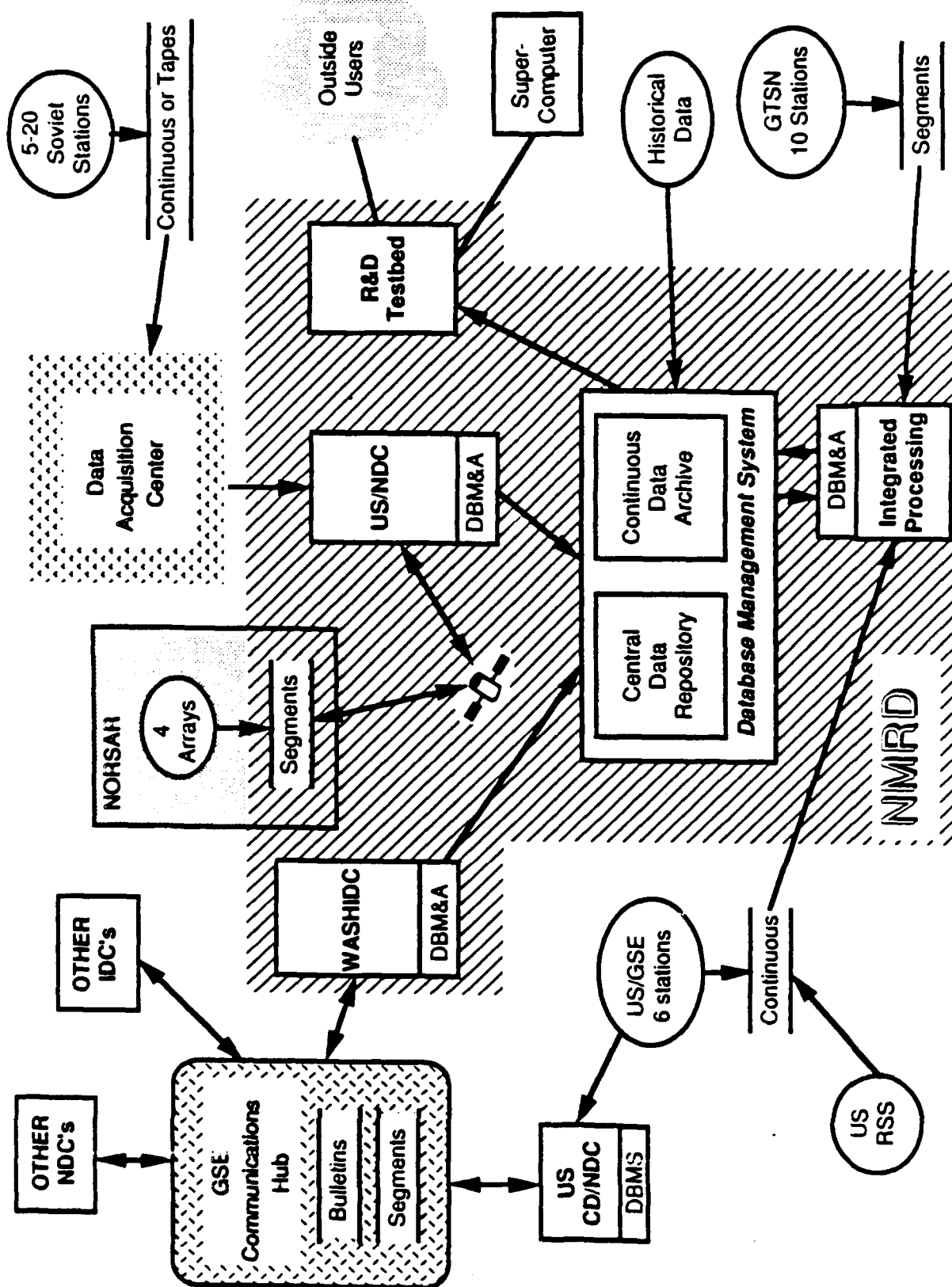


Figure 1. NMIRD subsystems and data sources

THE WASHINGTON INTERNATIONAL DATACENTER (*WASHIDC*)

The United Nations Conference on Disarmament Group of Scientific Experts (CD/GSE) is designing and developing a global system for exchanging seismic data and data analysis results to provide the information needed for participants to monitor compliance with nuclear test limitation agreements. The system includes National Data Centers (NDC's) which analyze data from national stations according to standard procedures. The analysis includes signal detection and measurement of specified characteristics (parameters) of the detected signals. The NDC's forward waveform "Segments" (containing the detected signals) and parameters characterizing the signals to the "GSE Communications Hub" from where they can be obtained by the other participants in the CD/GSE system. †

The central elements of the CD/GSE system are the four International Data Centers (IDC's) which analyze the data from the NDC's to associate signals with events, locate the events, and produce a coordinated seismic "Bulletin" which lists the located events and the data used to locate them. The IDC's are located in Washington (*WASHIDC*), Stockholm, Moscow, and Canberra. The IDC "Bulletins" are exchanged via the "GSE Communications Hub." The *WASHIDC* will be developed by NMRD using advanced technologies to comply with the processing requirements developed by the CD/GSE.

U.S. NATIONAL DATA CENTER (*US/NDC*)

This subsystem analyzes the data from a network of stations in northern Europe and the Soviet Union to detect, locate, and identify seismic events. The data are obtained from three seismic arrays in Scandinavia, a seismic array in Germany, and 5-20 seismic stations in the Soviet Union. The arrays are designed for detection of small regional events, but they also have excellent capability for detecting distant events. The Soviet Union stations are being installed under scientific exchange agreements, and they are designed to record three-component data up to high frequencies (40 Hz continuous and up to 250 Hz triggered).

Two of the arrays are now operational (NORESS and ARCESS), and the data are telemetered to NORSAR (near Oslo). The data from these two arrays is being analyzed by the *Intelligent Array System (IAS)* which is to be completed in the summer of 1989. The primary signal processing in *IAS* is done at NORSAR, where signals are detected and parameters describing them are computed automatically. NORSAR is linked via a wide-area network (WAN) bridge to the main elements of *IAS* at the *Center*. The *Center* elements of *IAS* automatically retrieve the parameters from NORSAR and analyze them to locate and identify seismic events. The system then automatically retrieves the event waveform data from NORSAR and stages them for subsequent human review.

The *US/NDC* is a major extension and enhancement of the *IAS* to analyze the data from the much larger and more diverse network indicated in Figure 1. The signal processing of the array data will remain at NORSAR. The plan is not yet final for transmission of data from the Soviet stations, but our expectation is that there will be continuous transmission of some data via satellite telemetry and transfer of other data on magnetic tape (i.e., with a long time delay). All these data will be collected by a "Data Acquisition Center" at Scripps Institute of Oceanography in San Diego. The *US/NDC* will acquire these data from the "Data Acquisition Center" and integrate it with the data from the four arrays to obtain a detailed interpretation of seismic events in northern Europe and the Soviet Union.

† In another DARPA-sponsored project six "US/GSE Stations" are being installed, and these will provide the U.S. contribution to the CD/GSE network via the "US CD/NDC" which analyzes the data to extract the "Segments." These data sources are also indicated in Figure 1.

INTEGRATED PROCESSING

This subsystem is similar to *US/NDC* in many ways, but it is designed for different data sources and operational requirements. As shown in Figure 1, the *Integrated Processing* subsystem has the capability to process telemetered continuous data from the six US/GSE stations. It can also process telemetered continuous data from the "Regional Seismic Stations (RSS)" being installed by DOE. The "Global Telemetered Seismic Network (GTSN)" stations are being installed in the southern hemisphere by the U.S. Geological Survey. These stations have automatic detectors that extract waveform segments and telemeter them to a data acquisition center from where they will be retrieved for further analysis in the NMRD system. Finally, the *Integrated Processing* subsystem has the capability to retrieve from the *Database Management System* data previously processed by the *WASHDC* and *US/NDC*. The previous solutions can then be refined by adding data from other stations in the "Integrated Processing" subsystem.

The *Integrated Processing* system should be viewed as a flexible R&D resource since it will have the capability for automatic analysis of any combination of these various data sources. This provides a powerful resource for testing and evaluating new concepts using appropriate input data.

DATABASE MANAGEMENT SYSTEM

Each of the data processing subsystems (*WASHDC*, *US/NDC*, *Integrated Processing*) has a local database management and archiving ("DBM&A") system adequate for a limited time period (typically a few weeks). The data then migrate to the NMRD *Database Management System* which manages and archives the data from all subsystems for the life of the system. This *Database Management System* has two major elements. The first is the "Continuous Data Archive" which stores all input data in unprocessed form (e.g., continuous waveform data). Since requests for these data should be rare, they will be stored on 8mm cartridge tapes.

The more important "Central Data Repository" manages the processed data, which include all seismic "Bulletins," the data (including the waveform segments) contributing to each event solution, and explanations of the reasoning leading to each solution. The "Central Data Repository" will provide the capability to retrieve with little delay (seconds to a few minutes) all parameter data from the previous several years and the waveform segments from approximately the past year. Older data will be migrated into a very large (essentially unbounded for this application) storage system which will allow retrieval of even large volumes of data with a delay of at most a few hours.

A large volume of "Historical Data" is archived on magnetic tape at the *Center*. Storage and retrieval of data from this archive now requires extensive effort by *Center* staff, and requests often require weeks to fill. In NMRD the plan is to install the important "Historical Data" in the new *Database Management System* so they can be retrieved by the user (rather than a specialist on the *Center* staff).

The database management problem in NMRD is one of the most complex to be addressed anywhere. The current version of the relational database organization in *IAS* has more than 250 attributes in more than 50 tables. The number of attributes and tables will greatly increase (perhaps even double) for NMRD. The volume of data to be stored in the "Central Data Repository" is expected to be generated at a rate of 30-100 Gigabytes per year at full operation. There is a strong requirement for interactive retrieval of data for selected events, which means that the waveforms and relevant event data should appear on a screen (with a map) within a few seconds.

R&D TESTBED

The *WASHIDC* and *US/NDC* subsystems process specified input data according to relatively rigorous operational procedures, while the *Integrated Processing* system is designed to process data from a variety of network configurations using flexible operational procedures. The software architecture of these systems anticipates enhancement with new techniques and knowledge, but the effort required should not be undertaken until the proposed enhancements have been evaluated thoroughly elsewhere. To meet this need and support other important R&D activities, the NMRD system includes an *R&D Testbed* subsystem designed to support:

- Exploratory R&D
- Preliminary testing and evaluation of new concepts using small specialized datasets
- Access to the NMRD system by "outside" users (remote or resident at the *Center*)
- Database browsing and retrieval
- A software infrastructure and analysis tools to reduce substantially the effort required to test new techniques on suitable datasets
- Computer capabilities adequate to support the R&D requirements of authorized *Center* users, including access to the San Diego Supercomputer Center (SDSC)

The emphasis in the *R&D Testbed* subsystem development is on easy-to-learn, easy-to-use software for research applications. Many software modules needed to acquire, process, manipulate, and display seismic data are available in the other subsystems, but a more friendly man-machine interface is needed to support the occasional user. New software tools being added include a natural language interface to select and retrieve data with english language queries. The *R&D Testbed* will also include hypermedia tools for reviewing documentation and organizing information.

NMRD SOFTWARE ARCHITECTURE

The basic architecture of the *WASHIDC*, *US/NDC*, and *Integrated Processing* subsystems is shown in Figure 2. The major software modules include:

- *Data Acquisition*
NMRD has a variety of data sources, and different software is needed to acquire the data from each. In general, incoming data are spooled in batches into a "first in, first out" buffer. The "expert system" starts a process to retrieve needed data from this buffer.
- *Signal Processing*
This module processes the data to detect signals and extract characteristic features. For array data the features include slowness and azimuth from f-k power, f-k quality, slowness and azimuth error bounds (based on S/N, f-k quality, and f-k resolution), amplitude, dominant frequency, polarization (using 3-component elements), and spectrum (including an estimate for the noise spectrum). For non-array data the design is the same, but fewer features can be extracted and the error bounds are generally larger.
- *Event Location*
Signals are identified by phase type and associated with events by a rule-based expert system. This expert system starts with the detected signals and their features and uses the rules to group the phases by event and phase type. These event-associated phases are

† The *IAS* system described under *US/NDC* above has the same architecture (at this level of abstraction), so working versions of each module in Figure 2 now exist as part of *IAS*.

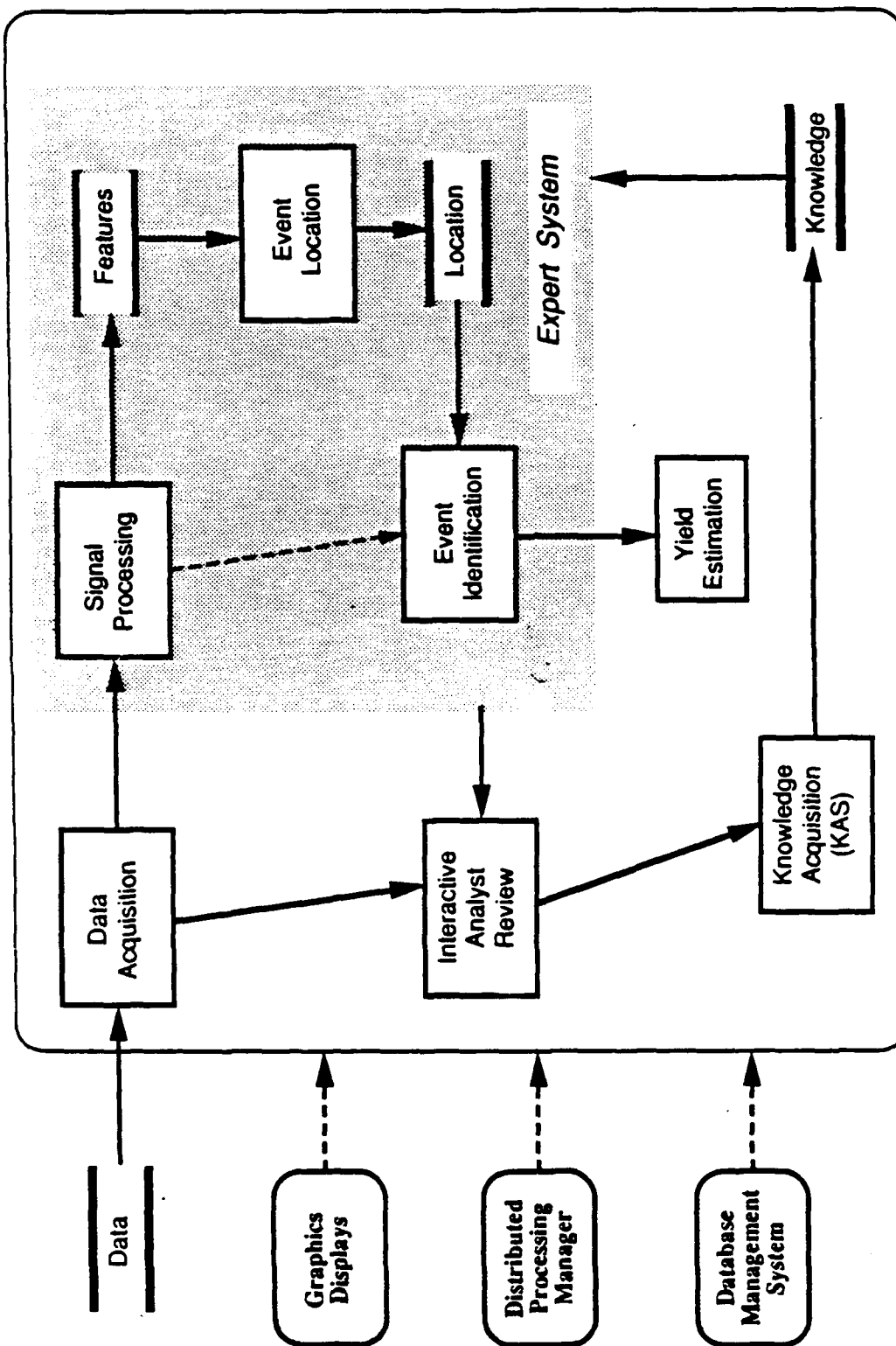


Figure 2. Software architecture for NMRD data analysis subsystems

input to a conventional location program to obtain an initial estimate of the location. This process can be viewed as a knowledge-rich implementation of "automatic association." In IAS a rule-based expert system for initial location was programmed in Flavors and Lisp by Advanced Decision Systems. In NMRD the automatic association and location problem involves data from much larger networks and analysis of all (local, regional, and teleseismic) events. This module is being developed by SAIC and Inference Corporation using ART, an expert system building tool from Inference Corporation.

The initial location hypothesis is based on seismic travel times, and it can be improved substantially by using knowledge obtained from past events in the vicinity. The IAS performs this function with a "script-match" process, where scripts are statistical representations for the pattern of detections for past events.[†] This can be viewed as a knowledge-rich implementation of "master-event" location techniques. In NMRD similar concepts are being programmed within the ART framework.

- *Event Identification*

Many events can be identified immediately from their location, and this is done with a rule-based expert system. Also, some events can be identified by their similarity to past events at the same location (e.g., repeated mine blasts), and this is implemented as a rule-based analysis of the script-match results described above. For other events additional signal processing is done to extract features needed for identification (e.g., spectral ratios, analysis of the cepstrum, magnitude ratios, etc.), and rule-based reasoning is applied to interpret these features.

- *Yield Estimation*

Estimation of the yield is important for identified nuclear explosions. Since these events are relatively rare, extensive automation of the knowledge-based reasoning involved is not so important, and this process is shown outside the "Expert System." The "yield estimation" module is being developed by S-Cubed.

- *Interactive Analyst Review*

A powerful interactive seismic analysis workstation is a key part of the system. The analyst is needed for two reasons. First, he can provide quality-control of the bulletin produced. Second, analyst review and validation of the automatic solutions is an important part of the "knowledge acquisition" process described below. Therefore, an interactive seismic analysis workstation is being developed to allow an analyst to review and correct the solutions. The tools provided include a flexible, interactive mapping capability, and the waveform display, manipulation, and measurement tools needed to change, add, delete, and reassociate detections and relocate and identify events.

- *Knowledge Acquisition (KAS)*

The "knowledge acquisition" concept for NMRD is shown in Figure 3. An unconventional (compared to most expert systems) aspect central to this concept is that the "Expert System" caches an "audit trail" in the relational database. This audit trail represents the reasoning process leading to the solution. "Explanation" of each solution is provided as part of the seismic analysis workstation, and this explanation is obtained from the audit trail records. The "Performance Validation" module is itself an expert system. When the analyst changes a solution, this module uses the audit trail to determine which element of the knowledge base has been "invalidated" and marks it accordingly in the database. The "Performance Analysis" module is used after much data

[†] This portion of the IAS system is being developed by Ensco and ISX.

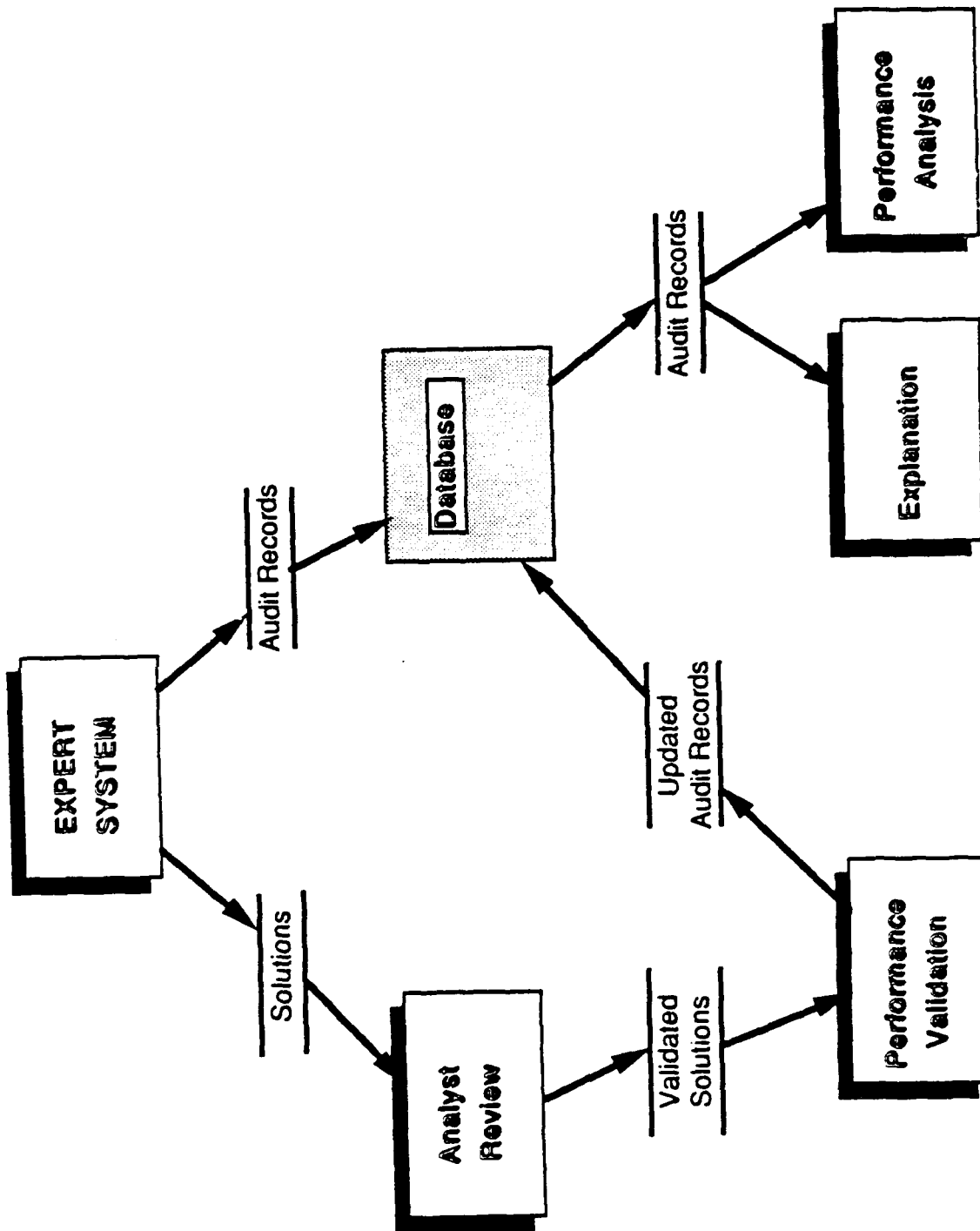


Figure 3. The knowledge acquisition concept for the NMRD data analysis subsystems

has been processed to compile and display statistics about the performance of the knowledge base to focus attention on weak elements. Since all relevant information is cached in the same relational database, it is straightforward to find the event solutions which depend on selected elements of the knowledge base, display them on a map, compare waveforms, etc. Other seismological tools needed to develop additions to the knowledge base (e.g., tools for analyzing travel-time data, etc.) are also integrated into the KAS.

- *Graphics Displays*

The NMRD hardware architecture is based on Sun workstations, and bit-mapped displays are ubiquitous. These displays show maps, satellite photographs, waveforms, and process monitoring and administration information. Nearly all graphical actions are being implemented with object-oriented families of widgets in X Windows. This choice has great advantages for producing transportable, reusable and maintainable graphics code. At this stage of implementation of the X Windows standard, code development is tedious and complex figures are slow to draw. The popularity of X Windows makes it nearly certain that these problems are temporary.

- *Distributed Processing Manager*

Each major subsystem of NMRD has a distributed processing design modeled on the IAS experience. Unix provides inter-process communication primitives (i.e., sockets), but software is needed to monitor the communication, detect faults, recover from failures, rehost crucial processes, etc. For the multiple LAN NMRD system a "Distributed Operating System" or D-OS is being implemented as a software layer built on ISIS (a system developed at Cornell University to provide robust inter-process communication capabilities in Unix). This D-OS provides process management, monitoring, and fault tolerance capabilities for the overall system.

- *Database Management System*

The only practical way to address the imposing complexity of the NMRD database management problem is with a commercial relational database management system (RDBMS). Oracle has been chosen. All parameter data are stored in tables in the RDBMS, and the data objects incompatible with this structure (most prominently, the time series data) are stored as Unix files with pointers to these files stored in the RDBMS. Embedded SQL queries are used to access data from application programs. For example, the signal processing module stores its results in the RDBMS and sends a message to the expert system informing it that new data are available for analysis. Subsequent processes then retrieve data from the RDBMS, store their results, send messages to other processes that are to use the new data, etc.

The response time to SQL queries is very sensitive to the organization of the database and detailed query structure. Experience has demonstrated that the desired performance goals (retrieval times of seconds) can be met for queries that are anticipated in the design even when the database is huge (millions of records in some tables). Naive queries to retrieve essentially the same information can take days. Therefore, software tools that provide menu or other structured capabilities to search the database are very important for occasional users.

NMRD HARDWARE ARCHITECTURE

The basic building block for the NMRD hardware architecture is a Local-Area Network consisting of 5-8 workstations. The IAS LAN at the Center is shown in Figure 4 as an example of the design concept. The Megatek is basically a Sun 4/260 with a Megatek graphics

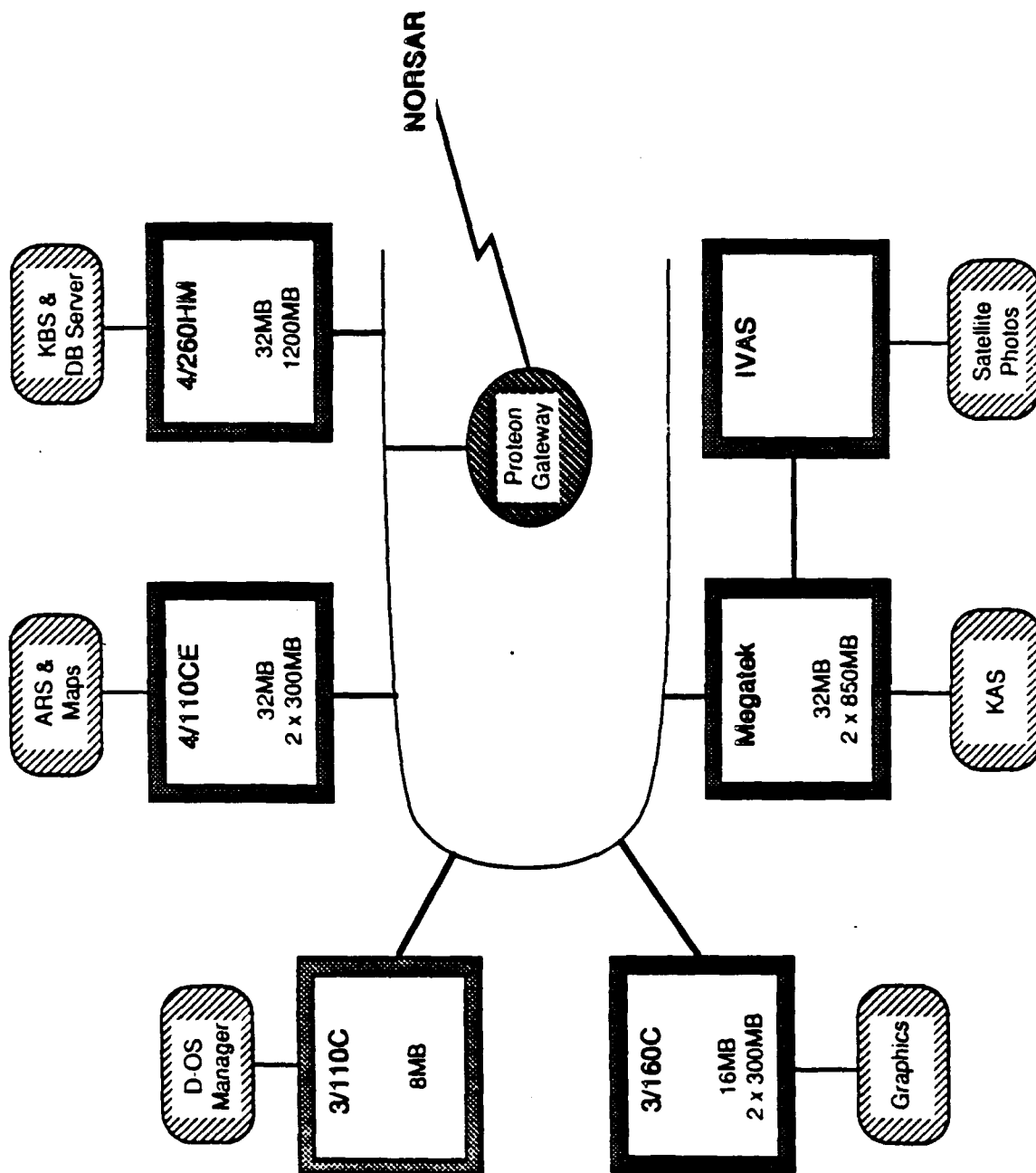


Figure 4. The hardware architecture for IAS modules generated at the Center

accelerator board added. The IVAS is special purpose hardware (from International Imaging Systems) for displaying satellite photographs and digital maps.

The tentative design for NMRD is shown in Figure 5. An allocation of functions consistent with this architecture is also indicated (FS = file server, SigPro = signal processing, KBS = expert system for location and identification, ARS = interactive analyst review workstation, KAS = knowledge acquisition workstation, DBA = database administrator). This function assignment is for illustration, since the system administrators are expected to move the various processes around the network depending on the workload and priorities.

The final NMRD system will be different in detail from the design in Figure 5 because new machines will be preferable by the time some of the workstations are purchased. For example, the selection of the Sequent S81 for the main database server is tentative, and the appropriate choice for this element is still being evaluated.

Not shown in the figure are the NMRD computers in Norway. These consist of one Sun 4/260 per array. These computers host the SigPro process for beamforming, detection, and feature extraction, the RDBMS, and the software for communicating with the *US/NDC* at the *Center*.

NMRD AND ADVANCED TECHNOLOGY

The automation of seismic data analysis to obtain results comparable to those obtained by human analysts is a long-sought goal in earthquake and explosion seismology. An even more venerable goal in this data-rich empirical science is a capability to retrieve quickly and conveniently the seismic data bearing on a particular question. In the NMRD system many advanced technologies are being brought together to make major advances toward these two important long-term goals in seismology.

We have described the NMRD system in terms of its main functions. But it is also useful to describe it in terms of the new technology that is being used to perform these functions. The major elements include:

- *Signal Processing*

Automated signal processing is by now routine in many applications. However, NMRD represents a significant advance in the scale and variety of the automated processing and in the way the processing is dynamically reconfigured (under control of the expert system) depending on the character of the data.

- *Embedded Expert Systems*

Expert systems are certainly new to the seismic data analysis problem. Further, the NMRD expert systems are embedded in a large and complex system with many cooperating elements, and this use of expert system technology remains rare.

- *Semi-Automated Knowledge Acquisition*

"Explanation" and "Knowledge Acquisition" capabilities are important for all expert systems. The concept sketched above (i.e., Figure 3) is unusual in many ways, but especially in the central role of a relational database for storing the history of the reasoning process.

- *Database Management*

As described earlier, the NMRD DBMS problem is one of the most complex to be addressed anywhere. The major complexity is the large volumes of data including both tables (flat files) and user-defined objects (e.g., time series) coupled with the requirement for rapid response to automatic and interactive queries. Also, some of the features being used (especially dynamic embedded SQL queries) have only recently been added to commercial RDBMS products.

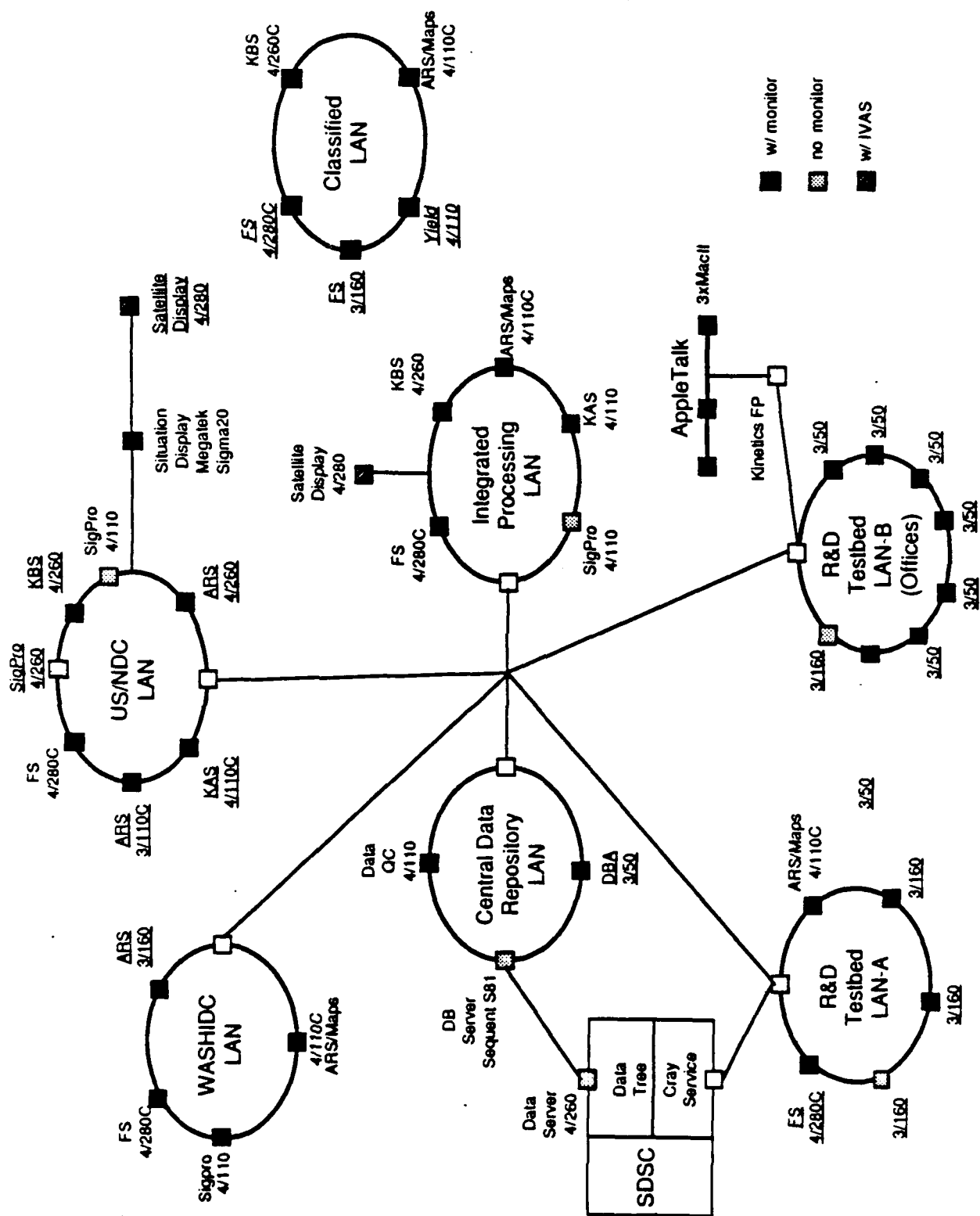


Figure 5. The NMRD hardware design

- *Distributed Processing*

The distributed processing architecture chosen for NMRD has many potential advantages in its flexibility and fault tolerance. However, the software for fully exploiting this potential does not yet exist in Unix. A "Distributed Operating System" is being developed to provide the capabilities needed for NMRD, but most of this "D-OS" should have much wider application.

- *Man-Machine Interface*

The NMRD system includes a variety of interactive processes for retrieving and analyzing seismic data, and a consistent and easy-to-use man-machine interface is important for these applications. For this purpose MMI standards are being imposed based on the Macintosh paradigm (select-then-choose). A natural-language interface to the database is also used extensively, and a new class of tools using hypermedia is being developed.

- *Software Engineering*

Flexibility, portability, and maintainability are emphasized in the NMRD software architecture. That is, when choices must be made, designs that ease future enhancement and expansion are preferred over designs that optimize current software productivity and system performance. Compliance with open architecture standards is central to this approach. NMRD is being developed with Unix, ISIS (for the distributed processing support), X Windows (for graphics), ANSI-standard SQL and Oracle (for database access), and Sun workstations. Software is being developed according to written NMRD coding, design, and documentation standards that express our interpretation of the "Rapid Prototyping" method of software development.[†]

DEVELOPMENT SCHEDULE

The NMRD project began in December, 1989, and the planned duration is 30 months. All systems are to be delivered to the *Center* after 22 months, with the final 8 months of the contract being devoted to testing, training, and knowledge acquisition (to enhance the performance of the expert systems). In the first year of the project the emphasis is on *WASHIDC* and *US/NDC*. The *IAS* is being incorporated into the larger *US/NDC*, with the initial capability to handle additional arrays and Soviet stations planned for October, 1989. The key milestone for *WASHIDC* is a major CD/GSE data exchange experiment scheduled to begin in January, 1990. Warmup tests of elements of *WASHIDC* to prepare for this experiment are scheduled to begin in the summer of 1989. These two subsystems provide most of the software needed to develop the *Integrated Processing* subsystem, and the plans are to develop it as a distinct system during 1990 when the new data sources come on line. The *Database Management System* will grow to provide the capabilities needed by the other subsystems, with the full capability scheduled to be available in the Fall of 1990.

Center users will begin to see significant new *R&D Testbed* capabilities in the summer of 1989 as data processed by *IAS* becomes available with the software tools to retrieve and review it. These tools and the data available will increase steadily over the course of the NMRD project. Emphasis during the first half of the project is on developing the functionality, and in the second half the emphasis shifts to streamlining the performance and ease of use.

[†] *Software Policies and Procedures* (Revision 2.3), SAIC-88/1596, March, 1988.

A Geophysical Data Base for NTS:
A New Interpretation for the Shallow Structure
of Silent Canyon Caldera, Pahute Mesa, Nevada

J. F. Ferguson, A. H. Cogbill*, R. G. Warren*

and H. D. Axilrod

The University of Texas at Dallas
Center for Lithospheric Studies
P. O. Box 688
Richardson, TX 75080

* Los Alamos National Laboratory
Earth and Space Sciences Division
MS F659
Los Alamos, NM 87545

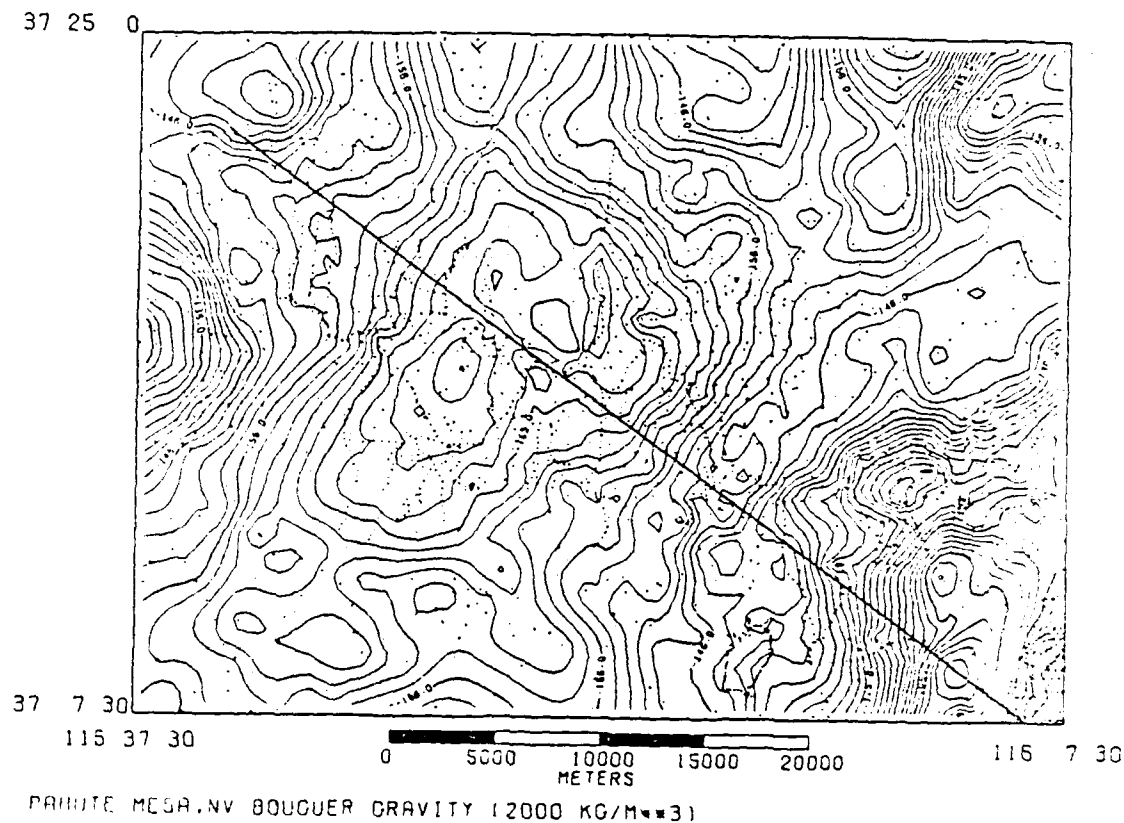
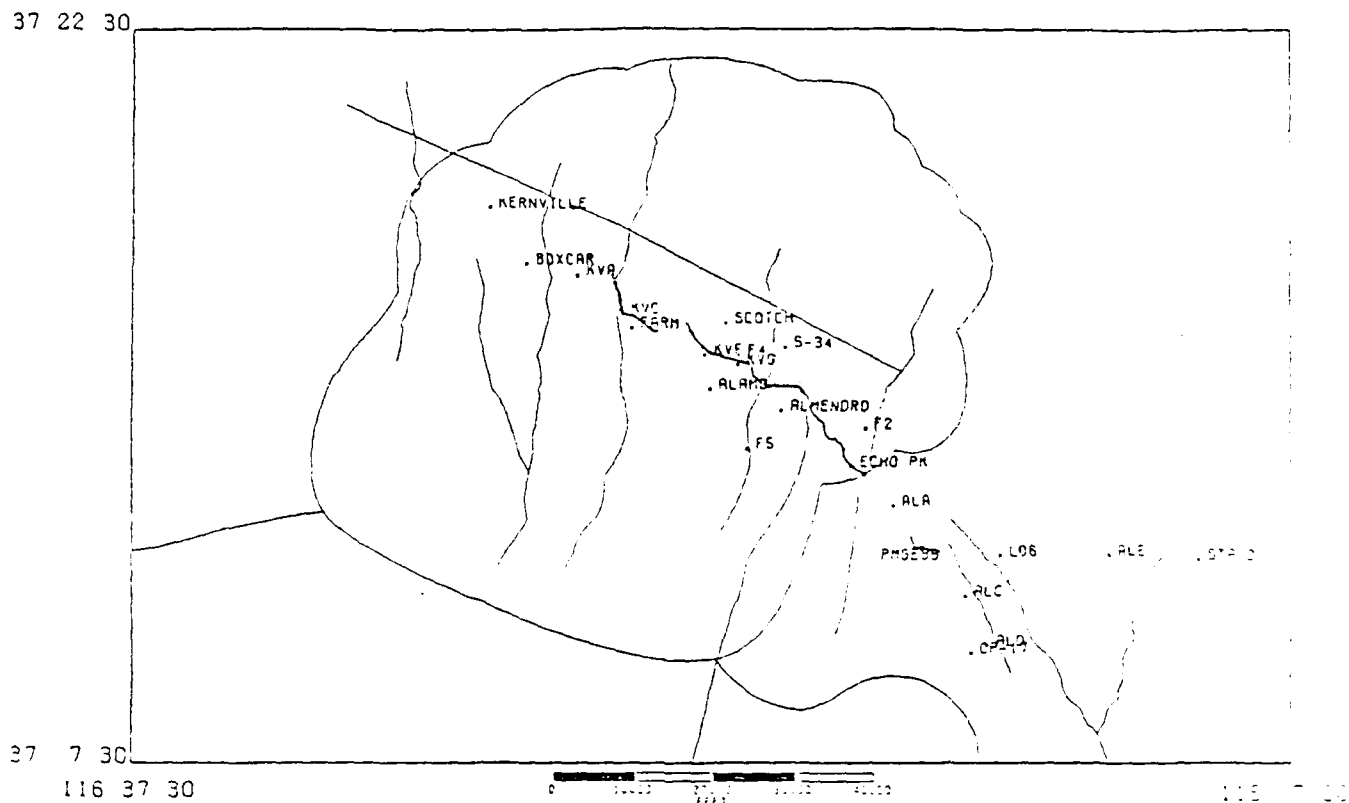


Figure 1. The Bouguer Gravity Map for the Pahute Mesa Area. This map shows the generally elliptical low associated with the Silent Canyon Caldera. The prominent anomaly due to the Black Mountain volcanic center is visible on the west. The gravity high in the southeast corner of the map is associated with outcrop of Paleozoic sediments, which along with Mesozoic intrusive rocks, form the basement under the volcanics from the Silent Canyon, Timber Mountain, Black Mountain and other regional centers. The heavy black line shows the location of a transect through the caldera which has been modeled using gravity, seismic traveltimes and borehole data.



PAHUTE MESA, NV SEISMIC STATIONS AND SHOT LOCATIONS

Figure 2. The Location of Seismic Shot Points and Stations at Pahute Mesa.

Six nuclear tests, Kernville, Boxcar, Farm, Scotch, Alamo and Almendro have been instrumented and recorded at sparse stations. Traveltimes for these events have been gathered from various sources. In 1986 UTD and Los Alamos National Laboratory ran a seismic experiment (PMSE86) with a shot point in Big Burn Valley, southeast of Pahute Mesa. These conventional explosive shots were recorded on a dense array from 3.5 to 15 km from the shot point on Pahute Mesa. These traveltimes provide reversed coverage of the critical structure on the margin of the Silent Canyon Caldera.

Figure 3. A Geologic Profile of the Pahute Mesa Transect. Shallow volcanic units have been correlated on the bases of occurrence in boreholes and outcrop. New stratigraphic relationships based on geochemical analysis have been used in this process. The youngest units from the Black and Timber Mountain volcanic centers tend to obscure all older units at Pahute Mesa. A geophysically important unit is shown with the heavy stippled pattern, the peralkaline rocks associated with the Silent Canyon caldera collapse and formation. Generally lower density and velocity units fill in the hole created by the caldera. It is also apparent that the caldera lacks the symmetry normally associated with such structures. The major NNE trending faults of basin and range type have been responsible for creating a asymmetrical graben with the greatest structural relief on the east side. About 2 km of post-Silent Canyon relief is found.

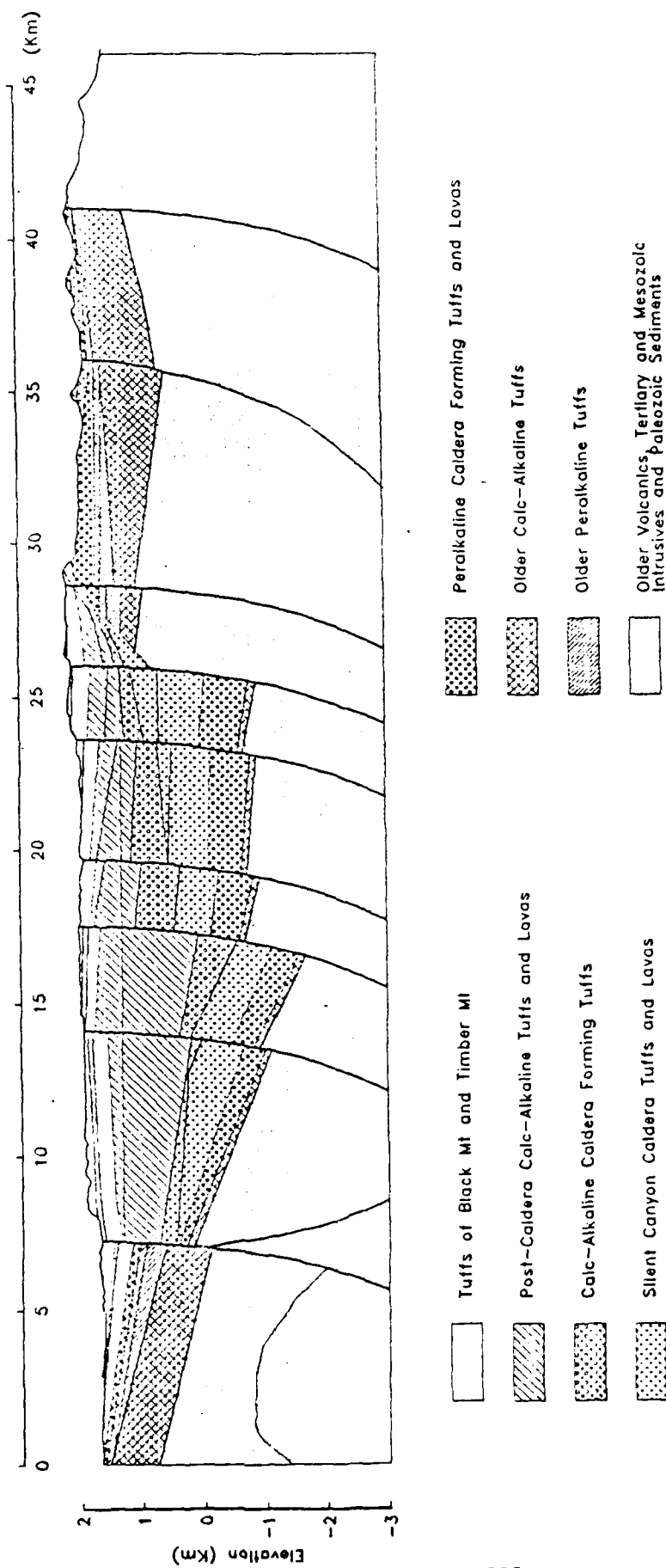


Figure 3. A Geologic Profile of the Pahute Mesa Transect.

Figure 4. A Gravity Model for the Pahute Mesa Transect.

This forward gravity calculation is based on the known shallow geologic structure and density functions determined from borehole gravity and as inferred from other physical properties. With a suitable regional trend included, the the average fit is better than 1 mGal between the observed and theoretical anomalies. An arbitrary 95 mGal has been added to the observed gravity from a 2 km wide corridor in this figure.

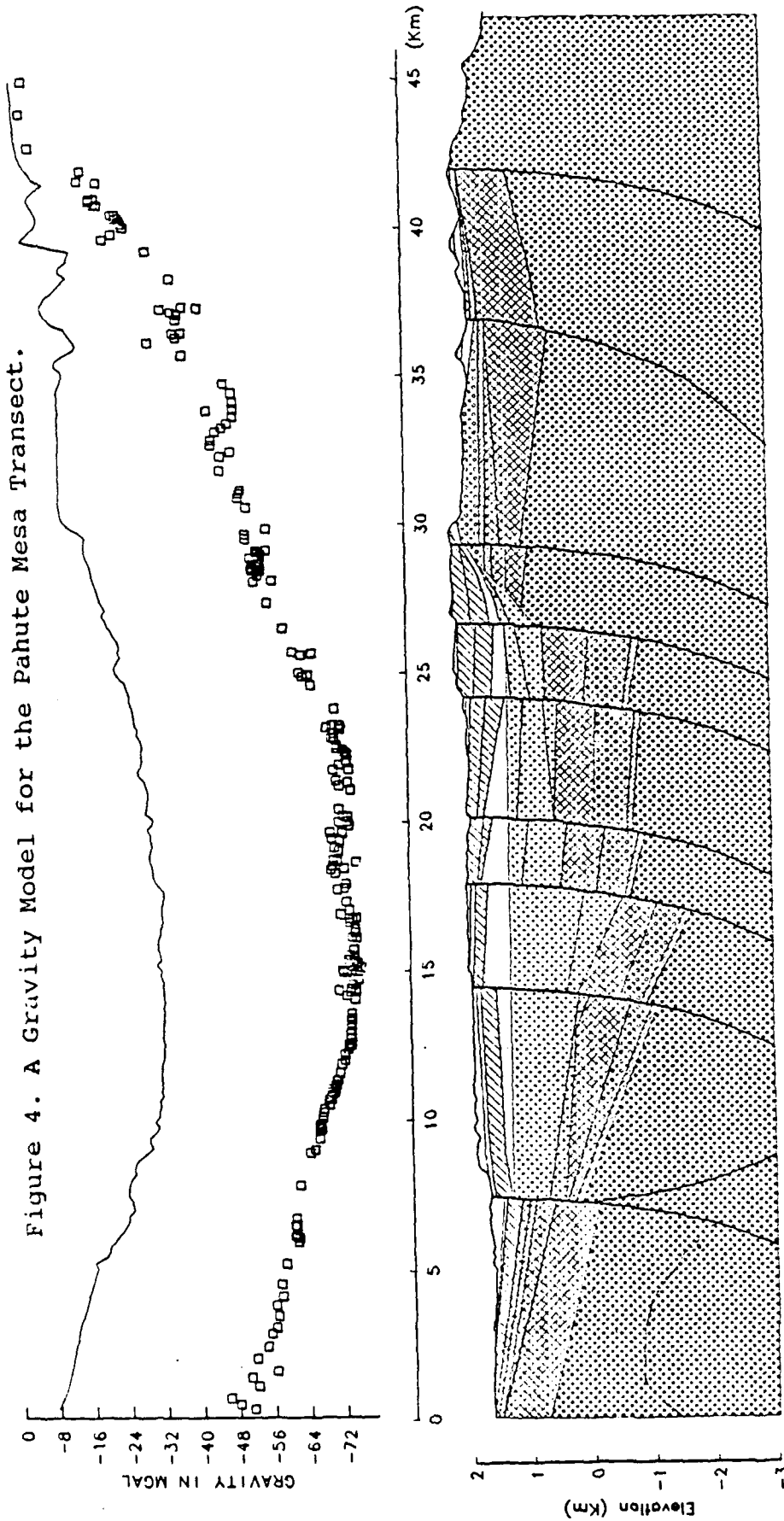
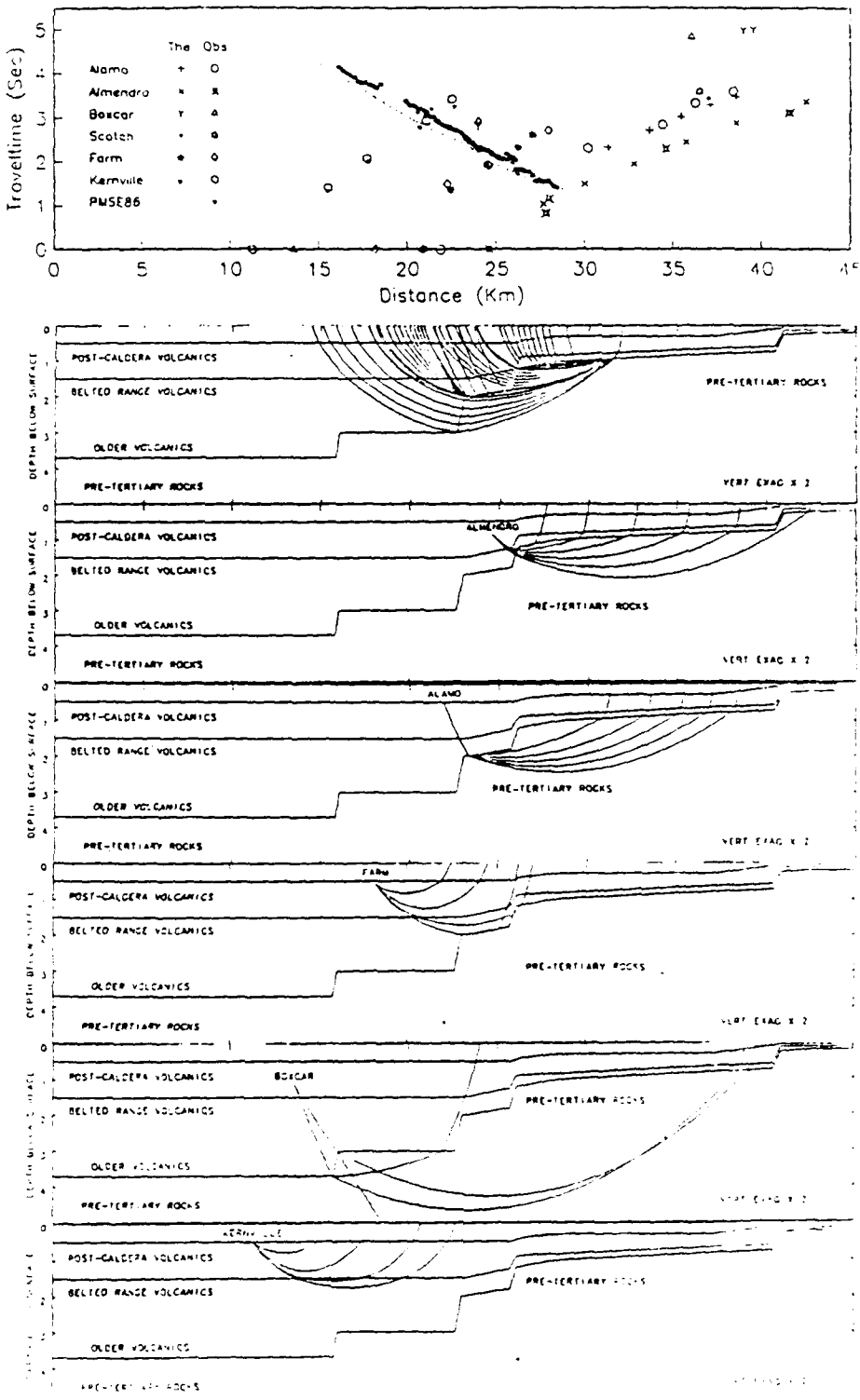


Figure 5. A Seismic Velocity Model of the Pahute Mesa Transect.

A relatively simple seismic model has been constructed to fit observed travel times of P and S-waves for the shots and stations illustrated in Figure 2. A composite of the P-wave travel time data is shown in this figure. Shot location is denoted by the observed data symbol plotted on the distance axis at traveltime 0.0. Selected ray paths for six of the seven shot points are shown below. The traveltimes for these raypaths are also plotted. The fit is generally to within about 0.1 s. The S-wave traveltime results are of similar quality. Within the caldera, on the northwest end of the profile, the velocity structure agrees well with the one dimensional model of Leonard and Johnson (1987). The contact between volcanics and basement (either Paleozoic sediment or Mesozoic intrusives) is inferred to be at about 3.5 km beneath Pahute Mesa. The total structural relief is thus at least 3.5 km between the basement high to the southeast and Pahute Mesa. The important faulted structure on the caldera margin is well covered by raypaths with this data.

Figure 5. A Seismic Velocity Model of the Pahute Mesa Transect.



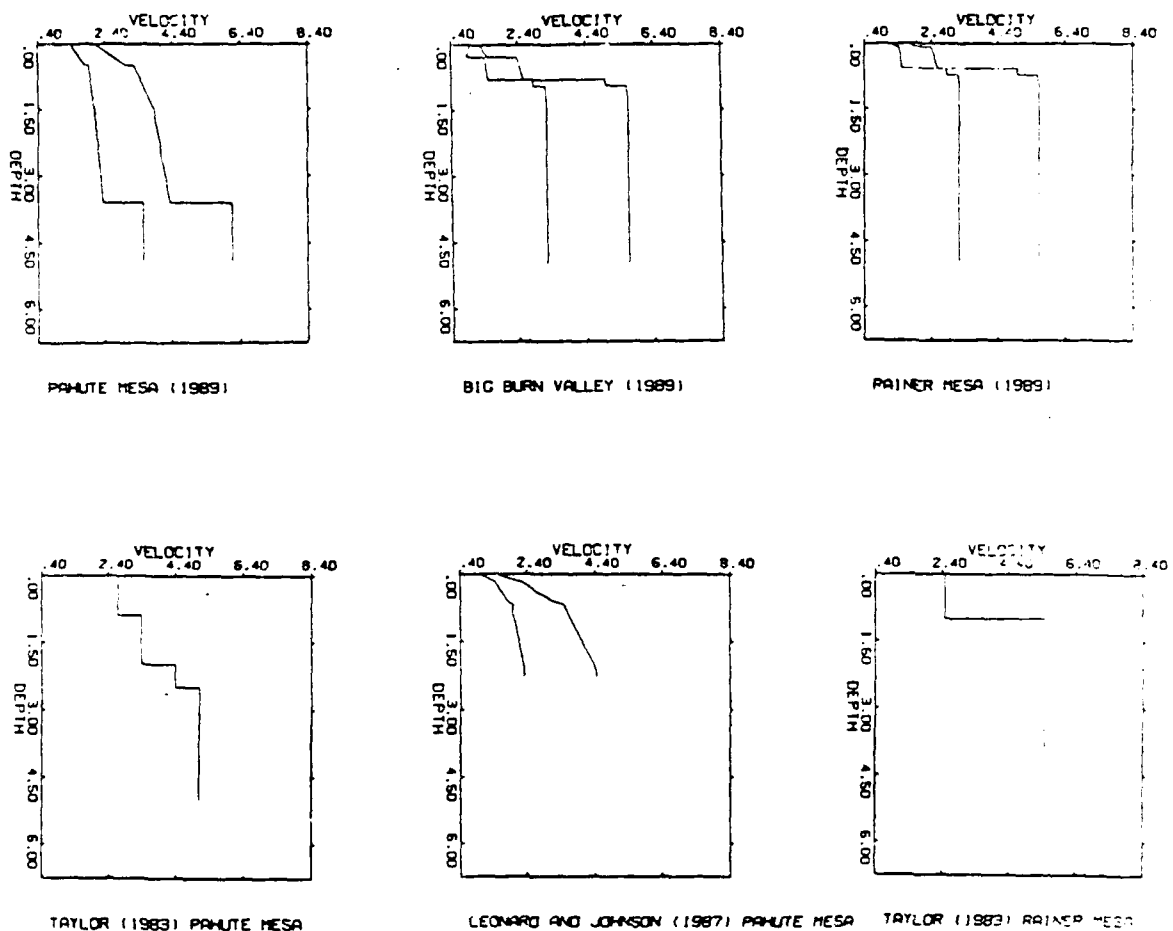


Figure 6. Velocity Profiles on the Pahute Mesa Transect.

Three stations were selected at 15, 32 and 39 km to illustrate the velocity function contained in the model. These profiles may be compared to the one dimensional model of Leonard and Johnson (1987), which was derived by inversion of traveltimes from explosions and stations within the Silent Canyon caldera area. They are also comparable to profiles from the tomographic regional and teleseismic traveltimes inversion of Taylor (1983). The total thickness of volcanics is best constrained by the two dimensional model presented here.